CHARACTERIZATION AND OPTIMIZATION OF SATURATION TRANSFER NMR WITH EXCHANGING XENON IN DIFFERENT HOST–GUEST SYSTEMS

Im
Fachbereich Physik
der
Freien Universität Berlin
eingereichte

DISSERTATION

zur Erlangung des Grades eines
Doctor rerum naturalium (Dr. rer. nat.)

vorgelegt von

Diplom-Physiker Martin Kunth

Januar 2016
Berlin

Martin Kunth: *Characterization and Optimization of Saturation Transfer NMR with Exchanging Xenon in Different Host-Guest Systems,* Dissertation, January 7th, 2016

GUTACHTER:

1. GUTACHTER: Dr. rer. nat. Leif Schröder (Betreuer)
Leibniz-Institut für Molekulare Pharmakologie (FMP), Berlin
2. GUTACHTER: Prof. Dr. rer. nat. Joachim Heberle
Freie Universität Berlin
3. GUTACHTER: Prof. Dr. rer. nat. Gerd Buntkowsky
Technische Universität Darmstadt

Thesis defense: October 20th, 2016

ELECTRONIC MAIL: kunth@fmp-berlin.de

meiner Familie

Die vorliegende Arbeit wurde in der Arbeitsgruppe von Dr. Leif Schröder am Leibniz-Institut für Molekulare Pharmakologie (FMP) in Berlin durchgeführt.

ABSTRACT

Molecular imaging modalities that aim for early detection of small biochemical changes in combination with spatial information would revolutionize our currently existing medical diagnostic and treatment system, as it could focus on the conservation of the state of health and not on its recovery. Such molecular imaging concepts are based on the noninvasive detection of labeled cells by sensitive methods such as positron emission tomography, single-photon emission computed tomography, X-ray computed tomography, or magnetic resonance imaging (MRI). Of these, only MRI is based on non-ionizing radiation. However, the low sensitivity of MRI for conventional, relaxation-based contrast agents limits its application for molecular imaging purposes in which sensitivity down to nanomolar concentrations of a contrast agent is required.

A *ca.* 10^5-fold gain in sensitivity for MRI is achieved when detecting spin-hyperpolarized xenon and its reversible binding to xenon-host molecules using the method of hyperpolarized xenon detection through chemical exchange saturation transfer (Hyper-CEST). This sensitivity gain is achieved by the combination of the two processes of a) LASER-induced spin-exchange optical pumping and b) the indirect CEST detection method. The latter depletes the spin hyperpolarization of the biological compatible noble gas xenon when it is temporarily bound to a host structure using a selective RF saturation pulse. Continuous xenon exchange transfers this depleted signal to that of free and unbound xenon as a measurable signal change. However, initial Hyper-CEST MRI implementations were experimentally time-consuming. Furthermore, different Hyper-CEST sensitivities have been reported empirically when switching the xenon host molecule. Moreover, as the Hyper-CEST technique relies on RF saturation pulses, the pulse strengths and durations become new degrees of freedom to generate signal contrast. Overall, the mechanism of the Hyper-CEST technique is quantitatively unknown.

This thesis presents approaches for quantitative xenon-host system exchange characterization and optimization with saturation transfer. By using single-shot MR imaging techniques that encode the required information within one working step, the first time-resolved xenon-host diffusion studies could be demonstrated. With this significant MR imaging speed improvement, the spectral dimension of the Hyper-CEST technique was studied to characterize xenon-host systems. A novel quantification method could be established that determines for the first time the xenon-host exchange kinetics at high sensitivity. This enabled for the first time the determination of optimal saturation pulse parameters. These results were obtained using the most prominent xenon host for biosensing, cryptophane-A (CrA). It could further quantitatively be demonstrated for the first time that switching to the CrA-alternative xenon host molecule cucurbit[6]uril provides substantial sensitivity improvement for the Hyper-CEST detection method.

Therefore, this thesis provides the fundamentals to characterize and optimize the Hyper-CEST mechanism for general xenon-host systems. Such a characterization and optimization is essential to successfully translate the Hyper-CEST technique towards a possible molecular imaging modality with potential *in vivo* applications or preclinical implementations but also for investing gas binding structures in general.

KURZZUSAMMENFASSUNG

Molekulare Bildgebungsverfahren, die biochemische Veränderungen frühzeitig und räumlich aufgelöst detektieren, könnten unser aktuelles medizinisches Diagnostik- und Behandlungssystem revolutionieren, da sie nicht auf der Wiederherstellung, sondern auf der Erhaltung unseres Gesundheitszustandes beruhen. Solche Verfahren basieren auf der sensitiven nicht-invasiven Detektion von markierten Zellen mit Techniken wie Positronen-Emissions-Tomographie, Einzelphotonen-Emissionscomputertomographie, Computertomographie oder Magnetresonanztomographie (MRT). Unter diesen nutzt lediglich das MRT-Verfahren keine ionisierende Strahlung. Jedoch ist die Sensitivität von MRT gegenüber den Zellmarkern aufgrund konventioneller, relaxations-basierten Kontrastmitteln beschränkt.

Unter der Verwendung von Spin-hyperpolarisiertem Xenon und dessen reversibler Bindung zu Xenon-Wirtsstrukturen mittels Sättigungstransfer MRT (englisch: hyperpolarized xenon detection through chemical exchange saturation transfer; Hyper-CEST) wird eine *ca.* 10^5-fache Sensitivitätssteigerung der MRT erreicht. Diese Verstärkung wird durch die zwei Teilprozesse a) des LASER-induzierten "spin-exchange optical pumping" und b) der indirekten CEST Methode erzielt. Bei der Letzteren wird die Spin-Hyperpolarisation des ungiftigen Edelgases Xenon, das temporär im Wirt bindet, selektiv durch einen HF-Sättigungspuls zerstört. Durch den reversiblen Bindungscharakter wird dieses ausgeschaltete Signal auf das des freien und ungebundenen Xenons transferiert und als Signalrückgang messbar. Erste Realisierungen dieser Hyper-CEST MR-Bildgebung waren experimentell sehr zeitaufwändig. Zudem wurde bisher durch den Einsatz verschiedener Wirtsstrukturen empirisch unterschiedliche Sensitivitätssteigerungen mit Hyper-CEST berichtet. Da die Hyper-CEST-Technik HF-Sättigungspulse ausnutzt, tragen die Pulsstärke und -dauer als weitere Freiheitsgrade bei. Die genauen Hyper-CEST-Mechanismen waren bislang quantitativ unverstanden.

Diese Arbeit präsentiert Methoden zur beschleunigten quantitativen Charakterisierung des Xenon-Wirt-Systems und Optimierung des Sättigungstransfers. Bei der Beschleunigung handelt es sich um den Einsatz sogenannter "single-shot" Bildgebungsverfahren, die in einem einzigen Arbeitsschritt die erforderliche Information aufnehmen und kodieren. Damit konnten zum ersten Mal zeitaufgelöste Diffusionsstudien des Xenon-Wirts gezeigt werden. Mit dieser signifikanten Bildgebungsbeschleunigung konnte zudem die spektrale Dimension der Hyper-CEST Methode untersucht werden. Mit Hilfe dieser konnte eine neue Quantifizierungstechnologie etabliert werden, welche es erstmals ermöglichte, die Xenon-Austauschkinetiken hochsensitiv zu ermitteln. Damit konnten auch erstmalig optimale Sättigungspulsparameter bestimmt werden. Diese Charakterisierung und Optimierung wurde mit dem weit verbreiteten Xenon-Wirt Cryptophan-A (CrA) durchgeführt. Darüber hinaus konnte quantitativ zum ersten Mal gezeigt werden, dass der CrA-alternative Xenon-Wirt Cucurbit[6]uril eine erhebliche Sensitivitätssteigerungen für die Hyper-CEST Detektion mit sich bringt.

Die vorgelegte Arbeit liefert die Grundlagen für eine detaillierte *In vitro*-Charakterisierung und Optimierung des Hyper-CEST Mechanismus für allgemeine Xenon-Wirt-Systeme. Eine solche Charakterisierung ist die Voraussetzung für eine erfolgreiche Übertragung auf weitere Xenon-Wirt-Systeme mit maßgeschneiderten Eigenschaften für potentiell zukünftige *In vivo*-Anwendungen oder mögliche präklinische Einsätze auf dem Gebiet der molekularen Bildgebung, sowie der Untersuchung Gas-bindender Substanzen im Allgemeinen.

CONTENTS

LIST OF FIGURES

LIST OF TABLES

LIST OF MATLAB-CODES

ABBREVIATIONS AND SYMBOLS

ABBREVIATIONS

^{1}H	hydrogen-1
^{129}Xe	xenon-129
α-CD	α-cyclodextrin
APT	amide proton transfer
BM	Bloch–McConnell
BS	bacterial spores
bSSFP	balanced steady-state free precession
CA	contrast agent
CB6	cucurbit[6]uril
CBn	cucurbit[n]uril
CCD	charge-coupled device
CEST	chemical exchange saturation transfer
CrA	cryptophane-A (= Cr-222)
CrA-PEG	polyethylene glycol-coupled CrA
Cr	cryptophane
CSI	chemical shift imaging
CTV	cyclotriveratrylene
CT	X-ray computed tomography
cw	continuous-wave
diaCEST	diamagnetic CEST
DMSO	dimethyl sulfoxide
DNP	dynamic nuclear polarization
DS	double sampling
EPI	echo-planar imaging
EXSY	exchange spectroscopy
FHC	full Hyper-CEST
FID	free induction decay
FLEX	frequency-labeled exchange

FOV	field-of-view
FT	Fourier transform
FWHM	full width at half-maximum
GAG	glycosaminoglycan
glycoCEST	glycogen CEST
GRE	gradient (recalled) echo
GUI	graphical user interface
GV	gas vesicles
HP	hyperpolarized
Hyper-CEST	hyperpolarized xenon detection through CEST
IC	inner compartment
IR	infrared
LEIPNIX	LASER enabled increase of polarization for nuclei of imprisoned xenon
lipoCEST	liposome CEST
MR	magnetic resonance
MRI	magnetic resonance imaging
MT	magnetization transfer
NMR	nuclear magnetic resonance
OC	outer compartment
ODE	ordinary differential equation
paraCEST	paramagnetic CEST
PBS	phosphate-buffered saline
PC	packing coefficient
PET	positron emission tomography
PFA	perfluoroalkoxy alkane
PFOB	perfluoroctyl bromid
PHIP	*para*-hydrogen-induced polarization
ppm	parts per million
qHyper-CEST	quantitative hyperpolarized xenon detection and analysis through CEST
QUESP	quantifying exchange using saturation power
QUEST	quantifying exchange using saturation time
RARE	rapid acquisition with relaxation enhancement

RBC	red blood cells
Rb	rubidium
RF	radio frequency
ROI	region-of-interest
SAR	specific absorption rate
SEOP	spin-exchange optical pumping
SLM	standard liter per minute
smashCEST	shared magnetization after single hyperpolarization CEST
SNR	signal-to-noise ratio
SPECT	single photon emission computed tomography
SSP	strong saturation pulse
US	ultra sound
VFA	variable flip angle
WEX	water exchange
WKS	Whittaker–Kotelnikow–Shannon
WSP	weak saturation pulse
Xe	xenon

SYMBOLS

A_0	initial amplitude
$\hat{A}$	coefficient matrix of the BM equations (in s^{-1})
$\vec{b}$	inhomogeneity of the BM equations (in s^{-1})
$\vec{B}_0$	external static magnetic field (in T)
$\vec{B}_1$	RF or saturation pulse field (in T)
$\vec{B}_{eff}$	effective RF or saturation pulse field (in T)
$\vec{B}_{HH}$	magnetic induction of Helmholtz coils (in T)
BT	bubbling time (in s)
c	speed of light (299 792 458 m s^{-1})
$\hat{D}$	diagonal matrix (in s^{-1})
E	energy (in J)
f_A	relative size of pool A (normally $f_A = 1$)
f_B	fraction of (pool B) bound Xe to free Xe
G	magnetic field gradient strength (in T m^{-1})

h	Planck's constant ($6.626207 \cdot 10^{-34}$ J s)
$\hbar$	reduced Planck's constant ($h/(2 \cdot \pi)$)
$\hat{\mathcal{H}}_{\text{spin}}$	spin Hamiltonian
I	spin quantum number
$I_{\text{center/out}}$	current of center/outer coil (in A)
$\vec{J}$	total angular momentum
k_{AB}	exchange rate from pool A to pool B (in s^{-1})
K_A	binding (or association) constant (in M^{-1})
k_{BA}	exchange rate from pool B to pool A (in s^{-1})
k_B	Boltzmann constant ($1.38065 \cdot 10^{-23}$ J K^{-1})
$\vec{l}$	angular momentum
$\vec{M}$	macroscopic net magnetization
M_x, M_y, M_z	orthogonal components of the macroscopic net magnetization
$\vec{M}_0$	initial available macroscopic magnetization (either thermally or HP)
$\vec{M}_{th}$	thermally polarized macroscopic magnetization
M_i^j	component i of the macroscopic magnetization of the spin ensemble j
$M_{i,\text{on/off}}^j$	component i of the macroscopic magnetization of the spin ensemble j after on/off-resonant cw saturation
$M_\perp$	macroscopic transverse magnetization
m	magnetic quantum number
m_e	electron mass ($9.109383 \cdot 10^{-31}$ kg)
N_A	Avogadro constant ($6.022141 \cdot 10^{23}$ mol^{-1})
N_n	total number of nucleons
n_{rep}	number of repetitions
P_0	power (in W)
P_A	relative population of pool A
P_B	relative population of pool B
P_{HP}	hyperpolarized polarization
P_T	transverse component of positronium momentum (in kg m s^{-1})
P_{th}	thermal polarization
PL	RF pulse length or duration (in s; is equal to t_{sat} for saturation pulses)
$\hat{R}$	relaxation rate matrix (in s^{-1})
R_1	longitudinal relaxation rate (in s^{-1})

$R_{1,\mathrm{eff}}$	effective longitudinal relaxation rate (in s^{-1})
R_2	transverse relaxation rate (in s^{-1})
$\vec{s}$	spin
T	temperature (in K or °C)
$\hat{T}$	matrix of eigenvectors
T_1	longitudinal relaxation time (in s)
T_2	transverse relaxation time (in s)
T_2^*	apparent transverse relaxation time (in s)
TA	acquisition time (in s)
TE	echo time (in s)
TR	repetition time (in s)
t_{sat}	saturation pulse time or duration (in s; is equal to PL for RF pulses)
W	width of the field-of-view (in m)
$Z^{\mathrm{FHC}}_{\mathrm{Hyper-CEST}}$	Hyper-CEST *z*-spectrum model function of the FHC solution
α	flip angle (in °) or Hyper-CEST labeling efficiency (in %/100)
β	host occupancy (in %)
$\beta \cdot k_{BA}$	gas turnover rate (in % s^{-1})
γ	gyromagnetic ratio (in rad s^{-1} T^{-1})
Γ	Ostwald solubility coefficient (in L/atm) or full width at half-maximum of depolarization rate (in s^{-1})
δ_A	chemical shift of pool A (in ppm)
δ_B	chemical shift of pool B (in ppm)
ΔE	energy difference (in J)
$\Delta\delta$	chemical shift difference (in ppm)
$\Delta\omega_{\mathrm{sat}}$	RF or saturation pulse carrier frequency difference (in Hz)
η	signal enhancement factor by hyperpolarization
θ	effective (or variable) flip angle (in °) or residual positronium momentum annihilation angle (in °)
κ	Xe exchange rates in kick-out model (in s^{-1})
$\kappa_{+,-}$	chemically Xe exchange rates (in s^{-1})
$\lambda_{1,\ldots,n}$	eigenvalues of matrix of eigenvectors $\hat{T}$ (in s^{-1})
λ_{depol}	total ^{129}Xe depolarization rate (in s^{-1})
$\lambda_{\mathrm{direct}}$	direct ^{129}Xe depolarization rate of free Xe (in s^{-1})
$\lambda^{\mathrm{AB}}_{\mathrm{CEST}}$	^{129}Xe depolarization rate of (pool B) bound Xe (in s^{-1})

λ_{on-res}	on-resonant ^{129}Xe depolarization rate (in s^{-1})
$\vec{\mu}$	nuclear magnetic dipole moment
ν_0	Larmor frequency (in Hz)
σ	shielding constant
τ	exponential decay rate (in s or min)
τ_{AB}	residence time of Xe free in solution (in s)
τ_{BA}	host-bound Xe residence time (in s)
τ_P	phase encoding time (in s)
φ_0	phase (in °)
$\vert\psi_{full}(t)\rangle$	full wavefunction
$\vert\psi_{spin}(t)\rangle$	nuclear spin wavefunction
ω_0	Larmor frequency (in rad s^{-1})
ω_1	RF or saturation pulse amplitude frequency (in rad s^{-1})
$\omega_{A,B}$	Larmor frequency of pool A or B (in rad s^{-1})
ω_{sat}	RF or saturation pulse carrier frequency (in Hz)

Part I

Introduction

1 INTRODUCTION

> *"Human cancers when first detected usually have an average diameter of at least 1 cm and contain about 10^9 cancer cells, [. . .]."*
>
> — Schreiber and Rowley[185] – 2010

Contents

In living organisms (including humans), microscopic biochemical changes of healthy tissue are the origin of macroscopic anatomical, and physiological changes within a certain time frame. Due to the lack of methods that are capable to detect microscopic biochemical changes in living organisms (*i. e.*, *in vivo*), the much more coarse and temporally delayed identification of macroscopic changes is common practice in diagnostic imaging. Wagner and Wechsler[222] described that early detection of such small biochemical changes in combination with spatial information would revolutionize our current existing health care and treatment system, as it could focus on the conservation of the state of health and not on the recovery of the state of health.

Therefore, a modality that is able to scan the human body noninvasively and identifies diverse kinds of diseases while the patient does not perceive any harm is a highly desired medical imaging modality.[1] By now, however, this goal has not yet been reached. This thesis aims to make important contributions to achieve this worthy goal. As such, we introduce molecular imaging, identify magnetic resonance imaging as a promising molecular imaging modality and show how the noble gas xenon overcomes several sensitivity limitations.

1.1 MOLECULAR IMAGING

Molecular imaging is an innovative concept that combines the spatially resolved detection of biochemical events on a molecular level with anatomical

---

[1] The meaning of *"invasive"* in medical context is to penetrate the human body. This for example implies the removal of tissue samples for examinations while destroying or irreversible altering the tissue.

reference scale imaging modalities. While still in its infancy, the goal of molecular imaging is to localize disease markers as early as possible to facilitate an individualized therapy. The different imaging modalities that have the potential to achieve this use **contrast agent**s (CAs) that give the desired contrast. At the same time, the concentration of such CAs should be minimized to avoid toxicity and to not influence the biological system. Consequently, the CA detection method must be extremely sensitive to detect such small amounts of molecular markers.

Since future studies should additionally give information about therapy monitoring, molecular imaging must be minimize harm as the examination could be applied multiple times within a short time window, or observing the progression of chronic diseases over many years, to the same patient. Both, short- and long-term therapy monitoring additionally requires quantitative data of the imaging modality to permit correct signal interpretation, *e. g.*, growing or shrinking of the tumor while under therapy. Furthermore, molecular imaging should have the ability to image/visualize multiple molecular targets simultaneously, a concept also called multiplexing. This technique can minimize the number of examinations.

In summary, the ideal molecular imaging modality should provide the following features:

1. targeted and specific uptake,
2. harmless,
3. large penetration depth of the detected signal,
4. high sensitivity,
5. high spatial resolution,
6. multiplexing option, and
7. quantitative signal analysis.

The following overview lists currently existing modalities that have molecular imaging capabilities (predominantly noninvasive), including their strengths and limitations. All are fields of active research:[2]

X-RAY COMPUTED TOMOGRAPHY (CT): The CT method relies on X-ray attenuation by tissues or media that a) strongly absorb or scatter X-rays (such as bones) and b) others that poorly absorb/scatter X-rays. To further enhance spatial resolution and soft tissue contrast, imaging agents such as iodine can be used. Since X-rays have high energy, CT's main strengths are 1) high spatial resolution, 2) short acquisition time, and 3) large penetration depth (regarding the human body). The main limitations of CT are 1) its high radiation exposure, 2) low specificity, 3) no quantitative data and 4) no multiplexing, although it could technically be possible.

---

[2] The field of molecular imaging is steadily progressing. Due to space limitations, the following comprehensive literature is recommended for further reading: James and Gambhir[107], Weissleder and Mahmood[228], Weissleder[227], Modo and Bulte[155], or Bryan[35], while many more can be found.

magnetic resonance imaging (mri): Atomic nuclei with spin (*i. e.*, they exhibit a nuclear magnetic moment) interact with strong external magnetic fields. Spin-1/2 nuclei populate two energy levels according to the Boltzmann distribution which averages at body temperature to a very small macroscopic net magnetization or spin polarization. After a perturbation of this macroscopic magnetization (*e. g.*, by **radio frequency** (RF) fields perpendicular to the external magnetic field), the magnetization relaxes back to this thermal equilibrium with two different time constants: the longitudinal and transverse relaxation times. The systematic timing of perturbation and relaxation (a so-called pulse sequence) generates image contrast that depends on microscopic relaxation behavior and spin density. Spatial reconstruction is conventionally done through **Fourier transformation** (FT) after rendering the resonance frequency of the detected nuclei spatially dependent with additional magnetic field gradients. The MRI technique 1) has superior soft tissue contrast, 2) is harmless as it uses non-ionizing radiation, 3) provides high spatial resolution (from µm to 1 mm for preclinical and clinical settings, respectively), 4) comes with large penetration depth, 5) offers quantitative data, and 6) has excellent clinical availability. A main limitation is 1) its poor sensitivity and 2) inability to be multiplexed. More details will be given in Chapter 2.

positron emission tomography (pet): Radioactive nuclides (or radionuclides) emit either one of three types of radiation with differing abilities to penetrate matter: alpha-rays (He^{2+} particles), beta-rays (positron or electron particle radiation) or gamma-rays (radiation in the form of photons). PET exploits the beta-plus decay β^+, in which, contrary to the more frequent β^- decay, an excess of protons over neutrons is present in the nucleus. During decay, a proton becomes converted into a neutron under emission of an electron antineutrino and a positron. Therefore, the mass number of the nucleus is unchanged while its charge number has decreased by 1. The free ionizing positron interacts with matter, becomes slowed down due to collisions until it eventually forms positronium with an available electron.[3] As this system is unstable, the two particles annihilate each other under the emission of two gamma-photons that move in approximately opposite directions.[4] Since these gamma-photons have large energy (511 keV), they merely interact with tissue and hit the surrounding detectors. By different post-processing techniques, the three-dimensional distribution of radionuclide-marked biological targets can be reconstructed at nanomolar concentration. The strengths of PET are therefore 1) excellent sensitivity (*i. e.*, ≈ nM to pM detection limit), 2) limitless penetration depth, and 3) quantitative data analysis. Main limitations are 1) the use of ionizing radiation, 2) inability to be multiplexed, 3) relative poor spatial resolution, and 4) the elaborate incorporation of radionuclides into biological tracers.

single photon emission computed tomography (spect): In contrast to PET, SPECT uses radionuclides that decay under emission of single gamma rays. As this emission is spherical, localized information of

---

[3] Positronium is an unstable system formed by an electron and its anti-particle, a positron.

[4] This also causes a limitation regarding spatial resolution. If the positron is not slow enough, the positronium has a residual momentum and the emitted two gamma-photons do not enclose 180° but a difference to 180° of $\tan\theta = p_T/(m_e \cdot c)$ with p_T being the transverse component of the positroniums momentum, m_e electron mass and c the speed of light.

the radionuclides is achieved using gamma-ray detectors that measure the intensity for different positions (so-called projections). The Radon transformation-based reconstruction of such projections shows the tomographic spatial distribution of the radionuclides throughout the body. Thus, the strengths of SPECT are 1) high sensitivity (although slightly lower than that of PET), 2) limitless penetration depth, 3) quantitative data analysis, and 4) the ability to be multiplexed. Main limitations are 1) the use of ionizing radiation, 2) relative poor spatial resolution and 3) no anatomical reference images.

OPTICAL IMAGING: Various optical imaging methods exist and they all rely on the same basic instrument combination: a source of light and a light detector. Such a detector can be a microscope or a **charge-coupled device** (CCD) camera to enable macroscopic optical imaging. The following sources of light are widely used:

1. Fluorescence: The source of light are fluorescent molecules that are provided to the target either as genetically encoded fluorescent proteins or as a dye. An external source of radiation is additionally required to excite these molecules which then relax to their ground state under emission of a photon with lower energy (*i. e.*, larger wavelength). Since the image intensity contains the number of photons for each region, fluorescence provides quantitative data.
2. Bioluminescence: Internally produced emission of light is generated by the enzymatic oxidation reaction of luciferase with its substrate. Thus, in contrast to fluorescence, no external excitation is required. Often, a cooled CCD camera is used to further enhance sensitivity.

Therefore, the main strengths of optical imaging methods are 1) excellent sensitivity (bioluminescence even more than fluorescence), 2) a high safety profile (*i. e.*, no ionizing radiation), 3) low background signal, 4) relative low costs, 5) quantitative image analysis and 6) multiplexing capabilities. However, the main limitation is 1) small penetration depth and 2) relatively low spatial resolution if scattering is involved. For bioluminescence, also substrate requirements may limit clinical translatability.

ULTRA SOUND (US): US uses frequencies above the frequency range of human hearing. Short-pulses of sound generated by piezoelectric crystals at recorded time intervals are transmitted to the subject. *Via* a coupling gel, the sound waves couple into the subject and travel through the body until a tissue interface is reached. Some interfaces cause the wave to partially transmit and to partially reflect. The reflected wave can interfere with the incoming wave, build up echoes, and eventually couples out of the body. There, it hits the detector on which the sound signature becomes analyzed according to its time of arrival, axis of the sound wave, amplitude, and frequency to generate a two-dimensional image. Therefore, one major advantage of US is 1) its good safety profile as it uses no ionizing radiation. When microbubbles are used as CA, further advantages such as 2) excellent sensitivity is achieved, and US provides 3) quantitative data, 4) is widely used and 5) is cost effective. Limitations are 1) difficulties in imaging structures such as bones and 2) no multiplexing option.

Table 1.1: Comparison of molecular imaging modalities (adapted from James and Gambhir[107]). The spatial resolution ranges from preclinical to clinical used systems. The term *Limitless* is referring relative to the human body size. Modalities that are marked with a dagger (†) employ ionizing radiation.

Modality	Spat. Resol.	Penetr. Depth	Sensitivity	Multi-plexing	Quanti-tative
CT†	0.05-1 mm	Limitless	ND[a]	no[b]	no
MRI	0.03-1 mm	Limitless	10^{-3}-10^{-5} M	no	yes
PET†	1-7 mm	Limitless	10^{-11}-10^{-12} M	no	yes
SPECT†	1-10 mm	Limitless	10^{-10}-10^{-11} M	yes	no
US	0.1-2 mm	mm - cm	10^{-12} M[c]	no[b]	yes
Fluorescence	2-3 mm	$<$ 1 cm	10^{-12} M	yes	yes
Bio-luminescence	3-5 mm	1-2 cm	10^{-17} M	yes	yes[112]

[a] Not determined. [b] Could be possible. [c] If microbubbles are used.

The summary in Table 1.1 shows that these modalities rather complement each other, instead of revealing a superior molecular imaging modality. For example, the sensitivity of PET is excellent, while it employs ionizing radiation. Another example is optical imaging: the sensitivity is outstanding but the restricted penetration depth of 1-2 cm limits clinical translation. Nevertheless, the medical imaging modality that pairs many requirements best is MRI but with inherently low sensitivity. The improvement of this everlasting challenge is currently an active field of research. In the following, we describe how MRI's sensitivity is significantly increased.

1.2 MAGNETIC RESONANCE IMAGING

The MRI signal is proportional to a) concentration of nuclei, b) gyromagnetic ratio, and c) spin polarization.[5] Since the **nuclear magnetic resonance** (NMR)-active isotope **hydrogen-1** (^{1}H; referred to as proton in the context of NMR) is the most abundant nucleus in biological tissue (Table 1.2), it typically provides the largest NMR signal (including the gyromagnetic ratio and spin polarization).

1.2.1 Proton Magnetic Resonance Imaging

Although the polarization at current clinical MRI magnets is inherently low at room temperature, most MRI studies are performed with ^{1}H as their large abundance ($\sim$ 110 M in water) greatly compensates for the low polarization (see Chapter 2 and Chapter 4 for detail). The contrast between different types of tissue is usually proportional to the concentration differences of the nuclei, the polarization, and the differences in longitudinal and transverse relaxation times. The larger the difference in these parameters is, the better is the pulse sequence able to generate maximal contrast in the final image. In practice, however, such differences are very small and the introduction of CAs is often mandatory. In the following, two types of CAs are described.

---

[5] The ratio of angular momentum to nuclear magnetic moment is unique for each magnetically active nucleus and known as the gyromagnetic ratio.

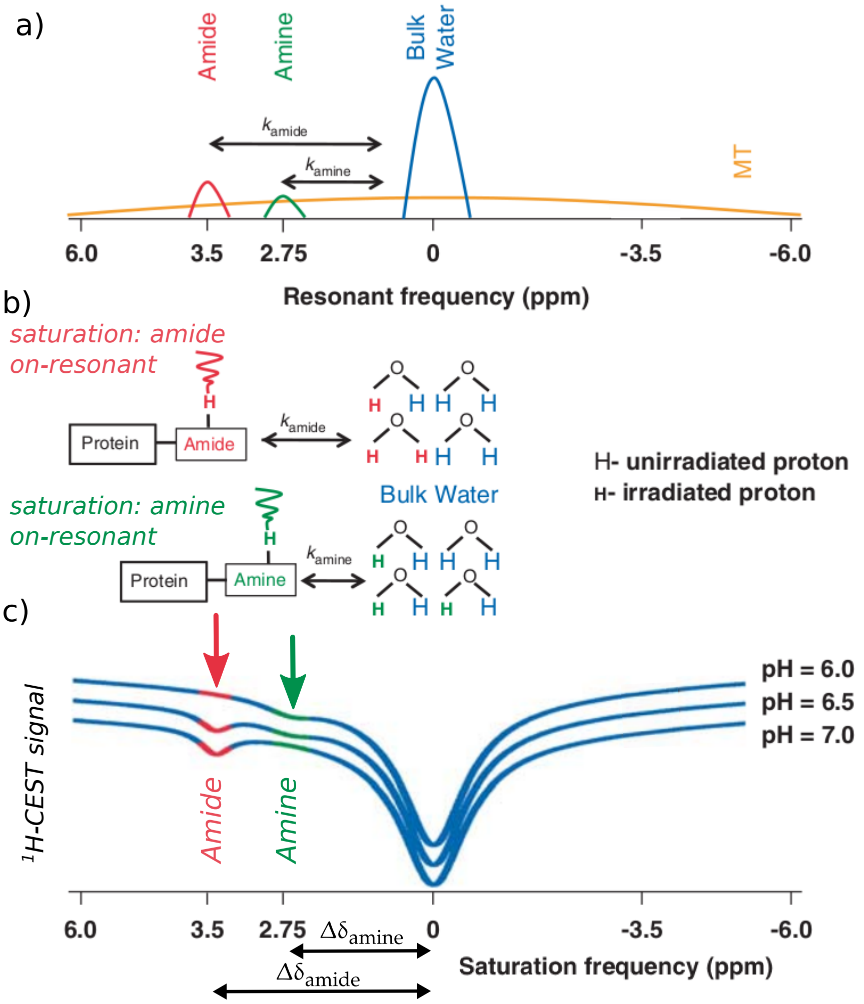

Figure 1.1: Sensitivity increased protein detection by **proton-chemical exchange saturation transfer** (^{1}H-CEST). a) The concentrations of the protein-associated amide protons –NH (at 3.5 ppm; red population), and amine protons –NH_2 (at 2.75 ppm; green population) are usually so highly diluted that their NMR signals are far below the noise for MR imaging puropses. In addition, their resonances often overlap with the bulk water (blue population) signal. However, the protons of these groups chemically exchange with the protons of the bulk water with the exchange rates k_{amide} and k_{amine}, respectively. b) On-resonant saturation on either the amide or amine protons decreases their magnetization. Due to chemical exchange, this vanishing net magnetization becomes transfered to the large detection signal of bulk water. Thus, amide or amine protons on-resonant saturation transfers their invisibility into a detectable decrease of the large bulk water signal (red and green irradiated protons H). c) At saturation frequencies where exchangeable protons resonate, a loss in the detection signal is observed (amide protons: red arrow, amine protons: green arrow). Moreover, the proton exchange is pH-dependent. In addition, **magnetization transfer** (MT) from protons that originate from macromolecules (orange population) with short relaxation times exchange with the bulk water and cause a broad interference with the detected water signal and other exchangeable proton groups. Image adapted from McVicar *et al.*[149]. Reprinted with permission. Copyright © 2014, © SAGE Publications.

Contrast Agents that Disturb the Local Magnetic Field

The effect of longitudinal and/or transversal relaxivity is related to local magnetic field fluctuations. These can be produced by paramagnetic CAs, *e. g.*, gadolinium (Gd^{3+}; which is toxic when not chelated like in DOTA complexes), iron-oxide nano-particles or manganese.[6] Following the uptake into certain tissue, they all alter the contrast compared to the surrounding tissue and make particular tissue types such as tumors visible in MR images. A first drawback is that typical CA concentrations for sufficient influence on the detected water magnetization need to be about 10^{-5} to 10^{-3} mole per liter (*i. e.*, sub-millimolar). Thus, specific targeting is not possible anymore for many dilute markers, and these CAs typically accumulate non-specifically in the extracellular space. A second drawback is that methods which use such CAs rely on comparing MR images before (*pre*) and after (*post*) CA injection. Thus, they are prone to errors if the patient is, *e. g.*, moving between different measurements.

A CA class that overcomes these concerns is described next.

Signal Amplification by Chemical Exchange Saturation Transfer

In 2000, another class of MRI CAs was proposed by Ward *et al.*[226] that are based on **chemical exchange saturation transfer** (CEST; also referred to as ^{1}H-CEST when performed with ^{1}H; Figure 1.1).

Since ^{1}H-CEST can make dilute species (or pools) detectable that are otherwise far below the noise by conventional ^{1}H NMR, CEST bears the potential for early disease detection and is currently under active investigation. Generally speaking, ^{1}H-CEST experiments exploit the chemical exchange of species that are able to exchange protons with bulk water protons, such as labile amide protons –NH, amine protons $–NH_2$, hydroxyl protons –OH, or as entire H_2O molecules.[7] The resonance of such amide protons –NH, or amine protons $–NH_2$ is shifted relative to the dominant bulk water signal by several **parts per million** (ppm; see Equation (2.26)) which is referred to as chemical shift difference $\Delta\delta_{\text{amide}}$ and $\Delta\delta_{\text{amine}}$, and their NMR signal is usually far below the noise. The application of a so-called saturation pulse that is on-resonant with the amide or amine protons (at 3.5 ppm: red population in Figure 1.1 or at 2.75 ppm: green population) decreases their magnetization. Due to chemical exchange with rates k_{amide} and k_{amine}, this vanishing net magnetization becomes transfered to the large detection signal of bulk water (blue population in Figure 1.1), which then decreases significantly in signal intensity. Therefore, the on-resonant saturation of amide or amine protons transfers their invisibility into a visible decrease of the large bulk water signal (red and green irradiated protons H in Figure 1.1b). Thus, CEST provides large signal amplification capabilities – typically around 1,000-fold – since a single exchangeable proton site (*e. g.*, from amides or amines) can manipulate the signal of thousands of exchanging protons while under RF saturation for several seconds. A further strength of this method is its activeable contrast mechanism by the use of a saturation pulse that can either be turned on or turned off. This replaces the *pre* and *post* injection character of other conventional CAs. The typical spectral resolution (and therefore its limitation) of CEST experiments is given by the

---

[6] DOTA is the common name for 1,4,7,10-tetraazacyclododecane-1,4,7,10-tetraacetic acid.

[7] The empirical effect of chemical exchange on the NMR signal and its theoretical concept on saturation transfer experiments will be discussed in detail in Section 2.1.5 and Chapter 3, respectively.

ratio of the exchange rate and the chemical shift difference relative to the resonance of the detection signal in Hertz (Hz). This is known as the chemical exchange regime and depending on its value it is either slow, intermediate or fast exchange. Whereas signals under slow and intermediate exchange can be distinguished in a CEST experiment, this becomes impossible for fast exchange.

As a background for the need of this thesis, we introduce in the following ^{1}H-CEST approaches that are promising as potential molecular imaging modality and we also discuss their limitations.

In the last decade, numerous ^{1}H-CEST applications have been demonstrated in the literature. Whereas a somewhat complete classification of ^{1}H-CEST CAs is provided by van Zijl and Yadav[260], we will simplify this and introduce here two large classes which are endogenous and exogenous CAs.

The endogenous CAs are by definition substances that originate from within an organism. Thus, their main advantage is that a **Food and Drug Administration** (FDA) approval is not required and a translation to clinics is relative straight forward. For example, endogenous **diamagnetic CEST** (diaCEST; Figure 1.1 and Figure 1.2a; reviewed by Zhou and van Zijl[258]) CAs such as protons of amide groups have been demonstrated by Zhou *et al.*[256] for noninvasive *in vivo* pH imaging *via* **amide proton transfer** (APT) and further for *in vivo* APT tumor imaging in rat brain by Zhou *et al.*[255]. Furthermore, APT imaging has been used for ischemia detection as demonstrated by Sun *et al.*[206] and for acute stroke detection which was shown by Zhou *et al.*[256], Sun *et al.*[203], Zhao *et al.*[254], Zaiss *et al.*[245] and Harston *et al.*[94]. Another endogenous CA is glycogen. The exchanging hydroxyl protons of glycogen can be detected *in vivo* using the method **glycogen CEST** (glycoCEST) which was reported by van Zijl *et al.*[259]. More recently, *in vivo* imaging of glucose uptake in tumors using glycoCEST was reported by Walker-Samuel *et al.*[224]. Another endogenous CA is **glycosaminoglycan** (GAG). As GAG is one of the main constituents of cartilaginous tissue, it is involved in many cartilage diseases such as osteoarthritis and intervertebral disc degeneration. Recently, GAG could be detected *in vivo* using the CEST based method, gagCEST, which was proposed by Ling *et al.*[136]. Moreover, McMahon *et al.*[147] reported new polypeptides for multicolor diaCEST imaging and endogenous genetically engineered diaCEST CAs have been reported by Gilad *et al.*[81]. Nonetheless, Liu *et al.*[137] showed ^{1}H-CEST-based *in vivo* temperature mapping with no contrast agent and simply using direct water saturation. However, a drawback of most diaCEST CAs is their small chemical shift difference relative to water (Figure 1.1) at already fairly large exchange rates. This limits the lowest CA concentration that can be detected.

The second class of ^{1}H-CEST CAs, the exogenous CAs, do not originate in the human body and have therefore to be administered externally to the patient. As these require FDA approval, they are less straight forward to clinical translation, but they provide multiple advantages regarding the ^{1}H-CEST sensitivity. A main member of exogenous CAs are **paramagnetic CEST** (paraCEST; Figure 1.2b; generally reviewed by Zhang *et al.*[249]) agents.[8] They can provide larger chemical shifts which in turn allows for

---

[8] Although many diaCEST CAs are endogenous and *vice versa* many paraCEST CAs are exogenous, this classification is not strict and some diaCEST CAs are exogenous whereas some paraCEST CAs are endogenous.

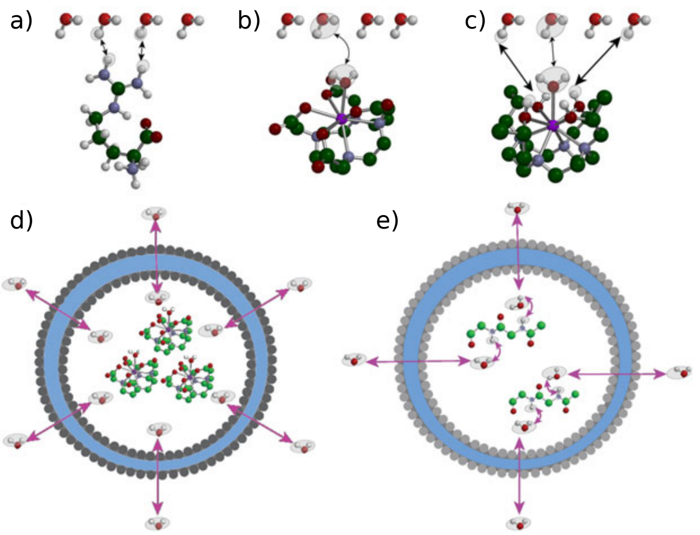

Figure 1.2: Different ^{1}H-CEST systems that are characterized by their exchange pathways: a) proton exchange (typically diaCEST agents), b) molecule exchange (typically paraCEST agents), c) simultaneously by protons and molecules, d) compartment exchange (typically lipoCEST agents) and e) molecule-mediated compartment exchange. Image reproduced from Liu *et al.*[138]. Reprinted with permission. Copyright © 2013 John Wiley & Sons, Ltd.

exploiting faster exchange rates in order to detect lower CA concentrations:

> *"[...], [O]ne advantage of a paramagnetic complex*
> *that displays a large [chemical shift] is*
> *that faster exchange can take place [...]*
> *without approaching the fast exchange limit."*
>
> — Zhang *et al.*[247] – 2001

This was exploited with a europium(III)-based MRI CA proposed by Zhang *et al.*[247] that was further developed to be pH sensitive as presented by Aime *et al.*[3]. Even a lactate concentration sensitive paraCEST CA has been reported by Aime *et al.*[5]. Zhang *et al.*[250] described a sharp dependence of the water exchange rate on the radii of such europium(III)-based paraCEST CAs and *in vitro* MRI thermometry based on exogenous paraCEST CA was reported by Zhang *et al.*[248]. Further, the detection of enzymatic activity could be shown by Yoo and Pagel[239] and Yoo *et al.*[240]. Recently, Jones *et al.*[109] demonstrated DOTA based paraCEST CA detection *in vivo* in the mouse kidney. As a highly sensitive method, Aime *et al.*[6] demonstrated that water entrapped in liposomes loaded with paramagnetic shift agents shifts by 3 ppm and liposomes in picomolar (pM) concentrations could be detected with **liposome CEST** (lipoCEST; Figure 1.2d). In addition, this chemical shift of water within such liposomes could be tuned highly sensitive as described by Terreno *et al.*[209]. Recently, pH nanosensors for *in vivo* sensing of transplanted-cell viability using lipoCEST was reported by Chan *et al.*[209].

All these ^{1}H-CEST approaches – and only a few could be mentioned here – demonstrated promising results with potential as molecular imaging modal-

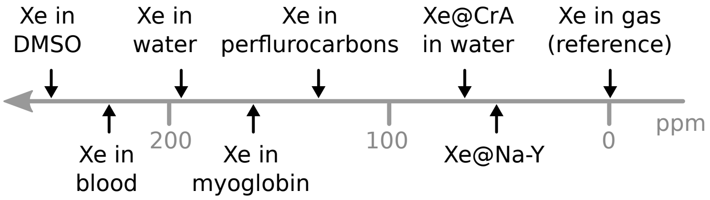

Figure 1.3: Xe shows remarkable large chemical shift sensitivity in different chemical environments. Image adapted from Pietraiß and Gaede[163] and Goodson[82].

Table 1.2: Nuclear spin numbers, natural abundance, gyromagnetic ratio and NMR frequencies (calculated for a magnetic field strength of 9.4 T) for the NMR-active isotopes ^{1}H, ^{2}H, ^{13}C, ^{129}Xe and ^{131}Xe. This Table is adapted from Levitt [132].

Isotope	Spin	Natural Abundundance	Gyromagnetic Ratio / rad s^{-1} T^{-1}	NMR Freq. / MHz
^{1}H	1/2	~ 100 %	$267.52 \cdot 10^{6}$	400
^{2}H	1	0.015 %	$41.06 \cdot 10^{6}$	61
^{13}C	1/2	1.1 %	$67.28 \cdot 10^{6}$	101
^{129}Xe	1/2	24.4 %	$-74.52 \cdot 10^{6}$	- 110
^{131}Xe	3/2	21.3 %	$22.09 \cdot 10^{6}$	33

ity including *in vivo* experiments.[9] However, the use of water protons has also the following two restrictions:

1. Limited chemical shift sensitivity (*e.g.*, about ± 6 ppm for most diaCEST CAs (compare with Figure 1.1) and about + 50 ppm for most DOTA-based paraCEST CAs).

2. The reported ^{1}H-CEST effects for most diaCEST studies are typically within a few percent (*i.e.*, 2 - 8 %) until steady-state saturation is reached although the typical concentration of CAs is in the millimolar to micromolar regime [Vinogradov *et al.*[220]] (except for the lipoCEST approach). This limitation arises because a very large ^{1}H nuclei concentration in biological tissue (which is about 110 M in water) must be manipulated *via* saturated magnetization transfer.

To potentially further gain sensitivity, these issues can be overcome using a different detection nucleus, for example xenon.

1.2.2 Xenon Magnetic Resonance Imaging

The hydrophobic noble gas **xenon** (Xe) has two NMR-active isotopes, xenon-129 and xenon-131 (see Table 1.2).[10] Whereas xenon-131 exhibits a nuclear spin of 3/2 with more complicated resonance patters, **xenon-129** (^{129}Xe, ^{129}Xe) is a spin-1/2 system which is similar to ^{1}H (see Table 1.2). Furthermore, as Xe is naturally not present in the human body, ^{129}Xe MRI has inherently no unwanted background signal.

---

[9] Comprehensive reviews on ^{1}H-CEST are given (in chronologically order) by Zhang *et al.*[249], Aime *et al.*[2], Zhou and van Zijl[258], Woods *et al.*[237], Sherry and Woods[194], Castelli *et al.*[47], Aime *et al.*[4], Hancu *et al.*[88], van Zijl and Yadav[260], Liu *et al.*[138], Vinogradov *et al.*[220], Zaiss and Bachert[242] or Bar-Shir *et al.*[16].

[10] As a noble gas, xenon is considered to be chemically inert [Schröder[186]], although it has been used as anesthetic when applied in very high amounts.

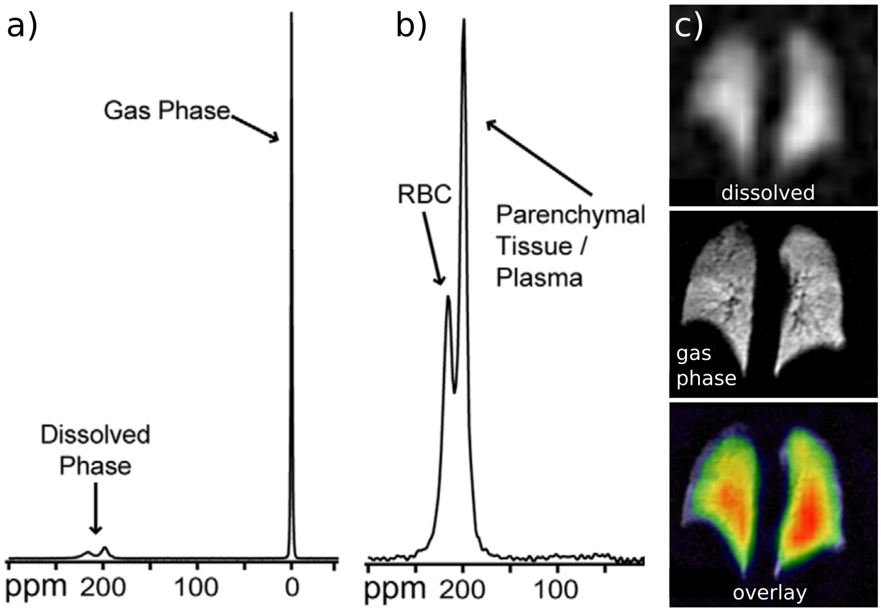

Figure 1.4: Xe shows exquisite sensing properties within the human lung. a) shows the ^{129}Xe NMR spectrum revealing a dominant ^{129}Xe signal in the gas phase and two separated signals of Xe associated with human lung tissue. b) The amplification of the dissolved phase ^{129}Xe signals reveals two peaks: one of Xe that is associated with **red blood cells** (RBC) and another one which is tissue associated. c) shows ^{129}Xe MR images acquired through the dissolved phase (top) or gas phase (middle) signal that facilitated false-color encoded overlay of both images (bottom). Images adapted from Cleveland *et al.*[55].

Increased Chemical Shift Sensitivity

In contrast to ^{1}H, ^{129}Xe has outstanding chemical shift sensitivity over several hundreds of ppm as reported by Goodson[82] (see Figure 1.3). This is due to its large electron cloud. Xenon's van der Waals radius is reported to be 2.16 Å [Bondi[27]]. Thus, its van der Waals volume yields $V_{\mathrm{vdW,Xe}} \sim 42.2$ Å^3. This will later be important for evaluating host structures.

Signal Amplification by Hyperpolarization

Another advantage using Xe is that its NMR signal originating from the Boltzmann distribution can be amplified by a technique known as **spin-exchange optical pumping** (SEOP) [Walker and Happer[223]], which increases the polarization far beyond thermal equilibrium. The resulting NMR signal of so-called **hyperpolarized** (HP) Xe is then up to ~ 25,000-fold increased, compared to thermally polarized Xe [Witte *et al.*[231]] (details given in Chapter 4). In turn, this allows the NMR detection of very low amounts of HP Xe which enabled human lung imaging of void spaces by ^{129}Xe MRI (Figure 1.4). Cleveland *et al.*[55] described that inhaled HP Xe gas in the human lung shows a) a distinct NMR signal at 0 ppm (Figure 1.4) but also b) two separated lung tissue-associated signals around 200 ppm. Under closer examination, these correspond to Xe dissolved in **red blood cells** (RBC) and Xe dissolved in parenchymal lung tissue. This further demonstrates Xe's excellent chemical shift sensitivity. Moreover, they reported tissue-associated

^{129}Xe MR images (Figure 1.4c) which were acquired either through the dissolved phase (top) or gas phase (middle) signal. The false-color encoded overlay of both images (bottom) shows the ^{129}Xe tissue-associated signal with "anatomical" reference of void spaces of the human lung. This experiment highlights the unique specific molecular environment information which Xe conveys in its NMR signal that is not possible with ^{1}H MRI.

In addition, Xe is not only able to probe its molecular environment, it also undergoes non-covalent interactions with local small-scale structures such as specific hydrophobic binding sites on proteins. This was first detected by X-ray crystallography [Schoenborn *et al.*[184] and Schoenborn[183]] and later by ^{129}Xe NMR. For example, one hydrophobic cavity was found on bacteriophage lysozymes as described by Desvaux *et al.*[58] and four binding sites on a lipid transfer protein from *Nicotiana tabacum* reported by Dubois *et al.*[67]. In addition, Gröger *et al.*[85] reported Xe binding to histidine, and surface explorations of different proteins with Xe was described by Bowers *et al.*[30], Rubin *et al.*[175], Rubin *et al.*[174] and Rubin *et al.*[173].

In a quantitative ^{129}Xe NMR study, Bartik *et al.*[18] reported Xe interaction with the hydrophobic cavity of the smallest member of the cyclic molecule family cyclodextrin, which is α-**cyclodextrin** (α-CD), but found rather weak Xe binding. In a follow up study, Bartik *et al.*[17] described for the first time the much stronger Xe binding to a so-called **cryptophane-A** (CrA) cage-like molecule.[11] They concluded that:

> *"The xenon-cryptophane-A complex [. . .] is probably*
> *the most stable xenon-host complex ever observed*
> *in the absence of hydrophobic forces."*
>
> — Bartik *et al.*[17] – 1998

The Xe Biosensor Prototype

Importantly, Bartik *et al.*[17] introduced the idea of *trapping* Xe on purpose by the outstanding large Xe affinity of CrA. This was realized by Spence *et al.*[198] to design the first CrA-based Xe biosensor prototype (Figure 1.5a). The biotin-avidin bonding is one of the strongest in nature. The construct is called a biosensor because the inert Xe is now functionalized to a biological targeting unit, *i. e.*, the biotin unit (red) *via* the high-affinity CrA cage and a linker. Biotin binds to the protein avidin as a model target. Real targets could be presented on the cell surface (Figure 1.5b). The remarkable property of this Xe based biosensor is its excellent chemical shift sensitivity of Xe for such binding scenarios. The ^{129}Xe NMR signal shifts accordingly upon formation of the biotin-avidin binding (Figure 1.5c; non-functionalized CrA, functionalized CrA = unbound biosensor, and bound-functionalized CrA = bound biosensor). Moreover, Xe is in continuous exchange (Figure 1.5b; green arrows) between the CrA-bound (blue Xe atom) and free state (gray Xe atom). Although the Xe biosensor concept is promising, and the reported biosensor concentration of 300 µM is about three orders of magnitude lower than what is used by conventional ^{1}H NMR/MRI, it is still considerably high and its ^{129}Xe NMR signal barely above the noise. Applications therefore need a further sensitivity enhancement. This can be achieved through the host-guest system itself.

---

[11] The first cryptophane molecule was described by Gabard and Collet[75]. In this publication it was not called cryptophane but (D_3)-Bis(cyclotriveratrylenyl) macrocage.

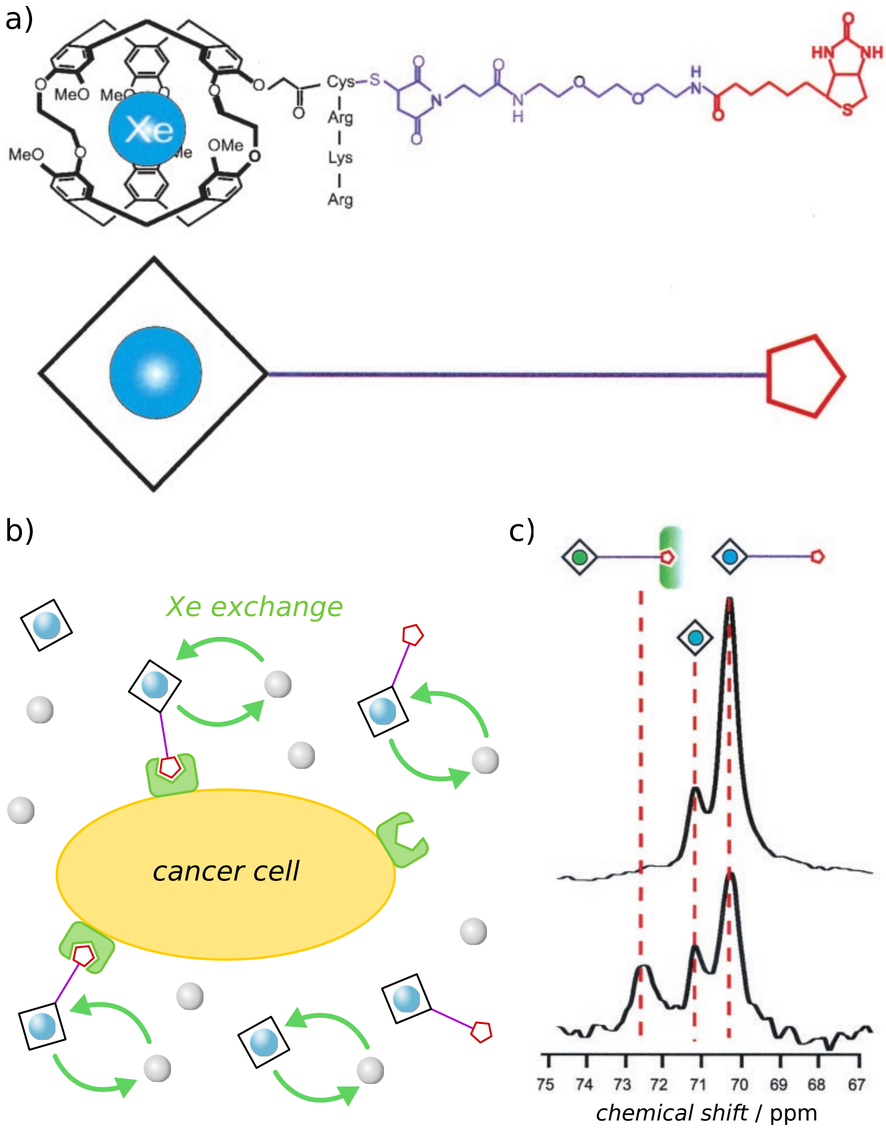

Figure 1.5: Prototype of a Xe biosensor using functionalized Xe *via* the Xe-encapsulating host molecule CrA. a) Design of the Xe biosensor prototype: The molecular cage CrA is connected to the highly specific targeting unit biotin (red) by a tether (purple). A simplified illustration is shown below. b) Illustration of a possible application. Some biosensors bind to cell surface expressed receptors (green), while other biosensors remain unbound. As a reference, non-functionalized CrA may also be added. As Xe dynamically binds to CrA (*i. e.*, Xe resides about 33 ms in CrA in aqueous solution), Xe is in continuous exchange (green arrows) between the CrA-bound (blue Xe atom) and free state in solution (gray Xe atom). c) This corresponds to a highly sensitive chemical shift in the ^{129}Xe NMR spectrum for the different sensor configurations. The upper spectrum is in the absence of the target, and the spectrum below in the presence of it. Figures a) and c) were adapted from Spence *et al.*[198]. Copyright © 2001, National Academy of Sciences, USA.

The Xe-Host: Cryptophane

In order to decrease the Xe biosensor concentration while keeping it detectable by ^{129}Xe NMR, the CrA-bound Xe signal needs to be increased. How this works will be introduced in the following.

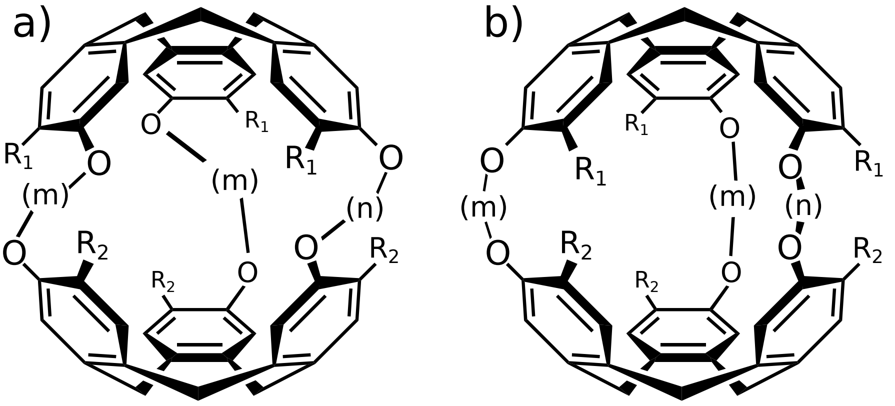

Figure 1.6: Cryptophane structure: *anti* and *syn*. a) *anti*: The O–(m/n)–O bridges (in Table 1.3 summarized by Y), joying two **cyclotriveratrylene** (CTV) units of the same handedness where the $R_{1,2}$ residues display an *anti* relationship results in a chiral *anti* cryptophane (D_3 symmetry). b) *syn*: The bridges, joying two CTV units of opposite handedness where the $R_{1,2}$ residues display a *syn* relationship results in a *syn* cryptophane (C_3 symmetry). Detailed description is given in Table 1.3.

The type of **cryptophane** (Cr) that was used for the Xe biosensor prototype was CrA (Figure 1.5a) [Spence *et al.*[198]]. However, CrA belongs to an entire family of cryptophanes (compare Figure 1.6 and Table 1.3), in which CrA is better known as cryptophane-222 or Cr-222.[12]

Generally, all Cr's consist of two **cyclotriveratrylene** (CTV) units that are connected by three alkoxy groups *via* $(CH_2)_{m/n}$ bridges (Figure 1.6). Thus, the cavity size of Cr can be adjusted by the length of these bridges, which is done by repeating the methylene units ($-CH_2-$) m and n times. Depending on the type of these bridges (diagonal or parallel), Cr's appear in so-called *anti* (Figure 1.6a) and *syn* (Figure 1.6b) configurations. In addition, each CTV unit has three residues $R_{1,2}$ that are natively methoxyl groups (*i.e.*, $R_1 = R_2 =$ MeO). Therefore, native Cr's are hydrophobic and have poor water solubility. However, the residues can be used to make the native Cr's water-soluble, and, moreover, to equip Cr's with specific targeting units (Figure 1.5). Due to symmetric or asymmetric repetitions of the methylene units, Cr's have versatile modification options (compare Table 1.3), with different bound Xe signal intensities.

To increase the ^{129}Xe NMR sensitivity for the detection limit of Cr, it has been shown that a decrease in cavity size changes its binding properties. More specifically, Huber *et al.*[105] demonstrated that water-soluble (*i.e.*, $R_1 = R_2 = CH_2COOH$) *anti* structure Cr's with symmetric (*i.e.*, $m = n =$ [2 or 3]) and asymmetric (*i.e.*, $m \neq n$ [2 or 3]) methylene unit repetitions, resulted in different Cr cavity sizes. The intensity of the bound Xe NMR signal (which correlates with the Xe association or binding constant K_A) increases with decreasing cavity size (Figure 1.7). This experiment confirms that the largest Xe signal intensity was observed for the smallest of the Cr versions under investigation, in this case CrA. The reason why in Figure 1.7 the bound Xe signal to the Cr derivative with the largest cavity **4** is inferior

---

[12] Unfortunately, the reason why exactly cryptophane-222 (Cr-222 or CrA) was chosen in the study by Bartik *et al.*[17] out of many possible Cr versions (Table 1.3) was referred to another publication *"(5) Garcia, C.; Venturo, M.-A.; Antoine, C.; Dutasta, J.-P.; Le Letty, M.; Perrin, M.; Collet, A. To be submitted for publication."* which seems never been published to date.

Table 1.3: Nomenclature for cryptophanes. It appears to be alphabetically ordered with the size of Cr, although **B** is missing, and somewhat historically, since Cr-222, which is attributed to **A**, was published first. The bridge Y mainly determines the size of the Cr by increasing the number of repetitions of the methylene unit $-CH_2-$. The residues $R_{1,2}$ can be used to make the hydrophobic Cr's water-soluble, and, moreover, to equip Cr's with specific binding targeting units (see Figure 1.5). This table is adapted from a book chapter reviewed by Holman[102].

Structure			Name		
Bridges, $-Y-$	R_1	R_2	*anti*	*syn*	Ref.
$3 \times O(CH_2)_1O$	H	H	**111**		[73]
$3 \times O(CX_2)_2O$, where X = H/D	OCX_2	OCX_2	**A = 222**		[76, 33]
$3 \times O(CX_2)_2O$	OCH_2CO_2H	OCH_2CO_2H	**A3**		[43]
$3 \times O(CX_2)_2O$	OCH_2	H	**C**	**D**	[40, 41]
$3 \times O(CH_2)_3O$	OCH_2	OCH_2	**E = 333**	**F**	[42, 39]
$3 \times O(CH_2)_3O$	OCH_2CO_2H	OCH_2CO_2H	**E3**		[77]
$3 \times O(CH_2)_5O$	OCH_2	OCH_2	**O = 555**	**P**	
$3 \times O(CH_2)_5O$	OCH_2CO_2H	OCH_2CO_2H	**O3**		[77]
$2 \times O(CH_2)_2O$, $1 \times O(CH_2)_3O$	OCH_2	OCH_2	**223**		[34]
$1 \times O(CH_2)_2O$, $2 \times O(CH_2)_3O$	OCH_2	OCH_2	**233**		[34]
$2 \times O(CH_2)_2O$, $1 \times O(CH_2)_4O$	OCH_2	OCH_2	**224**		[34]
$2 \times O(CH_2)_2O$, $1 \times O(CH_2)_3O$	OCH_2CO_2H	OCH_2CO_2H	**223**		[105]
$1 \times O(CH_2)_2O$, $2 \times O(CH_2)_3O$	OCH_2CO_2H	OCH_2CO_2H	**233**		[105]
$3 \times O(CH_2)_3O$	OCH_2CO_2H	OCH_2CO_2H	**333**		[105]

lies also in the Xe exchange rate k_{BA} from the Cr-bound state (in the later chapters called pool B) to the free state in solution (in the later chapters called pool A; indicated by the green arrows in Figure 1.5b). This exchange rate k_{BA} is obviously larger for less tight bound Xe atoms. As a result, with increased exchange rate k_{BA} the NMR signal broadens, while the area below the NMR signal (that corresponds to the Cr concentration) is conserved.[13] This means that much lower concentrations of CrA-bound Xe will still give an NMR signal, while that bound to Cr-333 (Xe@**4** in Figure 1.7) is already below the noise level.

Based on these findings, the following straightforward definition of an ideal Xe biosensor applies:

> *"The conditions required for xenon-binding biosensors to be effective for possible* in vivo *applications are as follows:*
>
> A. *a high xenon binding constant (K_A) in biological media;*
>
> B. *slow in-out exchange conditions on the ^{129}Xe NMR time scale, yet sufficient in-out exchange rates to allow optimization of sensitivity by renewal of the host cavity with hyperpolarized xenon;*
>
> C. *adequate longitudinal relaxation times of the bound xenon nucleus; and*
>
> D. *amenity to chemical functionalization."*
>
> — Fairchild *et al.*[70] – 2010

Such a definition was also earlier outlined by Berthault *et al.*[21]. The optimization of the binding constant K_A and the Xe exchange rate k_{BA} gives already a trade-off, as both are related to each other. Therefore, especially points A. and B. are important for ^{129}Xe NMR detection of Xe biosensors, or more specific, for *direct* ^{129}Xe NMR detection.

---

[13] This technical issue will be addressed in Section 2.1.5.

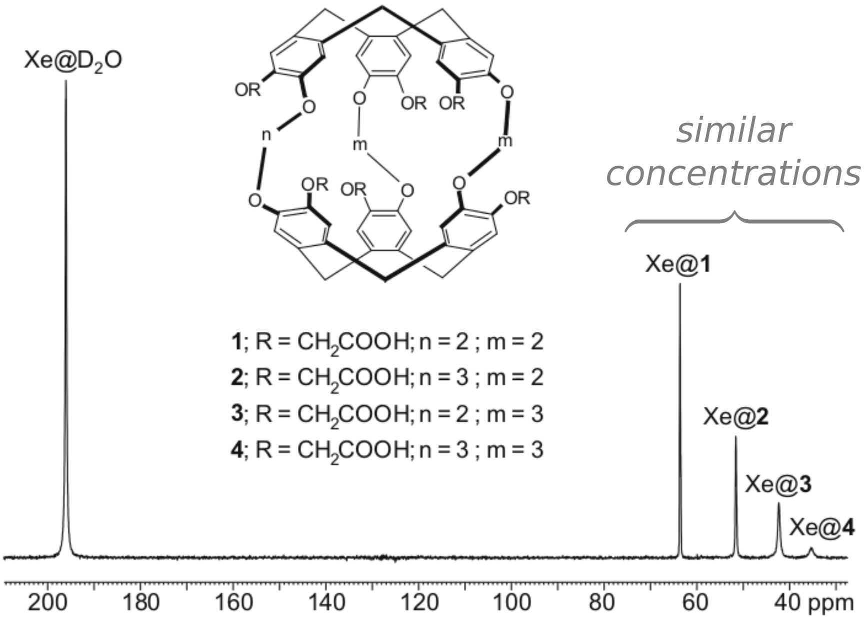

Figure 1.7: Cr cavity size and related ^{129}Xe NMR sensitivity [Huber *et al.*[105]]. ^{129}Xe NMR spectrum of water-soluble (*i. e.*, $R_1 = R_2 = CH_2COOH$) Cr derivatives (with similar concentrations ranging from 500 µM to 740 µM) with symmetric (*i. e.*, $m = n = [2 \text{ or } 3]$) and asymmetric (*i. e.*, $m \neq n$ [2 or 3]) CTV units connecting bridges. Thus, the Cr cavity size increases from derivate **1** → **4**. This study demonstrates that 1) Xe has excellent chemical shift sensitivity for such small structural changes on the host, and 2) the Cr-bound Xe signal increases for smaller cavity sizes. Image adapted from Berthault *et al.*[21]. Reproduced with permission. Copyright © 2009 Elsevier B.V. All rights reserved.

However, as shown in Figure 1.5, the ^{129}Xe NMR signal of the Xe biosensor prototype that used the superior CrA was at a concentration of about 300 µM just above the noise (for realistic measurement times). This concentration is still considerably high for non-toxic biological applications and needed further improvement.

According to Figure 1.7 and to the citation above, the Xe biosensor sensitivity improves by increasing the Xe binding constant K_A, while keeping the minimum necessary Xe exchange rate k_{BA} to refill the used Xe magnetization with fresh HP Xe. Therefore, the design of tailor-made Cr's with huge Xe affinity is a highly active field of research. For example, the CrA decoration with tris(triazole propionic acid)- and triacetic acid-functionalized groups were reported by Hill *et al.*[99] and Hill *et al.*[100], respectively, to demonstrate increase in Xe binding by one order of magnitude for a CrA core. In addition, as demonstrated in Figure 1.7 by Huber *et al.*[105], the Xe binding constant can also be increased by moving to even smaller Cr core sizes than CrA, such as Cr-111 (Table 1.3) and its native and water-soluble congenerics as reported by Fogarty *et al.*[73], Huber *et al.*[104], Chaffee *et al.*[49], Fairchild *et al.*[70], Traore *et al.*[211], Dubost *et al.*[68] and Joseph *et al.*[111]. Also these Cr's showed excellent increase in Xe binding by one order of magnitude, while slowing down the Xe exchange rate k_{BA}, as the core size is smaller. However, the reported sensor concentrations were still in the low µM regime and a further decrease in Cr cavity size might be too tight to bind Xe at all.

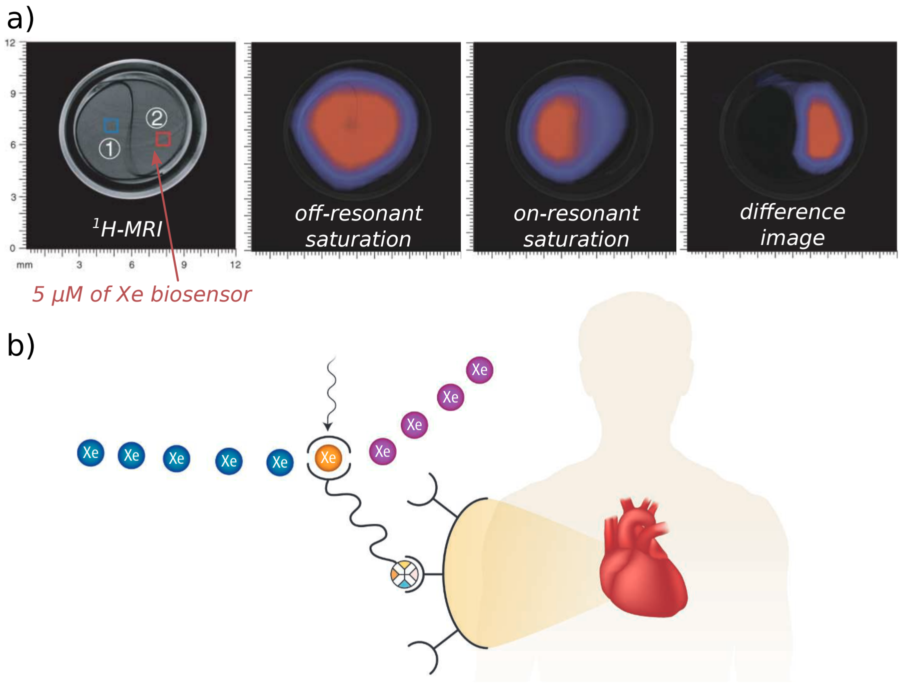

Figure 1.8: Xe Hyper-CEST Biosensor MRI. a) ^{1}H-MRI of a two-compartment phantom. Only compartment 2 contains 5 µM of the biosensor construct. Off-resonant saturation does not deplete the Xe signal. On-resonant saturation on biosensor-bound Xe shows signal depletion at areas where the biosensor is present. The difference image of the off-resonant MR image and the on-resonant MR image reveals an exclusive mapping of compartment 2, *i. e.*, a moleuclar image of the Xe biosensor. Images adapted from Schröder *et al.*[187]. Reprinted with permission. Copyright © 2006, American Association for the Advancement of Science (AAAS). b) A future Xe Hyper-CEST biosensor MRI may visualize molecular binding events in the human body (blue: HP Xe; purple: depolarized Xe; orange: Cr-bound Xe). Illustration from Driehuys[65]. Reprinted with permission from AAAS.

We mentioned above the detection by *direct* ^{129}Xe NMR. We know that – similar to the sensitivity improved *indirect* ^{1}H-CEST method – Xe is in dynamic and continuous exchange between the Cr-bound and unbound state (Figure 1.5b). More specifically, depending on the sensor properties (the cavity size, the electrostatic potential, surrounding solvent, *etc.*) Xe binds to the sensor either with a close to static or dynamic behavior (*i. e.*, Xe's residence time in the small Cr-111 in organic solvent is *ca.* 400 ms [Fogarty *et al.*[73]], in CrA = Cr-222 in aqueous solution *ca.* 33 ms [Spence *et al.*[198]], and in the large Cr-333 in water *ca.* 1 ms [Huber *et al.*[105]]). In order to gain Xe biosensor sensitivity, it is also possible to apply saturation transfer to the Cr-bound Xe signal.

Combined Signal Amplification: Hyperpolarization and Chemical Exchange Saturation Transfer

Schröder *et al.*[187] reported that the dynamic nature of the non-covalent Xe interaction with Cr can be exploited by saturation transfer in order to detect Xe biosensors indirectly by **hyperpolarized Xe detection through CEST** (Hyper-CEST). As this method combines > 20,000-fold signal enhancement by hyperpolarization and 1,000-fold sensitivity enhancement of biosensor-bound Xe NMR signal, it demonstrated for the first time real MR imaging of the Xe biosensor at 5 μM biosensor concentration (Figure 1.8). Therefore, the Hyper-CEST method could become another candidate as possible molecular imaging modality. Nevertheless, the Xe biosensor signal is generated by the difference of two subsequent acquired data sets. This requires very stable and reproducible Xe redeliveries between these measurements, which can be problematic, especially for *in vivo* applications.

1.3 MOTIVATION FOR THIS THESIS

1.3.1 Initial Situation

To motivate the objectives of this thesis, the initial situation when this thesis started in 2011, is described in the following.

The goal of this thesis is the characterization and optimization of saturation transfer NMR with exchanging Xe in different host-guest systems. This requires quantitative knowledge of the Xe exchange kinetics, such as the Xe exchange rate k_{BA}, fraction of host-bound Xe f_B, the Xe-host occupancy β, the Xe binding constant K_A, the chemical shift differences to free Xe $\Delta\delta_{BA}$, and the relaxation times $T_{1,2}^{A,B}$. So-called Hyper-CEST *z*-spectra are relevant to derive these Xe exchange kinetics. However, one point in such a *z*-spectrum is obtained from one ^{129}Xe MR image. When this study started in 2011, the state-of-the-art Hyper-CEST experiment took ~ 11 minutes for each ^{129}Xe MR image (thus ~ 22 minutes to acquire one Hyper-CEST image of the biosensor distribution, with a rather low image resolution of 8 × 8 pixels per field-of-view) [Schröder *et al.*[187]]. Consequently, the acquisition time of an entire *z*-spectrum is therefore very time consuming, using the original implementation. Thus, to achieve the goal of this thesis the objectives were defined as follows.

1.3.2 Objectives of this Thesis

The improvement and characterization of the sensitivity amplification concepts for xenon Hyper-CEST biosensor MRI is conceptually divided into four main objectives. The related literature as well as the achievements for each objective are further described in the corresponding chapters within the results Part III.

Objective 1: Single-Shot Hyper-CEST MRI

The first objective is to accelerate the Hyper-CEST imaging process. Therefore, different Xe MRI pulse sequences and data acquisition strategies have to be tested and compared in order to minimize acquisition time, while maximizing the signal-to-noise ratio of the achieved Xe MR image. Since the Hyper-CEST technique is a difference technique that requires at minimum two data sets, the repeated Xe redeliveries must be very stable and reproducible. This is problematic if the Hyper-CEST method shall be translated into *in vivo* applications and contribute as molecular imaging modality. Therefore, the faster the imaging process of one ^{129}Xe MR image, the less prone would be this Hyper-CEST technique to Xe delivery instabilities. Decreasing the total Hyper-CEST image acquisition time down to several minutes would also enable fast acquisition of entire spatially localized Hyper-CEST *z*-spectra, which can be exploited in the next objective of this thesis.

Objective 2: Quantitative Hyper-CEST MRI

The second objective is to quantify the Xe exchange kinetics at high sensitivity. These exchange kinetics are the Xe exchange rate k_{BA}, fraction of host-bound Xe f_B, the Xe-host occupancy β, the Xe binding constant K_A, the chemical shift differences to free Xe $\Delta\delta_{BA}$, and the relaxation times $T_{1,2}^{A,B}$. Moreover, the host occupancy also remained elusive in previous studies. As different these parameters are, just as well different quantification methods were previously required. Unfortunately, most of these methods fail considering the low concentrations that are desirable for the biosensor approach (*e.g.*, by direct ^{129}Xe NMR). However, Hyper-CEST also provides the potential to derive all these parameters from its spectral dimension, the Hyper-CEST *z*-spectra. Since the Hyper-CEST experiment is a non-linear system in the exchange kinetics and experimental conditions, fundamental Bloch-McConnell modeling [McConnell[146]] for coupled spin systems that exchange magnetization must be used to investigate this objective. In addition and as for every novel quantification method, their correctness as well as their range of validity has to be proven.

Objective 3: Optimal Saturation for Hyper-CEST MRI

As the innovative Hyper-CEST technique takes advantage of saturation pulses, new degrees of freedom in form of the saturation strength and duration provide an entirely new parameter space with potential for improvement and optimization. Therefore, the third objective is to characterize the saturation pulse impact on the Hyper-CEST signal. As such, strategies must be designed and developed that are capable to address this objective. It is unknown how these saturation pulse parameters change the Hyper-CEST signal intensity and how far these can compensate for ultrahigh dilutions of Xe biosensors. Moreover, it would be very useful if such an optimal saturation pulse could be expressed in terms of the Xe exchange kinetics, because this would facilitate a direct prediction of optimal saturation simply after its initial quantification.

Objective 4: High Gas Turnover Hyper-CEST MRI

The Hyper-CEST signal intensity is coupled to the exchange rate and, contrary to the conventional definition of an ideal Xe biosensor as stated above, Hyper-CEST takes advantage of faster exchange rates. The forth objective is to exploit fast Xe exchange rates and larger host occupancies to systematically amplify Hyper-CEST signal intensity. This may be achieved by purposefully changing the Xe-host molecule from CrA to another one. It is entirely unknown how much this exchange rate influences the Hyper-CEST signal quantitatively, and where its optimum is. Care has to be taken what causes the absence of a bound Xe signal in direct ^{129}Xe NMR: Is it indeed no binding or strong binding but paired with rather fast exchange rates.

1.3.3 Structure of this Thesis

This thesis discusses the systematic characterization and optimization of saturation transfer NMR with exchanging Xe in different host-guest systems.

In Part II, the fundamentals of NMR spectroscopy, MRI and Hyper-CEST are briefly introduced as basic tools (Chapter 2). We further outline in Chapter 3 the theoretical models that were used to quantify the Xe-host exchange kinetics. The following Chapter 4 describes the experimental setup.

In the results Part III, the first straightforward approach to amplify the Hyper-CEST signal is by signal averaging which can be exploited by a fast single-shot MR imaging technique, which is discussed in Chapter 5. Other signal amplification strategies can be implemented through the Hyper-CEST itself. However, a deep understanding into the fundamental Hyper-CEST mechanism is required. For that purpose we developed a concept to quantify the Xe exchange kinetics using the ultra-sensitive Hyper-CEST technique, which is provided in Chapter 6. As a direct application, the next Chapter 7 takes advantage of the quantified Xe exchange kinetics and studies in detail the impact of a saturation pulse to maximize Hyper-CEST signal intensity. In addition, Chapter 8 highlights a further fundamental Hyper-CEST amplification question by identifying a CrA alternative 1:1 Xe-host complex that is inherently able to provide amplified Xe gas turnover rates, and hence, Hyper-CEST signal intensity.

Finally, we provide within Part IV the conclusion and outlook of further applications of the achievements made available within this thesis.

Part II

Background, Theory & Experimental Setup

2 FUNDAMENTALS

Contents

In this chapter, we will briefly introduce the fundamentals of NMR, MRI and Hyper-CEST as it is used for this thesis. It will be shown that NMR can provide quantitative data which is one of the main key strength of NMR based techniques related as molecular imaging modality. Section 2.1 and Section 2.2 follow to some extent the presentations in de Graaf[83], Levitt [132], and Liang[135]. Please refer to these books for more comprehensive information.

2.1 PRINCIPLES OF NUCLEAR MAGNETIC RESONANCE

In 1922, Otto Stern and Walter Gerlach reported that a beam of silver atoms splits into two discrete lines when traveling through an inhomogeneous magnetic field [Gerlach and Stern[80], Gerlach and Stern[79]]. This demonstrated for the first time the experimental proof for the concept of quantization of space. The interaction between an external magnetic field and the particle property is called spin and the fundamental requirement for MR. In 1943, Otto Stern was awarded the Nobel Prize for his contribution to the development of the molecular ray method and his discovery of the magnetic moment of the proton. Shortly afterwards in 1946, the nuclear induction was independently described by Bloch *et al.*[26] and Purcell *et al.*[166]. In 1952, both were awarded jointly the Nobel Prize in Physics for their elementary contribution.

2.1.1 Nuclear Spin

The spin of the nucleus of an atom is the total angular momentum, $\vec{J}$, which is the sum of the spins, $\vec{s}_i$, and angular momentums, $\vec{l}_i$, of the total number of nucleons, N_n:

$$\vec{J} = \sum_{i=1}^{N_n} (\vec{s}_i + \vec{l}_i) \quad . \tag{2.1}$$

It follows the quantum mechanic rule of the addition of angular momentums. The magnitude of the nuclear spin, $|\vec{J}|$, is quantized by

$$|\vec{J}| = \hbar\sqrt{I\,(I+1)} \quad , \tag{2.2}$$

where $\hbar = h/(2\cdot\pi)$ is the reduced Planck's constant and I is the spin quantum number. Since the nucleons are the positively elementary charged protons and uncharged neutrons both have the spin quantum number $1/2$ and integers as angular momentum numbers. Depending on the number of nucleons N_n which is either even or odd, the nuclear spin is either integer or half-integer.[1] The nucleus of hydrogen, ^{1}H , consists of only one proton, thus, N_n is odd and its nuclear spin is half-integer, I(^{1}H) = $1/2$. The nucleus of the xenon isotope, ^{129}Xe , has 54 protons and 75 neutrons. Thus, N_n is odd, its nuclear spin is half-integer, and sums up to the total nuclear spin of I(^{129}Xe) = $1/2$. With the nuclear angular momentum, $\vec{J}$, the spinning charge distribution produces the vectorial nuclear magnetic dipole moment or magnetic moment, $\vec{\mu}$, that is fundamentally related with the angular momentum by the Wigner–Eckart symmetry theorem to

$$\vec{\mu} = \gamma\,\vec{J} \quad . \tag{2.3}$$

This is illustrated in Figure 2.1a. The ratio of the nuclear magnetic moment to the angular momentum is known as gyromagnetic ratio, γ, which is unique for each nucleus (see Table 1.2). As this magnetic moment interacts with external magnetic fields, the study of matter within external magnetic fields enables to achieve information about the atomic environment of such nuclear spins.

2.1.2 Macroscopic Thermal Magnetization

The full wavefunction $|\psi_{\text{full}}(t)\rangle$, which contains all the informations of the positions, velocities, and spin states of all electrons and nuclei within the macroscopic sample, is fully described by the Hamiltonian $\hat{\mathcal{H}}_{\text{full}}$. However, it cannot be solved in any realistic situation. Therefore, NMR makes the (convenient) simplification of describing only the nuclear spin states, $|\psi_{\text{spin}}(t)\rangle$, by the Schrödinger equation

$$\frac{d}{dt}\,|\psi_{\text{spin}}(t)\rangle \cong -i\,\hat{\mathcal{H}}_{\text{spin}}\,|\psi_{\text{spin}}(t)\rangle \quad . \tag{2.4}$$

---

[1] More specifically, the value of nuclear spin quantum number, I, can be deduced by the following three rules: 1) nuclei with an odd mass number have half-integral spin (*i. e.*, I = 1/2, 3/2, 5/2, . . .), 2) nuclei with an even mass number and an even charge number have zero spin (*i. e.*, I = 0), and 3) nuclei with an even mass number but odd charge number have integral spin (*i. e.*, I = 1, 2, 3, . . .) [de Graaf[83]].

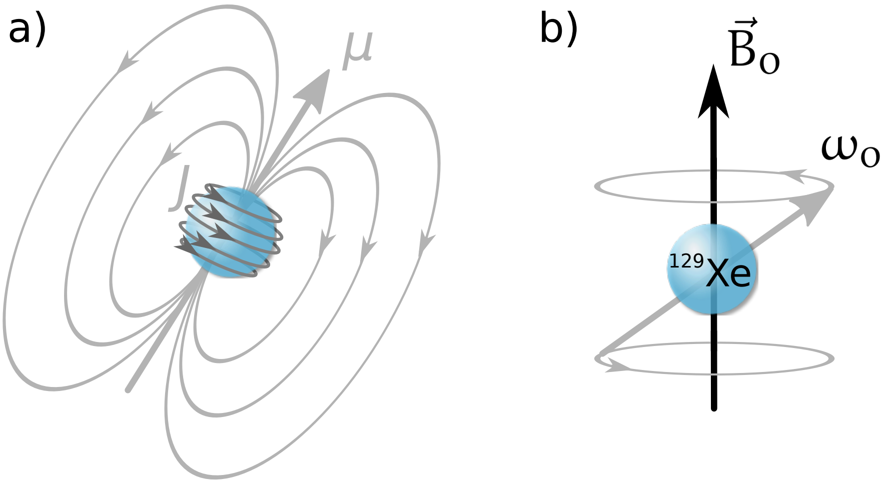

Figure 2.1: a) Illustration of nuclear spin with total angular momentum, $\vec{J}$, its magnetic moment $\vec{\mu}$, and its induced magnetic field lines. The ratio of magnetic moment to total angular momentum is known as gyromagnetic ratio. b) The magnetic moment $\vec{\mu}$ for a spin-1/2 nucleus (such as ^{129}Xe) that is placed into an external magnetic field produces two discrete energy states. Nuclei with negative gyromagnetic ratio such as ^{129}Xe precess with Larmor frequency, ω_0, anticlockwise as seen when looking against the direction of $\vec{B}_0$.

This simplification is known as the spin Hamiltonian hypothesis. The spin Hamiltonian for each individual spin, i, is abbreviated by $\hat{\mathcal{H}}_{\text{spin}} = \hat{\mathcal{H}}_i$, and contains all external and internal spin interactions. For spin-1/2 nuclei, both the external interactions (generated from the apparatus, *i. e.*, by the static external magnetic field $\vec{B}_0$, and the RF field), and the internal interactions (*i. e.*, generated from the sample) are purely magnetic.[2] Therefore, the total spin Hamiltonian for ^{1}H and ^{129}Xe (both spin-1/2 nuclei) for each spin considering only magnetic contributions sums up to

$$\hat{\mathcal{H}}_i = \hat{\mathcal{H}}_{i,\text{mag,ext}} + \hat{\mathcal{H}}_{i,\text{mag,int}} \quad . \tag{2.5}$$

The largest interaction comes from large external magnetic fields ($\hat{\mathcal{H}}_{i,\text{mag,ext}} > \hat{\mathcal{H}}_{i,\text{mag,int}}$), in particular, from the static magnetic induction field, $\vec{B}_0$ [Levitt [132]]. We therefore simplify and examine the external magnetic spin Hamiltonian $\hat{\mathcal{H}}_{i,\text{mag,ext}}$ in the following.

Without loss of generality we choose the external magnetic field induction field, $\vec{B}_0$, from now on and throughout the whole thesis to point into the z-direction ($\vec{B}_0 = \{0, 0, B_0\}^T$). Consequently, the external magnetic spin Hamiltonian for each spin, i, in interaction with the static external magnetic field, $\vec{B}_0$, is given by

$$\hat{\mathcal{H}}_i = -\gamma_i \, \vec{B}_0 \cdot \vec{J}_i = -\gamma_i \, B_0 \cdot J_{i,z} \quad , \tag{2.6}$$

which yields for all spins in the sample,

$$\hat{\mathcal{H}} = \sum_i \hat{\mathcal{H}}_i \quad . \tag{2.7}$$

---

[2] For spins with $I > 1/2$, electric multipoles have also taken into account.

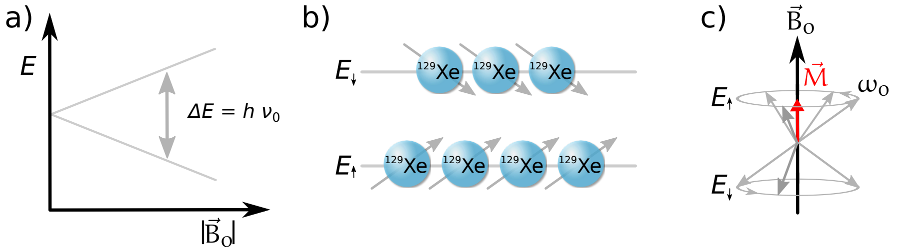

Figure 2.2: a) Zeeman-splitting of the spin-1/2 nucleus ^{129}Xe within a static magnetic field, $|\vec{B}_0|$. b) Illustration of ^{129}Xe occupied energy levels at thermal equilibrium given by the Boltzmann distribution with a small population difference. c) Larmor frequency, ω_0, precessing magnetic moments within the vectorial external magnetic field, $\vec{B}_0$. Summation over all randomly precessing vectorial magnetic moments yields the macroscopic magnetization, $\vec{M}$ (red).

Thus, only the z-components of the angular momentum and the magnetic moment are significant and, moreover, quantized along the longitudinal z-direction by

$$\mu_z = \gamma\, J_z = \gamma\, \hbar\, m \quad . \tag{2|8}$$

Here, m is the so-called magnetic quantum number. Thus, m has (2I + 1) values that range from m = -I, -I+1, -I+2, ..., I-1, I. Since both, ^{1}H and ^{129}Xe, are nuclei with nuclear spin quantum number I = 1/2, the magnetic quantum number, m, can either be $-1/2$ and $+1/2$. The nucleus acquires the magnetic energy

$$E = -\mu_z \cdot B_0 = -\gamma\, \hbar\, m \cdot B_0 = \begin{cases} E_\uparrow = -\frac{1}{2}\gamma\, \hbar\, B_0 & \text{for } m = +1/2 \\ E_\downarrow = +\frac{1}{2}\gamma\, \hbar\, B_0 & \text{for } m = -1/2 \end{cases} \tag{2|9}$$

for spins in the low-energy state (or referred to pointing-up spin state), $E_\uparrow$, and spins in the high-energy state (or pointing-down spin state), $E_\downarrow$, spins. The system is characterized by an energy difference of

$$\Delta E = E_\downarrow - E_\uparrow = \gamma\, \hbar \cdot B_0 \quad , \tag{2|10}$$

which is known as Zeeman-splitting [Zeeman[246]] (Figure 2.2a). For this contribution Pieter Zeeman and his advisor Hendrik Antoon Lorentz were jointly awarded the Nobel Prize in Physics in 1902. Transitions between these Zeeman levels are induced by the application of an oscillating magnetic field perpendicular to μ_z with a frequency, ν_0, such that the energy equals the magnetic energy difference

$$\Delta E = h\, \nu_0 \quad , \tag{2|11}$$

or in terms of the frequency

$$\nu_0 = \frac{\gamma}{2\pi} B_0 \quad . \tag{2|12}$$

The discovery of NMR was reported by Isidor Isaac Rabi *et al.*[167], using an oscillating magnetic field to induce nuclei to flip their magnetic orientation. In 1944, he received for this discovery the Nobel Prize in Physics.[3] Equation (2 | 12) is known as the Larmor frequency. The Larmor frequency in Hz (*i. e.*, $\omega_0 = 2\pi \cdot \nu_0$) for ^{1}H at a magnetic field strength of $|\vec{B}_0| = 9.4$ T as used in this thesis is about 400 MHz, whereas the Larmor frequency for ^{129}Xe is $\omega_0 = -110$ MHz (compare with Table 1.2) which are both in the RF regime. Moreover, each nuclear spin precesses with this Larmor frequency clockwise (for $\gamma > 0$ such as ^{1}H) or anticlockwise (for $\gamma < 0$ such as ^{129}Xe) as seen when looking against (or anti-parallel with) the direction of $\vec{B}_0$ (Figure 2.1b). The irradiation of an RF field with the Larmor frequency, $\omega_0 = 2\pi\nu_0$ (in Hz), causes a coupling of the spin to the RF field that inverts the spin orientation into the new energy state.

Unfortunately, $\vec{\mu}$ is too small to be detected as individual unit by Faraday's law of induction. A macroscopic sample within a magnetic field, however, contains an Avogadro number of spins (10^{23}) that are a collection of independent, identical systems, the so-called spin ensemble. Upon measurement, each spin of this ensemble occupies either the low-energy state or the high-energy state. This population difference is given by the Boltzmann distribution

$$\frac{N_\uparrow}{N_\downarrow} = \exp\left(\frac{\Delta E}{k_B T}\right) \approx 1 + \left(\frac{\Delta E}{k_B T}\right) \tag{2 | 13}$$

where $N_\uparrow$ and $N_\downarrow$ are the number of spins in the low-energy state and high-energy state, respectively, k_B is the Boltzmann constant and T the absolute temperature (Figure 2.2b). For room temperature, the thermal energy is much larger than the Zeeman splitting energy, $k_B T \gg \Delta E$, and the last approximation in Equation (2 | 13) was Taylor series expanded and truncated. Due to the population difference, a total net magnetic moment, $\vec{M}$, adds up as summation over all individual magnetic moments, $\vec{\mu}$. Consequently, the amplitude of the macroscopic magnetization component that is parallel to $\vec{B}_0$, is given by [de Graaf[83]]:

$$M_{th} = (\gamma \hbar)^2 N \frac{|\vec{B}_0|}{4k_B T} \quad , \tag{2 | 14}$$

where $N = N_\uparrow + N_\downarrow$ is the total number of nuclear spins within the sample (Figure 2.2c). To exemplify, in a macroscopic sample of protons, ^{1}H, at physiological temperature of 37 °C (T ~ 310 K) within a magnet field of 9.4 T, only 31 out of one million spins build up the difference in population [de Graaf[83]] (Figure 2.2b and c). This is where the rather low sensitivity of NMR originates from (see Table 1.1). To overcome this intrinsic limitation in sensitivity, techniques that push the population difference far beyond Boltzmann distribution or thermal polarization can be used to obtain a so-called HP spin system (Figure 2.3).

---

[3] The Dutch physicist Cornelius J. Gorter was proposing this idea one year earlier, but he was not able to observe this effect due to experimental limitations. Gorter is therefore known as the man who almost discovered NMR.

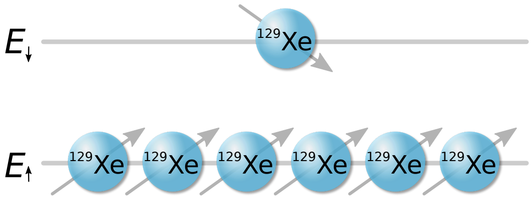

Figure 2.3: Illustration of the energy level occupancy of a hyperpolarized ^{129}Xe spin-1/2 system.

2.1.3 Hyperpolarization

Generally, the polarization P of a spin-1/2 system is given by [Witte and Schröder[233]]:

$$P_{th} = \frac{N_\uparrow - N_\downarrow}{N_\uparrow + N_\downarrow} = \tanh\left(\frac{\gamma \hbar B_0}{2 k_B T}\right) . \qquad (2|15)$$

For the example above, the population difference of 31 proton spins out of a million causes a small polarization of 0.0031 %. However, inspection of Equation (2|15) directly suggests that two *"brute force"* methods exist to achieve a strong polarization,

$$P_{HP} = \eta P_{th} \quad , \qquad (2|16)$$

where η is the signal enhancement factor by hyperpolarization. This can be obtained by either 1) the use of larger magnetic fields, $B_0 \gg 10$ T, or 2) to cool down the sample temperature close to 0 K. To achieve a significant increase in polarization, magnetic field strengths as they arise on neutron stars would be required which is impracticable. Also sample cooling below liquid helium temperature, *i. e.*, < 4 K, is unrealistic to perform in clinics as molecular imaging modality.

A more elegant way is to manipulate another spin system first and then transfer this polarization onto the nucleus of interest. Various hyperpolarization methods exist, including **dynamic nuclear polarization** (DNP; first reported by Overhauser[161]), ***para*-hydrogen-induced polarization** (PHIP; theoretically predicted by Bowers and Weitekamp[32] and later experimentally confirmed by the same authors [31]) or SEOP [Walker and Happer[223], Goodson[82]]. An overview of these methods and their reported maximal polarization is given in Table 2.1.[4] Although SEOP is limited to noble gases, it has been shown to achieve the highest polarization with up to 70 % and should be able to approach also the 100 % limit. Regarding biological applications, SEOP has already been demonstrated for mouse lung and heart ^{129}Xe MR imaging [Albert *et al.*[8], Driehuys *et al.*[66]] and can greatly be combined with Xe biosensors, since Xe can be trapped into other molecules. Thus, SEOP was used in this thesis.

The SEOP process consists of two steps. The first step is the production of highly polarized atoms with a 2S or 3S valence (such as the alkali metals) by optical pumping. In a second step, this polarization becomes transfered *via* spin-exchange from such optically pumped atoms onto the nucleus

---

[4] The theoretical limit of DNP is given by the Bohr magneton, μ_B, and the gyromagnetic ratio, γ, of the nucleus under investigation. A polarization of 100 % is in principle not possible.

Table 2.1: Overview of hyperpolarization methods. This Table is adapted from Witte and Schröder[233].

Method	Acting Nucleus	Reported max. Polarization
DNP	all	64 %
PHIP	*via* ^{1}H onto ^{13}C, ^{19}F,...	30 %
SEOP	all noble gases, mostly Xe	60 – 70 %

of ^{129}Xe.[5] In 1966, Alfred Kaster was awarded the Nobel Prize in Physics [Happer[92]] for his fundamental work on optical pumping and the discovery and development of optical methods for studying Hertzian resonances in atoms [Kastler[113]].

Optical Pumping of Rubidium

We use the alkali metal **rubidium** (Rb). We vaporize Rb within an optical pumping cell by heating (see Chapter 4 for experimental details). This pumping cell is placed inside a small (mT range), and homogeneous magnetic field to generate Zeeman-splitting of the Rb atoms (ground state: 5^2S, and excited state: 5^2P; see $m_{S,P} = \pm 1/2$ in Figure 2.4). The advantage of using Rb is that commercially available pre-assembled and powerful LASERs with narrow line profile exist for its D1 transition. The Rb vapor is irradiated with circularly polarized LASER light that is tuned to the Rb D1 transition from $5^2S_{1/2} \rightarrow 5^2P_{1/2}$ (*i.e.*, the energy difference of the excited state to the ground state corresponds to a wave length of $\lambda = 794.7$ nm [Walker and Happer[223]]). The left-circularly polarized LASER light excites Rb atoms

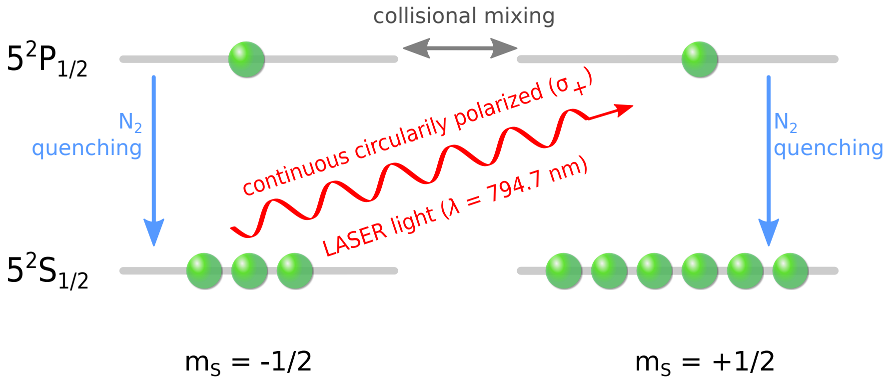

Figure 2.4: Principle of optical pumping of vaporized Rb atoms within a small, but homogeneous magnetic field. Only Rb atoms in the $m_S = -1/2$ ground state couple to left-circularly polarized LASER light that is tuned to the Rb D1 transition $5^2S_{1/2} \rightarrow 5^2P_{1/2}$. This includes a spin flip, $m_P = +1/2$. Due to collisional mixing within the gas, both excited sub-levels become rapidly, equally populated, $m_P = \pm 1/2$, before they equally relax radiation free into the ground state. This is caused by N_2 quenching. Since the circular polarized LASER light is still selectively depopulating the $m_S = -1/2$ ground state, a large overpopulation is achieved for the $m_S = +1/2$ state, resulting in highly polarized Rb atoms. This figure is adapted from Walker and Happer[223].

---

[5] A comprehensive description about optically pumped atoms is further provided by Happer *et al.*[93].

with spin-down sub-level m_S = - 1/2 of the ground state into the spin-up sub-level m_P = + 1/2 of the excited state because of the quantum-mechanical selection rule $\Delta m = 0, \pm 1$. Due to collisions within the gas, both spin sub-levels in the excited state equally populate rapidly, $m_P = \pm 1/2$. Both ground state sub-levels become repopulated with almost equal probability *via* non-radiative N_2 quenching.[6] Since the circular polarized LASER light is still continuously depopulating selectively the m_S = - 1/2 sub-level in the ground state, a large overpopulation for the m_S = + 1/2 state is achieved. Over time, this results in a nearly 100 % spin polarization of the Rb atoms [Walker and Happer[223]].

Spin-Exchange to the Xe Nucleus

In a second step, the so-called spin-exchange, this large polarization of the Rb atoms is transfered to the nucleus of ^{129}Xe through spin-exchange collisions. Two processes contribute to this spin-exchange: 1) van der Waals interaction in short-lived (*i. e.*, ~ 1 ns) Rb-^{129}Xe-N_2 clusters and 2) binary Rb-^{129}Xe collisions. While the first spin-exchange contribution from van der Waals interactions of the Rb-^{129}Xe-N_2 clusters becomes dominant for low gas pressures [Walker and Happer[223]], it can be neglected at large pressures, as it was performed in this thesis (*i. e.*, 3.5 bar overpressure). Therefore, the major contribution of the spin-exchange process comes from binary Rb-^{129}Xe collisions. During such binary collisions, there is a small probability that the wave function of Rb penetrates that of the ^{129}Xe atom to the nucleus wave function. A spin flip of both, the Rb electron and the ^{129}Xe nucleus, is caused through Fermi-contact hyperfine interaction while transferring angular momentum from the Rb valence electron to the ^{129}Xe nucleus [Walker and Happer[223]]. Although, the probability for such an interaction is rather small, the large production of HP ^{129}Xe gas under continuous flow mode (up to 0.3 liter/h) with 64 % polarization was reported by Ruset *et al.*[176]. In addition, our custom-designed SEOP Xe polarizer (details will be given in Chapter 4) partly developed and used in this thesis produces a Xe polarization of 25 % under continuous Xe gas flow of *ca.* 0.5 **standard liter per minute** (SLM). This results in a signal enhancement factor, η, of about 25,000 compared to thermally polarized ^{129}Xe as reported by Witte *et al.*[231], providing a large macroscopic net magnetization $\vec{M}$.

In summary, the macroscopic net magnetization, $\vec{M}$, points parallel to the external magnetic field, $\vec{B}_0$, and is proportional to 1) concentration of nuclei, 2) gyromagnetic ratio, and 3) the (hyper-) polarization.

2.1.4 The NMR Signal

Experiments show that any disturbance of the macroscopic net magnetization away from the $\vec{B}_0$ magnetic field axis causes this macroscopic magnetization to realign (or to relax back) to this axis with an exponential behavior. At the same time, the generated transverse component decays. This process can be observed through Faraday induction with the coils placed perpendicular to the magnetic field. The time-dependent behavior of the thermally polarized or HP magnetization, $\vec{M}(t)$, within an arbitrary magnetic field in

---

[6] The excited Rb atoms transfer energy into rotational and vibrational motion on N_2 which causes a non-radiative decay. This is important as otherwise other excited Rb atoms could be stimulated to decay by the emitted photon.

time, $\vec{B}$, which points without loss of generality into the z-direction was empirically described by Bloch[25] and is given by the following so-called Bloch equations

$$\frac{dM_x(t)}{dt} = \gamma\,(\vec{M}(t) \times \vec{B})_x - \frac{M_x(t)}{T_2} \tag{2 | 17a}$$

$$\frac{dM_y(t)}{dt} = \gamma\,(\vec{M}(t) \times \vec{B})_y - \frac{M_y(t)}{T_2} \tag{2 | 17b}$$

$$\frac{dM_z(t)}{dt} = \gamma\,(\vec{M}(t) \times \vec{B})_z - \frac{M_z(t) - M_{th}}{T_1} \quad . \tag{2 | 17c}$$

Whereas the cross-product describes the precession of $\vec{M}$ about $\vec{B}$, the longitudinal magnetization component, M_z, recovers with the so-called longitudinal relaxation time, T_1, while both transverse magnetization components, M_x and M_y, decrease in time with the so-called transverse relaxation time, T_2. As a consequence, the total net magnetization, $\vec{M}$, relaxes back to align with the main magnetic field axis, $\vec{B}$, for $t \to \infty$. Its amplitude is solely given by the magnetic field strength and sample temperature, T, thus, the thermally polarized magnetization, M_{th} (see the green highlighted term in Equation (2 | 17c)).

The origins of these different relaxation mechanisms are described in the following. Note that for pure transverse relaxation with the time constant, T_2, it was assumed that the main magnetic field that is experienced by each spin within the sample is constant. This is an idealization. There is, however, on top of pure T_2 relaxation another and faster so-called apparent transverse relaxation time, T_2^*, as described in the following.

LONGITUDINAL RELAXATION TIME, T_1: The longitudinal relaxation time (or spin-lattice relaxation time) describes the return of longitudinal magnetization after a perturbation. This process is characterized by a transfer of energy from the spins to the surrounding *"lattice"* which can be either both solid or liquid.

TRANSVERSE RELAXATION TIME, T_2: The transverse relaxation time (or spin-spin relaxation time) is the characteristic disappearance of transverse magnetization. This relaxation is an entropy-process because spins interact between themselves causing an increased loss in phase coherence.

APPARENT TRANSVERSE RELAXATION TIME, T_2^*: Inhomogeneities in the external static magnetic field, $\vec{B}_0$, cause a locally varying $\vec{B}_0$ distribution across the sample with accordingly distributed Larmor frequencies. Thus, the loss of phase coherence during precession is even more increased as caused by pure T_2 relaxation. This is the so-called apparent T_2 relaxation time, T_2^*.

For the same nuclei, the relaxation times differ between different chemical environments and in different external fields and temperatures (Table 2.2). In addition, they differ between different nuclei (Table 2.2) and are therefore important measurement parameters for NMR and MRI.

Table 2.2: Overview of the large differences in longitudinal and transverse relaxation times, T_1 and T_2, between ^{1}H and ^{129}Xe nuclei. As typically $T_1 \geqslant T_2$, the order of magnitude (or trend) of the not reported values (indicated by a dash -) can be estimated to some extent.

Nucleus	Environment	T_1	T_2
^{1}H	cerebrospinalfluid	~ 4 s [69]	~ 2 s [69]
	gray matter	~ 1.1 s [69]	~ 88 ms [69]
	white matter	~ 700 ms [69]	~ 65 ms [69]
^{129}Xe	solid phase	~ 7 days [78]	-
	gas phase	hours [52]	-
	blood	~ 10 s [53, 9]	-
	PFOB [a)]	long [22, 236]	15 s [235]
	intralipid	40 s [22]	-
	water	> 100 s	5 s [160, 252]

[a)] **Perfluoroctyl bromide** (PFOB) nano droplets.

Experimental disturbances of $\vec{M}$ are achieved on purpose by irradiation of a magnetic RF field – a so-called RF pulse – perpendicular to $\vec{B}_0$ with Larmor frequency

$$\omega_0 = \gamma\,|\vec{B}_0| \ , \tag{2|18}$$

amplitude $|\vec{B}_1(t)|$, and for a specific pulse length PL *via* the RF coils (used in transmitter mode; see Figure 2.5). This on-resonant condition causes the pulse to interact with the macroscopic magnetization, $\vec{M}$, and to induce a well defined rotation of the macroscopic magnetization with a particular flip angle given by

$$\alpha(t) = \gamma \int_0^{PL} |\vec{B}_1(t)|\,dt \tag{2|19}$$

that is shown in Figure 2.5a for $\alpha = 90°$. After the pulse irradiation is finished, $\vec{M}$ relaxes back to thermal equilibrium (red trajectory). The transverse components of the rotating magnetization induce then a measurable alternating current through Faraday induction in the RF coils (now used in receiver mode; Figure 2.5a and b). This is the typical NMR signal (Figure 2.5b), the so-called **free induction decay** (FID) as $\vec{M}$ precesses freely. Since the transverse components of the magnetization, M_x and M_y, are recorded, it is instructive to define the transverse components of the magnetization with real and imaginary part as

$$M_\perp = M_x + i\,M_y \ , \tag{2|20}$$

which simplify the Bloch equations (Equation (2|17a)) to (Equation (2|17c)) to

$$\frac{dM_\perp(t)}{dt} = -\left(i\,\omega_0 + \frac{1}{T_2}\right)\cdot M_\perp(t) \tag{2|21a}$$

$$\frac{dM_z(t)}{dt} = \frac{M_{th} - M_z(t)}{T_1} \ . \tag{2|21b}$$

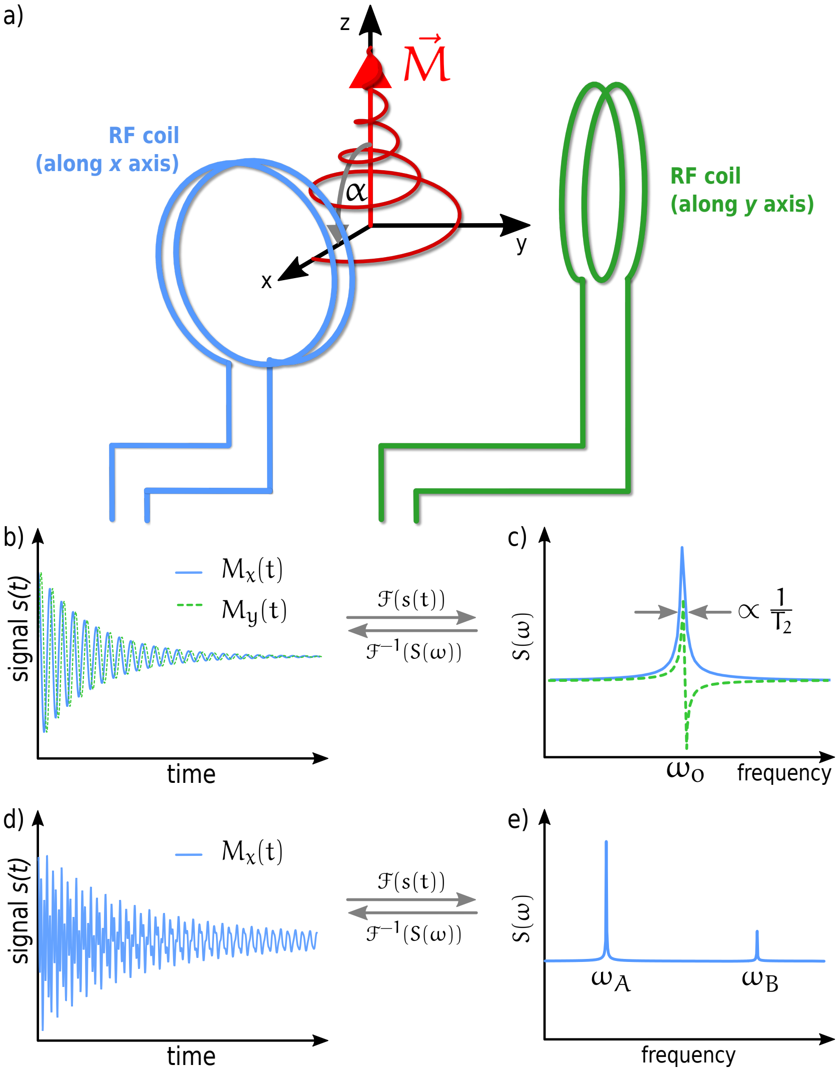

Figure 2.5: Free induction decay and related NMR spectrum. a) The time-behavior of the magnetization, $\vec{M}$, under relaxation shows a mono-exponential relaxation to thermal equilibrium (red curve corresponds to the tip of $\vec{M}$). This is recorded by Faraday's law of induction using two orthogonally placed RF coils. b) The typically recorded NMR signal is a **free induction decay** (FID) that consists of a real ($M_x(t)$ component; blue solid line) and an imaginary part ($M_y(t)$ component; green dashed line). The FID decays exponentially with the transverse relaxation time, T_2. c) The frequency spectrum of the FID, which is obtained by FT, shows real (blue solid line) and imaginary (green dashed line) part with one resonance at the Larmor frequency, ω_0. The total area below the peak is related to the spin ensemble size. The full width at half-maximum is proportional to the transverse relaxation time, T_2. As the FT is a reversible operation, the inverse FT of the NMR spectrum, $\mathcal{F}^{-1}$, yields back the FID. d-e) FID and FT for two different spin ensembles (summarized to so-called spin pools, pool A and pool B) that are resonating at its own Larmor frequency, ω_A and ω_B (only the real part is shown for better illustration).

This is now given in the rotating frame to omit the cross product terms. This system has the solutions

$$M_\perp(t) = M_{\perp,0} \cdot e^{-\left(i\,\omega_0 + \frac{1}{T_2}\right)\cdot t} \tag{2|22a}$$

$$M_z(t) = M_{z,0} \cdot e^{-\frac{t}{T_1}} + M_{th} \cdot \left(1 - e^{-\frac{t}{T_1}}\right) \quad . \tag{2|22b}$$

Here, $M_{\perp,0}$ and $M_{z,0}$ are the initial transverse and longitudinal magnetization components of $\vec{M}$, at the onset of relaxation, *i. e.*, immediately after the RF pulse. However, for $t \to \infty$ (which is commonly assumed for $t \geqslant 5 \cdot T_1$) the magnetization approaches thermal polarization, M_{th}, which is given by the magnetic field strength, $|\vec{B}_0|$, and temperature, T, according to Equation (2 | 14). Thus, the system is not hyperpolarized anymore.

Typically, two RF transmitter/receiver coils are used in an NMR experiment. They are orthogonally placed by each other in such a way that one coil is recording the x-component while the second coil acquires the y-component of the transverse magnetization, $M_\perp$, (Figure 2.5a). Mathematically, this is treated as real and imaginary part of $M_\perp$, respectively. Using Equation (2 | 22a), the measured FID is then (as illustrated in Figure 2.5b)

$$s(t) \propto M_{\perp,0} \cdot \overbrace{e^{-i\,\omega_0\,t}}^{\text{oscillation}} \cdot \underbrace{e^{\frac{t}{T_2}}}_{\text{exponential envelope}} \quad . \tag{2|23}$$

By exponential sine and cosine fitting of the measured FID in Figure 2.5b, one can identify the frequency components that were contained within the measured FID signal. For complicated FID structures, containing, however, multiple frequencies, relaxation times and amplitudes, this becomes an impracticable task. A sophisticated FID analysis is provided by the FT, $\mathcal{F}(s(t))$, which is at the heart of todays NMR techniques. The FT in combination with NMR FID analysis was investigated by Richard R. Ernst in Palo Alto in California in 1966. It underpins applications for high-resolution NMR and medical MRI as we know it today, and he was awarded the Nobel Prize in Chemistry in 1991 for this achievement [Alger[10]]. The FT of Equation (2 | 23) yields

$$S(\omega) \propto \mathcal{F}(s(t)) = \frac{M_{\perp,0} T_2}{1 + (\omega - \omega_0)^2 T_2^2} + i \left(\frac{M_{\perp,0} (\omega - \omega_0)^2 T_2^2}{1 + (\omega - \omega_0)^2 T_2^2} \right) \quad , \tag{2|24}$$

which is the so-called NMR spectrum that is typically evaluated. The NMR spectrum in Figure 2.5c shows one spin ensemble resonating at the Larmor frequency ω_0, where the line width is proportional to the transverse relaxation time, $1/(2\,\pi\,T_2)$, and the area of the line shape corresponds to the initial spin magnetization, $M_{\perp,0}$. This demonstrates one of the main strength of NMR based techniques as molecular imaging modality, which is providing quantitative data. As the FT is a linear operation, this requirement is matched. Furthermore, the FT is a reversible operation, which means that the inverse FT of the NMR spectrum, $\mathcal{F}^{-1}(S(\omega))$, yields back the FID (Figure 2.5b and c).

Chemical Shift in NMR

The NMR technique would not be a frequently used spectroscopy method if each nucleus albeit with different gyromagnetic ratios at the same static main magnetic field, $\vec{B}_0$, would resonate at the same frequency. Fortunately, the same type of nuclei is highly sensitive to its chemical environment. This is the so-called chemical shift sensitivity. As the Larmor frequency depends on the net magnetic field strength (Equation (2 | 18)) at the site of each nucleus, the chemical shift originates from shielding or deshielding of nuclei from the external magnetic field, $\vec{B}_0$, by surrounding electrons. Consequently, nuclei at different positions within the same molecule can show different chemical shifts in their NMR signal. In particular, the large and flexible electron cloud of the noble gas ^{129}Xe causes an efficient shielding and deshielding of the magnetic field that experiences the Xe nucleus [Goodson[82]]. By introducing a shielding constant, σ, the net magnetic field, $\vec{B}_{\mathrm{net}}$, on the nucleus after shielding is given by

$$\vec{B}_{\mathrm{net}} = \vec{B}_0 \cdot (1 - \sigma) \quad . \tag{2 | 25}$$

However, the Larmor frequency, $\omega_0 = \gamma\,|\vec{B}_0|$, changes linearly with the static magnetic field, $\vec{B}_0$. Consequently, the chemical shift of ^{1}H at different positions within the same molecule shows different absolute changes in chemical shift at different fields strengths $\vec{B}_0$. This makes it difficult to compare NMR spectra of the same molecule at different magnets. To make NMR signatures of the molecule independent of $\vec{B}_0$, and to provide comparable results throughout different static magnetic fields, the ppm scale has been introduced to

$$\delta_{\mathrm{MESE}} = \frac{\omega_{\mathrm{MESE}} - \omega_0}{\omega_0} \cdot 10^6 \quad . \tag{2 | 26}$$

Here, ω_{MESE} is the resonance frequency of the magnetically equivalent spin ensemble and ω_0 the Larmor frequency of the reference signal, *e.g.*, ^{1}H in tetramethylsilane or ^{129}Xe in gas each is set to 0 ppm. This ppm scale is commonly used, as also in this thesis.

In summary, the chemical shift is an important parameter in NMR. With respect to ^{129}Xe, such nuclei experience a significant shift when trapped in Cr cages. The change in chemical shift of ^{129}Xe is also influenced by the size of Cr's as shown in Figure 1.7. An explanation is that the aromatic rings of the CTV caps alter the effective magnetic field of the nuclei. These aromatic rings in Cr's posses a magnetic momentum that by itself and depending on the distance to the Xe atom cause a shielding or deshielding of the magnetic field. This impacts the Xe nucleus for which calculation concepts were performed in literature. As we treat the chemical shift as a single property of the whole Xe-host exchange kinetics fingerprint, such chemical shift calculations were beyond the focus of this thesis.

To now exemplify the complexity of the FID containing two spin ensembles with different Larmor frequencies, $\omega_{A,B}$, different concentration of nuclei, $M_{\perp,0}^{A,B}$, and different transverse relaxation times, $T_2^{A,B}$, Figure 2.5d shows such an FID in which it can hardly be distinguished whether two or more spin ensembles were participating. The FT of this FID, shown in Figure 2.5e, retrieves two populations at $\omega_{A,B}$ where the line width is proportional to $1/(2\,\pi T_2^{A,B})$, and the relative area corresponds to the number of nuclei of each ensemble, $M_{\perp,0}^{A,B}$. This again supports the quantitative character of NMR.

2.1.5 Asymmetric Chemical Exchange in NMR

We mentioned in Chapter 1 and the last paragraph above that commonly more than one spin ensemble is present in the sample or body. This results in a corresponding number of multiple sharp peaks in the NMR signal (compare Figure 2.5e). If these separated spin ensembles (pool A and pool B) become coupled such that these pools can exchange magnetization given by

$$A \underset{k_{BA}}{\overset{k_{AB}}{\rightleftharpoons}} B \ , \tag{2|27}$$

where $k_{AB,BA}$ are the exchange rates from pool $A \to B$ and *vice versa* from pool $B \to A$, then the shape of the NMR spectrum changes (Figure 2.6). This is observed for the exchange of amide protons – NH, amine protons – NH_2, or hydroxyl protons – OH, that are in exchange with free bulk water of tissue. For ^{129}Xe, the same occurs by temporally binding to Cr's or other binding sites. While the area under the exchanging NMR peaks is conserved by increasing the exchange rate, the signals broaden and become less distinguishable from the baseline (Figure 2.6). The most common case is the asymmetric chemical exchange in which two spin ensembles have unequal relative populations, $P_A = \frac{k_{BA}}{k_{AB}+k_{BA}}$ and $P_B = \frac{k_{AB}}{k_{AB}+k_{BA}}$ with $P_A + P_B = 1$, and, therefore, asymmetric peak appearance in the NMR spectrum (compare Figure 2.6). This is inherently a typical Xe biosensor prerequisite as it is about the optimized detection of low biosensor concentration.

In the slow exchange regime (two green NMR spectra in Figure 2.6), the total exchange rate, $k_{exch} = k_{AB} + k_{BA}$, is much smaller than the difference in Larmor frequency of each pool ($k_{exch}/|\Delta\omega| \ll 1$). The NMR signals are sharp and represent clearly the pool sizes.[7] For an increased exchange rate, both signals broaden and move towards each other. The system enters the so-called intermediate exchange regime (two yellow NMR spectra in Figure 2.6). Beyond a critical exchange rate, the two peaks start to merge until they form one single dominant signal in the fast exchange regime (two red NMR spectra in Figure 2.6). Both pools cannot be resolved anymore. This point is known as the so-called coalescence point. For asymmetric pool populations, the observed frequency, ω_{obs}, of the single peak is not centered between both resonances, but weighted by the center of mass ($\omega_{obs} = f_A\omega_A + f_B\omega_B$, where f_A and f_B are the mole fractions of each pool and conserved by $f_A + f_B = 1$; Figure 2.6). From an NMR spectrum beyond the coalescence point and without knowledge of the exchange rate, it is not possible to determine the number of spin pools or resonances. Moreover, a small NMR resonance which is in *"faster"* slow exchange with a dominant pool can even become invisible, as the signal area is significantly broadened (Figure 2.6).

Therefore, knowledge of the exchange rate is crucial, and another important NMR parameter which was one additional focus of this thesis. While we gave here a phenomenological introduction to the impact of chemical exchange on NMR spectra, its mathematical description using the Bloch equations (Equation (2|17a)) that are extended to the exchange of magnetization, the so-called **Bloch-McConnell** (BM) equations, is given in the next Chapter 3. As this provides the mathematical tools that were developed

---

[7] For highly asymmetric spin ensemble concentrations, *i.e.*, $P_A \gg P_B$, as it is the case for most of the Xe biosensor scenarios, the total chemical exchange rate, k_{exch}, approaches the off-rate, $k_{exch} \approx k_{BA}$, because $\frac{k_{BA}}{k_{AB}+k_{BA}} \gg \frac{k_{AB}}{k_{AB}+k_{BA}} \to k_{BA} \gg k_{AB}$.

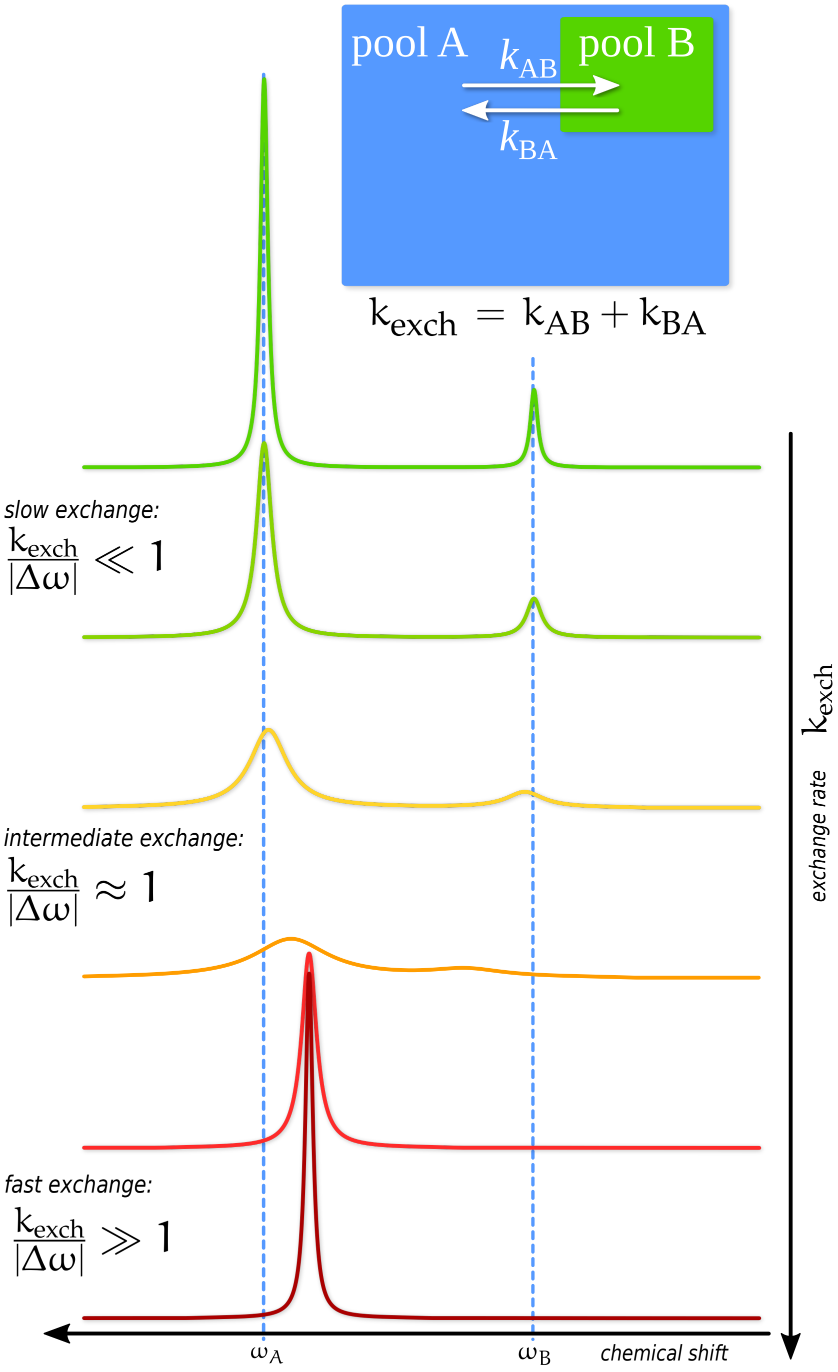

Figure 2.6: Principles of asymmetric (two spin ensembles with unequal populations) chemical exchange. The smaller pool B (top: green box) is nested into the much larger pool A (top: blue box) and both exchange magnetization with the exchange rates $k_{AB,BA}$ (white arrows). The difference in Larmor frequency of each pool, $\Delta\omega = \omega_B - \omega_A$, is constant, while the total exchange rate, k_{exch}, increases from green to red. This results in characteristic NMR line shapes within three exchange regimes: slow (green; $k_{exch}/|\Delta\omega| \ll 1$), intermediate (yellow; $k_{exch}/|\Delta\omega| \approx 1$) and fast (red; $k_{exch}/|\Delta\omega| \gg 1$) exchange regimes.

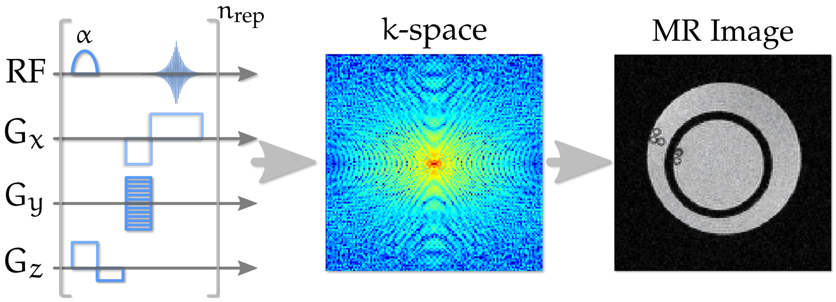

Figure 2.7: Principles of conventional MRI by magnetic field gradients, $\vec{G}$. The pulse program (left) acquires complex data in the so-called reciprocal image space, the k-space (middle; for better visibility the log(k-space) is shown), which contains the image information of the object for the MR image after 2D FT (right; showing the cross-section of two nested NMR tubes with 5 glass capillaries).

and used for this thesis to address sensitivity amplification strategies for Hyper-CEST, we dedicate an entire chapter for a detailed description.

2.2 PRINCIPLES OF HYPERPOLARIZED NUCLEI MAGNETIC RESONANCE IMAGING

With the use of additional magnetic field gradients, NMR can be turned to MR imaging (Figure 2.7). Paul C. Lauterbur and Sir Peter Mansfield were jointly awarded the Nobel Prize in 2003 in Physiology or Medicine for their discovery concerning magnetic resonance imaging.

There are some differences to consider when applying standard ^{1}H MRI pulse sequences to HP Xe. The NMR relaxation times of ^{1}H and ^{129}Xe are very different (Table 2.2). Contrary to ^{1}H and ^{129}Xe NMR spectroscopy where commonly a single RF pulse is sufficient to acquire the full FID after a single delivery of fresh HP Xe, for MR imaging multiple RF excitations are required to obtain the full image information. Here arises another difference between thermally polarized ^{1}H and HP ^{129}Xe as the magnetization of HP ^{129}Xe of the same nuclei is non-renewable, in contrast to ^{1}H. That means that each RF pulse uses up a certain fraction of the HP magnetization, depending on the flip angle, α, of the RF pulse and the number of pulse repetition, until no HP magnetization is left. The pulse sequence optimization for the behavior of HP ^{129}Xe MRI, which is described in the following, is therefore one important aspect of this thesis, and the results are given in Chapter 5.

2.2.1 Signal Localization by Magnetic Field Gradients

The key idea for conventional MR imaging of a three dimensional (3D) object is making the Larmor frequency spatially dependent. As the Larmor frequency (Equation (2.18)) is proportional to the static magnetic field, $\omega_0 \propto |\vec{B}_0|$, this can be achieved by assigning spins at one spatial position to a particular local magnetic field strength, while at another spatial position a different magnetic field strength is generated. This results in differently precessing magnetizations. In practice, 3D magnetic field gradients, $\vec{G}$, are

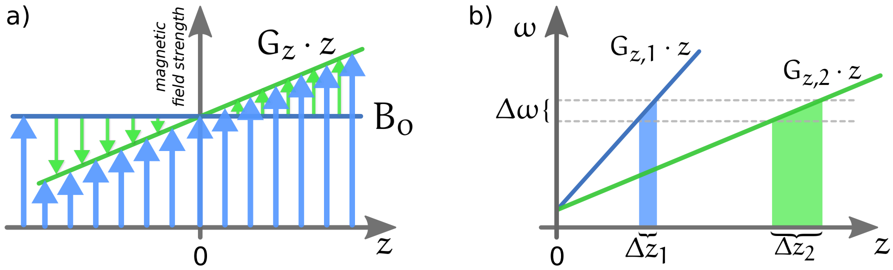

Figure 2.8: a) The addition of a magnetic field gradient G_z (green line and arrows) to the spatially uniform external magnetic field B_0, makes B_0, and hence the Larmor frequencies, spatially dependent. b) Different slice thicknesses $\Delta z_{1,2}$ are achieved for a constant RF excitation bandwidth $\Delta\omega$ using different magnetic field gradient strengths $G_{z,1} > G_{z,2}$.

added (Figure 2.8a) to $\vec{B}_0$ such that the Larmor frequency becomes spatially dependent:

$$\omega_0(\vec{x}) = \gamma \left(|\vec{B}_0| + \vec{G} \cdot \vec{x}\right) \quad , \tag{2.28}$$

where $\vec{x} = \{x, y, z\}$ represents the spatial vector. This principle is in the following – although each time slightly different – three times exploited to obtain sectioned images from the 3D object.

In the timing of a conventional pulse program, the first selection is the slice selection SS, usually followed by the phase encoding PE, and finally the frequency encoding FE. We will keep the corresponding gradients as in the literature as $G_{SS} \rightarrow G_z$, $G_{PE} \rightarrow G_y$, and $G_{FE} \rightarrow G_x$.

Slice Selection

The first sectioning of the 3D object is a selected slice. Without loss of generality, we chose the z-direction for this purpose. To make the Larmor frequency spatially depended, a gradient in z-direction, G_z, is added to B_0 (Figure 2.8a)

$$\omega_0(z) = \gamma \left(B_0 + G_z \cdot z\right) \quad . \tag{2.29}$$

Since now a whole distribution of Larmor frequencies exists an RF pulse with a certain bandwidth, $\Delta\omega$, will only couple to that spins which are within this bandwidth (Figure 2.8b). Only these excited magnetic moments produce measurable transverse magnetization that originates from the slice thickness, Δz, of

$$\Delta z = \frac{\Delta\omega}{\gamma\, G_z} \quad . \tag{2.30}$$

Therefore, using an RF pulse with a specific carrier frequency and a certain bandwidth, allows selection of an arbitrary slice position and thickness.[8]

---

[8] An infinitesimal thin slice is limited by both: 1) a maximal gradient strength, G_z, that can be produced by the hardware and 2) imperfections in the pulse profile generation to produce an infinitesimal small bandwidth. Additionally, a smaller slice thickness always means less number of spins that can contribute to the NMR signal. Thus, an infinitesimal thin slice results in signal-to-noise ratio close to zero.

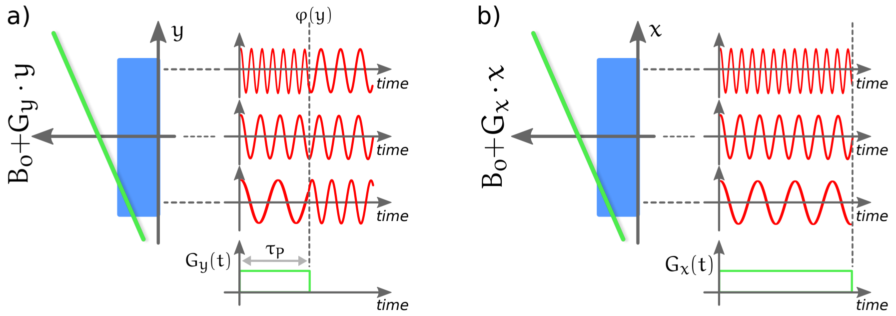

Figure 2.9: Principle of phase and frequency encoding. a) Phase encoding: The 1D object projection onto the y-axis is shown in blue. The phase encoding gradient, G_y, is turned on for a specific time, τ_P. While the spins at $-y_{max}$ precess the slowest, they precess with unchanged Larmor frequency at $y = 0$, and at $+y_{max}$ they precess the fastest. Thus, by turning off G_y, they have accumulated a spatially dependent phase difference, $\varphi(y)$. b) Frequency encoding: For simplicity, all spin have the same phase here. The orthogonal gradient, G_x, is turned on. Thus, the spins at $-x_{max}$ precess the slowest, they precess with unchanged Larmor frequency at $x = 0$, and at $+x_{max}$ they precess the fastest. The spins are spatially frequency encoded.

Spatial Encoding within the Slice

After the slice is selected, all the magnetization packages have the same precession frequency and phase, which is not enough as an image reconstruction would only correspond to an 1D projection of the object. Now, the orthogonal gradients in x and y-direction, G_x and G_y, are used to encode the magnetization spatially along these directions.

PHASE ENCODING All the x-y plane projected transverse magnetization induces in the RF coils the signal

$$S \propto \int_{\text{object}} M_\perp(x,y)\,dx\,dy \quad . \tag{2.31}$$

Turning on a gradient in y-direction, G_y, for a short time interval, τ_P (Figure 2.9a), causes the magnetic moments during the gradient application to dephase and accumulate a specific spatially-dependent phase, $\varphi(y)$, given by $\varphi(y) = \gamma\,(G_y \cdot y) \cdot \tau_P$, as the Larmor frequency was made spatially depended by $\omega(y) = \omega_0 + \gamma\,(G_y \cdot y)$. After the gradient G_y is turned off, all the magnetic moments at different positions, y, precess with the B_0-determined Larmor frequency, ω_0, again. The total signal S became phase $\varphi(y)$ encoded as described by

$$S(x,y,t) \propto \int_{\text{object}} M_\perp(x,y) \cdot e^{-i\,\omega(y)\cdot t}\,dx\,dy \tag{2.32}$$

$$S(x,y,t) \propto \left[\int_{\text{object}} M_\perp(x,y) e^{-i\,\gamma\,(G_y\cdot y)\cdot\tau_P}\,dx\,dy\right] e^{-i\,\omega_0\cdot t}\ ,$$

and is ready for the last encoding step.[9]

---

[9] The factor $e^{-i\,\omega_0\cdot t}$ is the carrier signal and is removed after demodulation.

FREQUENCY ENCODING We consider the 1D distributed object on the x-axis. Similar to phase encoding, the addition of a magnetic field gradient, G_x, on the static magnetic field, B_0, makes the Larmor frequencies spatially-dependent according to $\omega_0(x) = \omega_0 + \gamma\,(G_x \cdot x)$ for the time the gradient remains turned on, t (Figure 2.9b). Contrary to phase encoding which was essentially a preparation step, this gradient, G_x, is turned on while the data is recorded. Equation (2|32) is then extended to

$$\begin{aligned} S(x,y,t) &\propto \int_{\text{object}} M_\perp(x,y) \left[e^{-i\gamma\,(G_y\cdot y)\cdot\tau_P} \cdot e^{-i\gamma\,(G_x\cdot x)\cdot t} \right] \mathrm{d}x\,\mathrm{d}y \\ &\propto \int_{\text{object}} M_\perp(x,y) e^{-i\gamma\,((G_y\cdot y)\cdot\tau_P + (G_x\cdot x)\cdot t)}\,\mathrm{d}x\,\mathrm{d}y\,. \end{aligned} \tag{2|33}$$

Using the k-space notation (for constant magnetic field gradients in time) given by

$$k_x = \gamma \int_0^t G_x(t')\,\mathrm{d}t' = \gamma\,G_x \cdot t \tag{2|34a}$$

$$k_y = \gamma \int_0^{\tau_P} G_y(t')\,\mathrm{d}t' = \gamma\,G_y \cdot \tau_P \tag{2|34b}$$

(which will be further discussed in the next section), then Equation (2|33) yields after reordering

$$S(x,y,t) \propto \int_{\text{object}} M_\perp(x,y)\; e^{-i\,(k_x\cdot x + k_y\cdot y)}\,\mathrm{d}x\,\mathrm{d}y\,. \tag{2|35}$$

This corresponds to the Fourier transformation of the 2D transverse magnetization, $M_\perp(x,y)$. Thus, the inverse 2D FT of Equation (2|35) over the k-space recovers the spatial distribution of the object (the transverse magnetization $M_\perp(x,y)$; compare with Figure 2.7) according to

$$M_\perp(x,y) \propto \int_{k-\text{space}}^{\infty} {}_{-\infty}\; S(x,y)\; e^{i\,(k_x\cdot x + k_y\cdot y)}\,\mathrm{d}k_x\,\mathrm{d}k_y\,. \tag{2|36}$$

Pulse Sequences and k-Space Sampling

In the following we introduce the pulse sequences that were used in this thesis. A pulse sequence is the systematic timing of perturbation of the macroscopic magnetization by RF pulse and gradient application as well as relaxation that generates a certain image contrast for a given relaxation and spin density condition. The required data to reconstruct an image is recorded in Fourier space or k-space. Since each of the pulse sequences used in this thesis has different strategies to cover the k-space, the concept of each individual k-space trajectory is given in the following. In addition, we will highlight the differences of a pulse sequence for MR imaging of thermally polarized ^{1}H and hyperpolarized ^{129}Xe.

GRADIENT ECHO Probably the most commonly used pulse sequence is the **gradient (recalled) echo** (GRE), as it allows for fast image acquisition because fast RF pulse repetitions can be achieved. In addition, the GRE is the most simple pulse sequence.

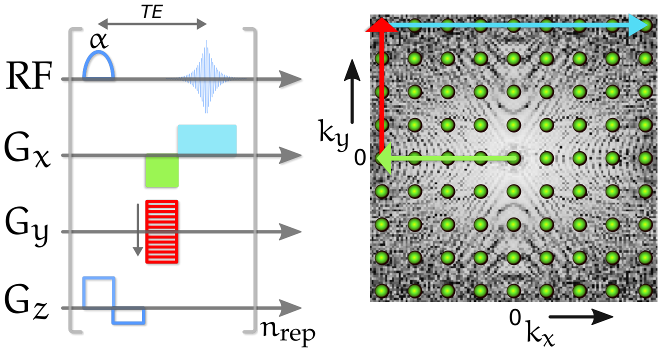

Figure 2.10: Gradient Echo (GRE) pulse sequence (left; with idealized rectangular gradient shapes) and corresponding k-space trajectory (right; each discrete $k_{x,y}$-value is illustrated by a green sphere; background: a representative k-space). The slice selection is obtained by the simultaneous irradiation of the RF pulse with flip angle, α, and gradient G_z (positive polarity; open blue rectangle). A rephase gradient with half the momentum and negative polarity, $-G_z$, follows to rephase the isochromates that dephased during excitation (definition of isochromates: see main text). This corrects for pulse profile imperfections and magnetic field inhomogeneities. Since all selected isochromates have same phase and frequency, this corresponds to a position in k-space center. The negative gradient momentum, $\gamma\,(-G_x)\cdot t$ (green rectangle) causes to move in negative k_x-direction (Equation (2.34a)) in k-space (green arrow in k-space). This causes the isochromates to dephase (hence, a signal loss in k-space). An orthogonal positive gradient momentum, $\gamma\,(+G_y)\cdot\tau_P$ (red rectangle) causes to move in positive k_y-direction. Now, the isochromates accumulate a spatially dependent phase. Up to here, this was the preparation phase of the isochromates. The signal acquisition is during the frequency encoding in positive k_x-direction. The positive G_x gradient (light blue rectangle) rephases the dephased isochromates which form an echo (blue oscillating signal on RF channel) at the echo time TE, when both G_x gradient areas (green and light blue) cancel each other. This was one single line in k-space. This pulse sequence has to be repeated until the entire k-space is acquired. The number of repetitions n_{rep} equals the number of phase encoding steps (if no under-sampling is performed).

The timing of the GRE pulse sequence is shown in Figure 2.10 (left). As introduced in Section 2.2.1, the slice selection is obtained by turning on G_z for a particular time and with particular strength, and the simultaneous irradiation of an RF pulse with a specific bandwidth, $\Delta\omega$, (Equation (2.30)), and flip angle α.

A specific spin system has a range of Larmor frequencies, *e.g.*, mostly dominated by the existence of inhomogeneities in B_0, or by the chemical shift effect. However, this is also caused by magnetic field gradients. Hence, each group of nuclear spins that share the same resonance frequency is called an isochromat. A pulse sequence can be understood more easily using isochromates rather than single spins.

The isochromates within this bandwidth couple to the RF pulse, rotate and produce transverse magnetization. The imperfections in the RF pulse as well as other inhomogeneities produce signal loss due to dephasing. This signal loss is recovered by refocusing the isochromates by exactly half the gradient momentum with opposite polarity (negative G_z gradient after the RF pulse α in Figure 2.10). All spins (thus, isochromates) have same frequency and phase that corresponds to the position exactly in the center of k-space. If data acquisition would take place now, this is nothing else as an FID from a particular selected slice without further spatial information. Turning on an orthogonal gradient in x-direction, G_x, with negative polarity for a specific time (green gradient in Figure 2.10) causes the isochromates to dephase, as different spatial Larmor frequencies are generated on purpose. Using the k-space notation (Equation (2.34a)), this effect is similar to a movement in negative k_x direction away from the center (green arrow in Figure 2.10), as the gradient is negative, $-k_x = \gamma(-G_x) \cdot t$. The application of the third orthogonal gradient in y-direction with positive polarity, G_y, the so-called phase encoding gradient (red gradient in Figure 2.10), for a short time τ_P, causes a spatially dependent phase accumulation of the isochromates (Figure 2.9 left). In k-space, this simultaneously corresponds to a movement in positive k_y direction (red arrow in Figure 2.10).

The ischromates are now spatially prepared for the data acquisition by a so-called echo that is caused by gradients (therefore, this pulse sequence is called gradient echo). The so-called read-gradient, which is the gradient in x-direction, G_x, now with opposite polarity (light blue gradient in Figure 2.10), causes the previously dephased isochromates to rephase until the gradient momentum is equal to the green gradient area. This is the time point where the isochromates are back in the center of k-space with maximum phase coherence. To cover the entire k-space, the read-gradient is still turned on, causing the isochormates to dephase again (light blue arrow in Figure 2.10). The entire echo is recorded by the RF coils (real and imaginary part) and collected as one single line in k-space. The maximum intensity of the echo is formed after the so-called echo time TE. To cover the entire k-space, this pulse sequence is n_{rep} times repeated (which is conventionally the number of the resolution of the final image) after the repetition time TR, and each time with a new RF pulse excitation, α, and a different strength of the phase encoding gradient, G_y, (red gradient in Figure 2.10).

When using HP magnetization (such as HP ^{129}Xe) for imaging, a main difference is the non-renewable character of the hyperpolarization, in contrast to thermally polarized ^{1}H. Since an RF pulse, α, uses up a certain amount of the HP magnetization it is entirely used up after some repetitions before the entire k-space is acquired, depending of the flip angle that is used. Or in contrast, for too small flip angles, the transverse magnetization might not be large enough to produce sufficient signal. Therefore, we investigated within this thesis the **variable flip angle** (VFA) approach by Zhao *et al.*[253], which is explained in the following.

VARIABLE FLIP ANGLE (VFA) APPROACH: The VFA θ_n divides a non-renewable HP signal into N equal portions of transverse magnetization $M_\perp$ by a non-linearly increased flip angle which is given by

$$\theta_n = \tan^{-1}\left(\frac{1}{\sqrt{N-n}}\right) \quad . \tag{2.37}$$

Here, each flip angle θ of the n^{th} excitation of the total number of excitation pulses N, maintains a constant transverse magnetization $M_\perp$ (by ignoring longitudinal relaxation of free Xe T_1 which is a valid assumption considering the much faster pulsing). The principle is illustrated in Figure 2.11. The flip angle of the last RF pulse is always 90° which tips the entire residual magnetization into the transverse plane. Thus, all the HP magnetization is efficiently used up for encoding and the VFA approach is the most effective way of distributing hyperpolarized magnetization.

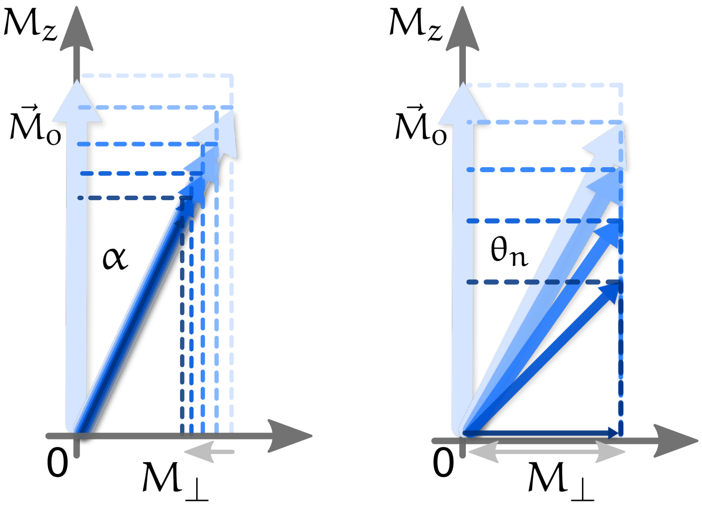

Figure 2.11: Comparison of the NMR signal produced by a constant flip angle α (left) and a variable flip angle (right) of HP magnetization (proportional to the transverse magnetization $M_\perp$). The initial magnetization vector $\vec{M}_0$ (light blue), is shown twice in each Figure: fully aligned with $\vec{B}_0$ and tipped under the first RF pulse with either the constant flip angle $\alpha = 25°$ (left) or with the first (smallest) variable flip angle, θ_1 (right). Since the HP magnetization is not renewable, only the longitudinal projection of the tipped magnetization vector, $\vec{M}_0$, onto the M_z-axis is available for the next RF pulse either with the constant flip angle $\alpha = 25°$ (left) or with the second variable flip angle. Thus, $\theta_2 > \theta_1$ is required to produce the same amount of transverse magnetization, $M_{\perp,2} = M_{\perp,1}$. For a total number of RF pulses, N (*i.e.*, $N = 5$), the last two flip angles in the VFA approach are always $\theta_{n=N-1} = 45°$ and $\theta_{n=N} = 90°$. Therefore, the measured transverse magnetization $M_\perp$ for HP nuclei gradually decreases for constant flip angles (left), whereas $M_\perp$ stays favorably constant for the variable flip angle approach (right).

An alternative way to address the non-renewable character of HP nuclei is to encode the entire required k-space information in one single-shot, which was also extensively used in this thesis. This is the method of choice if the transverse magnetization, $M_\perp$, from θ_n in the VFA approach does not yield sufficient signal.

ECHO-PLANAR IMAGING The **echo-planar imaging** (EPI) pulse sequence, introduced by Mansfield *et al.*[144], is a derivate of the GRE. It is the fastest (Cartesian) imaging sequence currently available. After a single 90° slice selective spin excitation, fast switching of a strong read-gradient (light blue gradients in Figure 2.12) is applied in order to generate gradient echoes during the FID period. This is covered by the faster apparent transverse relaxation time, T_2^*. By shortly turning on a phase encoding gradient during alternation of the read-gradient (so-called blips; red gradients in Figure 2.12), the entire k-space is covered with a single k-space trajectory. Whereas this technique allows extremely fast imaging with true snapshot capabilities, too fast T_2^* dephasing limits this method. Another drawback of single-shot EPI is its typical chemical-shift artifact. Further challenging is the need for more advanced gradients, since the switching of real gradients is not instantly, but delayed causing a gradient echo to be formed not perfectly in the center of k-space. This causes so-called ghost artifacts in the image. We, however,

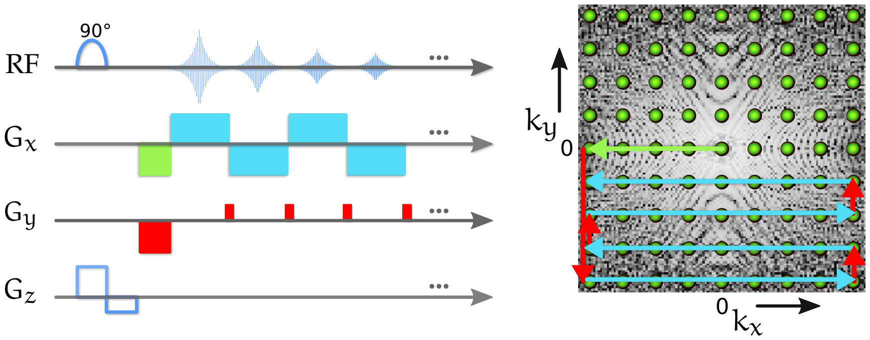

Figure 2.12: Single-shot echo-planar imaging (EPI) pulse sequence (left) and corresponding k-space trajectory (right). After one slice selective 90° excitation RF pulse and preparation of the isochromates to the most outer part in k-space (*i.e.*, $\{-k_x, -k_y\}$ by the green and first red preparation gradients), fast switching of strong read-gradients (light blue gradients) produce fast gradient echoes (blue oscillations on RF channel) during the FID period. Between the polarity change of the read-gradient, the phase encoding blips (red gradients) are shortly turned on. This results in a continuous, complete k-space trajectory, after one single excitation pulse.

overcame this problem by double sampling of each k-space line [Yang *et al.*[238]], as shown later in the results Part III in Section 5.3.1.

A further single-shot pulse sequence, which was also used for this thesis, is more stable regarding imaging artifacts compared to the EPI but slower, and is described in the following.

RAPID ACQUISITION WITH RELAXATION ENHANCEMENT The **rapid acquisition with relaxation enhancement** (RARE) pulse sequence was introduced by Hennig *et al.*[97] and belongs to the family of the spin-echo pulse sequences that were investigated by Hahn[87]. It employs a 90° excitation pulse, followed by multiple 180° refocusing pulses (Figure 2.13; in contrast to the gradient echoes that were used in the GRE and EPI pulse sequences). Therefore, the train of generated spin-echos is covered by the transverse relaxation time, T_2, and the data is T_2 weighted. Most frequently, a RARE sequence is used in a segmented mode in order to gain **signal-to-noise ratio** (SNR) at the cost of acquisition speed. For HP ^{129}Xe we, however, used the single-shot mode using a so-called RARE factor that is similar to the final image resolution. Since in ^{1}H-MR the transverse relaxation time is usually in the order of milliseconds to seconds (Table 2.2), such high RARE factors only add noise to the data. In contrast, Xe in water or DMSO has transverse relaxation times at the order of several seconds (compare with Table 2.2). We therefore exploited the long transverse relaxation times of free Xe T_2 to implement fast single-shot Hyper-CEST RARE pulse sequences. However, if too short T_2 decay times are present in the object, then typical artifacts in the reconstructed image are T_2 blurring.

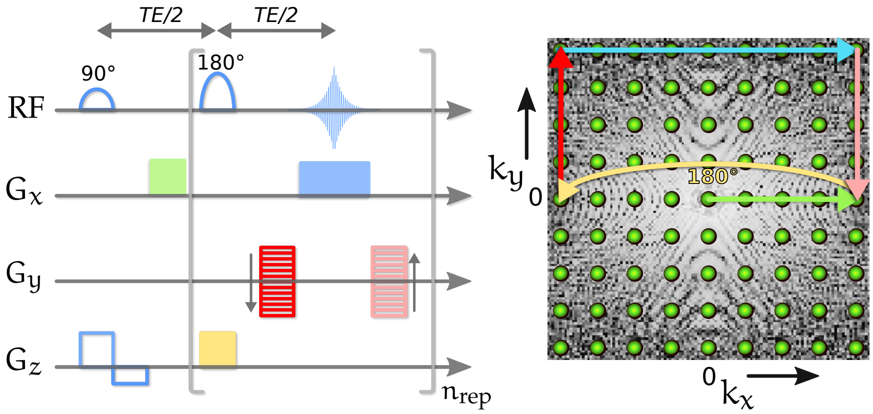

Figure 2.13: Single-shot rapid acquisition with relaxation enhancement (RARE) imaging pulse sequence (left) and k-space trajectory (right). After a single 90° slice selective RF excitation pulse, the isochromates start to dephase. After the time TE/2, a slice selective (yellow gradient, G_z) 180° refocusing RF pulse causes the isochromates to rotate around the RF pulse axis, but to keep their rotational direction. This is similar to a transformation in k-space from $+k_x$ to $-k_x$. Thus, the isochromates rephase and form a so-called spin-echo at time point TE (blue oscillations on RF channel). This is recored and corresponds to one line in k-space. To fully acquire all phase encoding steps (red gradients, G_y), the slice selective 180° refocusing RF pulse including echo recording is repeated n_{rep} times.

2.2.2 Image Reconstruction

Further MR image artifacts arise, if the following sampling theorem is violated.

WHITTAKER–KOTELNIKOW–SHANNON SAMPLING THEOREM The **Whittaker–Kotelnikow–Shannon** (WKS) sampling theorem [Whittaker[229], Kotelnikov[119], Shannon[191]] originates from information theory and signal processing. It states that the sampling time interval Δt of an oscillating signal with frequency f_{max} must be at least twice as fast as the inverse of that frequency to exactly reconstruct the original signal (*i. e.*, without aliasing artifacts): $\Delta t \leqslant 1/(2 \cdot f_{max})$. As the Larmor frequencies become spatially dependent by the gradient, the highest occurring frequency from the object to be imaged originates from farthest regions of the object. Therefore, the equidistant maximal k-space sampling distance Δk, is related to the width of the field-of-view W in x- and y-direction by

$$\Delta k_{x,y} \leqslant \frac{1}{W_{x,y}} \quad . \tag{2.38}$$

Thus, the minimum number of samples N_{min} for each direction is

$$N_{min} \geqslant 2 \cdot \frac{k_{max}}{\Delta k_{x,y}} \quad , \tag{2.39}$$

with k_{max} being the highest occurring frequency value. This is related to the matrix size and resolution of the final image.

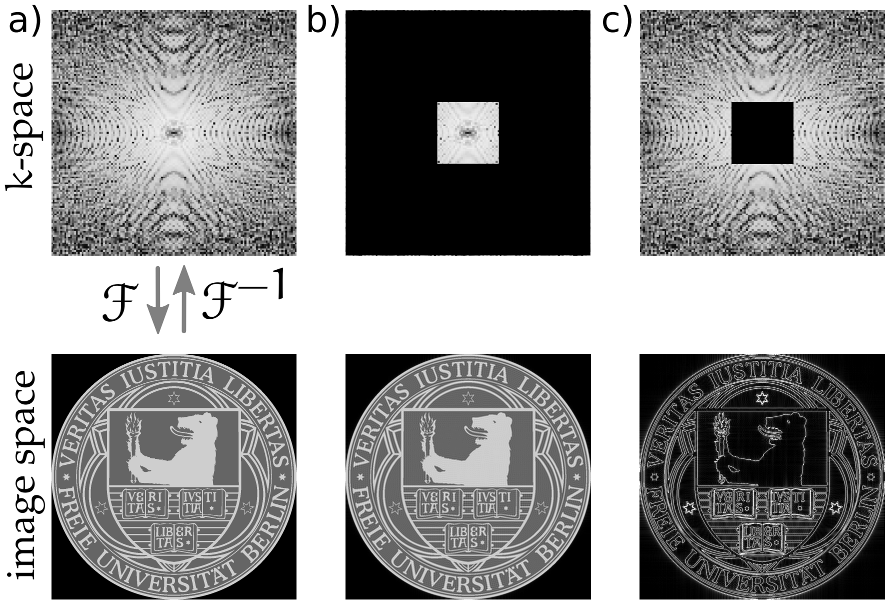

Figure 2.14: a) Sampling theorem accordingly full sampled k-space (top) of the Freie Universität Berlin logo (bottom). The 2D FT of the k-space $\mathcal{F}$ yields the image space, whereas the inverse 2D FT $\mathcal{F}^{-1}$ yields back the k-space. While the real part of the complex k-space data is shown (top row), the images are magnitude images. b) shows one fourth of the k-space of a) in each direction, k_x and k_y, that is centered around the center of k-space. In image space, these contain the main information, but details such as sharp edges or fine structures are missing, as they originate from the high frequency components from the outer k-space shown in c).

FOURIER-RELATION OF k-SPACE AND IMAGE SPACE Figure 2.14 gives an overview, how the information in k-space is related to the image space. a) shows the full k-space (*i. e.*, not violating the WKS sampling theorem) of the Freie Universität Berlin logo. Both, the k-space and the image space are related by the 2D Fourier-, $\mathcal{F}$, and inverse Fourier-transformation, $\mathcal{F}^{-1}$, respectively. The main image information is contained in the low frequency components in the k-space center. Thus, b) shows one fourth of the fully acquired k-space for each k_x and k_y direction which is centered around the k-space center. Details in the reconstructed MR image such as sharp edges or fine structures are missing, as they are contained in the high frequency components (Figure 2.14c).

2.3 PRINCIPLES OF HYPER-CEST

As mentioned in the introduction (Chapter 1) and above, besides its favorable non-invasive and quantitative character, NMR has a low sensitivity in comparison to other molecular imaging modalities (Table 1.1). This remains an everlasting challenge. The Hyper-CEST technique surpasses the detection limit of conventional direct ^{129}Xe NMR detection of biosensor bound Xe by several orders of magnitude by taking advantage of a so-called saturation pulse that transfers loss of signal from a small into a large spin pool.

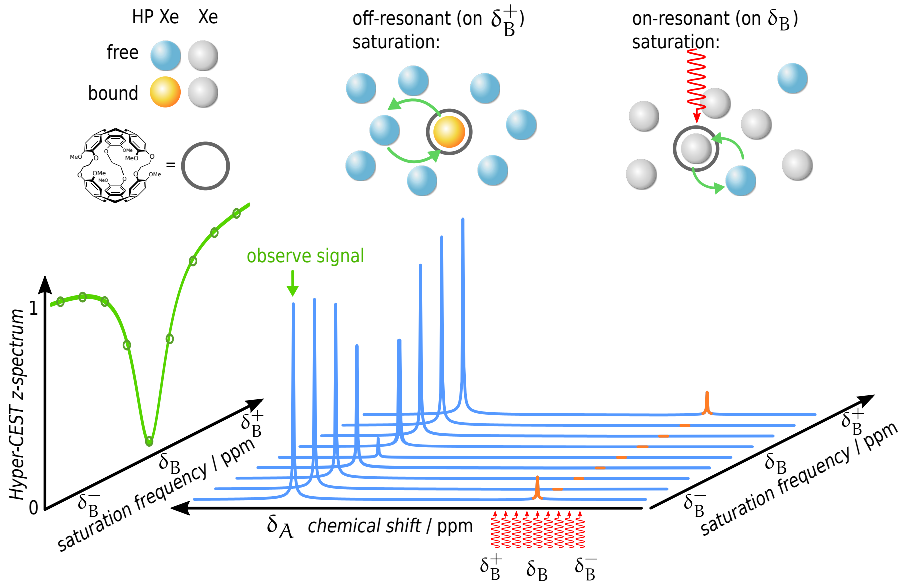

Figure 2.15: Principle of Hyper-CEST. The legend is shown in the top left including the host molecule CrA. While Xe is bound to CrA, its resonance frequency shifts remarkably large (indicated by the change in color from blue to orange). For illustration purposes, this bound Xe resonance in the direct ^{129}Xe NMR spectrum is drawn exaggeratedly large, but is usually far below the noise level at the low concentration of Xe biosensors. Xe freely exchanges in and out of CrA (green arrows) but remains its hyperpolarization, when the system is under off-resonant saturation (whose loss is then mainly driven by T_1 relaxation). Selective on-resonant saturation tuned to the CrA-encapsulated Xe signal cancels the magnetization of bound Xe (gray atoms). Due to continuous exchange, the depolarized Xe atoms are transfered to the free Xe pool which results in a measurable loss of the total Xe in solution signal (blue). By repeating this Hyper-CEST experiment multiple times, each time with a different saturation frequency, the spectral dimension of Hyper-CEST is obtained, the so-called Hyper-CEST *z*-spectrum (green projection of the dominant free Xe in solution signal on the left). This spectrum plots the *z*-component of the magnetization of pool A after saturation, M_z^A, after normalizing it to the initial magnetization, $M_{z,0}^A$. This Hyper-CEST *z*-spectrum is, in contrast to the direct ^{129}Xe NMR spectrum, an indirect ^{129}Xe NMR spectrum that shows a highly amplified signal of the bound Xe resonance with a characteristic line shape.

2.3.1 Hyper-CEST and its Spectral Dimension

The non-covalent interaction of the inert noble gas Xe with hydrophobic cavities of molecules, *i.e.*, CrA, for several milliseconds highlights its dynamic system character. While the sensitive Xe is encapsulated, its NMR signal largely shifts by several ppm (Figure 2.15; orange color-encoded). For illustration purposes, the bound Xe resonance in Figure 2.15 is drawn exaggeratedly large. However, at the concentrations we are looking for, this signal is typically far below the noise level and not identifiable by direct ^{129}Xe NMR. An off-resonant irradiated saturation pulse (*e.g.*, at δ_B^+) does not couple to the system and the dominant signal of free Xe (pool A) remains unchanged (blue color-encoded Xe atoms). In contrast, a saturation pulse that is tuned on-resonant with the encapsulated Xe resonance δ_B selectively cancels its magnetization (gray color-encoded Xe atoms). The depolarized Xe atoms

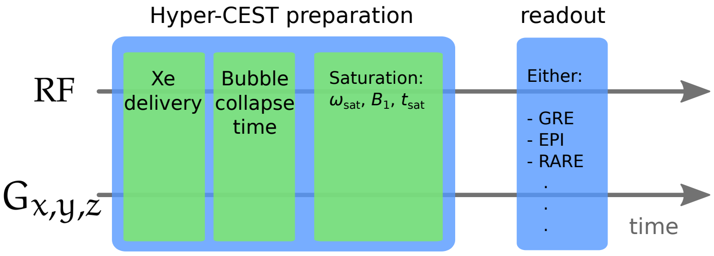

Figure 2.16: Hyper-CEST pulse sequence consisting of the Hyper-CEST preparation module and the readout module. The Hyper-CEST preparation module consists of the delivery of fresh HP Xe by bubbling into solution, and a waiting time delay to allow residual bubbles to collapse. Both are triggered by the pulse sequence. Subsequently, the saturation preparation is performed with a particular saturation pulse frequency ω_{sat}, strength B_1, and duration t_{sat}. This is followed by the MRI readout that can either be a GRE, EPI, RARE, *etc.* pulse sequence as described in Section 2.2.1.

become transferred to the spin pool of free Xe in solution and cause a measurable decrease of its dominant ^{129}Xe NMR signal. Since the Xe residence time within the host molecule is much shorter than the duration of the saturation pulse, several thousands of Xe atoms become depolarized per host molecule. Thus, this method provides large sensitivity amplification factors.

As the signal of bound Xe is usually below the noise level, the on-resonant irradiation frequency is *a priori* unknown. However, by repeating the Hyper-CEST experiment multiple times, each time with a different saturation frequency that covers a frequency range of the bound Xe resonance where it is expected to be (*i.e.*, from δ_B^- to δ_B^+), we obtain the spectral dimension of Hyper-CEST. A so-called Hyper-CEST *z*-spectrum is achieved by plotting the *z*-component of the magnetization of pool A after saturation M_z^A that is normalized to its initial magnetization $M_{z,0}^A$ (green projection in Figure 2.15). It shows a characteristic and highly amplified signal of the Xe host molecule. Therefore, by observing signal changes of the dominant pool of free Xe while irradiating a saturation pulse at frequencies where the bound Xe resonance is expected to be, we indirectly conclude about the presence of diluted Xe host molecules. Thus, the Hyper-CEST method is also referred to as an indirect ^{129}Xe NMR method.

2.3.2 Hyper-CEST Imaging

A general Hyper-CEST pulse sequence as designed, developed and used for this thesis is illustrated and described in Figure 2.16.

Figure 2.17a shows the principles of Hyper-CEST imaging of a so-called double bubbling phantom (which consists of two nested NMR tubes and five glass capillaries for Xe delivery: two within the **inner compartment** (IC) and three within the **outer compartment** (OC); see cross-section of the ^{1}H-MRI). While both compartments were filled with the same solvent, only the IC contained CrA. The direct ^{129}Xe NMR spectrum (Figure 2.17b) shows a dominant signal of the free Xe in solution resonance δ_A, and a small signal upfield at δ_B that is below the noise (illustrated by the gray sine curve). A ^{129}Xe-MR image acquired at the resonance frequency of the large signal of free Xe in solution δ_A, shows the full ^{129}Xe distribution throughout the phantom, but no CrA localization. This would straightforwardly be obtained by switching the MR image acquisition frequency to Xe bound to

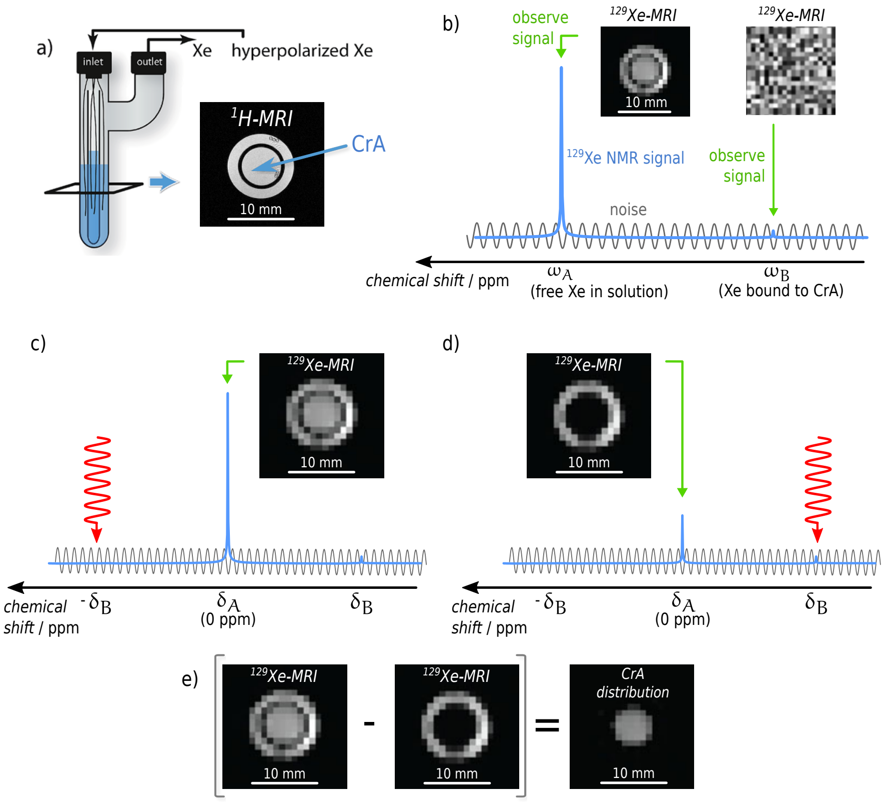

Figure 2.17: Principles of Hyper-CEST imaging. a) Double bubbling phantom that consists of two nested NMR tubes (see phantom cross-section by ^{1}H-MRI) filled with the same solvent, but only the inner compartment (IC) contains CrA. b) Direct (simulated) ^{129}Xe NMR spectrum of a) for illustration purposes. A ^{129}Xe-MR image acquired on the dominant signal of free Xe in solution shows the ^{129}Xe distribution throughout the entire phantom, but no CrA. As the ^{129}Xe NMR signal of CrA-bound Xe at δ_B is far below the noise (gray sine curve), a ^{129}Xe-MR image that is recorded directly on the CrA-bound Xe resonance shows noise. Hyper-CEST takes advantage of the large SNR of the dominant signal of free Xe in solution. Applying an off-resonant (at $-\delta_B$) saturation with specific strength and for certain time, the acquired large signal shows the full ^{129}Xe distribution (c). On-resonant saturation at $+\delta_B$ shows a signal loss at areas where CrA is present (which is the IC). e) The distribution of CrA is obtained by the subtraction of the off-resonant and on-resonant images reproducing the shape of the phantom.

CrA, δ_B. However, as the signal is below the noise, the ^{129}Xe -MRI also contains only noise and prevents CrA from identification (Figure 2.17b). In Hyper-CEST imaging, we take advantage of the large SNR of the free Xe in solution pool and acquire the images on this frequency. One image with off-resonant saturation (Figure 2.17c; at the exact same frequency offset but with opposite sign with respect to the solution pool as reference, *i. e.*, $-\delta_B$, if δ_A is set to zero, $\delta_A = 0$ ppm), and one on-resonant ^{129}Xe-MR image. While the off-resonant image shows the full Xe distribution throughout the phantom, the on-resonant image shows a signal loss at areas where CrA is present, in this case in the IC (Figure 2.17d). The localization of the highly diluted CrA molecules is then obtained by the subtraction of the off-resonant and the on-resonant ^{129}Xe-MR images (Figure 2.17e).

Similar to ^{1}H-CEST, the Hyper-CEST experiment is limited by the fast exchange regime as shown in Figure 2.6. Thus, the chemical shift difference of the exchanging dilute pool to the dominant detection pool resonance $\Delta\delta$ is critical for the detection of highly diluted molecular host concentrations (*e. g.*, to achieve sufficient spectral resolution for selective saturation). Commonly, the ppm scale of the ^{129}Xe NMR spectrum is referenced to the Xe in gas resonance. We, however, consider from now on throughout the whole thesis – similar to ^{1}H-CEST – all reported chemical shifts of dilute spin pools relative to the large detection pool of free Xe (*i. e.*, δ_A = 0 ppm).[10]

---

[10] This, however, has the potential disadvantage of loosing the overall chemical shift orientation which can change by temperature or molecular environment, if the relative chemical shift difference stays constant under such external changes.

3 MATHEMATICAL TOOLS

Contents

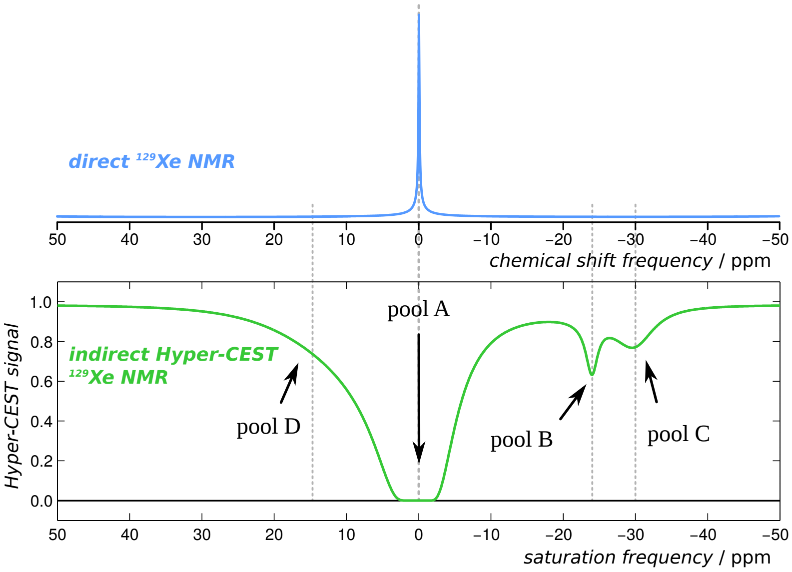

Figure 3.1: Simulated direct (top; blue curve) versus indirect Hyper-CEST (bottom; green curve; cw saturation of 5 μT for 2 s) ^{129}Xe NMR detection. The indirect Hyper-CEST method reveals in addition to the dominant large signal of free Xe in solution (pool A), three additional Xe-bound NMR signals that are hidden in the direct NMR spectrum as they are far below the noise of conventional detection. These have the following parameters: pool B at $\delta_B = -24$ ppm (pool B concentration 0.1 % relative to pool A, a Xe exchange rate of $k_{BA} = 500\ s^{-1}$); pool C at $\delta_C = -30$ ppm (relative pool C concentration 0.2 %, $k_{CA} = 2{,}300\ s^{-1}$); and pool D at $\delta_D = +15$ ppm (relative pool D concentration 1 %, $k_{DA} = 10{,}000\ s^{-1}$). Both spectra were simulated with the same parameters, using the BM equations that will be introduced in this Chapter. Noteworthy, in contrast to pool C and D, pool B is the most diluted system (*i. e.*, concentration of 0.1 %) but has superior resolution as Hyper-CEST signal.

In this chapter we derive the theory to analyze data of CEST, in particular Hyper-CEST experiments by the application of a saturation pulse as used within this thesis. This allows to maximize the Hyper-CEST signal by different approaches as will be shown in Chapter 7 and Chapter 8. We begin by describing one single spin ensemble, pool A, by the Bloch equations. The addition of another distinct magnetically equivalent spin ensemble, pool B, that is coupled to the first spin ensemble by the exchange of magnetization is described by the Bloch-McConnell equations. As in many Hyper-CEST experiments more than 2-spin ensembles or spin pools are present, we describe strategies to solve multiple coupled spin pools.

In addition, we show that these equations can be simplified under certain criteria and analytically solved. In this thesis, all presented methods were implemented to solve a system of up to 4-spin pools (Figure 3.1). We further demonstrate that these complicated equations can be handled conveniently with our developed Bloch-McConnell graphical user interface.

3.1 THEORY OF CHEMICAL EXCHANGE SATURATION TRANSFER

For state of the art *in vitro* Hyper-CEST experiments we introduce the theory to quantitatively access the Xe exchange kinetics using a **continuous-wave** (cw) saturation pulse.

3.1.1 1-Spin Pool: Bloch Equations

We consider an ensemble of magnetically equivalent spins with gyromagnetc ratio γ that resonants at Larmor frequency ω_0 within a static external magnetic field $\vec{B}_0$. The time evolution of the net magnetization, $\vec{M}(t)$, under RF irradiation, $\vec{B}_1(t)$ (for better identification of the different terms in the coming equations, we introduce this color encoding), is described by the Bloch equations (Equation (2.17)):

$$\frac{d\vec{M}(t)}{dt} = \gamma \vec{M}(t) \times (\vec{B}_0 + \vec{B}_1(t)) - \hat{R}(\vec{M}(t) - \vec{M}_{th}). \tag{3.1}$$

The first cross-product describes the Larmor precession term which rotates the net magnetization around the effective magnetic field, $\vec{B}_{eff} = \vec{B}_0 + \vec{B}_1(t)$. The second term describes the change of the length of the magnetization vectors by both the intrinsic longitudinal and transverse relaxation times, $T_{1,2}$, respectively, to the magnetization at thermal equilibrium, $\vec{M}_{th}$. Without loss of generality, we choose the saturation pulse, $\vec{B}_1(t)$, applied along the x-direction and the static magnetic field, $\vec{B}_0$, along the z-direction. Thus, with $\vec{B}_0 = \{0, 0, B_0\}^T$ the corresponding relaxation rate matrix, $\hat{R}$, is given by

$$\hat{R} = \begin{pmatrix} 1/T_2 & 0 & 0 \\ 0 & 1/T_2 & 0 \\ 0 & 0 & 1/T_1 \end{pmatrix}. \tag{3.2}$$

As stated in Chapter 2, a z-spectrum is similar to a direct NMR spectrum but diluted Xe signals at different chemicals shifts are stronger visible under saturation transfer. We obtain such a z-spectrum by variation of the carrier frequency of the saturation pulse ω_{sat}, as offset relative to the Larmor fre-

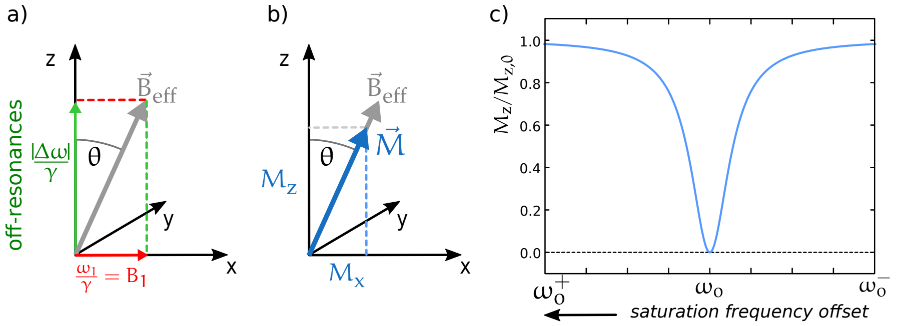

Figure 3.2: 1-Spin pool z-spectrum. a) Under irradiation of a saturation pulse along the x-axis, an effective magnetic field $\vec{B}_{eff}$ builds up that is tipped by the angle $\theta = \tan^{-1}(\omega_1/\Delta\omega)$ with respect to the z-axis. b) In steady-state, the magnetization $\vec{M}$ aligns with the effective magnetic field $\vec{B}_{eff}$. c) The z-spectrum is obtained by reading out the M_z component of $\vec{M}$ (as shown in b), normalized to the initial magnetization $M_{z,0}$ for a range of saturation frequency offsets $\Delta\omega$.

quency $\Delta\omega = \omega_{sat} - \omega_0$, and observation of the z-component of the magnetization, M_z, after saturation that is normalized to the initial magnetization, $M_{z,0}$. The time-dependent RF field, *i.e.*, the saturation pulse, with time-dependent amplitude $\omega_1(t)$, carrier or saturation frequency ω_{sat}, and a particular saturation frequency offset (*i.e.*, not on-resonant: $\omega_{sat} \neq \omega_0$) is given by $\vec{B}_1(\omega_1(t), \omega_{sat}, t)$. In the case for cw saturation, the amplitude is time independent, *i.e.*, $\omega_1(t) = \omega_1$. The linearly polarized RF field along the x-axis is given by

$$\vec{B}_1(t) = 2\frac{\omega_1}{\gamma}\cos(\omega_{sat} \cdot t)\,\vec{e}_x \quad . \tag{3.3}$$

By decomposing this linear field into two circularly polarized fields that rotate in opposite directions about the z-axis in the x-y-plane yields

$$\begin{aligned}\vec{B}_1(t) =& \frac{\omega_1}{\gamma}\left[\cos(\omega_{sat} \cdot t)\,\vec{e}_x + \sin(\omega_{sat} \cdot t)\,\vec{e}_y\right] \\ &+ \frac{\omega_1}{\gamma}\left[\cos(\omega_{sat} \cdot t)\,\vec{e}_x - \sin(\omega_{sat} \cdot t)\,\vec{e}_y\right] \quad .\end{aligned} \tag{3.4}$$

Only that field interacts with the magnetic moments which rotates in the same sense while the other component can in most cases be neglected.[1] Thus, the linearly polarized RF field is then equivalent to a rotating magnetic field in the x-y-plane which is given by

$$\vec{B}_1(\omega_1, \omega_{sat}, t) = \frac{\omega_1}{\gamma} \cdot \begin{pmatrix} \cos(\omega_{sat} \cdot t) \\ \sin(\omega_{sat} \cdot t) \\ 0 \end{pmatrix} \quad . \tag{3.5}$$

In total, an effective magnetic field $\vec{B}_{eff} = \frac{1}{\gamma} \cdot \{\omega_1, 0, \Delta\omega\}^T$ builds up that is tipped into the x-direction by an angle of $\theta = \tan^{-1}(\omega_1/\Delta\omega)$ relative to the z-axis (Figure 3.2a). In steady-state, the magnetization $\vec{M}$ aligns with the effective magnetic field $\vec{B}_{eff}$ (blue arrow in Figure 3.2b).[2] Subsequent repe-

---

[1] The counter rotating component influences the spins to the order of $(\frac{\omega_1}{\gamma 2 B_0})^2$ which is typically a very small number and known as Bloch-Siegert shift [Bloch and Siegert[24]].

[2] Note, θ is not the flip angle, α, as the magnetization rotates under on-resonant irradiation along the x-axis into the y-direction with flip angle, α.

tition of this procedure for different saturation frequency offsets $\Delta\omega$ by adjusting ω_{sat} (and hence different angles θ) and recording of the z-component of the magnetization, M_z, after each saturation pulse yields the z-spectrum as illustrated in Figure 3.2c. For saturation pulse frequencies that are irradiated far off-resonant (*i. e.*, $\omega_{\text{sat}} < \omega_0^-$ or $\omega_{\text{sat}} > \omega_0^+$) relative to the Larmor frequency, the M_z component remains unaffected as the spins do not couple to the RF pulse. At saturation pulse frequencies closer to ω_0, M_z drops as θ becomes larger until M_z is entirely saturated for frequencies that are on-resonant with ω_0. Therefore, Figure 3.2c shows one single resonance at the Larmor frequency ω_0.

3.1.2 2-Spin Pools: Bloch-McConnell (BM) Equations

We now add to the first spin pool system (pool A) another spin ensemble at a different resonance frequency, pool B, which is also much smaller in size than pool A. In addition, we allow both pools to exchange magnetization by coupling with exchange rates $k_{AB,BA}$ from pool A → B and *vice versa* from B to A (Figure 3.3a). The system obeys the rate equation in steady-state $k_{AB} = (|\vec{M}_{th}^B|/|\vec{M}_{th}^A|) \cdot k_{BA}$. Using the saturation pulse carrier frequency offset relative to each individual Larmor frequency of pool A and B, $\Delta\omega_{A,B} = \omega_{\text{sat}} - \omega_{A,B}$, two Bloch equations similar to Equation (3.1) for each spin pool are extended by coupling terms in order to exchange magnetization (indicated by the blue terms):

$$
\begin{aligned}
\frac{d\vec{M}^A(t)}{dt} &= \gamma\, \vec{M}^A(t) \times (\vec{B}_0 + \vec{B}_1(t)) - \hat{R}^A(\vec{M}^A(t) - \vec{M}_{th}^A) - k_{AB}\vec{M}^A(t) + k_{BA}\vec{M}^B(t) \\
\frac{d\vec{M}^B(t)}{dt} &= \gamma\, \vec{M}^B(t) \times (\vec{B}_0 + \vec{B}_1(t)) - \hat{R}^B(\vec{M}^B(t) - \vec{M}_{th}^B) - k_{BA}\vec{M}^B(t) + k_{AB}\vec{M}^A(t)\,,
\end{aligned}
\tag{3.6}
$$

or explicitly

$$
\begin{array}{ccllllll}
\frac{dM_x^A(t)}{dt} & = & -R_2^A M_x^A(t) & -\Delta\omega_A M_y^A(t) & & -k_{AB}M_x^A(t) & +k_{BA}M_x^B(t) \\
\frac{dM_y^A(t)}{dt} & = & -R_2^A M_y^A(t) & +\Delta\omega_A M_x^A(t) & +\omega_1 M_z^A(t) & -k_{AB}M_y^A(t) & +k_{BA}M_y^B(t) \\
\frac{dM_z^A(t)}{dt} & = & -R_1^A (M_z^A(t) - M_{th}^A) & -\omega_1 M_y^A(t) & & -k_{AB}M_z^A(t) & +k_{BA}M_z^B(t) \\
\hline
\frac{dM_x^B(t)}{dt} & = & -R_2^B M_x^B(t) & -\Delta\omega_B M_y^B(t) & & -k_{BA}M_x^B(t) & +k_{AB}M_x^A(t) \\
\frac{dM_y^B(t)}{dt} & = & -R_2^B M_y^B(t) & +\Delta\omega_B M_x^B(t) & +\omega_1 M_z^B(t) & -k_{BA}M_y^B(t) & +k_{AB}M_y^A(t) \\
\frac{dM_z^B(t)}{dt} & = & -R_1^B (M_z^B(t) - M_{th}^B) & -\omega_1 M_y^B(t) & & -k_{BA}M_z^B(t) & +k_{AB}M_z^A(t).
\end{array}
$$

Since this coupling was introduced by McConnell[146], these equations are known as the BM equations. In contrast to the BM equations, the Bloch-Solomon equations describe magnetization transfer by dipolar cross relaxation [Solomon[197]] and the Bloch-Torrey equations describe transfer of magnetization by diffusion [Torrey[210]]. The BM equations form a set of coupled first-order **ordinary differential equations** (ODEs). It is not possible to solve the 2-spin pool BM equations analytically without further simplifications.

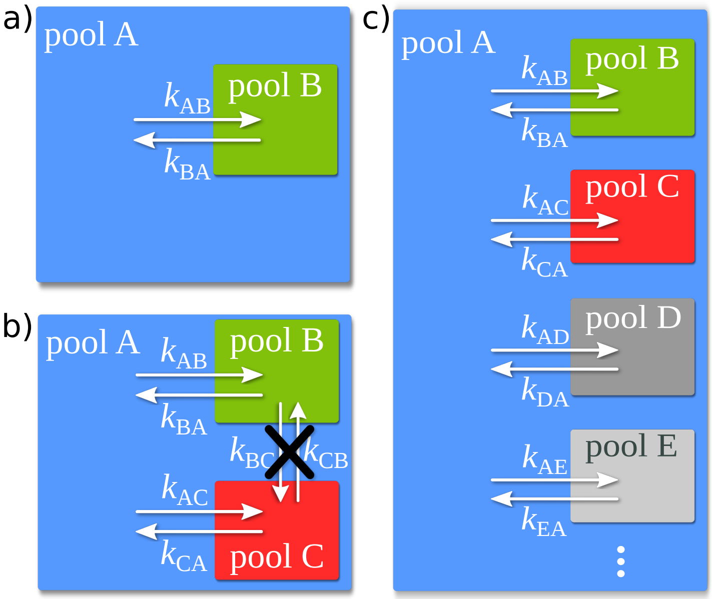

Figure 3.3: Magnetization exchange kinetics modeling. a) 2-Spin pools: Magnetization is transfered from free Xe in solution (pool A) to bound Xe, *i. e.*, from pool A to pool B with the exchange rate k_{AB}, and *vice versa* from pool B to pool A with k_{BA}. b) 3-Spin pools: Similar to a) but with an additional different spin ensemble, pool C. As it is assumed that Xe does not exchange from one host B-bound state to another host C-bound state (and *vice versa*) without going *via* the solution pool, pool C solely exchanges with the dominant free Xe in solution, pool A. Therefore, the direct Xe magnetization exchange between pool B and pool C is excluded ($k_{BC} = k_{CB} = 0\ s^{-1}$; black ×). c) Multiple spin pools: As in b) direct Xe magnetization exchange between bound Xe pools are neglected. All magnetically different spin ensembles solely exchange with free Xe in solution (pool A).

Experimentally, such an ideal 2-spin pool Hyper-CEST system is achieved by, *e. g.*, CrA in pure water or in pure **dimethyl sulfoxide** (DMSO; see Chapter 5, Chapter 6, Chapter 7, and Chapter 8). However, before we demonstrate ways how we treat this in this thesis, we will first extent the 2-spin pools to also the case of three or even multiple spin pools. The solutions presented afterwards can then be applied to any number of spin pools to model complex Xe binding systems.

3.1.3 3-Spin Pools: BM Equations

Although Hyper-CEST NMR encounters cases with only two pools, this is an idealized condition and real scenarios are more complex.

More specific, the Xe in target-bound biosensor and in unbound sensors (Figure 1.5) is one example for the following 3-spin pool model. We add one distinct spin ensemble, pool C, to pool A and pool B from the previous section. As it is reasonably unlikely for Xe atoms to exchange directly from a biosensor that is bound to its target to a biosensor that is not bound without traveling through the free Xe pool in solution, the exchange between both CEST pools is negligible, *i. e.*, $k_{BC} = k_{CB} = 0\ s^{-1}$ (compare with schematic in Figure 3.3b). Both CEST pools solely exchange with the dominant pool of free Xe, pool A. This is modeled by the following BM equations:

$$
\begin{aligned}
\frac{d\vec{M}^A(t)}{dt} &= \gamma\vec{M}^A(t)\times(\vec{B}_0+\vec{B}_1(t)) - \hat{R}^A(\vec{M}^A(t)-\vec{M}^A_{th}) \\
&\quad \underbrace{-\,k_{AB}\vec{M}^A(t)+k_{BA}\vec{M}^B(t)}_{\text{exchange with pool B}}\underbrace{-\,k_{AC}\vec{M}^A(t)+k_{CA}\vec{M}^C(t)}_{\text{exchange with pool C}} \\
\frac{d\vec{M}^B(t)}{dt} &= \gamma\vec{M}^B(t)\times(\vec{B}_0+\vec{B}_1(t)) - \hat{R}^B(\vec{M}^B(t)-\vec{M}^B_{th}) - k_{BA}\vec{M}^B(t)+k_{AB}\vec{M}^A(t) \\
\frac{d\vec{M}^C(t)}{dt} &= \gamma\vec{M}^C(t)\times(\vec{B}_0+\vec{B}_1(t)) - \hat{R}^C(\vec{M}^C(t)-\vec{M}^C_{th}) - k_{CA}\vec{M}^C(t)+k_{AC}\vec{M}^A(t)\;\;.
\end{aligned}
$$

Similar to the 2-spin pool model, this system obeys the two rate equations in steady-state: $k_{AB} = (|\vec{M}^B_{th}|/|\vec{M}^A_{th}|)\cdot k_{BA}$ and $k_{AC} = (|\vec{M}^C_{th}|/|\vec{M}^A_{th}|)\cdot k_{CA}$. In comparison with Equation (3|6), the time-dependency of the magnetization of pool A includes the additional exchange terms with pool C. In contrast, the magnetization of pool B does not change, while one new and similar equation for the magnetization of pool C is added.

In theory, this extension can be done to an infinitely large number of distinct magnetic environments.

3.1.4 Multiple-Spin Pools

> *"We consider a chemical reaction or conformational transition that exchanges a nuclear spin between n sites A_i with distinct magnetic environments, ..."*
> — Trott and Palmer[214] – 2004.

For more complex *in vitro* systems such as Xe-CrA interactions with cells [Klippel *et al.*[116]], biomembranes [Schnurr *et al.*[182]], bacteriophages on cancer cells [Palaniappan *et al.*[162]], alternative Xe-hosts such as genetically encoded **gas vesicles** (GV) [Shapiro *et al.*[192]], **bacterial spores** (BS) [Bai *et al.*[14]], PFOB nano emulsion [Wolber *et al.*[236], Stevens *et al.*[200], Klippel *et al.*[117]] or ultimately *in vivo*, it is, however, more likely that several pools are present or a whole distribution of exchange rate exists for one pool.

To address these issues quantitatively, we also extended the BM equations up to 4-spin pools using the schematic above (Figure 3.3c; equations not shown), with the similar principle: While for new CEST pools that solely exchange with the dominant pool of free Xe, pool A, only new equations are added to the system, the equation for pool A becomes longer as it sums up all the new exchanging CEST pools including their exchange rates $k_{Ai,iA}$ with $i \in [B, C, D, E, \ldots]$.

Further possible straightforward extensions of the BM equations by scaling to multiple pools was previously described for ^{1}H-CEST by Trott and Palmer[214], Li *et al.*[134] and Sun[201].

To understand the Hyper-CEST mechanism and how each parameter manifests in the Hyper-CEST signal, the behavior of the *z*-component of the magnetization, M_z, provides useful fundamental insights into this optimization task. Unfortunately, it is not possible to solve these BM equations analytically without further simplifications. We therefore demonstrate in the following section first straightforward numerical approaches to achieve Hyper-CEST *z*-spectra.

3.1.5 Numerical Solutions of the BM Equations

The methods described in the following can all be extended to an arbitrary number of spin pools. This description is therefore given for the most simplest system, the 2-spin pool Hyper-CEST system. In the following, we begin by describing the time evolution which is followed by the frequency evolution to obtain the typical Hyper-CEST *z*-spectra whose characteristic shape bears detailed information of the Xe exchange kinetics.

Time Evolution

Finding a solution of the BM equations is complicated as it is a coupled system of first-order ODEs that scales up in complexity with increasing number of CEST pools. We numerically solved this equation system using the following three methods which all differ in simulation time:

A. Runge-Kutta-Integrator,

B. two matrix evaluations proposed by Woessner *et al.*[234] in 2005, and

C. one exponential matrix evaluation proposed by Murase *et al.*[157] in 2011.

RUNGE-KUTTA-INTEGRATOR For this thesis, a Runge-Kutta-Integrator was implemented based on the Dormand and Prince[64] method to solve differential equations, as a first step to solve the BM equations and gain insights into chemical exchange saturation transfer experiments. It should be noted that Cramer's rule has also been used in the literature to solve the BM equations [Woessner *et al.*[234]].[3] However, due to the calculation of many determinants Cramer's rule is computationally inefficient [Poole[164]] and also numerically unstable even for 2 × 2 systems [Higham[98]]. In contrast, the Dormand-Prince integrator uses six function evaluations to accurately calculate up to the 4th and 5th order. The difference between these solutions is then taken to be the error of the 4th order solution. This error estimate is then used for adaptive step size integration which is then minimized to satisfy the tolerance threshold of 10^{-3} of the estimated error that is set by the user. Therefore, after each iteration the deviation of the exact solution is given within the tolerance threshold. The starting condition for two pools, $\vec{M}_0 = \{0, 0, \eta \cdot M_{th}^{A}, 0, 0, \eta \cdot M_{th}^{B}\}^{T}$, is chosen such that the initial available magnetization of all spin pools points parallel to $\vec{B}_0$. The signal enhancement factor η is $\geqslant 20{,}000$ for hyperpolarization or otherwise $\eta = 1$ for thermal polarization. This method was implemented for up to 4-spin pools (see later in the BM **graphical user interface** (GUI) Section 3.2) under cw saturation and can be extended to an arbitrary number of pools and shaped pulsed saturation. This solution of the BM equations was used here as the gold-standard method (the main idea of the implementation in MATLAB for a 2-spin pool system is shown in Code 1).[4]

---

[3] Cramer's rule was published in 1750. This rule was – as found out later – identical with a formula of a manuscript published by Gottfried Wilhelm Leibniz in 1678 [Chabert[48]].

[4] Faster algorithms in C/C++ can also be used. These were, however, outside the scope of this thesis.

Code 1: Bloch-McConnell Equations for Runge-Kutta-Integrator

```
function dMdt = BlochMcConnell_2Pool(t,M,DOmega,PoolA,PoolB,Pulse,System)

% function dMdt=BlochMcConnell_2Pool(t,M,DOmega,PoolA,PoolB,Pulse,System)
% Bloch-McConnell equations for 2-spin pools
% Author: M. Kunth (FMP-Berlin, 2012)

        % --------- parameters ---------
        R1A             = PoolA.R1;
        R2A             = PoolA.R2;
        dOmegaA_PPM     = PoolA.del;
        M0A             = PoolA.Mz0;

        R1B             = PoolB.R1;
        R2B             = PoolB.R2;
        dOmegaB_PPM     = PoolB.del;
        M0B             = PoolB.Mz0;
        kBA             = PoolB.kBA;             % 1/s
        kAB             = M0B/M0A*kBA;           % 1/s;

        gamma           = System.Gamma;
        B0              = System.B0;

        % --------- frequencies ---------
        OmegaRef = gamma*B0;
        Omega1 = B1Field(Pulse,t,System);

        dOmegaA = dOmegaA_PPM*1e-6*OmegaRef; % Hz
        DOmegaA = DOmega - dOmegaA;

        dOmegaB = dOmegaB_PPM*1e-6*OmegaRef; % Hz
        DOmegaB = DOmega - dOmegaB;

        % --------- initial values ---------
        MxA = M(1);     MyA = M(2);     MzA = M(3);
        MxB = M(4);     MyB = M(5);     MzB = M(6);

        % --------- preallocate memory ---------
        dMdt = zeros(size(M));

        % --------- ODE system ---------
        % MxA
        dMdt(1) = -R2A*MxA - kAB*MxA + kBA*MxB - DOmegaA*MyA;
        % MyA
        dMdt(2) = -R2A*MyA - kAB*MyA + kBA*MyB + DOmegaA*MxA +Omega1*MzA;
        % MzA
        dMdt(3) = -R1A*(MzA - M0A) - kAB*MzA + kBA*MzB - Omega1*MyA;

        % MxB
        dMdt(4) = -R2B*MxB + kAB*MxA - kBA*MxB - DOmegaB*MyB;
        % MyB
        dMdt(5) = -R2B*MyB + kAB*MyA - kBA*MyB + DOmegaB*MxB +Omega1*MzB;
        % MzB
        dMdt(6) = -R1B*(MzB - M0B) + kAB*MzA - kBA*MzB - Omega1*MyB;
end
```

TWO MATRIX EVALUATIONS A formal solution of the BM equations for 2-spin pools is found by rewriting Equation (3.6) into the following matrix form *with* inhomogeneity $\vec{b}$. Using the same order as above (*i. e.*, pool A $\{x, y, z\}$, pool B $\{x, y, z\}$), we obtain:

$$\frac{d}{dt}\underbrace{\begin{pmatrix} M_x^A \\ M_y^A \\ M_z^A \\ M_x^B \\ M_y^B \\ M_z^B \end{pmatrix}}_{=\vec{M}} = \underbrace{\begin{pmatrix} -(R_2^A+k_{AB}) & -\Delta\omega_A & 0 & +k_{BA} & 0 & 0 \\ +\Delta\omega_A & -(R_2^A+k_{AB}) & +\omega_1 & 0 & +k_{BA} & 0 \\ 0 & -\omega_1 & -(R_1^A+k_{AB}) & 0 & 0 & +k_{BA} \\ +k_{AB} & 0 & 0 & -(R_2^B+k_{BA}) & -\Delta\omega_B & 0 \\ 0 & +k_{AB} & 0 & +\Delta\omega_B & -(R_2^B+k_{BA}) & +\omega_1 \\ 0 & 0 & +k_{AB} & 0 & -\omega_1 & -(R_1^B+k_{BA}) \end{pmatrix}}_{=\hat{A}} \cdot \begin{pmatrix} M_x^A \\ M_y^A \\ M_z^A \\ M_x^B \\ M_y^B \\ M_z^B \end{pmatrix} + \underbrace{\begin{pmatrix} 0 \\ 0 \\ R_1^A M_{th}^A \\ 0 \\ 0 \\ R_1^B M_{th}^B \end{pmatrix}}_{=\vec{b}} .$$

As reported by Woessner *et al.*[234], the general solution is achieved by the exponential matrix operation and the inverse-matrix evaluation according to

$$\vec{M}(t) = \left(\vec{M}_0 + \frac{\vec{b}}{\hat{A}}\right) \cdot \exp(\hat{A} \cdot t) - \frac{\vec{b}}{\hat{A}} \quad , \tag{3.7}$$

where $\vec{M}_0 = \{0, 0, \eta \cdot M_{th}^A, 0, 0, \eta \cdot M_{th}^B\}^T$ is the initial available magnetization as starting condition. The segment in Code 2 shows the exponential matrix operation as well as the solution of the inverse-matrix problem which was implemented in MATLAB for this thesis and of further use.

Code 2: Two Matrix Evaluation

```
MStart = [0 0 Mz0A*HP 0 0 Mz0B*HP];

M_t = zeros(size(MStart,2),length(offset));

b = [0 0 R1A*Mz0A 0 0 R1B*Mz0B]';

%----- solve matrix -----------------
for  k=1:length(offset)
        DOmega = offset(k)*1e-6*omegaRef; % offset in Hz

        DOmegaA = DOmega - dOmegaA;
        DOmegaB = DOmega - dOmegaB;

        A = [...
        -(R2A+kAB)  -DOmegaA    0           kBA         0           0;...
        +DOmegaA    -(R2A+kAB)  +omega1     0           kBA         0;...
        0           -omega1     -(R1A+kAB)  0           0         kBA;...
        kAB         0           0       -(R2B+kBA)  -DOmegaB        0;...
        0           kAB         0       +DOmegaB   -(R2B+kBA) +omega1;...
        0           0           kAB         0       -omega1  -(R1B+kBA)];

        M_t(:,k) = (MStart + (A\ b)')*expm(A.*tSat) - (A\ b)';
end

% normalization
M_t = M_t./HP;
```

Code 3: Exponential Matrix Evaluation

```
M0Start = [ 0 0 0 0 HP*Mz0A HP*Mz0B 1]';

M_t = zeros(size(M0Start,1),size(satOffsets,2));

%----- solve matrix -----------------
for k=1:size(satOffsets,2)
        DomegaA = (satOffsets(k)-delA)*1e-6*omegaRef; % Hz
        DomegaB = (satOffsets(k)-delB)*1e-6*omegaRef; % Hz

        A=[...
        -(R2A+kAB) kBA      -DomegaA   0        0        0           0;...
        kAB      -(R2B+kBA)  0      -DomegaB     0        0           0;...
        +DomegaA   0     -(R2A+kAB)  kBA      +omega1     0           0;...
        0      +DomegaB     kAB    -(R2B+kBA)    0     +omega1        0;...
        0          0      -omega1     0     -(R1A+kAB)  kBA   R1A*Mz0A;...
        0          0           0    -omega1     kAB -(R1B+kBA) R1B*Mz0B;...
        0          0           0      0        0        0           0];

        M_t(:,k) = expm(A.*tSat)*M0Start;
end

% normalization
M_t = M_t./HP;
```

ONE EXPONENTIAL MATRIX EVALUATION More recently, Murase *et al.*[157] reported that Equation (3.6) can be rewritten in matrix form with different order: x {pool A, pool B}, y {pool A, pool B}, z {pool A, pool B}. This representation is now in contrast to the two matrix evaluation by Woessner *et al.*[234], *without* inhomogeneity $\vec{b}$. By the extension of one dimension (see 7th entry in $\vec{M}$ and $\hat{A}$), $\hat{A}$ becomes a square matrix again:

$$\frac{d}{dt}\underbrace{\begin{pmatrix} M_x^A \\ M_x^B \\ M_y^A \\ M_y^B \\ M_z^A \\ M_z^B \\ 1 \end{pmatrix}}_{=\vec{M}} = \underbrace{\begin{pmatrix} -(R_2^A+k_{AB}) & +k_{BA} & -\Delta\omega_A & 0 & 0 & 0 & 0 \\ +k_{AB} & -(R_2^B+k_{BA}) & 0 & -\Delta\omega_B & 0 & 0 & 0 \\ +\Delta\omega_A & 0 & -(R_2^A+k_{AB}) & +k_{BA} & +\omega_1 & 0 & 0 \\ 0 & +\Delta\omega_B & +k_{AB} & -(R_2^B+k_{BA}) & 0 & +\omega_1 & 0 \\ 0 & 0 & -\omega_1 & 0 & -(R_1^A+k_{AB}) & +k_{BA} & R_1^A M_{th}^A \\ 0 & 0 & 0 & -\omega_1 & +k_{AB} & -(R_1^B+k_{BA}) & R_1^B M_{th}^B \\ 0 & 0 & 0 & 0 & 0 & 0 & 0 \end{pmatrix}}_{=\hat{A}} \cdot \underbrace{\begin{pmatrix} M_x^A \\ M_x^B \\ M_y^A \\ M_y^B \\ M_z^A \\ M_z^B \\ 1 \end{pmatrix}}_{=\vec{M}} .$$

This has the simpler solution

$$\vec{M}(t) = \vec{M}_0 \cdot \exp(\hat{A} \cdot t) \ , \tag{3.8}$$

by computing $\exp(\hat{A} \cdot t) = \sum_{k=0}^{\infty} \frac{\hat{A}^k t^k}{k!}$. However, the summation of repeated powers of $\hat{A}^k$ is difficult to compute. As $\hat{A}$ is an $n \times n$ matrix and if $\hat{A}$ has a full set of eigenvectors (we use here the matrix of eigenvectors $\hat{T}$), then $\hat{A}$ is diagonalizable according to $\hat{T}^{-1}\,\hat{A}\,\hat{T} = \hat{D} \Leftrightarrow \hat{T}\,\hat{D}\,\hat{T}^{-1} = \hat{A}$. Thus, the diagonal matrix $\hat{D}$ is given by the eigenvalues, $\hat{D} = \operatorname{diag}[\lambda_1, \lambda_2, \dots, \lambda_2]$, and the exponential matrix computation yields then

$$\exp(\hat{A} \cdot t) = \hat{T} \operatorname{diag}[\exp(\lambda_1 t), \exp(\lambda_2 t), \dots, \exp(\lambda_n t)]\ \hat{T}^{-1} \ . \tag{3.9}$$

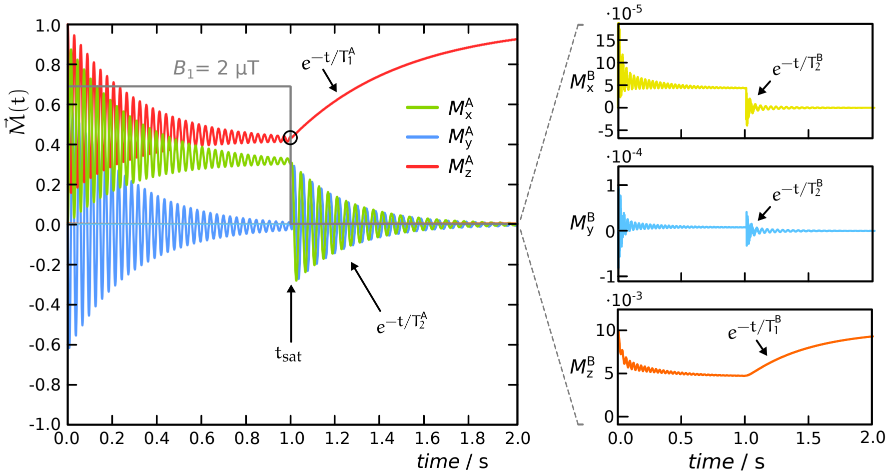

Figure 3.4: Numerically simulated time-evolution of the magnetization, $\vec{M}(t) = \{M_x^A$ (green), M_y^A (blue), M_z^A (red), M_x^B (light green), M_y^B (light blue), M_z^B (light red)$\}$, under cw irradiation of 2 μT for $t_{sat} = 1$ s (gray envelope) at a saturation frequency offset of $\Delta\omega = 1.4$ ppm for an artificial Xe system (for better illustration of the principle, the hyperpolarization is turned off: $\eta = 1$). The M_z^A component after the saturation pulse t_{sat} (black open circle), is used for the frequency evolution of Hyper-CEST (Figure 3.5). While the magnetization during saturation decays with effective relaxation times, afterwards it relaxes with the true longitudinal relaxation time $T_1^{A,B}$, and decays with transverse relaxation time $T_2^{A,B}$. Whereas this full time-evolution of the magnetization is mandatory for the Runge-Kutta-Integrator, the two matrix evaluation methods calculate the magnetization directly at the saturation time t_{sat}. Simulation parameters: 2-spin pool at clinical typically $B_0 = 1.5$ T, $T_1^A = 500$ ms, $T_2^A = 250$ ms, fractional size of pool A $f_A = 1$, $\delta_A = 0$ ppm, $T_1^B = 300$ ms, $T_2^B = 150$ ms, fractional size of pool B $f_B = 0.01$, Xe exchange rate $k_{BA} = 33$ s^{-1}, $\delta_B = -132$ ppm, saturation frequency offset = 1.4 ppm, total time evolution time = 2 s and time evolution increment = 0.001 s.

Similar to the two matrix evaluation method, $\vec{M}_0 = \{0, 0, 0, 0, \eta \cdot M_{th}^A, \eta \cdot M_{th}^B, 1\}^T$ is the initial available magnetization as starting condition. A MATLAB segment that was implemented for this thesis, which solves this task, is shown in Code 3.

Using these numerical methods, the Hyper-CEST system is fully described. To exemplify, similar to the Hyper-CEST experiment, the time-evolution for a 2-spin pool system with slow exchange rate of 33 s^{-1} under cw saturation of $B_1 = 2$ μT for $t_{sat} = 1$ s at a saturation frequency offset of $\Delta\omega = 1.4$ ppm is calculated (Figure 3.4; for better illustration with thermally polarization, $\eta = 1$). After saturation, the magnetizations relaxe with longitudinal relaxation times $T_1^{A,B}$, and decay with transverse relaxation times $T_2^{A,B}$.

z-Spectra through Frequency Evolution

Similar to the Hyper-CEST experiment, we simulate first the time-evolution of the magnetization under cw saturation pulse irradiation for one particular saturation pulse frequency offset $\Delta\omega$, and then read out directly after the saturation the z-component of the magnetization of the dominant pool A (black circle in Figure 3.4). This is then repeated multiple times, each time

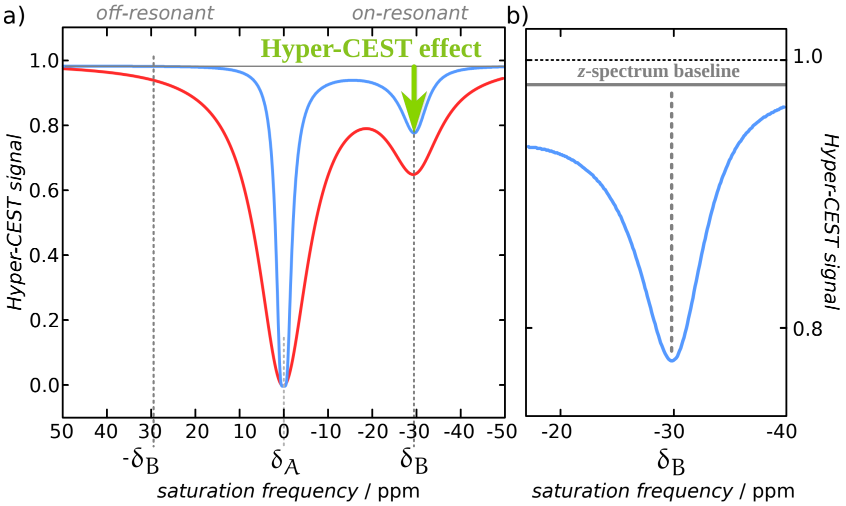

Figure 3.5: Numerically simulated 2-spin pool z-spectrum that is obtained through frequency evolution along the dimension of ω_{sat} by the following two steps: 1) time evolution for a particular saturation pulse frequency offset up to the saturation time, t_{sat}, and read out of the value M_z^A, as shown in Figure 3.4, and 2) frequency evolution by repetition of 1) for different saturation frequencies. While this is required for the Runge-Kutta-Integrator, the two matrix evaluation methods calculate directly the magnetization at the saturation time, t_{sat}. a) The Hyper-CEST effect, calculated by $(M_z^A(-\delta_B) - M_z^A(+\delta_B))/M_{z,0}^A$, corresponds to the length of the green arrow and takes also spillover into account (red curve; $B_{1,\text{red}} > B_{1,\text{blue}}$). b) The zoom in into the Hyper-CEST response of pool B shows that the baseline of a Hyper-CEST z-spectrum (gray line) decays with the longitudinal relaxation time T_1^A during the saturation time t_{sat}. Thus, if the data is normalized correctly to the initial (not just the off-resonant) z-component of the magnetization of pool A, $M_{z,0}^A$, the baseline is < 1. Therefore, 1 - baseline = T_1^A-effect.

with a different saturation frequency offset $\Delta\omega$. The resulting curve (Figure 3.5) is called a z-spectrum [Bryant[36]]. The aim is to maximize the Hyper-CEST effect, which is calculated by (compare with Figure 3.5, length of the green arrow)

$$\text{Hyper} - \text{CEST effect} = \frac{M_z^A(-\delta_B) - M_z^A(+\delta_B)}{M_{z,0}^A} \quad . \tag{3|10}$$

The Hyper-CEST effect is a useful measure, as it also takes spillover into account (red curve; $B_{1,\text{red}} > B_{1,\text{blue}}$). Spillover is the significant contribution to the depolarization of the CEST pool that originates from the direct resonance (visible at - δ_B), or generally, from any resonance that contributes, but is not belonging to this distinct magnetic environment. Spillover can make the Hyper-CEST effect appear larger then it actually is. Equation (3 | 10) corrects for this effect. However, the Hyper-CEST effect depends on the strength and duration of the saturation pulse and on the Xe exchange kinetics of the particular Xe-host molecule, making this optimization task complex.

Power and Limitations of Numerical Methods

The power of numerical methods to solve the BM equations is that they find highly accurate solutions without simplifications or approximations made

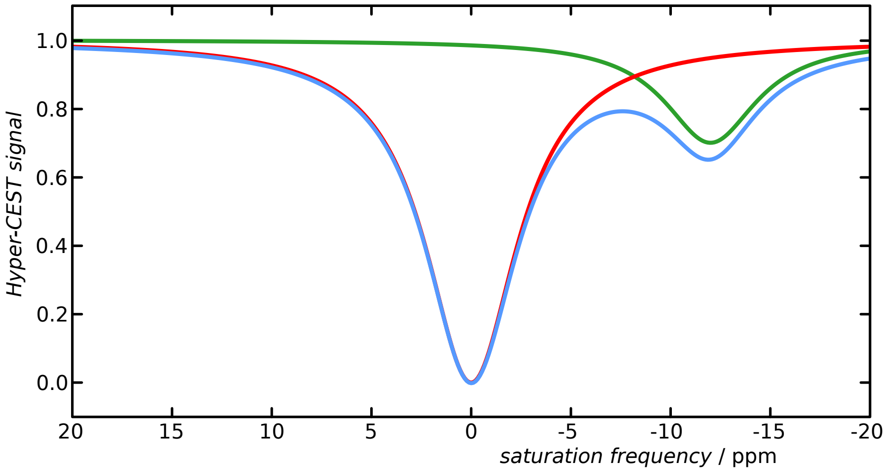

Figure 3.6: Decomposition of the total depolarization rate λ_{depol} of a 2-spin pool Hyper-CEST z-spectrum (blue curve) into two depolarization rates: 1) a direct saturation λ_{direct} (red curve), and 2) for the CEST pool saturation $\lambda_{\text{CEST}}^{\text{AB}}$ (green curve).

to the Hyper-CEST system. The main restriction is, however, their limited insight into the structure of a z-spectrum and the Xe-host exchange kinetics, without performing large number of simulations. In addition, their simulation speed can be time consuming. Analytical expressions, however, would provide insight into such structure of a z-spectrum and, in particular, how the different Xe-exchange parameters manifest in Hyper-CEST effect and in optimizing experimental designs.

3.1.6 Analytical Solutions of the BM Equations

For ^{1}H-CEST, different approximations were proposed that are all based on neglecting different terms in the BM equations in order to decouple them. In addition, further simplifications can be made when considering the steady-state condition of the magnetization, *i. e.*, the magnetization does not change for longer saturartion durations: $\frac{d\vec{M}}{dt} = 0$. Such simplifications can then yield analytical solutions with different ranges of validity. For example, the Henkelman model is valid for very fast transverse relaxation times such as magnetization transfer modeling [Henkelman *et al.*[95]]. The **weak saturation pulse** (WSP) approach assumes that only the CEST pool and no water pool is affected by the saturation pulse [Zhou *et al.*[257], Zhou and van Zijl[258]]. In contrast, the **strong saturation pulse** (SSP) approach is assuming a saturation pulse that is stronger compared to relaxation and exchange rate terms to neglect certain terms in the BM equations [Baguet and Roby[12]].

However, as the hyperpolarization is a highly artificial state far beyond thermal equilibrium that relaxes with longitudinal relaxation time towards thermally polarized magnetization, Hyper-CEST does not have such steady-state conditions (besides fully relaxed HP magnetization to thermal equilibrium for $t \to \infty$) and is always in a transient-state during the typical experimental time frame. However, in the following a proposed analytical approach for Hyper-CEST is reviewed which was actively used in this thesis.

The Full Hyper-CEST Solution

The transformation of $\hat{A}$ into a diagonal matrix allows to solve the BM equations by an eigenspace approach [Trott and Palmer[213], Trott *et al.*[212], Trott and Palmer[214], Zaiss and Bachert[242]]. Based on this eigenspace approach, Zaiss *et al.*[244] showed for the case of Hyper-CEST that the complex BM equations can be approximated analytically when the magnetization is always much larger than the stationary solution (as in Hyper-CEST). Under the assumption that the longitudinal relaxation times of both pools are similar, $T_1^A \approx T_1^B = T_1$, the **full Hyper-CEST** (FHC) model function for a Hyper-CEST z-spectrum yields

$$Z^{\mathrm{FHC}}_{\mathrm{Hyper-CEST}}(\Delta\omega) = \frac{M_z^A(t_{\mathrm{sat}})}{M_z^A(t_{\mathrm{sat}}=0)}(\Delta\omega) = e^{-\lambda_{\mathrm{depol}}(\Delta\omega)\cdot t_{\mathrm{sat}}} \quad , \tag{3|11}$$

with the total ^{129}Xe depolarization rate

$$\lambda_{\mathrm{depol}}(\Delta\omega) = -\lambda_{\mathrm{direct}}(\Delta\omega) - \lambda^{AB}_{\mathrm{CEST}}(\Delta\omega) \quad . \tag{3|12}$$

This total ^{129}Xe depolarization rate λ_{depol} consists of the direct saturation term of free Xe in solution $\lambda_{\mathrm{direct}}$, and the CEST pool depolarization term $\lambda^{AB}_{\mathrm{CEST}}$ (compare with Figure 3.6). Using the relaxation rates $R^{A,B}_{1,2} = 1/T^{A,B}_{1,2}$, both are given as follows:

$$-\lambda_{\mathrm{direct}}(\Delta\omega) = R_1^A \cos^2(\theta(\Delta\omega)) + R_2^A \sin^2(\theta(\Delta\omega)) \quad , \tag{3|13a}$$

$$-\lambda^{AB}_{\mathrm{CEST}}(\Delta\omega) = \frac{S_1 + S_2}{S_3 + S_4 + S_5 + S_6 + S_7 + S_8} \quad . \tag{3|13b}$$

Whereas θ in Equation (3|13a) is the angle between the effective magnetic field $\vec{B}_{\mathrm{eff}}$ and the z-axis (see Figure 3.2), Equation (3|13b) consists of the following terms:

$$S_1 = \omega_1^2 \frac{k_{AB}\cdot k_{BA}}{k_{AB}+k_{BA}} \cdot (\delta\omega_B - \delta\omega_A)^2 \tag{3|14a}$$

$$\begin{aligned} S_2 = {} & \frac{R_2^B}{k_{AB}+k_{BA}} \cdot \omega_1^2 k_{AB} \\ & \cdot (\Delta\omega_A^2 + (k_{AB}+k_{BA})^2 + k_{BA}R_2^B + \omega_1^2) \end{aligned} \tag{3|14b}$$

$$S_3 = (\Delta\omega_A(k_{BA}+R_2^B) + \Delta\omega_B k_{AB})^2 \tag{3|14c}$$

$$S_4 = (k_{AB}+k_{BA}+R_2^B)^2\omega_1^2 \tag{3|14d}$$

$$S_5 = (\Delta\omega_A\Delta\omega_B - k_{AB}R_2^B)^2 \tag{3|14e}$$

$$S_6 = \Delta\omega_B^2\omega_1^2 \tag{3|14f}$$

$$S_7 = k_{AB}R_2^B\omega_1^2 \tag{3|14g}$$

$$S_8 = \frac{k_{AB}+k_{BA}+R_2^B}{k_{AB}+k_{BA}}(\Delta\omega_A^2\omega_1^2 + \omega_1^4). \tag{3|14h}$$

For multiple spin pools, the FHC solution can be extended according to

$$\lambda_{\mathrm{depol}} = -\lambda_{\mathrm{direct}} - \lambda^{AB}_{\mathrm{CEST}} - \lambda^{AC}_{\mathrm{CEST}} - \lambda^{AD}_{\mathrm{CEST}} - \lambda^{AE}_{\mathrm{CEST}} - \ldots \quad . \tag{3|15}$$

Limits and Possibilities of the FHC Solution

As mentioned above, the FHC solution neglects the relaxation time of bound Xe T_1^B, and assumes that this is similar to that of free Xe in solution. For most cases this is sufficient. However, if this difference is large, *e.g.*, T_1^A = 125 s (typical for Xe in water or DMSO at 9.4 T and room temperature; Chapter 6) and T_1^B = 4 s (that may occur for some Cr derivatives [Huber *et al.*[104]]), and also in combination of exceeding a critical size of the bound Xe pool, then the FHC solution shows limitations and deviates from the solution obtained by numerical methods. We propose a correcting extension to the FHC solution by introducing the effective longitudinal relaxation rate $R_{1,\text{eff}}$ as the pool size weighted longitudinal relaxation rate average that is given by

$$\begin{aligned} R_{1,\text{eff}} &= \frac{f_A \cdot R_1^A + f_B \cdot R_1^B + f_C \cdot R_1^C + f_D \cdot R_1^D + \ldots}{f_A + f_B + f_C + f_D + \ldots} \\ &= \frac{\sum_{i=1}^{N} f_i \cdot R_1^i}{\sum_{i=1}^{N} f_i} \quad . \end{aligned} \tag{3|16}$$

Thus, the corrected baseline of the direct depolarization rate (Equation (3 | 13a)) yields then to

$$-\lambda_{\text{direct}}(\Delta\omega) = R_{1,\text{eff}} \cos^2(\theta) + R_2^A \sin^2(\theta) \quad , \tag{3|17}$$

as a more general modeling function.

The possibilities of the FHC solution is 1) its rather simple implementation, 2) straightforward application for multiple spin pools, 3) fast Hyper-CEST *z*-spectrum simulation time, and 4) potential for further approximations to intuitively show how the Xe exchange kinetics manifest in the Hyper-CEST effect and the structure of a Hyper-CEST *z*-spectrum.

3.2 BLOCH-MCCONNELL SOLVER (GRAPHICAL USER INTERFACE)

To systematically explore amplified Hyper-CEST sensitivity conditions and in order to plan Hyper-CEST experiments in advance, we designed and developed a GUI in MATLAB (screen shot given in Figure 3.7) solving the BM equations up to 4-spin pools (*i.e.*, a system of coupled first-order ODEs). As described in the previous sections, the following numerical methods were implemented:

a. Runge-Kutta-Integrator,

b. two matrix evaluations proposed by Woessner *et al.*[234] in 2005, and

c. one exponential matrix evaluation proposed by Murase *et al.*[157] in 2011.

In addition, the following analytical approximations were implemented (amongst others):

a. Henkelman model [Henkelman *et al.*[95]],

b. WSP approximation [Zhou *et al.*[257], Zhou and van Zijl[258]],

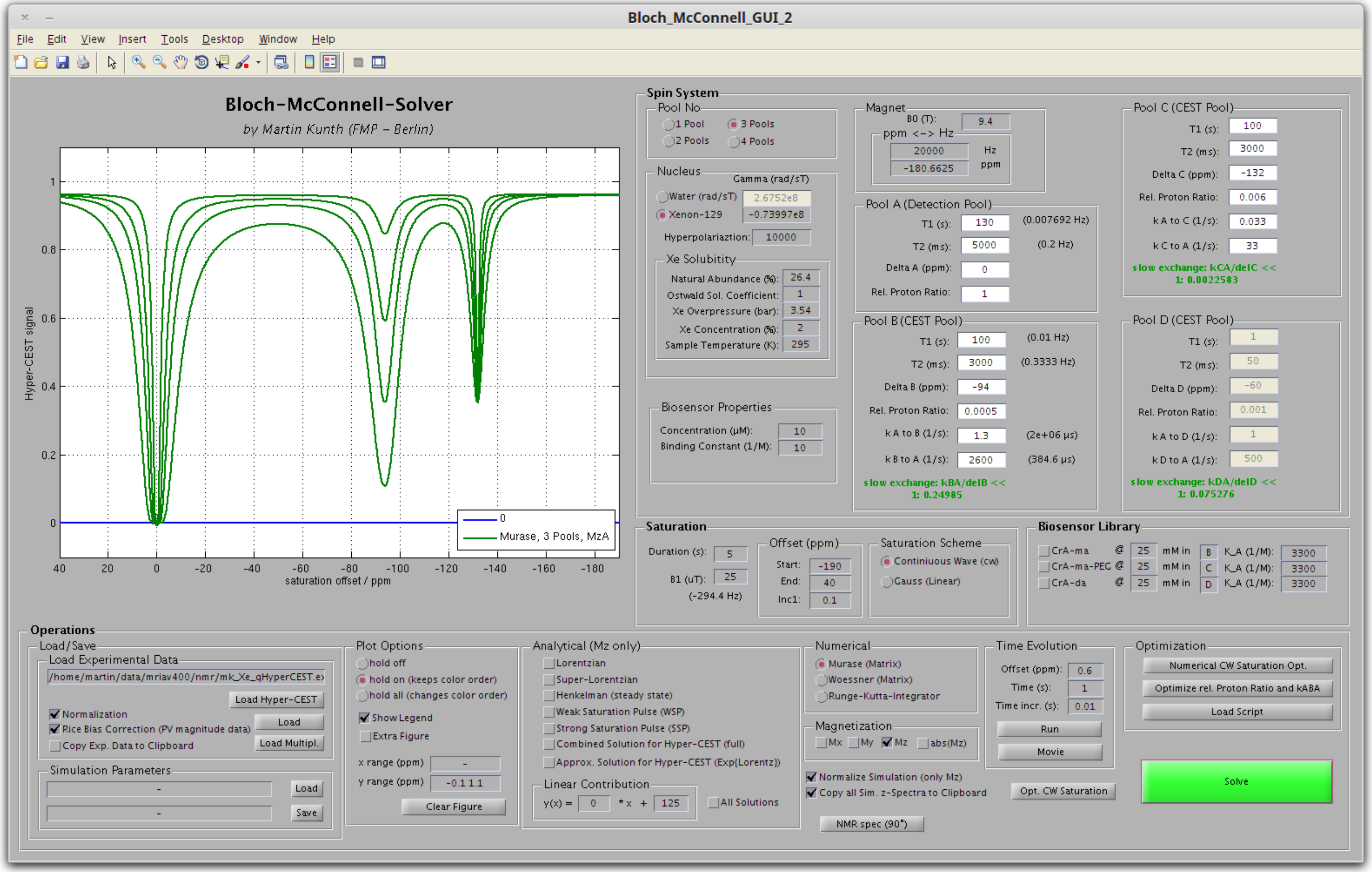

Spin System

Pool No: ○ 1 Pool ○ 2 Pools ● 3 Pools ○ 4 Pools

Nucleus: Gamma (rad/sT)
○ Water (rad/sT) 2.6752e8
● Xenon-129 -0.73997e8
Hyperpolariaztion: 10000

Xe Solubitity
Natural Abundance (%): 26.4
Ostwald Sol. Coefficient: 1
Xe Overpressure (bar): 3.54
Xe Concentration (%): 2
Sample Temperature (K): 295

Biosensor Properties
Concentration (µM): 10
Binding Constant (1/M): 10

Magnet
B0 (T): 9.4
ppm <-> Hz: 20000 Hz; -180.6625 ppm

Pool A (Detection Pool)
T1 (s): 130 (0.007692 Hz)
T2 (ms): 5000 (0.2 Hz)
Delta A (ppm): 0
Rel. Proton Ratio: 1

Pool B (CEST Pool)
T1 (s): 100 (0.01 Hz)
T2 (ms): 3000 (0.3333 Hz)
Delta B (ppm): -94
Rel. Proton Ratio: 0.0005
k A to B (1/s): 1.3 (2e+06 µs)
k B to A (1/s): 2600 (384.6 µs)
slow exchange: kBA/delB <<
1: 0.24985

Pool C (CEST Pool)
T1 (s): 100
T2 (ms): 3000
Delta C (ppm): -132
Rel. Proton Ratio: 0.006
k A to C (1/s): 0.033
k C to A (1/s): 33
slow exchange: kCA/delC <<
1: 0.0022583

Pool D (CEST Pool)
T1 (s): 1
T2 (ms): 50
Delta D (ppm): -60
Rel. Proton Ratio: 0.001
k A to D (1/s): 1
k D to A (1/s): 500
slow exchange: kDA/delD <<
1: 0.075276

Saturation
Duration (s): 5
B1 (uT): 25
(-294.4 Hz)

Offset (ppm)
Start: -190
End: 40
Inc1: 0.1

Saturation Scheme
● Continiuous Wave (cw)
○ Gauss (Linear)

Biosensor Library
☐ CrA-ma @ 25 mM in B K_A (1/M): 3300
☐ CrA-ma-PEG @ 25 mM in C K_A (1/M): 3300
☐ CrA-da @ 25 mM in D K_A (1/M): 3300

Operations

Load/Save
Load Experimental Data
/home/martin/data/mriav400/nmr/mk_Xe_qHyperCEST.e
☑ Normalization
☑ Rice Bias Correction (PV magnitude data)
☐ Copy Exp. Data to Clipboard
Simulation Parameters
-
-

Plot Options
○ hold off
● hold on (keeps color order)
○ hold all (changes color order)
☑ Show Legend
☐ Extra Figure
x range (ppm): -
y range (ppm): -0.1 1.1

Analytical (Mz only)
☐ Lorentzian
☐ Super-Lorentzian
☐ Henkelman (steady state)
☐ Weak Saturation Pulse (WSP)
☐ Strong Saturation Pulse (SSP)
☐ Combined Solution for Hyper-CEST (full)
☐ Approx. Solution for Hyper-CEST (Exp(Lorentz))
Linear Contribution
y(x) = 0 * x + 125
☐ All Solutions

Numerical
● Murase (Matrix)
○ Woessner (Matrix)
○ Runge-Kutta-Integrator

Magnetization
☐ Mx ☐ My ☑ Mz ☐ abs(Mz)
☑ Normalize Simulation (only Mz)
☑ Copy all Sim. z-Spectra to Clipboard

Time Evolution
Offset (ppm): 0.6
Time (s): 1
Time incr. (s): 0.01

Optimization

Figure 3.7: Bloch-McConnell Solver GUI, which was developed for this thesis, demonstrates simulations of Hyper-CEST *z*-spectra for two Xe hosts. In this simulation, the varying parameter is B_1 with values of {5, 10, 15, 25} µT, while all other parameters were constant and can be seen in the screen shot.

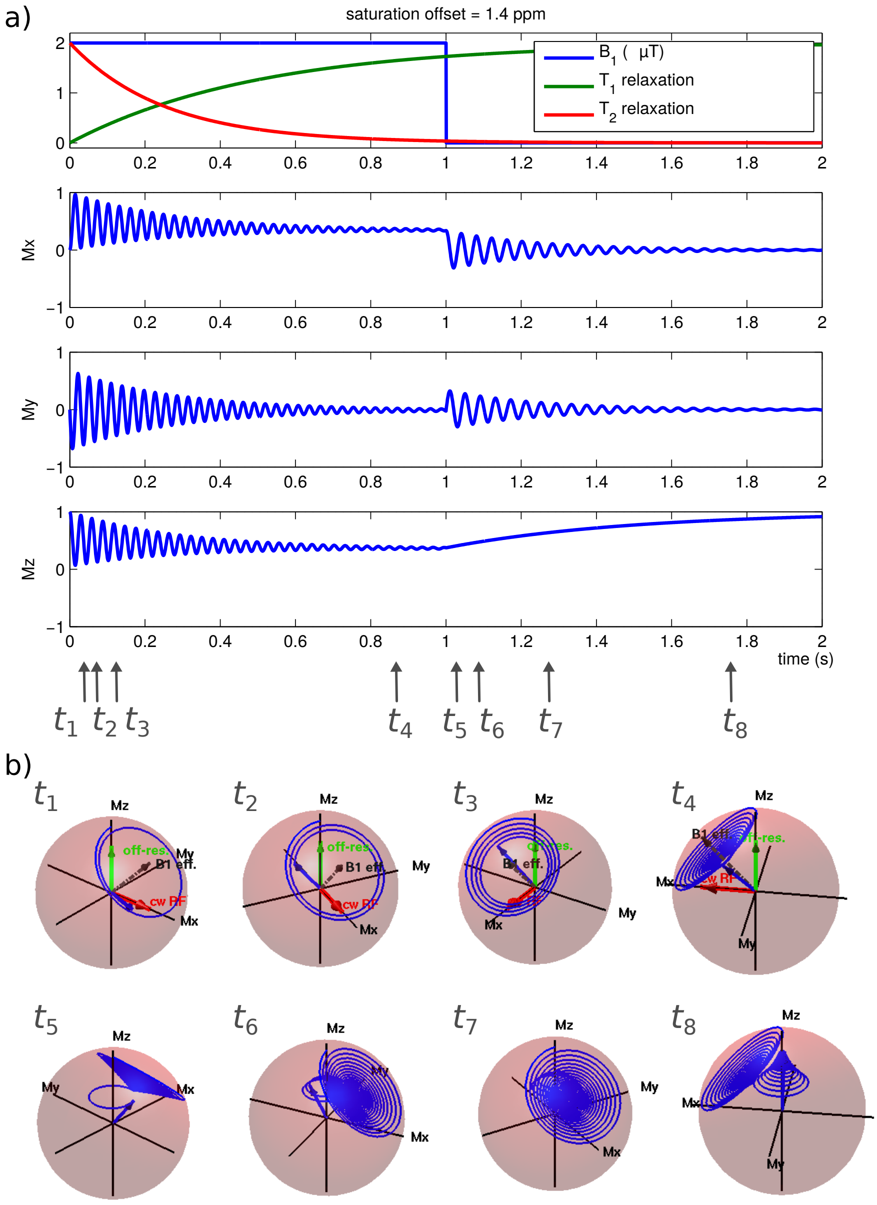

Figure 3.8: a) Time-evolution of the net magnetization (similar to Figure 3.4) under cw saturation including the relaxation time curves (top) as implemented in the BM solver GUI. All magnetization components, $\{M_x^A, M_y^A, M_z^A\}$, were numerically simulated by the BM equations and shown in the second, third, and forth plot from the top. b) Time-evolution of these magnetization components, $\{M_x^A, M_y^A, M_z^A\}$, within the Bloch-sphere (red transparent sphere) at time points $t_{1,\ldots,4} < 1$ s during saturation pulse irradiation. The superposition of the direction of the saturation pulse (*i.e.*, along the x-direction (red arrow; cw RF label)) and the off-resonances (*i.e.*, along the z-direction (green arrow; off-res. label)) spans an effective magnetic field (dashed dark brown arrow; B1 eff. label; analog to Figure 3.2a) about which the magnetization vector (blue arrow) precesses (blue trajectory of the arrow tip). After saturation, at time points $t_{5,\ldots,8} > 1$ s, the magnetization $\vec{M}$ precesses freely with respect to $\vec{B}_0 = \{0, 0, B_0\}^T$ and recovers along z with T_1, while decaying with T_2 in the x-y-plane.

c. SSP approximation [Baguet and Roby[12]], and

d. FHC solution [Zaiss *et al.*[244]].

The GUI is divided into five main parts: 1) the plot display, 2) the spin system, 3) the saturation, 4) the biosensor library and 5) the operations. In the spin system specification, the number of spin-pools, the type of nucleus and degree of hyperpolarization and the magnet with magnet strength corresponding conversion from ppm to Hz and *vice versa*, can be specified. In addition, the longitudinal and transverse relaxation times, the chemical shifts, the pool sizes relative to the detection pool (pool A) and the exchange rates can be entered directly to the respective CEST pools (up to three). The exchange regime on the NMR time scale with respect to the detection pool A is given below each CEST pool (additional font color encoding: slow (green), intermediate (yellow) and fast (red) exchange). The saturation pulse parameters such as the duration t_{sat} and strength B_1, the offset frequencies $\Delta\omega$ and the saturation scheme (cw, gauss-shaped or pulsed) is specified in the saturation part. In the options part, the different numerical and analytical solving methods can be chosen. Whereas the z-spectrum is the z-component of the magnetization vector, M_z^A, each component of the magnetization vector $\{M_x^A, M_y^A, M_z^A\}$ can be plotted.
Experimental ^{1}H-CEST or Hyper-CEST data can be loaded into the BM-GUI and manually be fitted.

TIME EVOLUTION In contrast to z-spectra, the time evolution of the net magnetization vector under RF irradiation (or saturation) can be animated (Figure 3.8) and/or saved as movie. This enables intuitive understanding of Hyper-CEST or ^{1}H-CEST experiments.

4 EXPERIMENTAL SETUP

Contents

This chapter describes the experimental setup, which is optimized for Hyper-CEST experiments with HP Xe. First, the custom-designed Xe polarizer is introduced. This is followed by the description of the NMR spectrometer. Putting both together, we report here the comparison of thermally polarized and HP ^{129}Xe gas NMR signals. In addition, we show the reproducibility of the Xe delivery into gas phase and for dissolved Xe in water and DMSO.

4.1 CUSTOM-DESIGNED XENON POLARIZER

The mobile custom-designed **LASER enabled increase of polarization for nuclei of imprisoned xenon** (LEIPNIX 150 duo) was developed at the FMP in the ERC BiosensorImaging group. The overview of the polarizer and the NMR magnet is shown in Figure 4.1. A schematic illustration is given in Figure 4.2.

In this thesis, the Xe gas mixture was either 2 % Xe (*i. e.*, 2/10/88 vol.-% Xe/N_2/He) or 5 % Xe (*i. e.*, 5/10/85 vol.-% Xe/N_2/He), all isotopes of natural abundance. The general procedure is as follows: The Xe gas mixture at 4.5 bar absolute pressure enters the polarizer and becomes hyperpolarized by SEOP. After hyperpolarization, HP Xe gas is guided through **perfluoroalkoxy alkane** (PFA) tubing into the NMR magnet. There, it is bubbled into solution within the bubbling phantom with a particular sample flow rate, for most experiments of 0.25 SLM.[1] The Xe flow through the sample was then stopped to perform the NMR measurement. After the measurement, the mostly depolarized, hence used, Xe is released to atmosphere. These timings were triggered by the individual pulse sequence (Figure 2.16).

At the heart of the LEIPNIX polarizer is a 150 W in cw mode operating **infrared** (IR) LASER system (wavelength of 795 nm and 0.5 nm bandwidth). The Xe gas pressure of 3.5 bar overpressure broadens the Rb absorption line allowing more of the pump LASER light to be absorbed. As the LASER light from the emitting diode bars is not 100 % linearly polarized (a prerequisite to produce circularly polarized LASER light for SEOP, described in Section 2.1.3; Figure 4.1a), the LASER beam is *"filtered"* by a beam splitter

---

[1] If for some experiments the sample flow rate was different from the value of 0.25 SLM, then it will be given in the text explicitly.

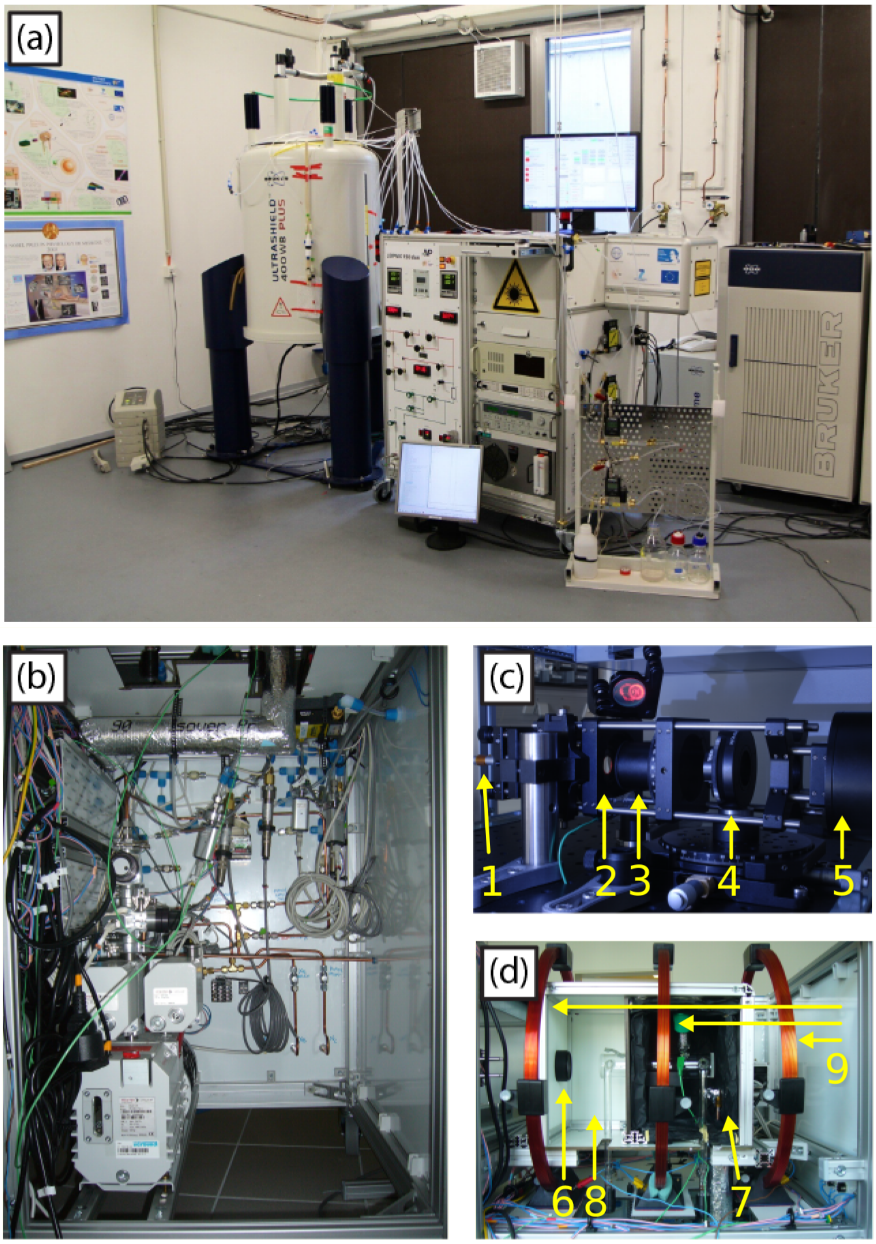

Figure 4.1: a) Experimental setup of the NMR magnet and the custom-designed LEIPNIX 150 duo polarizer. b-c) Inside of the polarizer (pictures taken from the back). b) Tubings were chosen to be made of copper and **perfluoroalkoxy alkane** (PFA), *pre* and *post* hyperpolarization within the optical pumping cell, respectively. PFA minimizes shortening of the Xe longitudinal relaxation time by Xe-wall interactions inside the tubings. c) Optics from left to right: the LASER fiber (1), collimator with temperature sensor (green wire; 2), beam splitter cube (including the reflection mirror to the beam dump; shown here with red light from the aiming beam; 3), $\lambda/4$ plate (4) and beam expander (5). d) shows the optical pumping glass cell inside the oven (in which LASER light enters from the left (6); the oven box is divided into two chambers: a heated one (right with black insulation; 7) and an actively cooled one (left; 8)). The oven sits within a modified Helmholtz coil configuration (orange coils; 9).

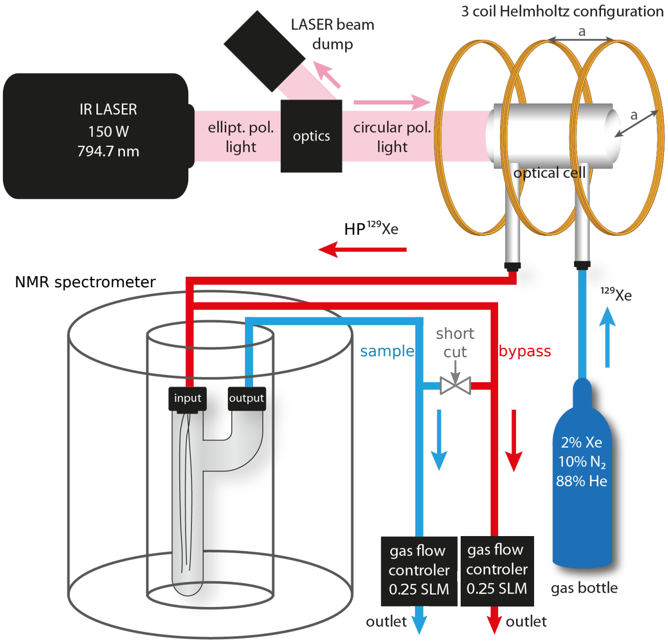

Figure 4.2: Schematic of the experimental setup shown in Figure 4.1. Bottom right: The 2 % Xe gas mixture leaves the gas bottle and enters the optical pumping cell at an overpressure of 3.5 bar. The optical pumping cell is placed within a modified Helmholtz coil configuration (each with same radius and distance, a, placed on the same axis). Xe becomes hyperpolarized *via* SEOP in the optical pumping cell using **infrared** (IR) left-circularly polarized LASER light. The HP Xe (red tube) is then guided into the phantom that sits inside the NMR spectrometer. If the Xe gas flow through the sample is stopped for NMR measurements the bypass maintains the Xe gas flow through the optical pumping cell. To disperse Xe bubbles inside the phantom immediately after stopping the gas flow a short cut valve connects the sample with the bypass flow.

cube (Figure 4.1c) that was adjusted for maximal LASER light transmission (polarization optimization shown in Figure 4.3). Left-circularly polarized light was then produced with a $\lambda/4$ plate.

One important requirement for Hyper-CEST (as a difference image method; Figure 2.17e), and in particular for quantitative Hyper-CEST experiments is a stable and reproducible Xe delivery into the sample with stable Xe starting signals between different measurements. Therefore, one fundamental requirement for our setup is that the Xe flow through the optical pumping cell must stay constant over a large period of repeated measurements to produce the same degree of Xe hyperpolarization. If the Xe gas flow through the sample, however, is stopped during an NMR measurement, then this would normally also stop the Xe flow through the optical pumping cell. This results in a significant increased Xe residence time within the optical pumping cell. Consequently, the degree of hyperpolarization will be different. Once the Xe gas flow is turned on again, this different degree of hyperpolarization travels to the phantom and becomes delivered to the sample of investigation. Thus, the calculated Hyper-CEST effect may show a signal change, although it was only a change in Xe hyperpolarization. To avoid this effect, we maintain the total flow rate within the optical cell constant by

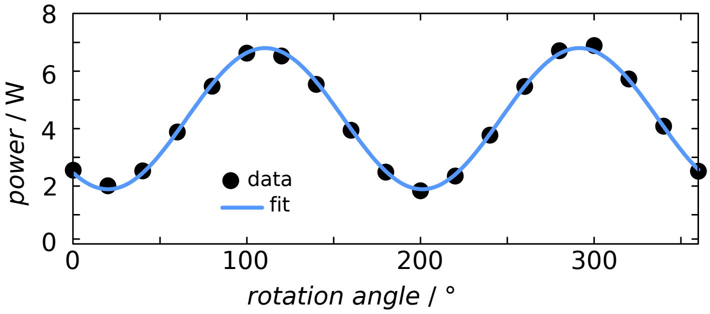

Figure 4.3: LASER polarization optimization by beam splitter cube rotation angle adjustment. Data (black closed circles) were fitted to the function $P(\alpha) = P_0 + A_0 \cdot \left(\sin\{\pi/\alpha_{\text{period}} \cdot (\alpha + \varphi_0)\}\right)^2$ (blue curve; fitting parameters: P_0 = (1.89 ± 0.04) W, A_0 = (4.91 ± 0.06) W, α_{period} = (180.9 ± 0.6)° and φ_0 = (- 20.1 ± 0.7)°). Thus, the optimal angle with maximum linear polarized LASER light transmission is given by $\alpha_{\text{opt}} = \alpha_{\text{period}}/2 - \varphi_0$ = (110.5 ± 0.9)°.

bypassing the Xe gas mixture around the sample, while the flow through the sample is stopped for data acquisition (Figure 4.2).

In addition, the LEIPNIX polarizer has the following two special key features:

1. One problem in conventional optical pumping setups is the Rb runaway effect. The Rb runaway effect means that Rb in the *"wrong"* spin state *"steal back"* some hyperpolarization from the already polarized Xe nuclei, in the worst case directly before the Xe leaves the optical pumping cell. This results in a significant decrease of the Xe NMR signal. By actively cooling the optical pumping cell at the Xe exit with air at room temperature causes a strong temperature gradient relative to the heated part of the cell (at 190 ° C). This forces the Rb vapor to preferably stay in the hot part of the optical pumping cell and HP Xe can exit while remaining hyperpolarized. Therefore, as a particular feature of the LEIPNIX polarizer, the glass cell sits in an oven box that is divided into two compartments to generate a hot and cold volume (Figure 4.1d; this is the dou in the name) [Patent application[188]]. This prevents the Rb runaway effect [Witte *et al.*[231]]. A simple heater underneath the glass cell maintains constant temperatures usually between 90 °C to 160 °C (see Table 4.1) while the Xe gas mixture is continuously flowing.

2. Another special feature is the three Helmholtz coil configuration to save space in the setup of the mobile polarizer (Figure 4.1d and Figure 4.2). We optimized the current of the center coil, I_{center}, such that the produced total magnetic induction of the three Helmholtz coil configuration, $\vec{B}_{\text{HH}}$, shows minimized variations in amplitude and vectorial directions (Figure 4.4). We modeled the magnetic induction by extending the analytical expressions for the magnetic field of a single circular current loop (given by Simpson *et al.*[195]) to three current loops that are placed similar to the Helmholtz coil pair with distances which are equal to the radius (compare with Figure 4.2). By searching for the optimum current of the coil that is placed in the center between the outer coils, we found that minimal variations in the amplitude of the magnetic induction is obtained for the current of the center coil

Table 4.1: Operating pumping cell temperatures of LEIPNIX. Once the polarizer is stabilized in equilibrium, these temperatures reproducibly adjust depending on the Xe concentration [Xe], the LASER diode current (here fix at 38 A), and the total flow rate (*i. e.*, the sum of the flow rate through the sample and the bypass; former was varied here, while the latter one was constant at 0.25 SLM for all listed entries). The overpressure at the inlet and outlet was 3.48 bar. The silicon heater set temperature was 190 °C.

Xe	Sample Flow Rate / SLM	Hot 1 / °C	Hot 2 / °C	Cold / °C
2 %	0.18	130	102	99
2 %	0.1	146	114	121
2 %	0.07	131	102	101
5 %	0.1	145	117	109

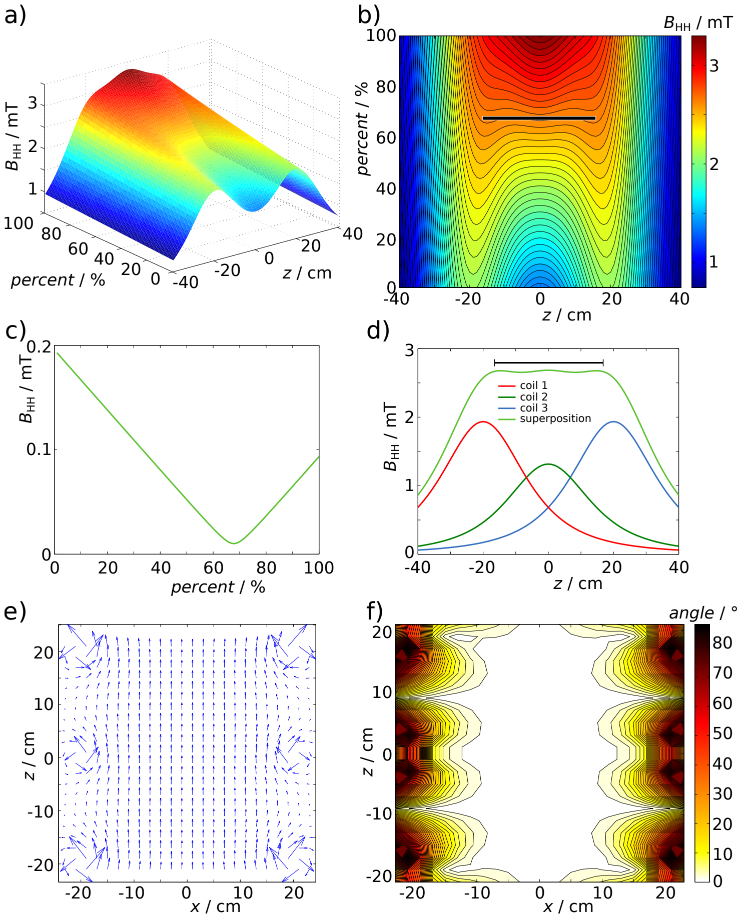

Figure 4.4: Optimization of the modified Helmholtz coil configuration (three coils as shown in Figure 4.1d and Figure 4.2). Setup: number of windings, N = 154 per coil, each coil has a radius of $a = 20$ cm, the current of the two outer coils was $I_{out} = 4$ A each. The LASER light traveling direction is in z-direction. a) and b) show the total magnetic field strength, $B_{HH} = |\vec{B}_{HH}|$, at $x = y = 0$ cm along the z-axis with respect to the percentage value of the center coil current, $I_{center} = \text{percent} \cdot I_{out}$, as surface and contour plot. c) shows the standard deviation of the magnetic field strength calculated from a pathway along the black line in b) (between - 17 cm to 17 cm), which minimizes for 68 % (*i. e.*, $I_{center} = 0.68 \cdot I_{out}$). The particular profile of (b) is shown in d). e-f) show that for this optimal center coil current the deviation angle of the field to the quantization axis which is given by the LASER light travel direction results in deviations of less than 2° (one contour line step corresponds to 2°).

of $I_{center} = 0.68 \cdot I_{out}$ (see Figure 4.4a-d). The deviation angle of the field to the quantization axis given by the LASER light travel direction shows deviations of less than 2° in the center where the glass cell sits (Figure 4.4e,f). However, larger Xe NMR signals were obtained for different values of I_{center}, demonstrating that the magnetic fringe field where the HP Xe travels out of the optical pumping cell through field vortexes has also to be taken into account [Kunth *et al.*[128]].

In summary, the following hardware was used:
The glass cell for optical pumping was custom-designed using Pyrex glass and planar windows.

The 2 % or 5 % Xe gas mixtures were purchased from PRAXAIR NV, Belgien (filling pressure: 150 bar; volume: 7,500 liter; valve typ: N14 HPSS TD). When replacing an empty gas bottle, all tubings of the entire polarizer were evacuated (preferably over night) using a vacuum unit with turbo pump unit from PFEIFFER VACUUM to remove potential contamination with H_2O and oxygen that can react with Rb within the glass cell. The IR LASER system (795 nm, 0.5 nm bandwidth) was manufactured by QPC Lasers, Sylmar, CA, USA. It is driven by a high power LASER diode current source from ILX Lightwave (Model LDX-3690). The LASER chiller (QPC Lasers, Inc.) was set to 16.5°C when using 2 % Xe for a LASER current of 38 A or to 17.5°C when using 5 % Xe and 36 A. In order to adjust the LASER optics without running the invisible IR LASER, a visible red light aiming beam was used that was driven at 3 V and 30 mA DC power supply (Agilent Technologies, model N6700B, 400 Watt; Figure 4.1c; red circle in the mirror above the optics).

Below the optical pumping cell a silicon heater was placed and controlled using a PID device from OMEGA (CN7800) that had a temperature setting point of 190°C. All the valves were purchased from Swagelok. To minimize loss of hyperpolarization by Xe-wall interactions, all the tubings after Xe hyperpolarization were made of PFA, whereas all the tubings before the optical pumping cell were made of copper (Figure 4.1b). The overpressure meters were from NEWPORT. The typical Xe gas overpressure was 3.5 bar, thus, a total pressure of 4.5 bar of Xe is applied to the solution. The Xe flow rate was controlled by two different mass flow controllers: 1) for the sample: OMEGA FMA5408 with 0-100 mL/min = 0-0.1 SLM, and 2) for the bypass: OMEGA FMA5516 with 0-2 SLM. All these elements were arranged to be able to control the polarizer by custom-designed software in DASYLab11 (V 11.00.00 Sep 21 2009).

While not running Xe experiments, the polarizer was backed up with an overpressure of > 2 bar using the (less expensive) noble gas argon that was purchased from AIR LINDE (pressure at 15°C: 200 bar; volume: 10,700 liter; valve typ: DIN 477, No. 6).

4.2 NMR SPECTROMETER

In this thesis, the BRUKER ULTRASHIELD 400 WB PLUS NMR magnet (Bruker Biospin, Ettlingen, Germany) with field strength B_0 of 9.4 T was used (causing a ^{1}H Larmor frequency of 400 MHz; Table 1.2). It is equipped with gradient coils for MR imaging and a variable temperature unit that was – if not stated otherwise – adjusted to room temperature (T = 295 K ~ 22 °C). A 10 mm inner-diameter double-resonant probe (^{129}Xe and ^{1}H) was used for excitation and detection. As variable temperature unit, the

BRUKER BVT 3000 Digital was used. The amplifier model was BLAX 300 RS for x-nuclei, and BLAH 300 for protons. For signal acquisition, the AQS CHASSIS (Z003414) was used. The transmitter/receiver unit was BSMS/2 (Z002798).

For MR imaging, the gradient unit BRUKER GREAT 3/60 MASTER UNIT (amplifier X: GREAT 1/40A, amplifier Y: GREAT 1/40A, amplifier Z: GREAT 1/40A) was used. The GREAT B0 COMPENSATION UNIT B0+H0, compensates the B_0 drift. For tuning and matching of the proton channel, the HPPR 1H LNA MODULE 400 - PREAMPLIFIER, whereas for the x-nuclei channel the HPPR X-BB19F 2HP MODULE 400 - PREAMPLIFIER, were used.

Whereas the NMR magnet was controlled with the software TopSpin Version 2.0PV (July 2010) to acquire NMR spectra, ParaVision Version 5.1 (Apr-2010) was used for MR imaging.

4.3 EXPERIMENTAL PROTOCOLS

4.3.1 Phantom Preparation

A typical phantom was either a single bubbling phantom (Figure 4.2) or a double compartment bubbling phantom (see Figure S2 in Supporting Information of Kunth and Döpfert *et al.*[121] which is attached in Appendix Section D.1). The phantom was filled with Xe host-containing solutions (mostly water or DMSO) that were then measured. After the measurements the phantom was at least three times rinsed with pure water and each time carefully brushed using pipe cleaners. Finally, to remove residual compounds inside the phantom, it was rinsed with acetone and dried using nitrogen gas.

Care has to be taken in ultra high diluted Xe-host concentrations as residual molecules from previous measurements may stuck on the phantom walls or the silica glass capillaries. For published measurements, the silica glass capillaries were always replaced by new ones.

4.3.2 Thermally Polarized versus Hyperpolarized ^{129}Xe NMR

Putting both the polarizer and the NMR magnet together, the comparison between higher concentrated thermally polarized Xe gas mixture (with 90 % Xe that contains naturally abundant ^{129}Xe) and 2 % HP Xe gas containing naturally abundant ^{129}Xe shows a signal enhancement factor by hyperpolarization of approximately, $\eta \cong 25{,}000$ (Figure 4.5). This enables effortless the NMR detection of extremely low amounts of HP Xe (*e. g.*, < 400 µM at room temperature in water at a total pressure of 4.5 bar).

4.3.3 Xenon Delivery

The stable Xe delivery into the sample is crucial for Hyper-CEST measurements and, in particular, for quantitative Hyper-CEST measurements. To validate its stability, we recorded 64 times the ^{129}Xe NMR signal of pure Xe gas that is continuously flowing through the phantom (Figure 4.6a). It shows an excellent shot-to-shot noise of below 1 % (Figure 4.6b).

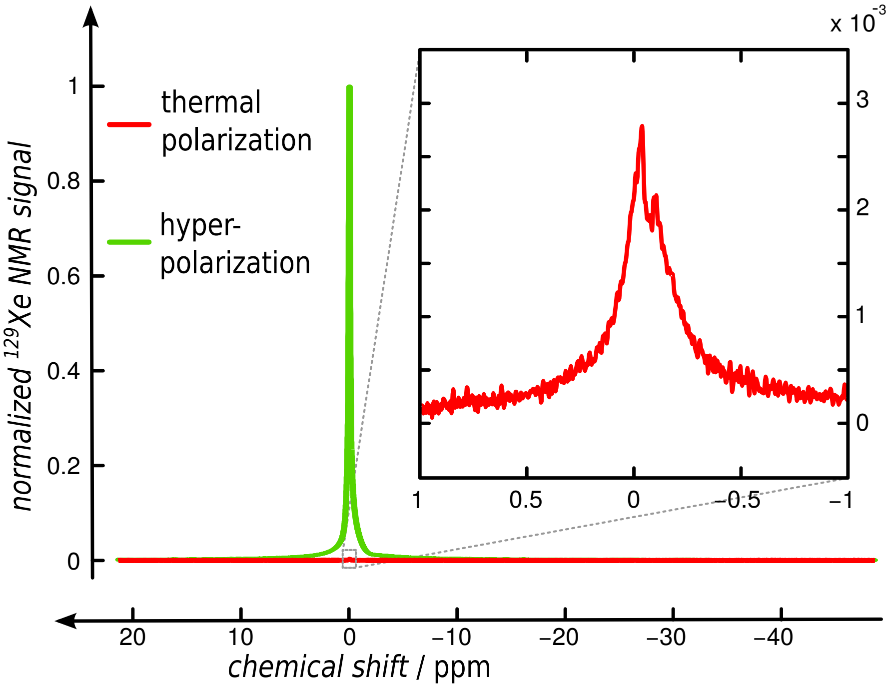

Figure 4.5: Thermally polarized versus hyperpolarized ^{129}Xe NMR signal. Whereas the red curve corresponds to the signal of thermally polarized Xe gas mixture of 90 % Xe containing naturally abundant ^{129}Xe at a total pressure of 2.79 bar, the HP Xe (green) was 2 % at a total pressure of 4.5 bar. Thus, the signal enhancement factor by hyperpolarization is about $\eta \cong 25{,}000$.

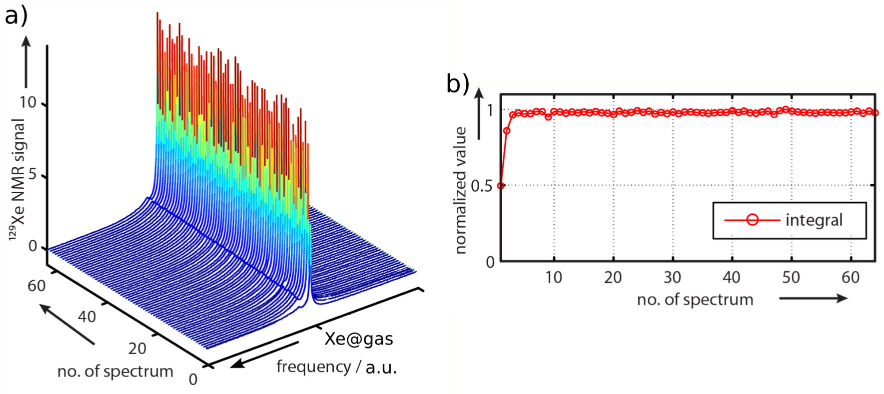

Figure 4.6: Reproducibility of HP Xe gas re-delivery. a) A total of 64 ^{129}Xe NMR spectra (90° excitation RF pulse) using a TR = 10 s while HP Xe gas is continuously flowing through the phantom. b) The integrated Xe NMR signal shows first an increase of signal as Xe gas flow was turned on and reaches a constant value (here normalized to 1). The shot-to-shot noise for the integrated signal is below < 1 %.

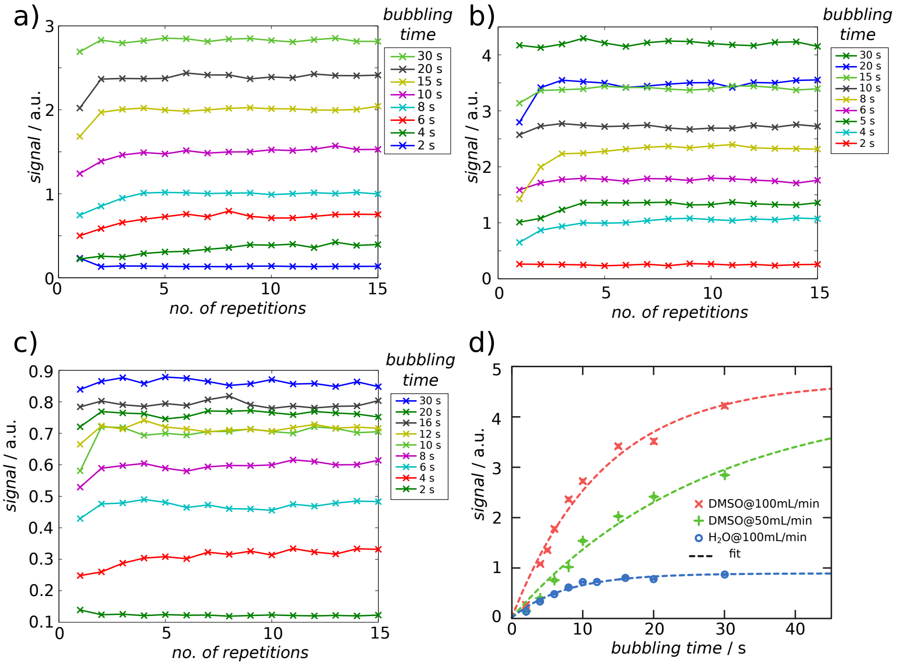

Figure 4.7: Delivery of 2 % Xe gas mixture into different solvents at different flow rates. a) Xe bubbling time into a solution of pure dimethyl sulfoxide (DMSO) at a flow rate of 50 mL per minute. b) Xe bubbling time into DMSO at a flow rate of 100 mL per minute. c) Xe bubbling time into water at a flow rate of 100 mL per minute. (a-c) shows that for small flow rates and short bubbling times four repetitions of Xe re-delivery are required to achieve stable Xe signal. Some combinations of flow rate and bubbling time show oscillations in the repetitive Xe NMR signal. Therefore, the Xe NMR signal versus the bubbling time, plotted in (d), was averaged for the last 10 data points and monoexponentially fitted to a saturation function (dashed line; published in Kunth *et al.*[126]).

Moreover, we investigated the stability of the Xe NMR signal of Xe that is dissolved in water and DMSO for multiple repetitions and with respect to the Xe bubbling time. As expected, while the shot-to-shot noise for Xe in DMSO (< 3 %) and water (< 5 %) is low, it increases as the Xe solubility decreases according to the Ostwald solubility coefficient (Figure 4.7). We fitted the signal in Figure 4.7d with respect to the bubbling time BT using the function $S(BT) = A_0 \cdot (1 - \exp\{-BT/\tau\})$ with the following fit results:

- H_2O at 100 mL per minute: A_0 = (0.88 ± 0.04), τ = (8 ± 1) s,
- DMSO at 100 mL per minute: A_0 = (4.7 ± 0.4), τ = (13 ± 2) s, and
- DMSO at 50 mL per minute: A_0 = (4.4 ± 0.9), τ = (27 ± 8) s.

The ratio of $A_{0,DMSO}/A_{0,H_2O} \sim 5$ and differs from the value 6, as expected from the ratio of both Ostwald coefficients. Thus, the total measured signal is influenced by the build up due to HP Xe bubbling while HP Xe starts to decay with its longitudinal relaxation time $T_1{}^A$ (~ 125 s for both solvents).

In summary, the LEIPNIX 150 dou provides a huge NMR signal enhancement factor of > 20,000 (compared to thermally polarized Xe), and excellent reproducible Xe delivery, thus, optimal conditions for the Hyper-CEST method.

Part III

Results & Discussion

5 SINGLE-SHOT HYPER-CEST MRI

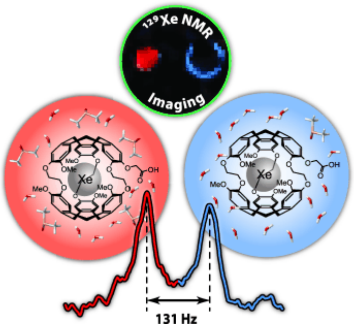

The work described in this chapter was done in collaboration with Dr. Jörg Döpfert and is partly published. It has been honored with a jointly awarded Gorter-Award of the German Chapter of the International Society for Magnetic Resonance in Medicine 2012. This chapter describes several advantages that can be achieved by single-shot Hyper-CEST MRI. For example, multiplexed MR imaging of two CAs that are separated by 131 Hz (or 1.2 ppm at 9.4 T), while preserving high spectral sensitivity (Figure left).

Contents

5.1 INTRODUCTION

An important contribution to the Xe biosensor field was the first spatial encoding with spectrally resolved MR image of Xe biosensors that was demonstrated by Hilty *et al.*[101]. Whereas this image was a 1D projection of immobilized Xe biosensors, the CrA concentration was with 82 µM rather high, and the scanning time was with 135 minutes challenging for biomedical applications. As Xe binds reversibly to such host structures, the reversible Xe binding has been used in two ways:

1. direct detection by repetitive sensor-selective excitation that was reported by Berthault *et al.*[19], and
2. indirect detection by Hyper-CEST proposed by Schröder *et al.*[187].

The first method shows the ability to readout the bound Xe NMR signal by excitation directly on-resonant and incorporate a defined waiting time to let fresh HP Xe exchange back into the Cr-host. This is followed by the next selective excitation and so forth. As it uses a fast GRE imaging pulse sequence, the total acquisition time was with 25 s already fast but, however, without the ability of slice selection. As this method is a direct ^{129}Xe NMR technique, all the challenges that were discussed in the Chapter 1 apply, also here: 1) a large Xe-host concentration is required (*i. e.*, [Cr-111 and Cr-222] = 300 μM), 2) for multiplexing, a large chemical shift difference between both bound Xe resonances is needed (here $\Delta\delta$ = 60 ppm - 37 ppm = 23 ppm; further resonance broadening is expected when slice selection imaging gradients will be turned on additionally), and 3) if the Xe exchange rate is too fast, then the resonance broadens and the Xe NMR signal may not be visible (compare with Figure 2.6).

The second MR imaging method, Hyper-CEST, comes with very high sensitivity. In the first implementation, the detection of [Cr] ~ 5 μM was demonstrated with room for further sensitivity improvements. Moreover, the Hyper-CEST method comes with the ability to use any readout scheme (*i. e.*, spectroscopic or imaging, *e. g.*, GRE, spin-echo, EPI, RARE, *etc.*; see Figure 2.16) after the saturation preparation. However, the first implementation was very time consuming, as for a matrix size of 8×8 for one image was acquired after ~11 minutes. For illustrating the spatial distribution of the biosensors, two Hyper-CEST data sets are required, which sums up to a total measurement time of 22 minutes.

Here, we report drastic improvement in Xe biosensor MR imaging acquisition time for the Hyper-CEST technique by combining it with the fastest single-shot pulse sequence currently available (Cartesian k-space coverage), the EPI. We report that this speed in image acquisition time has several advantages such as nanomolar imaging, true single-shot sub-second imaging (with the ability of intrinsic Hyper-CEST effect normalization), and being that fast to be able to monitor Cr diffusion through a dialysis tubing with a whole image series in a short time frame down to < 10 minutes. To address sensitivity amplification strategies of Hyper-CEST as a potential molecular imaging modality, we exploited here – as intermediate step – the imaging speed to acquire entire *z*-spectra from spatially resolved data within the same amount of time as used for two on-/off-resonance images using the original implementation. The shape of such *z*-spectra is characteristic and can provide – under careful analysis – insights into the fundamental Hyper-CEST mechanism (see next chapter Chapter 6).

5.2 POLARIZER OPTIMIZATIONS

A high initial magnetization from HP nuclei is a prerequisite for single-shot ^{129}Xe MR imaging techniques, such as EPI or RARE pulse sequences. In order to fulfill this condition, we designed our LEIPNIX 150 duo Xe polarizer accordingly to effortless yield signal enhancement factors $\eta > 20{,}000$ as described in Chapter 4.

5.3 RESULTS AND DISCUSSION

5.3.1 Pulse Sequence Optimization

In the following, we compare the SNR of a multiple-shot GRE pulse sequence that is optimized for best use of a hyperpolarized signal through the VFA approach [Zhao *et al.*[253]] (introduced in Section 2.2.1), with a single-shot EPI.

Multiple-Shot Gradient Echo

CONSTANT VERSUS VARIABLE FLIP ANGLE We first measured and compared the signal decay of HP ^{129}Xe under repeated RF pulse excitation without redelivery of fresh HP Xe between the pulses. This was performed for various constant flip angles of $\alpha = \{2.5^\circ, 5^\circ, 7.5^\circ, 10^\circ, 12.5^\circ, 15^\circ, 20^\circ, 25^\circ\}$ and a tailored VFA schedule for 32 RF pulses (Figure 5.1). By switching off phase encoding we could display the signal decay in k-space. Each k_y-line corresponds therefore to a $k_y = 0\,\mathrm{s}^{-1}$ value. This had the advantage that the signal decay did not interfere with the phase encoding gradient signal dephasing effect along this direction (Figure 5.1a top). Below each k-space the 2D FT reconstructed ^{129}Xe MR image with enabled linear phase encoding is shown. For repeated RF pulse excitation with a small constant flip angle of 2.5°, the transverse component of the HP magnetization $M_\perp$ is equally distributed for all 32 pulses, while the signal is barely above the noise (compare averaged signal profile between the two dashed black lines around k_x-center that is plotted in Figure 5.1b; dark blue down pointing triangles). This shows that "unused" HP magnetization is left in the sample as this flip angle was constant but the signal not decaying. In contrast, large constant flip angles of 25° produce large signal at the beginning for the first few pulse repetitions, but use up larger amounts of the HP magnetization which results in a quick signal decay (blue crosses in Figure 5.1b). Such nonuniform signal distribution in k-space can result in not optimal reconstructed ^{129}Xe MR images.

However, the VFA schedule for 32 RF pulses shows excellent equally distributed HP magnetization throughout all 32 excitation pulses (green stars in Figure 5.1b) with optimal distributed overall signal, as described in Figure 2.11. This results in optimal ^{129}Xe MR image quality.

These experiments demonstrated that each RF pulse uses up a certain fraction of the HP magnetization. Therefore, less number of RF pulse excitations results in larger SNR in the ^{129}Xe MR images. We therefore optimized the pulse sequences to record less data than the fully sampled k-space (described in Section 2.2.2) using partial Fourier acceleration.

PARTIAL FOURIER ACCELERATION We exploit the symmetry in k-space to actually omit larger fractions in k-space, while being able to reconstruct the missing data by an algorithm as a post-processing step, known as partial Fourier acceleration. This has the large advantage to acquire less data which results in larger HP magnetization portions per data block and eventually in larger ^{129}Xe MR image SNR and contrast.

As two quadrants of the k-space are the complex conjugated of the other two (Figure 5.2), it can – in theory – be enough to acquire only two quadrants and reconstruct the missing two parts. In practice, however, imperfect

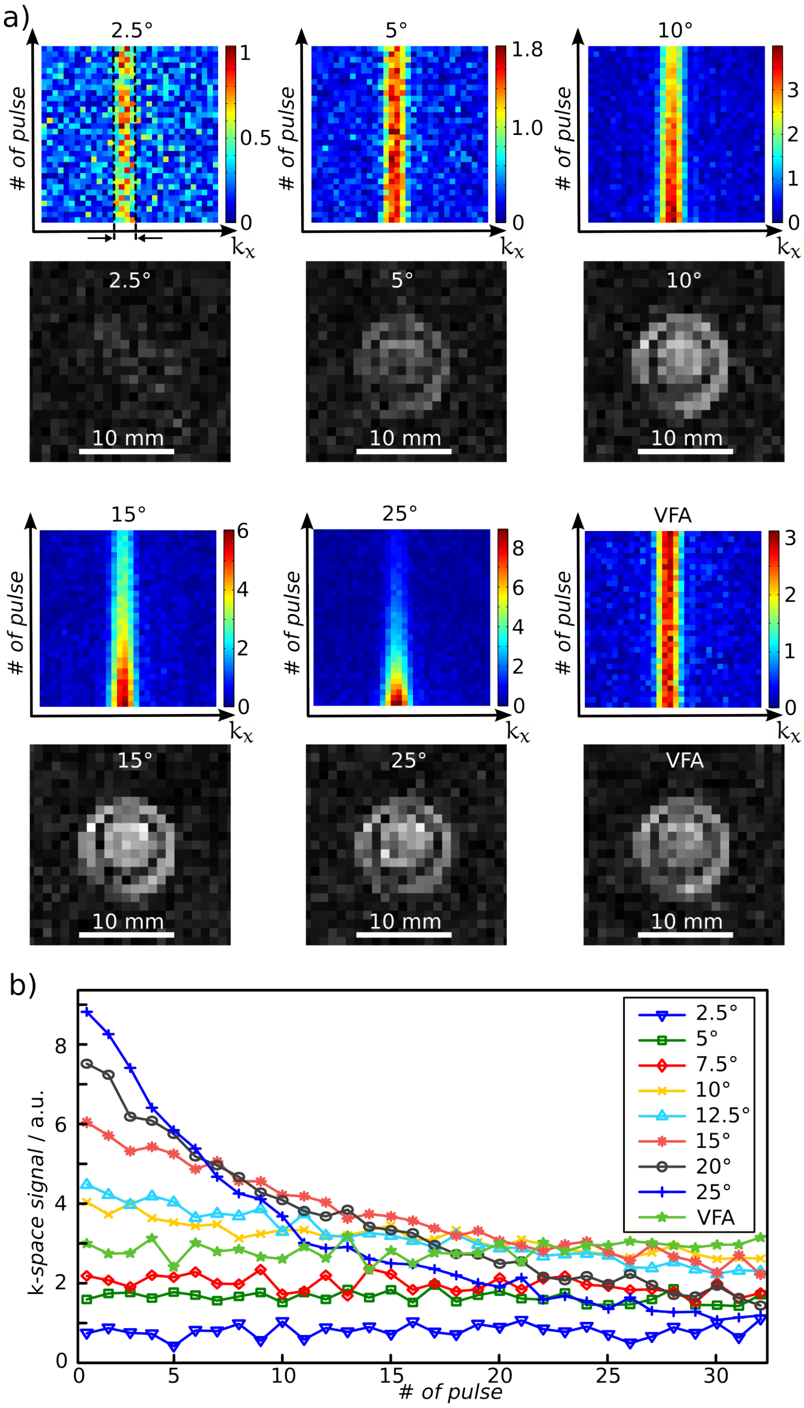

Figure 5.1: Constant versus VFA approach and ^{129}Xe MR images for a single delivery of fresh HP Xe. a) k-space without phase encoding steps. Thus, each k_y line corresponds to the $k_y = 0$ s^{-1} value. The signal between the dashed lines was integrated and plotted in b). Exemplary, the data for the constant flip angles of 2.5°, 5°, 10°, 15° and 25° are shown. The ^{129}Xe MR images below each k-space is a weighting of the normal k-space (with linear phase encoding) with the decreased HP signal contribution caused by each RF pulse. The tailored VFA schedule for 32 RF pulses is the most effective way of distributing HP signal (similar to Figure 2.11). Experimental conditions: DMSO solution, bubbling time = 20 s, bubble collapse time = 8 s, TE = 6 ms, TR = 100 ms, in-plane resolution = 625 μm^2 (**field-of-view** (FOV) = 20 × 20 mm^2 with 32 × 32 matrix size), slice thickness = 20 mm.

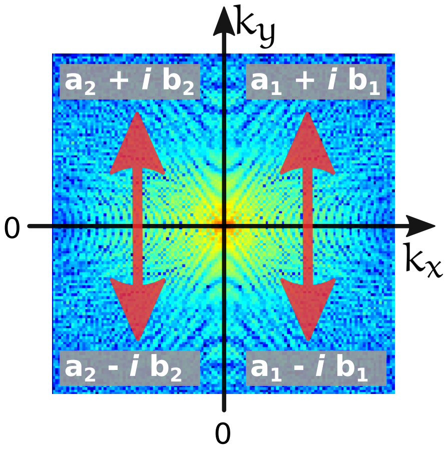

Figure 5.2: Redundancy in k-space. Whereas k_x corresponds to the real part $\Re$, k_y corresponds to the imaginary part $\Im$. Thus, the complex plane quadrants are related to each other by the complex conjugate: $(a_1 + ib_1)^* = a_1 - ib_1$ and $(a_2 + ib_2)^* = a_2 - ib_2$.

magnetic field gradients cause the center of k-space not to be in the symmetrical center of complex space. As a result, a few additional calibration lines close to the k-space center must be acquired which suggest an optimal partial Fourier acceleration factor.

Figure 5.3 shows the effect of different partial Fourier acceleration factors ranging from no partial Fourier acceleration (*i. e.*, 1.0; the reference image) up to maximal partial Fourier acceleration (*i. e.*, 1.9) on the SNR of the reconstructed ^{129}Xe MR image. The SNR was, contrary to the publication [Kunth and Döpfert *et al.*[121]], calculated without further scaling factor by the evaluation of a **region-of-interest** (ROI) according to `mean`(blue or red signal ROI)/ `standard deviation` (green ROI in noise), which is normalized to the number of pixels. While the blue signal ROI was the signal of solely the **outer compartment** (OC) of the double phantom, the red signal ROI contained the signal of the entire double phantom.[1] The precision of the SNR values were determined as the standard deviation of 4 times independently repeated determined SNR values (error bars). The blue lines in k-space were skipped in acquisition, but reconstructed for 2D FT to obtain the ^{129}Xe MR image. A GRE with VFA (*i. e.*, for each partial Fourier acceleration factor the number of total VFAs were calculated accordingly) was used as MRI pulse sequence. Thus, the smaller the fraction of acquired data, the smaller the fraction of the HP magnetization that is used up. This results in larger SNR (compare, *e. g.*, 1.4 with 1.0). However, the reconstructed images suffer from artifacts for too large acceleration factors (*i. e.*, > 1.4).

With increasing factor of partial Fourier acceleration ranging from 1.0 to 1.9, the total image acquisition time decreases accordingly, TA = {295.1, 267.5, 249.2, 230.8, 212.4, 194.0, 184.8, 175.6, 166.4, 157.2} ms, respectively. Therefore, the T_1 relaxation during the imaging readout even in human blood with < 10 s (see Table 2.2), can be neglected.

While increasing partial Fourier acceleration factor corresponds to increasing SNR it also increases the MR image artifacts. For this particular experi-

---

[1] While the SNR value in the OC (blue signal ROI in Figure 5.3) is the SNR that corresponds to Xe in 100 % DMSO, the phantom overall SNR (red signal ROI in Figure 5.3) is the one that should be optimized when adjusting the partial Fourier acceleration factor before the measurement.

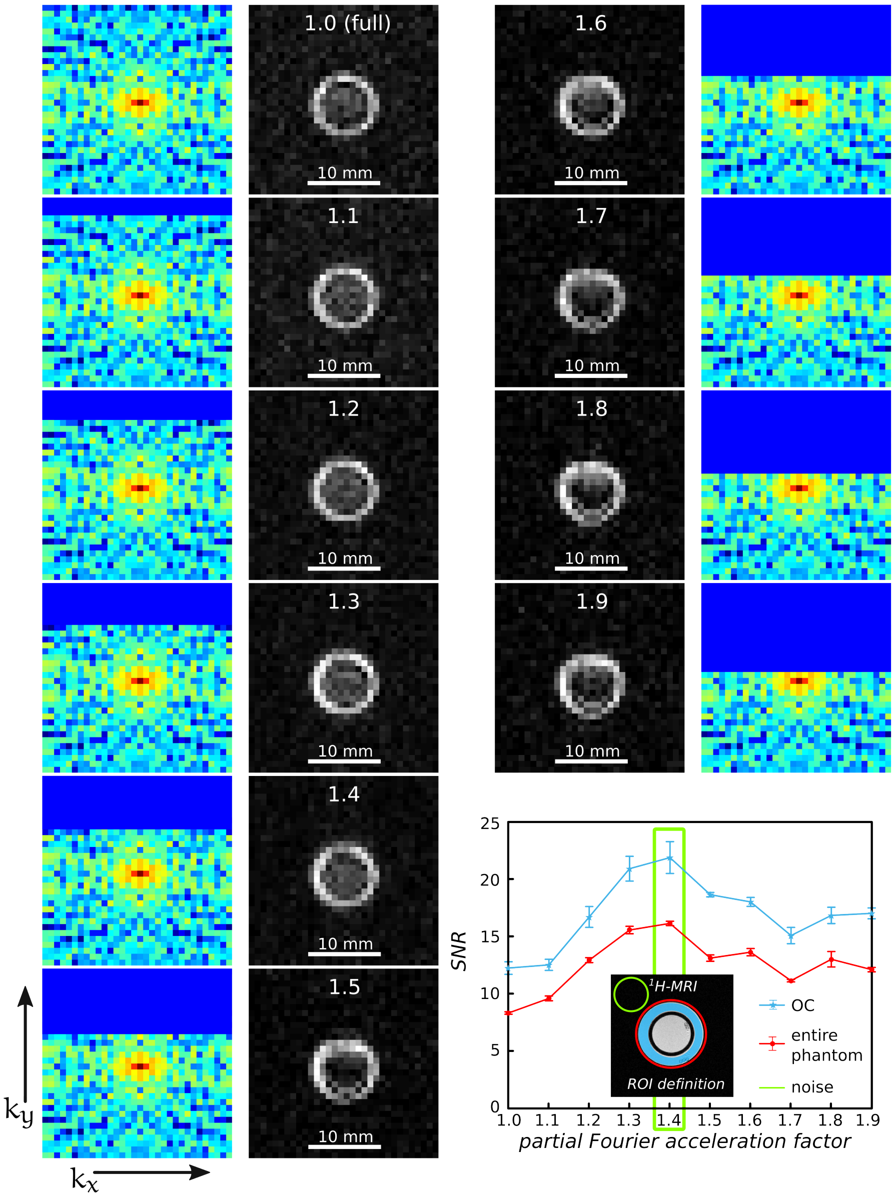

Figure 5.3: k-Spaces, ^{129}Xe MR images and SNR for different partial Fourier acceleration factors. No partial Fourier acceleration, *i. e.*, a fully sampled k-space, is denoted by the acceleration factor of 1.0. Maximal partial Fourier acceleration is denoted by the acceleration factor of 1.9, as nearly half the data is omitted. This nearly halves the acquisition time. The blue lines in k-space were skipped in acquisition, but reconstructed for 2D FT. The reconstructed images suffer from artifacts for too large acceleration factors (*i. e.*, for > 1.4 the IC begins to lose signal). The calculated SNR values are normalized to the number of pixels. They were calculated as the standard deviation of 4 times independently repeated determined SNR values (error bars). Experimental conditions: **inner compartment** (IC): 70 % DMSO + 30 % water (hence reduced Xe solubility), **outer compartment** (OC): 100 % DMSO, both without CrA. Bubbling time = 20 s, bubble collapse time = 8 s, TE = 2.98 ms (minimum), TR = 6.17 ms, in-plane resolution = 625 µm^2 (FOV = 20×20 mm^2 with 32×32 matrix size), slice thickness = 20 mm. For this particular experimental setup, a partial Fourier acceleration of 1.4 yielded largest SNR while negligible MR image distortions.

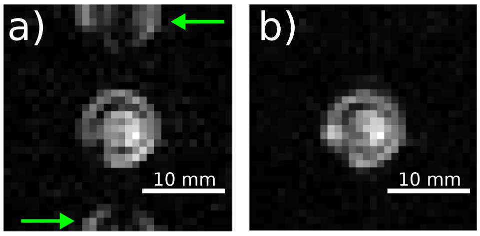

Figure 5.4: Single-shot EPI of the double phantom sample containing DMSO in both compartments. a) shows a Nyquist ghost artifact in the reconstructed ^{129}Xe MR image (green arrows) for conventionally blipped EPI k-space trajectory (as described in Figure 5.5). b) shows the **double sampling** (DS)-EPI reconstructed ^{129}Xe MR image without Nyquist ghosts and increased SNR from (21 ± 1) to (33 ± 1). The SNR increased due to both 1) increased signal by averaging of two images, and 2) reduced Nyquist ghost noise. Experimental conditions: Bubbling time = 20 s, bubble collapse time = 8 s, $\mathrm{TE_a} = 7.7\,\mathrm{ms}/\mathrm{TE_{b,DS}} = 11.6\,\mathrm{ms}$, $\mathrm{TA_a} = 18.6\,\mathrm{ms}/\mathrm{TA_{b,DS}} = 28.4\,\mathrm{ms}$, in-plane resolution = 625 $\mu\mathrm{m}^2$ (FOV = $20 \times 20\,\mathrm{mm}^2$ with 32×32 matrix size), slice thickness = 20 mm, no partial Fourier acceleration.

mental setup, a partial Fourier acceleration of 1.4 yielded optimal SNR and negligible MR image distortions. Thus, we nearly doubled the SNR of the VFA-GRE pulse sequence using a partial Fourier acceleration factor of 1.4.

Other clever strategies to acquire less data in k-space than a factor of two is parallel MRI [Pruessmann *et al.*[165], Griswold *et al.*[84], Blaimer *et al.*[23], Seiberlich *et al.*[189], Deshmane *et al.*[57]] and compressed sensing [Candes and Tao[45], Donoho[59], Lustig *et al.*[141], Candes and Wakin[44], Lustig *et al.*[140]]. In particular, applications to HP nuclei have been reported such as resolution enhanced compressed sensing of HP ^{13}C spectroscopic imaging [Hu *et al.*[103]], and compressed sensing in HP ^{3}He human lung MRI [Ajraoui *et al.*[7]]. However, as our experimental setup consisted of a single receiver coil only, parallel MRI was not an option and compressed sensing was outside the scope of this thesis.

Single-Shot Echo-Planar Imaging

In contrast to the multiple-shot GRE pulse sequence, single-shot MR imaging techniques maximize the signal by a full 90° RF pulse excitation and encode the entire k-space after that single excitation pulse. We used the fastest (Cartesian) single-shot technique that is currently available, the EPI (introduced in Section 2.2.1). A ^{129}Xe MR image of the double phantom filled with DMSO using the conventionally blipped EPI (Figure 2.12) is shown in Figure 5.4a. Defining the SNR similar to the red signal containing ROI as defined in Figure 5.3, the EPI yielded an overall SNR of (21 ± 1), which is slightly larger than the maximum SNR obtained with the VFA-GRE with optimal partial Fourier acceleration factor of 1.4. However, also an image artifact appeared that is centered at half of the field-of-view (FOV) away from the image in phase encoding direction (green arrows in Figure 5.4a). This artifact is known as Nyquist ghost.

The Nyquist ghost is a typical blipped EPI image artifact and arises due time-reversal asymmetry between even and odd gradient-recalled echoes.

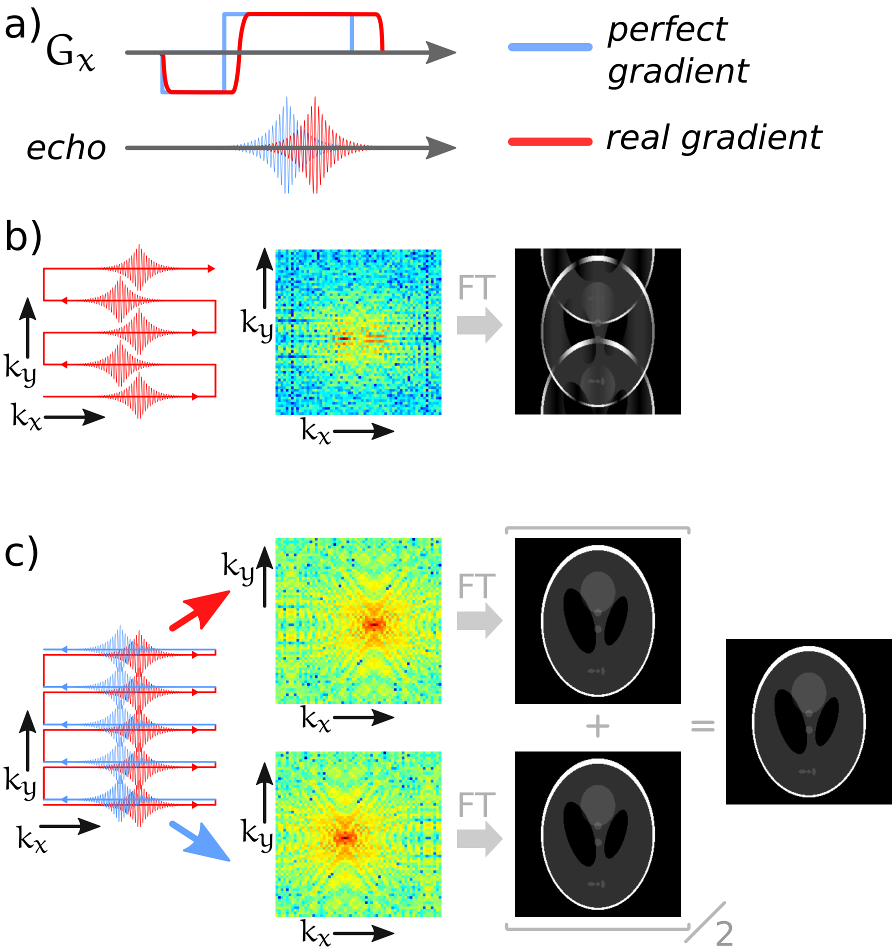

Figure 5.5: Simulation of double sampling on a Shepp-Logan[193] phantom. a) In contrast to perfect gradients (blue), real gradients (red) cause a delayed gradient-recalled echo. b) In a conventional blipped EPI k-space trajectory (compare Figure 2.12), such delayed gradient echoes manifest in a phase error accumulation in k-space due to time-reversal asymmetry between even and odd echoes. The MR image after 2D FT gains a so called Nyquist ghost artifact with significantly reduced SNR as this artifact can interfere with the object. c) By double sampling each k_y-line in k-space twice (forth (red) and back (blue)), two separate k-spaces with shifted k-space centers are recorded and each with a Nyquist ghost free reconstructed MR image, while the true EPI single-shot character is maintained. The SNR of the final image is increased by $\sqrt{2}$ due to averaging of two images.

This time-reversal asymmetry is caused by the imperfections in gradient waveform, the gradient eddy currents and modulations due to the static magnetic field inhomogeneities (Figure 5.5a). We simulated this image artifact using a Shepp-Logan[193] phantom in MATLAB . The gradient-recalled echoes of the blipped EPI k-space trajectory form slightly delayed with respect to the center of the readout interval and accumulate a phase error in k-space (Figure 5.5b). This phase error results after 2D FT in signal intensity displacement in the phase encoding direction. As the Nyquist ghost can interfere with the image (depending on the size of the object to FOV ratio) it reduces the image SNR and can become a serious image artifact.

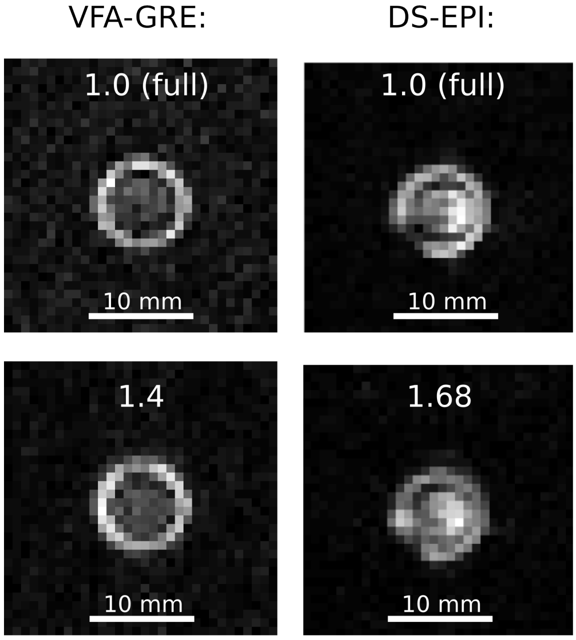

Figure 5.6: Comparison of the optimized sequences VFA-GRE and **double sampling** (DS)-EPI for both partial Fourier acceleration factors, 1.0 (both), 1.4 (VFA-GRE) and 1.68 (DS-EPI). The SNR improved with partial Fourier acceleration for VFA-GRE from (11 ± 1) to (20 ± 1) and for DS-EPI from (33 ± 1) to (44 ± 1). Thus, SNR of the DS-EPI is more than twice increased in comparison to the optimized VFA-GRE pulse sequence. The comparison made here is not entirely fair as the IC of the VFA-GRE sample contained 70 % DMSO + 30 % water that reduces Xe solubility. Accordingly, the used SNR ROI was for both the OC. However, it sufficiently illustrates the large SNR improvement of the optimized single-shot DS-EPI versus the VFA-GRE pulse sequence. The experimental conditions are given in Figure 5.3 and Figure 5.4.

To remove Nyquist ghosts in the image while maintaining true single-shot character of EPI, Yang *et al.*[238] proposed double sampling of each line in k-space as simulated in Figure 5.5c. All even (blue) and odd (red) echoes are arranged into two individual k-spaces with shifted centers of k-space. Each 2D FT reconstructed MR image is without the Nyquist ghost. By averaging both MR images, the SNR additionally gained a factor of $\sqrt{2}$. By employing double sampling on the EPI pulse sequence we successfully suppressed the Nyquist ghost in the ^{129}Xe MR image and increased the SNR from (21 ± 1) to (33 ± 1) (Figure 5.4b). The MR image acquisition time was with 28.4 ms slightly increased when compared to no double sampling (18.6 ms).

In addition, we further increased the SNR from (33 ± 1) to (44 ± 1) by reducing the number of recorded data using a partial Fourier acceleration factor of 1.68, which was carefully optimized similar to Figure 5.3. Thus, the MR image acquisition time reduced from 28.4 ms to 19.8 ms (see comparison in Figure 5.6) making now the HP Xe delivery and the Hyper-CEST saturation pulse scheme the most time consuming part of the detection sequence.

In summary, we implemented the single-shot Hyper-CEST EPI with double sampling and partial Fourier acceleration factor of 1.68 (Figure 5.7) that increased the SNR by a factor of about 4 in comparison to the not optimized VFA-GRE in Figure 5.3 (*i. e.*, fully sampled; SNR = (11 ± 1)). In combination with the improved HP Xe signal from the optimized polarizer, the single-

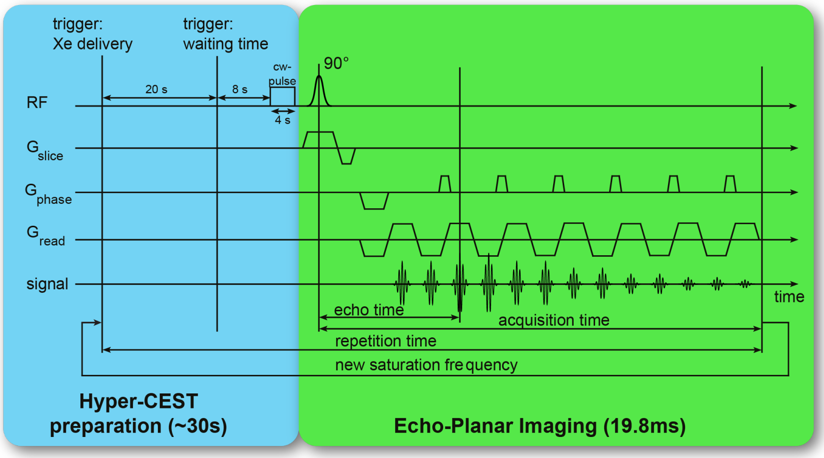

Figure 5.7: Hyper-CEST echo-planar imaging (EPI) pulse sequence with double sampling. The triggering of the Xe bubbling into the phantom was controlled by trigger pulses in the pulse sequence. After 20 s of bubbling and 8 s of bubble collapse time, a cw saturation pulse with a particular carrier frequency was turned on for 4 s if not stated otherwise in the text. Slice selection and excitation was achieved by a selective 90° Gaussian shaped RF pulse of 1 ms duration.

shot Hyper-CEST EPI yielded several experimentally significant improvements, including

1. nanomolar imaging,
2. full *z*-spectra acquisition and multicolor imaging,
3. **shared magnetization after single hyperpolarization CEST** (smashCEST), and
4. time-resolved studies of CrA diffusion

that are described in the following.

5.3.2 Nanomolar Imaging

We demonstrated for the first time that a cryptophane-222 (CrA) Xe-host molecule concentration of 250 nM in a solution of 95 vol. % $H_2O/5$ vol. % DMSO was enough to be imaged with our Hyper-CEST EPI pulse sequence introduced in the previous Section 5.3.1 (Figure 5.8). We increased the Xe exchange rate and hence, the Hyper-CEST efficiency by increasing the temperature up to physiological temperature, *i. e.*, $T = 310$ K $\approx$ 37°C. The Hyper-CEST data show excellent response with clear localization of CrA as depicted in Figure 5.8. More details are given in the caption of Figure 5.8.

The nanomolar imaging experiment demonstrates the tremendous increase in sensitivity of the single-shot Hyper-CEST imaging method. At that time, even for ^{129}Xe NMR spectroscopy in which the ^{129}Xe NMR signal averages over the total sample without spatial information, has not been reported with nanomolar sensitivity for CrA. Using the repetitive sensor-selective

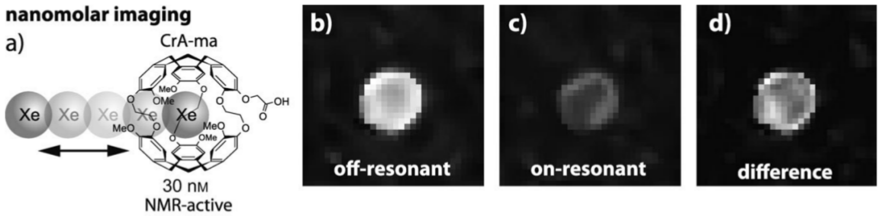

Figure 5.8: Principles of nanomolar imaging. The schematic in a) shows the chemical structure of the CrA molecule (in a solution of 95 vol. % H_2O/ 5 vol. % DMSO) with exchangeable Xe atoms. Since only a fraction of the total CrA concentration is occupied by Xe and of all Xe atoms only 26 % are detectable by NMR, the detected NMR-active CrA concentration was 30 nM out of 250 µM. b) shows the off-resonant ($SNR_b \approx 5$; here with scaling factor of 0.655 as given in supporting section 12 and Figure S10 in [121] which is attached in Appendix Section D.1) and c) the on-resonant ($SNR_c \approx 3$) images that were obtained by a cw-saturation pulse with strength of 19 µT and duration of 26 s. The difference image in d) illustrates localized caged Xe ($SNR_{CEST,d} \approx 2$). Prior to each measurement, fresh HP Xe was bubbled into solution for 25 s. Reprinted with permission from Kunth and Döpfert *et al.*[121]. Copyright © 2012 WILEY-VCH Verlag GmbH & Co. KGaA, Weinheim.

excitation method, Kotera *et al.*[120] reported the detection of a Cr concentration of 83 µM within an acquisition time of 15 s at a Xe concentration of [Xe] = 4,500 µM. Our approach detected a [Cr] = 30 nM in 100 s at a Xe concentration of [Xe] = 361 µM. Therefore, our sensitivity is 83,000 nM/ 30 nM ≅ 2,750-fold increased [Kunth and Döpfert *et al.*[121]]. To achieve such an increase in sensitivity with their method requires averaging for 2,750 times each time for 15 s measurement time, resulting in $2{,}750^2 \cdot 15$ s ≅ 3.6 years of signal averaging. By taking the different Xe concentrations into account that were required, another factor of 12.5^2 would increase their measurement time to several hundreds of years.

5.3.3 Multicolor Imaging and z-Spectra

We further used the imaging speed to exploit for the first time the spectral dimension of Hyper-CEST in an MR image series. In contrast to the original Hyper-CEST **chemical shift imaging** (CSI) implementation in which 11 minutes per ^{129}Xe MR image including Xe delivery and Hyper-CEST saturation were required, we were able to acquire Hyper-CEST images every 33 s. We demonstrated the acquisition of entire Hyper-CEST *z*-spectra within a few minutes (Figure 5.9b; data fitted to Lorentzian lines; dashed lines). This imaging speed is an important step, as the shape of such Hyper-CEST *z*-spectra with respect to the Xe exchange kinetics provides highly useful insights into the fundamental Hyper-CEST mechanism (see next Chapter 6).

Moreover and contrary to the missing multiplexing option of MRI that is listed in Table 1.1, we exploited the Hyper-CEST *z*-spectra information to show for the first time multicolor imaging with Hyper-CEST of two different Cr's. We simulated differently functionalized sensors by taking advantage of the effect of the solvent on the Xe-CrA chemical shift and added different amounts of DMSO to the pure water solution (see section 6 and Figure S8 in Supporting Information of Kunth and Döpfert *et al.*[121] that is attached in Appendix Section D.1). We adjusted a chemical shift difference between both Xe@CrA resonances to be 131 Hz at 9.4 T (*i. e.*, 1.2 ppm, see Figure 5.9a) by adding to the inner/outer compartment 20/10 % DMSO, respectively.

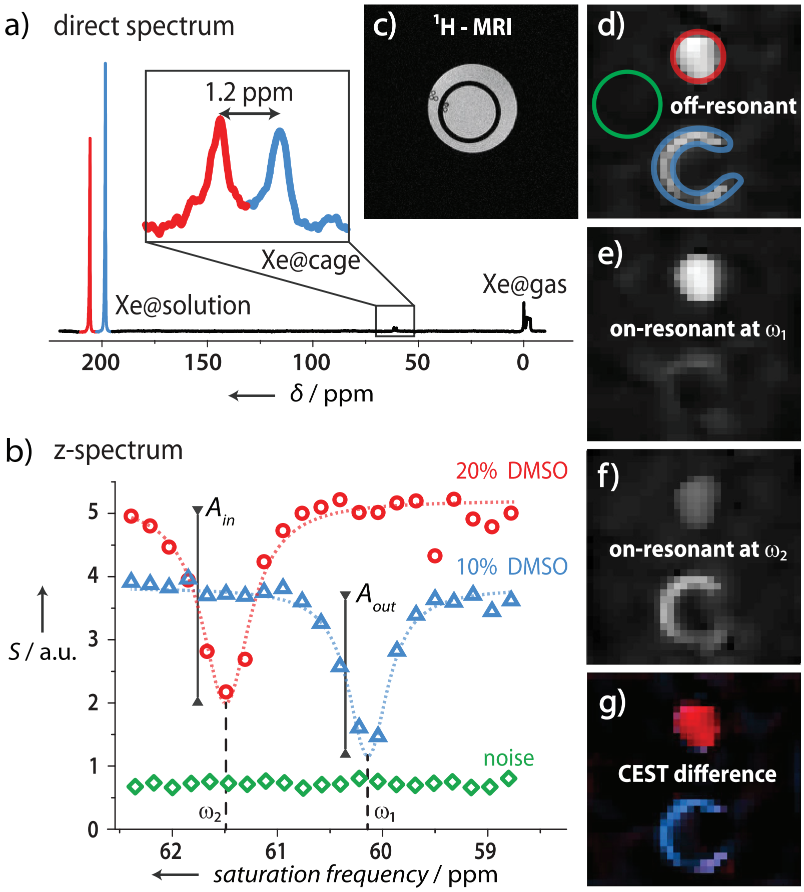

Figure 5.9: Principles of Xe multicolor (or chemically selective) imaging at $T = 293$ K. a) Direct ^{129}Xe NMR spectrum (16 averages) of 10 μM of cage that is dissolved in water. Different DMSO fractions were added (IC: 20 % and OC: 10 %) into the bubbling phantom (cross-section shown in ^{1}H-MRI (c)) that lead to a chemical shift separation for both the bound Xe (Xe@cage) and free Xe (Xe@solution) resonances. The Xe@cage resonances are separated by $\omega_2 - \omega_1 = 1.2$ ppm (131 Hz at 9.4 T). The *z*-spectrum (20 Hz ($\delta = 0.18$ ppm) increments of the saturation frequency) depicted in (b) illustrates the high sensitivity and selectivity of the CEST response. The data points were obtained from averaging the signal over the ROIs which are shown in the off-resonant CEST image (d). The amplitudes of the CEST response $A_{\text{in}} = 3.2$ and $A_{\text{out}} = 2.7$ were obtained from Lorentzian fits (dashed lines). This corresponds to CEST effects of approximately $3.2/5.5 = 58$ % and $2.7/4 = 68$ %, respectively. Subtraction of the two on-resonant images (e) and (f) from the off-resonant image (d) yields the color-encoded CEST difference image (g), which allows for a clear spatial discrimination of the two Xe@cage resonances ($\text{SNR}_{\text{CEST,red}}/\text{SNR}_{\text{CEST,blue}} \approx 3/2$ referred to the raw ^{129}Xe images). The displacement between the inner and the outer compartment in (d-g) is a chemical shift artifact that originates from the frequency separation of the Xe@solution peaks (805 Hz; *ca.* 17 pixel shift). Reprinted with permission from Kunth and Döpfert *et al.*[121]. Copyright © 2012 WILEY-VCH Verlag GmbH & Co. KGaA, Weinheim.

Whereas the ^{1}H-MR image shows the cross-section of the double phantom (see Figure 5.9c), the ^{129}Xe EPI MR image shows a EPI typical chemical-shift artifact (Figure 5.9d). This appears when the bandwidth per pixel in the phase encoding direction is less than the chemical shift difference between the free Xe resonances of both solutions. The *z*-spectra in Figure 5.9b were acquired with a saturation pulse strength of $B_1 = 1\,\mu T$, a duration of $t_{sat} = 4\,s$ and steps of 20 Hz in saturation frequency taking images every 33 s after Xe re-delivery. This method could separate both solutions and shows a Hyper-CEST response in one compartment while the other remains untouched (Figure 5.9e, f). Further, false-color encoding of the separate responses yields multicolor ^{129}Xe MR images (Figure 5.9g)[Kunth and Döpfert *et al.*[123]]. It shows good selectivity with unprecedented high chemical specificity while still performing slice selection. In contrast, the demonstrated selective readout of resonances separated by 235 Hz [Kotera *et al.*[120]] was without the ability of slice selection.

5.3.4 smashCEST

As Hyper-CEST requires two independent measurements (Figure 2.17), it is prone to instabilities in the Xe delivery. This has two drawbacks, because it is

1. time consuming, and
2. prone to incorrect calculations of the Hyper-CEST effects.

The first statement becomes clear by considering that all initial Xe signal was used for the first off-resonant image. Thus, for the second on-resonant image new freshly HP Xe must be delivered which increases the total acquisition time. If any instability of the Xe supply occurs between the subsequent off- and the on-resonant image acquisition, then the calculated difference image will have an incorrect calculated Hyper-CEST effect, which justifies the second statement. Whereas our polarizer is optimized for such accurate and precise Hyper-CEST experiments (*i. e.*, a shot-to-shot noise in the ^{129}Xe NMR signal of $< 1\,\%$; Section 4.3.3; [Witte *et al.*[230], Witte *et al.*[231]]), other groups with differently realized Xe polarizer setups might have higher instabilities in the Xe supply. Ultimately, *in vivo* experiments might also provide conditions with unstable Xe delivery.

Therefore, we developed a method that takes advantage of the VFA approach and is able to prepare and encode two ^{129}Xe -MR images (one with off-resonant and one with on-resonant saturation) after one single HP Xe delivery, the so-called **shared magnetization after single hyperpolarization chemical exchange saturation transfer** (smashCEST) technique. We took advantage of the VFA approach and used Equation (2 | 37) in the extreme case for two excitations, *i. e.*, $N = 2$ (Figure 5.10a). Then, Equation (2 | 37) reduces to

$$n = 1: \qquad \theta_1 = \tan^{-1}(1) = 45^\circ, \tag{5|1}$$

$$n = 2: \qquad \theta_2 = \tan^{-1}(\to \infty) = 90^\circ. \tag{5|2}$$

The first application of smashCEST is fast sub-second Hyper-CEST imaging that is shown in Figure 5.10b. We first saturated off-resonant for 450 ms with $19\,\mu T$, excited the spin-system with a flip angle of 45° and applied the single-shot EPI readout immediately afterwards for 19.8 ms. Secondly, this was followed by on-resonant saturation with same parameters, a 90° excitation and the single-shot readout. As shown in Figure 5.10b, the difference image of both acquired data sets yield the localized CrA distribution of $50\,\mu M$ image in $< 1\,s$ (940 ms). This is a tremendous increase in acquisition speed when compared to the 22 minutes of the original implementation.

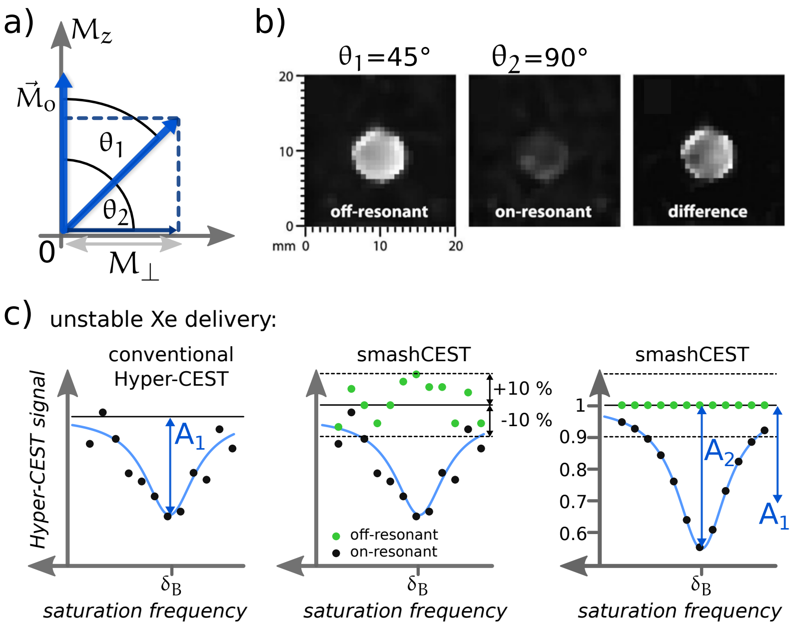

Figure 5.10: Principles of smashCEST. a) smashCEST exploits the VFA approach (Figure 2.11) in the minimum case of two excitations. After a single Xe delivery, for a flip angle of 45° and a second flip angle of 90°, the HP magnetization is entirely used up while both produced transverse magnetizations have the same magnitude $M_\perp$. For each excitation, a double sampled EPI records within milliseconds an entire ^{129}Xe MR image. b) Sub-second sensor imaging is obtained by off-resonant saturation before the first excitation with 45° and on-resonant saturation before the second excitation with 90°. c) Left: Conventional Hyper-CEST z-spectrum with unstable Xe delivery. After the fit (blue curve) a data baseline (horizontal black line) and the CEST amplitude A_1 is assigned. Middle: However, a smashCEST acquisition additionally records the off-resonant value (green data) to each on-resonant saturation (black data), providing an internal reference for a single Xe delivery. Thus, in this illustration the baseline (black line) is actually larger and the Xe delivery was fluctuating by ± 10 %. Right: By normalization to each individual off-resonant value, a clean and accurate z-spectrum is obtained. This has in contrast to the left about 33 % larger CEST effect. Thus, the smashCEST method provides a useful tool for Hyper-CEST z-spectra acquisition with highly unstable Xe delivery, as expected *in vivo*. Figure 5.10b is reprinted with permission from Kunth and Döpfert *et al.*[121]. Copyright © 2012 WILEY-VCH Verlag GmbH & Co. KGaA, Weinheim.

A second smashCEST application is the acquisition of full Hyper-CEST z-spectra similar to Figure 5.9b, but in the presence of incoherent and largely unstable HP Xe supply (a simulation is illustrated in Figure 5.10c). A conventional Hyper-CEST z-spectrum (black data points) under unstable Xe delivery is noisy. The data fit (blue curve) finds a baseline of the z-spectrum (black solid line) and a certain amplitude A_1. In contrast, the smashCEST method reveals two properties: 1) the noise of the off-resonant data points (green data points) is about ± 10 %, and 2) a different baseline level of the z-spectrum (middle; here increased in comparison to plot on the left). By normalization of the on-resonant data to the off-resonant data, the z-spectrum is corrected for any unstable HP Xe delivery during measurements (right). Indeed, the true Hyper-CEST effect was larger, *i. e.*, $A_2 > A_1$. Thus, what-ever extreme HP Xe delivery conditions are present, the smashCEST method always corrects for it and produces valuable *z*-spectra for further analysis.

In summary, if the HP Xe NMR signal is large enough to divide it into two measurements, smashCEST allows correct acquisition of full Hyper-CEST *z*-spectra in particular under strongly fluctuating Xe delivery. This is possible because of the internal reference scan (*i. e.*, off-resonant data and on-resonant data come from the same batch of HP Xe delivery) by renormalization of the data as a simple post-processing step. In addition, smashCEST allows for very fast sub-second Hyper-CEST imaging. It is noteworthy that Boutin *et al.*[28] reported the same idea as smashCEST by using the VFA approach for two excitations for a ultrafast *z*-spectroscopy method, one year later.

5.3.5 Imaging of Sensor Diffusion

In addition, we exploited the fast single-shot Hyper-CEST technique for monitoring for the first time a dynamic process, *e. g.*, CrA-sensor diffusion through a dialysis tubing. This experiment would be impossible to perform by either the Hyper-CEST CSI implementation or the repetitive sensor-selective excitation. We divided the bubbling phantom which contained DMSO into two compartments using a dialysis tubing with molecular weight cut-off of 10,000 Da, filled the inner compartment with 500 µM of CrA to generate a concentration gradient and observed the Hyper-CEST response after RF saturation every 33 s. The image series in Figure 5.11a shows an increase of the Hyper-CEST effect, *i. e.*, a signal loss in the images, at areas where CrA is present. The signal decrease in the outer compartment agreed well with a monoexponential decay with time constant $\tau_{\mathrm{intact}} = 53$ min, as can be seen in Figure 5.11b. We further accelerated the diffusion process by piercing the membrane 2 or 3 times ($\tau_{2\ \mathrm{holes}} = 17$ min and $\tau_{3\ \mathrm{holes}} = 4$ min, respectively) using a 350 µm needle, as shown in Figure 5.11c. The Hyper-CEST effect overlayed with the ^{1}H-MR image is shown in Figure 5.11d that corresponds to some extend to the CrA concentration. Entire movies of the CrA diffusion process can be found in Kunth and Döpfert *et al.*[121]. Note that the Hyper-CEST response is not linearly related to the CrA concentration making a simple quantification demanding.

Additionally, we reported sensor diffusion of two different CrAs, namely CrA and **polyethylene glycol-coupled CrA** (CrA-PEG), through a dialysis tubing into opposite directions (Figure 5.12) [Kunth *et al.*[124]]. To slow down the Xe exchange rate and to make both Xe resonances more narrow, we chose the phantom solution to contain 20 %/80 % vol. DMSO/H_2O. By the acquisition of ^{129}Xe MR images with the Hyper-CEST EPI (cw saturation on 0.3 µT for 8 s) and alternating the on-resonant frequencies between Xe@CrA and Xe@CrA-PEG for every second image, we could monitor a *ca.* 9-fold slower exponential signal decay for CrA-PEG compared to CrA ($\tau_{\mathrm{CrA}} = 5.1$ min, $\tau_{\mathrm{CrA-PEG}} = 43.5$ min). This could indeed be attributed to the larger size of the CrA-PEG molecules. Thus, this demonstrates the large potential of Hyper-CEST for tracking multiple time-depended biochemical events simultaneously.

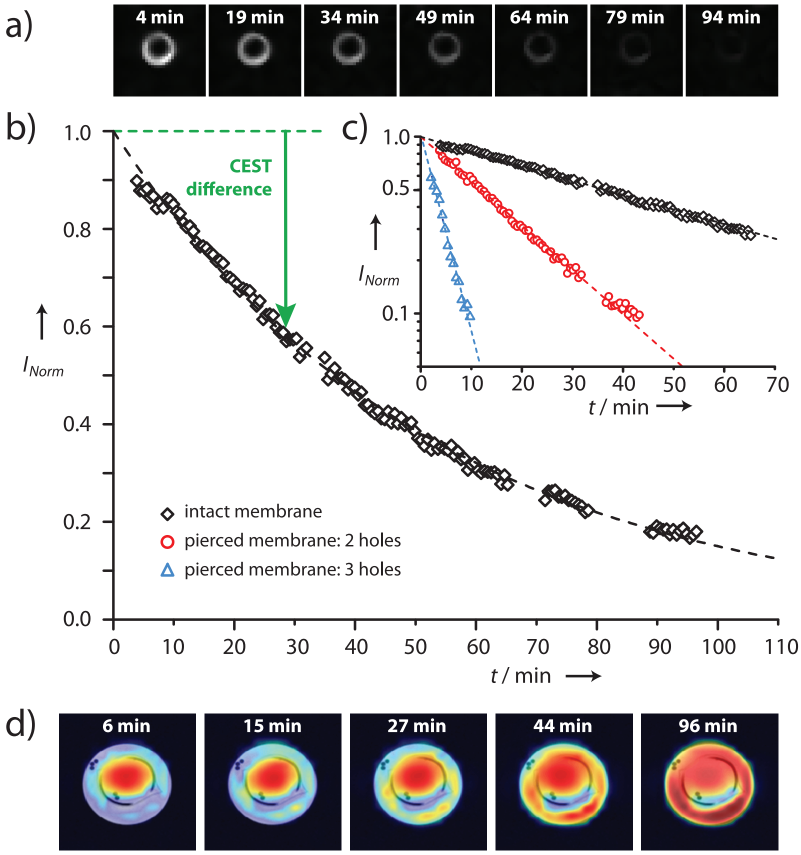

Figure 5.11: Visualization of CrA diffusion at $T = 295$ K through dialysis tubing with Hyper-CEST EPI. At $t = 0$ min, CrA is only present in the inner compartment (500 µM concentration). a) ^{129}Xe Hyper-CEST EPI images with presaturation at the Xe@cage frequency ($t_{sat} = 7$ s, $B_1 = 12$ µT) at different times t illustrates the gradual decay of the signal in the outer compartment owing to diffusion of cage molecules through the intact membrane ($SNR_{image,1} \approx 16.7$). b) The time-dependent mean signal of a ROI in the outer compartment shows an exponential decay. The dashed green line represents the extrapolated off-resonant signal intensity; the length of the green arrow corresponds to the CEST difference which increases in time. Missing data points in the plot are due to acquisitions of high-resolution multislice proton images to monitor the position of the membrane. c) Signal decays show good agreement with monoexponential behavior (dashed lines) for the intact membrane (black diamonds) and intentionally pierced membranes with two (red circles) and three (blue triangles) 350 µm holes. The obtained decay constants of $\tau_{intact} = 53$ min, $\tau_{2\text{ holes}} = 17$ min, and $\tau_{3\text{ holes}} = 4$ min, respectively, indicate faster diffusion through damaged membranes. d) Visualization of the increase in cage concentration in the outer compartment for the intact membrane by overlaying a ^{1}H-MR image with false-color encoded CEST difference images. In comparison, within this time frame only 5 images would be possibly obtained using the original implementation. Reprinted with permission from Kunth and Döpfert *et al.*[121]. Copyright © 2012 WILEY-VCH Verlag GmbH & Co. KGaA, Weinheim.

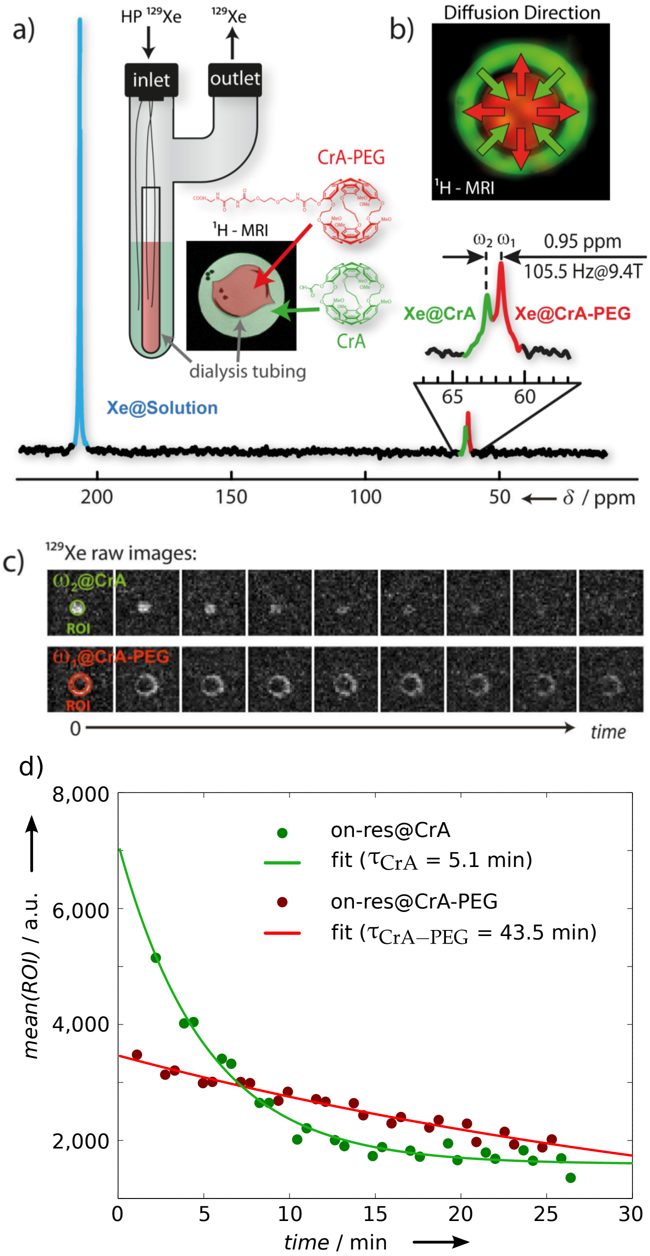

Figure 5.12: Multiplexed sensor diffusion MRI. a) Sample setup: Double bubbling phantom containing 20 %/80 % vol. DMSO/H_2O solution. The compartments were separated by a dialysis tubing similar as used in a previous setup (Figure 5.11). While only the inner compartment contained [CrA-PEG] = 100 µM (red), the outer compartment was filled with only [CrA] = 100 µM (green). The direct ^{129}Xe NMR spectrum of this sample shows three distinct resonances; one of free Xe in solution at δ_A = 210 ppm (blue; with respect to the gas signal) and two of bound Xe, one to CrA at δ_{CrA} = 62.75 ppm (green) and one to CrA-PEG at $\delta_{CrA-PEG}$ = 61.80 ppm (red). Both were separated by only 0.95 ppm (*i. e.*, 105.5 Hz at 9.4 T). b) Simulated illustration of the bidirectional diffusion of both CrA compounds. c) ^{129}Xe MRI series on-resonant on CrA (green) and CrA-PEG (red). d) ROI averaged signal evolution in time that is achieved from c). Reproduced from Kunth *et al.*[124].

5.4 CONCLUSION

The idea of single-shot Hyper-CEST demonstrates the capability to acquire Hyper-CEST images with imaging speed comparable to typical clinical scanner pulse sequences while using the full potential of the Xe biosensors. This enables for the first time the performance of many diverse experiments in a decent amount of time at unprecedented high sensitivity and chemical specificity, such as true sub-second Xe sensor imaging, nanomolar imaging, multicolor imaging, and the acquisition of full Hyper-CEST z-spectra including spatial resolution. Especially the dynamic study of sensor diffusion is impossible with the original Hyper-CEST CSI implementation or direct detection by repetitive sensor-selective excitation.

The Hyper-CEST EPI method has recently been used by others for probing biomembrane fluidity [Schnurr *et al.*[182]], and for the smart detection of toxic metal ions, *i. e.*, Pb^{2+} and Cd^{2+} [Tassali *et al.*[208]]. In addition, the idea of single-shot Hyper-CEST imaging has been used for: Xe Hyper-CEST MRI of brain endothelial cells that were targeted *via* a peptide-functionalized liposomal carrier [Schnurr *et al.*[180]], cell tracking with caged Xe [Klippel *et al.*[116]], multiplexed mammalian cell labeling by Hyper-CEST MRI [Klippel *et al.*[117]], multi-modular cell targeting/tracking [Rose *et al.*[170]], and live-cell MRI with Xe Hyper-CEST biosensors that were targeted to metabolically labeled cell-surface glycans [Witte *et al.*[232]]. These results motivate the Xe biosensor field to move towards first Hyper-CEST *in vivo* demonstrations.

However, while the EPI has the capability for true snap-shot ultra fast MR imaging, it also comes with the following drawbacks: 1) chemical shift artifact, 2) Nyquist ghost artifact, 3) large initial signal required, and 4) $T_2^* > 3$ to 5 times TA (acquisition time). Also the fast gradient switching is demanding to the hardware.

An alternative single-shot method will be the RARE pulse sequence (Figure 2.13) that exploits the larger transverse relaxation times T_2, instead of the faster T_2^* values. In addition, the SNR of the multiple-shot GRE pulse sequence can be further improved using constant flip angles, but centric phase encoding in order to exploit the large HP signal at the beginning to arrange it close to the center of k-space to maximize image contrast (Figure 2.14). Other potential pulse sequences that were investigated also in the case for HP nuclei is the class of **balanced steady-state free precession** (bSSFP) sequences. Deppe and Wild[56] reported for HP ^{3}He bSSFP human lung MR imaging in conjunction with a VFA schedule to reduce blurring in the image in contrast to constant flip angles. In addition, for ^{1}H its combination with CEST was proposed using a ^{1}H-CEST bSSFP pulse sequence for fast and sensitive CEST contrast on 7 T MRI scanner by Shah *et al.*[190].

However, MR imaging of HP nuclei could in particular benefit from non-Cartesian trajectories, such as multiple-shot radial k-space coverage or single-shot spiral k-space trajectories. As most ^{129}Xe MR image contrast is contained in center of k-space, radial trajectories 1) traverse with each projection the center of k-space (therefore all of them can contribute to the overall signal), and 2) have better possibilities for larger undersampling factors. This results in larger portions of the HP magnetization per projection and hence increased SNR. Alternatively, a single-shot Hyper-CEST pulse sequence with spiral k-space trajectory (Figure 5.13a-b) keeps the single-shot character of the pulse sequence and is much less demanding to the gradient hardware as these switch harmonically, compared to the conventionally

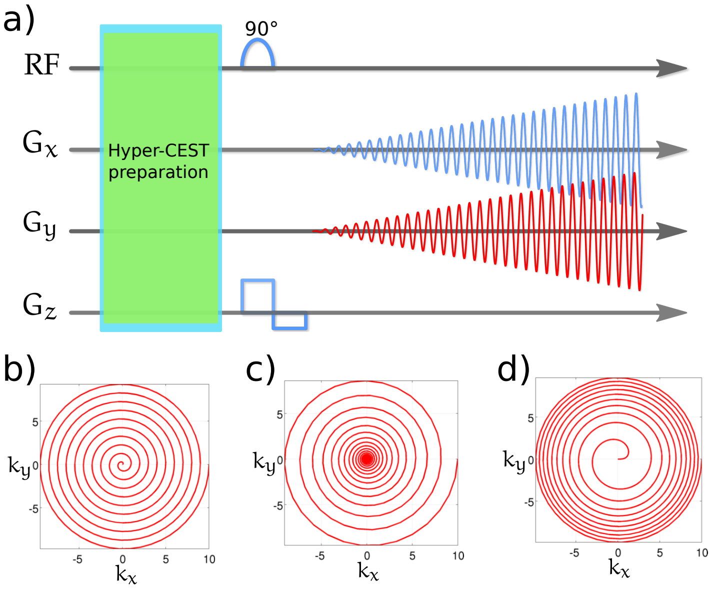

Figure 5.13: a) Spiral Hyper-CEST pulse sequence and b-c) three possible k-space trajectories for imaging. Whereas b) shows *uniform* dense sampling, c) is *nonuniform* dense sampling with WKS sampling theorem oversampling of the k-space center and the outer regions being undersampled. This maximizes image contrast for fast decaying nuclei. d) *Nonuniform* dense sampling (in opposite to c). Spiral trajectories can arbitrarily be oversampled, undersampled or take other possible combinations. In contrast to rectangular sampling, *e.g.*, in EPI, the gradient hardware requirement is less demanding as harmonics are used, at the cost of rather advanced image reconstruction. As all spiral trajectories shown here sample from the inside to the outside of k-space (see gradient in the pulse sequence), the largest HP signal is arranged at the k-space center. This could provide further contrast and signal improvements.

blipped EPI or DS-EPI. In particular, spiral trajectories can be adjusted to the natural decaying nonrenewable character of HP Xe, to maximize image contrast, as the acquired data at the beginning of the T_1 decay curve are arranged close to the center of k-space (Figure 5.13c).

Compared to the EPI, spiral data acquisition provides further increased SNR for the same number of images [Viallon *et al.*[219], Klarhöfer *et al.*[115]]. In addition, such spiral trajectories have been used in fast imaging [Marseille *et al.*[145]] and for the reduction of undersampling errors [Tsai and Nishimura[215]]. The price for the benefits of non-Cartesian trajectories is that the sampled data are not uniformly distributed on a discrete Cartesian grid, but trajectory-dependent in between, causing image artifacts by conventional 2D FT. However, a nonuniform fast Fourier transform image reconstruction toolbox for such purposes was made available by Fessler and Sutton[71], which is actively used, for example by Ma *et al.*[142], Yutzy *et al.*[241], Ehses *et al.*[69], Döpfert *et al.*[63], Neumann *et al.*[158], Völker *et al.*[221], Kunth *et al.*[125].[2]

In summary, our developed single-shot Hyper-CEST method enabled for the first time the possibility to perform complex experiments in a feasible amount of time. This highlights the outstanding capabilities of Xe Hyper-CEST biosensors. The imaging speed is useful for increasing the Hyper-

---

[2] Webpage of the image reconstruction toolbox: `http://web.eecs.umich.edu/~fessler/code/`

CEST sensitivity in the most straightforward approach, *i. e.*, by signal averaging. In addition, the imaging speed can greatly be used to explore the fundamental Hyper-CEST mechanism, as there are several unknown parameters to ultimately amplify the Hyper-CEST sensitivity. To exemplify and as shown in Figure 5.11d, the Hyper-CEST effect is influenced by the concentration of CrA, but non-linearly. The impact of the Xe exchange rate and how it improves the Hyper-CEST effect is not yet known. Further, the optimal saturation pulse parameters play a crucial role for maximal Hyper-CEST effect, but its optimal combination is unknown. In theory, all these parameters can be quantified to understand the fundamental Hyper-CEST mechanism and to address these issues, including the longitudinal and transverse Xe relaxation times. In the next chapter, we demonstrate a novel quantitative Hyper-CEST (qHyper-CEST) approach to build a mathematical basis towards further Hyper-CEST sensitivity amplifications.

The results for *Single-Shot Hyper-CEST MRI* can also be found within the following publication.

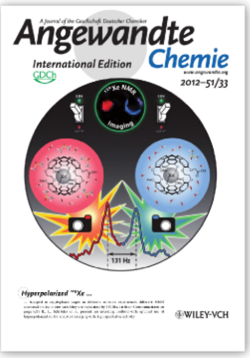

FULL REFERENCE (attached in Section D.1):
Martin Kunth*, Jörg Döpfert*, Christopher Witte, Federica Rossella, and Leif Schröder. Optimized use of reversible binding for fast and selective NMR localization of caged xenon *Angewandte Chemie International Edition*, 51(33):8217-8220, 2012; Kunth and Döpfert *et al.*[121] and German edition[122].
*contributed equally.

(highlighted as hot paper, inside back cover article and honored with a Gorter-Award)

AUTHOR CONTRIBUTIONS: M.K. and J.D. designed research; M.K., J.D. and F.R. performed research; M.K., J.D., C.W., F.R. and L.S. analyzed data; M.K., J.D., C.W. and L.S. wrote the paper.

6 QUANTITATIVE HYPER-CEST MRI

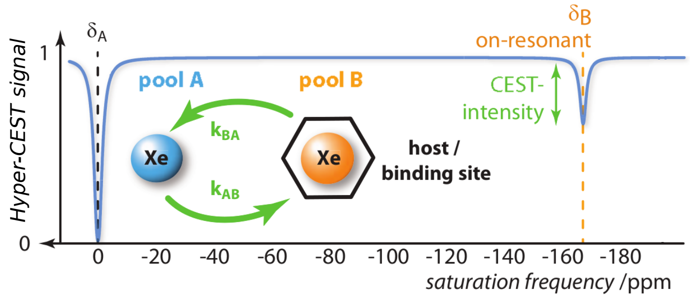

The work described in this chapter provides an approach to quantify the fundamental Xe exchange kinetics. Parts of these results have been published.

Contents

6.1 INTRODUCTION

In the previous Chapter 5 we demonstrated the first MRI sensitivity amplification concept that is achieved using a single-shot Hyper-CEST method. This opens the horizon for entirely new data acquisition concepts that can address further data dimensions (temporal or spectral resolution) for Xe Hyper-CEST biosensor MRI. Therefore, we exploit the greatly reduced data acquisition time for recording entire image series to obtain Hyper-CEST z-spectra with spatial assignment within several minutes. As described in Chapter 1 and similar to ^{1}H-CEST, the intensity of the resulting MRI signal depends on multiple parameters such as the contrast agent concentration, the number of bound Xe atoms relative to the number of unoccupied host cavities (which is related to the Xe binding constant K_B and the – so far only speculated – host occupancy β in different solvents), the exchange rate k_{BA}, longitudinal and transverse relaxation times $T_{1,2}^{A,B}$, the chemical shift difference $\Delta\delta$, but also on the experimental parameters of the saturation pulse strength B_1 and duration t_{sat}. More challenging for the Hyper-CEST effect quantification is that some intrinsic parameters can compensate for others; for example, the exchange rate and the host concentration. Therefore, this sensitive interference between all these parameters impacts the Hyper-CEST effect and makes a proper data analysis and interpretation necessary, but challenging. The knowledge and understanding of these parameters is of crucial importance for general Hyper-CEST predictions and optimizations.

To address this fundamental question, the BM equations (McConnell[146]; Equation (3.6)) can be used. Whereas ^{1}H-CEST is empirically described by the BM equations, it is *ad-hoc* not obvious that these describe Hyper-CEST sufficiently, as also diffusion effects of Xe in solution might be an issue. Then the Bloch-Torrey equations [Torrey[210]] should additionally be considered. However, first quantitative modeling of Hyper-CEST experiments using the BM equations was reported by Ramirez *et al.*[168]. Further evidence for BM modeled Hyper-CEST experiments was reported by Stevens *et al.*[200].

Whereas Ramirez *et al.*[168] reported the simulation of individual Hyper-CEST *z*-spectra with reasonable numbers, Stevens *et al.*[200] demonstrated already individual fitting of Hyper-CEST *z*-spectra to the Xe exchange kinetics using the BM equations. Unfortunately, no errors were given for the fitting results. In addition, the quantification was mainly focused only on the exchange rate k_{BA} and the chemical shift difference $\Delta\delta$. The connection to the Xe host concentration, the binding constant K_A, the host occupancy, and the determination of both the longitudinal and transverse relaxation times of free Xe in solution by Hyper-CEST remained elusive.

Here, we exploit the imaging speed by the acquisition of entire Hyper-CEST *z*-spectra and develop a **quantitative hyperpolarized xenon detection and analysis through CEST** (qHyper-CEST) concept. This qHyper-CEST concept makes minimal approximations to the Hyper-CEST system that is under investigation and is therefore as comprehensive as possible. We demonstrate the quantification of the Xe exchange kinetics on a previously undescribed and idealized Hyper-CEST system, *i. e.*, CrA in pure DMSO (assumed to be a true 2-spin pool system). In addition, we show on simulations that both the longitudinal and transverse relaxation times of free Xe in solution can be quantified reasonably accurate with qHyper-CEST. Thus, our technology is able to determine all relevant parameters for which multiple methods were required earlier.

6.2 OVERVIEW OF EXISTING QUANTIFICATION METHODS

The Hyper-CEST mechanism of a 2-spin pool system involves the following Xe NMR parameters and exchange kinetics: 1) the longitudinal relaxation time of free Xe T_1^A, 2) the transverse relaxation time of free Xe T_2^A, 3) the chemical shift difference $\Delta\delta$, 4) the Xe exchange rate k_{BA}, 5) the association constant K_A, and 6) the host occupancy β. To determine 5) and 6) the free Xe concentration must be known. The Xe solubility in tissue is challenging to determine. However, for *in vitro* measurements it is possible to calculate the Xe concentration from the Ostwald solubility coefficient Γ at a given temperature T and pressure p. For *in vivo* situations, a previously characterized system behavior might then be extrapolated.

Table 6.1: Overview of some Xe exchange quantification methods.

Parameter	Method	Reference
exchange rate: k_{BA}	direct NMR line width determination	[148]
	WEX $^{a)}$ spectroscopy	[257]
	2D EXSY $^{b)}$	[108, 172]
	inversion recovery	
	saturation recovery	
	inverse Hyper-CEST	[118]
	FLEX $^{c)}$ transfer	[74]
	saturation transfer: QUEST $^{d)}$	[148]
	saturation transfer: QUESP $^{e)}$	[148]
chem. shift diff.: $\Delta\delta$	direct NMR	
long. relax. time: T_1^A	inversion recovery	
	Xe delivery waiting time variation	[129]
	bSSFP	[178, 69, 125]
transv. relax. time: T_2^A	spin echo	
	Carr-Purcell-Meiboom-Gill	
	bSSFP	[178, 69, 125]
mole fraction of pool B: f_B	FLEX transfer	[74]
	peak ratio of direct NMR	
association constant: K_A	peak ratio of direct NMR	
	ITC $^{f, \dagger)}$	[99, 114, 100]
	fluorescence quenching of Xe $^{\dagger)}$	[99, 100]
host occupancy: β	direct NMR	[172]

$^{a)}$ water exchange (WEX). $^{b)}$ exchange spectroscopy (EXSY).
$^{c)}$ frequency-labeled exchange (FLEX).
$^{d, e)}$ quantifying exchange using saturation time/power (QUEST/QUESP) dependence.
$^{f)}$ isothermal titration calorimetry (ITC). † not NMR related.

Table 6.1 lists different methods that have been used or have the potential to be used to determine these relevant parameters. Whereas most of them rely on direct NMR spectroscopy or MRI, they therefore suffer from the low sensitivity of the exchangeable peak due to dilute concentrations. Such methods include line width determinations, 2D **exchange spectroscopy** (EXSY), inversion and saturation recovery, inverse Hyper-CEST (*i. e.*, observing bound Xe resonance while manipulating the free Xe in solution), bSSFP, spin echo or Carr-Purcell-Meiboom-Gill experiments. In **water exchange** (WEX), **frequency-labeled exchange** (FLEX) and saturation transfer based methods such as **quantifying exchange using saturation time/power** (QUEST/QUESP) dependence, the dominant water signal is observed while encoding information in the "invisible" dilute bound signal. Such techniques are therefore suitable for the quantification of dilute Xe-host concentrations.

Other methods have been reported in literature that determine the Xe binding constant such as **isothermal titration calorimetry** (ITC) or fluorescence quenching of Xe (Table 6.1). However, the results provided by such methods can significantly differ from those obtained by more accurate NMR measurements:

> *"A large discrepancy is often found between binding constants measured by NMR and by other methods, e.g. isothermal titration calorimetry."*
> — Fairchild *et al.*[70] – 2010

Moreover, they also require additional instrumental equipment which is rather disadvantageous.

We wanted to design a quantification technology for all these parameters that is 1) purely based on NMR and 2) ultra-sensitive to highly dilute Xe-host concentrations. Hence, we took advantage of the indirect NMR detection feature of saturation transfer in order to gain sensitivity to the quantification method by observing the dominant signal of free Xe in solution. Noteworthy, we developed the qHyper-CEST framework as comprehensive as possible. This has the additional advantage that we need a minimal amount of prior knowledge.

6.3 RESULTS AND DISCUSSION

In the development of a quantitative method with absolute numbers, the results of this method must be confirmed and additionally checked for the range of validation. We therefore show its validation based on BM simulations first, face then experimental issues that can bias or corrupt the results, and finally quantify the Xe exchange kinetics of the previously unquantified Xe-host system CrA in DMSO.

6.3.1 Simulation-Supported Method Validation

Implementation of Bloch-McConnell Fitting

Fitting of *z*-spectra can be seen as a multi-dimensional parameter space optimization of many iterative simulated *z*-spectra. Therefore, the faster the simulation time for one single *z*-spectrum, the faster is the whole fitting process. We therefore implemented such fitting routines in MATLAB, THE MATHWORKS using the build-in function `lsqcurvefit` and measured the calculation time per simulated *z*-spectrum (Figure 6.1 and Table 6.2). We studied both ^{1}H-CEST (Figure 6.1a) and Hyper-CEST systems (Figure 6.1b) for each numerical method that is introduced in Section 3.1.5, *i. e.*, the Runge-Kutta-Integrator, the inverse and exponential matrix evaluation [Woessner *et al.*[234]] and the exponential matrix evaluation [Murase *et al.*[157]], and the FHC solution [Zaiss *et al.*[244]] in Section 3.1.6 (for Hyper-CEST). All of them were implemented from a single spin pool up to 4 coupled spin pools. This has the further benefit of cross-checking for similar depolarization behavior of a newly implemented CEST pool.

All methods agreed very well with each other (in fact, the curves almost completely match each other; Figure 6.1). For Hyper-CEST, however, all numerical solutions for 1-spin pool on-resonant with free Xe in solution ($\Delta\omega = 0$ ppm) did not reach total depolarization (exactly zero: "0"; Figure 6.1). This was because relative to the system intrinsic relaxation times,

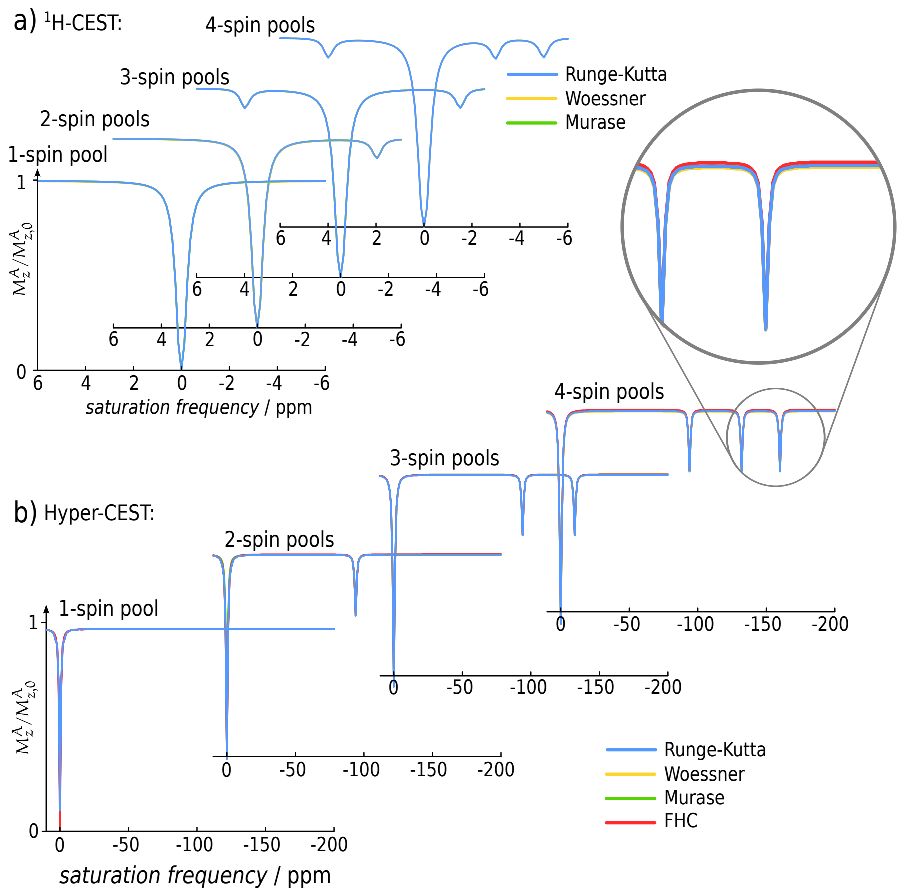

Figure 6.1: *z*-Spectra for simulation time comparison (Table 6.2) for the two artificial CEST systems: a) ^{1}H-CEST and b) Hyper-CEST that range from 1-spin pool to 4-spin pools (as introduced in Chapter 3). The y-axis is shown once for 1-spin pool and omitted for the others for better illustration purposes. The scaling, however, is equal. *z*-Spectra were calculated by the Runge-Kutta-Integrator (blue), the inverse and exponential matrix evaluation (Woessner *et al.*[234]; yellow), the exponential matrix evaluation (Murase *et al.*[157]; green) and for b) also by the full Hyper-CEST (FHC) solution (Zaiss *et al.*[244]; red). All methods agreed very well with each other. The simulation parameters for a) were: $B_0 = 9.4$ T, hyperpolarized signal enhancement factor $\eta = 1$, gyromagnetic ratio: $^{\mathrm{H}}\gamma$ (see Table 1.2), cw saturation of 0.8 µT for 2 s, offset range from - 6 ppm to 6 ppm with an increment of 0.125 ppm, *i. e.*, a total of 97 offsets. The parameters for the water pool (pool A), were: $T_1^A = 3$ s, $T_2^A = 0.2$ s, $\delta_A = 0$ ppm, $f_A = 1$; pool i: $T_1^i = 1$ s, $T_2^i = 0.05$ s, $f_i = 0.001$, $k_{iA} = 500$ s^{-1}, $k_{Ai} = f_i/f_A \cdot k_{iA} = 0.5$ s^{-1} with $i \in$ [B, C, D]. They differ in chemical shifts of $\delta_B = -5$ ppm, $\delta_C = +4$ ppm and $\delta_D = -3$ ppm. For b): $B_0 = 9.4$ T, hyperpolarized signal enhancement factor $\eta = 10{,}000$, gyromagnetic ratio: $^{\mathrm{Xe}}\gamma$ (see Table 1.2), cw saturation of 5 µT for 2 s, offset range from - 200 ppm to 10 ppm with an increment of 1 ppm, *i. e.*, a total of 211 offsets. The parameters for the free Xe pool (pool A) were: $T_1^A = 125$ s, $T_2^A = 5$ s, $\delta_A = 0$ ppm, $f_A = 1$. All CEST pools i with $i \in$ [B, C, D] had: $T_1^i = 100$ s, $T_2^i = 5$ s, $f_i = 0.001$, $k_{iA} = 300$ s^{-1}, $k_{Ai} = f_i/f_A \cdot k_{iA} = 0.3$ s^{-1}. They only differ in chemical shifts of $\delta_B = -94$ ppm, $\delta_C = -132$ ppm and $\delta_D = -160$ ppm. To crosscheck for correct implementation (*i. e.*, the CEST responses are similar in amplitude and width) the simulation parameters were purposefully chosen such that the CEST pools have equal exchange rates, k_{BA}, and sizes, f_B, while they only differ in chemical shift, $\delta_{B,C,D}$. Since all CEST resonances showed equal depolarization characteristics, we successfully implemented the CEST pool extension up to 4-spin pools.

Table 6.2: Simulation time comparison for a single z-spectrum using the Runge-Kutta-Integrator, the matrix inverse and exponential evaluation by Woessner *et al.*[234], the exponential matrix evaluation by Murase *et al.*[157] and the full Hyper-CEST (FHC) solution by Zaiss *et al.*[244] for ^{1}H-CEST and Hyper-CEST systems (Figure 6.1). All methods have identical sets of CEST parameters (detailed simulation parameters are provided in the caption of Figure 6.1). The listed times were rounded to 3 significant digits.

No. of Spin Pools	Runge-Kutta	Woessner	Murase	FHC
^{1}H-CEST				
1	715 s	0.0198 s	0.0172 s	-
2	846 s	0.0216 s	0.0206 s	-
3	927 s	0.0253 s	0.0237 s	-
4	962 s	0.0272 s	0.0252 s	-
Hyper-CEST				
1	16200 s	0.0370 s	0.0360 s	0.0000920 s
2	18300 s	0.0467 s	0.0402 s	0.000145 s
3	20800 s	0.0486 s	0.0422 s	0.000203 s
4	22600 s	0.0532 s	0.0478 s	0.000357 s

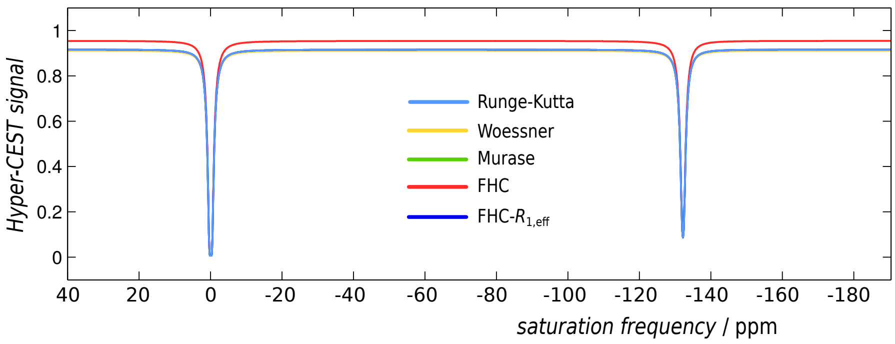

Figure 6.2: Limits of the FHC solution. Comparison of z-spectra simulation by the Runge-Kutta-Integrator (light blue), the inverse and exponential matrix evaluation (yellow), the exponential matrix evaluation (green), the FHC solution (red) and the $R_{1,\mathrm{eff}}$ extended FHC solution (dark blue; see Equation (3 | 16)). Simulation parameters: B_0 = 9.4 T, cw saturation was 2 μT for 7 s. Pool A: T_1^A = 125 s, T_2^A = 5 s. Pool B: T_1^B = 1 s, T_2^B = 0.5 s, chemical shift of δ_B = - 132 ppm, ratio of bound to free Xe, f_B = 0.006, exchange rate k_{BA} = 300 s^{-1} (and $k_{AB} = f_B/f_A \cdot k_{BA} = 1.8$ s^{-1}). The baseline of the FHC solution deviates from the three numerical solutions, since the FHC solution assumes a T_1^B that is similar to T_1^A. Thus, T_1^B is ignored in the FHC calculation. However, considering T_1^B by averaging the longitudinal relaxation rates according to Equation (3 | 16) ($R_{1,\mathrm{eff}}$) excellently matches the results of the numerical methods.

such particular cw saturation causes the magnetization to still precess around the effective field $\vec{B}_{\mathrm{eff}}$ (Figure 3.8). In contrast, the signal of the FHC solution (red) approximates the effective field $\vec{B}_{\mathrm{eff}}$ immediately and does not precess (Figure 3.8). Hence, its signal reached zero. Despite these negligible deviations between these methods, they agreed very well. The simulation time for each method (Table 6.2) relative to the Runge-Kutta-Integrator revealed an enormous decrease in fitting time for the method by Woessner *et al.*[234] and even a further decrease for the Murase *et al.*[157] method for both ^{1}H-CEST and Hyper-CEST throughout all spin pool extensions. For example, the Woessner *et al.*[234] solution was – in the case for a 2-spin pool ^{1}H-CEST model – 39,000 times faster than the straightforward Runge-Kutta-Integrator (see Table 6.2) and for a 4-spin pool Hyper-CEST model 425,000 times faster while calculating almost an identical *z*-spectrum with negligible deviation (Figure 6.1). The Murase *et al.*[157] solution was with 473,000 times (compared to the Runge-Kutta-Integrator) even faster for the 4-spin pool Hyper-CEST system than the Woessner *et al.*[234] method. However, for the same 4-spin pool system, the superior FHC solution was more than $60 \cdot 10^6$ times faster than the Runge-Kutta-Integrator, which is important for the use as fitting routine.

We further studied the limits of the FHC solution. Zaiss *et al.*[244] made the assumption that T_1^B is similar to T_1^A, and ignores T_1^B in the FHC calculation. However, Huber *et al.*[104] reported that $T_1^B = 4$ s of Xe within some Cr derivatives can also occur. This is fairly different from the commonly assumed large T_1^A values of free Xe in solution (Table 2.2). In the following we refer to the measured signal $M_z^A/M_{z,0}^A$ for both ^{1}H-CEST and Hyper-CEST systems as ^{1}H/Hyper-CEST signal (for *y*-axis scaling of *z*-spectra). We simulated a 2-spin pool Hyper-CEST system with the same parameters as in Figure 6.1, decreased the $T_1^B = 1$ s, $T_2^B = 0.5$ s (as $T_1 \geqslant T_2$) and increased 6 times the concentration of bound Xe $f_B = 0.006$ (Figure 6.2). While the CEST response was modeled correctly, the baseline of the FHC solution (red curve) was overestimated compared to the results of all numerical solutions. This was because the Xe is overall much faster depolarized within the fast relaxing moiety of Cr, which is simulated correctly by the numerical methods. By correcting the FHC solution with an effective longitudinal relaxation rate $R_{1,\text{eff}} = (f_A \cdot R_1^A + f_B \cdot R_1^B)/(f_A + f_B)$ that is weighted by the mole fractions of pool A and B (using Equation (3 | 16) and Equation (3 | 17)), we could excellently approximate the numerical solutions (Figure 6.2; dark blue curve). Our FHC-$R_{1,\text{eff}}$ solution yields optimal results even in the limit of largely different longitudinal relaxation times, while being as fast as the FHC solution. However, for this and the next two chapters, the original FHC solution was used, since the *z*-spectrum baseline deviation became significant only for large differences between T_1^A and T_1^B, and was even then less than < 5 % (as displayed in Figure 6.2).

Overall, numerical BM fitting by the Runge-Kutta-Integrator would take 60 million times longer per iteration step in comparison to the analytical FHC solution (for a 4-spin pool Hyper-CEST system). Since the exponential matrix evaluation by Murase *et al.*[157] was the fastest of all three numerical methods that were investigated here, we used from now on the exponential matrix evaluation by Murase *et al.*[157] as gold-standard numerical method. As gold-standard analytical solution we used the full Hyper-CEST (FHC) solution by Zaiss *et al.*[244]. A simulated *z*-spectrum can be fitted to the true exchange parameters which gains powerful insights into the Xe exchange dynamics and binding affinities. We next fitted a simulated *z*-spectrum to validate the fitting routine for qHyper-CEST.

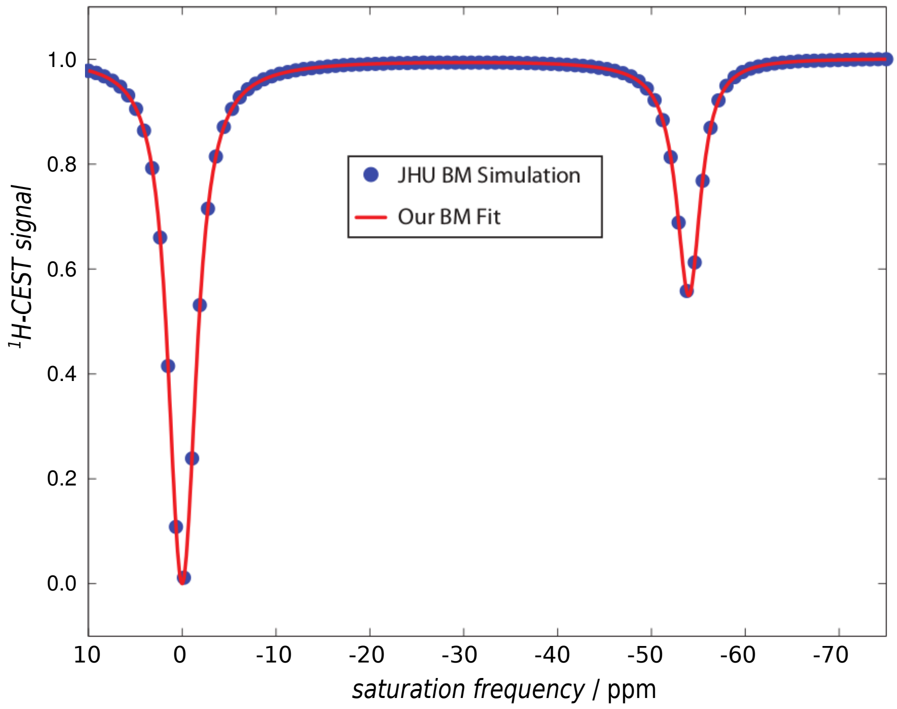

Figure 6.3: Validation of our implemented BM fitting routine. We fitted this ^{1}H-CEST system (blue data; simulated independently by a BM implementation of Craig Jones from the Johns-Hopkins University (JHU), Baltimore, USA [Jones *et al.*[110]] with cw saturation of 2.5 µT for 4 s at $B_0 = 9.4$ T) with our qHyper-CEST based fitting routine by adapting parameters accordingly to ^{1}H-CEST (see Table 6.3 for fitting results).

Fitting Routine Validation: ¹H-CEST

First, we validated our implemented qHyper-CEST fitting routine that is based on the fastest BM equations evaluation method, the exponential matrix evaluation by Murase *et al.*[157] (Table 6.2), on a BM equations-based simulator developed by Jones *et al.*[110] from the Johns-Hopkins University (JHU), Baltimore, USA, and Nirbhay Yadav, Ph.D. .[1] By adapting our qHyper-CEST fitting routine to ^{1}H-CEST, *i. e.*, 1) from Xe to proton: $\gamma^{^{129}Xe} \rightarrow \gamma^{^{1}H}$ and 2) from HP to thermally polarized initial magnetization: $M_0^{A,B} = M_{th}^{A,B} \cdot \eta \rightarrow M_0^{A,B} = M_{th}^{A,B}$, it excellently recovered all relevant exchange kinetics (Figure 6.3 and Table 6.3) demonstrating reliable implementation. Thus, we could correctly recover the following 6 parameters 1) T_1^A, 2) T_2^A, 3) δ_A, 4) δ_B, 5) k_{BA} and 6) f_B, for each of which conventionally multiple different methods would be required (Table 6.1).

By adapting back to Hyper-CEST, we aimed to quantify the Xe-CrA exchange kinetics in the following. Before we do that, we similarly validated the fitting routine on a Hyper-CEST system.

---

[1] Thanks for support at the CEST-Workshop 2014 in Turino, Italy, where the following ^{1}H-CEST simulator was introduced to the author: `http://www.nirbhay.info/`

Table 6.3: The parameter recovery of the artificial ^{1}H-CEST *z*-spectrum (Figure 6.3) is listed. Whereas the middle column shows the simulation parameters, the right column shows the fitting results of our BM equation-based qHyper-CEST fitting routine that was adapted to ^{1}H-CEST (by both 1) from Xe to proton: $\gamma^{^{129}Xe} \rightarrow \gamma^{^{1}H}$ and 2) from HP to thermally polarized initial magnetization: $M_0^{A,B} = M_{th}^{A,B} \cdot \eta \rightarrow M_0^{A,B} = M_{th}^{A,B}$). As a known and common issue, the relaxation rates of the bound species $R_{1,2}^B$ were not reliably accessible.

		JHU Simulator	Our Fitting Routine
pool A	δ_A / ppm	0	0.0001 ± 0.0017
	R_1^A / s^{-1}	0.333	0.345 ± 0.006
	R_2^A / s^{-1}	10	10.24 ± 0.15
	f_A	1	1 (fix)
pool B	δ_B / ppm	-54	-54.0004 ± 0.0035
	k_{BA} / s^{-1}	3,000	3,044 ± 20
	R_1^B / s^{-1}	0.33	1.40 ± 1.14
	R_2^B / s^{-1}	10	0.333 ± 16
	f_B	0.0022	0.002329 ± 0.00003

Fitting Routine Validation: Hyper-CEST

We next tested Xe exchange kinetics recovery by simulating experimental Hyper-CEST data. We simulated Hyper-CEST *z*-spectra using the exponential matrix evaluation method [Murase *et al.*[157]].

We fitted these simulated *z*-spectra again with both the numerical Murase *et al.*[157] method and analytically with the FHC solution. This procedure had the benefit of adding large amounts of noise onto the data and explore the fitting stability and reliability of the numbers obtained from our method. For some cases we found perfect parameter recovery even in presence of 10 % noise (Figure 6.4), with the FHC solution being much more precise than the BM fitting. However, with increased saturation pulse strength B_1, the recovery failed even for noiseless *z*-spectra (Figure 6.5a). The combination of both *z*-spectra enabled parameter recovery (Figure 6.5b). Clearly, there is some redundancy in the data that prevents from perfect parameter recovery. As a first guess, one might assume that this behavior was due to data averaging as the fit was based on twice the number of data points and, thus, clearly improved. However, for a total of three simulated *z*-spectra, the simultaneous fitting, so-called global fitting, successfully recovered the Xe exchange kinetics (Figure 6.6, noiseless and with 10 % noise), whereas for increased saturation pulse strengths B_1, the parameter recovery was poor (Figure 6.6, noiseless and with 10 % noise), although the fit was based on the same amount of data. As this was not expected, we explored this effect by examining the Xe depolarization behavior using the BM equations but with the more intuitive and simpler FHC solution (introduced in Section 3.1.6).

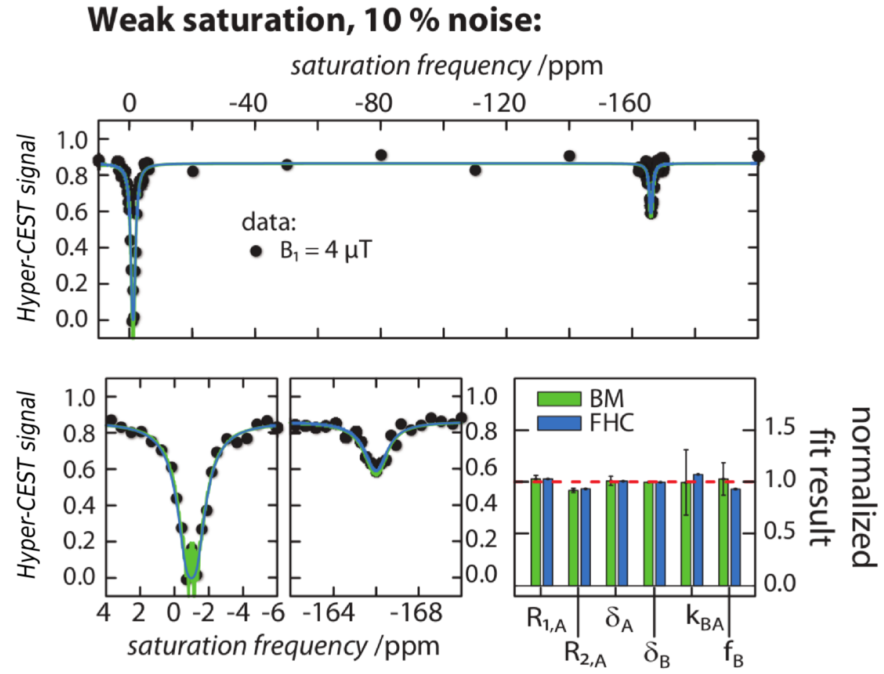

Figure 6.4: Validation of the implemented fitting routines. The Hyper-CEST z-spectrum was simulated (using the Murase *et al.*[157] method; dots: data) with weak saturation of $B_1 = 4\ \mu T$ for 10 s and 10 % noise and then fitted numerically with BM equations (using the Murase *et al.*[157] method; green line) and analytically with the FHC solution (blue line) with $B_1 = 4\ \mu T$ (top). A zoom in of the Xe in solution (bottom left) and bound Xe (bottom middle) resonance is shown below. The fit results normalized to the simulation values are shown in the bar plot (bottom right, green: BM equations, blue: FHC solution). A perfect retrieval returns all normalized fit values as 1 (red dashed line). The error bars were the standard deviation of the individual results of fitting five times, each time with a new randomly distributed set of initial values (see Table 2 in Kunth *et al.*[129]). The simulation parameters were: $B_0 = 9.4$ T; pool A: $T_1^A = 70$ s, $T_2^A = 5$ s, chemical shift: $\delta_A = 0$ ppm, $f_A = 1$; pool B: $T_1^B = 10$ s, $T_2^B = 0.5$ s, chemical shift: $\delta_B = -166$ ppm, ratio of bound to free Xe: $f_B = 0.00027$, and exchange rate: $k_{BA} = 270\ s^{-1}$. Reproduced with permission from Kunth *et al.*[129]. Copyright 2014, AIP Publishing LLC.

Dynamic Range of Xenon Depolarization Rate

Since we observed both successful and failed Xe exchange kinetic parameter recovery with respect to the saturation pulse strength B_1, we further examined this effect. In contrast to the BM equations (Equation (3.6)), the FHC solution gives an analytical but still complicated solution. Zaiss *et al.*[244] also proposed a simplified solution that we further approximated. This approximation intuitively shows how the different Xe exchange parameters manifest themselves into the Hyper-CEST effect as outlined in the following:

We consider 1) saturation that is tuned on-resonant with the bound Xe resonance, and 2) no spillover from direct saturation (*i. e.*, $\lambda_{\text{direct}} = 0\ s^{-1}$).[2] When

---

[2] The complete ^{129}Xe depolarization rate is obtained by the summation of the isolated direct depolarization rate $\lambda_{\text{direct}}(\Delta\omega)$ according to Equation (3.12) by $\lambda_{\text{depol}}(\Delta\omega) = -\lambda_{\text{direct}}(\Delta\omega) - \lambda_{\text{CEST}}^{AB}(\Delta\omega)$.

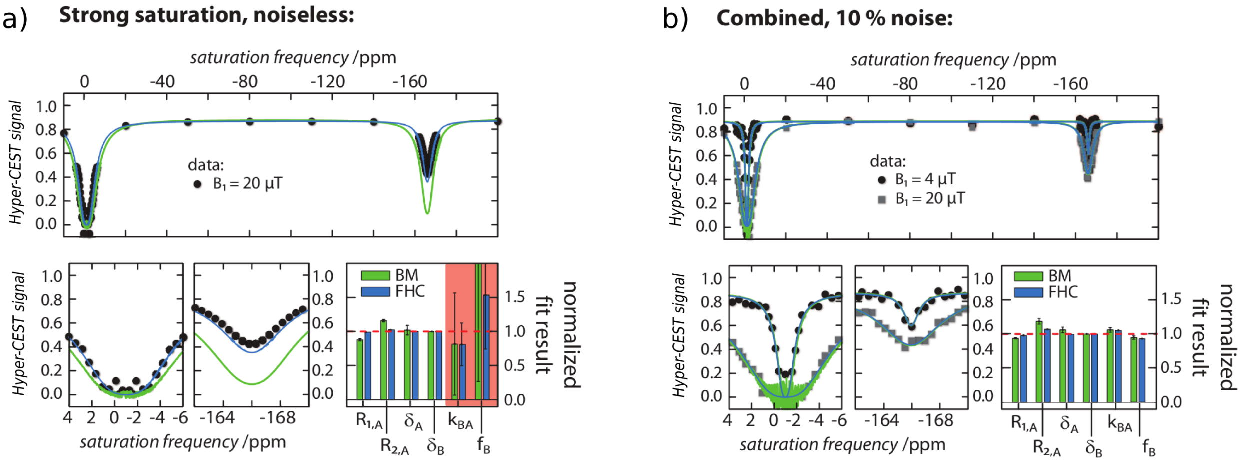

Figure 6.5: Validation of the implemented fitting routines. The method and parameters were similar as given in Figure 6.4, but a) with strong saturation of $B_1 = 20\ \mu\text{T}$ for 10 s on noiseless data, and b) the simultaneous fitting (global fitting) of the combined Hyper-CEST z-spectra ($B_1 = 4\ \mu\text{T}$ (circles) and $20\ \mu\text{T}$ (rectangles)) with 10 % noise. Note that the quantification failed even on noiseless data for strong saturation (a). The exchange rate k_{BA} and the relative bound Xe concentration f_B were not accurately determined (red box). Reproduced with permission from Kunth *et al.*[129]. Copyright 2014, AIP Publishing LLC.

$k_{BA} \gg R_2^B$ (*e.g.*, $k_{BA} = 270\ \text{s}^{-1}$ and $R_2^B = 2\ \text{s}^{-1}$, which are indeed realistic parameters for Xe and CrA in DMSO at room temperature), then the ^{129}Xe depolarization rate of the CEST pool $\lambda_{\text{CEST}}^{\text{AB}}(\Delta\omega)$ (compare with Equation (3 | 13b)) reduces to

$$\lambda_{\text{depol}}(B_1, k_{BA}) = f_B \cdot k_{BA} \cdot \frac{(\gamma B_1)^2}{(\gamma B_1)^2 + k_{BA}^2} \quad . \tag{6 | 1}$$

Equation (6 | 1) with respect to the saturation pulse strength B_1 is shown in Figure 6.6 bottom where we can identify two regimes:

1. a regime within the dynamic range of the ^{129}Xe depolarization rate where the quantification is successful (green circles and global fitting on the left hand side; green frame), and
2. a plateau regime of the ^{129}Xe depolarization rate in which the quantification failed (red circles and global fitting on the right hand side; red frame).

Therefore, Xe exchange kinetics quantification by qHyper-CEST was successful when (multiple) Hyper-CEST *z*-spectra were acquired within this dynamic range of the ^{129}Xe depolarization rate – typically around its own exchange rate k_{BA}, which is calculated in µT, *i.e.*, $B_1 = k_{BA}/\gamma$ [Kunth *et al.*[127]] (Chapter 7) and failed if these were within the plateau the ^{129}Xe depolarization rate. Whereas this exchange rate is *a priori* unknown (if the system under investigation has not been characterized before), the goal of the qHyper-CEST analysis is to determine – apart from other parameters – this very exchange rate. This results in a somewhat redundant task.

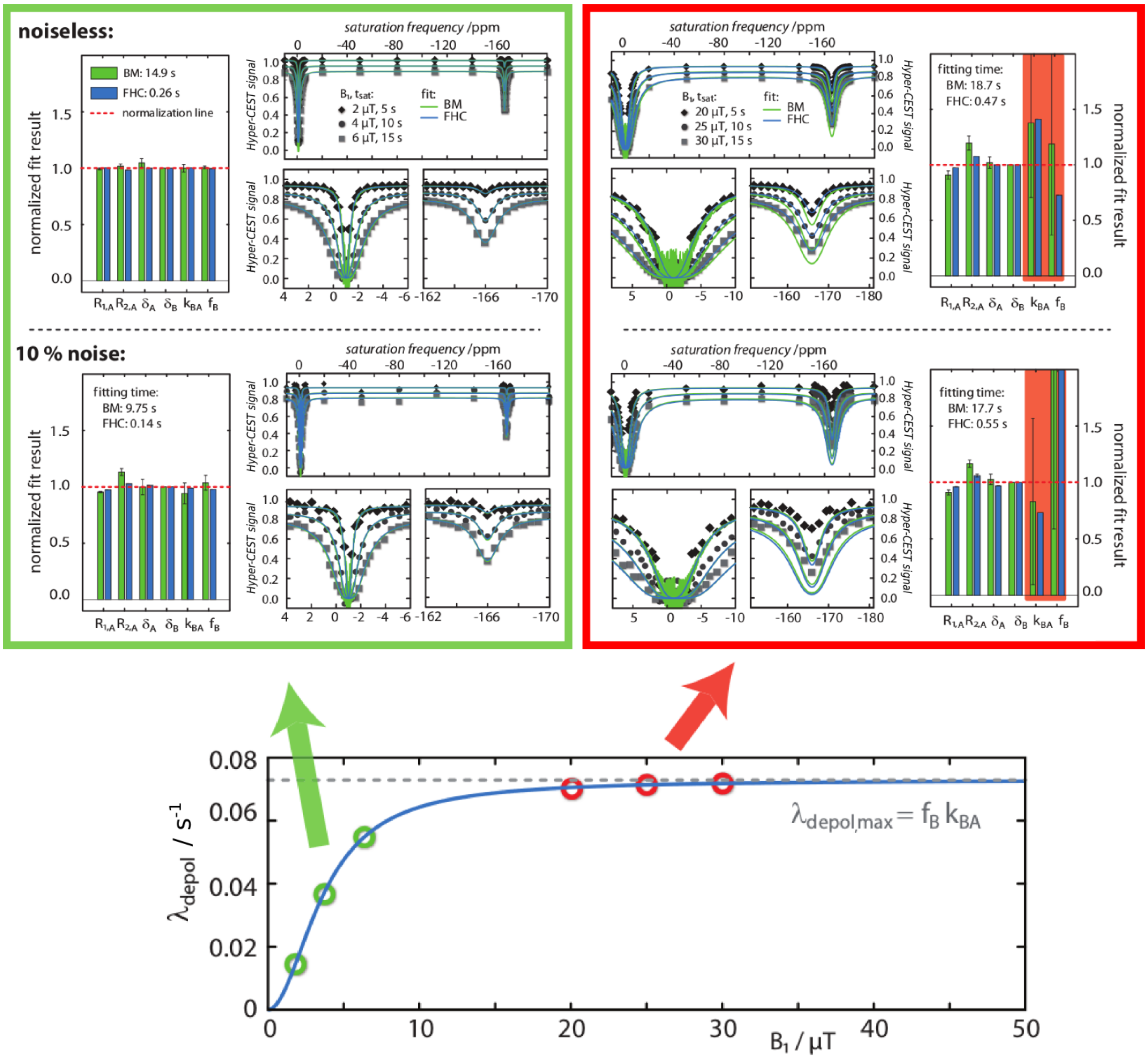

Figure 6.6: Validation of the implemented fitting routines. Quantitative information range in Hyper-CEST z-spectra based on simulations and global fitting. The data simulation and analysis was performed as described in Figure 6.4. Left green frame: Low B_1 values allowed for successful global fitting with separate determination of f_B and k_{BA} for both the BM equations (green in bar plot; including fitting time) and the FHC solution (blue in bar plot; including fitting time) even for 10 % noise on z-spectra. Right red frame: For large B_1 values the global fit was not able to determine f_B and k_{BA} individually (transparent red boxes) and fails in the correct quantification of the system even for noiseless z-spectra. Bottom: Depolarization rate λ_{depol} calculated with Equation (6.1) using the parameters listed in the caption of Figure 6.4. The maximum possible Hyper-CEST depolarization for a specific Xe-host system is $\lambda_{depol,max}(B_1 \to \infty) = f_B\, k_{BA}$ (indicated by the dashed gray line). For B_1 values within the transition regime of λ_{depol} (green circles), global fitting recovered all simulation parameters (green frame). For B_1 values within the plateau of λ_{depol} (red circles), global fitting was not able to individually determine f_B and k_{BA} (red frame). Reproduced with permission from Kunth *et al.*[129]. Copyright 2014, AIP Publishing LLC.

However, one way to achieve this experimentally is the following: acquisition of z-spectra around the bound Xe resonance with constant saturation time but for different saturation pulse strengths B_1 and identifying for changes in the amplitude of the Hyper-CEST effect, prior to the quantitative Hyper-CEST experiments that are used for the Xe exchange kinetics analysis. If the amplitude of the response is not changing but the resonance spectrally broadens with B_1 then the saturation pulse strength is too large and must be reduced. This gives a clear limitation of this technique as a reasonable amount of bound Xe signal must be present. For extreme dilutions of pool B, large B_1 values are already required to produce any Hyper-CEST effect, which in turn leads to maximum depolarization and hinders successful quantification. Moreover, within the plateau regime the fitting routine lost its boundary condition to the Hyper-CEST effect, since the saturation pulse strength B_1 was *a priori* knowledge for the fit. Therefore, the fit was unable to individually extract the exchange rate k_{BA}, and the ratio of bound to free Xe f_B, but only their product $f_B \cdot k_{BA}$. The difficulties of separating k_{BA} and f_B has also been reported for ^{1}H-CEST systems and studied with different approaches [Sun *et al.*[205]].

The meaning of different quantitative information regimes of the ^{129}Xe depolarization rate is similar to other methods, *e.g.*, optical absorption in optically thin or thick regimes. When all signal is saturated/absorbed, then no further information can be achieved from the system. This is also true for the quantification of the Xe exchange kinetics using Hyper-CEST: If all Xe atoms that are encapsulated by CrA (or later more general: by any host or binding site) are labeled through the saturation pulse, then the system does not notice a further increase of the saturation pulse strength, and no further Xe magnetization can be "turned off" during the saturation period. This Xe labeling process is limited by the exchange rate k_{BA} that is given by the host (see also in Chapter 7 about cw saturation pulse considerations for efficient Xe depolarization).

In summary, the analytical FHC solution was more 100 times faster than the numerical the exponential matrix evaluation of the BM equations [Murase *et al.*[157]] in computational fitting time but also more precise. In addition, the approximation of the FHC solution (Equation (6 | 1)) allows effective interpretation of the z-spectra affected by diverse parameters such as the exchange kinetics or the saturation pulse, where the parameters manifest themselves intuitively. Before we quantify the Xe-CrA system in DMSO, some B_1 concerns have to be addressed, which will be discussed in the following.

6.3.2 RF Field Issues

The value of the saturation pulse strength B_1 is the central component for the meaningful quantification of the Xe exchange kinetics by qHyper-CEST. Thus, its accuracy must be verified for any issues on the instrumental site, *i. e.*, 1) for amplifier linearity, 2) for correct flip angles and 3) the exclusion of RF field inhomogeneities. In the following sections we address each of these concerns.

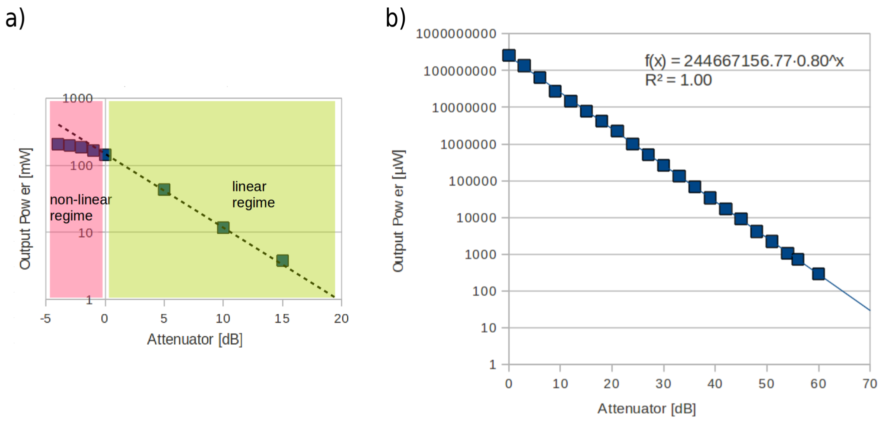

Figure 6.7: Amplifier linearity of a) the ^{1}H amplifier BLAH 300 and b) the ^{129}Xe amplifier BLAX 300. Both showed excellent linear behavior for positive attenuations, *i. e.*, > 0 dB.

Amplifier Linearity

The linearity of the amplifier between the controlled applied attenuation and the effective power output is mandatory. We measured this behavior using an oscilloscope and multiple resistors for both the ^{1}H channel and the ^{129}Xe channel (Figure 6.7). Both channels showed excellent linear relationships for positive attenuations, *i. e.*, > 0 dB. This linearity is also important to know when calculating the subject **specific absorption rate** (SAR). The deposited power P during a RF pulse of length PL is proportional to the square of the main magnetic field strength B_1, and the irradiation RF field according to

$$P \approx \omega_0^2 \int_0^{PL} B_1^2(t)\, dt \quad . \tag{6.2}$$

The SAR over the entire repetition time TR of the sequence yields then to

$$\mathrm{SAR} = \frac{t_{RF}}{\mathrm{TR}} \cdot \frac{P}{m} \quad , \tag{6.3}$$

where m equals the mass of the object (or sample) and t_{RF}/TR is the duty cycle for the RF pulses [de Graaf[83]]. Since the tissue resistivity and the B_1 strength is spatially distributed and not constant, the evaluation of Equation (6.3) is complex. However, for clinical ^{1}H-CEST applications, SAR of the object to be investigated is limited. For this reason, pulsed saturation schemes including different presaturation models are an active area of research to reduce the RF power deposition in the clinics [Jones *et al.*[110], Liu *et al.*[138], Vinogradov *et al.*[220]]. However, it is also known that cw saturation is more efficient than pulsed saturation schemes [Meißner *et al.*[151]].

Flip Angle Calibration

The flip angle calibration is very important in as much as saturation pulse parameters are derived from it. For this thesis the following flip angle calibration methods were under investigation and frequently used:

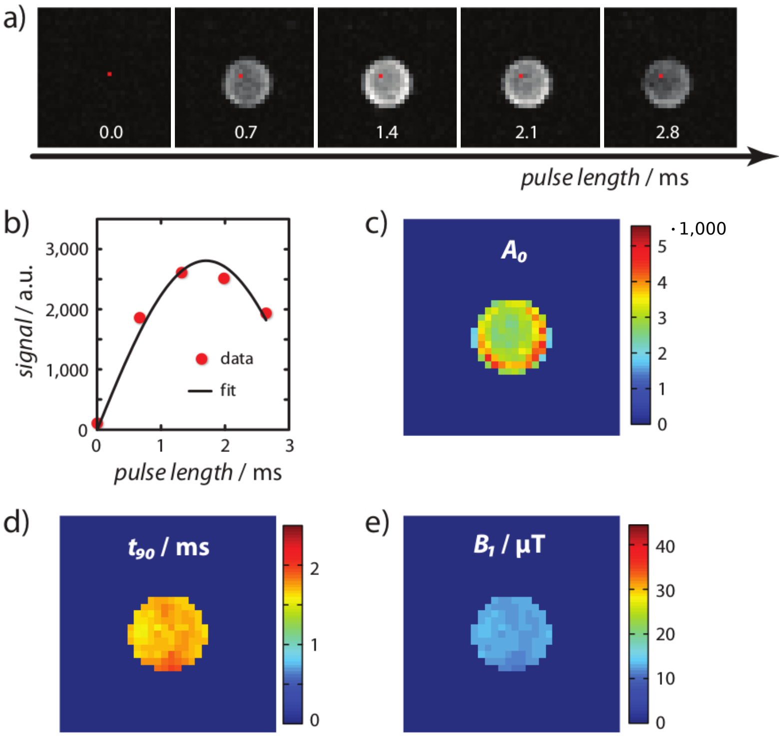

Figure 6.8: Traditional flip angle calibration and mapping. a) shows the image series obtained from a ^{129}Xe EPI pulse sequence with increased excitation pulse length (PL) using a block pulse shape. b) shows the signal S (red dots) of the red pixel in a). This was fitted to the function $S(PL) = A_0 \cdot |\sin\{(\pi/2 \cdot PL/t_{90} \cdot 1,000\}|$ (black line) with an amplitude of A_0 = 2,640 ± 130 and the 90° time, t_{90} = (1,800 ± 70) μs. (c-d) shows the fitting results of A_0 and t_{90} for each pixel of the whole phantom. e) The B_1 values were calculated by $B_1 = (\pi/2)/(2 \cdot \pi \cdot 11.777\ \text{MHz/T} \cdot t_{90})$.

TRADITIONAL FLIP ANGLE CALIBRATION: The rotation of the total net magnetization M_0 yields maximal NMR signal for the maximal projection of M_0 onto the transverse x–y plane, $M_\perp$. This occurs for a flip angle of α = 90°. Since the flip angle increases with the RF pulse strength B_1 and pulse length PL according to $\alpha = \gamma \int_0^{PL} |B_1(t)|\, dt$, (see Equation (2 | 19)), the following two gold-standard methods for the flip angle calibration exist (of which we used the first):

1. constant RF pulse strength B_1 and incremental increase of the pulse length PL (as used for this thesis; see Figure 6.8) and *vice versa*
2. constant RF pulse length PL and incremental increase of the pulse strength B_1.

While very accurate, both methods are time consuming since new HP Xe must be delivered into the sample for each incremental measurement.

FAST SINGLE-DELIVERY FLIP ANGLE CALIBRATION: An extremely fast single-delivery flip angle calibration was developed by Jörg Döpfert at the FMP-Berlin in the ERC BiosensorImaging Group. After a single delivery of fresh HP Xe, the non-renewable total magnetization is, in con-

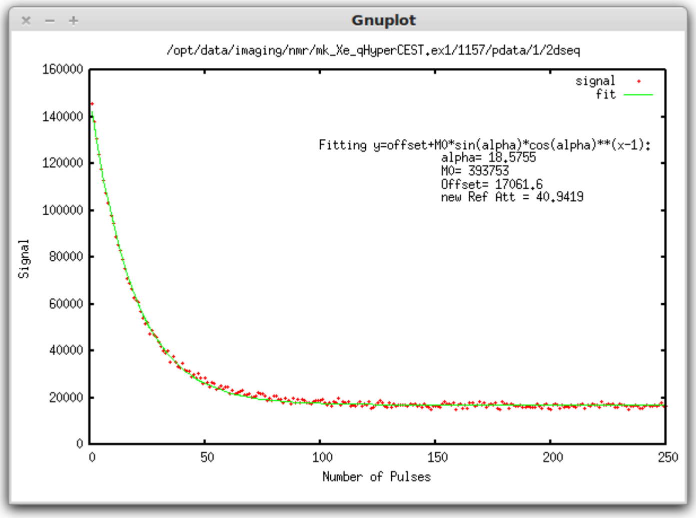

```
Fitting y=offset+M0*sin(alpha)*cos(alpha)**(x-1):
                 alpha= 18.5755
                 M0= 393753
                 Offset= 17061.6
                 new Ref Att = 40.9419
```

Figure 6.9: Single-delivery flip angle calibration.

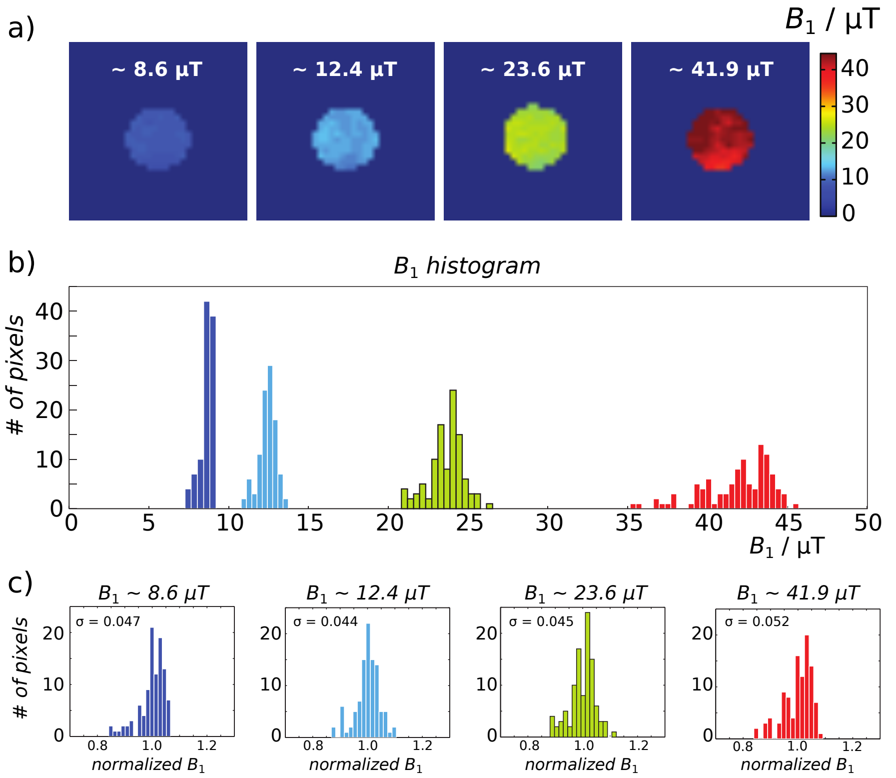

Figure 6.10: RF field homogeneity distribution by measured B_1 maps and homogeneity analysis. a) shows B_1 maps as obtained in Figure 6.8 for pulse strengths of $B_1 \sim \{8.6, 12.4, 23.6, 41.9\}$ µT. b) displays the histogram analysis for each B_1 map with adaptive bin number to keep the bin size constant regarding B_1. The results do not follow a Gaussian distribution. c) shows these histogram values normalized to its mean value (displayed with a constant bin number of 14). The results show a trend of slightly increased inhomogeneities at higher strength.

trast to the variable flip angle approach (see Equation (2.37)), used up by a known constant flip angle. This results in an RF pulse induced decay of the signal with respect to the number of excitation pulses (see Figure 6.9). By fitting this signal to $y = \text{offset} + M_0 \cdot \sin(\alpha) \cdot \cos(\alpha)^{x-1}$ one obtains for the particular reference attenuation the flip angle α of this RF pulse. As this pulsing happens on a time scale faster than the Xe-host system intrinsic longitudinal and transverse relaxation, this method neglects these relaxation terms.

The fast single-delivery flip angle calibration was used for about 80 % of the experiments for this thesis. However, we observed differences in the results of both methods when Xe relaxation times enhanced or exchange rate enhanced Xe-host systems were under investigation, *e. g.*, CB6 in water, CrA in DMSO, PFOB in PBS buffer, gas vesicles in water, CrA in cell associated aqueous environments, *etc*. It is therefore recommended to carefully compare the results of both and, moreover, potentially extend the single-delivery flip angle calibration by including both longitudinal and transverse relaxation times. This, in contrast, requires prior knowledge of the system to be investigated.

RF Field Homogeneity Distribution

It is known for ^{1}H-CEST experiments that the RF field of the saturation pulse that is produced by the transmitter coil close to the sample distributes inhomogeneously across the sample [Sun *et al.*[204]]. The impact of such RF field inhomogeneities induces an error for the quantified exchange kinetics due to pixel-averaging within a ROI of a whole distribution of RF field strengths. To estimate its magnitude on our micro-imaging system, we mapped the RF fields for four different commonly used saturation pulse strengths $B_1 \sim \{8.6$ (dark blue), 12.4 (blue), 23.6 (yellow), 41.9 (red)$\}$ μT (Figure 6.10a), and analyzed the distribution across the sample. As expected, this distribution was not-Gaussian. In addition, it was broadened with increasing B_1 values (Figure 6.10b). However, the relative broadening becomes insignificant with respect to B_1 by normalizing this distribution to its actual B_1 value (Figure 6.10c). We therefore conclude that RF field inhomogeneities are less of a concern for our micro-imaging system.

Nevertheless, as this is an important issue, we validated in a second step the impact of the B_1 field inhomogeneities on the quantification of the Xe exchange kinetics as it would be similar to the experiment by the application of a ROI. This ROI causes one averaged B_1 value that actually consisted of a whole distribution of pixel-related B_1 values. To test this impact, we simulated for three B_1 maps of 2.2 μT, 8.6 μT and 12.4 μT (Figure 6.10 and Supplemental Material S6 Figure 9 in Kunth *et al.*[129] that is attached in Appendix Section D.2) 104 Hyper-CEST *z*-spectra, hence a total of 312 *z*-spectra, each of which with its particular pixel-corresponding B_1 value. As the B_1 field distribution is not-Gaussian shaped, the three pixel-wise averaged *z*-spectra were not centered around the data points but distribution corresponding weighted. Strikingly, global BM fitting of these more "realistic" obtained Hyper-CEST *z*-spectra showed excellent parameter recovery of the Xe exchange kinetics. This demonstrates high stability of the qHyper-CEST method on our micro-imaging system (in the presence of RF inhomogeneities with magnitude observed in Figure 6.10a).

6.3.3 Xenon Exchange Kinetics for Cryptophane-A in Dimethyl Sulfoxide

After successful validation of the fitting method and exploring the RF field issues of our hardware, we could proceed to quantify the Xe exchange kinetics for CrA in DMSO using Hyper-CEST.

Rician-Correction

The images for data evaluation were obtained with the Hyper-CEST EPI protocol [Kunth and Döpfert *et al.*[121]] and are magnitude data. Thus, the noise level is above zero. As a consequence, the signals for total saturation of the free Xe resonance as well as the bound Xe CEST resonance are above zero. This results in a non-linear data distortion. For accurate and precise quantification *via* z-spectra fitting, we therefore corrected for this issue by performing a Rician-correction (see Supplemental Material S2 in Kunth *et al.*[129] which is attached in Appendix Section D.2).

Exchange Kinetics

To understand the entire system with minimal, while controllable and expectable changes in the Hyper-CEST mechanism, we changed the CrA concentration, while keeping all other parameters constant. This should clearly isolate these parameters that depend on the Xe-host concentration, while others remain unchanged. As a hypothesis, the binding constant is a constant by definition and should be independent on the Xe-host concentration. The fraction of bound Xe f_B, should directly give the CrA concentration (by knowing the Xe concentration in solution, which we do). But what about the Xe exchange rate k_{BA}? Will it be twice as large if twice the amount of CrA is present?

The direct ^{129}Xe NMR spectra for [CrA] = {1, 5, 10, 50, 100, 150} μM taken with 64 averages showed a bound Xe resonance detection limit of 100 μM in DMSO at room temperature (Figure 6.11). Thus, an exchange kinetics quantification on such data sets is limited. Instead, the qHyper-CEST *z*-spectra MRI (Figure 6.12; exemplary shown for the detection limit of direct ^{129}Xe NMR at 100 μM) showed greatly improved sensitivity using Hyper-CEST. The global BM and FHC *z*-spectra fitting results for each CrA concentration conveyed this large sensitivity to the quantification of the Xe exchange kinetics with accurate results down to 5 μM (Figure 6.13). While the chemical shift difference $\Delta\delta$ showed slight dependence on the CrA concentration (Figure 6.13a), the Xe exchange rate k_{BA} and the binding constant were insensitive to the CrA concentration (Figure 6.13b,c). The insensitivity of the binding constant K_A is expected, but not of the exchange rate as one might think if twice more host molecules are present, then twice more Xe atoms per time unit should be exchanged. This is represented in the BM equations by the magnetization transfer, which summarizes all these effects in two effective pools that exchange magnetization. Thus, the exchange rate k_{BA} is the off-rate for Xe to leave the CrA-bound state that is always the same, independent of the CrA concentration. As expected, the parameter of bound Xe, f_B, increased linearly with the CrA concentration (Figure 6.13d). However, the absolute numbers were not intuitive at all. For example, a CrA concentration of 50 μM produced an f_B of 0.0014. Since Xe forms 1:1 complexes with CrA and knowing the Xe in solution concentration of [Xe] = 2,340 μM according to the Ostwald solubility coefficient,

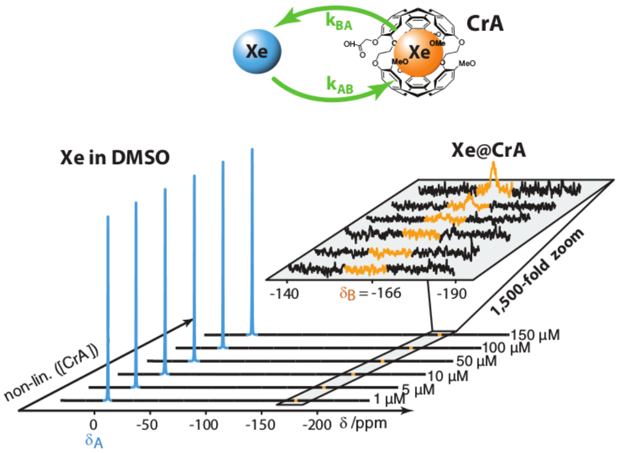

Figure 6.11: Direct ^{129}Xe NMR spectra of CrA in DMSO at room temperature. The CrA concentrations varied between 1 µM and 150 µM. The detection limit of CrA-bound Xe (orange) in DMSO was about 100 µM. Reproduced with permission from Kunth *et al.*[129]. Copyright 2014, AIP Publishing LLC.

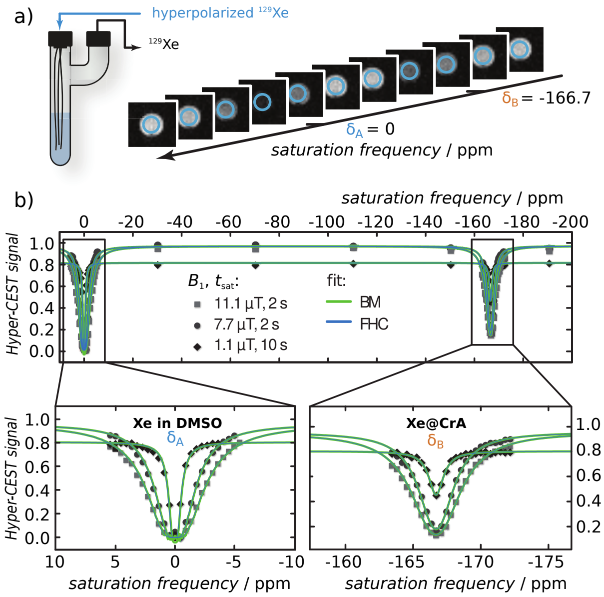

Figure 6.12: qHyper-CEST *z*-spectra MRI. a) shows the bubbling phantom containing the sample and the ^{129}Xe MR image series for different saturation frequencies. The Hyper-CEST *z*-spectra shown in b) were obtained by ROI signal averaging (blue ROI shown in a). Exemplary, the detection limit of direct ^{129}Xe NMR at 100 µM is shown in b (green: BM fitting; blue: fitting to the FHC solution). The number of offsets were 55 for each *z*-spectrum. The different saturation pulse strengths B_1 produced different pronounced Hyper-CEST effects and therefore ensure a successful quantification of the exchange kinetics. The different saturation times t_{sat} allow an estimation of the longitudinal relaxation time of free Xe in solution T_1^A. The longer the saturation time (until approximation to the true T_1^A), the more accurate the quantified value. Thus, the Hyper-CEST system is fully described by this method. Reproduced with permission from Kunth *et al.*[129]. Copyright 2014, AIP Publishing LLC.

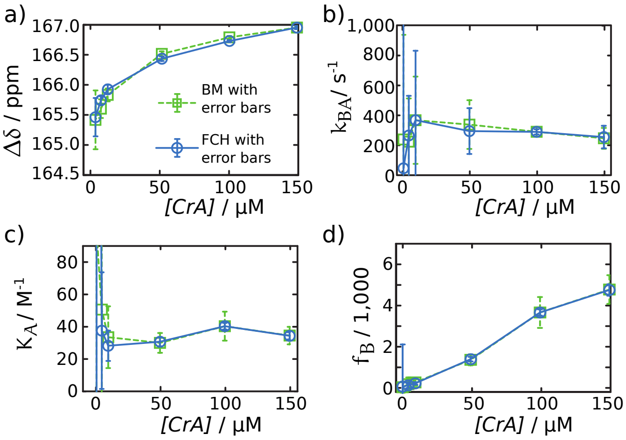

Figure 6.13: Xe exchange kinetics for CrA in DMSO at room temperature with respect to the CrA concentration (green: BM fitting results; blue: fitting results of the FHC solution) for a) the chemical shift difference $\Delta\delta$, b) the Xe exchange rate k_{BA}, c) the Xe binding constant K_A, and d) the relative bound Xe concentration f_B. Reproduced with permission from Kunth *et al.*[129]. Copyright 2014, AIP Publishing LLC.

an f_B = [CrA]/[Xe] = 50 µM/2,340 µM = 0.0214 would be expected, which is about one order of magnitude deviation. The fit was validated on simulations to be correct.

Speculated Host Occupancy

We now discuss in more detail the meaning of the parameter of the ratio of bound to free Xe f_B. Since Xe forms 1:1 complexes with CrA, the ratio of bound to free Xe f_B should somewhat reflect the concentration of CrA. As introduced in the method overview section (Section 6.2), f_B can be achieved from a direct ^{129}Xe NMR spectrum. We performed such quantitative measurements with both direct ^{129}Xe NMR and qHyper-CEST and both found similar values for f_B (data not shown). Contrary to intuitive expectation, this ratio did not represent the CrA concentration. To exclude any implementation or experimental errors, we further validated our method on a known ^{1}H-CEST system, more specific on a ^{1}H PARACEST system (similar to Figure 1.2b) using an **Eu-DOTA-4AmC** (further abbreviated with Eu-DOTA) complex.[3] Its chemical structure is shown in Figure 6.14a. It has a single water coordination site that is able to chemically exchange with water molecules of the surrounding environment (Figure 6.14b). When this complex is placed into water it acts as a PARACEST agent (Figure 6.14c). We designed a phantom, consisting of 7 sub-phantoms each of which filled with water and a different Eu-DOTA concentration of {0, 7.5, 15, 30, 45, 60, 90} mM (Figure 6.14d). Our qHyper-CEST analysis, which was adapted to ^{1}H-CEST, of exemplary [Eu-DOTA] = 30 mM revealed an exchange rate of k_{BA} = 29,800 s^{-1} that agrees well with literature [van Zijl and Yadav[260]] and an f_B of 0.00062286 (Figure 6.14e), while f_A = 1. This includes the chemical relations that 55 M of H_2O molecules exist in water, thus, $2 \cdot 55$ M = 110 M detectable NMR-active protons (*i. e.*, since one entire H_2O molecule exchanges, then f_A = 55 M). Then, the absolute Eu-DOTA concentration regarding this f_B value yielded 55 M $\cdot$ 0.00062286 $\sim$ 34 mM, which greatly

---

[3] The chemical formula of Eu-DOTA-4AmC is $EuC_{24}H_{37}N_8O_{12} \cdot 8\,H_2O$. It was purchased from Macrocyclics Inc., Dallas, USA: `http://macrocyclics.com/shop`

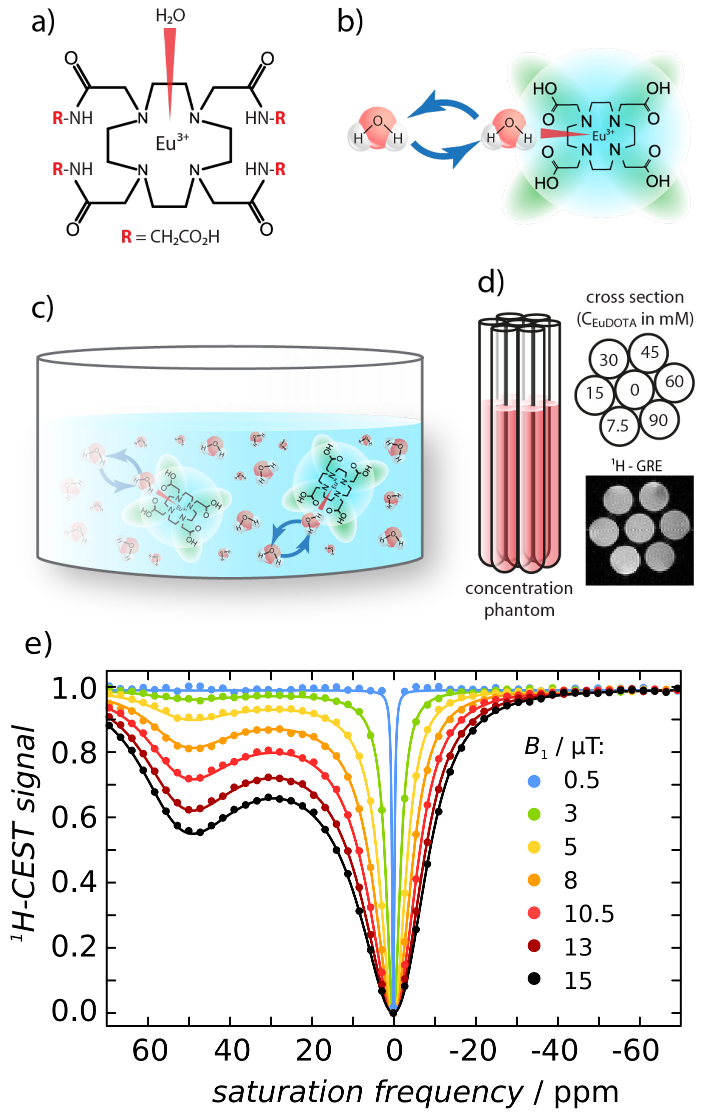

Figure 6.14: Quantification of the water Eu-DOTA exchange kinetics. a) Eu-DOTA complex with coordinated water molecule that is in chemical exchange (b). c) Eu-DOTA complex in pure water acts as PARACEST agent. d) Phantom with Eu-DOTA concentrations of {0, 7.5, 15, 30, 45, 60, 90} mM and ^{1}H-GRE cross section image. e) Exemplary *z*-spectra for an Eu-DOTA concentration of 30 mM at room temperature, $T = 295$ K. The cw saturation was $B_1 = \{0.5$ (blue), 3 (green), 5 (red), 8 (light blue), 10.5 (magenta), 13 (yellow), 15 (black)$\}$ μT for $t_{sat} = 5.5$ s. Fitting results of the Murase *et al.*[157] method were for pool A: $T_1^A = 2.5$ s, $T_2^A = 2$ s, $\delta_A = 0$ ppm, $f_A = 1$ and pool B: $T_1^B = 2$ s, $T_2^B = 1.5$ s, $\delta_B = 52$ ppm, $f_B = 0.00062286$, $k_{BA} = 29{,}800\ s^{-1}$ and $k_{AB} = k_{BA} \cdot f_B/f_A = 18.6235\ s^{-1}$. Setting $f_A = 55$ M (*i.e.*, 55 M H_2O molecules in water; thus, $2 \cdot 55$ M = 110 M detectable NMR-active protons in water) recovered the absolute Eu-DOTA concentration (55 M · 0.00062286 ~ 34 mM).

recovers the Eu-DOTA concentration within this sample. This is an accurate result which validates that our implementation was correct.[4]

---

[4] Figure 6.14e emphasizes the sensitivity of this Eu-DOTA ^{1}H PARACEST contrast agent. Note that CEST effects of < 50 % were achieved for the strongest saturation pulse of 15 μT for an Eu-DOTA concentration of 30 mM. In contrast, Hyper-CEST effortless achieves CEST effects larger > 60 % (*e.g.*, Figure 5.9b) at CrA concentrations of 10 μM which is more than three

It took advantage from the knowledge that always one water molecule is coordinated to the Eu-DOTA complex. Thus, the H_2O molecule occupancy is 100 %, as for many ^{1}H-CEST systems.

However, according to Figure 6.13d, the Xe ensemble appears to not entirely occupy all available CrA hosts. As this behavior was linear (within the range we studied here), we fitted the signal to

$$f_B([\mathrm{CrA}]) = \underbrace{\frac{\beta}{[\mathrm{Xe}]}}_{\text{linear slope}} \cdot [\mathrm{CrA}]\,, \tag{6.4}$$

where we introduced the host occupancy β, as a new parameter. Or *vice versa*:

$$\beta = f_B \cdot \frac{[\mathrm{Xe}]}{[\mathrm{CrA}]}\,. \tag{6.5}$$

Surprisingly, we found the host occupancy to be 8 % for this particular Xe-host system of CrA in DMSO at room temperature, T = 295 K (compare with Supplemental Material S3 in Kunth *et al.*[129] that is attached in Appendix Section D.2). One explanation for this unexpected low number could be the hydrophobic nature of Xe. Accordingly, the probability for Xe to stay in the non-polar environment that is provided by DMSO is larger than what we expected and causes 92 % of the total CrAs to be Xe free.

The Xe Binding Constant

From a direct ^{129}Xe NMR spectrum and considering chemical equilibrium the binding constant is given by[5]

$$K_A = \frac{f_B}{[\mathrm{CrA}] - f_B \cdot [\mathrm{Xe}]}. \tag{6.6}$$

We determined K_A by measuring f_B for a particular [CrA] (Figure 6.13c). From Equation (6.6) it is not obvious that the binding constant is constant in [CrA], as it occurs in the denominator. However, as f_B also changes with [CrA], Equation (6.6) can be expressed in terms of the introduced host occupancy using Equation (6.4) and the Xe concentration free in solution. The following equations emphasize its true constant character (given that the host occupancy β is constant):

$$K_A = \frac{1}{[\mathrm{Xe}]} \cdot \frac{\beta}{1-\beta}\,, \tag{6.7a}$$

$$\beta = \frac{K_A \cdot [\mathrm{Xe}]}{1 + K_A \cdot [\mathrm{Xe}]}\,. \tag{6.7b}$$

Equation (6.7a) and Equation (6.7b) should describe the system sufficiently for 1:1 complexes with $\beta \in [0, \ldots, 1]$.

---

orders of magnitude less. This is possible because the concentration of the detection pool (pool A) that has to be manipulated for any change by the contrast agent is for Xe by far less than 110 M protons in water (400 µM for Xe in water or 2,340 µM for Xe in DMSO).

[5] In chemical equilibrium $\mathrm{Xe} + \mathrm{CrA} \underset{\kappa_-}{\overset{\kappa_+}{\rightleftharpoons}} \mathrm{Xe@CrA}$ with $\kappa_\pm$ being the forward and backward chemical exchange rate, respectively.

6.4 CONCLUSION

We demonstrated a novel quantitative Hyper-CEST (qHyper-CEST) concept that is able to determine the Xe exchange kinetics, binding parameters and relaxation times with one type of ^{129}Xe NMR experiment at unprecedented high sensitivity. We showed excellent agreement of experimental data and the developed theoretical description. More specific, we showed that qHyper-CEST retrieved 1) the longitudinal relaxation time of free Xe T_1^A, 2) the transverse relaxation time of free Xe T_2^A, 3) the chemical shift difference $\Delta\delta$, 4) the Xe exchange rate k_{BA}, 5) the association constant K_A, and 6) the host occupancy β in one type of ^{129}Xe NMR experiment. A fundamental finding was that Xe occupies CrA in DMSO only by a fraction of $< 10\,\%$.

The theoretical and experimental combination enabled for the first time a qHyper-CEST approach that comprehensively sets the fundamentals for the determination of the Xe-host exchange kinetics without prior knowledge (except for two concentrations: that of Xe in solution and the Xe host). The small deviation from experimental data further supports that the Bloch-Torrey equations [Torrey[210]] are not required in addition to the BM equations.

In case of incoherent Xe supply with large delivery fluctuations between measurements, the successful quantification could fail or the results may be corrupted. Then the smashCEST *z*-spectra acquisition concept could be promising to recover the real shape of the *z*-spectrum (Figure 5.10c).

To improve Hyper-CEST sensitivity, further studies benefit from increasing the host occupancy. Although very fast in contrast to the original implementation, the entire qHyper-CEST data acquisition was still relative time consuming. Therefore, the combination of qHyper-CEST with ultrafast Hyper-CEST *z*-spectroscopy methods [Döpfert *et al.*[61], Boutin *et al.*[28]] could become a valuable research tool for the fast quantification of the Xe exchange kinetics of novel Xe-hosts or optimization of an existing one (at the cost of the slice selection possibility). Moreover, with methods as we introduced in Chapter 3, the qHyper-CEST concept can straightforwardly be expanded to more than 2-spin pools and might be of even larger interest for the characterization of the fundamental behavior of more complicated Xe-host systems.

The combination of theoretical and experimental validations of our qHyper-CEST concept also clearly showed the limits and possibilities of this method.

Limitations and Possibilities of qHyper-CEST

The method works if multiple saturation pulse strengths are used that produce different Hyper-CEST effects; hence, if they are within the dynamic range of the ^{129}Xe depolarization rate. This gives a clear limitation of the method, as sufficient large amounts of CrA must be present in the sample. Or *vice versa*: The quantification fails if large saturation pulse strengths B_1 are used that barely produce any Hyper-CEST effect due to low CrA concentration.[6] The accuracy of the quantification of the longitudinal relaxation

---

[6] It has to be noted here that the individual BM fitting results of the PFOB nanodroplets demonstrated by Stevens *et al.*[200] should be accurate and relative precise. According to our developed theory, individual fitting (*i.e.*, of one single *z*-spectrum) is only successful if saturation pulse strengths well within the dynamic range of the ^{129}Xe depolarization rate are used (Figure 6.6).

time of free Xe T_1^A is coupled to the length of the saturation pulse. This limits the total acquisition time. In most cases, the quantification of the Xe exchange kinetics for the CEST pool are not very sensitive to T_1^A. Therefore, this is less of a concern. We also showed that the FHC solution has a limitation if the longitudinal relaxation times of both free and bound Xe are too different. We found an effective relaxation rate $R_{1,\mathrm{eff}}$ that corrects for this deviation.

We validated our method for a pure 2-spin pool system. If, however, due to a too high host concentration a clustering is present, then a whole distribution of exchange rates, chemical shifts or host occupancies can occur. Then the global fitting of such altered *z*-spectra is expected to fail. However, the extension to multiple spin pools is straightforward.

The possibilities of our qHyper-CEST concept are the highly sensitive and simultaneous determination of relevant Xe exchange parameters, for which diverse experiments were previously required (Table 6.1). This provides a highly useful approach for

- analyzing plausibility of new Hyper-CEST systems of even complex systems such as pillar[5]arenes [Adiri *et al.*[1]], PFOB nanodroplets [Stevens *et al.*[200]], genetically encoded gas vesicles [Shapiro *et al.*[192]], bacterial spores [Bai *et al.*[14]], Xe encapsulating self-assembled Fe_4L_6 metallosupramolecular cages [Roukala *et al.*[172]], and for the modeling of Xe-CrA interaction with lipid environments and cell membranes [Meldrum *et al.*[153], Boutin *et al.*[29], Schnurr *et al.*[182], Schnurr *et al.*[180]];
- simulating a large number of Hyper-CEST experiments and designing complex experiments on the screen without the use of expensive Xe-gas, samples, sample preparation time, cells, and/or seldom host systems in advance;
- Xe-host classification beyond the single dimension of the chemical shift (*i. e.*, chemical shift, exchange rate and host occupancy/binding constant as whole package that are similar to a unique fingerprint);
- even more comprehensive temperature-dependent studies of the Xe-host exchange kinetics [Schilling *et al.*[177]];
- sensitive pH-studies [Berthault *et al.*[20]];
- the prediction and prospectives of general Hyper-CEST behavior as we will see in the next chapter in analyzing general rules for efficient Xe depolarization of any 2-spin pool system, or
- the development of general Xe Hyper-CEST biosensor MRI sensitivity amplification concepts.

In summary, qHyper-CEST allows to comprehensively describe the Hyper-CEST effect, formulate predictions and exploit them to amplify Hyper-CEST sensitivity. Therefore, qHyper-CEST could become an indispensable NMR

Their reported exchange rates (droplet size dependent) range from 37,000 s^{-1} to 9,600 s^{-1}. Their cw saturation was $B_1 = 21\ \mu T$ for 2 s even for the smaller exchange rate measurements. This corresponds to the very beginning of the depolarization rate curve (Figure 8.6) and should therefore be reasonably precise. Unfortunately, the errors were not reported in their publication.

tool for characterization of fundamental Hyper-CEST mechanism. The build-up of the measured Hyper-CEST effect is complex and relies on the intrinsic specific Xe-host system properties as well as the extrinsic applied saturation pulse strength and duration. However, our qHyper-CEST concept provides now the basis to individually optimize both 1) the applied saturation pulse strength and duration, and 2) the specific Xe-host system properties, independently and separately for further Hyper-CEST effect signal amplifications. Whereas we focus on point 1) in detail in the next Chapter 7 on cw pulse optimization, point 2) about the identification, classification and signal amplification capabilities for high turnover gas binding hosts will be discussed in Chapter 8.

The results for *Quantitative Hyper-CEST MRI* can also be found within the following publication.

FULL REFERENCE (attached in Section D.2):
Martin Kunth, Christopher Witte, and Leif Schröder. Quantitative chemical exchange saturation transfer with hyperpolarized nuclei (qHyper-CEST): Sensing xenon-host exchange dynamics and binding affinities by NMR. *The Journal of Chemical Physics*, 141:194202, 2014; Kunth *et al.*[129].

AUTHOR CONTRIBUTIONS: M.K. designed research and analyzed data; M.K. and C.W. performed research; M.K., C.W. and L.S. wrote the paper.

7 OPTIMAL SATURATION FOR HYPER-CEST MRI

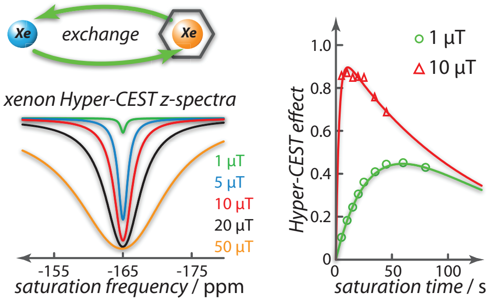

The work described in this chapter provides guidance for optimal cw saturation for maximizing the Hyper-CEST effect for a Xe-host system that was previously quantified with qHyper-CEST (see Chapter 6). Contrary to ^{1}H-CEST, Hyper-CEST has an optimal saturation time. Parts of this chapter have been published.

Contents

7.1 INTRODUCTION

The goal of this study – and a new approach in the optimization of the sensitivity of Hyper-CEST – is the identification of cw saturation pulse conditions that yield maximum possible Hyper-CEST effect. Crucially, this optimum combination of the saturation pulse strength and duration is *a priori* unknown. The build-up of the measured Hyper-CEST effect is complex and relies on the specific Xe-host system properties such as the Xe exchange rate k_{BA}, the host concentration, the host occupancy β, and the relaxation times of free Xe in solution, as well as the applied saturation pulse strength B_1 and duration t_{sat} [Kunth *et al.*[129]]. Intuitively hypothesized, the Hyper-CEST sensitivity should improve by increasing either the saturation pulse strength B_1 or the saturation pulse duration t_{sat} or both.

While Xe shows outstanding sensing properties to explore hydrophobic Xe-binding sites (*e.g.*, on lipid transfer proteins from *nicotiana tabacum*

[Dubois *et al.*[67]] or tripropargyl CrA encapsulated Xe that interacts as a whole complex with human carbonic anhydrase [Chambers *et al.*[50]]), the combination with the Hyper-CEST technique has additionally been used for the highly sensitive detection of such Xe-hosts. Most commonly, cw saturation schemes are used [chronologically ordered: Schröder *et al.*[187], Kunth and Döpfert *et al.*[121], Stevens *et al.*[200], Döpfert *et al.*[61], Boutin *et al.*[28], Klippel *et al.*[116], Rose *et al.*[170], Shapiro *et al.*[192], Schnurr *et al.*[180], Witte *et al.*[232]]. Alternatively, pulsed saturation schemes were also under investigation [Meldrum *et al.*[152], Bai *et al.*[13], Tassali *et al.*[208], Bai *et al.*[14], Wang and Dmochowski[225], Riggle *et al.*[169]] . However, from ^{1}H-CEST it is also known that cw saturation is more efficient than pulsed saturation schemes [Meißner *et al.*[151]], and it is expected that this behavior is similar for Hyper-CEST. However, the saturation parameters often appear to be randomly chosen, while all of these studies could potentially detect the Xe-host at even higher dilutions using optimal saturation parameters.

Here, we investigated a concept for the determination of such optimal saturation pulse parameters using the efficient cw saturation. We provide for the first time a very simple rule of thumb for a saturation pulse to produce maximal while still spectrally narrow Hyper-CEST responses. This was achieved first by quantifying the Xe exchange kinetics of the Xe-host system of interest (*e.g.*, by qHyper-CEST; see Chapter 6; Kunth *et al.*[129]), and use then simulations that are based on the FHC solution. As a fundamental result, we found that a saturation pulse strength of $\sqrt{2}$ times the exchange rate (*i.e.*, $B_1 = \sqrt{2} \cdot k_{BA}/\gamma$) showed best ratio of CEST amplitude to spectral width of the produced CEST resonance, whereas a strength of 5 times the exchange rate (*i.e.*, $B_1 = 5 \cdot k_{BA}/\gamma$) generated 96 % of the maximal possible Hyper-CEST effect. Contrary to ^{1}H-CEST, we further demonstrate that the superposition of the longitudinal relaxation time of free Xe in solution T_1^A and the actively driven depolarization yields an optimum saturation time. We show that saturating for longer than T_1^A becomes inefficient. This finding can be extrapolated for the Hyper-CEST detection of any general dilute Xe-host system.

7.2 RESULTS AND DISCUSSION

7.2.1 System Characterization

We consider the previously quantified Xe-host system CrA in DMSO at room temperature with known Xe exchange kinetics (Chapter 6; Kunth *et al.*[129]) at a concentration of 50 µM. We quantified the exchange rate to be k_{BA} = (317 ± 17) s^{-1}, the fractional size of pool B f_B = (13.4 ± 0.4)·10^{-4}, the occupancy β = 6 %, and the longitudinal relaxation time of free Xe T_1^A = (125 ± 26) s with qHyper-CEST (Figure 7.1). These numbers will be used for the following optimizations.

7.2.2 Optimization using Numerical BM Equation Tools

One way to address the question of maximizing the Hyper-CEST effect by the choice of optimal cw saturation pulse parameters is to numerically solve the BM equations (Equation (3.6)) for a range of saturation pulse strengths B_1 and durations t_{sat} (Figure 7.2). Full simulated Hyper-CEST *z*-spectra for cw saturation of B_1 = {1, 50, 100, 200, 300} µT each for t_{sat} = 2 s (Figure 7.2a)

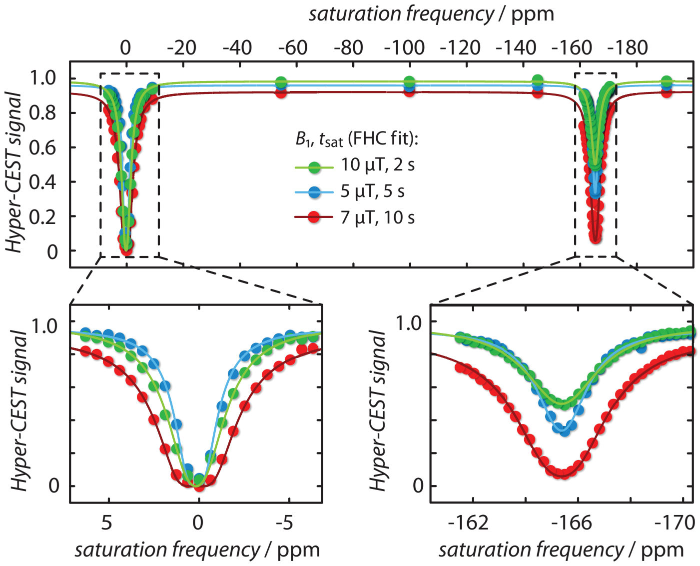

Figure 7.1: System characterization. qHyper-CEST analysis of [CrA] = 50 µM in DMSO at T = 295 K by simultaneously fitting *z*-spectra obtained from ^{129}Xe MR image series with the full Hyper-CEST (FHC) solution (solid lines) of multiple *z*-spectra with saturation pulse strengths B_1, and times t_{sat} of B_1/t_{sat} = {10/2 (green), 5/5 (blue), 7/10 (red)} µT/s. Reprinted with permission from Kunth *et al.*[127]. Copyright © 2015 John Wiley & Sons, Ltd.

showed that for weak saturation strengths, *i.e.*, < 50 µT, the maximal Xe depolarization of the CEST pool is not yet reached, while for larger values there is no improvement in its depolarization (even for unrealistic large B_1 values of 300 µT). In fact, saturation strengths beyond an optimal B_1 value cause the Hyper-CEST effect to decrease again. This happens because both resonances, that of free Xe in solution (direct saturation) and CrA-bound Xe, spectrally broaden with increasing B_1. The Hyper-CEST effect is calculated (according to Equation (3 | 10)) as

$$\text{Hyper}-\text{CEST effect} = \frac{M_z^A(-\delta_B) - M_z^A(+\delta_B)}{M_{z,0}^A} \cdot 100\,\% \ . \qquad (7\,|\,1)$$

The broader solution resonance at 0 ppm reaches into the CEST resonance as seen at the opposite side (Figure 7.2; off-resonant signal at gray dashed line) that decreases the calculated Hyper-CEST effect. Thus, the Hyper-CEST effect of strong saturation pulses is prone to concomitant effects due to so-called spillover contribution from the free Xe in solution resonance. This increasingly reduces the Hyper-CEST effect (Figure 7.2a). We found the system intrinsic maximum Hyper-CEST effect of ~ 90 % for a cw saturation pulse strength of B_1 = 30 µT (compare with Hyper-CEST effect surface plot in Figure 7.2b). Contrary to ^{1}H-CEST, we additionally found an optimal saturation time of 9.4 s for which this Hyper-CEST effect becomes maximal (Figure 7.2b). This is due to the superposition of the longitudinal relaxation time of free Xe in solution T_1^A and the actively driven depolarization.

While this numerical solution straightforwardly finds the maximal Hyper-CEST effect with its optimal cw saturation parameters, it does not gain any insights into the Xe exchange kinetics, is time consuming and rather empiri-

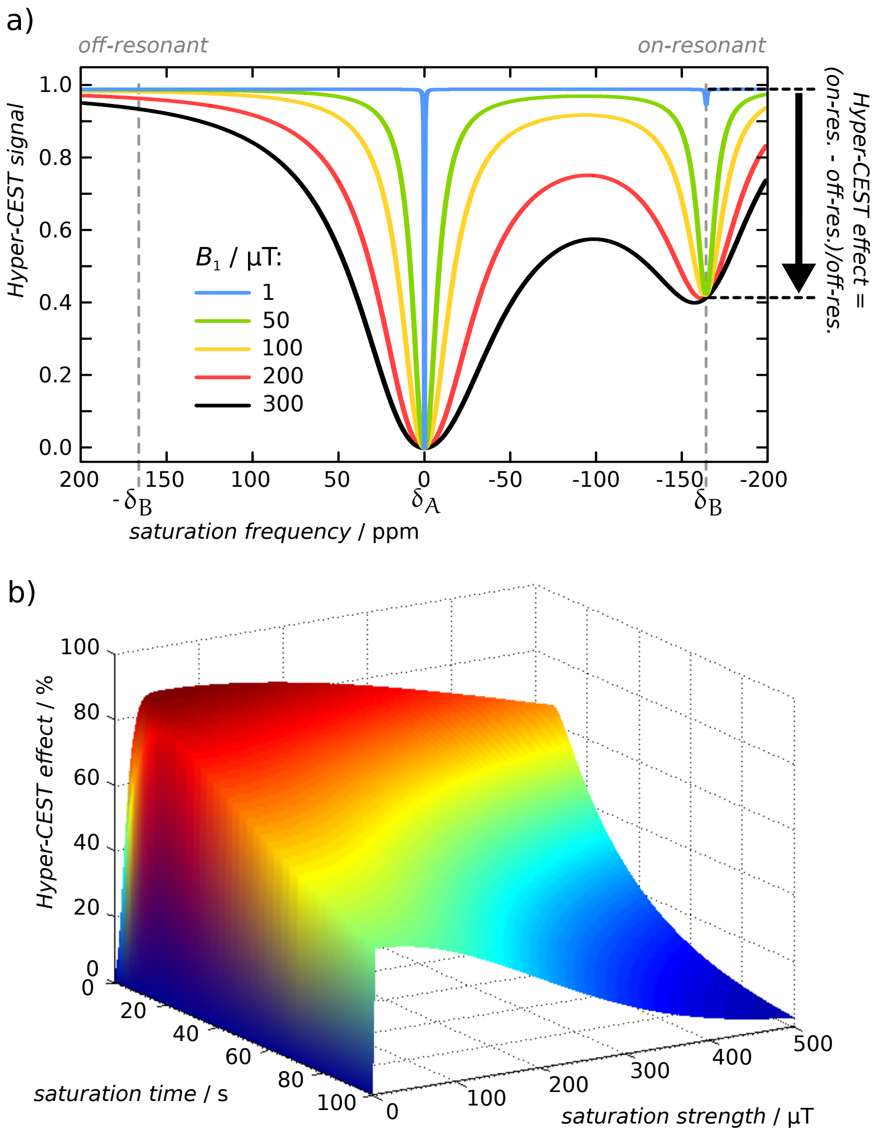

Figure 7.2: Numerical optimization of the cw saturation pulse parameters of the Xe-host system CrA in DMSO at room temperature. a) *z*-Spectra were simulated using cw saturation of $B_1 = \{1$ (blue), 50 (green), 100 (yellow), 200 (red), 300 (black)$\}$ µT, each for $t_{sat} = 2$ s using the exponential matrix evaluation by Murase *et al.*[157] for a 2-spin pool system (Equation (3|6)). With increasing B_1 beyond 50 µT, there is no improvement in the Xe depolarization even for unrealistic large saturation pulse strengths, *e.g.*, 300 µT. Instead, the Hyper-CEST effect starts to decrease because of spillover effects from direct saturation of the free Xe in solution resonance (off-resonant gray dashed line on the opposite side). b) The Hyper-CEST effect surface plot with respect to the saturation pulse strength B_1 and time t_{sat} was calculated by $(M^A_{z,off} - M^A_{z,on})/M^A_{z,off}$ (similar to Equation (3|10)). Thus, only two data points from each of the z-spectra shown in (a) were considered. The total simulation time of this 150^2 matrix-size based Hyper-CEST effect surface plot was ~ 30 s. The maximal Hyper-CEST effect of ~ 90 % was generated for optimal cw saturation of $B_1 = 30$ µT and optimal saturation time of 9.4 s. The simulation parameters were for the pool of free Xe in solution (pool A): $T_1^A = 125$ s, $T_2^A = 5$ s, $\delta_A = 0$ ppm, $f_A = 1$; CrA-bound Xe (pool B): $T_1^B = 10$ s, $T_2^B = 0.5$ s, $\delta_B = -165$ ppm, $f_B = 0.00134$, $k_{BA} = 317$ s^{-1} and $k_{AB} = k_{BA} \cdot f_B/f_A = 0.42478$ s^{-1} at $B_0 = 9.4$ T (as quantified in Section 7.2.1). Critically, this method straightforwardly finds the saturation parameters that generate maximal Hyper-CEST effect, but does not yield an intuitive rule of thumb how these are related to the fundamental Xe exchange kinetics.

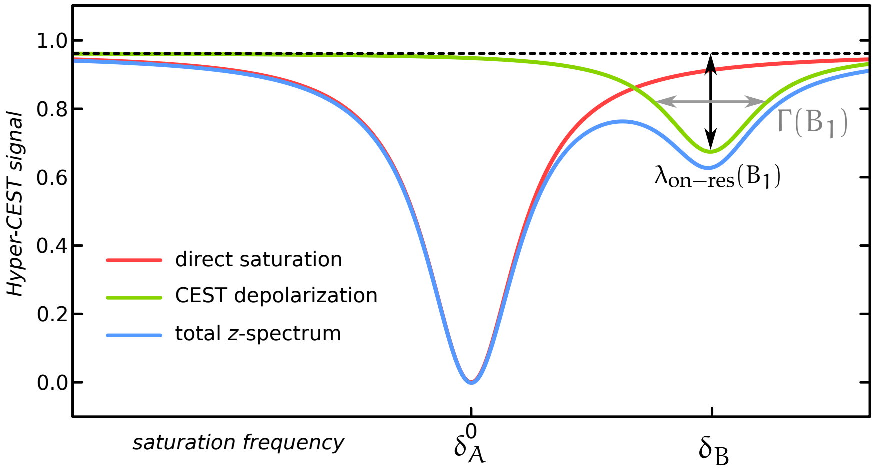

Figure 7.3: Decoupling of a 2-spin pool *z*-spectrum (blue curve) into a superposition of two independent depolarization pools of free Xe in solution (pool A; direct saturation; red curve), and of bound Xe (pool B or CEST pool; green curve). It has to be noted that $\lambda_{\text{on-res}}(B_1)$ (black) and $\Gamma(B_1)$ (gray) correspond to the amplitude and full width at half-maximum of the ^{129}Xe depolarization rate, and not to the shape of the *z*-spectrum as drawn here. For the shape of the *z*-spectrum the depolarization rate must further be considered using the exponential function in Equation (7.2). This here is for illustration purposes to convey the idea using the familiar *z*-spectrum representation.

cal. An alternative is to derive analytical expressions that couple such optimal cw saturation pulse parameters to the intrinsic Xe-host exchange kinetics. This may allow general expressions for intuitive rules of thumb to gain maximal Hyper-CEST effect directly without running such numerical simulations.

7.2.3 Optimization using Analytical BM Equation Tools

We decouple the *z*-spectrum into a superposition of two independent depolarization pools, *i.e.*, free Xe in solution (pool A) and bound Xe (pool B or CEST pool), similar to the FHC solution [Zaiss *et al.*[244]] (described in Section 3.1.6; Figure 7.3). The Hyper-CEST signal as a function of the cw saturation pulse irradiation frequency $\Delta\omega$, the strength B_1, and the duration time t_{sat} is given by

$$\text{Hyper}-\text{CEST signal}(\Delta\omega, B_1, t_{\text{sat}}) = 1 - e^{-\lambda_{\text{depol}}(\Delta\omega, B_1)\cdot t_{\text{sat}}} \quad , \tag{7.2}$$

with the Lorentzian line shaped Xe depolarization rate

$$\lambda_{\text{depol}}(\Delta\omega, B_1) = C(\Delta\omega) + \frac{\lambda_{\text{on-res}}(B_1)\cdot\frac{\Gamma(B_1)^2}{4}}{\frac{\Gamma(B_1)^2}{4} + (\Delta\omega_B(\Delta\omega) + x_0(B_1))^2} \quad . \tag{7.3}$$

The parameters $C(\Delta\omega)$, $\Delta\omega_B(\Delta\omega)$ and $x_0(B_1)$ are the direct saturation line shape (thus, the baseline), the true chemical shift and its shift away under disproportional strong saturation, respectively, (further discussed in the Supplemental Material S1 in Kunth *et al.*[127] which is attached in Appendix Section D.3). The two useful parameters for the pulse optimization are the maximum depolarization rate for on-resonant irradiation onto the CEST pool, given by (compare with Figure 7.3)

$$\lambda_{\text{on-res}}(B_1) \approx f_B\, k_{BA} \frac{(\gamma B_1)^2}{(\gamma B_1)^2 + k_{BA}^2} \ , \tag{7.4}$$

and the full width at half-maximum of the depolarization rate in Equation (7.3), Γ, which is given by (compare with Figure 7.3)

$$\Gamma(B_1) \approx 2\sqrt{(\gamma B_1)^2 + k_{BA}^2} \ . \tag{7.5}$$

Note that Equation (7.3) is similar to a framework for ^{1}H-CEST. For protons, we have $\lambda_{\text{depol}}(\Delta\omega, B_1) = R_{1\rho} = R_{\text{eff}} + R_{\text{ex}}$, with the longitudinal relaxation rate of the detection pool in the rotating frame $R_{1\rho}$, the effective relaxation rate R_{eff} and the exchange-dependent relaxation rate in the rotating frame R_{ex} [Zaiss and Bachert[242], Zaiss and Bachert[243]]. Also here the R_{ex} part should be dominated by the saturation pulse in order to produce a CEST effect before the R_{eff} part intrinsically cancels the total signal. For ^{1}H-CEST analysis, it has also been shown that it is beneficial to remove the steady-state signal [Sun[202]] or to perform the measurement in the transient state [Zaiss and Bachert[243]]. In contrast to ^{1}H-CEST, Hyper-CEST is special, since a negligible steady-state amplitude exists and the system is always in the transient state.

In the following, we derive guidelines that find optimal saturation pulse parameters using Equation (7.4) and Equation (7.5).

Optimal Saturation Pulse Strength

Since the Hyper-CEST signal is related to the saturation pulse as the argument of an exponential function (Equation (7.2)), we consider – for the sake of convenience – the Xe depolarization rate and not the shape of the CEST resonance in the *z*-spectrum. However, the general behavior is similar.

The Hyper-CEST *z*-spectra for cw saturation of $B_1 = \{1$ (green), 5 (blue), 10 (red), 20 (black), 50 (orange)$\}$ µT for 5 s each (Figure 7.4) show, similar to Figure 7.2a, with increasing saturation pulse strength B_1 first a large increase of the on-resonant Hyper-CEST effect, and then only spectral broadening. To analyze this behavior, we investigated the on-resonant Xe depolarization rate $\lambda_{\text{on-res}}$ (Equation (7.4)). We found a Xe-host concentration dependent and system intrinsic maximum saturation transfer onto free Xe given by $f_B \cdot k_{BA} = 0.425\ \text{s}^{-1}$ (Figure 7.5a).[1]

A potential interpretation of this number is given in the following: Considering in chemical equilibrium the law of conservation, the forward and backward Xe exchange rates are related by $k_{AB} = f_B \cdot k_{BA}$. This leads to the following two Xe exchange rates:

- The Xe exchange rate to leave the CrA-bound state $k_{BA} = 317\ \text{s}^{-1}$, and
- the Xe exchange rate to leave the free state in solution $f_B \cdot k_{BA} = k_{AB} = 0.425\ \text{s}^{-1}$.

---

[1] This limit is reached for an infinitely high saturation pulse strength, *i. e.*, $\lambda_{\text{on-res}}(B_1 \to \infty) = f_B \cdot k_{BA}$.

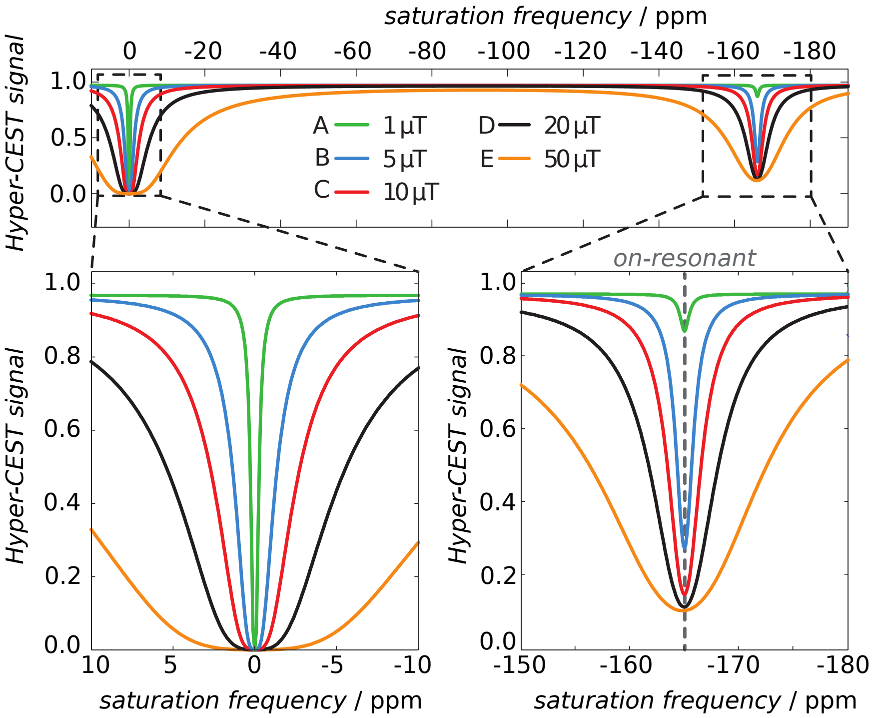

Figure 7.4: Simulated z-spectra using the FHC solution by Zaiss *et al.*[244]. The simulation parameters used are listed in the caption of Figure 7.2. A cw saturation of $B_1 = \{1$ (green), 5 (blue), 10 (red), 20 (black), 50 (orange)$\}$ µT for 5 s each was used. Note that in the on-resonant Hyper-CEST response (gray dashed line) the difference between 20 µT (orange) and 50 µT (black) in maximal Hyper-CEST effect is small but the loss of spectral resolution significant. This line marks the on-resonant Hyper-CEST signal that is further analyzed in the following three subfigures Figure 7.5a–c. Reprinted with permission from Kunth *et al.*[127]. Copyright © 2015 John Wiley & Sons, Ltd.

More intuitively, these exchange rates can be expressed as two average residence times for Xe (compare with Figure 7.6):

- The CrA-bound Xe residence time $\tau_{BA} = 1/k_{BA} = 3.3$ ms, and
- the residence time of Xe free in solution $\tau_{AB} = 1/k_{AB} = 2.35$ s.

On average, every 2 s one Xe atom binds to a CrA molecule. In contrast, if the host occupancy β would be 100 % (instead of 6 %), then nearly 17 Xe atoms could cycle through the Cr within the same time frame and manipulate the large detection pool of free Xe in solution more efficiently. This finding leaves large room for further Hyper-CEST sensitivity amplifications, as will be exploited in the next Chapter 8.

We further analyzed Equation (7.4) with respect to the saturation pulse strength B_1 and, in addition, generalize B_1 in terms of the unit-less parameter $B_1 \cdot \gamma / k_{BA}$. This has the advantage that the effect is generalized to the system intrinsic exchange rate k_{BA} and can be extrapolated to any Xe-host system. Using this generalization we found the following three general regimes of the behavior of the Xe depolarization rate:

1. $B_1 \gg k_{BA}/\gamma$: then $\lambda_{on-res} \approx f_B \cdot k_{BA}$ reaches the Xe-host system intrinsic maximum possible depolarization rate.

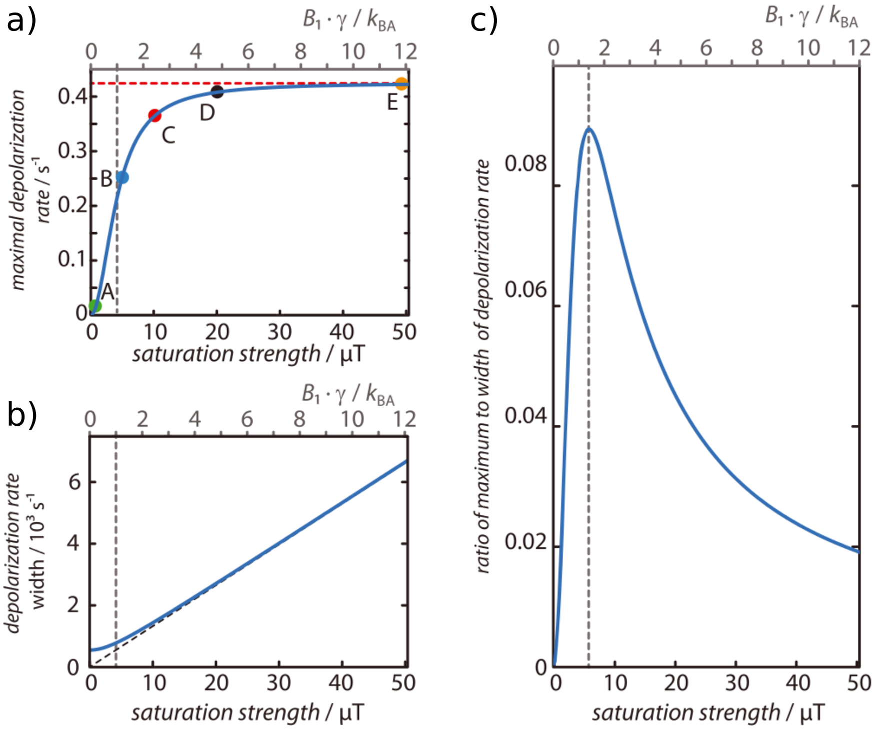

Figure 7.5: Comparison of the depolarization rate λ_{on-res}, the full width at half-maximum of the depolarization rate Γ, and the ratio of both (as a measure of how much Hyper-CEST effect is gained at the cost of spectral selectivity) λ_{on-res}/Γ, with respect to the saturation pulse strength B_1, and it unit-less equivalent scale $B_1 \cdot \gamma / k_{BA}$ (gray scale on top of each plot). a) The color-encoded closed circles correspond to the on-resonant ^{129}Xe depolarization in Figure 7.4. Its maximum, *i. e.*, $\lambda_{on-res}(B_1 \to \infty) \approx f_B \cdot k_{BA}$, reaches 0.425 s^{-1} (indicated by the red dashed line). 50 % of the maximum possible depolarization rate is reached for $B_1 = k_{BA}/\gamma \sim 4.3\ \mu T$ (vertical gray dashed line), whereas 96 % is reached for $B_1 = 5\,k_{BA}/\gamma \sim 21.4\ \mu T$ (approximately at the black circle; D). b) The full width at half-maximum of the depolarization rate Γ shows a y-intercept of $\Gamma(B_1 \to 0) = 2 \cdot k_{BA} \sim 634\ s^{-1}$ as pure exchange rate driven line broadening. This becomes dominated by the linear increasing saturation pulse strength line broadening (diagonal black dashed line) for larger B_1 values. c) The ratio of the maximal depolarization rate and the full width at half-maximum of the depolarization rate λ_{on-res}/Γ shows a distinct maximum for $B_1 = \sqrt{2}\ k_{BA}/\gamma \approx 6\ \mu T$ (gray dashed line). Contrary to Figure 7.2, plots a-c intuitively show the Xe depolarization behavior with saturation pulse strength relative to their own exchange rate k_{BA}. Reprinted with permission from Kunth *et al.*[127]. Copyright © 2015 John Wiley & Sons, Ltd.

2. $B_1 = k_{BA}/\gamma$: then $\lambda_{on-res} = (f_B \cdot k_{BA})/2$ is 50 % of the maximum possible depolarization rate.
3. $B_1 \ll k_{BA}/\gamma$: then $\lambda_{on-res} \approx (f_B/k_{BA}) \cdot (\gamma B_1)^2$ which is parabolic in saturation pulse strength B_1.

The identification of a maximum possible Xe depolarization rate means that the amplification effect from Xe which binds to CrA – or more generally a host or binding site – is limited. Consequently, if all Xe atoms are labeled by the saturation pulse, the system cannot translate more pulse strength into further depolarization of the HP free Xe pool A.

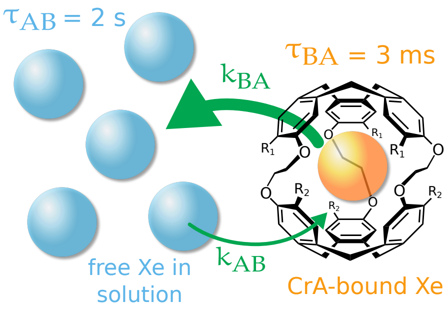

Figure 7.6: Xe exchange rates and residence times for 50 μM of CrA (with $R_1 = R_2 =$ MeO) in DMSO (*i. e.*, $f_B = 0.00134$; Section 7.2.1). While the Xe exchange rate leaving CrA is $k_{BA} \sim 300\ s^{-1}$ (thick green arrow), the slower Xe exchange rate leaving the free unbound state is $k_{AB} = f_B \cdot k_{BA} = 0.425\ s^{-1}$ (thin green arrow). Therefore, the residence time of one Xe atom in the CrA-bound state is on average $\tau_{BA} = 1/k_{BA} \sim 3.3$ ms, while it is on average for $\tau_{AB} = 1/k_{AB} \sim 2$ s free in solution.

However, a notable contribution of high saturation pulse strengths to the Hyper-CEST *z*-spectrum is a loss of spectral resolution due to line broadening. By comparing the shape of the *z*-spectra for 20 μT (*ca.* 4-5 k_{BA}/γ; Figure 7.4; black curve) with results for 50 μT (*ca.* 12 k_{BA}/γ; Figure 7.4; orange curve), it becomes obvious that the gain of the Xe depolarization rate is small but the loss of spectral selectivity is significant. To further investigate this effect, we analyzed the full width at half-maximum of the depolarization rate (Equation (7.5)) for the same unit-less scaling as for the pulse strength B_1. We found the following two general regimes:

1. $B_1 \gg k_{BA}/\gamma$: $\Gamma \approx 2\gamma B_1$ and depends linearly on the saturation pulse strength B_1.
2. $B_1 \ll k_{BA}/\gamma$: $\Gamma \approx 2k_{BA}$, which is the minimum possible width given by the Xe exchange rate.

For our study of CrA in DMSO at room temperature the minimum possible full width at half-maximum of the depolarization rate Γ for very weak saturation pulse strengths is determined by twice the Xe exchange rate and approaches $\Gamma(B_1 \to 0) = 634\ s^{-1}$ (Figure 7.5b). A more narrow line width cannot be achieved.

It is now interesting to ask which B_1 strength should be used to gain maximal possible Hyper-CEST effect in relation to how much spectral resolution is lost. Since both λ_{on-res} and Γ increase monotonically, we proposed to look at the ratio of the maximal depolarization rate and its full width at half-maximum λ_{on-res}/Γ as a function of B_1 (Figure 7.5c). We found a distinct maximum for pulses with strength $B_1 = \sqrt{2} \cdot k_{BA}/\gamma$ (Figure 7.5c; gray dashed line), which means that the CEST resonance for such a B_1 value shows best amplitude to width ratio. Moreover, a pulse strength of $B_1 = 5 \cdot k_{BA}/\gamma$ generates 96 % of the maximal possible Hyper-CEST effect while (at least to some extent) preserves spectral selectivity (Figure 7.4).

The two saturation pulse strengths, *i. e.*, $B_1 = \sqrt{2}\, k_{BA}/\gamma$ and $B_1 = 5\, k_{BA}/\gamma$, are of fundamental interest for the Xe biosensor Hyper-CEST MRI detection method because they provide decent to nearly maximal Hyper-CEST effect, respectively. However, for multiplexing experiments with two resonances being spectrally close together, the $\sqrt{2}$ pulse would be ideal (compare in Figure 7.4 for maximal Hyper-CEST response: $\sqrt{2} \cdot k_{BA}/\gamma \approx 6$ µT (blue curve; B) with $5 \cdot k_{BA}/\gamma \approx 21.4$ µT (black curve; D)). As shown in Section 6.3.2, SAR limitations (Equation (6 | 3)) are an additional aspect of saturation pulse limitation to the system. Moreover, SAR also increases with the duration of pulse irradiation. It is therefore – beside its influence of the intrinsic longitudinal relaxation time of free Xe in solution, T_1^A – of interest to optimize the saturation time with respect to two aspects: 1) signal maximization of the Hyper-CEST effect and 2) SAR confinements.

Optimal Saturation Pulse Time

> *"One of the main challenges to practical application of [^{1}H-]CEST (on the clinical scanners) is achieving RF irradiation long enough to get to the maximum saturation."*
>
> — Vinogradov *et al.*[220] – 2013

In contrast to ^{1}H-CEST, for which the longitudinal relaxation opposes the CEST effect, for Hyper-CEST it further accelerates the driven depolarization, due to non-equilibrium starting conditions. Thus, Hyper-CEST systems therefore have an optimal saturation time beyond which the Hyper-CEST effect decreases again. We addressed this optimal saturation time by data acquisition off-resonant (Figure 7.7; black closed circles) and on-resonant for three saturation pulse strengths $B_1 = \{1$ (blue open circles), 7 (red rectangles), 10 (green triangles)$\}$ µT for increasing saturation time. Whereas the off-resonant signal is pure longitudinal relaxation T_1^A, we calculated (and not fitted) the on-resonant signal using Equation (7 | 4) and substituting into Equation (7 | 2). They excellently represent the data and emphasize, as expected, that an optimal saturation time t_{sat} exists for which the difference of the off-resonant and on-resonant Hyper-CEST signal becomes maximal (Figure 7.7b). From this analytical model, we calculated the optimal saturation times for these three B_1 values according to

$$t_{sat} = \frac{1}{\lambda_{on-res}} \cdot \ln\left(\lambda_{on-res} \cdot T_1^A + 1\right) \quad , \tag{7 | 6a}$$

$$= \frac{\left((\gamma B_1)^2 + k_{BA}^2\right)}{f_B\, k_{BA}\, (\gamma B_1)^2} \cdot \ln\left(\frac{f_B\, k_{BA}\, (\gamma B_1)^2}{(\gamma B_1)^2 + k_{BA}^2} \cdot T_1^A + 1\right) \tag{7 | 6b}$$

to $t_{sat} = \{59.3, 11.8, 10.6\}$ s, respectively (using Equation (7 | 6b)). The derivation is given in the Supplemental Material S3 in Kunth *et al.*[127] which is attached in Appendix Section D.3. The meaning of Equation (7 | 6a) and Equation (7 | 6b) is that

1. if the ^{129}Xe depolarization rate is small (*i. e.*, $\lambda_{on-res} \to 0$), then the saturation time approaches the longitudinal relaxation time of free Xe in solution ($t_{sat} \to T_1^A$). This is the case for:
   a) highly dilute concentrations of bound Xe (*i. e.*, $f_B \to 0$),
   b) weak saturation pulse strength (*i. e.*, $B_1 \to 0$), and/or
   c) for very small or large Xe exchange rates (*i. e.*, $k_{BA} \to \{0, \infty\}$).

   Thus, one should not exceed the intrinsic longitudinal relaxation time of free Xe as saturation time, *i. e.*, $t_{sat} \leqslant T_1^A$, independently of the exchange rate k_{BA}.

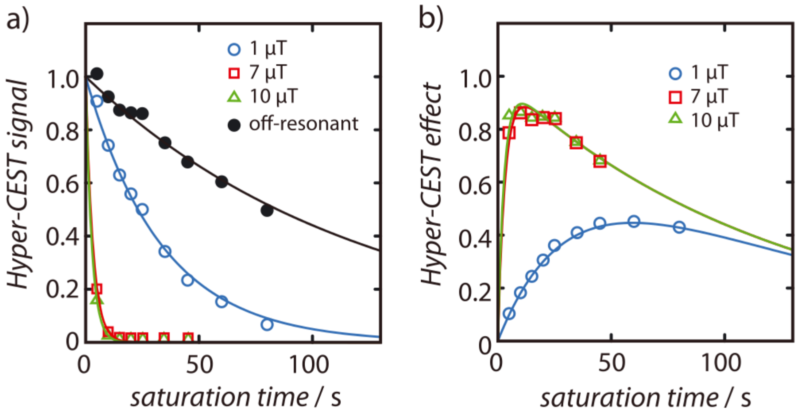

Figure 7.7: Analytical optimization of the cw saturation pulse duration t_{sat} for signal maximization of the Hyper-CEST effect. a) The Hyper-CEST signal with respect to the saturation time t_{sat} for on-resonant saturation on bound Xe with three different saturation pulse strength: $B_1 = \{1$ (blue open circles), 7 (red rectangles), 10 (green triangles)$\}$ µT is shown. The signal with off-resonant saturation (black closed circles) corresponds to pure longitudinal relaxation of free Xe T_1^A. b) shows the Hyper-CEST effect (calculated as the difference between the off-resonant and on-resonant signal) with respect to the saturation time t_{sat}. The corresponding curves (solid lines) in both subfigures (a, b) were not fitted but analytically calculated using Equation (7 | 2) (with substitution of Equation (7 | 4)) and the Xe exchange kinetics which were quantified by qHyper-CEST. The optimal saturation times regarding these B_1 values were $t_{sat} = \{59.3, 11.8, 10.6\}$ s, respectively (calculated using Equation (7 | 6b)). Reprinted with permission from Kunth *et al.*[127]. Copyright © 2015 John Wiley & Sons, Ltd.

2. if the ^{129}Xe depolarization rate is large (*i. e.*, $\lambda_{on-res} \rightarrow \infty$), then the saturation time approaches $t_{sat} \rightarrow 0$. This is the case for
   a) high concentrations of bound Xe (*i. e.*, $f_B \rightarrow \infty$), and
   b) strong saturation pulse strengths (*i. e.*, $B_1 \rightarrow \infty$).

   The Xe exchange rate in Equation (7 | 6b) is less of a concern since k_{BA} gives λ_{on-res} only a value (even for favorable resonant $k_{BA} \leftrightarrow (\gamma B_1)$ conditions for which λ_{on-res} becomes maximal, but $\lambda_{on-res} \nrightarrow \infty$; see Chapter 8).

The arguments regarding the influence of the exchange rate k_{BA} in point 1.c and 2 will become clear when considering the Hyper-CEST signal build-up in more detail as discussed in Chapter 8.

7.2.4 Comparison of Both Optimizations

To compare the numerical solution with the analytical one, we match their saturation pulse strength and compare their provided optimal saturation time. Thus, we search for the optimal saturation time according to Equation (7 | 6b), by knowing that the numerical method found the optimal saturation pulse strength of $B_1^{opt,num} = B_1^{opt,ana} = 30$ µT. Using these values for the analytical calculation of the optimal saturation time according to Equation (7 | 6b) yielded $t_{sat}^{opt,ana} = 9.5$ s. This is in excellent agreement with the optimal cw saturation time found numerically, *i. e.*, $t_{\mathrm{sat}}^{\mathrm{opt,num}} = 9.4$ s (see Figure 7.2b) although spillover was excluded in the analytical solution. Moreover, using our analytically proposed saturation pulse strength of $B_1^{\mathrm{opt,ana}} = 5 \cdot k_{BA}/\gamma \approx 21.4$ µT, the optimal saturation time according to Equation (7 | 6b) yields then to $t_{\mathrm{sat}}^{\mathrm{opt,ana}} = 9.67$ s, which is still decent. Thus, both methods agree very well with each other.

The cw saturation pulse optimization was also implemented into the Bloch-McConnell-Solver GUI (Figure 3.7). It calculates the optimal parameters for any general 2-spin pool Hyper-CEST system with a particular exchange rate k_{BA}, occupied host concentration f_B, and longitudinal relaxation time of free Xe T_1^A.

7.3 CONCLUSION

We demonstrated for the first time the connection between the cw saturation pulse and the Xe exchange kinetics and derived an optimal cw saturation condition to achieve maximal Xe depolarization while preserving spectral selectivity. Instead of running extensive large numbers of experiments, we quantified once the fundamental Xe exchange kinetics with qHyper-CEST and used simulations to make significant predictions on the Hyper-CEST performance of this system. Simulations in general have the advantage that they can reveal the behavior of a system for experimentally difficult accessible parameters and, thus, allow the finding of general laws of this system.[2] As a rule of thumb, we found that a saturation pulse strength of $\sqrt{2}$ times the exchange rate (*i. e.*, $B_1 = \sqrt{2} \cdot k_{BA}/\gamma$) showed best ratio of amplitude to spectral width of the produced CEST resonance, whereas a strength of 5 times the exchange rate (*i. e.*, $B_1 = 5 \cdot k_{BA}/\gamma$) generated 96 % of the maximal possible Hyper-CEST effect. Contrary to ^{1}H-CEST, we further provide evidence that Hyper-CEST has an optimum saturation time (for which we propose a formula) and to saturate for longer than T_1^A becomes inefficient.

However, in some studies it might be too detailed to analyze the system by qHyper-CEST. For such cases one can rely on the fact that the Xe depolarization rate is assumed to be monoexponential [Zaiss *et al.*[244]]. One can therefore achieve a quick estimate of the optimal saturation time by fitting the data in Figure 7.7a monoexponentially, use the decay rates τ as the inverse of $\lambda_{\mathrm{on-res}}$ and calculate the optimal saturation time for a specific preselected saturation pulse strength B_1, and sample concentration (using Equation (7 | 6a); see Supplemental Material S3 in Kunth *et al.*[127] which is attached in Appendix Section D.3). Considering the reduced complexity, the following restrictions remain when recording this simple exponential decay: The determined saturation times t_{sat} are only valid for 1) exactly this one concentration of bound Xe f_B, and 2) the saturation pulse strength B_1 that were used.

Limitations and Possibilities

If the exchange rate k_{BA}, the fractional size of pool B f_B, and the longitudinal relaxation time of free Xe T_1^A are known, then this method should be generally applicable for the optimal Xe-host detection by Hyper-CEST.

---

[2] This assumes that the simulation has been validated and sufficiently describes the system within the regime which is under investigation.

For multiplexing experiments, which often require large spectral selectivity, our method could even be extended to the corresponding number of spin pools to predict the cw saturation that optimally resolves multiple species that resonate close to each other.

In summary, we exploited the imaging speed provided by single-shot Hyper-CEST (see Chapter 5) and the quantification of the Xe exchange kinetics with qHyper-CEST (see Chapter 6) to develop an optimal cw saturation pulse. This plays a crucial role for sensitivity amplification of Xe biosensor MRI by maximizing the Hyper-CEST effect. We also demonstrated that the intrinsic maximum possible Xe depolarization improves with the Xe exchange rate k_{BA} as long as B_1 can be strong enough. This opens an entire new sensitivity amplification concept for Hyper-CEST that will be exploited in the next Chapter 8.

The results for *Optimal Saturation for Hyper-CEST MRI* can also be found within the following publication.

FULL REFERENCE (attached in Section D.3):
Martin Kunth, Christopher Witte, and Leif Schröder. Continuous-wave saturation considerations for efficient xenon depolarization. *NMR in Biomedicine*, 28: 601-606, 2015; Kunth *et al.*[127].

AUTHOR CONTRIBUTIONS: M.K. designed research, performed research and analyzed data; M.K., C.W. and L.S. wrote the paper.

8 HIGH GAS TURNOVER HYPER-CEST MRI

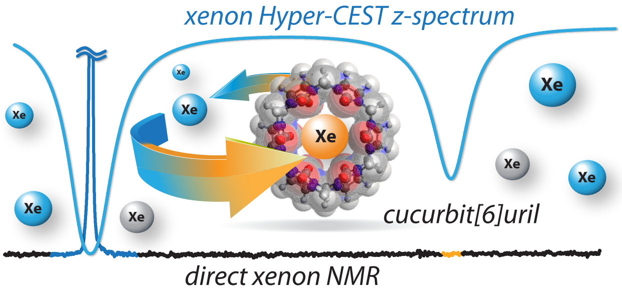

The work described in this chapter was done in collaboration with Dr. Andreas Hennig from the Jacobs University Bremen, Department of Life Sciences and Chemistry, Germany and is partly published. It investigates the CrA-alternative Xe-host **cucurbit[6]uril** (CB6) with the aim of sensitivity improvement. As CB6 is poorly soluble in water, direct ^{129}Xe NMR was too insensitive to study Xe binding to CB6 in pure water up to now. We quantified the Xe exchange kinetics in pure water at unprecedented sensitivity with qHyper-CEST (see Chapter 6) and found that the Xe gas turnover rate for CB6 is 100-fold increased compared to CrA. This turns CB6 into a novel very powerful ^{129}Xe MRI contrast agent.

Contents

8.1 INTRODUCTION

In the previous Chapter 7, we investigated how Hyper-CEST signal maximization can be achieved by the optimal choice of the cw saturation pulse strength and duration. This chapter now focuses on a Hyper-CEST signal amplification strategy that is implemented through the Xe-host itself. Motivated by the hypothesis in Chapter 6 and Chapter 7 that the Xe depolarization improves with higher exchange rate, we were systematically looking for

Xe-hosts which are similar in size to CrA but with a geometry enabling potentially faster Xe dissociation/re-association (*i.e.*, exchange rate). Despite of their excellent affinity for Xe, cryptophanes suffer from multi-step synthesis and separation of enantiomers. In addition, their Xe exchange rate in water is rather low. One could therefore investigate different Cr derivatives with potentially higher exchange rates (Table 1.3), but the synthesis remains challenging, time consuming and of low yield. Thus, we also sought commercially available macro molecules that still have decent Xe affinity but allow faster Xe exchange.

As one promising macrocyclic supramolecular family, we investigated two members of the **cucurbit[n]urils** (CBns) family with $n \in [5, 6, 7, 8, 10]$ [Lagona *et al.*[130]]. The name is derived from resemblance of this molecule with a pumpkin. Cucurbiturils are highly important in the fields of molecular self-assembly and nano-technology [Lagona *et al.*[130]]. Due to their nontoxicity [Uzunova *et al.*[217]], new biological applications with cucurbiturils are currently emerging, such as drug carriers, as molecular recognition units for insulin or β-amyloid fibers [Chinai *et al.*[54]], as well as pH-responsive supramolecular nanovalves [Angelos *et al.*[11]] or in fluorescence assays [Hennig *et al.*[96], Florea and Nau[72]]. The **packing coefficient** (PC) can be used as a general measure of non-covalent Xe affinity to a general Xe-host. The PC is the ratio of the guest volume V_{Xe} and the internal cavity volume that is provided by the host V_{cavity} ($PC = V_{Xe}/V_{cavity}$). Based on van der Waals interaction and London dispersion calculations, strongest binding is expected when the PC is 55 % (*i.e.*, 0.55) [Mecozzi and Rebek[150]]. For cucurbiturils, the smallest reported homologue of the CBn family with 5 repetitions of the glycolurils, CB5, has an empty cavity volume of 41 Å^3 [Lee *et al.*[131]] (assuming cylinder volume with a height of 9.1 Å).[1] Therefore, CB5 has a theoretical PC of 1.2, presumably causing some induced fit to accommodate the guest atom at all. While its Xe binding constant is comparable to that of CrA in water, the Xe exchange rate is only less than three times per day (*i.e.*, $k_{BA} = 2.4\ d^{-1}$) [Huber *et al.*[106]]. While the Xe chemical shifts for cucurbiturils appear promising, its exchange rates were considered to be slow:

> *"For the biosensing application, an interesting property*
> *of [. . .] [the cucurbituril] family of molecules [. . .] resides in*
> *the slow exchange [. . .], as well as the chemical shift for bound xenon,*
> *being very different [. . .] from that of xenon*
> *encapsulated in cryptophanes [. . .]."*
>
> — Berthault *et al.*[21] – 2009

According to our hypothesis which is *"Improving the Hyper-CEST depolarization with larger exchange rates"*, CB6 should be a more suitable candidate (Figure 8.1).

Indeed, nearly 15 years ago, CB6 has been reported in literature to bind Xe in aqueous solution [Haouaj *et al.*[91], Haouaj *et al.*[90]]. It has a inner cavity volume of 109 Å^3 and therefore a more favorable PC of 0.387 (Figure 8.1). For potential usage of CB6 as a biosensor, a proper Xe exchange kinetics and binding affinity quantification is mandatory. However, in contrast to

---

[1] The word glycoluril (with chemical structure: $C_4H_2N_4O_2$) is made up of *"glyco"*, which comes from the organic compound glyoxal, and *"uril"* which originates from the two cyclic urea groups joined across the same two-carbon chain.

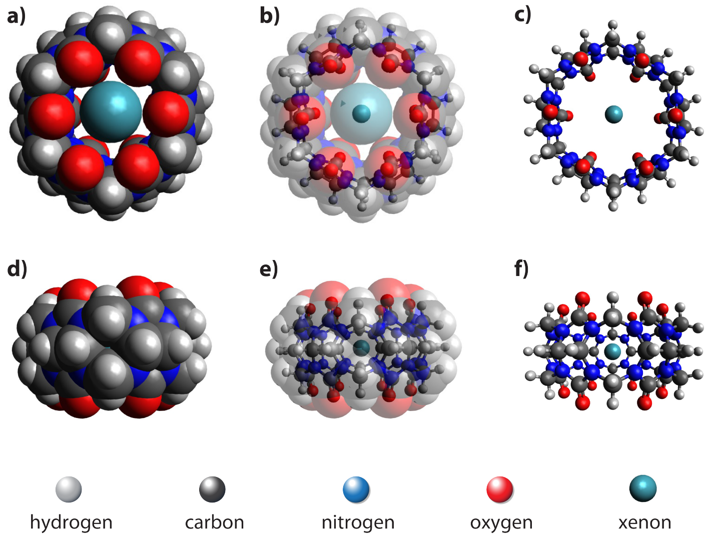

Figure 8.1: Cucurbit[6]uril (CB6; $C_{36}H_{36}N_{24}O_{12}$) and Xe modeling. a) Xe encapsulation by CB6 in the van der Waals radius representation from the top view of the molecule. b) transparent overlay of the van der Waals radius representation shown in a) with the ball-and-stick model that is solely shown in c). d-f) displays the side view representation of a-c), respectively. Molecular modeling was performed using the open-source molecular builder and visualization tool, Avogadro – Version 1.1.1 [Hanwell *et al.*[89]] (`http://avogadro.openmolecules.net`).

CB5 and CB7, the water solubility of CB6 (and also CB8) is very poor (< 18 μM) [Buschmann *et al.*[37], Lee *et al.*[131]]:

> *"One of the potential limitations of the [cucurbit[n]uril (CB[n])] family is their relatively poor solubility in water: CB[6] and CB[8] are essentially insoluble, whereas CB[5] and CB[7] possess modest solubility in water [...]."*
>
> — Lagona *et al.*[130] – 2005

Thus, bound Xe signal detection with common techniques is difficult. It is known from literature that salts, *e.g.*, sodium sulfate (Na_2SO_4), increase the solubility of CB6 in water [Haouaj *et al.*[91], Haouaj *et al.*[90]]. However, the Xe exchange kinetics of CB6 in salty water cannot be inter-/extrapolated to CB6 in pure water since the quantification is inferred by competitive binding of cations to the carbonyl groups at the portals of CB6. An active field of research is the investigation of further CB6 derivatives to increase water solubility [Lewin *et al.*[133], El-Barghouthi *et al.*[15]]. Benzene rings on the outside of CB6 overcome this low water solubility (so called water-soluble CB6 derivate, CB6*) [Zhao *et al.*[251], Kim *et al.*[114]], but it is commercially unavailable. Importantly, a high Xe exchange rate for this CB6* in pure water has been reported (k_{BA} = 2,300 s^{-1} using 2D direct ^{129}Xe NMR EXSY at a CB6 concentration of about 2.5 mM [Kim *et al.*[114]]) that is about 70-fold (*i.e.*, 2,300/33 = 69.7) faster than that of CrA. How these benzene rings influence the Xe exchange kinetics is unknown. So far and to the best of our knowledge, no Xe exchange kinetics quantification by NMR of unmodified CB6 in pure water exists due to poor CB6-bound Xe NMR signal.

Here, we investigate binding of Xe to CB6 under previously inaccessible conditions and binding to CrA in water as two different model systems, and compare it with the previously quantified Xe exchange kinetics of CrA in

DMSO. The Xe complexation with CB6 is extremely difficult to access by conventional NMR due to its low water solubility. We successfully quantified the exchange kinetics of this system and found that the absence of Xe signals related to encapsulated Xe in conventional HP ^{129}Xe NMR is due to line broadening and not due to low binding. By introducing for the first time a measure for the gas turnover during constant association-dissociation, we demonstrate that the signal amplification from a dilute pool of CB6 can turn this host into a very powerful contrast agent for Xe MRI applications. However, labile systems only provide improved signal amplification for suitable saturation conditions and otherwise become disadvantageous. The method is applicable to many hosts where Xe is a suitable spy nucleus to probe for non-covalent interactions and should foster reinvestigation of several systems to delineate true absence of interaction from labile complex formation. By contrasting these three different Xe-host systems, we further developed the idea of the Xe exchange kinetics fingerprint. To this end, we investigate further sensitivity amplification strategies. This includes the influence of the external static magnetic field B_0 on the Hyper-CEST effect, and the design of an optimal cw saturation for Hyper-CEST detection of highly diluted CB6 (*i. e.*, 680 pM) in water. Finally, we discuss other alternative Xe-hosts and their possibilities.

8.2 RESULTS AND DISCUSSION

We first quantify the Xe exchange kinetics to CrA in water to have a further external verification of the qHyper-CEST method. We then apply this to the unknown Xe exchange kinetics of unmodified CB6 in pure water. The methodology and experimental details to obtain these results are given in full detail in the original publication [Kunth *et al.*[126]].

8.2.1 Xenon Exchange Kinetics for CrA in Water

Whereas we designed and developed the qHyper-CEST technology on CrA in the organic solvent DMSO (see Chapter 6; [Kunth *et al.*[129]]), the numbers could not be put into relation to previous studies, as it was previously unquantified. We, therefore, apply quantitative saturation transfer to this system in water such that comparison to previous studies are possible. This provides a reference for the subsequently studied more labile system and illustrates the consequences in saturation transfer performance under different RF exposures.

The Xe binding constant to the prominent synthetic Xe host CrA has been measured using ITC [Hill *et al.*[99]] and the kinetics has been studied by direct detection of the caged Xe in a different organic solvent [Berthault *et al.*[21], Bartik *et al.*[17]] and in water [Spence *et al.*[199], Korchak *et al.*[118]]. Again, before qHyper-CEST multiple different methods were required to obtain these results (compare with Chapter 6). The direct ^{129}Xe NMR spectrum for [CrA] = 11 μM showed a sharp and distinct CrA-bound Xe signal (see Figure 8.2a). The corresponding Xe exchange kinetics were quantified with the qHyper-CEST analysis (*z*-spectra shown in Figure 8.2b) and can be found in Table 8.1. The determined exchange rate k_{BA} of (38 ± 6) s^{-1} is in

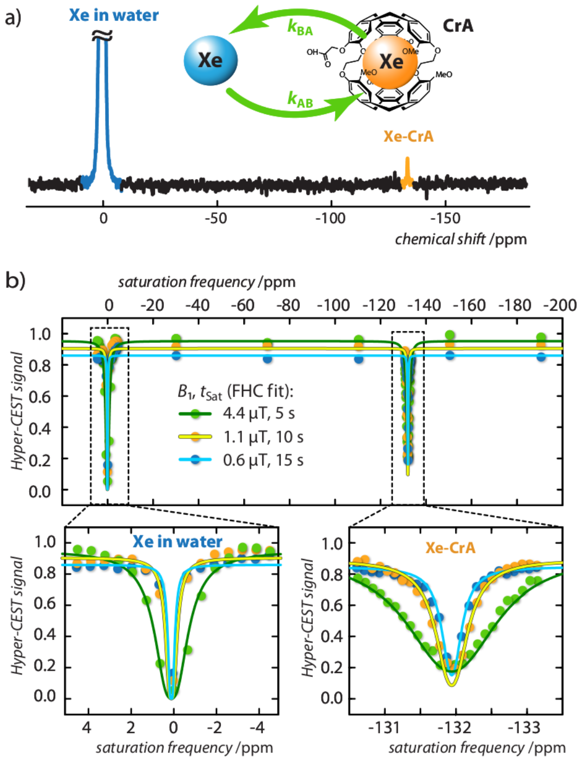

Figure 8.2: Direct and indirect (Hyper-CEST) ^{129}Xe NMR measurements for [CrA] = 11 µM dissolved in pure water at room temperature, T = 295 K. a) ^{129}Xe NMR spectrum with 64 averages. The Xe-CrA resonance appears at δ_B = -132 ppm. b) Hyper-CEST *z*-spectra (dots) for cw saturation of B_1/t_{sat} = {4.4/5 (green), 1.1/10 (orange), 0.6/15 (blue)} µT/s including global fitting curves of the FHC solution (solid lines). The Xe exchange kinetics obtained from the fitting results are listed in Table 8.1 and confirmed the host occupancy of 29 %.

excellent agreement with previous studies [Spence *et al.*[199], Korchak *et al.*[118]]. As such, the Xe-CrA complexation in water is well within the slow exchange regime ($k_{BA}/\Delta\omega = 0.0024 \ll 1$). The results of the other exchange parameters are listed in Table 8.1. This proves the validity of our qHyper-CEST method. Having verified our saturation transfer quantification concept for another system, we now explore the unknown Xe exchange kinetics of unmodified CB6 in pure water.

8.2.2 Xenon Exchange Kinetics for CB6 in Water

In contrast to CB5, one single Xe atom fits geometrically sufficiently lose into the cavity of CB6 (compare van der Waals radius and ball-and-stick molecular modeling of CB6 in Figure 8.1).[2]

The smaller PC of 0.387 is more favorable for labile binding than CB5 or CrA and not too small for too fast exchange. In addition, CB6 should be more rigid and stable than CrA as no imploded, saddle or crown confirmations of CB6 have been reported so far [Mough *et al.*[156], Huber *et al.*[105], Taratula *et al.*[207], Haberhauer *et al.*[86]].

---

[2] The molecular modeling of CB6 was done using the open-source molecular builder and visualization tool, Avogadro – Version 1.1.1 [Hanwell *et al.*[89]] (`http://avogadro.openmolecules.net`).

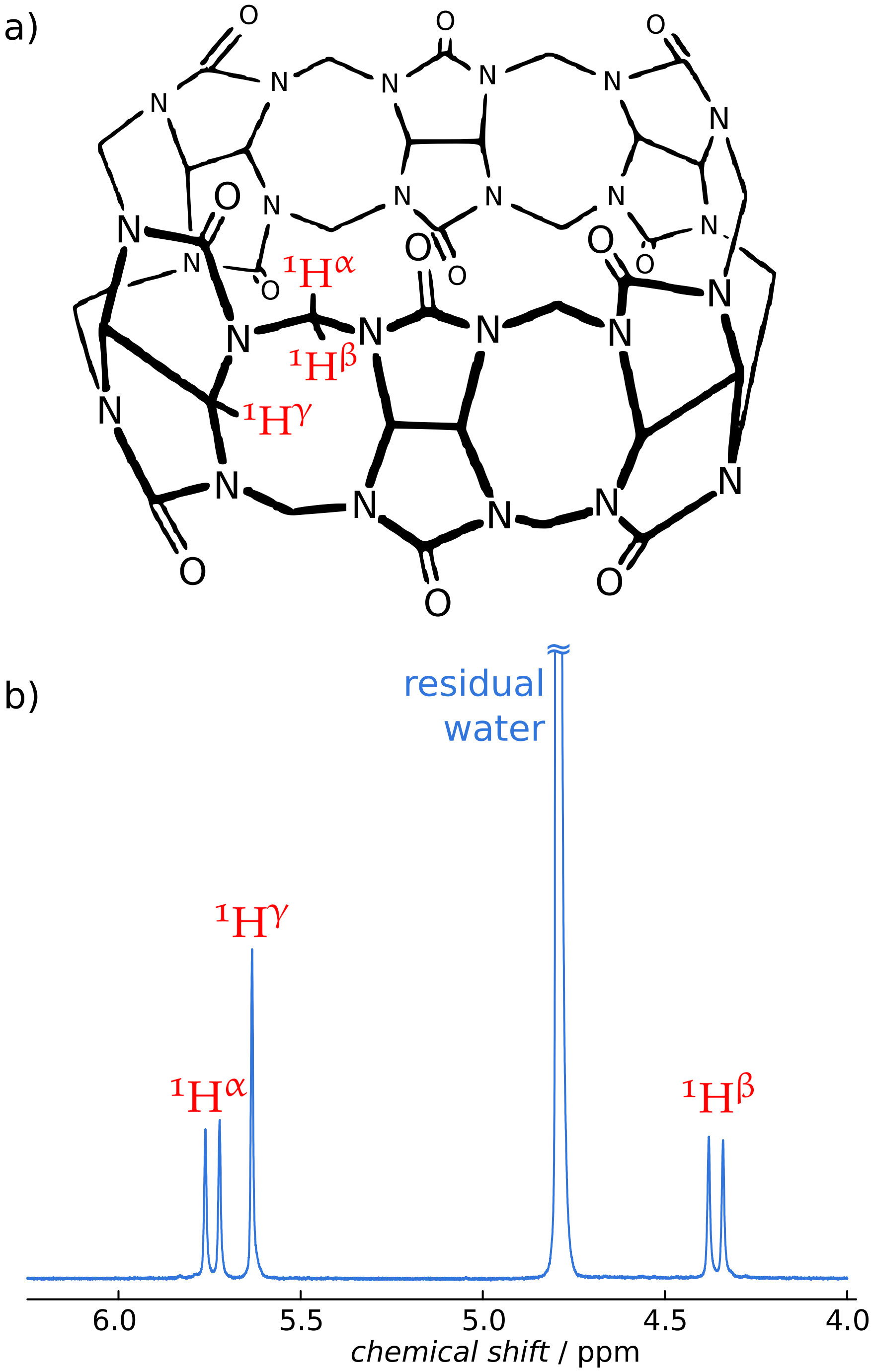

Figure 8.3: a) ^1H labeling within the CB6 molecule (adapted from Haouaj *et al.*[91]). b) The direct ^1H-NMR spectrum of a saturated CB6 solution in 0.2 M Na_2SO_4 in D_2O (temperature T = 295 K) was similar to that in other literature [Haouaj *et al.*[91]], and showed signals from intact CB6 molecules of the commercially available sample. Whereas the dominant resonance at 4.793 ppm corresponds to residual ^1H water signal, the five sharp resonances at 5.761 ppm, 5.722 ppm, 5.633 ppm, 4.380 ppm and 4.340 ppm belong to the $^1H^\alpha$ (doublet), two $^1H^\gamma$ (singlet), and $^1H^\beta$ (doublet), respectively.

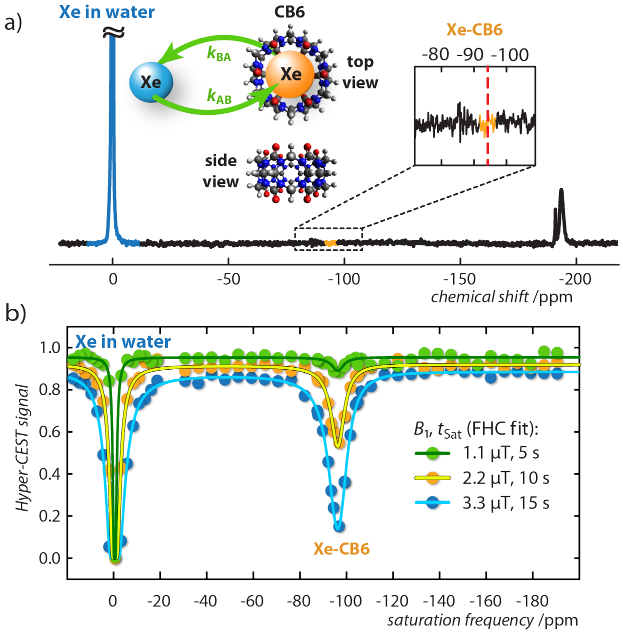

Figure 8.4: Direct and indirect (Hyper-CEST) ^{129}Xe NMR measurements for CB6 (substance provided by Dr. Andreas Hennig) at a concentration of 3.4 µM dissolved in pure water. a) ^{129}Xe NMR spectrum with 64 averages at $T = 295$ K. Retrospectively, the Xe-CB6 bound resonance is expected to appear at *ca.* $\delta_B = -96$ ppm (red dashed line). The insert shows the CB6 structure as top and side view including the Xe exchange $k_{AB,BA}$. b) Hyper-CEST *z*-spectra (dots) for cw saturation of $B_1/t_{sat} = 1.1/5$ (green), $2.2/10$ (orange), $3.3/15$ (blue) µT/s including fitting curves of the full Hyper-CEST (FHC) solution (solid lines); host occupancy of 49 %; results are listed in Table 8.1. Note that we observed 10 % blocking of the CB6 portals by unknown impurities of the commercially available sample (thus a host occupancy of only 5 %; see S6 in the Supporting Information of Kunth *et al.*[126] which is attached in Appendix Section D.4). Reprinted with permission from Kunth *et al.*[126]. Published by The Royal Society of Chemistry.

We first validated the purity of our CB6 sample by direct ^{1}H-NMR (compare Figure 8.3). Similar to literature [Haouaj *et al.*[91], Haouaj *et al.*[90]], we added 0.2 M of Na_2SO_4 at neutral pH in D_2O solution to solubilize a sufficiently high amount of pure CB6 ([CB6] $\leqslant$ 20 mM). The direct ^{1}H-NMR spectrum showed a similar peak signature ($^1H^{\alpha}$ (doublet) at 5.761 ppm and 5.722 ppm, two $^1H^{\gamma}$ (singlet) at 5.633 ppm, and $^1H^{\beta}$ (doublet) at 4.380 ppm and 4.340 ppm, respectively; the dominant peak at 4.793 ppm belonged to the free residual water molecules). We therefore concluded that our sample exhibited intact CB6 molecules without noticeable impurities.

We then examined the Xe interaction with CB6 by ^{129}Xe NMR. As mentioned in this chapter's introduction and known from literature, CB6 has a poor water solubility (< 18 µM; [Buschmann *et al.*[37], Lee *et al.*[131]]) and did therefore show no Xe signal that was associated with CB6. To exemplify, we recorded a direct ^{129}Xe NMR spectrum of CB6 (3.4 µM) with 64 signal averages in pure water, which, contrary to CrA at comparable concentration (Figure 8.2), showed no signal from the Xe-CB6 complex (Figure 8.4a). A first direct conclusion would be that Xe does not bind in detectable amounts to CB6 in water. Or if it binds, is it just low binding or even strong binding but with exchange broadening that causes the absence of the signal.

Table 8.1: Xe exchange kinetics fingerprint prototype (excluding the relaxation times) obtained with qHyper-CEST at room temperature. The fractional size of pool B f_B, the chemical shift difference $\Delta\delta$, the exchange rate of Xe exiting the host k_{BA}, the Xe host occupancy β, and the Xe binding constant K_A are listed for the following three Xe-host systems: CrA in DMSO, CrA in water and CB6. The Xe concentration free in solution [Xe] was calculated using the overpressure, and the Ostwald solubility coefficient Γ, as shown in the experimental section in Kunth *et al.*[126].

Solvent	[Xe] (μM)	Host	[host$_{tot}$] (μM)	f_B (10^{-4})	$\Delta\delta$ (ppm)	k_{BA} (s^{-1})	β (%)	K_A (M^{-1})
water	390	CB6	3.4	43 ± 1	-96.1 ± 0.1	2,100 ± 300	49	2,500 ± 400
water	390	CrA	11	70 ± 11	-132.06 ± 0.02	38 ± 6	29	850 ± 250
DMSO	2,340	CrA	50	18 ± 1	-166.37 ± 0.04	250 ± 130	9	38 ± 4

In contrast, Hyper-CEST z-spectra that were obtained from the same CB6 sample clearly revealed a distinct signature of the Xe-CB6 complex at - 95.6 ppm upfield from free Xe (Figure 8.4b). The varying cw saturation pulse conditions facilitated the corresponding qHyper-CEST analysis (Table 8.1). This clearly demonstrates that studying hosts at the low concentrations used here may be misleading with direct ^{129}Xe NMR and easily lead to the wrong assumption of no complexation. Both the exchange rate k_{BA} and association constant K_A obtained by the qHyper-CEST analysis are in good agreement with expectations based on literature results with a water-soluble CB6 derivative, which has been measured by conventional hyperpolarized ^{129}Xe NMR spectroscopy at 10^3-fold higher concentration [Haouaj *et al.*[91], Zhao *et al.*[251], Kim *et al.*[114]]. Most strikingly, only the qHyper-CEST analysis was able to reveal that CB6 has a higher occupancy (β = 50 %) than CrA (β = 29 %) under the given experimental conditions suggesting that Xe binding to CB6 is more efficient than to CrA in pure water where the portals are freely accessible. Moreover, the Xe-CB6 system enters the intermediate exchange regime on the NMR time scale ($k_{BA}/\Delta\omega = 0.2 < 1$; the corresponding value for CrA in water is 100-fold lower and in the slow regime), which should additionally contribute to a higher Hyper-CEST signal compared to CrA. As a consequence, the signal of bound Xe in the direct ^{129}Xe NMR spectrum is most likely only below the noise level because of extreme line broadening and not because of insufficient binding (for more details see S3 in the Supporting Information in Kunth *et al.*[126] which is attached in Appendix Section D.4).

8.2.3 Xenon Exchange Kinetics Fingerprint

Adding now the previously quantified CrA in DMSO into the discussion ([Kunth *et al.*[129], Kunth *et al.*[127]]), and comparing the Xe exchange kinetics of all the three different Xe-host systems – CrA in DMSO, CrA in water and CB6 in water – with each other (Table 8.1) showed large deviations within the parameters between these different systems. Remarkably, the identical Xe-host CrA within two different solvents, DMSO and H_2O, showed entirely different exchange kinetics for a given temperature. This behavior strongly supports the idea of a characteristic Xe-host specific exchange kinetics fingerprint that each system owns. This extends the Xe biosensor classification capability far beyond the chemical shift dimension as used so far. One could model such a fingerprint using an n-tuple where the entries consist of all exchange kinetic parameters of the particular Xe-host system. A prototype for a 2-spin pool system fingerprint could look as in the following:

Unique Xe-host system exchange kinetics fingerprint:

$$\langle T_1^A \,|\, T_2^A \,|\, \Delta\delta \,|\, k_{BA} \,|\, \beta \,|\, K_A \,|\, T \,|\, \Gamma \rangle.$$

Such an exchange kinetics fingerprint could potentially be able to easily sense complex scenarios. For example,

1. the solvent (or chemical environment) in which the Xe-host is in.[3]
2. if the Xe-host is blocked.[4]
3. the surrounding temperature the Xe-host is in.[5]

Just mentioning only three possible applications.

The question remains which of the fingerprint parameters $\langle T_1^A \,|\, T_2^A \,|\, \Delta\delta \,|\, k_{BA} \,|\, \beta \,|\, K_A \,|\, T \,|\, \Gamma \rangle$ gives information about Hyper-CEST effect amplification at a given host concentration? Thus, which parameter is a measure about the Hyper-CEST effect amplification possibilities of a particular Xe-host system?

Intuitively, the saturation transfer increases by both a large number of Xe atoms continuously moving through the host during the saturation period (*i. e.*, a high Xe exchange rate k_{BA}) and a large amount of Xe atoms that bind in chemical equilibrium to the hosts (*i. e.*, a high Xe association constant K_A). Unfortunately, an increase in one parameter is often associated with a decrease in the other and, as a consequence, makes the sensitivity improvement insignificant. Consider for example the Xe exchange kinetics for CrA in the two solvents H_2O and DMSO (Table 8.1). While the Xe exchange rate can be improved by more than 6-fold when switching from H_2O to DMSO, the binding constant, in contrast, decreases by a factor of 22. Thus, the Xe exchange rate of CrA improves at the cost of the binding constant. Which system has superior ^{129}Xe depolarization, thus, Hyper-CEST sensitivity? This question becomes even more complex considering that in DMSO, 6 times more free Xe atoms are in solution (Table 8.1) and the manipulation of this large signal *via* saturation transfer requires more nuclei to be involved. Surprisingly, we found that CB6 in pure water has both a superior Xe exchange rate of k_{BA} = 2,100 s^{-1}, and a superior Xe binding constant K_A = 2,500 M^{-1} of all three systems. The question remains how to compare these Xe-host systems with each other.

---

[3] At a specific temperature T, all tuple entries change, when only the solvent changes (compare Xe-CrA exchange kinetics in H_2O and DMSO in Table 8.1). Potentially, this fingerprint could be useful in exploiting Xe-CrA biomembrane interactions [Meldrum *et al.*[153], Sloniec *et al.*[196], Schnurr *et al.*[181] Schnurr *et al.*[182], Schnurr *et al.*[180]] when the tuple is extended to the corresponding number of CEST pools. Further, structural probing of, *e. g.*, bacterial spores [Bai *et al.*[14]] could be described in even more detail.

[4] We observed in water a blocking of the freely accessible CB6 portals of about 10 % by impurities (compare Figure 8.4 and Table 8.1 with Table II provided in S6 in the Supporting Information of Kunth *et al.*[126] which is attached in Appendix Section D.4. Here, all tuple members remained constant, except for the fraction of CB6-bound Xe f_B and the host occupancy β (and therefore the binding constant K_A and the gas turnover rate as the product of $\beta \cdot k_{BA}$).

[5] With a change in temperature T, the chemical shift $\Delta\delta$ and the exchange rate k_{BA} should change, while the other parameters of the fingerprint should (mainly) remain constant (for example monitored for ^{1}H-CEST by Döpfert *et al.*[62]).

8.2.4 Gas Turnover Rate and Labeling Efficiency

A classification of labeling efficiency should first allow the objective comparison of these systems in terms of their Hyper-CEST performance, and second specifically classify novel Xe-host systems with highly optimized properties for Hyper-CEST detection.

Initially, the first approach was to consider the ^{129}Xe depolarization rate λ_{depol} (Equation (6 | 1)). However, contrary to our needs and according to the discussion above, λ_{depol} depends on the host concentration *via* the parameter of the fractional size of pool B f_B. As stated in the previous Section 8.2.3, we wanted to have the measure host concentration independent. We thus normalized λ_{depol} by [host] to

$$\lambda_{\text{depol}}(B_1, k_{BA})/[\text{host}] = \frac{f_B \cdot k_{BA}}{[\text{host}]} \cdot \frac{(\gamma B_1)^2}{(\gamma B_1)^2 + k_{BA}^2} \quad . \tag{8 | 1}$$

Using this measure, the maximum possible depolarization (*i. e.*, for infinite large B_1 [Kunth *et al.*[127]]) is $f_B \cdot k_{BA}/[\text{host}]$. By neglecting from Table 8.1 10^{-6} for μ and 10^{-4} from f_B, yields for each system the following numbers:

- CrA in DMSO: 90 $(\text{s}\cdot\text{M})^{-1}$,
- CrA in water: 240 $(\text{s}\cdot\text{M})^{-1}$, and
- CB6 in water: 26,560 $(\text{s}\cdot\text{M})^{-1}$.

As expected, CB6 in water is the superior system. Controversy and against intuitive expectations, CrA in DMSO appears to be the inferior Xe-host system, although it has about 10-fold increased exchange rate compared to CrA in water and 6 times more Xe atoms to depolarize during the saturation period (see the Xe concentration [Xe] in Table 8.1). This would directly conclude that – assuming all Xe exchange kinetic parameters do not change – the less free [Xe] in solution is available, the more sensitive becomes the very same Xe-host system. This is not correct. While this is indeed the case for most Hyper-CEST effect calculations that are done experimentally, it is a not valid criterium for Xe-host system comparisons throughout different solvents.[6] Therefore, for comparing the *"true"* Hyper-CEST potential of the Xe-host system, also the concentration of free Xe in solution [Xe] must be taken into account.

By including [Xe] into the normalization for $f_B \cdot k_{BA}/[\text{host}]$, we found the following relationship

$$\lambda_{\text{depol}}(B_1, k_{BA}) \cdot \frac{[\text{Xe}]}{[\text{host}]} = \beta \cdot k_{BA} \cdot \underbrace{\frac{(\gamma B_1)^2}{(\gamma B_1)^2 + k_{BA}^2}}_{\text{labeling efficiency, } \alpha} \quad , \tag{8 | 2}$$

---

[6] Consider the following two systems with identical concentration of CrA but one is in cell environment and the other in water. A further assumption is that this environment only changes the free Xe concentration in solution, but not the relaxation times, the exchange rate, binding constant, chemical shifts and host occupancy for both systems. For identical cw saturation pulses, both systems will generate different Hyper-CEST effects although they have the same CrA concentration [CrA], and identical exchange kinetics. The larger *"calculated"* Hyper-CEST effect is where less free Xe concentration is present that is used for the off-resonant reference image, *i. e.*, for the cell environment. This becomes apparent when the free Xe concentration in water is – assuming – twice as large as the Xe concentration in cells. Then, this smaller free Xe in solution signal is manipulated two times faster *via* saturation transfer than the twice larger free Xe concentration in water. Therefore, Hyper-CEST effects calculated for solvents or molecular environments that barely contain free Xe always appear much larger, when compared to the actual host concentration [host] that was present [*e. g.*, Klippel *et al.*[117], Rose *et al.*[170], Witte *et al.*[232]].

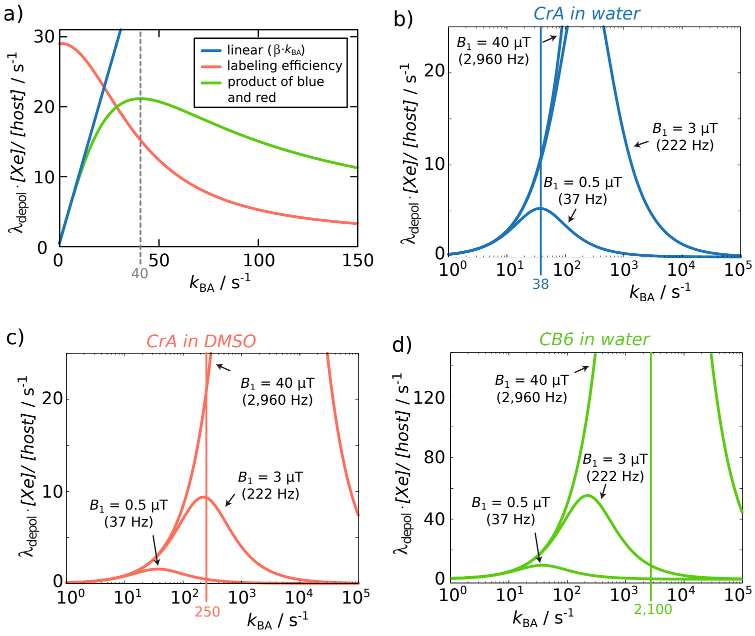

Figure 8.5: Xe depolarization per host molecule with respect to the exchange rate. a) Composition of Equation (8 | 2) (with $\beta = 1$) of each of the curves that are shown in b-d). Note that in a) k_{BA} is linear scaled at the x-axis, whereas in b-d) base 10 logarithmic. a) The blue curve shows the linear exchange rate contribution ($f(k_{BA}) = k_{BA}$). The red curve shows the labeling efficiency (with an amplitude of 28 s^{-1} for better illustration and a FWHM of $k_{BA,FWHM} = \gamma \cdot B_1 = 40$ s^{-1}): $f(k_{BA}) = (40\ \text{s}^{-1})^2/((40\ \text{s}^{-1})^2 + k_{BA}{}^2) \cdot 28\ \text{s}^{-1}$. Thus, the saturation pulse labeling is most effective for an exchange rate of $k_{BA} = 0$ s^{-1}. However, the entire Equation (8 | 2) produces a shift of the maximum according to $f(k_{BA}) = k_{BA} \cdot (40\ \text{s}^{-1})^2/((40\ \text{s}^{-1})^2 + k_{BA}{}^2) \cdot 28\ \text{s}^{-1}$ (green curve) to $\gamma \cdot B_1 = 40$ s^{-1}. This green curve is always shown in b-d) for $B_1 = \{0.5, 3, 40\}$ µT for the systems: CrA in water (b; blue; $k_{BA} = 38$ s^{-1}), CrA in DMSO (c; red; $k_{BA} = 250$ s^{-1}) and CB6 in water (d; green; $k_{BA} = 2{,}100$ s^{-1}). These B_1 values roughly correspond to the Xe exchange rates of the three systems and were purposefully chosen. The most effective pulse coupling into the system occurs at its corresponding frequency (*i.e.*, $B_1 = k_{BA}/\gamma$). b) CrA in water has a Xe exchange rate of 38 s^{-1} (Table 8.1). Saturation pulses that are B_1 on-resonant with the exchange rate (*i.e.*, $B_1 = k_{BA}/\gamma \sim 0.5$ µT) have most efficient coupling, while depolarizing/labeling half of the maximal possible bound Xe atoms (see curve intersection with vertical blue line; compare also with Chapter 7). In contrast, the Xe depolarization for 3 µT (6 times the exchange rate), which is similar as for 40 µT (80 times the exchange rate), reaches its intrinsic maximum. c) CrA in DMSO has a Xe exchange rate of 250 s^{-1} (Table 8.1). Whereas (relative to this system intrinsic exchange rate) weak pulses with $B_1 = 0.5$ µT barely depolarize bound Xe atoms (compare intersection with vertical line), B_1 on-resonant pulses (*i.e.*, $B_1 = k_{BA}/\gamma \sim 3$ µT) depolarize 50 %, and strong pulses ($B_1 = 40$ µT; ~ 12 times the exchange rate) up to 100 % of all bound Xe atoms. d) CB6 in water has a Xe exchange rate of 2,100 s^{-1} (Table 8.1). In addition, the y-axis is more than 5 times increased due to both a higher exchange rate and a higher host occupancy, in contrast to b) and c). Therefore, already weak pulses of 3 µT depolarize a similar amount of bound Xe as for b) and c), although it is 13 times less than the B_1 on-resonant condition ($B_1 = k_{BA}/\gamma \sim 28$ µT) for maximal energy transfer that leaves large room for improvement. A less complex representation of b-d) is shown in the next Figure 8.6.

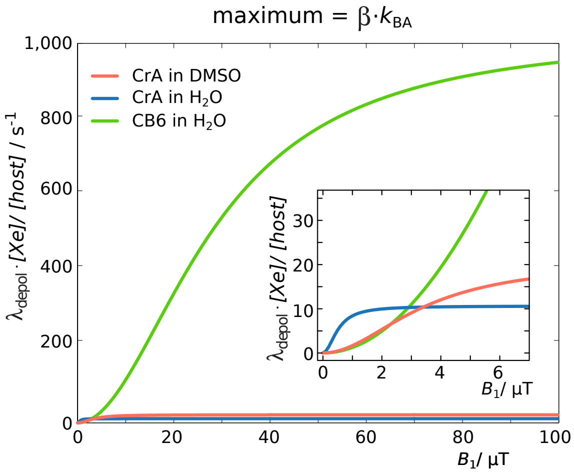

Figure 8.6: Hyper-CEST labeling efficiency α with respect to the saturation pulse strength B_1 and gas turnover rate $\beta \cdot k_{BA}$. The systems are CrA in DMSO (red), CrA in water (blue), and CB6 in water (green; Table 8.1; Kunth *et al.*[126]). The CB6 in water system is 100 times more efficient than CrA in water. This plot is a more intuitive representation of Figure 8.5b-d.

which now represents a fair comparison of the Xe-host systems throughout the surrounding chemical environment these systems are in. Again, the maximum (*i. e.*, for infinite large B_1 [Kunth *et al.*[127]]) is now given by a product that we termed the **gas turnover rate** ($\beta \cdot k_{BA}$). Here, the host occupancy β can be related to the binding constant as $K_A = [Xe]^{-1} \cdot \{\beta/(1-\beta)\}$ [Kunth *et al.*[129]]. As expected, the gas turnover rate of CrA in DMSO is more efficient than in H_2O, as it has more free Xe to depolarize (Table 8.2). Moreover, CB6 in H_2O stays the most sensitive Xe-host system and is 100 times more efficient than CrA in H_2O. Hence, CB6 has the potential to be a much better Hyper-CEST contrast agent. Yet the question remains, if CB6 has superior Hyper-CEST performance under all saturation conditions?

To address this question, we consider Equation (8.2) in more detail and analyze the energy coupling of a particular saturation pulse with strength B_1 to the Xe-host system that has a specific exchange rate k_{BA}. We separate this transfer into two contributions of the exchange rate k_{BA}:

1. the linear contribution originating from the gas turnover rate $\beta \cdot k_{BA}$ (blue line in Figure 8.5a), and
2. the labeling efficiency α (similar to a Lorentzian line) that is centered at $k_{BA} = 0\ s^{-1}$ with a **full width at half-maximum** (FWHM) of $k_{BA,FWHM} = \gamma \cdot B_1$ (see Figure 8.5a; red curve: $\gamma \cdot B_1 = 40\ s^{-1}$).

The net effect (*i. e.*, Equation (8.2) with β = 1) is given by the product (Figure 8.5a; green curve). In total, we have an exchange rate driven linear shifted saturation pulse strength sensitivity of the Xe-host system. It demonstrates that if a Xe-host system wants to benefit from larger saturation pulse strength then it requires large exchange rates accordingly (Figure 8.5). Using a base 10 logarithmic scale, Figure 8.5b-d shows that the Xe depolarization with respect to the Xe exchange rate k_{BA} (vertical line in Figure 8.5b-d) for three pulse strengths B_1 can be seen as a spectral line. The maximum of each spectral line shifts to its own B_1 value that is expressed in s^{-1} (*i. e.*, $B_1 = k_{BA}/\gamma$). At these B_1 values the transfer is most efficient. Therefore, these B1 values in Figure 8.5b-d were chosen on purpose to match the Xe exchange rates of the three Xe-host systems. Further increase of B_1 further depolarizes Xe, while the spectral line further shifts away from the system intrinsic exchange rate k_{BA}. Then, the Xe depolarization has reached its maximum value – the gas turnover rate $\beta \cdot k_{BA}$. Further increase of B_1 does not improve the Xe depolarization. This demonstrates the large potential of CB6 in H_2O (Figure 8.5d) over CrA in H_2O (Figure 8.5b) and CrA in DMSO (Figure 8.5c).

More intuitively, we inspected Equation (8.2) by variation of B_1 for the three Xe-host systems CB6 in H_2O (Figure 8.6; green curve), CrA in H_2O (blue curve) and CrA in DMSO (red curve). It shows the superior gas turnover rate of CB6. It also shows that the most efficient pulses with $B_1 = k_{BA}/\gamma$ correspond to the point of inflection of the labeling efficiency α and label 50 % of the maximum gas turnover rate. Similar as already discussed in Chapter 7, if $B_1 \approx 5 \cdot k_{BA}/\gamma$, then 96 % of the maximum possible Xe atoms are labeled [Kunth *et al.*[127]], which is very close to gas turnover rate $\beta \cdot k_{BA}$ for infinitely strong pulses $B_1 \rightarrow \infty$ µT. In Figure 8.5b-d, each crossing point between the spectral line of a saturation pulse strength and the Xe exchange rate of the particular Xe-host system (vertical line) corresponds in Figure 8.6 to one value of the labeling efficiency curves.

In the following, we describe the related consequences for ^{129}Xe MR imaging.

8.2.5 Signal Amplification Strategies

If Xe-hosts differ in their Xe exchange rates, then care has to be taken considering which saturation parameters and which Xe host were used for correct interpretation of Hyper-CEST contrast. Only saturation pulses that are strong enough to cancel the Xe net magnetization during the rather short residence time within CB6 will fully take advantage of its signal amplification potential. Having said that, this aspect at the same time has consequences for the image contrast similar to the film speed in optical detection but with a somewhat inverse behavior: efficient amplification build-up at high RF *"exposure"* comes along with poor sensitivity at low exposure (for 1:1 Xe-host complexation and occupancy of $\leqslant$ 100 %). To illustrate this, we compare the gas turnover of two dilute host structures side by side in an inhomogeneous setup. Two solutions were prepared and studied under different exposure conditions: one of CB6 and the other CrA (both at identical concentrations of [CB6] = [CrA] = 12.9 µM). These solutions were placed into separate, concentric compartments, CrA in the inner compartment and CB6 in the outer compartment (Figure 8.7a) and studied by MRI. As can be seen in the Hyper-CEST *z*-spectra in Figure 8.7b, when increasing the saturation pulse strength from 5.5 µT to 33.3 µT (both with 2 s saturation duration) there is almost no change in the CrA Hyper-CEST effect (Figure 8.7c). Due to its slower exchange rate (Table 8.1) CrA has reached its intrinsic depolarization maximum (*i.e.*, 60 % Hyper-CEST effect). In contrast, CB6 showed with its faster exchange rate a significant amplification in the Hyper-CEST effect as the saturation strength is increased, namely from < 30 % to ~ 100 % (Figure 8.7d). Best comparison of the gas turnover and the related signal amplification is possible for high RF exposure. It should, however, be noted that CrA can still remain the host of choice, if saturation pulse strength is limited, *e.g.*, due to SAR concerns (see *z*-spectra in Figure 8.7b). Weak pulses are only capable of saturating Xe with longer residence times, as is the case for the slower exchange of the Xe-CrA system. In such cases, the

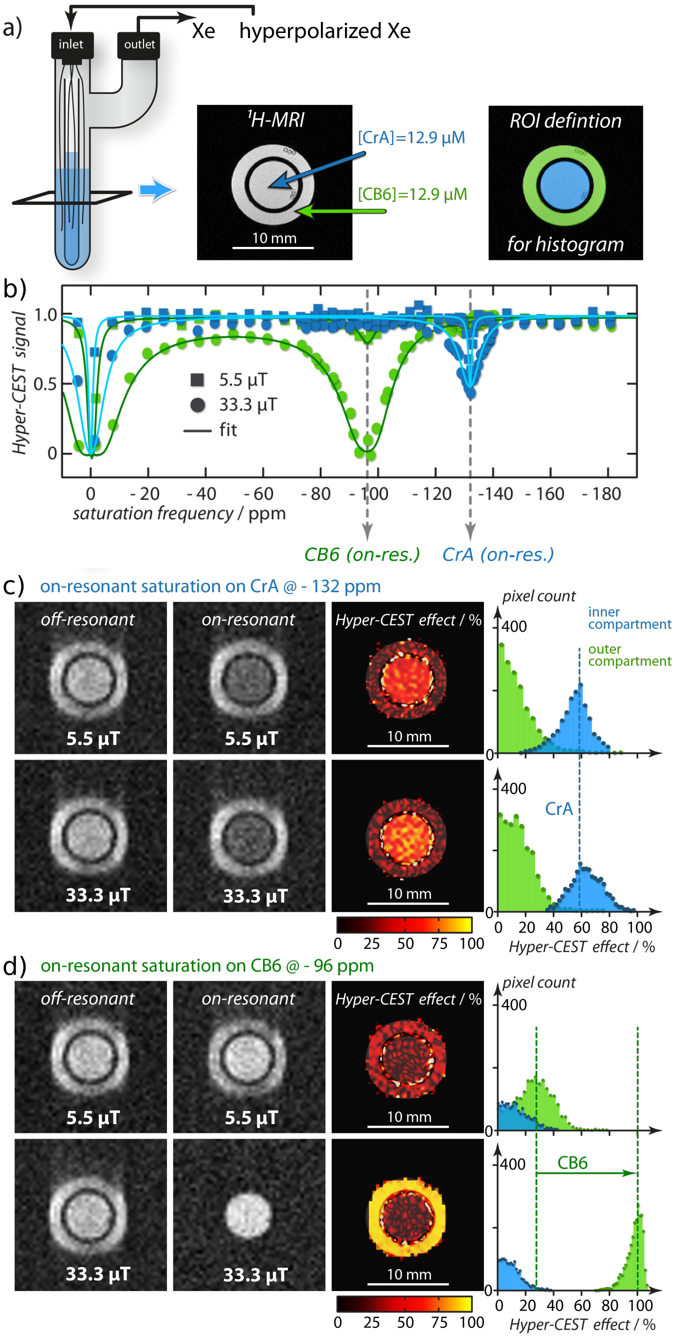

Figure 8.7: Signal amplification capabilities and multiplexing. a) shows the experimental setup of [CB6] = [CrA] = 12.9 µM in pure H_2O at T = 295 K and the ROI definition for histogram shown in c-d. b) The cw saturation pulse strength was either 5.5 µT ("low RF exposure") or 33.3 µT ("high RF exposure"), both for 2 s. The *z*-spectra were globally fitted with the FHC solution. Xe that is bound to CrA has a longer residence time (26 ms; *i. e.*, the inverse of the exchange rate of k_{BA} = 38 s^{-1}) than in CB6 (480 µs; *i. e.*, with a much faster exchange rate of k_{BA} = 2,100 s^{-1}). Thus, the full Xe gas turnover capability of CrA is already reached for low RF exposures and high RF exposure does not increase the Hyper-CEST effect anymore. In contrast, the Xe gas turnover of CB6 is highly increased. Therefore, low RF exposure poorly labels this fast exchange, whereas high RF exposure greatly depolarizes a large faction of bound Xe. c-d) ^{129}Xe MRI off- and on-resonant either on CrA-bound Xe (- 132 ppm) or CB6-bound Xe (- 96 ppm) for low and high RF exposure. The Hyper-CEST effect maps were further analyzed by a histogram (corresponding ROI definition illustrated in a). CB6 fully takes advantage of the high RF exposure and depolarizes up to 100 %. Note that for this experiment the Xe-CB6 occupancy β was about 5 %. Reprinted with permission from Kunth *et al.*[126]. Published by The Royal Society of Chemistry.

Table 8.2: Derived parameters from Xe exchange kinetics fingerprint (Table 8.1). The occupied host concentration $[\text{host}_{occ}] = \beta \cdot [\text{host}_{tot}]$ were chosen such that the systems are comparable. The other listed parameters are the gas turnover rate $\beta \cdot k_{BA}$, the average residence time for one Xe atom in the host $\tau_{BA} = 1/k_{BA}$, the average exchange rate for Xe to leave the free solution state $k_{AB} = f_B \cdot k_{BA}$, and the average residence time for Xe to stay free in solution $\tau_{AB} = 1/k_{AB}$.

Solvent	[Xe] (µM)	Host	$[\text{host}_{tot}]$ (µM)	$[\text{host}_{occ}]$ (µM)	$\beta \cdot k_{BA}$ (% s^{-1})	τ_{BA} (ms)	k_{AB} (s^{-1})	τ_{AB} (s)
water	390	CB6	3.4	1.7	1,029	0.48	9.03	0.111
water	390	CrA	11	3.2	11	26	0.27	3.76
DMSO	2,340	CrA	50	4.5	23	4	0.45	2.22

Hyper-CEST performance as a function of the saturation pulse strength B_1 should also be considered (Figure 8.6).

It should be noted here that the concept of different hosts allows for multiplexing *via* the saturation pulse strength rather than the chemical shift, as long as they are spatially separated (similar to the variation of the saturation time, which was reported by Schnurr *et al.*[182]). In particular, it should work even if the CAs resonate at the same frequency. To exemplify, we consider the following system: Two CA resonances are equal and overlap spectrally, but the exchange rate is different. Under low RF exposure, the system with the slow exchange rate responses according to their labeled gas turnover rate with large Hyper-CEST effect, while the other system with the larger exchange rate shows minor Hyper-CEST response. Under large RF exposure, the system with the slow exchange rate does not further gain Hyper-CEST effect, while the other system with the larger exchange rate shows superior Hyper-CEST contrast.

Further analysis of the Xe exchange kinetics fingerprint in Table 8.1 revealed, beside the gas turnover rate $\beta \cdot k_{BA}$, also the following Xe residence times for the three different systems (Table 8.2): the average residence time for one Xe atom to leave the host $\tau_{BA} = 1/k_{BA}$, the average exchange rate for Xe to leave the free solution state $k_{AB} = f_B \cdot k_{BA}$, the average residence time for one Xe atom to stay free in solution $\tau_{AB} = 1/k_{AB}$. The occupied host concentration $[\text{host}_{occ}]$ was purposefully chosen such that all these systems achieved about the same values. A remarkably interpretation of our data analysis is that Xe resides for 3.4 µM of CB6 for about 100 ms freely in water, whereas for about 4 s in the presence of about 4 times more CrA (11 µM; Table 8.2; both values depend on the host concentration). In addition, Xe resides for only about 500 µs in CB6 whereas for about 26 ms bound to CrA. This further illustrates the superior gas turnover rate of CB6 in comparison to CrA.

In summary, the gas turnover rate proves useful and is a very simple parameter to predict the Hyper-CEST performance of a particular Xe-host system.

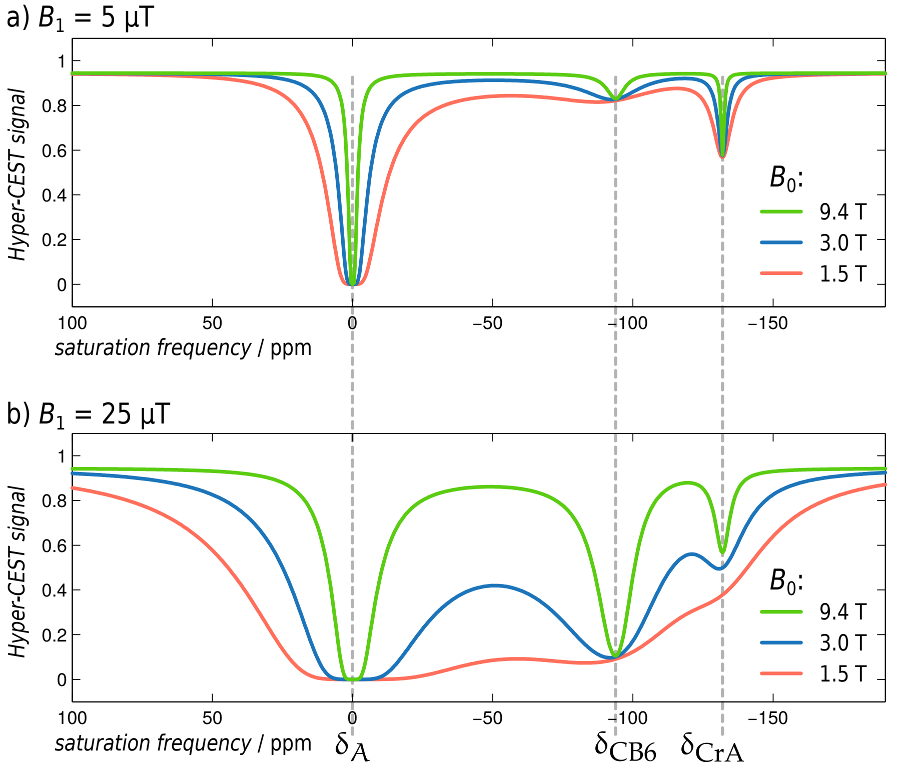

Figure 8.8: The static magnetic field B_0 improves spectral resolution in Hyper-CEST z-spectra, but not the Hyper-CEST effect. 3-Spin pool simulation using the FHC-$R_{1,eff}$ solution (Equation (3 | 16)) for cw saturation of a) B_1 = 5 µT, and b) B_1 = 25 µT for 5 s. As static magnetic field B_0 = {1.5 (red), 3 (blue), 9.4 (green)} T was used. The Xe-host systems were CB6 (12.9 µM) and CrA (12.9 µM) in water. This simulation assumed that both relaxation times of the dominant free Xe pool T_1^A and T_2^A, and the Xe exchange rate k_{BA} were not influenced by B_0. All simulation parameters are shown in Figure 3.7.

8.2.6 Further Signal Amplification Strategies

Static Magnetic Field Influence on z-Spectra

So far, we have not examined the impact of the external static magnetic field B_0 onto the Hyper-CEST effect sensitivity. The Larmor frequency of a nuclear spin that exchanges between two sites is proportional to the value of the static magnetic field of the NMR spectrometer ($\omega_0 = \gamma \cdot B_0$; Equation (2 | 18)) and the local magnetic fields of each site. Hence, the Larmor frequency ω_0 increases with B_0, while the exchange rate of the Xe-host system remains constant (and assuming for now negligible B_0 impact on both longitudinal and transverse relaxation times). However, the ppm scale (Equation (2 | 26) in Chapter 2) makes those Larmor frequency shifts independent of the B_0 strength.

We investigated the impact of the static magnetic field B_0 for a typical field strength of research NMR systems (B_0 = 9.4 T; green curves in Figure 8.8a,b) and two typical field strengths of clinical MRI machines (B_0 = 1.5 T; red curves and B_0 = 3.0 T; blue curves) by simulating Hyper-CEST z-spectra for CB6 and CrA in water (Table 8.1) using the FHC-$R_{1,eff}$ solution

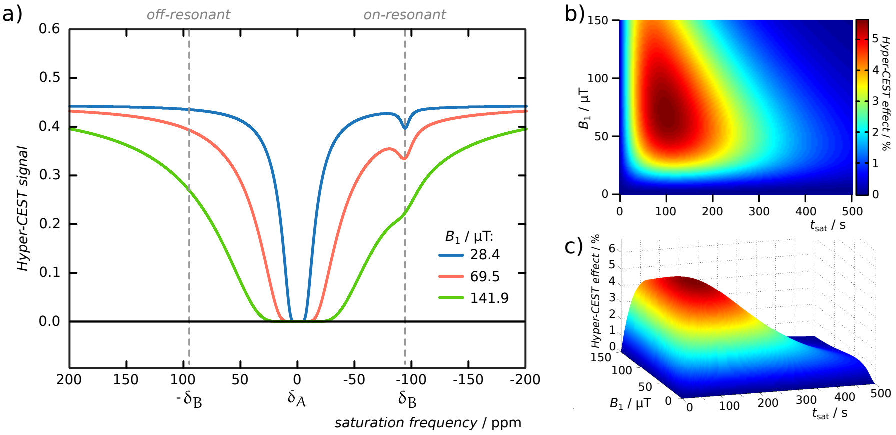

Figure 8.9: CW saturation pulse optimization for 680 pM of CB6 in water at room temperature. a) Simulated Hyper-CEST *z*-spectra with optimal cw saturation pulses of B_1 = {28.4 (analytical; corresponding to k_{BA}/γ), 69.5 (numerically found), 141.9 (analytical; corresponding to $5 \cdot k_{BA}/\gamma$)} µT for t_{sat} = 101 s and the Hyper-CEST surface plots as top view (b) and side view (c) obtained from the numerical approach (similar to Section 7.2.2). The numerically determined solution yielded 5.6 % as maximal achievable Hyper-CEST effect. The simulation parameters were for the pool of free Xe in solution (pool A): T_1^A = 125 s, T_2^A = 5 s, δ_A = 0 ppm, f_A = 1; CB6-bound Xe (pool B): T_1^B = 100 s, T_2^B = 3 s, δ_B = - 94 ppm, f_B = $8.6 \cdot 10^{-7}$, k_{BA} = 2,100 s^{-1} and $k_{AB} = k_{BA} \cdot f_B/f_A$ = 0.0018 s^{-1} at B_0 = 9.4 T and a hyperpolarization of 10,000. Whereas the analytical solution excludes spillover and considers the CEST depolarization without interference with the direct saturation of free Xe in solution [Kunth *et al.*[127]], the numerical approach includes such effects.

(Equation (3 | 16)) for low (a; B_1 = 5 µT) and high (b; B_1 = 25 µT) saturation pulse exposure and a saturation time of 5 s. At higher static magnetic fields B_0, the Hyper-CEST response is spectrally more resolved (Figure 8.8), while the Hyper-CEST effect remains unchanged. Therefore, the spectral resolution is improved at larger B_0, but the Hyper-CEST effect remains constant.

Optimal cw Saturation for CB6 in Water

We further addressed the question which CB6 concentration in water could potentially be the lowest that is detectable by Hyper-CEST. Thus, we address the optimal cw saturation for highly diluted CB6 in water.

We used the numerical cw saturation pulse optimization approach as described in Section 7.2.2 and shown in Figure 7.2, and iteratively decreased the fractional size of bound Xe f_B until the generated Hyper-CEST effect approached 5 % under optimal cw saturation (Figure 8.9). This Hyper-CEST effect should be fairly above the experimental noise and thus measurable. We found that an f_B of $8.6 \cdot 10^{-7}$ was able to generate a Hyper-CEST effect of 5.6 % with B_1 = 69.5 µT for t_{sat} = 101 s (see red Hyper-CEST *z*-spectrum in Figure 8.9a and Hyper-CEST effect surface plots in b-c). This f_B value corresponds to a CB6 concentration of $8.6 \cdot 10^{-7}/0.0043 \cdot 3.4$ µM = $6.8 \cdot 10^{-4}$ µM = 680 pM (Table 8.1; assuming a constant host occupancy β), which is considerably low for a 1:1 Xe host complex.

In comparison to the analytically found optimal cw saturation (which, contrary to the numerical approach, excludes spillover effects), we calculated a $B_1^{opt,ana} = k_{BA}/\gamma$ = 28.4 µT which generates for a saturation time of 101 s a Hyper-CEST effect of 3.8 %, and a $B_1^{opt,ana} = 5 \cdot k_{BA}/\gamma$ = 141.9 µT which generates for a saturation time of 101 s a Hyper-CEST effect of 4.2 % (Figure 8.9a). Both are in good agreement with the numerical approach. The analytical optimal saturation time for 680 pM of CB6 was calculated to be $t_{sat}^{opt,ana}$ = 114 s using the optimal saturation pulse strength of B_1 = 69.5 μT (Equation (7.6b)), which is also in good agreement with the numerically found $t_{sat}^{opt,num}$ = 101 s.

In summary, the large Xe gas turnover rate of CB6 in water and optimal cw saturation of B_1 = 69.5 μT for t_{sat} = 101 s should enable the detection of extremely low amounts of CB6 in water of about 700 pM by Hyper-CEST. This sensitivity can compete with other molecular imaging modalities, such as PET and SPECT but without using ionizing radiation (compare with Table 1.1). However, CB6 is also known for competitive binding and some blocking of the portals. It would therefore be of large interest to maintain such high Xe gas turnover rates to design and establish a CB6 derivative that has a similar Xe exchange kinetics fingerprint in water as pure unmodified CB6, but more exclusive Xe binding. On the other hand, one could look at different derivatives of Cr that provide similar gas turnover rates as CB6 in water, but with more exclusive Xe specificity and less competitive binding. An alternative approach to maintain large gas turnover rates, while keeping the Xe exchange rate below that of CB6, would be to increase the number of Xe atoms that bind to one host. So far, most reported Xe binding hosts in literature were studied by direct ^{129}Xe NMR which provides limited information if the Xe exchange rate is too fast (Figure 8.4). However, that is exactly the favored condition in which the Hyper-CEST detection scheme is beneficial. Therefore, it is now interesting to revise the literature for different Xe-hosts and analyze their Xe exchange kinetics fingerprint to identify novel or overseen Xe-hosts with promising properties for future Hyper-CEST studies, in particular for highly sensitive *in vivo* applications.

Alternative Xe-Hosts

Similar to the finding of the Xe gas turnover rate for CB6 in water, other alternative Xe-hosts might exist with related Xe exchange properties. While many studies were done using the Xe-host CrA as the preferred module for Xe Hyper-CEST biosensing [Meldrum *et al.*[153], Sloniec *et al.*[196], Schnurr *et al.*[181] Schnurr *et al.*[182], Schnurr *et al.*[180], Döpfert *et al.*[60], Döpfert *et al.*[61], Tyagi *et al.*[216], Klippel *et al.*[116], Klippel *et al.*[117], Rossella *et al.*[171], Rose *et al.*[170], Witte *et al.*[232]], we focus here on quantitative studies regarding their exchange kinetics. We summarized in Table 8.3 currently available (preferably quantitative) Xe-host studies that have been reported so far in literature regarding their host cavity volume, the Xe host concentration used in the study (generally three orders of magnitude differences if detected either by direct or indirect Hyper-CEST ^{129}Xe NMR), chemical shift differences $\Delta\delta_{BA}$, the Xe exchange rate k_{BA}, the Xe binding constant K_A, and at which temperature T the study was done. Importantly, the temperature influences in particular the reported chemical shift, the Xe exchange rate and the binding constant. The determination methods are also indicated. We classified the overview in Table 8.3 into two groups: 1:1 Xe host complexes (top) and multiple Xe atoms per host (bottom). The caption can be found in the following.

Table 8.3: Cucurbit[6]uril (CB6) has superior Xe exchange k_{BA} of all listed 1:1 Xe host complexes. This Table's description can be found in this Caption.

Host	Name (residue R; if any)	Cavity Volume / Å³	PC	Solvent	[host]	$\Delta\delta_{BA}$ / ppm	k_{BA} / s⁻¹	K_A / M⁻¹	T / K	Literature
	1:1 Xe HOST COMPLEXES									
Cr-111	cryptophane-111 (R=H)	81	0.521	TCE	15 mM $^{h)}$	- 194	2.4 $^{d)}$	10,000 $^{h,o)}$	293	[73]
Cr-111	cryptophane-111 [(Cp*Ru)$_6$Cr-111]Cl$_6$ (R=H)	32	1.319	D_2O	1.7 mM $^{h)}$	+ 112	13 $^{e)}$	29,000 $^{h)}$	293	[70]
Cr-222	cryptophane-A (R=MeO)	95[34]	0.444	H_2O	~ 10 µM $^{c)}$	- 132	38 $^{q)}$	850 $^{q)}$	295	[126]
Cr-222	cryptophane-A (R=MeO)	95[34]	0.444	DMSO	~ 10 µM $^{c)}$	- 166	250 $^{q)}$	40 $^{q)}$	295	[129, 127, 126]
Cr-222	cryptophane-A (R=OCH$_2$COOH)	95[34]	0.444	H_2O	0.74 mM $^{h)}$	- 133	3.2 $^{d)}$	6,800 $^{h)}$	289, 293	[105]
Cr-223	cryptophane-223 (R=OCH$_2$COOH)	102[34]	0.414	H_2O	0.50 mM $^{h)}$	- 145	11 $^{d)}$	2,200 $^{h)}$	289, 293	[105]
Cr-233	cryptophane-233 (R=OCH$_2$COOH)	117[34]	0.361	H_2O	0.69 mM $^{h)}$	- 155	37 $^{d)}$	2,200 $^{h)}$	289, 293	[105]
Cr-333	cryptophane-E (R=OCH$_2$COOH)	89[77] or 121[34]	0.474 or 0.349	H_2O	0.69 mM $^{h)}$	- 162	90 $^{d)}$	1,000 $^{h)}$	289, 293	[77, 105]
Cr-222	cryptophane-A (R=OCH$_3$)	95[34]	0.444	TCE	~ 40 mM $^{h)}$	- 156	66 $^{e,p)}$	3,900 $^{h,o)}$	278	[139, 34]
Cr-223	cryptophane-223 (R=OCH$_3$)	102[34]	0.414	TCE	~ 40 mM $^{h)}$	- 164	71 $^{e,p)}$	2,810 $^{h,o)}$	278	[34]
Cr-233	cryptophane-233 (R=OCH$_3$)	117[34]	0.361	TCE	~ 40 mM $^{h)}$	- 177	70 $^{e,p)}$	810 $^{h,o)}$	278	[34]
Cr-224	cryptophane-224 (R=OCH$_3$)	110[34]	0.384	TCE	~ 40 mM $^{h)}$	-	-	9.5 $^{n)}$	278	[34, 104]
Cr-333	cryptophane-E (R=MeO)	89[77] or 121[34]	0.474 or 0.349	TCE	~ 300 mM $^{h)}$	- 186	-	5-10	278	[77, 198, 34]
Cr-555	cryptophane-O (R=MeO or R=OCH$_2$COOH)	115[77]	0.367	TCE or D_2O	-	-	-	-	300	[77, 105]
TTPC	tris(triazole propionic acid) cryptophane-A	95[34]	0.444	phosphate buffer	60 µM $^{h)}$	- 126	-	17,300 $^{f,g)}$	293	[99]
TAAC	triacetic acid cryptophane-A	95[34]	0.444	H_2O	140 µM $^{h)}$ → pM $^{c,r)}$	- 129	45 $^{d,e)}$	33,000 $^{f,g)}$	297, 293	[13, 100]
α-CD	α-cyclodextrin	137	0.308	H_2O	~ 10 mM $^{h)}$	+ 3	-	22 $^{n)}$	298	[18]
α-CD	α-cyclodextrin	137	0.308	DMSO	~ 10 mM $^{h)}$	- 50	-	2 $^{n)}$	298	[18]
CB5	cucurbit[5]uril	41 $^{b)}$	1.03	D_2O	~ mM $^{h)}$	+ 29	0.127 $h^{-1,\ n)}$ ~ 3.0 d^{-1}	1,320 $^{h)}$	316	[106]
CB6	cucurbit[6]uril	109 $^{b)}$	0.387	H_2O	3.4 µM $^{c)}$	- 96.1	2,100 $^{q)}$	2,500 $^{q)}$	295	[126]
CB6*	cucurbit[6]uril derivative	109 $^{b)}$	0.387	H_2O	2.49 mM $^{h)}$	- 93	2,300 $^{e)}$	3,400 $^{g)}$	295	[114]
CB6	cucurbit[6]uril	109 $^{b)}$	0.387	H_2O + 0.2 M Na_2SO_4	20 mM $^{h)}$	- 68	-	200 $^{n)}$	298	[90, 91]
CB6*	cucurbit[6]uril derivative	109 $^{b)}$	0.387	H_2O + 0.2 M Na_2SO_4	2.28 mM $^{h)}$	- 69	310 $^{e)}$	180 $^{h)}$	295	[114]
CB7	cucurbit[7]uril	208 $^{b)}$	0.203	-	-	-	-	-	-	-
PA5	pillar[5]arene	137 $^{m)}$	0.308	D_2O	100 mM $^{h)}$	- 80 to - 64	-	-	298	[1]
Fe_4L_6	self-assembled metallo cage	141[143]	0.299	H_2O	8.3 mM $^{h)}$	+ 17	10 $^{e)}$	16 $^{h)}$	298	[172]
	MULTIPLE Xe ATOMS PER HOST									
GV	gas vesicles	(4-16) $\cdot 10^{9,\ b)}$	-	PBS	100 - 400 pM $^{c)}$	- 164	-	-	295	[192]
PFOB	nano droplets	(2-15) $\cdot 10^{9,\ a)}$	-	H_2O	~ pM $^{c)}$	- 92	(10-37) $\cdot 10^3$	-	310	[200]
BS	bacterial spores	770 $\cdot 10^{9,\ b)}$	-	H_2O	~ fM $^{c)}$	+ 3	-	10-100	278	[46, 14]

a) assuming sphere volume: $V_{sp} = 4/3 \cdot \pi \cdot r^3$.
b) assuming cylinder volume: $V_{cy} = \pi \cdot r^2 \cdot h$.
c) by Hyper-CEST.
d) by ^{129}Xe NMR line width.
e) by 1D or 2D ^{129}Xe NMR EXSY.
f) by Xe fluorescence quenching.
g) by ITC.
h) by direct ^{129}Xe NMR.
m) assuming size of α-CD [159].
n) by own Eqs. in paper.
o) by competition experiment.
p) at T = 243 K.
q) by qHyper-CEST.
r) at T = 320 K.

CAPTION OF Table 8.3: The table is divided into two groups: 1:1 Xe host complexes (top) and multiple Xe atoms per host (bottom). The cavity volume was either reported within the actual study that is referenced, or it was reported in a separate publication (then it is marked as superscript above the value). Otherwise it was calculated according to the geometry. The internal cavity volumes of the native cryptophane derivatives 222, 223, 233, 224 and 333 were estimated by minimizing the cryptophanes with MACROMODEL 7.1, Amberforce field, followed by the program GRASP that estimated the volume of the internal cavities as done by Brotin and Dutasta[34] and described earlier by Mecozzi and Rebek[150]. The residues of Cr, R, are consistent with the chemical structure shown in Figure 1.6. The cavity volumes of the cucurbiturils were calculated using the inner diameters listed in Table 1 by Lagona *et al.*[130] assuming a cylinder volume. Accordingly, the α-cyclodextrin assumes a torus volume. The dimensions of the GVs were determined using transmission electron microscopy (diameter ~ 145 nm and lengths that range from 250 to 1,000 nm [Shapiro *et al.*[192]]). Their volumes were calculated assuming cylindric shape. The cavity volume of the PFOB nano droplets was calculated assuming spherical volume using the radii reported in the original publication. From the cavity volume, the PC was calculated by PC = V_{Xe}/V_{cavity} (using V_{Xe} = 42.2 Å^3; Figure 1.2.2). The following solvents are listed: **1,1,2,2-tetrachloroethane** (TCE), **phosphate-buffered saline** (PBS), (deuterated) water (D_2/H_2O) or DMSO. The host concentrations [host] that were used in the study have a superscript marking the detection method (either direct or indirect Hyper-CEST ^{129}Xe NMR). The relative chemical shift difference $\Delta\delta_{BA}$ is always referred to free Xe in solution (not to Xe in gas phase). The definition of an upfield chemical shift is towards more negative ppm or Hz values with respect to the reference signal of free Xe in solution. The Xe exchange rates k_{BA}, and binding constants K_A are supplied with an index referencing about the actual quantification method (and hence its accuracy and precision; compare Chapter 6), which was used within the study. Since the temperature T influences in particular the reported chemical shift, the Xe exchange rate and the binding constant of each study it is listed. Noteworthy, CB6 provides superior Xe exchange k_{BA} of all listed 1:1 Xe host complexes at room temperature.

We first compare the sensitivities of direct and indirect Hyper-CEST ^{129}Xe NMR. Regarding the lowest possible host concentration that can be detected by direct detection, it is obvious that large binding constants and rather slow Xe exchange rates are required, whereas with indirect Hyper-CEST ^{129}Xe NMR detection, faster exchange rates can compensate for low binding constants. This is reflected by the fact that detection of small Xe-host concentrations was often achieved using saturation transfer experiment (*e.g.*, Hyper-CEST; marked with $^{c)}$), whereas direct ^{129}Xe NMR requires larger host concentrations. Larger binding constants and slower exchange rates can enable host detection down into the upper μM-regime by direct ^{129}Xe NMR. For the strongest binding constants of 17,300 M^{-1} [Hill *et al.*[99]] and 33,000 M^{-1} [Hill *et al.*[100], Bai *et al.*[13]], mid μM values could be detected by direct ^{129}Xe NMR. The multiple Xe atoms per hosts listed here are poorly detectable by direct ^{129}Xe NMR due to their large exchange rates, and are only accessible by indirect Hyper-CEST.

We now discuss the link between the host cavity size and its Xe binding properties. Within the same host series (Cr-222, Cr-223, Cr-233, and Cr-333) in the same solvent, such as Brotins series of native Cr's in TCE [Brotin and Dutasta[34]] or Hubers series of water-soluble Cr's [Huber *et al.*[105]], the predicted correlation between cavity size and optimal binding when the PC approaches the value of 0.55, is confirmed in Table 8.3. Moreover, Cr-111 in TCE [Fogarty *et al.*[73]] further supports this theory.[7] At the same time, the Xe exchange rate increases with increasing cavity volume [Huber *et al.*[105]]. This intuitive behavior is also reported for the native Cr's in TCE [Brotin and Dutasta[34]] and means that the host should have a rather lose Xe binding property to be favorable for highly diluted Hyper-CEST detection. However, the water-soluble Cr-111 $[(Cp^{*}Ru)_6\text{Cr-111}]Cl_6$ has a PC of 1.3 and even larger Xe affinity, although the PC is beyond its optimal value of 0.55. This shows that the PC is not sufficient to solely describe this behavior. While the Xe binding constant of CB5 in water is comparable to that of CrA in water, the Xe exchange rate is less than three times per day (*i. e.*, $k_{BA} = 2.4\ d^{-1}$ at room temperature; Table 8.3; [Huber *et al.*[105], Huber *et al.*[106], Kunth *et al.*[126]]) making it unsuitable for Hyper-CEST detection. In addition, the detection with HP Xe becomes less beneficial for such low exchange rates, since HP Xe becomes depolarized for the readout and does not further gain new fresh HP signal to the bound state. Then, thermally polarized Xe studies can provide useful informations, at the cost of sensitivity.

The same trends can also be formulated for the cucurbiturils, although only CB5 and CB6 were under quantitative direct and quantitative indirect Hyper-CEST ^{129}Xe NMR investigation so far. Consistently, CB6 and CB6* behave very similar in their Xe exchange kinetics in both water and in 0.2 M Na_2SO_4 aqueous solution (Table 8.3), indicating that the benzene rings at the outside of CB6* influence the Xe exchange dynamics not significantly. According to the trend mentioned above, CB7 should facilitate even faster Xe exchange rates than CB6, as the cavity size increases. Therefore, CB7 should be able to be detected at even lower concentrations by taking advantage of the larger exchange rate using Hyper-CEST. However, an about 100-fold higher concentration of CB7 in pure water was required to produce about the same Hyper-CEST effect for comparable cw saturation as with CB6 in pure water [Kunth *et al.*[126], Schnurr *et al.*[179]]. Further quantitative studies on CB7 are therefore required to fully discover the potential of CB7. It should be mentioned that a strength of CB6 are its excellent properties for molecular recognition, it binds other ions in competition to Xe [Schnurr *et al.*[179], Wang and Dmochowski[225]]. This offers opportunities for further investigation of overseen or novel Xe hosts with similar exchange kinetics as for CB6 in pure water, but with reduced competitive binding. The same is the case for pillararenes. They are structurally similar to the cucurbiturils and play an important role in host-guest chemistry. The inner cavity of pillar[5]arene is negatively charged and electron rich. The cavity size is comparable to α-CD [Ogoshi *et al.*[159]].

Huber could show with his water-soluble Cr series that the Xe exchange rate improves by a factor of 30 when changing from CrA (*i. e.*, Cr-222) to CrE (*i. e.*, Cr-333) in water. Using CB6, we achieved a factor of 55 within the same solvent which further highlights their potential. In Section 8.2.4, we

---

[7] It has to be noted that this trend was reported to be the opposite when switching the solvent from water and the organic solvent TCE [Berthault *et al.*[21]; Table 1].

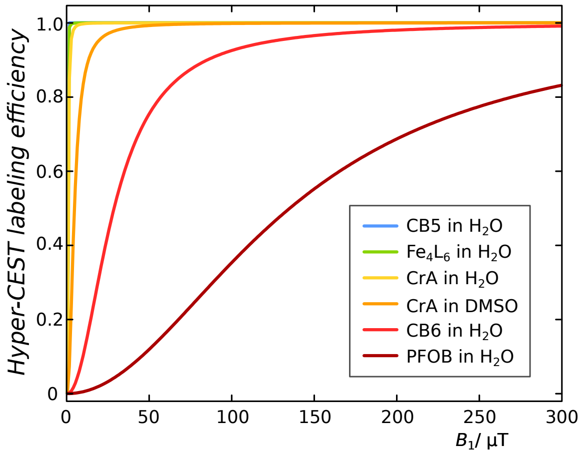

Figure 8.10: Normalized Hyper-CEST labeling efficiency α with respect to the saturation pulse strength B_1 for some Xe-host systems of Table 8.3 with exchange rates of k_{BA} = {2.7 · 10⁻⁵ (CB5 in water: blue); 10 (Fe_4L_6 in water: green); 38 (CrA in water: yellow); 317 (CrA in DMSO: orange); 2,100 (CB6 in water: red); 10,000 (PFOB in water: brown)} s^{-1}.

discussed the Hyper-CEST labeling efficiency dependence with respect to the exchange rate. Figure 8.10 shows the Hyper-CEST labeling efficiency for some Xe-hosts of Table 8.3: CB5 in water, Fe_4L_6 in water, CrA in water, CrA in DMSO, CB6 in water, and PFOB in water. It shows that faster Xe exchange rates become less efficiently labeled by the saturation pulse. If there is a B_1 limitation (*e.g.*, by SAR), then Xe hosts with too fast exchange rates must be discarded as the labeling is not sufficient. Furthermore, for *in vivo* applications, the temperature will be physiological 37° C, which significantly increases the exchange rate. Therefore, a too high exchange rate at room temperature will become less useful for *in vivo* applications. In summary, the Xe gas turnover rate should provide a trade-off between a high exchange rate to amplify Hyper-CEST sensitivity, and a certain upper limit to be able to label all Xe atoms within the saturation period.

The class of hosts that bind multiple Xe atoms per host are excellent CEST agents, as they provide large host occupancies and fast exchange rates. These CAs hold the record in ultra-diluted detection down to pico and femto molar using Hyper-CEST. However, their disadvantages are limited stability over time (*e.g.*, PFOB), and their suitability to become delivered to the biological target as their rather large dimensions limit this process. However, genetically encoded contrast agents such as the gas vesicles overcome this limitation and may take full advantage of the sensitive Hyper-CEST detection of *in vivo* applications.

A so far overlooked while promising Xe-host for Hyper-CEST detection might be the Cr-224 cage (Table 1.3, Figure 1.6 and Table 8.3). The exchange rate could be promisingly high, as no Cr-224 bound Xe signal was observed by direct ^{129}Xe NMR [Brotin and Dutasta[34]]. The possibilities of the Cr-224 host in contrast to CB6 is to provide similar favorable exchange kinetics, while offering minimal competitive binding options for other guests than Xe. Also other larger Cr derivatives and all combinations of the CTV unit linker lengths (Cr-333, Cr-334, Cr-344, Cr-444, Cr-234, *etc.*) can now be studied with quantitative Hyper-CEST for obtaining Xe exchange kinetics fingerprints with the potential achievement of no competitive binding.

8.3 CONCLUSION

The work described in this chapter takes together all the achieved advantages from the previous three chapters (Chapter 5, Chapter 6 and Chapter 7) to obtain unprecedented Hyper-CEST sensitivity. We demonstrated that a dilute host is providing a binding site for labile complex formation with Xe (in the intermediate exchange regime). This can be identified and classified by saturation transfer NMR where conventional detection fails. The gas turnover rate is accessible through qHyper-CEST as a highly sensitive method for the comprehensive quantification of Xe exchange kinetics and binding affinities. In particular, we successfully quantified the Xe interaction with CB6 in pure water, a Xe-host system which is extremely difficult to access by conventional NMR owing to the exceedingly low solubility of CB6. This indicated that CB6 can be a much more efficient Hyper-CEST agent than previously assumed, because the absence of a detectable signal from the Xe-CB6 complex in direct NMR precluded its comprehensive characterization. Given proper saturation conditions, CB6 is 100 times more efficient than CrA, which is the most widely used host so far in Xe biosensing. We could attribute the superior performance of CB6 to its fast exchange rate k_{BA}, and high occupancy β. We additionally suggest that other Xe-host systems are worthy to be reinvestigated, since their performance may have similarly been overlooked if the combination of a high exchange rate and low solubility led to the absence of a signal in direct Xe NMR. In addition, we provide the gas turnover rate $\beta \cdot k_{BA}$ as a simple parameter to classify the constant complex association/dissociation and to assess the prospective Hyper-CEST performance of particular Xe-host systems. This is not restricted to macrocyclic host systems, but will be similarly applicable to other emerging potential contrast agents such as bacterial spores [Bai *et al.*[14]], nanodroplets [Stevens *et al.*[200]] or genetically encoded gas vesicles (gas-binding protein nanostructures) [Shapiro *et al.*[192]]. It is also noteworthy that the different exchange parameters (Table Table 8.1) in combination with their determination at low concentrations by Hyper-CEST, paves the way for analytical multiplexing applications by exploiting these parameters as unique fingerprints assignable to different Xe-host systems.

The negligible influence on the Hyper-CEST effect with the external static magnetic field B_0 showed that same Hyper-CEST sensitivity can be obtained even at low fields. However, the spectral resolution of Hyper-CEST improves with B_0 which appreciates the trend of clinical MRI magnets to move towards larger field strengths. Our proposed optimal cw saturation produced a Hyper-CEST effect of about 5 % for a highly diluted CB6 concentration of about 700 pM (using BM simulations). This dramatic improvement for the detection of highly dilute concentrations for a 1:1 Xe-host complexation highlights the large potential of Hyper-CEST as molecular imaging modality as it can compete with PET and SPECT without using ionizing radiation (compare with Table 1.1). Moreover, we showed that the Xe exchange rate of CB6 in water is superior to all other 1:1 Xe-host complexes that are listed in Table 8.3, which manifests the outstanding detection potential of Hyper-CEST for Xe hosts with a high gas turnover rate. Moreover, constructs that bind multiple Xe atoms per host multiply their Hyper-CEST sensitivity accordingly. Similar for the bacterial spores [Bai *et al.*[14]], PFOB [Stevens *et al.*[200]], and the GV [Shapiro *et al.*[192]] is that they are able to passively bind multiple Xe atoms per host. On the other hand, multiple copies of 1:1 Xe binding host molecules can be attached to one single biosensor in order to bind multiple Xe atoms per biosensor to increase the Hyper-CEST sensitivity. This concept of binding multiple Xe atoms per biosensor has been exploited for the ultra-sensitive detection of CrA-targeted bacteriophages [Palaniappan *et al.*[162]], MS2 viral capsid scaffolds [Meldrum *et al.*[154]], an antibody based, modular biosensor with up to four CrA molecule copies per biosensor that target clusters of differentiation 14-expressing cells [Rose *et al.*[170]], or multiple CrA molecules within single liposomes [Schnurr *et al.*[180]] by Hyper-CEST.

Limitations and Possibilities

Labile systems with fast exchange only provide improved signal amplification for suitable saturation conditions and become otherwise disadvantageous. To fully activate the signal amplification using high exchange rates, also high saturation pulse strengths are required. However, these can be limited by SAR (Equation (6 | 3)) or hardware related limitations. This effect is modeled by the Hyper-CEST labeling efficiency (Equation (8 | 2), Figure 8.6 and Figure 8.10) and can therefore be optimized by tailored Xe-hosts for the particular question that is under investigation.

Further limitations of unmodified CB6 are its known promiscuous binding properties. Future CB6 congenerics may be synthesized such that they do not present polar carbonyl groups on the portals or to bind Xe more exclusively while keeping their Xe exchange kinetics.

The possibilities of the concept of the gas turnover rate are the application to many hosts where Xe is a suitable spy nucleus to probe for non-covalent interactions and it should foster reinvestigation of several systems to delineate true absence of interaction from labile complex formation. Our characterization framework allows to derive the full Hyper-CEST sensitivity capabilities of a particular Xe-host. A further possibility is to derive an unique Xe-host system exchange kinetics fingerprint $\langle T_1^A, T_2^A, \Delta\delta, k_{BA}, \beta, K_A, T, L \rangle$, which provides comprehensive biosensor characterization possibilities that expand the single chemical shift dimension as done previously. For example, this fingerprint changes uniquely when the same Xe-host switches between different chemical environments, or is able to tell when the Xe-host is blocked, *e.g.*, 10 % of CB6 in water were blocked by impurities for a commercial sample.


Chemical Science

The results for *High Gas Turnover Hyper-CEST MRI* can also be found within the following publication.

FULL REFERENCE (attached in Section D.4):
Martin Kunth, Christopher Witte, Andreas Hennig, and Leif Schröder. Identification, classification, and signal amplification capabilities of high-turnover gas binding hosts in ultra-sensitive NMR *Chemical Science*, 6:6069-6075, 2015; Kunth *et al.*[126].

(highlighted as front cover article)

AUTHOR CONTRIBUTIONS: M.K. designed research and analyzed data; M.K. and C.W. performed research; A.H. provided CB6; M.K., C.W., A.H. and L.S. wrote the paper.

Part IV

Conclusion

9 CONCLUSION & OUTLOOK

Contents

9.1 CONCLUSION

The goal of this thesis was to characterize and optimize saturation transfer NMR with exchanging Xe in different host-guest systems. To achieve this, we could successfully realize all objectives that were mentioned in the introduction and conclusions can be drawn.

9.1.1 Single-Shot Hyper-CEST MRI

The first objective was to accelerate the Hyper-CEST imaging process. We tested therefore different Xe MRI pulse sequences and data acquisition strategies that maximize the signal-to-noise ratio of the achieved Xe MR image, while reducing the acquisition time. To this end, we implemented fast single-shot encoding techniques that provide efficient use of the non-renewable hyperpolarized magnetization. The initial Hyper-CEST implementation achieved one Hyper-CEST MR image of the spatial biosensor distribution with a concentration of 5 μM in 22 minutes, with a matrix size of 8×8 that corresponds to a spatial resolution of $1.5 \times 1.5 \times 10\ \mathrm{mm}^3$. Using the ultrafast echo-planar imaging concept and a Xe polarizer that is optimized for Hyper-CEST to provide a high initial magnetization, we could drastically improve the sensitivity, spatial resolution and acquisition time, *e. g.*, for the detection of 250 nM of contrast agent in 102 s with a matrix size of 32×32 that corresponds to a spatial resolution of $0.6 \times 0.6 \times 20\ \mathrm{mm}^3$, with further room for improvement. Using an alternative biosensor detection based on direct ^{129}Xe NMR detection [Kotera *et al.*[120]], such sensitivity would require signal averaging for several hundreds of years.

To overcome the challenge of stable and reproducible Xe redeliveries for potential *in vivo* applications, we developed the clever data acquisition concept smashCEST to encode both the reference and the saturation image with one single Xe delivery. This makes the Hyper-CEST technology completely independent of a reliable, reproducible and stable Xe delivery between the two required measurements. This has the consequence that smashCEST enables further acceleration of the Hyper-CEST imaging speed which yields true sub-second imaging capabilities of the biosensor at sufficient high (50 μM) concentrations. Finally, we could also demonstrate the first time-resolved Hyper-CEST MRI studies with these new approaches. We could monitor contrast agent diffusion through a dialysis tubing recording every 33 seconds a Hyper-CEST image of the actual CrA situation and observed exponential signal behavior with (situation dependent) time constants of 53 minutes, 17 minutes and 4 minutes. Considering the diffusion time frame and the sensitivity, such diffusion monitoring is impossible with the original implementation or other approaches that are based on direct detection by repetitive sensor-selective excitation.

By drastically decreasing the total Hyper-CEST image acquisition time down to several seconds even for low concentrations we then had a tool for fast acquisition of entire Hyper-CEST *z*-spectra on hand. This leads to the conclusion for the second objective of this thesis that is based on fast single-shot Hyper-CEST MRI, a novel (and comprehensive) quantification technique of the Xe exchange kinetics.

9.1.2 Quantitative Hyper-CEST MRI

The second objective was to quantify the Xe exchange kinetics at high sensitivity. These are the Xe exchange rate k_{BA}, fraction of host-bound Xe f_B, the Xe-host occupancy β, the Xe binding constant K_A, the chemical shift differences to free Xe $\Delta\delta_{BA}$, and the relaxation times $T_{1,2}^{A,B}$. Additionally, the host occupancy has only been speculated before. The Hyper-CEST technique provides the potential to derive all these parameters from its spectral dimension, the Hyper-CEST *z*-spectra.

We addressed the non-linearity of the Hyper-CEST system in the exchange kinetics and experimental conditions, using fundamental Bloch-McConnell modeling for coupled spin systems that exchange magnetization. As for every novel quantification method, we verified its correctness as well as its range of validity. Under consideration of all these aspects, we successfully designed and investigated such a quantitative method which we termed qHyper-CEST. This qHyper-CEST technology 1) provided for the first time the capabilities to address the required Xe exchange kinetics, and 2) opens entire new possibilities when screening for novel CAs. Regarding point 1), a surprising result for CrA in DMSO (at room temperature) was that the Xe host occupancy for this very system was only about 8 % which we attributed to the hydrophobic nature of Xe to reside longer in the non-polar DMSO solvent than expected. Beyond the other parameters, we focus on the result of the Xe exchange rate as it is of further use in the conclusion of objective 4. We found the Xe exchange rate to be about $300\,s^{-1}$.

With respect to point 2), such new possibilities are the optimization of the Hyper-CEST system itself that is summarized in the following two conclusions for objective 3 and 4.

9.1.3 Optimal Saturation for Hyper-CEST MRI

The third objective was to characterize the saturation pulse impact on the Hyper-CEST signal. As such, two strategies (*i. e.*, a numerical and an analytical approach) were designed and developed that are capable to address this objective. As the innovative Hyper-CEST technique takes advantage of saturation pulses, new degrees of freedom in form of the saturation strength and duration provide an entirely new parameter space with potential for improvement and optimization. We used the novel qHyper-CEST technology and could quantitatively analyze the Xe depolarization behavior to CrA for various possible combinations of the saturation pulse parameters to maximize the Hyper-CEST response. In contrast to ^{1}H-CEST, Hyper-CEST has an optimal saturation time which has not been investigated before. Furthermore, we could successfully express the optimal saturation parameters by simple rules of thumbs that only depend on the exchange kinetics and the longitudinal relaxation time of free Xe itself. This enabled for the first time to predict the maximal intrinsic possible Hyper-CEST effect for any Xe-host system (by calculating its optimal saturation parameters) simply after its exchange kinetics quantification.

Finally, another Hyper-CEST signal amplification concept is expected when purposefully changing the Xe-host molecule. This was focused in objective 4.

9.1.4 High Gas Turnover Hyper-CEST MRI

The forth objective was to exploit fast Xe exchange rates and larger host occupancies in alternative host systems to systematically amplify Hyper-CEST signal intensity.

Using the novel qHyper-CEST technology, we could investigate three different Xe-host systems that provided the diversity that is required to identify improved conditions for Hyper-CEST performance. We designed and investigated for the first time the novel concept of the Xe gas turnover rate (which is the product of the Xe exchange rate and the host occupancy $k_{BA} \cdot \beta$) to identify and classify Xe-host systems regarding their Hyper-CEST performance, independently of the host concentration and the solvent that is used. We showed that the purposefully chosen CrA-alternative 1:1 Xe-host complex CB6 in water inherently provides a Xe host occupancy of about 50 % and a Xe exchange rate of about 2,100 s^{-1} at room temperature (to compare: CrA in water has a Xe host occupancy of about 30 % and an exchange rate of about 38 s^{-1}). This causes CB6 to facilitate an up to 100-fold increased gas turnover rate as to CrA, and can turn CB6 into a very powerful Xe MRI contrast agent. We simulated that optimal saturation parameters should enable the detection of extremely low amounts of CB6 in water of about 700 pM by Hyper-CEST. This sensitivity can compete with other molecular imaging modalities, such as PET and SPECT without ionizing radiation (compare with Table 1.1). We further demonstrated that the absence of CB6-bound Xe signal in direct ^{129}Xe NMR is not due to insufficient binding but rather due to a high exchange rate. This evidenced that previously studied Xe binding sites may be overseen and worthwhile to revisit with qHyper-CEST. Finally, we could design the idea to extend the monitoring capabilities of Xe biosensors beyond the conventionally used chemical shift dimension by introducing the concept of the Xe exchange kinetics fingerprint which is sensitive to many more scenarios. For example, this fingerprint monitors Xe host blocking by impurities in solution, something impossible if focusing only on the conventional chemical shift readout.

In summary, within this thesis the most simple Xe hosts, *i.e.*, 1:1 Xe-host complexes, could systematically be studied. This could minimize unwanted lateral effects and uncertainties of the Hyper-CEST system itself. Therefore, the results provide substantial improvement in the fundamental understand-

Table 9.1: Comparison of molecular imaging modalities considering results of this thesis (compare with Table 1.1; adapted from James and Gambhir[107]). The spatial resolution ranges from preclinical to clinical used systems. The term *Limitless* is referring relative to the human body size. Modalities that are marked with a dagger (†) employ ionizing radiation.

Modality	Spat. Resol.	Penetr. Depth	Sensitivity	Multi-plexing	Quanti-tative
CT †	0.05-1 mm	Limitless	ND a)	no b)	no
MRI	0.03-1 mm	Limitless	10^{-3}-10^{-5} M	no c)	yes
PET †	1-7 mm	Limitless	10^{-11}-10^{-12} M	no	yes
SPECT †	1-10 mm	Limitless	10^{-10}-10^{-11} M	yes	no
US	0.1-2 mm	mm - cm	10^{-12} M b)	no c)	yes
Fluorescence	2-3 mm	< 1 cm	10^{-12} M	yes	yes
Bio-luminescence	3-5 mm	1-2 cm	10^{-17} M	yes	yes[112]
Hyper-CEST MRI	0.625-1 mm	Limitless	10^{-9}-10^{-12} M d)	yes e)	yes f)

a) Not determined. b) If microbubbles are used. c) Could be possible.
d) Concepts for further improvements developed by Kunth *et al.*[126] and Kunth *et al.*[127].
e) Demonstrated by Kunth and Döpfert *et al.*[121], Klippel *et al.*[117] and Shapiro *et al.*[192].
f) Enabled by Kunth *et al.*[129].

ing of the Hyper-CEST mechanism. Doubtlessly, the approaches achieved within this thesis will help contributing to identify and classify novel types of Xe biosensors that are highly optimized for Hyper-CEST as a molecular imaging modality and, moreover, for future *in vivo* applications.

9.2 OUTLOOK

9.2.1 Hyper-CEST as Molecular Imaging Modality

In the following, we prospect the Hyper-CEST technique from the perspective as potential molecular imaging modality. We therefore revise Table 1.1 from Chapter 1 in form of Table 9.1.

Initially, the Hyper-CEST technique was time consuming, prone to instabilities in the Xe delivery, with 5 μM of biosensor concentration still on the lower sensitivity level, had rather low spatial resolution and a quantitative data analysis remained elusive. In addition, multiplexing was not established yet. By now, fast single-shot pulse sequences enable to largely increase the spatial resolution of ^{129}Xe MR images. Moreover, the combination of CEST MRI and HP Xe provides extraordinary sensitivity down to picomolar (as discussed in Chapter 8) that is comparable to the excellent sensitivity of PET and SPECT. Altogether, Hyper-CEST provides two important advantages: 1) avoiding ionizing radiation, and 2) at least 10-fold increased spatial resolution (which is limited by the hardware and can further be improved using stronger magnetic field gradients or innovative pulse sequences). In addition, the Hyper-CEST MRI technique achieves its anatomical reference frame from ^{1}H MRI, while PET or SPECT have to be combined with such modalities, *e.g.*, with ^{1}H MRI facilities. As discussed above, the demonstrated multiplexing feature of Hyper-CEST provides the possibility to screen multiple targets, *e.g.*, different types of diseases, simultaneously as a single imaging technique. The quantitative concept achieved within this thesis provides the fundamentals of the challenging potential of quantitatively follow tumor size progression and changing over time by

Hyper-CEST MRI noninvasively while under therapy. Based on the clever smashCEST technology, the Hyper-CEST method becomes immune to instabilities in the Xe delivery, given that the Xe magnetization is sufficiently large. In summary, Hyper-CEST MRI ranks favorable under all listed molecular imaging modalities given in Table 9.1.

9.2.2 Hyper-CEST for *in vivo* Applications

A critical step will be the translation of the Hyper-CEST concept to *in vivo* applications. It has to be ensured that sufficient amount of Xe magnetization can be detected within the organ of interest. Recently, the first HP Xe MR images of the human brain by simple HP Xe gas inhalation could be shown (Rao *et al.*, Sheffield-University, UK, unpublished yet; XeMAT Conference in Dresden, September 2015). This emphasizes the promising capabilities of HP Xe MRI.

Innovative pulse sequences and image reconstructions may be key features for this translation. As soon as a Xe NMR signal is detectable then Hyper-CEST can be applied to destroy that signal and to conclude about the presence of the Xe biosensor. As discussed in Chapter 5, one possibility might be in using non-Cartesian data acquisition strategies, such as radial or spiral trajectories. Both can be designed such that they become sensitive for very short relaxation times. While we discussed this case for possible spiral Hyper-CEST MR imaging in Chapter 5, radial readout strategies could be based on ultra-short echo time or zero echo time MR imaging techniques [Bydder *et al.*[38]]. In this regard, keyhole CEST MR imaging could also be promising for HP Xe to achieve further SNR improvements [Varma *et al.*[218]]. As we concluded above, the choice of the Xe-host is an additional key feature for the translation to *in vivo* applications. Whether 1:1 Xe-host complexes or biosensors that bind multiple Xe atoms will become the host of choice may depend on the type of application. This thesis provides the fundamental basis for efficient characterization of novel Xe biosensors.

While the Hyper-CEST concept is an excellent tool of fundamental research in biochemistry and material science, the translation to preclinical or ultimately clinical *in vivo* applications would in parallel be the next logical long-term goal. To this end, the biosensor should additionally be able to be stored for longer periods of time after it has been synthesized and needs therefore to be stable (a property that, for example, the PFOB nano-droplets lack, but 1:1 Xe-host complexes rather fulfill). Thus, the chances of Hyper-CEST as molecular imaging modality concept for *in vivo* applications point towards an exiting future.

Part V

Bibliography

BIBLIOGRAPHY

[1] Tal Adiri, Daniele Marciano, and Yoram Cohen. “Potential ^{129}Xe-NMR biosensors based on secondary and tertiary complexes of a water-soluble pillar[5]arene derivative.” In: *Chemical Communications* 49 (2013), pp. 7082–7084. DOI: 10.1039/C3CC43253J. URL: http://dx.doi.org/10.1039/C3CC43253J (Cited on pages 130, 165).

[2] S. Aime, S. Geninatti Crich, E. Gianolio, G.B. Giovenzana, L. Tei, and E. Terreno. “High sensitivity lanthanide(III) based probes for MR-medical imaging.” In: *Coordination Chemistry Reviews* 250.11-12 (2006). Inorganic Chemistry in Italy, pp. 1562–1579. DOI: http://dx.doi.org/10.1016/j.ccr.2006.03.015. URL: http://www.sciencedirect.com/science/article/pii/S0010854506000749 (Cited on page 12).

[3] Silvio Aime, Alessandro Barge, Daniela Delli Castelli, Franco Fedeli, Armando Mortillaro, Flemming U. Nielsen, and Enzo Terreno. “Paramagnetic Lanthanide(III) complexes as pH-sensitive chemical exchange saturation transfer (CEST) contrast agents for MRI applications.” In: *Magnetic Resonance in Medicine* 47.4 (2002), pp. 639–648. DOI: 10.1002/mrm.10106. URL: http://dx.doi.org/10.1002/mrm.10106 (Cited on page 11).

[4] Silvio Aime, Daniela Delli Castelli, Simonetta Geninatti Crich, Eliana Gianolio, and Enzo Terreno. “Pushing the Sensitivity Envelope of Lanthanide-Based Magnetic Resonance Imaging (MRI) Contrast Agents for Molecular Imaging Applications.” In: *Accounts of Chemical Research* 42.7 (2009), pp. 822–831. DOI: 10.1021/ar800192p. URL: http://dx.doi.org/10.1021/ar800192p (Cited on page 12).

[5] Silvio Aime, Daniela Delli Castelli, Franco Fedeli, and Enzo Terreno. “A Paramagnetic MRI-CEST Agent Responsive to Lactate Concentration.” In: *Journal of the American Chemical Society* 124.32 (2002), pp. 9364–9365. DOI: 10.1021/ja0264044. URL: http://dx.doi.org/10.1021/ja0264044 (Cited on page 11).

[6] Silvio Aime, Daniela Delli Castelli, and Enzo Terreno. “Highly Sensitive MRI Chemical Exchange Saturation Transfer Agents Using Liposomes.” In: *Angewandte Chemie International Edition* 44.34 (2005), pp. 5513–5515. DOI: 10.1002/anie.200501473. URL: http://dx.doi.org/10.1002/anie.200501473 (Cited on page 11).

[7] Salma Ajraoui, Kuan J. Lee, Martin H. Deppe, Steven R. Parnell, Juan Parra-Robles, and Jim M. Wild. “Compressed sensing in hyperpolarized ^{3}He Lung MRI.” In: *Magnetic Resonance in Medicine* 63.4 (2010), pp. 1059–1069. DOI: 10.1002/mrm.22302. URL: http://dx.doi.org/10.1002/mrm.22302 (Cited on page 93).

[8] M. S. Albert, G. D. Cates, B. Driehuys, W. Happer, B. Saam, C. S. Springer, and A. Wishnia. “Biological magnetic resonance imaging using laser-polarized ^{129}Xe.” In: *Nature* 370.6486 (1994), pp. 199–201. DOI: 10.1038/370199a0. URL: http://dx.doi.org/10.1038/370199a0 (Cited on page 30).

[9] Mitchell S. Albert, Daniel F. Kacher, Dilip Balamore, Arvind K. Venkatesh, and Ferenc A. Jolesz. “T_1 of ^{129}Xe in Blood and the Role of Oxygenation.” In: *Journal of Magnetic Resonance* 140.1 (1999), pp. 264–273. DOI: `http://dx.doi.org/10.1006/jmre.1999.1836`. URL: `http://www.sciencedirect.com/science/article/pii/S1090780799918360` (Cited on page 34).

[10] Jeffrey R. Alger. “The 1991 Nobel Prize in Chemistry Awarded to an MRI Investigator.” In: *Journal of Computer Assisted Tomography* 16.1 (1992), pp. 1–2. DOI: `00004728-199201000-00001`. URL: `http://journals.lww.com/jcat/Citation/1992/01000/The_1991_Nobel_Prize_in_Chemistry_Awarded_to_an.1.aspx` (Cited on page 36).

[11] Sarah Angelos, Ying-Wei Yang, Kaushik Patel, J. Fraser Stoddart, and Jeffrey I. Zink. “pH-Responsive Supramolecular Nanovalves Based on Cucurbit[6]uril Pseudorotaxanes.” In: *Angewandte Chemie International Edition* 47.12 (2008), pp. 2222–2226. DOI: `10.1002/anie.200705211`. URL: `http://dx.doi.org/10.1002/anie.200705211` (Cited on page 148).

[12] Evelyne Baguet and Claude Roby. “Off-Resonance Irradiation Effect in Steady-State NMR Saturation Transfer.” In: *Journal of Magnetic Resonance* 128.2 (1997), pp. 149–160. DOI: `http://dx.doi.org/10.1006/jmre.1997.1230`. URL: `http://www.sciencedirect.com/science/article/pii/S1090780797912301` (Cited on pages 67, 72).

[13] Yubin Bai, P. Aru Hill, and Ivan J. Dmochowski. “Utilizing a Water-Soluble Cryptophane with Fast Xenon Exchange Rates for Picomolar Sensitivity NMR Measurements.” In: *Analytical Chemistry* 84.22 (2012), pp. 9935–9941. DOI: `10.1021/ac302347y`. URL: `http://pubs.acs.org/doi/abs/10.1021/ac302347y` (Cited on pages 134, 165, 166).

[14] Yubin Bai, Yanfei Wang, Mark Goulian, Adam Driks, and Ivan J. Dmochowski. “Bacterial spore detection and analysis using hyperpolarized ^{129}Xe chemical exchange saturation transfer (Hyper-CEST) NMR.” In: *Chemial Science* 5 (8 2014), pp. 3197–3203. DOI: `10.1039/C4SC01190B`. URL: `http://dx.doi.org/10.1039/C4SC01190B` (Cited on pages 60, 130, 134, 155, 165, 169).

[15] Musa I. El-Barghouthi, Hamzeh M. Abdel-Halim, Feryal J. Haj-Ibrahim, and Khaleel I. Assaf. “Molecular dynamics simulation study of the structural features and inclusion capacities of cucurbit[6]uril derivatives in aqueous solutions.” In: *Supramolecular Chemistry* 27.1-2 (2014), pp. 80–89. DOI: `10.1080/10610278.2014.910601`. URL: `http://dx.doi.org/10.1080/10610278.2014.910601` (Cited on page 149).

[16] Amnon Bar-Shir, Jeff W. M. Bulte, and Assaf A. Gilad. “Molecular Engineering of Nonmetallic Biosensors for CEST MRI.” In: *ACS Chemical Biology* 10.5 (2015), pp. 1160–1170. DOI: `10.1021/cb500923v`. URL: `http://dx.doi.org/10.1021/cb500923v` (Cited on page 12).

[17] Kristin Bartik, Michel Luhmer, Jean-Pierre Dutasta, André Collet, and Jacques Reisse. “^{129}Xe and ^{1}H NMR Study of the Reversible Trapping of Xenon by Cryptophane-A in Organic Solution.” In: *Journal of the American Chemical Society* 120.4 (1998), pp. 784–791. DOI: `10.1021/ja972377j`. URL: `http://dx.doi.org/10.1021/ja972377j` (Cited on pages 14, 16, 150).

[18] Kristin Bartik, Michel Luhmer, Stephen J. Heyes, Robert Ottinger, and Jacques Reisse. "Probing Molecular Cavities in α-Cyclodextrin Solutions by Xenon NMR." In: *Journal of Magnetic Resonance, Series B* 109.2 (1995), pp. 164–168. DOI: `http://dx.doi.org/10.1006/jmrb.1995.0005`. URL: `http://www.sciencedirect.com/science/article/pii/S1064186685700052` (Cited on pages 14, 165).

[19] Patrick Berthault, Aurore Bogaert-Buchmann, Hervé Desvaux, Gaspard Huber, and Yves Boulard. "Sensitivity and Multiplexing Capabilities of MRI Based on Polarized 129-Xe Biosensors." In: *Journal of the American Chemical Society* 130.49 (2008), pp. 16456–16457. DOI: `10.1021/ja805274u`. eprint: `http://pubs.acs.org/doi/pdf/10.1021/ja805274u`. URL: `http://pubs.acs.org/doi/abs/10.1021/ja805274u` (Cited on page 87).

[20] Patrick Berthault, Hervé Desvaux, Thierry Wendlinger, Marina Gyejacquot, Antoine Stopin, Thierry Brotin, Jean-Pierre Dutasta, and Yves Boulard. "Effect of pH and Counterions on the Encapsulation Properties of Xenon in Water-Soluble Cryptophanes." In: *Chemistry – A European Journal* 16.43 (2010), pp. 12941–12946. DOI: `10.1002/chem.201001170`. URL: `http://dx.doi.org/10.1002/chem.201001170` (Cited on page 130).

[21] Patrick Berthault, Gaspard Huber, and Hervé Desvaux. "Biosensing using laser-polarized xenon NMR/MRI." In: *Progress in Nuclear Magnetic Resonance Spectroscopy* 55.1 (2009), pp. 35–60. DOI: `10.1016/j.pnmrs.2008.11.003`. URL: `http://www.sciencedirect.com/science/article/pii/S007965650800068X` (Cited on pages 17, 18, 148, 150, 167).

[22] A. Bifone, Y.-Q. Song, R. Seydoux, R. Seydoux, B. M. Goodson, T. Pietraiß, T. F. Budinger, G. Navon, and A. Pines. "NMR of laser-polarized xenon in human blood." In: *Proceedings of the National Academy of Sciences* 93.23 (1996), pp. 12932–12936. URL: `http://www.pnas.org/content/93/23/12932.abstract` (Cited on page 34).

[23] Martin Blaimer, Felix Breuer, Matthias Mueller, Robin M. Heidemann, Mark A. Griswold, and Peter M. Jakob. "SMASH, SENSE, PILS, GRAPPA: How to Choose the Optimal Method." In: *Topics in Magnetic Resonance Imaging* 15.4 (2004), pp. 223–236. URL: `http://www.ncbi.nlm.nih.gov/pubmed/15548953` (Cited on page 93).

[24] F. Bloch and A. Siegert. "Magnetic Resonance for Nonrotating Fields." In: *Physical Review* 57 (6 1940), pp. 522–527. DOI: `10.1103/PhysRev.57.522`. URL: `http://link.aps.org/doi/10.1103/PhysRev.57.522` (Cited on page 57).

[25] Felix Bloch. "Nuclear Induction." In: *Physical Review* 70 (7-8 Oct. 1946), pp. 460–474. DOI: `10.1103/PhysRev.70.460`. URL: `http://link.aps.org/doi/10.1103/PhysRev.70.460` (Cited on page 33).

[26] Felix Bloch, W. W. Hansen, and Martin Packard. "Nuclear Induction." In: *Physical Review* 69 (3-4 Feb. 1946), pp. 127–127. DOI: `10.1103/PhysRev.69.127`. URL: `http://link.aps.org/doi/10.1103/PhysRev.69.127` (Cited on page 25).

[27] A. Bondi. "van der Waals Volumes and Radii." In: *The Journal of Physical Chemistry* 68.3 (1964), pp. 441–451. DOI: `10.1021/j100785a001`. URL: `http://dx.doi.org/10.1021/j100785a001` (Cited on page 13).

[28] Céline Boutin, Estelle Léonce, Thierry Brotin, Alexej Jerschow, and Patrick Berthault. "Ultrafast Z-Spectroscopy for 129-Xe NMR-Based Sensors." In: *The Journal of Physical Chemistry Letters* 4.23 (2013), 4172–4176. DOI: `10.1021/jz402261h`. URL: `http://pubs.acs.org/doi/abs/10.1021/jz402261h` (Cited on pages 101, 129, 134).

[29] Célline Boutin, Antoine Stopin, Fatimazohra Lenda, Thierry Brotin, Jean-Pierre Dutasta, Nadélge Jamin, Alain Sanson, Yves Boulard, François Leteurtre, Gaspard Huber, Aurore Bogaert-Buchmann, Nawal Tassali, Hervé Desvaux, Marie Carriélre, and Patrick Berthault. "Cell uptake of a biosensor detected by hyperpolarized ^{129}Xe NMR: The transferrin case." In: *Bioorganic & Medicinal Chemistry* 19.13 (2011), pp. 4135–4143. DOI: `10.1016/j.bmc.2011.05.002`. URL: `http://www.sciencedirect.com/science/article/pii/S0968089611003476` (Cited on page 130).

[30] C. R. Bowers, V. Storhaug, C. E. Webster, J. Bharatam, A. Cottone, R. Gianna, K. Betsey, and B. J. Gaffney. "Exploring Surfaces and Cavities in Lipoxygenase and Other Proteins by Hyperpolarized Xenon-129 NMR." In: *Journal of the American Chemical Society* 121.40 (1999), pp. 9370–9377. DOI: `10.1021/ja991443+`. URL: `http://dx.doi.org/10.1021/ja991443+` (Cited on page 14).

[31] C. Russell Bowers and Daniel P. Weitekamp. "Parahydrogen and synthesis allow dramatically enhanced nuclear alignment." In: *Journal of the American Chemical Society* 109.18 (1987), pp. 5541–5542. DOI: `10.1021/ja00252a049`. URL: `http://dx.doi.org/10.1021/ja00252a049` (Cited on page 30).

[32] C. Russell Bowers and Daniel P. Weitekamp. "Transformation of Symmetrization Order to Nuclear-Spin Magnetization by Chemical Reaction and Nuclear Magnetic Resonance." In: *Physical Review Letters* 57 (21 1986), pp. 2645–2648. DOI: `10.1103/PhysRevLett.57.2645`. URL: `http://link.aps.org/doi/10.1103/PhysRevLett.57.2645` (Cited on page 30).

[33] Thierry Brotin, Thomas Devic, Anne Lesage, Lyndon Emsley, and André Collet. "Synthesis of Deuterium-Labeled Cryptophane-A and Investigation of Xe@Cryptophane Complexation Dynamics by 1D-EXSY NMR Experiments." In: *Chemistry - A European Journal* 7.7 (2001), pp. 1561–1573. DOI: `10.1002/1521-3765(20010401)7:7<1561::AID-CHEM1561>3.0.CO;2-9`. URL: `http://dx.doi.org/10.1002/1521-3765(20010401)7:7%3C1561::AID-CHEM1561%3E3.0.CO;2-9` (Cited on page 17).

[34] Thierry Brotin and Jean-Pierre Dutasta. "Xe@cryptophane Complexes with C_2 Symmetry: Synthesis and Investigations by ^{129}Xe NMR of the Consequences of the Size of the Host Cavity for Xenon Encapsulation." In: *European Journal of Organic Chemistry* 2003.6 (2003), pp. 973–984. DOI: `10.1002/ejoc.200390153`. URL: `http://dx.doi.org/10.1002/ejoc.200390153` (Cited on pages 17, 165–168).

[35] R. Nick Bryan. *Introduction to the Science of Medical Imaging*. Cambridge Universtity Press, 2010 (Cited on page 4).

[36] Robert G. Bryant. "The Dynamics of Water-Protein Interactions." In: *Annual Review of Biophysics and Biomolecular Structure* 25 (1996), pp. 29–53. DOI: `10.1146/annurev.bb.25.060196.000333`. URL: `http://www.`

annualreviews.org/doi/abs/10.1146/annurev.bb.25.060196.000333 (Cited on page 66).

[37] Hans-Jürgen Buschmann, Ernst Cleve, Klaus Jansen, Andreas Wego, and Eckhard Schollmeyer. "The determination of complex stabilities between different cyclodextrins and dibenzo-18-crown-6, cucurbit[6]uril, decamethylcucurbit[5]uril, cucurbit[5]uril, *p-tert*-butylcalix-[4]arene and *p-tert*-butylcalix[6]arene in aqueous solutions using a spectrophotometric method." In: *Materials Science and Engineering: C* 14.1-2 (2001), pp. 35–39. DOI: 10.1016/S0928-4931(01)00206-5. URL: http://www.sciencedirect.com/science/article/pii/S0928493101002065 (Cited on pages 149, 153).

[38] Graeme M. Bydder, Gary D. Fullerton, and Ian R. Young. *MRI of Tissue with short* T_2*s or* T_2^*. WILEY, 2012 (Cited on page 177).

[39] Josette Canceill, Michèle Cesario, André Collet, Jean Guilhem, Liliane Lacombe, Bénédicte Lozach, and Claudine Pascard. "Structure and Properties of the Cryptophane-E/$CHCl_3$ Complex, a Stable van der Waals Molecule." In: *Angewandte Chemie International Edition* 28.9 (1989), pp. 1246–1248. DOI: 10.1002/anie.198912461. URL: http://dx.doi.org/10.1002/anie.198912461 (Cited on page 17).

[40] Josette Canceill, Michèle Cesario, André Collet, Jean Guilhem, and Claudine Pascard. "A new bis-cyclotribenzyl cavitand capable of selective inclusion of neutral molecules in solution. Crystal structure of its CH2Cl2 cavitate." In: *Journal of the Chemical Society, Chemical Communications* (6 1985), pp. 361–363. DOI: 10.1039/C39850000361. URL: http://dx.doi.org/10.1039/C39850000361 (Cited on page 17).

[41] Josette Canceill, Michèle Cesario, André Collet, Jean Guilhem, Claude Riche, and Claudine Pascard. "Selective recognition of neutral molecules: ^{1}H NMR Study of the complexation of CH_2Cl_2 and CH_2Br_2 by cryptophane-D in solution and crystal structure of its CH_2Cl_2 cavitate." In: *Journal of the Chemical Society, Chemical Communications* (4 1986), pp. 339–341. DOI: 10.1039/C39860000339. URL: http://dx.doi.org/10.1039/C39860000339 (Cited on page 17).

[42] Josette Canceill, Liliane Lacombe, and André Collet. "A new cryptophane forming unusually stable inclusion complexes with neutral guests in a lipophilic solvent." In: *Journal of the American Chemical Society* 108.14 (1986), pp. 4230–4232. DOI: 10.1021/ja00274a067. URL: http://dx.doi.org/10.1021/ja00274a067 (Cited on page 17).

[43] Josette Canceill, Liliane Lacombe, and André Collet. "Water-soluble cryptophane binding lipophilic guests in aqueous solution." In: *Journal of the Chemical Society, Chemical Communications* (3 1987), pp. 219–221. DOI: 10.1039/C39870000219. URL: http://dx.doi.org/10.1039/C39870000219 (Cited on page 17).

[44] E. J. Candes and M. B. Wakin. "An Introduction To Compressive Sampling." In: *Signal Processing Magazine, IEEE* 25 (2008), pp. 21–30. DOI: 10.1109/MSP.2007.914731. URL: http://ieeexplore.ieee.org/xpl/freeabs_all.jsp?arnumber=4472240 (Cited on page 93).

[45] E.J. Candes and T. Tao. "Near-Optimal Signal Recovery From Random Projections: Universal Encoding Strategies?" In: *Information Theory, IEEE Transactions on* 52.12 (Dec. 2006), pp. 5406–5425. DOI: 10.1109/TIT.2006.885507. URL: http://ieeexplore.ieee.org/xpl/articleDetails.jsp?arnumber=4016283 (Cited on page 93).

[46] M. Carrera, R. O. Zandomeni, J. Fitzgibbon, and J. L. Sagripanti. "Difference between the spore sizes of Bacillus anthracis and other Bacillus species." In: *Journal of Applied Microbiology* 102.2 (2007), pp. 303–312. URL: `http://www.ncbi.nlm.nih.gov/pubmed/17241334?dopt=Abstract` (Cited on page 165).

[47] Daniela Delli Castelli, Eliana Gianolio, Simonetta Geninatti Crich, Enzo Terreno, and Silvio Aime. "Metal containing nanosized systems for MR-Molecular Imaging applications." In: *Coordination Chemistry Reviews* 252.21-22 (2008), pp. 2424–2443. DOI: `http://dx.doi.org/10.1016/j.ccr.2008.05.006`. URL: `http://www.sciencedirect.com/science/article/pii/S0010854508001008` (Cited on page 12).

[48] Jean-Luc Chabert. *A History of Algorithms. From the Pebble to the Microchip*. 284 - 287: Springer-Verlag, 1999. URL: `http://www.springer.com/de/book/9783540633693` (Cited on page 61).

[49] Kathleen E. Chaffee, Heather A. Fogarty, Thierry Brotin, Boyd M. Goodson, and Jean-Pierre Dutasta. "Encapsulation of Small Gas Molecules by Cryptophane-111 in Organic Solution. 1. Size- and Shape-Selective Complexation of Simple Hydrocarbons." In: *The Journal of Physical Chemistry A* 113.49 (2009), pp. 13675–13684. DOI: `10.1021/jp903452k`. URL: `http://dx.doi.org/10.1021/jp903452k` (Cited on page 18).

[50] Jennifer M. Chambers, P. Aru Hill, Julie A. Aaron, Zhaohui Han, David W. Christianson, Nicholas N. Kuzma, and Ivan J. Dmochowski. "Cryptophane Xenon-129 Nuclear Magnetic Resonance Biosensors Targeting Human Carbonic Anhydrase." In: *Journal of the American Chemical Society* 131.2 (2009), pp. 563–569. DOI: `10.1021/ja806092w`. URL: `http://pubs.acs.org/doi/abs/10.1021/ja806092w` (Cited on page 134).

[51] Kannie W. Y. Chan, Guanshu Liu, Xiaolei Song, Heechul Kim, Tao Yu, Dian R. Arifin, Assaf A. Gilad, Justin Hanes, Piotr Walczak, Peter C. M. van Zijl, Jeff W. M. Bulte, and Michael T. McMahon. "MRI-detectable pH nanosensors incorporated into hydrogels for *in vivo* sensing of transplanted-cell viability." In: *Nature Materials* 12.3 (2013), pp. 268–275. DOI: `10.1038/nmat3525`. URL: `http://dx.doi.org/10.1038/nmat3525` (Cited on page 11).

[52] B. Chann, I. A. Nelson, L. W. Anderson, B. Driehuys, and T. G. Walker. "$^{129}\mathrm{Xe}-\mathrm{Xe}$ Molecular Spin Relaxation." In: *Physical Review Letters* 88 (11 2002), p. 113201. DOI: `10.1103/PhysRevLett.88.113201`. URL: `http://link.aps.org/doi/10.1103/PhysRevLett.88.113201` (Cited on page 34).

[53] Andrea Cherubini and Angelo Bifone. "Hyperpolarised xenon in biology." In: *Progress in Nuclear Magnetic Resonance Spectroscopy* 42 (2003), pp. 1–30. DOI: `10.1016/S0079-6565(02)00052-3`. URL: `http://www.sciencedirect.com/science/article/pii/S0079656502000523` (Cited on page 34).

[54] Jordan M. Chinai, Alexander B. Taylor, Lisa M. Ryno, Nicholas D. Hargreaves, Christopher A. Morris, P. John Hart, and Adam R. Urbach. "Molecular Recognition of Insulin by a Synthetic Receptor." In: *Journal of the American Chemical Society* 133.23 (2011), pp. 8810–8813. DOI: `10.1021/ja201581x`. URL: `http://dx.doi.org/10.1021/ja201581x` (Cited on page 148).

[55] Zackary I. Cleveland, Gary P. Cofer, Gregory Metz, Denise Beaver, John Nouls, S. Sivaram Kaushik, Monica Kraft, Jan Wolber, Kevin T. Kelly, H. Page McAdams, and Bastiaan Driehuys. “Hyperpolarized ^{129}Xe MR Imaging of Alveolar Gas Uptake in Humans.” In: *PLoS ONE* 5.8 (2010), e12192. DOI: `10.1371/journal.pone.0012192`. URL: `http://journals.plos.org/plosone/article?id=10.1371/journal.pone.0012192` (Cited on page 13).

[56] Martin H. Deppe and Jim M. Wild. “Variable flip angle schedules in bSSFP imaging of hyperpolarized noble gases.” In: *Magnetic Resonance in Medicine* 67 (2012), pp. 1656–1664. DOI: `10.1002/mrm.23155`. URL: `http://dx.doi.org/10.1002/mrm.23155` (Cited on page 104).

[57] Anagha Deshmane, Vikas Gulani, Mark A. Griswold, and Nicole Seiberlich. “Parallel MR imaging.” In: *Journal of Magnetic Resonance Imaging* 36.1 (2012), pp. 55–72. DOI: `10.1002/jmri.23639`. URL: `http://dx.doi.org/10.1002/jmri.23639` (Cited on page 93).

[58] Hervé Desvaux, Lionel Dubois, Gaspard Huber, Michael L. Quillin, Patrick Berthault, and Brian W. Matthews. “Dynamics of Xenon Binding Inside the Hydrophobic Cavity of Pseudo-Wild-type Bacteriophage T4 Lysozyme Explored through Xenon-Based NMR Spectroscopy.” In: *Journal of the American Chemical Society* 127.33 (2005), pp. 11676–11683. DOI: `10.1021/ja053074p`. URL: `http://pubs.acs.org/doi/abs/10.1021/ja053074p` (Cited on page 14).

[59] D.L. Donoho. “Compressed sensing.” In: *Information Theory, IEEE Transactions on* 52 (2006), pp. 1289–1306. URL: `http://ieeexplore.ieee.org/xpl/freeabs_all.jsp?arnumber=1614066` (Cited on page 93).

[60] Jörg Döpfert, Christopher Witte, Martin Kunth, and Leif Schröder. “Sensitivity enhancement of (Hyper-)CEST image series by exploiting redundancies in the spectral domain.” In: *Contrast Media & Molecular Imaging* 9.1 (2014), pp. 100–107. DOI: `10.1002/cmmi.1543`. URL: `http://dx.doi.org/10.1002/cmmi.1543` (Cited on page 164).

[61] Jörg Döpfert, Christopher Witte, and Leif Schröder. “Fast Gradient-Encoded CEST Spectroscopy of Hyperpolarized Xenon.” In: *ChemPhysChem* 15.2 (2014), pp. 261–264. DOI: `10.1002/cphc.201300888`. URL: `http://dx.doi.org/10.1002/cphc.201300888` (Cited on pages 129, 134, 164).

[62] Jörg Döpfert, Christopher Witte, and Leif Schröder. “Slice-selective gradient-encoded CEST spectroscopy for monitoring dynamic parameters and high-throughput sample characterization.” In: *Journal of Magnetic Resonance* 237 (2013), pp. 34–39. DOI: `http://dx.doi.org/10.1016/j.jmr.2013.09.007`. URL: `http://www.sciencedirect.com/science/article/pii/S1090780713002280` (Cited on page 155).

[63] Jörg Döpfert, Moritz Zaiss, Christopher Witte, and Leif Schröder. “Ultrafast CEST imaging.” In: *Journal of Magnetic Resonance* 243 (2014), pp. 47–53. DOI: `http://dx.doi.org/10.1016/j.jmr.2014.03.008`. URL: `http://www.sciencedirect.com/science/article/pii/S1090780714000962` (Cited on page 105).

[64] J. R. Dormand and P. J. Prince. “A family of embedded Runge-Kutta formulae.” In: *Journal of Computational and Applied Mathematics* 6 (1980), pp. 19–26. DOI: `10.1016/0771-050X(80)90013-3`. URL: `http://www.sciencedirect.com/science/article/pii/0771050X80900133` (Cited on page 61).

[65] Bastiaan Driehuys. “Toward Molecular Imaging with Xenon MRI.” In: *Science* 314.5798 (2006), pp. 432–433. DOI: `10.1126/science.1134532`. URL: `http://www.sciencemag.org/content/314/5798/432.short` (Cited on page 19).

[66] Bastiaan Driehuys, Gary P. Cofer, Jim Pollaro, Julie Boslego Mackel, Laurence W. Hedlund, and G. Allan Johnson. “Imaging alveolar-capillary gas transfer using hyperpolarized ^{129}Xe MRI.” In: *Proceedings of the National Academy of Sciences* 103.48 (2006), pp. 18278–18283. DOI: `10.1073/pnas.0608458103`. URL: `http://www.pnas.org/content/103/48/18278.abstract` (Cited on page 30).

[67] Lionel Dubois, Pedro Da Silva, Céline Landon, J. Gaspard Huber, Michel Ponchet, Françoise Vovelle, Patrick Berthault, and Hervé Desvaux. “Probing the Hydrophobic Cavity of Lipid Transfer Protein from *Nicotiana tabacum* through Xenon-Based NMR Spectroscopy.” In: *Journal of the American Chemical Society* 126.48 (2004), pp. 15738–15746. DOI: `10.1021/ja046195i`. URL: `http://pubs.acs.org/doi/abs/10.1021/ja046195i` (Cited on pages 14, 134).

[68] Emmanuelle Dubost, Naoko Kotera, Sébastien Garcia-Argote, Yves Boulard, Estelle Léonce, Céline Boutin, Patrick Berthault, Christophe Dugave, and Bernard Rousseau. “Synthesis of a Functionalizable Water-Soluble Cryptophane-111.” In: *Organic Letters* 15.11 (2013), pp. 2866–2868. DOI: `10.1021/ol4012019`. URL: `http://dx.doi.org/10.1021/ol4012019` (Cited on page 18).

[69] Philipp Ehses, Nicole Seiberlich, Dan Ma, Felix A. Breuer, Peter M. Jakob, Mark A. Griswold, and Vikas Gulani. “IR TrueFISP with a golden-ratio-based radial readout: Fast quantification of T_1, T_2, and proton density.” In: *Magnetic Resonance in Medicine* 69.1 (2013), pp. 71–81. DOI: `10.1002/mrm.24225`. URL: `http://dx.doi.org/10.1002/mrm.24225` (Cited on pages 34, 105, 109).

[70] Robert M. Fairchild, Akil I. Joseph, K. Travis Holman, Heather A. Fogarty, Thierry Brotin, Jean-Pierre Dutasta, Ceéline Boutin, Gaspard Huber, and Patrick Berthault. “A Water-Soluble Xe@cryptophane-111 Complex Exhibits Very High Thermodynamic Stability and a Peculiar 129Xe NMR Chemical Shift.” In: *Journal of the American Chemical Society* 132.44 (2010), pp. 15505–15507. DOI: `10.1021/ja1071515`. URL: `http://pubs.acs.org/doi/abs/10.1021/ja1071515` (Cited on pages 17, 18, 110, 165).

[71] J.A. Fessler and B.P. Sutton. “Nonuniform fast Fourier transforms using min-max interpolation.” In: *Signal Processing, IEEE Transactions on* 51.2 (Feb. 2003), pp. 560–574. DOI: `10.1109/TSP.2002.807005`. URL: `http://ieeexplore.ieee.org/xpl/articleDetails.jsp?arnumber=1166689` (Cited on page 105).

[72] Mara Florea and Werner M. Nau. “Strong Binding of Hydrocarbons to Cucurbituril Probed by Fluorescent Dye Displacement: A Supramolecular Gas-Sensing Ensemble.” In: *Angewandte Chemie International Edition* 50.40 (2011), pp. 9338–9342. DOI: `10.1002/anie.2011`

04119. URL: http://dx.doi.org/10.1002/anie.201104119 (Cited on page 148).

[73] Heather A. Fogarty, Patrick Berthault, Thierry Brotin, Gaspard Huber, Herveé Desvaux, and Jean-Pierre Dutasta. "A Cryptophane Core Optimized for Xenon Encapsulation." In: *Journal of the American Chemical Society* 129.34 (2007), pp. 10332–10333. DOI: 10.1021/ja073771c. URL: http://pubs.acs.org/doi/abs/10.1021/ja073771c (Cited on pages 17–19, 165, 167).

[74] Joshua I. Friedman, Michael T. McMahon, James T. Stivers, and Peter C. M. Van Zijl. "Indirect Detection of Labile Solute Proton Spectra via the Water Signal Using Frequency-Labeled Exchange (FLEX) Transfer." In: *Journal of the American Chemical Society* 132.6 (2010), pp. 1813–1815. DOI: 10.1021/ja909001q. URL: http://dx.doi.org/10.1021/ja909001q (Cited on page 109).

[75] Jacqueline Gabard and André Collet. "Synthesis of a (D_3)-bis(cyclotriveratrylenyl) macrocage by stereospecific replication of a (C_3)-subunit." In: *Journal of the Chemical Society, Chemical Communications* (21 1981), pp. 1137–1139. DOI: 10.1039/C39810001137. URL: http://dx.doi.org/10.1039/C39810001137 (Cited on page 14).

[76] Laurent Garel, Jean-Pierre Dutasta, and André Collet. "Complexation of Methane and Chlorofluorocarbons by Cryptophane-A in Organic Solution." In: *Angewandte Chemie International Edition* 32.8 (1993), pp. 1169–1171. DOI: 10.1002/anie.199311691. URL: http://dx.doi.org/10.1002/anie.199311691 (Cited on page 17).

[77] Laurent Garel, Bénédicte Lozach, Jean Pierre Dutasta, and André Collet. "Remarkable effect of the receptor size in the binding of acetylcholine and related ammonium ions to water-soluble cryptophanes." In: *Journal of the American Chemical Society* 115.24 (1993), pp. 11652–11653. DOI: 10.1021/ja00077a096. URL: http://dx.doi.org/10.1021/ja00077a096 (Cited on pages 17, 165).

[78] M. Gatzke, G. D. Cates, B. Driehuys, D. Fox, W. Happer, and B. Saam. "Extraordinarily slow nuclear spin relaxation in frozen laser-polarized ^{129}Xe." In: *Physical Review Letters* 70 (5 1993), pp. 690–693. DOI: 10.1103/PhysRevLett.70.690. URL: http://link.aps.org/doi/10.1103/PhysRevLett.70.690 (Cited on page 34).

[79] Walther Gerlach and Otto Stern. "Das magnetische Moment des Silberatoms." In: *Zeitschrift für Physik* 9.1 (1922), pp. 353–355. ISSN: 0044-3328. DOI: 10.1007/BF01326984. URL: http://dx.doi.org/10.1007/BF01326984 (Cited on page 25).

[80] Walther Gerlach and Otto Stern. "Der experimentelle Nachweis der Richtungsquantelung im Magnetfeld." In: *Zeitschrift für Physik* 9.1 (1922), pp. 349–352. ISSN: 0044-3328. DOI: 10.1007/BF01326983. URL: http://dx.doi.org/10.1007/BF01326983 (Cited on page 25).

[81] Assaf A. Gilad, Michael T. McMahon, Piotr Walczak, Paul T. Winnard, Venu Raman, Hanneke W. M. van Laarhoven, Cynthia M. Skoglund, Jeff W. M. Bulte, and Peter C. M. van Zijl. "Artificial reporter gene providing MRI contrast based on proton exchange." In: *Nature Biotechnology* 25.2 (2007), pp. 217–219. DOI: 10.1038/nbt1277. URL: http://dx.doi.org/10.1038/nbt1277 (Cited on page 10).

[82] Boyd M. Goodson. "Nuclear Magnetic Resonance of Laser-Polarized Noble Gases in Molecules, Materials, and Organisms." In: *Journal of Magnetic Resonance* 155.2 (2002), pp. 157–216. ISSN: 1090-7807. DOI: 10.1006/jmre.2001.2341. URL: http://www.sciencedirect.com/science/article/pii/S1090780701923419 (Cited on pages 12, 13, 30, 37).

[83] Robin A. de Graaf. in vivo *NMR Spectroscopy: Principles and Techniques*. 2$^{\text{nd}}$. John Wiley & Sons, Ltd, 2007 (Cited on pages 25, 26, 29, 120).

[84] Mark A. Griswold, Peter M. Jakob, Robin M. Heidemann, Mathias Nittka, Vladimir Jellus, Jianmin Wang, Berthold Kiefer, and Axel Haase. "Generalized autocalibrating partially parallel acquisitions (GRAPPA)." In: *Magnetic Resonance in Medicine* 47.6 (2002), pp. 1202–1210. DOI: 10.1002/mrm.10171. URL: http://dx.doi.org/10.1002/mrm.10171 (Cited on page 93).

[85] Christian Gröger, Andreas Möglich, Miguel Pons, Brigitte Koch, Wolfgang Hengstenberg, Hans Robert Kalbitzer, and Eike Brunner. "NMR-Spectroscopic Mapping of an Engineered Cavity in the I14A Mutant of HPr from *Staphylococcus carnosus* Using Xenon." In: *Journal of the American Chemical Society* 125.29 (2003), pp. 8726–8727. DOI: 10.1021/ja030113t. URL: http://pubs.acs.org/doi/abs/10.1021/ja030113t (Cited on page 14).

[86] Gebhard Haberhauer, Sascha Woitschetzki, and Heinz Bandmann. "Strongly underestimated dispersion energy in cryptophanes and their complexes." In: *Nature Communications* 5 (2014), p. 3542. DOI: 10.1038/ncomms4542. URL: http://dx.doi.org/10.1038/ncomms4542 (Cited on page 151).

[87] Erwin L. Hahn. "Spin Echoes." In: *Physical Review* 80 (4 1950), pp. 580–594. DOI: 10.1103/PhysRev.80.580. URL: http://link.aps.org/doi/10.1103/PhysRev.80.580 (Cited on page 47).

[88] Ileana Hancu, W. Thomas Dixon, Mark Woods, Elena Vinogradov, A. Dean Sherry, and Robert E. Lenkinski. "CEST and PARACEST MR contrast agents." In: *Acta Radiologica* 51.8 (2010), pp. 910–923. DOI: 10.3109/02841851.2010.502126. URL: http://acr.sagepub.com/content/51/8/910.abstract (Cited on page 12).

[89] Marcus D. Hanwell, Donald E. Curtis, David C. Lonie, Tim Vandermeersch, Eva Zurek, and Geoffrey R. Hutchison. "Avogadro: an advanced semantic chemical editor, visualization, and analysis platform." In: *Journal of Cheminformatics* 4 (2012), p. 17. DOI: 1186/1758-2946-4-17. URL: http://www.jcheminf.com/content/4/1/17 (Cited on pages 149, 151).

[90] Mustapha El Haouaj, Young Ho Ko, Michel Luhmer, Kimoon Kim, and Kristin Bartik. "NMR Investigation of the complexation of neutral guests by cucurbituril." In: *Journal of the Chemical Society Perkin Transactions 2* (11 2001), pp. 2104–2107. DOI: 10.1039/B105535F. URL: http://dx.doi.org/10.1039/B105535F (Cited on pages 148, 149, 153, 165).

[91] Mustapha El Haouaj, Michel Luhmer, Young Ho Ko, Kimoon Kim, and Kristin Bartik. "NMR study of the reversible complexation of xenon by cucurbituril." In: *Journal of the Chemical Society Perkin Transactions 2* (2001), pp. 804–807. URL: http://pubs.rsc.org/en/content

/articlehtml/2001/p2/b008623l (Cited on pages 148, 149, 152–154, 165).

[92] William Happer. “Alfred Kastler.” In: *Physics Today* 37.5 (May 1984), pp. 101–102. DOI: http://dx.doi.org/10.1063/1.2916219. URL: http://scitation.aip.org/content/aip/magazine/physicstoday/article/37/5/10.1063/1.2916219 (Cited on page 31).

[93] William Happer, Yuan-Yu Jau, and Thad Walker. *Optically Pumped Atoms*. WILEY-VCH, 2010 (Cited on page 31).

[94] George W. J. Harston, Yee Kai Tee, Nicholas Blockley, Thomas W. Okell, Sivarajan Thandeswaran, Gabriel Shaya, Fintan Sheerin, Martino Cellerini, Stephen Payne, Peter Jezzard, Michael Chappell, and James Kennedy. “Identifying the ischaemic penumbra using pH-weighted magnetic resonance imaging.” In: *Brain* 138.1 (2015), pp. 36–42. DOI: 10.1093/brain/awu374. URL: http://brain.oxfordjournals.org/content/138/1/36 (Cited on page 10).

[95] R. Mark Henkelman, Xuemei Huang, Qing-San Xiang, G. J. Stanisz, Scott D. Swanson, and Michael J. Bronskill. “Quantitative interpretation of magnetization transfer.” In: *Magnetic Resonance in Medicine* 29.6 (1993), pp. 759–766. ISSN: 1522-2594. DOI: 10.1002/mrm.1910290607. URL: http://dx.doi.org/10.1002/mrm.1910290607 (Cited on pages 67, 69).

[96] Andreas Hennig, Hüseyin Bakirci, and Werner M. Nau. “Label-free continuous enzyme assays with macrocycle-fluorescent dye complexes.” In: *Nature Methods* 4.8 (2007), pp. 629–632. DOI: 10.1038/nmeth1064. URL: dx.doi.org/10.1038/nmeth1064 (Cited on page 148).

[97] Jürgen Hennig, A. Nauerth, and H. Friedburg. “RARE imaging: a fast imaging method for clinical MR.” In: *Magnetic Resonance in Medicine* 3.6 (1986), pp. 823–833. URL: http://onlinelibrary.wiley.com/doi/10.1002/mrm.1910030602/pdf (Cited on page 47).

[98] Nicholas J. Higham. *Accuracy and Stability of Numerical Algorithms*. 2nd. Society for Industrial and Applied Mathematics, 2002. DOI: 10.1137/1.9780898718027. URL: http://dx.doi.org/10.1137/1.9780898718027 (Cited on page 61).

[99] P. Aru Hill, Qian Wei, Roderic G. Eckenhoff, and Ivan J. Dmochowski. “Thermodynamics of Xenon Binding to Cryptophane in Water and Human Plasma.” In: *Journal of the American Chemical Society* 129.30 (2007), pp. 9262–9263. DOI: 10.1021/ja072965p. URL: http://pubs.acs.org/doi/abs/10.1021/ja072965p (Cited on pages 18, 109, 150, 165, 166).

[100] P. Aru Hill, Qian Wei, Thomas Troxler, and Ivan J. Dmochowski. “Substituent Effects on Xenon Binding Affinity and Solution Behavior of Water-Soluble Cryptophanes.” In: *Journal of the American Chemical Society* 131.8 (2009), pp. 3069–3077. DOI: 10.1021/ja8100566. URL: http://pubs.acs.org/doi/abs/10.1021/ja8100566 (Cited on pages 18, 109, 165, 166).

[101] Christian Hilty, Thomas J. Lowery, David E. Wemmer, and Alexander Pines. “Spectrally Resolved Magnetic Resonance Imaging of a Xenon Biosensor.” In: *Angewandte Chemie International Edition* 45.1 (2006), pp. 70–73. DOI: 10.1002/anie.200502693. URL: http://dx.doi.org/10.1002/anie.200502693 (Cited on page 87).

[102] K. Travis Holman. *Encyclopedia of Supramolecular Chemistry*. Cryptophanes: Molecular Containers. Marcel Dekker, Inc: p. 340, 2004. DOI: `10.1081/E-ESMC120012740`. URL: `http://faculty.georgetown.edu/kth7/Research/EncycloSupramolChem_2004_340-348.pdf` (Cited on page 17).

[103] Simon Hu, Michael Lustig, Albert P. Chen, Jason Crane, Adam Kerr, Douglas A.C. Kelley, Ralph Hurd, John Kurhanewicz, Sarah J. Nelson, John M. Pauly, and Daniel B. Vigneron. "Compressed sensing for resolution enhancement of hyperpolarized ^{13}C flyback 3D-MRSI." In: *Journal of Magnetic Resonance* 192.2 (2008), pp. 258–264. DOI: `10.1016/j.jmr.2008.03.003`. URL: `http://www.sciencedirect.com/science/article/pii/S109078070800092X` (Cited on page 93).

[104] Gaspard Huber, Lætitia Beguin, Hervé Desvaux, Thierry Brotin, Heather A. Fogarty, Jean-Pierre Dutasta, and Patrick Berthault. "Cryptophane-Xenon Complexes in Organic Solvents Observed through NMR Spectroscopy." In: *The Journal of Physical Chemistry A* 112.45 (2008), pp. 11363–11372. DOI: `10.1021/jp807425t`. URL: `http://pubs.acs.org/doi/abs/10.1021/jp807425t` (Cited on pages 18, 69, 113, 165).

[105] Gaspard Huber, Thierry Brotin, Lionel Dubois, Hervé Desvaux, Jean-Pierre Dutasta, and Patrick Berthault. "Water Soluble Cryptophanes Showing Unprecedented Affinity for Xenon: Candidates as NMR-Based Biosensors." In: *Journal of the American Chemical Society* 128.18 (2006), pp. 6239–6246. DOI: `10.1021/ja060266r`. URL: `http://pubs.acs.org/doi/abs/10.1021/ja060266r` (Cited on pages 16–19, 151, 165, 167).

[106] Gaspard Huber, François-Xavier Legrand, Véronique Lewin, Delphine Baumann, Marie-Pierre Heck, and Patrick Berthault. "Interaction of Xenon with Cucurbit[5]uril in Water." In: *ChemPhysChem* 12.6 (2011), pp. 1053–1055. DOI: `10.1002/cphc.201100068`. URL: `http://dx.doi.org/10.1002/cphc.201100068` (Cited on pages 148, 165, 167).

[107] Michelle L. James and Sanjiv S. Gambhir. "A Molecular Imaging Primer: Modalities, Imaging Agents, and Applications." In: *Physiological Reviews* 92.2 (2012), pp. 897–965. DOI: `10.1152/physrev.00049.2010`. URL: `http://physrev.physiology.org/content/92/2/897` (Cited on pages 4, 7, 176).

[108] J. Jeener, B. H. Meier, P. Bachmann, and R. R. Ernst. "Investigation of exchange processes by two-dimensional NMR spectroscopy." In: *The Journal of Chemical Physics* 71.11 (1979), pp. 4546–4553. DOI: `10.1063/1.438208`. URL: `http://scitation.aip.org/content/aip/journal/jcp/71/11/10.1063/1.438208` (Cited on page 109).

[109] Craig K. Jones, Alex X. Li, Mojmir Suchy, Robert H. E. Hudson, Ravi S. Menon, and Robert Bartha. "In vivo detection of PARACEST agents with relaxation correction." In: *Magnetic Resonance in Medicine* 63.5 (2010), pp. 1184–1192. DOI: `10.1002/mrm.22340`. URL: `http://dx.doi.org/10.1002/mrm.22340` (Cited on page 11).

[110] Craig K. Jones, Daniel Polders, Jun Hua, He Zhu, Hans J. Hoogduin, Jinyuan Zhou, Peter Luijten, and Peter C. M. van Zijl. "In vivo three-dimensional whole-brain pulsed steady-state chemical exchange saturation transfer at 7 T." In: *Magnetic Resonance in Medicine* 67.6 (2012), pp. 1579–1589. DOI: `10.1002/mrm.23141`. URL: `http://dx.doi.org/10.1002/mrm.23141` (Cited on pages 114, 120).

[111] Akil I. Joseph, Gracia El-Ayle, Céline Boutin, Estelle Léonce, Patrick Berthault, and K. Travis Holman. "Rim-functionalized cryptophane-111 derivatives via heterocapping, and their xenon complexes." In: *Chemical Communications* 50 (100 2014), pp. 15905–15908. DOI: 10.1039/C4CC08001G. URL: http://dx.doi.org/10.1039/C4CC08001G (Cited on page 18).

[112] Song-Yi Jung and Scott T. Willard. "Quantitative bioluminescence imaging of transgene expression in intact porcine antral follicles *in vitro*." In: *Reproductive Biology and Endocrinology* 12.11 (2014), pp. 1–10. DOI: 10.1186/1477-7827-12-11. URL: http://www.rbej.com/content/12/1/11 (Cited on pages 7, 176).

[113] Alfred Kastler. "Quelques suggestions concernant la production optique et la dtection optique d'une inégalité de population des niveaux de quantifigation spatiale des atomes. Application à l'expérience de Stern et Gerlach et à la résonance magnétique." In: *Le Journal de Physique et le Radium* 11.6 (1950), pp. 255–265. DOI: http://dx.doi.org/10.1051/jphysrad:01950001106025500. URL: http://jphysrad.journaldephysique.org/articles/jphysrad/abs/1950/06/jphysrad_1950__11_6_255_0/jphysrad_1950__11_6_255_0.html (Cited on page 31).

[114] Byoung Soo Kim, Young Ho Ko, Youngkook Kim, Hyeong Ju Lee, N. Selvapalam, Hee Cheon Lee, and Kimoon Kim. "Water soluble cucurbit[6]uril derivative as a potential Xe carrier for 129-Xe NMR-based biosensors." In: *Chemical Communications* (24 2008), pp. 2756–2758. DOI: 10.1039/B805724A. URL: http://dx.doi.org/10.1039/B805724A (Cited on pages 109, 149, 154, 165).

[115] Markus Klarhöfer, Markus Barth, and Ewald Moser. "Comparison of multi-echo spiral and echo planar imaging in functional MRI." In: *Magnetic Resonance Imaging* 20.4 (2002), pp. 359–364. DOI: 10.1016/S0730-725X(02)00505-2. URL: http://www.sciencedirect.com/science/article/pii/S0730725X02005052 (Cited on page 105).

[116] Stefan Klippel, Jörg Döpfert, Jabadurai Jayapaul, Martin Kunth, Federica Rossella, Matthias Schnurr, Christopher Witte, Christian Freund, and Leif Schröder. "Cell Tracking with Caged Xenon: Using Cryptophanes as MRI Reporters upon Cellular Internalization." In: *Angewandte Chemie International Edition* 53.2 (2014), pp. 493–496. DOI: 10.1002/anie.201307290. URL: http://dx.doi.org/10.1002/anie.201307290 (Cited on pages 60, 104, 134, 164).

[117] Stefan Klippel, Christian Freund, and Leif Schröder. "Multi-Channel MRI Labeling of Mammalian Cells by Switchable Nanocarriers for Hyperpolarized Xenon." In: *Nano Letters* 14.10 (2014), pp. 5721–5726. DOI: 10.1021/nl502498w. URL: http://dx.doi.org/10.1021/nl502498w (Cited on pages 60, 104, 156, 164, 176).

[118] Sergey Korchak, Wolfgang Kilian, and Lorenz Mitschang. "Degeneracy in cryptophane-xenon complex formation in aqueous solution." In: *Chem. Commun.* 51 (2015), pp. 1721–1724. DOI: 10.1039/C4CC08601E. URL: http://dx.doi.org/10.1039/C4CC08601E (Cited on pages 109, 150, 151).

[119] Vladimir A. Kotelnikov. “On the transmission capacity of “ether” and wire in electrocommunications.” In: *Izd. Red. Upr. Swjasi RKKA* (1933). URL: `http://ict.open.ac.uk/classics/1.pdf` (Cited on page 48).

[120] Naoko Kotera, Nawal Tassali, Estelle Léonce, Céline Boutin, Patrick Berthault, Thierry Brotin, Jean-Pierre Dutasta, Léa Delacour, Ténin Traoré, David-Alexandre Buisson, Frédéric Taran, Sylvie Coudert, and Bernard Rousseau. “A Sensitive Zinc-Activated 129Xe MRI Probe.” In: *Angewandte Chemie International Edition* 51 (2012), pp. 4100–4103. DOI: `10.1002/anie.201109194`. URL: `http://dx.doi.org/10.1002/anie.201109194` (Cited on pages 97, 99, 173).

[121] Martin Kunth, Jörg Döpfert, Christopher Witte, Federica Rossella, and Leif Schröder. “Optimized Use of Reversible Binding for Fast and Selective NMR Localization of Caged Xenon.” In: *Angewandte Chemie International Edition* 51.33 (2012), pp. 8217–8220. ISSN: 1521-3773. DOI: `10.1002/anie.201202481`. URL: `http://dx.doi.org/10.1002/anie.201202481` (Cited on pages 81, 91, 97, 98, 100–102, 106, 124, 134, 176, 221).

[122] Martin Kunth, Jörg Döpfert, Christopher Witte, Federica Rossella, and Leif Schröder. “Schnelle und selektive NMR-spektroskopische Lokalisierung von eingeschlossenem Xenon durch optimales Einbeziehen der reversiblen Bindung.” In: *Angewandte Chemie* 124 (2012), pp. 8341–8344. DOI: `10.1002/anie.201202481`. URL: `http://dx.doi.org/10.1002/anie.201202481` (Cited on pages 106, 221).

[123] Martin Kunth, Jörg Döpfert, Christopher Witte, and Leif Schröder. “Fast and selective MRI of xenon biosensors.” In: *Proceedings of the 20th Annual Meeting of the ISMRM; Melbourne, Australia* 1677 (2012) (Cited on page 99).

[124] Martin Kunth, Jörg Döpfert, Christopher Witte, and Leif Schröder. “Simultaneous MRI Monitoring of Diffusion of Multiple Hyper-CEST Contrast Agents.” In: *Proceedings of the 54th ENC Conference; Pacific Grove, CA, USA* 107 (2013) (Cited on pages 101, 103).

[125] Martin Kunth, Nicole Seiberlich, Philipp Ehses, Vikas Gulani, and Mark Griswold. “Improvement of Quantitative MRI using Radial GRAPPA in Conjunction with IR-TrueFISP.” In: *Proceedings of the 18th Annual Meeting of the ISMRM; Stockholm, Sweden* 2895 (2010) (Cited on pages 105, 109).

[126] Martin Kunth, Christopher Witte, Andreas Hennig, and Leif Schröder. “Identification, classification, and signal amplification capabilities of high-turnover gas binding hosts in ultra-sensitive NMR.” In: *Chemical Science* 6 (2015), pp. 6069–6075. DOI: `10.1039/C5SC01400J`. URL: `http://dx.doi.org/10.1039/C5SC01400J` (Cited on pages 83, 150, 153–155, 158, 160, 165, 167, 170, 176, 285).

[127] Martin Kunth, Christopher Witte, and Leif Schröder. “Continuous-wave saturation considerations for efficient xenon depolarization.” In: *NMR in Biomedicine* 28 (2015), pp. 601–606. DOI: `10.1002/nbm.3307`. URL: `http://dx.doi.org/10.1002/nbm.3307` (Cited on pages 117, 135, 137, 139, 140, 142–145, 154, 156, 158, 159, 163, 165, 176, 269).

[128] Martin Kunth, Christopher Witte, and Leif Schröder. "Fringe field effects on hyperpolarized 129-Xe for a continuous flow SEOP setup." In: *Proceedings of the 20th Annual Meeting of the ISMRM; Melbourne, Australia* 2581 (2012) (Cited on page 80).

[129] Martin Kunth, Christopher Witte, and Leif Schröder. "Quantitative chemical exchange saturation transfer with hyperpolarized nuclei (qHyper-CEST): Sensing xenon-host exchange dynamics and binding affinities by NMR." In: *Journal of Chemical Physics* (2014), p. 194202. DOI: `10.1063/1.4901429`. URL: `http://scitation.aip.org/content/aip/journal/jcp/141/19/10.1063/1.4901429` (Cited on pages 109, 116–118, 123–126, 128, 131, 133, 134, 150, 154, 158, 165, 176, 239).

[130] Jason Lagona, Pritam Mukhopadhyay, Sriparna Chakrabarti, and Lyle Isaacs. "The Cucurbit[n]uril Family." In: *Angewandte Chemie International Edition* 44.31 (2005), pp. 4844–4870. DOI: `10.1002/anie.200460675`. URL: `http://dx.doi.org/10.1002/anie.200460675` (Cited on pages 148, 149, 166).

[131] Jae Wook Lee, S. Samal, N. Selvapalam, Hee-Joon Kim, and Kimoon Kim. "Cucurbituril Homologues and Derivatives: New Opportunities in Supramolecular Chemistry." In: *Accounts of Chemical Research* 36.8 (2003), pp. 621–630. DOI: `10.1021/ar020254k`. URL: `http://pubs.acs.org/doi/abs/10.1021/ar020254k` (Cited on pages 148, 149, 153).

[132] Malcom H. Levitt. *Spin Dynamics*. John Wiley and Sons, LTD, 2005 (Cited on pages 12, 25, 27).

[133] Véronique Lewin, Julie Rivollier, Sylvie Coudert, David-Alexandre Buisson, Delphine Baumann, Bernard Rousseau, François-Xavier Legrand, Hana Kouřilová, Patrick Berthault, Jean-Pierre Dognon, Marie-Pierre Heck, and Gaspard Huber. "Synthesis of Cucurbit[6]uril Derivatives and Insights into Their Solubility in Water." In: *European Journal of Organic Chemistry* 2013.18 (2013), pp. 3857–3865. DOI: `10.1002/ejoc.201300229`. URL: `http://dx.doi.org/10.1002/ejoc.201300229` (Cited on page 149).

[134] Alex X. Li, Robert H.E. Hudson, John W. Barrett, Craig K. Jones, Stephen H. Pasternak, and Robert Bartha. "Four-pool modeling of proton exchange processes in biological systems in the presence of MRI-paramagnetic chemical exchange saturation transfer (PARACEST) agents." In: *Magnetic Resonance in Medicine* 60.5 (2008), pp. 1197–1206. ISSN: 1522-2594. DOI: `10.1002/mrm.21752`. URL: `http://dx.doi.org/10.1002/mrm.21752` (Cited on page 60).

[135] Zhi-Pei Liang and Paul C. Lauterbur. *Principles of Magnetic Resonance Imaging: A Signal Processing Perspective*. 1999 (Cited on page 25).

[136] Wen Ling, Ravinder R. Regatte, Gil Navon, and Alexej Jerschow. "Assessment of glycosaminoglycan concentration in vivo by chemical exchange-dependent saturation transfer (gagCEST)." In: *Proceedings of the National Academy of Sciences* 105.7 (2008), pp. 2266–2270. DOI: `10.1073/pnas.0707666105`. URL: `http://www.pnas.org/content/105/7/2266.abstract` (Cited on page 10).

[137] Guanshu Liu, Qin Qin, Kannie W. Y. Chan, Yuguo Li, Jeff W. M. Bulte, Michael T. McMahon, Peter C. M. van Zijl, and Assaf A. Gilad. "Non-invasive temperature mapping using temperature-responsive water saturation shift referencing (T-WASSR) MRI." In: *NMR in Biomedicine*

27.3 (2014), pp. 320–331. DOI: `10.1002/nbm.3066`. URL: `http://dx.doi.org/10.1002/nbm.3066` (Cited on page 10).

[138] Guanshu Liu, Xiaolei Song, Kannie W. Y. Chan, and Michael T. McMahon. "Nuts and bolts of chemical exchange saturation transfer MRI." In: *NMR in Biomedicine* 26.7 (2013), pp. 810–828. DOI: `10.1002/nbm.2899`. URL: `http://dx.doi.org/10.1002/nbm.2899` (Cited on pages 11, 12, 120).

[139] Michel Luhmer, Boyd M. Goodson, Yi-Qiao Song, David D. Laws, Lana Kaiser, Michelle C. Cyrier, and Alexander Pines. "Study of Xenon Binding in Cryptophane-A Using Laser-Induced NMR Polarization Enhancement." In: *Journal of the American Chemical Society* 121.14 (1999), pp. 3502–3512. DOI: `10.1021/ja9841916`. URL: `http://pubs.acs.org/doi/abs/10.1021/ja9841916` (Cited on page 165).

[140] M. Lustig, D.L. Donoho, J.M. Santos, and J.M. Pauly. "Compressed Sensing MRI." In: *Signal Processing Magazine, IEEE* 25 (2008), pp. 72–82. URL: `http://ieeexplore.ieee.org/xpl/freeabs_all.jsp?arnumber=4472246` (Cited on page 93).

[141] Michael Lustig, David Donoho, and John M. Pauly. "Sparse MRI: The application of compressed sensing for rapid MR imaging." In: *Magnetic Resonance in Medicine* 58.6 (2007), pp. 1182–1195. DOI: `10.1002/mrm.21391`. URL: `http://dx.doi.org/10.1002/mrm.21391` (Cited on page 93).

[142] Dan Ma, Vikas Gulani, Nicole Seiberlich, Kecheng Liu, Jeffrey L. Sunshine, Jeffrey L. Duerk, and Mark A. Griswold. "Magnetic resonance fingerprinting." In: *Nature* 495 (2013), pp. 187–192. DOI: `10.1038/nature11971`. URL: `http://dx.doi.org/10.1038/nature11971` (Cited on page 105).

[143] Prasenjit Mal, David Schultz, Kodiah Beyeh, Kari Rissanen, and Jonathan R. Nitschke. "An Unlockable-Relockable Iron Cage by Subcomponent Self-Assembly." In: *Angewandte Chemie International Edition* 47.43 (2008), pp. 8297–8301. DOI: `10.1002/anie.200803066`. URL: `http://dx.doi.org/10.1002/anie.200803066` (Cited on page 165).

[144] Peter Mansfield. "Multi-planar image formation using NMR spin echoes." In: *Journal of Physics C: Solid State Physics* 10.3 (1977), pp. L55–L58. DOI: `10.1088/0022-3719/10/3/004`. URL: `http://iopscience.iop.org/0022-3719/10/3/004` (Cited on page 46).

[145] G.J. Marseille, R. de Beer, M. Fuderer, A.F. Mehlkopf, and D. van Ormondt. "Nonuniform Phase-Encode Distributions for MRI Scan Time Reduction." In: *Journal of Magnetic Resonance, Series B* 111.1 (1996), pp. 70–75. DOI: `http://dx.doi.org/10.1006/jmrb.1996.0061`. URL: `http://www.sciencedirect.com/science/article/pii/S1064186696900618` (Cited on page 105).

[146] Harden M. McConnell. "Reaction Rates by Nuclear Magnetic Resonance." In: *Journal of Chemical Physics* 28 (1958), pp. 430–431. DOI: `10.1063/1.1744152`. URL: `http://jcp.aip.org/resource/1/jcpsa6/v28/i3/p430_s1` (Cited on pages 21, 58, 108).

[147] Michael T. McMahon, Assaf A. Gilad, Marco A. DeLiso, Stacey M. Cromer Berman, Jeff W. M. Bulte, and Peter C. M. van Zijl. "New "multicolor" polypeptide diamagnetic chemical exchange saturation transfer (DIACEST) contrast agents for MRI." In: *Magnetic Resonance in Medicine* 60.4 (2008), pp. 803–812. DOI: `10.1002/mrm.21683`. URL: `http://dx.doi.org/10.1002/mrm.21683` (Cited on page 10).

[148] Michael T. McMahon, Assaf A. Gilad, Jinyuan Zhou, Phillip Z. Sun, Jeff W. M. Bulte, and Peter C. M. van Zijl. "Quantifying exchange rates in chemical exchange saturation transfer agents using the saturation time and saturation power dependencies of the magnetization transfer effect on the magnetic resonance imaging signal (QUEST and QUESP): Ph calibration for poly-L-lysine and a starburst dendrimer." In: *Magnetic Resonance in Medicine* 55.4 (2006), pp. 836–847. DOI: `10.1002/mrm.20818`. URL: `http://dx.doi.org/10.1002/mrm.20818` (Cited on page 109).

[149] Nevin McVicar, Alex X. Li, Daniela F. Goncalves, Miranda Bellyou, Marco A.M. Meakin Susan O. Prado, and Robert Bartha. "Quantitative tissue pH measurement during cerebral ischemia using amine and amide concentration-independent detection (AACID) with MRI." In: *Journal of Cerebral Blood Flow & Metabolism* 34 (2014), pp. 690–698. DOI: `10.1038/jcbfm.2014.12`. URL: `http://dx.doi.org/10.1038/jcbfm.2014.12` (Cited on page 8).

[150] Sandro Mecozzi and Julius Rebek Jr. "The 55% Solution: A Formula for Molecular Recognition in the Liquid State." In: *Chemistry - A European Journal* 4.6 (1998), pp. 1016–1022. DOI: `10.1002/(SICI)1521-3765(19980615)4:6<1016::AID-CHEM1016>3.0.CO;2-B`. URL: `http://dx.doi.org/10.1002/(SICI)1521-3765(19980615)4:6%3C1016::AID-CHEM1016%3E3.0.CO;2-B` (Cited on pages 148, 166).

[151] Jan-Eric Meißner, Steffen Goerke, Eugenia Rerich, Karel D. Klika, Alexander Radbruch, Mark E. Ladd, Peter Bachert, and Moritz Zaiss. "Quantitative pulsed CEST-MRI using Ω-plots." In: *NMR in Biomedicine* 28.10 (2015), pp. 1196–1208. DOI: `10.1002/nbm.3362`. URL: `http://dx.doi.org/10.1002/nbm.3362` (Cited on pages 120, 134).

[152] Tyler Meldrum, Vikram S. Bajaj, David E. Wemmer, and Alexander Pines. "Band-selective chemical exchange saturation transfer imaging with hyperpolarized xenon-based molecular sensors." In: *Journal of Magnetic Resonance* 213.1 (2011), pp. 14–21. DOI: `10.1016/j.jmr.2011.06.027`. URL: `http://www.sciencedirect.com/science/article/pii/S109078071100214X` (Cited on page 134).

[153] Tyler Meldrum, Leif Schröder, Philipp Denger, David E. Wemmer, and Alexander Pines. "Xenon-based molecular sensors in lipid suspensions." In: *Journal of Magnetic Resonance* 205.2 (2010), pp. 242–246. DOI: `10.1016/j.jmr.2010.05.005`. URL: `http://www.sciencedirect.com/science/article/pii/S1090780710001485` (Cited on pages 130, 155, 164).

[154] Tyler Meldrum, Kristen L. Seim, Vikram S. Bajaj, Krishnan K. Palaniappan, Wesley Wu, Matthew B. Francis, David E. Wemmer, and Alexander Pines. "A Xenon-Based Molecular Sensor Assembled on an MS2 Viral Capsid Scaffold." In: *Journal of the American Chemical Society* 132.17 (2010), pp. 5936–5937. DOI: `10.1021/ja100319f`. URL: `http://pubs.acs.org/doi/abs/10.1021/ja100319f` (Cited on page 170).

[155] Michael M. J. Modo and Jeff W. M. Bulte. *Molecular and Cellular MR Imaging*. CRC Press, Taylor and Francis Group, 2007 (Cited on page 4).

[156] Scott T. Mough, John C. Goeltz, and K. Travis Holman. "Isolation and Structure of an "Imploded" Cryptophane." In: *Angewandte Chemie International Edition* 43.42 (2004), pp. 5631–5635. DOI: `10.1002/anie.200460866`. URL: `http://dx.doi.org/10.1002/anie.200460866` (Cited on page 151).

[157] Kenya Murase and Nobuyoshi Tanki. "Numerical solutions to the time-dependent Bloch equations revisited." In: *Magnetic Resonance Imaging* 29.1 (2011), pp. 126–131. DOI: `10.1016/j.mri.2010.07.003`. URL: `http://www.sciencedirect.com/science/article/pii/S0730725X10002043` (Cited on pages 61, 64, 69, 110–116, 119, 127, 136).

[158] Daniel Neumann, Felix A. Breuer, Michael Völker, Tobias Brandt, Mark A. Griswold, Peter M. Jakob, and Martin Blaimer. "Reducing contrast contamination in radial turbo-spin-echo acquisitions by combining a narrow-band KWIC filter with parallel imaging." In: *Magnetic Resonance in Medicine* 72.6 (2014), pp. 1680–1686. DOI: `10.1002/mrm.25081`. URL: `http://dx.doi.org/10.1002/mrm.25081` (Cited on page 105).

[159] Tomoki Ogoshi, Suguru Kanai, Shuhei Fujinami, Tada-aki Yamagishi, and Yoshiaki Nakamoto. "*para*-Bridged Symmetrical Pillar[5]arenes: Their Lewis Acid Catalyzed Synthesis and Host-Guest Property." In: *Journal of the American Chemical Society* 130.15 (2008), pp. 5022–5023. DOI: `10.1021/ja711260m`. URL: `http://dx.doi.org/10.1021/ja711260m` (Cited on pages 165, 167).

[160] Ana-Maria Oros and N. Jon Shah. "Hyperpolarized xenon in NMR and MRI." In: *Physics in Medicine and Biology* 49.20 (2004), R105. URL: `http://stacks.iop.org/0031-9155/49/i=20/a=R01` (Cited on page 34).

[161] Albert W. Overhauser. "Polarization of Nuclei in Metals." In: *Physical Review* 92 (2 1953), pp. 411–415. DOI: `10.1103/PhysRev.92.411`. URL: `http://link.aps.org/doi/10.1103/PhysRev.92.411` (Cited on page 30).

[162] Krishnan K. Palaniappan, R. Matthew Ramirez, Vikram S. Bajaj, David E. Wemmer, Alexander Pines, and Matthew B. Francis. "Molecular Imaging of Cancer Cells Using a Bacteriophage-Based ^{129}Xe NMR Biosensor." In: *Angewandte Chemie International Edition* 52.18 (2013), pp. 4849–4853. DOI: `10.1002/anie.201300170`. URL: `http://dx.doi.org/10.1002/anie.201300170` (Cited on pages 60, 170).

[163] Tanja Pietraiß and Holly C. Gaede. "Optically Polarized ^{129}Xe in NMR Spectroscopy." In: *Advanced Materials* 7.10 (1995), pp. 826–838. DOI: `10.1002/adma.19950071003`. URL: `http://dx.doi.org/10.1002/adma.19950071003` (Cited on page 12).

[164] David Poole. *Linear Algebra: A Modern Introduction*. 3rd. Brooks/Cole Cengage Learning, 2014 (Cited on page 61).

[165] Klaas P. Pruessmann, Markus Weiger, Markus B. Scheidegger, and Peter Boesiger. "SENSE: Sensitivity encoding for fast MRI." In: *Magnetic Resonance in Medicine* 42.5 (1999), pp. 952–962. DOI: `10.1002/(SICI)1522-2594(199911)42:5<952::AID-MRM16>3.0.CO;2-S`. URL: `http://dx.doi.org/10.1002/(SICI)1522-2594(199911)42:5%3C952::AID-MRM16%3E3.0.CO;2-S` (Cited on page 93).

[166] Edward M. Purcell, Henry C. Torrey, and Robert V. Pound. "Resonance Absorption by Nuclear Magnetic Moments in a Solid." In: *Physical Review* 69 (1-2 1946), pp. 37–38. DOI: `10.1103/PhysRev.69.37`. URL: `http://link.aps.org/doi/10.1103/PhysRev.69.37` (Cited on page 25).

[167] I. I. Rabi, J. R. Zacharias, S. Millman, and P. Kusch. "A New Method of Measuring Nuclear Magnetic Moment." In: *Physical Review* 53 (4 1938), pp. 318–318. DOI: `10.1103/PhysRev.53.318`. URL: `http://link.aps.org/doi/10.1103/PhysRev.53.318` (Cited on page 28).

[168] R. Matthew Ramirez, Todd K. Stevens, Monica A. Smith, David E. Wemmer, and Alexander Pines. "Exchange Dynamics of a Cryptophane-based Xenon Molecular Sensor." In: *Proceedings of ISMRM 19th Annual Meeting, Montreal* 19 (2011), p. 3542 (Cited on page 108).

[169] Brittany A. Riggle, Yanfei Wang, and Ivan J. Dmochowski. "A "Smart" 129-Xe NMR Biosensor for pH-Dependent Cell Labeling." In: *Journal of the American Chemical Society* ja (), null. DOI: `10.1021/jacs.5b01938`. URL: `http://dx.doi.org/10.1021/jacs.5b01938` (Cited on page 134).

[170] Honor M. Rose, Christopher Witte, Federica Rossella, Stefan Klippel, Christian Freund, and Leif Schröder. "Development of an antibody-based, modular biosensor for 129-Xe NMR molecular imaging of cells at nanomolar concentrations." In: *Proceedings of the National Academy of Sciences* 111.32 (2014), pp. 11697–11702. DOI: `10.1073/pnas.1406797111`. URL: `http://www.pnas.org/content/early/2014/07/24/1406797111.abstract` (Cited on pages 104, 134, 156, 164, 170).

[171] Federica Rossella, Honor May Rose, Christopher Witte, Jabadurai Jayapaul, and Leif Schröder. "Design and Characterization of Two Bifunctional Cryptophane A-Based Host Molecules for Xenon Magnetic Resonance Imaging Applications." In: *ChemPlusChem* 79.10 (2014), pp. 1463–1471. DOI: `10.1002/cplu.201402179`. URL: `http://dx.doi.org/10.1002/cplu.201402179` (Cited on page 164).

[172] Juho Roukala, Jianfeng Zhu, Chandan Giri, Kari Rissanen, Perttu Lantto, and Ville-Veikko Telkki. "Encapsulation of Xenon by a Self-Assembled Fe_4L_6 Metallosupramolecular Cage." In: *Journal of the American Chemical Society* 137.7 (2015), pp. 2464–2467. DOI: `10.1021/ja5130176`. URL: `http://dx.doi.org/10.1021/ja5130176` (Cited on pages 109, 130, 165).

[173] Seth M. Rubin, Seok-Yong Lee, E. Janette Ruiz, Alexander Pines, and David E. Wemmer. "Detection and Characterization of Xenon-binding Sites in Proteins by ^{129}Xe NMR Spectroscopy." In: *Journal of Molecular Biology* 322.2 (2002), pp. 425–440. DOI: `http://dx.doi.org/10.1016/S0022-2836(02)00739-8`. URL: `http://www.sciencedirect.com/science/article/pii/S0022283602007398` (Cited on page 14).

[174] Seth M. Rubin, Megan M. Spence, Ivan E. Dimitrov, E. Janette Ruiz, Alexander Pines, and David E. Wemmer. “Detection of a Conformational Change in Maltose Binding Protein by ^{129}Xe NMR Spectroscopy.” In: *Journal of the American Chemical Society* 123 (2001), 8616–8617. DOI: `10.1021/ja0110325`. URL: `http://pubs.acs.org/doi/pdf/10.1021/ja0110325` (Cited on page 14).

[175] Seth M. Rubin, Megan M. Spence, Boyd M. Goodson, David E. Wemmer, and Alexander Pines. “Evidence of nonspecific surface interactions between laser-polarized xenon and myoglobin in solution.” In: *Proceedings of the National Academy of Science* 97 (2000), pp. 9472–9475. DOI: `10.1073/pnas.170278897`. URL: `http://www.pnas.org/content/97/17/9472` (Cited on page 14).

[176] I. C. Ruset, S. Ketel, and F. W. Hersman. “Optical Pumping System Design for Large Production of Hyperpolarized ^{129}Xe.” In: *Physical Review Letters* 96 (5 2006), p. 053002. DOI: `10.1103/PhysRevLett.96.053002`. URL: `http://link.aps.org/doi/10.1103/PhysRevLett.96.053002` (Cited on page 32).

[177] Franz. Schilling, Leif Schröder, Krishnan K. Palaniappan, Sina Zapf, David E. Wemmer, and Alexander Pines. “MRI thermometry based on encapsulated hyperpolarized xenon.” In: *ChemPhysChem* 11 (2010), pp. 3529–3533. DOI: `10.1002/cphc.201000507`. URL: `http://onlinelibrary.wiley.com/doi/10.1002/cphc.201000507/abstract` (Cited on page 130).

[178] Peter Schmitt, Mark A. Griswold, Peter M. Jakob, Markus Kotas, Vikas Gulani, Michael Flentje, and Axel Haase. “Inversion recovery TrueFISP: quantification of T_1, T_2, and spin density.” In: *Magnetic resonance in medicine* 51.4 (2004), pp. 661–667. DOI: `10.1002/mrm.20058` (Cited on page 109).

[179] Matthias Schnurr, Jagoda Sloniec-Myszk, Jörg Döpfert, Leif Schröder, and Andreas Hennig. “Supramolecular Assays for Mapping Enzyme Activity by Displacement-Triggered Change in Hyperpolarized ^{129}Xe Magnetization Transfer NMR Spectroscopy.” In: *Angewandte Chemie International Edition* 54.45 (2015), pp. 13444–13447. DOI: `10.1002/anie.201507002`. URL: `http://dx.doi.org/10.1002/anie.201507002` (Cited on page 167).

[180] Matthias Schnurr, Karl Sydow, Honor May Rose, Margitta Dathe, and Leif Schröder. “Brain Endothelial Cell Targeting Via a Peptide-Functionalized Liposomal Carrier for Xenon Hyper-CEST MRI.” In: *Advanced Healthcare Materials* 4.1 (2015), pp. 40–45. DOI: `10.1002/adhm.201400224`. URL: `http://dx.doi.org/10.1002/adhm.201400224` (Cited on pages 104, 130, 134, 155, 164, 170).

[181] Matthias Schnurr, Christopher Witte, and Leif Schröder. “Depolarization Laplace Transform Analysis of Exchangeable Hyperpolarized ^{129}Xe for Detecting Ordering Phases and Cholesterol Content of Biomembrane Models.” In: *Biophysical Journal* 106.6 (2014), pp. 1301–1308. ISSN: 0006-3495. DOI: `http://dx.doi.org/10.1016/j.bpj.2014.01.041`. URL: `http://www.sciencedirect.com/science/article/pii/S0006349514001441` (Cited on pages 155, 164).

[182] Matthias Schnurr, Christopher Witte, and Leif Schröder. "Functionalized 129-Xe as a potential biosensor for membrane fluidity." In: *Physical Chemistry Chemical Physics* 15 (2013), pp. 14178–14181. DOI: `10.1039/C3CP51227D`. URL: `http://dx.doi.org/10.1039/C3CP51227D` (Cited on pages 60, 104, 130, 155, 161, 164).

[183] Benno P. Schoenborn. "Binding of Xenon to Horse Haemoglobin." In: *Nature* 208.5012 (1965), pp. 760–762. DOI: `10.1038/208760a0`. URL: `http://dx.doi.org/10.1038/208760a0` (Cited on page 14).

[184] Benno P. Schoenborn, Herman C. Watson, and John C. Kendrew. "Binding of Xenon to Sperm Whale Myoglobin." In: *Nature* 207.4992 (1965), pp. 28–30. DOI: `10.1038/207028a0`. URL: `http://dx.doi.org/10.1038/207028a0` (Cited on page 14).

[185] Hans Schreiber and Donald A. Rowley. "Awakening Immunity." In: *Science* 330.6005 (2010), pp. 761–762. DOI: `10.1126/science.1198345`. URL: `http://www.sciencemag.org/content/330/6005/761.short` (Cited on page 3).

[186] Leif Schröder. "Xenon for NMR biosensing – Inert but alert." In: *Physica Medica* 29.1 (2013), pp. 3–16. DOI: `10.1016/j.ejmp.2011.11.001`. URL: `http://www.sciencedirect.com/science/article/pii/S1120179711001384` (Cited on page 12).

[187] Leif Schröder, Thomas J. Lowery, Christian Hilty, David E. Wemmer, and Alexander Pines. "Molecular Imaging Using a Targeted Magnetic Resonance Hyperpolarized Biosensor." In: *Science* 314.5798 (2006), pp. 446–449. DOI: `10.1126/science.1131847`. URL: `http://www.sciencemag.org/content/314/5798/446.abstract` (Cited on pages 19, 20, 87, 134).

[188] Leif Schröder, Christopher Witte, Martin Kunth, Federica Rossella, and Jörg Döpfert. "Improved Production of LASER-Polarized Xenon." In: PCT/EP2012/072114 (8.11.2012). URL: `https://patentscope.wipo.int/search/en/detail.jsf?docId=WO2013068448` (Cited on page 78).

[189] Nicole Seiberlich, Philipp Ehses, Jeff Duerk, Robert Gilkeson, and Mark Griswold. "Improved radial GRAPPA calibration for real-time free-breathing cardiac imaging." In: *Magnetic Resonance in Medicine* 65.2 (2011), pp. 492–505. DOI: `10.1002/mrm.22618`. URL: `http://dx.doi.org/10.1002/mrm.22618` (Cited on page 93).

[190] T. Shah, L. Lu, K. M. Dell, M. D. Pagel, M. A. Griswold, and C. A. Flask. "CEST-FISP: A novel technique for rapid chemical exchange saturation transfer MRI at 7 T." In: *Magnetic Resonance in Medicine* 65 (2011), pp. 432–437. DOI: `10.1002/mrm.22637`. URL: `http://dx.doi.org/10.1002/mrm.22637` (Cited on page 104).

[191] Claude E. Shannon. "Communication In The Presence Of Noise." In: *Proceedings of the IEEE* 86.2 (Feb. 1998), pp. 447–457. ISSN: 0018-9219. DOI: `10.1109/JPROC.1998.659497`. URL: `https://www.ieee.org/publications_standards/publications/proceedings/introduction_shannon.pdf` (Cited on page 48).

[192] Mikhail G. Shapiro, R. Matthew Ramirez, Lindsay J. Sperling, George Sun, Jinny Sun, Alexander Pines, David V. Schaffer, and Vikram S. Bajaj. "Genetically encoded reporters for hyperpolarized xenon magnetic resonance imaging." In: *Nature Chemistry* 6 (2014), pp. 629–634. DOI: 10.1038/nchem.1934. URL: http://dx.doi.org/10.1038/nchem.1934 (Cited on pages 60, 130, 134, 165, 166, 169, 176).

[193] L.A. Shepp and B.F. Logan. "The Fourier reconstruction of a head section." In: *Nuclear Science, IEEE Transactions on* 21.3 (1974), pp. 21–43. DOI: 10.1109/TNS.1974.6499235. URL: http://ieeexplore.ieee.org/xpl/articleDetails.jsp?arnumber=6499235 (Cited on page 94).

[194] A. Dean Sherry and Mark Woods. "Chemical Exchange Saturation Transfer Contrast Agents for Magnetic Resonance Imaging." In: *Annual Review of Biomedical Engineering* 10.1 (2008), pp. 391–411. DOI: 10.1146/annurev.bioeng.9.060906.151929. URL: http://dx.doi.org/10.1146/annurev.bioeng.9.060906.151929 (Cited on page 12).

[195] James Simpson, John Lane, Christopher Immer, and Robert Youngquist. "Simple Analytic Expressions for the Magnetic Field of a Circular Current Loop." In: *NASA-KSC* 10-9800 I (2001), pp. 1–3. URL: http://ntrs.nasa.gov/archive/nasa/casi.ntrs.nasa.gov/20010038494_2001057024.pdf (Cited on page 78).

[196] Jagoda Sloniec, Matthias Schnurr, Christopher Witte, Ute Resch-Genger, Leif Schröder, and Andreas Hennig. "Biomembrane Interactions of Functionalized Cryptophane-A: Combined Fluorescence and ^{129}Xe NMR Studies of a Bimodal Contrast Agent." In: *Chemistry – A European Journal* 19.9 (2013), pp. 3110–3118. DOI: 10.1002/chem.201203773. URL: http://dx.doi.org/10.1002/chem.201203773 (Cited on pages 155, 164).

[197] I. Solomon. "Relaxation Processes in a System of Two Spins." In: *Physical Review* 99 (2 1955), pp. 559–565. DOI: 10.1103/PhysRev.99.559. URL: http://link.aps.org/doi/10.1103/PhysRev.99.559 (Cited on page 58).

[198] Megan M. Spence, Seth M. Rubin, Ivan E. Dimitrov, E. Janette Ruiz, David E. Wemmer, Alexander Pines, Shao Qin Yao, Feng Tian, and Peter G. Schultz. "Functionalized xenon as a biosensor." In: *Proceedings of the National Academy of Sciences* 98.19 (2001), pp. 10654–10657. DOI: 10.1073/pnas.191368398. URL: http://www.pnas.org/content/98/19/10654.abstract (Cited on pages 14–16, 19, 165).

[199] Megan M. Spence, E. Janette Ruiz, Seth M. Rubin, Thomas J. Lowery, Nicolas Winssinger, Peter G. Schultz, David E. Wemmer, and Alexander Pines. "Development of a Functionalized Xenon Biosensor." In: *Journal of the American Chemical Society* 126.46 (2004), pp. 15287–15294. DOI: 10.1021/ja0483037. URL: http://pubs.acs.org/doi/abs/10.1021/ja0483037 (Cited on pages 150, 151).

[200] Todd K. Stevens, R. Matthew Ramirez, and Alexander Pines. "Nanoemulsion Contrast Agents with Sub-picomolar Sensitivity for Xenon NMR." In: *Journal of the American Chemical Society* 135.26 (2013), 9576–9579. DOI: 10.1021/ja402885q. URL: http://pubs.acs.org/doi/abs/10.1021/ja402885q (Cited on pages 60, 108, 129, 130, 134, 165, 169).

[201] Phillip Zhe Sun. “Simplified and scalable numerical solution for describing multi-pool chemical exchange saturation transfer (CEST) MRI contrast.” In: *Journal of Magnetic Resonance* 205.2 (2010), pp. 235–241. DOI: `10.1016/j.jmr.2010.05.004`. URL: `http://www.sciencedirect.com/science/article/pii/S1090780710001473` (Cited on page 60).

[202] Phillip Zhe Sun. “Simplified quantification of labile proton concentration-weighted chemical exchange rate (k_{ws}) with RF saturation time dependent ratiometric analysis (QUESTRA): Normalization of relaxation and RF irradiation spillover effects for improved quantitative chemical exchange saturation transfer (CEST) MRI.” In: *Magnetic Resonance in Medicine* 67.4 (2012), pp. 936–942. DOI: `10.1002/mrm.23068`. URL: `http://dx.doi.org/10.1002/mrm.23068` (Cited on page 138).

[203] Phillip Zhe Sun, Thomas Benner, William A. Copen, and A. Gregory Sorensen. “Early Experience of Translating pH-Weighted MRI to Image Human Subjects at 3 Tesla.” In: *Stroke* 41.10 (2010), S147–S151. DOI: `10.1161/STROKEAHA.110.595777`. URL: `http://stroke.ahajournals.org/content/41/10_suppl_1/S147.abstract` (Cited on page 10).

[204] Phillip Zhe Sun, Christian T. Farrar, and A. Gregory Sorensen. “Correction for artifacts induced by B_0 and B_1 field inhomogeneities in pH-sensitive chemical exchange saturation transfer (CEST) imaging.” In: *Magnetic Resonance in Medicine* 58.6 (2007), pp. 1207–1215. DOI: `10.1002/mrm.21398`. URL: `http://dx.doi.org/10.1002/mrm.21398` (Cited on page 123).

[205] Phillip Zhe Sun, Yu Wang, ZhuoZhi Dai, Gang Xiao, and Renhua Wu. “Quantitative chemical exchange saturation transfer (qCEST) MRI - RF spillover effect-corrected omega plot for simultaneous determination of labile proton fraction ratio and exchange rate.” In: *Contrast Media & Molecular Imaging* 9.4 (2014), pp. 268–275. DOI: `10.1002/cmmi.1569`. URL: `http://dx.doi.org/10.1002/cmmi.1569` (Cited on page 119).

[206] Phillip Zhe Sun, Jinyuan Zhou, Weiyun Sun, Judy Huang, and Peter C. M. van Zijl. “Detection of the ischemic penumbra using pH-weighted MRI.” In: *Journal of Cerebral Blood Flow and Metabolism* 27.6 (2007), pp. 1129–1136. DOI: `10.1038/sj.jcbfm.9600424`. URL: `http://dx.doi.org/10.1038/sj.jcbfm.9600424` (Cited on page 10).

[207] Olena Taratula, P. Aru Hill, Najat S. Khan, Patrick J Carroll, and Ivan J. Dmochowski. “Crystallographic observation of ’induced fit’ in a cryptophane host-guest model system.” In: *Nature Communications* 1 (2010), p. 148. DOI: `10.1038/ncomms1151`. URL: `http://dx.doi.org/10.1038/ncomms1151` (Cited on page 151).

[208] Nawal Tassali, Naoko Kotera, Céline Boutin, Estelle Léonce, Yves Boulard, Bernard Rousseau, Emmanuelle Dubost, Frédéric Taran, Thierry Brotin, Jean-Pierre Dutasta, and Patrick Berthault. “Smart Detection of Toxic Metal Ions, Pb^{2+} and Cd^{2+}, Using a 129-Xe NMR-Based Sensor.” In: *Analytical Chemistry* 86.3 (2014), pp. 1783–1788. DOI: `10.1021/ac403669p`. URL: `http://pubs.acs.org/doi/abs/10.1021/ac403669p` (Cited on pages 104, 134).

[209] Enzo Terreno, Claudia Cabella, Carla Carrera, Daniela Delli Castelli, Roberta Mazzon, Simona Rollet, Joseph Stancanello, Massimo Visigalli, and Silvio Aime. “From Spherical to Osmotically Shrunken Paramagnetic Liposomes: An Improved Generation of LIPOCEST MRI Agents with Highly Shifted Water Protons.” In: *Angewandte Chemie International Edition* 46.6 (2007), pp. 966–968. doi: 10.1002/anie.200604027. url: http://dx.doi.org/10.1002/anie.200604027 (Cited on page 11).

[210] Henry C. Torrey. “Bloch Equations with Diffusion Terms.” In: *Physical Review* 104 (3 1956), pp. 563–565. doi: 10.1103/PhysRev.104.563. url: http://link.aps.org/doi/10.1103/PhysRev.104.563 (Cited on pages 58, 108, 129).

[211] Ténin Traoré, Guillaume Clavé, Léa Delacour, Naoko Kotera, Pierre-Yves Renard, Anthony Romieu, Patrick Berthault, Céline Boutin, Nawal Tassali, and Bernard Rousseau. “The first metal-free water-soluble cryptophane-111.” In: *Chemical Communications* 47 (34 2011), pp. 9702–9704. doi: 10.1039/C1CC13378K. url: http://dx.doi.org/10.1039/C1CC13378K (Cited on page 18).

[212] Oleg Trott, Daniel Abergel, and Athur G. Palmer III. “An average-magnetization analysis of $R_{1\rho}$ relaxation outside of the fast exchange limit.” In: *Molecular Physics* 101.6 (2003), pp. 753–763. doi: 10.1080/0026897021000054826. url: http://dx.doi.org/10.1080/0026897021000054826 (Cited on page 68).

[213] Oleg Trott and Arthur G. Palmer III. “$R_{1\rho}$ Relaxation outside of the Fast-Exchange Limit.” In: *Journal of Magnetic Resonance* 154.1 (2002), pp. 157–160. doi: http://dx.doi.org/10.1006/jmre.2001.2466. url: http://www.sciencedirect.com/science/article/pii/S1090780701924668 (Cited on page 68).

[214] Oleg Trott and Arthur G. Palmer III. “Theoretical study of $R_{1\rho}$ rotating-frame and R_2 free-precession relaxation in the presence of n-site chemical exchange.” In: *Journal of Magnetic Resonance* 170.1 (2004), pp. 104–112. doi: http://dx.doi.org/10.1016/j.jmr.2004.06.005. url: http://www.sciencedirect.com/science/article/pii/S1090780704001752 (Cited on pages 60, 68).

[215] Chi-Ming Tsai and Dwight G. Nishimura. “Reduced aliasing artifacts using variable-density k-space sampling trajectories.” In: *Magnetic Resonance in Medicine* 43.3 (2000), pp. 452–458. doi: 10.1002/(SICI)1522-2594(200003)43:3<452::AID-MRM18>3.0.CO;2-B. url: http://dx.doi.org/10.1002/(SICI)1522-2594(200003)43:3%3C452::AID-MRM18%3E3.0.CO;2-B (Cited on page 105).

[216] Rahul Tyagi, Christopher Witte, Rainer Haag, and Leif Schröder. “Dendronized Cryptophanes as Water-Soluble Xenon Hosts for ^{129}Xe Magnetic Resonance Imaging.” In: *Organic Letters* 16.17 (2014), pp. 4436–4439. doi: 10.1021/ol501951z. url: http://dx.doi.org/10.1021/ol501951z (Cited on page 164).

[217] Vanya D. Uzunova, Carleen Cullinane, Klaudia Brix, Werner M. Nau, and Anthony I. Day. “Toxicity of cucurbit[7]uril and cucurbit[8]uril: an exploratory *in vitro* and *in vivo* study.” In: *Organic & Biomolecular Chemistry* 8.9 (2010), pp. 2037–2042. doi: 10.1039/B925555A. url: http://dx.doi.org/10.1039/B925555A (Cited on page 148).

[218] G. Varma, R. E. Lenkinski, and E. Vinogradov. "Keyhole chemical exchange saturation transfer." In: *Magnetic Resonance in Medicine* 68.4 (2012), pp. 1228–1233. DOI: `10.1002/mrm.23310`. URL: `http://dx.doi.org/10.1002/mrm.23310` (Cited on page 177).

[219] Magalie Viallon, Yves Berthezene, Virginie Callot, Marc Bourgeois, Hubert Humblot, André Briguet, and Yannick Crémillieux. "Dynamic imaging of hyperpolarized ^{3}He distribution in rat lungs using interleaved-spiral scans." In: *NMR in Biomedicine* 13.4 (2000), pp. 207–213. DOI: `10.1002/1099-1492(200006)13:4<207::AID-NBM641>3.0.CO;2-G`. URL: `http://dx.doi.org/10.1002/1099-1492(200006)13:4%3C207::AID-NBM641%3E3.0.CO;2-G` (Cited on page 105).

[220] Elena Vinogradov, A. Dean Sherry, and Robert E. Lenkinski. "CEST: From basic principles to applications, challenges and opportunities." In: *Journal of Magnetic Resonance* 229 (2013), pp. 155–172. DOI: `10.1016/j.jmr.2012.11.024`. URL: `http://www.sciencedirect.com/science/article/pii/S1090780712003680` (Cited on pages 12, 120, 142).

[221] Michael Völker, Philipp Ehses, Stefan Weick, Felix Arno Breuer, Martin Blaimer, Christian Hintze, Jürgen Biederer, and Peter Michael Jakob. "Free breathing ^{1}H MRI of the human lung with an improved radial turbo spin-echo." In: *Magnetic Resonance Materials in Physics, Biology and Medicine* 28.3 (2015), pp. 227–238. DOI: `10.1007/s10334-014-0468-x`. URL: `http://dx.doi.org/10.1007/s10334-014-0468-x` (Cited on page 105).

[222] Volker Wagner and Dietmar Wechsler. "Nanobiotechnologie II: Anwendungen in der Medizin und Pharmazie." In: *VDI Technologiezentrum* (2004), pp. 1–194. URL: `http://www.vditz.de/fileadmin/media/publications/pdf/50.pdf` (Cited on page 3).

[223] Thad G. Walker and William Happer. "Spin-exchange optical pumping of noble-gas nuclei." In: *Reviews of Modern Physics* 69 (2 1997), pp. 629–642. DOI: `10.1103/RevModPhys.69.629`. URL: `http://link.aps.org/doi/10.1103/RevModPhys.69.629` (Cited on pages 13, 30–32).

[224] Simon Walker-Samuel, Rajiv Ramasawmy, Francisco Torrealdea, Marilena Rega, Vineeth Rajkumar, S. Peter Johnson, Simon Richardson, Miguel Goncalves, Harold G. Parkes, Erik Årstad, David L. Thomas, R. Barbara Pedley, Mark F. Lythgoe, and Xavier Golay. "*In vivo* imaging of glucose uptake and metabolism in tumors." In: *Nature Medicine* 19.8 (2013), pp. 1067–1072. DOI: `10.1038/nm.3252`. URL: `http://dx.doi.org/10.1038/nm.3252` (Cited on page 10).

[225] Yanfei Wang and Ivan J. Dmochowski. "Cucurbit[6]uril is an ultrasensitive ^{129}Xe NMR contrast agent." In: *Chemical Communcations* 51 (43 2015), pp. 8982–8985. DOI: `10.1039/C5CC01826A`. URL: `http://dx.doi.org/10.1039/C5CC01826A` (Cited on pages 134, 167).

[226] K. M. Ward, A. H. Aletras, and R. S. Balaban. "A New Class of Contrast Agents for MRI Based on Proton Chemical Exchange Dependent Saturation Transfer (CEST)." In: *Journal of Magnetic Resonance* 143.1 (2000), pp. 79–87. DOI: `10.1006/jmre.1999.1956`. URL: `http://www.sciencedirect.com/science/article/pii/S1090780799919560` (Cited on page 9).

[227] Ralph Weissleder. "Molecular Imaging in Cancer." In: *Science* 312.5777 (2006), pp. 1168–1171. DOI: 10.1126/science.1125949. URL: http://www.sciencemag.org/content/312/5777/1168.abstract (Cited on page 4).

[228] Ralph Weissleder and Umar Mahmood. "Molecular Imaging." In: *Radiology* 219.2 (2001), pp. 316–333. DOI: 10.1148/radiology.219.2.r01ma19316. URL: http://dx.doi.org/10.1148/radiology.219.2.r01ma19316 (Cited on page 4).

[229] Edmund T. Whittaker. "On the Functions which are represented by the Expansions of the Interpolation-Theory." In: *Proceedings of the Royal Society of Edinburgh* 35 (Jan. 1915), pp. 181–194. DOI: 10.1017/S0370164600017806. URL: http://journals.cambridge.org/article_S0370164600017806 (Cited on page 48).

[230] Christopher Witte, Martin Kunth, Jörg Döpfert, Federica Rossella, and Leif Schröder. "Hyperpolarized Xenon for NMR and MRI Applications." In: *Journal of Visualized Experiments* 67 (2012), e4268. DOI: 10.3791/4268. URL: http://www.jove.com/video/4268/hyperpolarized-xenon-for-nmr-and-mri-applications (Cited on page 99).

[231] Christopher Witte, Martin Kunth, Federica Rossella, and Leif Schröder. "Observing and preventing rubidium runaway in a direct-infusion xenon-spin hyperpolarizer optimized for high-resolution Hyper-CEST (chemical exchange saturation transfer using hyperpolarized nuclei) NMR." In: *The Journal of Chemical Physics* 140.8, 084203 (2014), p. 084203. DOI: 10.1063/1.4865944. URL: http://scitation.aip.org/content/aip/journal/jcp/140/8/10.1063/1.4865944 (Cited on pages 13, 32, 78, 99).

[232] Christopher Witte, Vera Martos, Honor May Rose, Stefan Reinke, Stefan Klippel, Leif Schröder, and Christian P. R. Hackenberger. "Live-cell MRI with Xenon Hyper-CEST Biosensors Targeted to Metabolically Labeled Cell-Surface Glycans." In: *Angewandte Chemie International Edition* 54.9 (2015), pp. 2806–2810. DOI: 10.1002/anie.201410573. URL: http://dx.doi.org/10.1002/anie.201410573 (Cited on pages 104, 134, 156, 164).

[233] Christopher Witte and Leif Schröder. "NMR of hyperpolarised probes." In: *NMR in Biomedicine* 26 (2012), pp. 788–802. DOI: 10.1002/nbm.2873. URL: http://dx.doi.org/10.1002/nbm.2873 (Cited on pages 30, 31).

[234] Donald E. Woessner, Shanrong Zhang, Matthew E. Merritt, and A. Dean Sherry. "Numerical solution of the Bloch equations provides insights into the optimum design of PARACEST agents for MRI." In: *Magnetic Resonance in Medicine* 53.4 (2005), pp. 790–799. DOI: 10.1002/mrm.20408. URL: http://dx.doi.org/10.1002/mrm.20408 (Cited on pages 61, 63, 64, 69, 110–113).

[235] Jan Wolber, Simon J. Doran, Martin O. Leach, and Angelo Bifone. "Measuring diffusion of xenon in solution with hyperpolarized ^{129}Xe {NMR}." In: *Chemical Physics Letters* 296.3-4 (1998), pp. 391–396. DOI: http://dx.doi.org/10.1016/S0009-2614(98)01050-1. URL: http://www.sciencedirect.com/science/article/pii/S0009261498010501 (Cited on page 34).

[236] Jan Wolber, Ian J. Rowland, Martin O. Leach, and Angelo Bifone. "Perfluorocarbon emulsions as intravenous delivery media for hyperpolarized xenon." In: *Magnetic Resonance in Medicine* 41.3 (1999), pp. 442–449. DOI: `10.1002/(SICI)1522-2594(199903)41:3<442::AID-MRM3>3.0.CO;2-7`. URL: `http://dx.doi.org/10.1002/(SICI)1522-2594(199903)41:3%3C442::AID-MRM3%3E3.0.CO;2-7` (Cited on pages 34, 60).

[237] Mark Woods, Donald E. Woessner, and A. Dean Sherry. "Paramagnetic lanthanide complexes as PARACEST agents for medical imaging." In: *Chemical Society Reviews* 35 (6 2006), pp. 500–511. DOI: `10.1039/B509907M`. URL: `http://dx.doi.org/10.1039/B509907M` (Cited on page 12).

[238] Qing X. Yang, Stefan Posse, Denis Le Bihan, and Michael B. Smith. "Double-Sampled Echo-Planar Imaging at 3 Tesla." In: *Journal of Magnetic Resonance, Series B* 113.2 (1996), pp. 145–150. ISSN: 1064-1866. DOI: `10.1006/jmrb.1996.0167`. URL: `http://www.sciencedirect.com/science/article/pii/S1064186696901673` (Cited on pages 47, 95).

[239] Byunghee Yoo and Marty D. Pagel. "A PARACEST MRI Contrast Agent To Detect Enzyme Activity." In: *Journal of the American Chemical Society* 128.43 (2006), pp. 14032–14033. DOI: `10.1021/ja063874f`. URL: `http://dx.doi.org/10.1021/ja063874f` (Cited on page 11).

[240] Byunghee Yoo, Manu S. Raam, Rachel M. Rosenblum, and Mark D. Pagel. "Enzyme-responsive PARACEST MRI contrast agents: a new biomedical imaging approach for studies of the proteasome." In: *Contrast Media & Molecular Imaging* 2.4 (2007), pp. 189–198. DOI: `10.1002/cmmi.145`. URL: `http://dx.doi.org/10.1002/cmmi.145` (Cited on page 11).

[241] Stephen R. Yutzy, Nicole Seiberlich, Jeffrey L. Duerk, and Mark A. Griswold. "Improvements in multislice parallel imaging using radial CAIPIRINHA." In: *Magnetic Resonance in Medicine* 65.6 (2011), pp. 1630–1637. DOI: `10.1002/mrm.22752`. URL: `http://dx.doi.org/10.1002/mrm.22752` (Cited on page 105).

[242] Moritz Zaiss and Peter Bachert. "Chemical exchange saturation transfer (CEST) and MR Z-spectroscopy in vivo: a review of theoretical approaches and methods." In: *Physics in Medicine and Biology* 58.22 (2013), R221. DOI: `10.1088/0031-9155/58/22/R221`. URL: `http://stacks.iop.org/0031-9155/58/i=22/a=R221` (Cited on pages 12, 68, 138).

[243] Moritz Zaiss and Peter Bachert. "Exchange-dependent relaxation in the rotating frame for slow and intermediate exchange – modeling off-resonant spin-lock and Chemical Exchange saturation transfer." In: *NMR in Biomedicine* 26.5 (2013), pp. 507–518. ISSN: 1099-1492. DOI: `10.1002/nbm.2887`. URL: `http://dx.doi.org/10.1002/nbm.2887` (Cited on page 138).

[244] Moritz Zaiss, Matthias Schnurr, and Peter Bachert. "Analytical solution for the depolarization of hyperpolarized nuclei by chemical exchange saturation transfer between free and encapsulated xenon (HyperCEST)." In: *The Journal of Chemical Physics* 136.14, 144106 (2012), p. 144106. DOI: `10.1063/1.3701178`. URL: `http://link.aip.org/`

link/?JCP/136/144106/1 (Cited on pages 68, 72, 110–113, 116, 137, 139, 144).

[245] Moritz Zaiss, Junzhong Xu, Steffen Goerke, Imad S. Khan, Robert J. Singer, John C. Gore, Daniel F. Gochberg, and Peter Bachert. "Inverse Z-spectrum analysis for spillover-, MT-, and T_1-corrected steady-state pulsed CEST-MRI – application to pH-weighted MRI of acute stroke." In: *NMR in Biomedicine* 27.3 (2014), pp. 240–252. DOI: 10.1002/nbm.3054. URL: http://dx.doi.org/10.1002/nbm.3054 (Cited on page 10).

[246] Pieter Zeeman. "The Effect of Magnetisation on the Nature of Light Emitted by a Substance." In: *Nature* 55.1424 (1897), pp. 347–347. DOI: 10.1038/055347a0. URL: http://www.nature.com/nature/journal/v55/n1424/abs/055347a0.html (Cited on page 28).

[247] S. Zhang, P. Winter, K. Wu, and A.D. Sherry. "A novel europium(III)-based MRI contrast agent." In: *Journal of the American Chemical Society* 123 (2001), pp. 1517–1518. DOI: 10.1021/ja005820q. URL: http://dx.doi.org/10.1021/ja005820q (Cited on page 11).

[248] Shanrong Zhang, Craig R. Malloy, and A. Dean Sherry. "MRI Thermometry Based on PARACEST Agents." In: *Journal of the American Chemical Society* 127.50 (2005), pp. 17572–17573. DOI: 10.1021/ja053799t. URL: http://dx.doi.org/10.1021/ja053799t (Cited on page 11).

[249] Shanrong Zhang, Matthew Merritt, Donald E. Woessner, Robert E. Lenkinski, and A. Dean Sherry. "PARACEST Agents: Modulating MRI Contrast via Water Proton Exchange." In: *Accounts of Chemical Research* 36.10 (2003), pp. 783–790. DOI: 10.1021/ar020228m. URL: http://dx.doi.org/10.1021/ar020228m (Cited on pages 10, 12).

[250] Shanrong Zhang, Kuangcong Wu, and A. Dean Sherry. "Unusually Sharp Dependence of Water Exchange Rate versus Lanthanide Ionic Radii for a Series of Tetraamide Complexes." In: *Journal of the American Chemical Society* 124.16 (2002), pp. 4226–4227. DOI: 10.1021/ja017133k. URL: http://dx.doi.org/10.1021/ja017133k (Cited on page 11).

[251] Jianzhang Zhao, Hee-Joon Kim, Jinho Oh, Soo-Young Kim, Jae Wook Lee, Shigeru Sakamoto, Kentaro Yamaguchi, and Kimoon Kim. "Cucurbit[n]uril Derivatives Soluble in Water and Organic Solvents." In: *Angewandte Chemie International Edition* 40.22 (2001), pp. 4233–4235. DOI: 10.1002/1521-3773(20011119)40:22<4233::AID-ANIE4233>3.0.CO;2-D. URL: http://dx.doi.org/10.1002/1521-3773(20011119)40:22%3C4233::AID-ANIE4233%3E3.0.CO;2-D (Cited on pages 149, 154).

[252] L. Zhao, A.K. Venkatesh, D. Balamore, F.A. Jolesz, and Albert M. In: *6th Proc. ISMRM Sydney, Australia* (1998) (Cited on page 34).

[253] Lei Zhao, Robert Mulkern, Ching-Hua Tseng, Daniel Williamson, Samuel Patz, Robert Kraft, Ronald Walsworth, Ferenc A. Jolesz, and Mitchell S. Albert. "Gradient-Echo Imaging Considerations for hyperpolarized 129-Xe MR." In: *Journal of Magnetic Resonance, Series B* 113.2 (Nov. 1996), pp. 179–183. URL: http://www.cfa.harvard.edu/Walsworth/pdf/Zhao_gradecho.pdf (Cited on pages 45, 89).

[254] Xuna Zhao, Zhibo Wen, Fanheng Huang, Shilong Lu, Xianlong Wang, Shuguang Hu, Donglin Zu, and Jinyuan Zhou. "Saturation power dependence of amide proton transfer image contrasts in human brain tumors and strokes at 3 T." In: *Magnetic Resonance in Medicine* 66.4 (2011), pp. 1033–1041. DOI: `10.1002/mrm.22891`. URL: `http://dx.doi.org/10.1002/mrm.22891` (Cited on page 10).

[255] Jinyuan Zhou, Bachchu Lal, David A. Wilson, John Laterra, and Peter C.M. van Zijl. "Amide proton transfer (APT) contrast for imaging of brain tumors." In: *Magnetic Resonance in Medicine* 50.6 (2003), pp. 1120–1126. DOI: `10.1002/mrm.10651`. URL: `http://dx.doi.org/10.1002/mrm.10651` (Cited on page 10).

[256] Jinyuan Zhou, Jean-Francois Payen, David A. Wilson, Richard J. Traystman, and Peter C. M. van Zijl. "Using the amide proton signals of intracellular proteins and peptides to detect pH effects in MRI." In: *Nature Medicine* 9 (2003), pp. 1085–1090. DOI: `10.1038/nm907`. URL: `http://dx.doi.org/10.1038/nm907` (Cited on page 10).

[257] Jinyuan Zhou, David A. Wilson, Phillip Zhe Sun, Judith A. Klaus, and Peter C.M. van Zijl. "Quantitative description of proton exchange processes between water and endogenous and exogenous agents for WEX, CEST, and APT experiments." In: *Magnetic Resonance in Medicine* 51.5 (2004), pp. 945–952. DOI: `10.1002/mrm.20048`. URL: `http://dx.doi.org/10.1002/mrm.20048` (Cited on pages 67, 69, 109).

[258] Jinyuan Zhou and Peter C. M. van Zijl. "Chemical exchange saturation transfer imaging and spectroscopy." In: *Progress in Nuclear Magnetic Resonance Spectroscopy* 48.2-3 (2006), pp. 109–136. DOI: `10.1016/j.pnmrs.2006.01.001`. URL: `http://www.sciencedirect.com/science/article/pii/S0079656506000033` (Cited on pages 10, 12, 67, 69).

[259] Peter C. M. van Zijl, Craig K. Jones, Jimin Ren, Craig R. Malloy, and A. Dean Sherry. "MRI detection of glycogen *in vivo* by using chemical exchange saturation transfer imaging (glycoCEST)." In: *Proceedings of the National Academy of Sciences* 104.11 (2007), pp. 4359–4364. DOI: `10.1073/pnas.0700281104`. URL: `http://www.pnas.org/content/104/11/4359.abstract` (Cited on page 10).

[260] Peter C. M. van Zijl and Nirbhay N. Yadav. "Chemical exchange saturation transfer (CEST): What is in a name and what isn't?" In: *Magnetic Resonance in Medicine* 65.4 (2011), pp. 927–948. DOI: `10.1002/mrm.22761`. URL: `http://dx.doi.org/10.1002/mrm.22761` (Cited on pages 10, 12, 126).

Part VI

Appendix

A ACKNOWLEDGEMENTS

First of all I thank my supervisors Dr. Leif Schöder and Prof. Dr. Joachim Heberle for their excellent intellectual and personal support.

I would like to thank Dr. Leif Schöder in particular for providing an outstanding research facility and inspiring working atmosphere. He always contributed to my work with smart and brilliant ideas. I learned from him how passioned and beautiful research is. He made it possible that I could show my work at national and international conferences in Europe, Australia, USA and Asia. I further like to thank Prof. Dr. Joachim Heberle for his confidence. His enthusiasms into my research project was always stimulating.

I am deeply grateful to the ”Team Biosensor” for the extraordinary atmosphere I was supported with throughout the entire project including: Dr. Honor May Rose, Dr. Christopher Witte, Dr. Jabadurai Jayapaul and Dr. Jan-Oliver Jost as well as Dr. Jörg Döpfert, Dr. Matthias Schnurr, Dr. Stefan Klippel and Dr. Federica Rossella. I will always remember our great time that we had at conferences, during work, in the office, the lab and beyond.

In particular, I would like to thank Chris. He was my mentor during the entire project and he taught me to think different and independently. Without his endless enthusiasm and contributions of knowledge, this work would have been impossible. A special thank goes to Jörg with whom I had fantastic times in the lab, working on single-shot sequences, diffusion, multiplexing, smashCEST, radial, compressed sensing, and org-mode.

A further special thank goes to Dr. B”**art**”h-Jan van Rossum for this beautiful cover. I would also like to thank Dr. Andreas Hennig for the fantastic cooperation. He provided pure cucurbit[6]uril in the right spot at the right time.

I would like to thank all members of the FMP for helping with new devices or techniques, paperwork and the IT. The guys from the machine shop in particular because they made lots of custom-designed devices for our polarizer.

For enabling me to represent my work also internationally, I am grateful for funding by the German Academic Exchange Service (DAAD), and World Molecular Imaging Congress (WMIC).

Finally, I would like to thank Dr. Christopher Witte and Dr. Jan-Oliver Jost for proof reading this thesis very carefully.

Outside the MR world, I would like to thank my physics teacher during high school, Peter Dammann, for his very inspiring lessons (for life), especially about Brownian motion. I highly enjoyed his intuitive contact with physics and his gift for education. A very special thank goes to my friends who are always welcoming me after I was working in the lab for longer. Thank you for your invaluable support and the great laughing time we share together. Finally, my deepest and most grateful thank goes to my family for their unquestioning trust, help and support during my entire life. Truly, it is hard to express my thankfulness with words. This thesis is dedicated to you.

Thank you all.

B CURRICULUM VITAE

The curriculum vitae is omitted in this electronic version for reasons of data privacy.

C

LIST OF PUBLICATIONS

PEER-REVIEWED JOURNAL PUBLICATIONS

1. **Martin Kunth**, Christopher Witte, Andreas Hennig, Leif Schröder: Identification, classification, and signal amplification capabilities of high-turnover gas binding hosts in ultra-sensitive NMR, *Chemical Science* **6**:6069-6075 (2015)
   (highlighted as front cover article)

2. **Martin Kunth**, Christopher Witte, Leif Schröder: Continuous-wave saturation considerations for efficient xenon depolarization, *NMR in Biomedicine* **28**:601-606 (2015)

3. **Martin Kunth**, Christopher Witte, Leif Schröder: Quantitative chemical exchange saturation transfer with hyperpolarized nuclei (qHyper-CEST): Sensing xenon-host exchange dynamics and binding affinities by NMR, *Journal of Chemical Physics* **141**:194202 (2014)

4. Christopher Witte, **Martin Kunth**, Jörg Döpfert, Federica Rossella, Leif Schröder: Observing and preventing rubidium runaway in a direct-infusion xenon-spin hyperpolarizer optimized for high-resolution Hyper-CEST NMR, *Journal of Chemical Physics* **140**:084203 (2014)

5. Stefan Klippel, Jörg Döpfert, Jabadurai Jayapaul, **Martin Kunth**, Federica Rossella, Matthias Schnurr, Christopher Witte, Leif Schröder, Christian Freund: Xenon Based Hyper-CEST-MRI of Cryptophane Labeled Cells, *Angewande Chemie International Edition* **53**:493–496 (2014)
   (highlighted as back cover article; Back Cover: *Angew. Chem. Int. Ed.*, **53**:600-600, 2014 – Reprinted with permission. Copyright © 2014 WILEY-VCH Verlag GmbH & Co. KGaA, Weinheim.)

6. Jörg Döpfert, Christopher Witte, **Martin Kunth**, Leif Schröder: Sensitivity Enhancement of (Hyper-)CEST Image Series by Exploiting Redundancies in the Spectral Domain, *Contrast Media & Molecular Imaging* **9**:100–107 (2014)

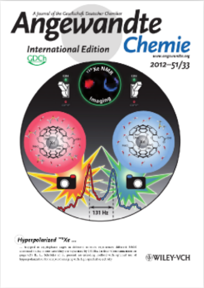

7. **Martin Kunth***, Jörg Döpfert*, Christopher Witte, Federica Rossella, Leif Schröder: Optimized use of reversible binding for fast and selective NMR localization of caged xenon, *Angewande Chemie International Edition* **51**(33):8217–8220 (2012); *Angewande Chemie* **124**:8341–8344 (2012), *contributed equally.
   (highlighted as 'hot paper' by editors, inside back cover article and honored with Gorter-Award)

8. Christopher Witte, **Martin Kunth**, Jörg Döpfert, Federica Rossella, Leif Schröder: Hyperpolarized Xenon for NMR and MRI Applications, *Journal of Visualized Experiments* **67**:e4268 (2012)

9. Alexander Ziegler, **Martin Kunth**, Susanne Müller, Christian Bock, Rolf Pohmann, Leif Schröder, Cornelius Faber, Gonzalo Giribet: Ap-

plication of magnetic resonance imaging in zoology, *Zoomorphology* **130**(4):227–254 (2011)

CONFERENCE CONTRIBUTIONS

1. **Martin Kunth**, Christopher Witte, Andreas Hennig, Leif Schröder: Impact of Gas Turnover Rate for Improving Hyper-CEST Sensitivity in Xe Biosensor MRI, XeMAT Conference 2015, Dresden, Germany (2015)
2. **Martin Kunth**, Christopher Witte, Jörg Döpfert, Leif Schröder: Determination of Absolute Xenon-Host Concentration by Quantitative ^{129}Xe MRI Using Hyper-CEST, # 1992846, WMIC 2014 – World Molecular Imaging Congress, Seoul, Korea (2014)
3. **Martin Kunth**, Christopher Witte, Jörg Döpfert, Leif Schröder: Xenon Exchange Rate Determination for Cryptophane-A in Water Using Hyper-CEST, #115, CEST 2014 – 4th International Workshop on Chemical Exchange Saturation Transfer Imaging, Ivrea, Italy (2014)
4. Stefan Klippel, Jörg Döpfert, Jabadurai Jayapaul, **Martin Kunth**, Federica Rossella, Matthias Schnurr, Christopher Witte, Leif Schröder, Christian Freund: Xenon Based Hyper-CEST-MRI of Cryptophane Labeled Cells, #115, 54th ENC Conference, Pacific Grove, CA, USA (2013)
5. Matthias Schnurr, Jörg Döpfert, **Martin Kunth**, Federica Rossella, Christopher Witte, Leif Schröder: Depolarization-Time Mapping of Functionalized ^{129}Xe in Biomembranes Possessing Different Fluidity, #113, 54th ENC Conference, Pacific Grove, CA, USA (2013)
6. **Martin Kunth**, Jörg Döpfert, Christopher Witte, Leif Schröder: Simultaneous MRI Monitoring of Diffusion of Multiple Hyper-CEST Contrast Agents, #107, 54th ENC Conference, Pacific Grove, CA, USA (2013)
7. Jörg Döpfert, Christopher Witte, **Martin Kunth**, Leif Schröder: Subsampling for Improved Use of Magnetization in Spectral Hyper-CEST Image Series, #105, 54th ENC Conference, Pacific Grove, CA, USA (2013)
8. Christopher Witte, **Martin Kunth**, Federica Rossella, Leif Schröder: Monitoring and Preventing Rubidium Runaway in a Compact Xenon Hyperpolariser for Hyper-CEST Applications, #88, 54th ENC Conference, Pacific Grove, CA, USA (2013)
9. **Martin Kunth**, Jörg Döpfert, Federica Rossella, Christopher Witte, Leif Schröder: Monitoring Xenon Biosensor Diffusion with MRI, 14th MDC/FMP PhD Retreat, Liebenwalde (2012)
10. Jörg Döpfert, Christopher Witte, **Martin Kunth**, Michael Beyermann, Leif Schröder: Improved evaluation of (Hyper)CEST images using the spectral dimension, 14th MDC/FMP PhD Retreat, Liebenwalde (2012)
11. **Martin Kunth**, Jörg Döpfert, Christopher Witte, Federica Rossella, Leif Schröder: Fast and selective MRI of xenon biosensors, ISMRM, Melbourne, Australia, p.1677 (2012)

12. **Martin Kunth**, Christopher Witte, Leif Schröder: Frindge field effects on hyperpolarized ^{129}Xe for a contiuous flow SEOP setup, ISMRM, Melbourne, Australia, p.2581 (2012)
13. Jörg Döpfert, Christopher Witte, **Martin Kunth**, Michael Beyermann, Leif Schröder: Improved evaluation of (Hyper)CEST images using the spectral dimension, ISMRM, Melbourne, Australia, p.1677 (2012)
14. Christopher Witte, Jörg Döpfert, **Martin Kunth**, Federica Rossella, Leif Schröder: Xenon based nuclear magnetic resonance biosensors using Hyper-CEST, XVI School of pure and Applied Biophysics - Multimodal Methods for Cell Imaging and Tracking, Venice, Italy (2012)
15. Jörg Döpfert, **Martin Kunth**, Christopher Witte, Federica Rossella, Leif Schröder: Fast and selective MRI of xenon biosensors, Deutsche Physikalische Gesellschaft, Berlin, ST 4.4, F, 2012
16. Christopher Witte, **Martin Kunth**, Federica Rossella, Leif Schröder: Preventing rubidium runaway in a compact continuous-flow SEOP hyperpolarizer for xenon NMR, Deutsche Physikalische Gesellschaft, Berlin, ST 4.3, F, 2012
17. Christopher Witte, **Martin Kunth**, Federica Rossella, Leif Schröder: Design of a continuous flow hyperpolarizer for Xenon based nuclear magnetic resonance biosensors, 11th HFSP Awardees Meeting, Montreal, Canada (2011)
18. **Martin Kunth**, Jörg Döpfert, Christopher Witte, Federica Rossella, Leif Schröder: Fast and selective MRI of xenon biosensors, 13th MDC/FMP PhD Retreat, Liebenwalde (2011)
19. **Martin Kunth**, Federica Rossella, Christopher Witte, Leif Schröder: Optimizing spin exchange optical pumping for xenon-129 biosensor NMR imaging, Campus Buch Symposium, Berlin (2011)
20. Federica Rossella, Sina Meyer, Vera Martos Riano, Katharina Koschek, Christopher Witte, **Martin Kunth**, Jörg Rademann, Leif Schröder: Targeting MMP-11 with xenon-129 MRI: preliminary results, Campus Buch Symposium, Berlin (2011)
21. **Martin Kunth**, Nicole Seiberlich, Philipp Ehses, Vikas Gulani, Mark Griswold: Improvement of Quantitative MRI Using Radial GRAPPA in Conjunction with IR-TrueFISP, ISMRM, Stockholm, Sweden, 2895 (2010)

D FIRST AUTHOR PUBLICATIONS

The following objective related publications could be achieved as first author.

D.1 SINGLE-SHOT HYPER-CEST MRI

FULL REFERENCE:
Martin Kunth*, Jörg Döpfert*, Christopher Witte, Federica Rossella, and Leif Schröder. Optimized use of reversible binding for fast and selective NMR localization of caged xenon *Angewandte Chemie International Edition*, 51(33):8217-8220, 2012; Kunth and Döpfert *et al.*[121] and German edition[122].
*contributed equally.
(highlighted as hot paper, inside back cover article and honored with a Gorter-Award)

AUTHOR CONTRIBUTIONS: M.K. and J.D. designed research; M.K., J.D. and F.R. performed research; M.K., J.D., C.W., F.R. and L.S. analyzed data; M.K., J.D., C.W. and L.S. wrote the paper.

On the next following 14 pages, the original publication including Supplemental Material is attached.

- Inside Back Cover: *Angew. Chem. Int. Ed.*, 51(33):8393-8393, 2012 – Reprinted with permission. Copyright © 2012 WILEY-VCH Verlag GmbH & Co. KGaA, Weinheim.
- Full Article: *Angew. Chem. Int. Ed.*, 51(33):8217-8220, 2012 – Reprinted with permission. Copyright © 2012 WILEY-VCH Verlag GmbH & Co. KGaA, Weinheim.

A Journal of the Gesellschaft Deutscher Chemiker
Angewandte Chemie
International Edition
GDCh
www.angewandte.org
2012–51/33

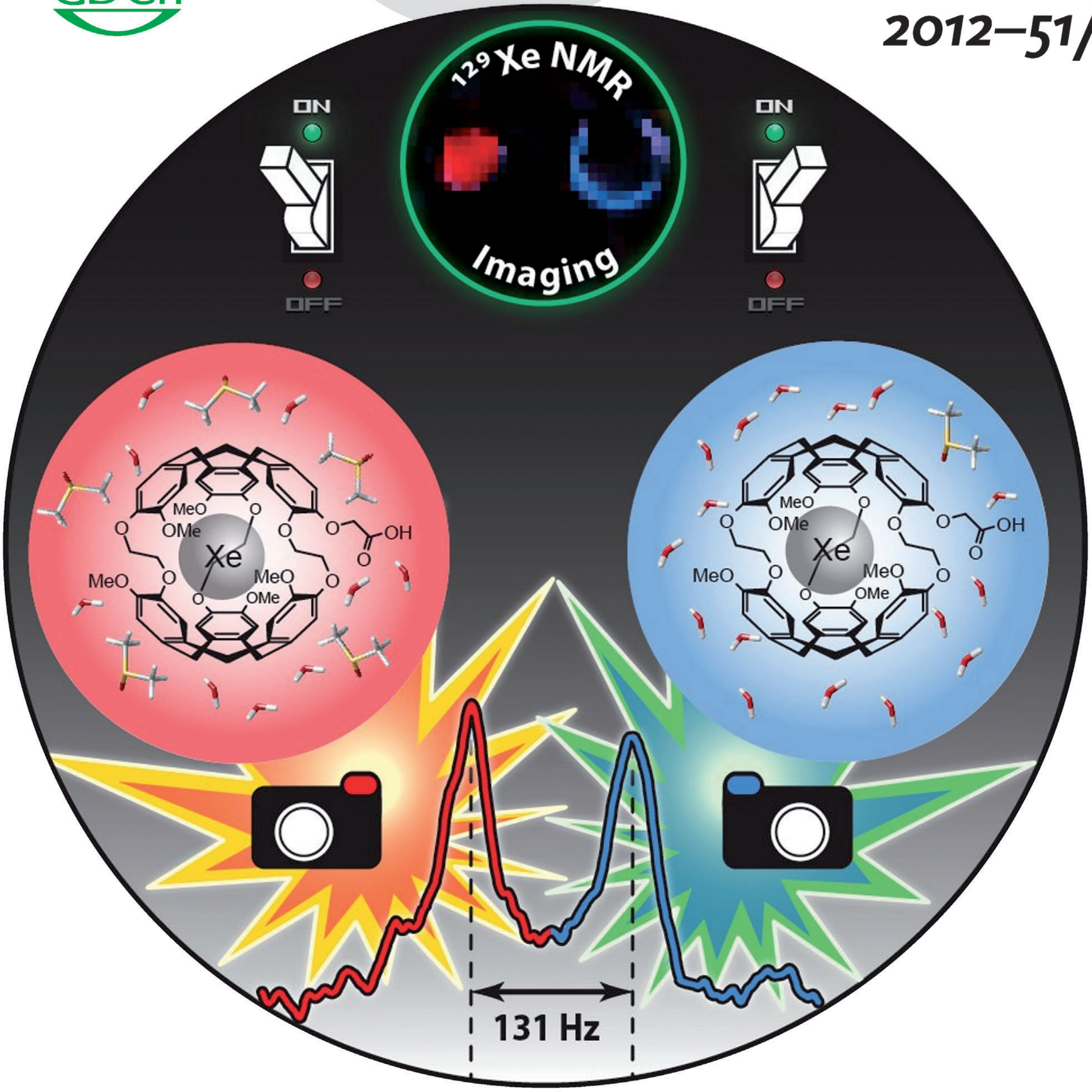

Hyperpolarized ^{129}Xe ...

... trapped in cryptophane cages in different solvents experiences different NMR chemical shifts; in one case they are separated by 131 Hz. In their Communication on page 8217 ff., L. Schröder et al. present an encoding method with optimal use of hyperpolarization for snapshot imaging with high spectral selectivity.

WILEY-VCH

DOI: 10.1002/anie.201202481

Biosensors

Optimized Use of Reversible Binding for Fast and Selective NMR Localization of Caged Xenon**

*Martin Kunth, Jörg Döpfert, Christopher Witte, Federica Rossella, and Leif Schröder**

Xenon-129 is an extremely sensitive NMR probe, as illustrated by its large chemical shift range in many different molecular environments.[1] The noble gas can be spin-hyperpolarized (hp) to achieve a 10^4-fold increase in NMR signal and in solution it can reversibly bind to host structures (for example, cryptophanes), inducing a large change in resonance frequency.[2] These properties have motivated the design of xenon biosensors[3] with the biologically compatible gas acting as a functionalized contrast agent for "molecular imaging". Improved detection techniques are crucial to realize the potential of xenon biosensors. It was recently speculated[4] that chemical exchange saturation transfer (CEST) could improve detection of xenon biosensors, as it is mainly limited by the signal-to-noise ratio (SNR) of the Xe@solution peak. Herein, NMR localization of caged xenon is demonstrated by free dissolved xenon with single-shot echo-planar imaging (EPI) and optimized use of reversible binding by CEST. This yields several significant improvements, including subsecond detection of caged xenon, magnetic resonance imaging (MRI) with xenon host concentrations in the nanomolar range, high spectral selectivity, and time-resolved studies of cryptophane diffusion.

Xenon-based sensors have been developed to detect the presence of a certain analyte[4,5] or reveal various biochemical binding events,[3,6–8] including transferrin-mediated uptake.[9] They often rely on small changes in chemical shift (typically $\delta \approx 1$ ppm) to determine if they are bound to their target and to differentiate between different sensors; thus any detection method should conserve high spectral selectivity. As the amount of caged ^{129}Xe is expected to be small, direct detection requires extensive signal averaging, especially for MRI.[10] Exploiting the reversible binding of xenon to its host has been suggested as a way to utilize all available hyperpolarized atoms in solution. Two such methods have been developed: direct detection by repetitive cage-selective excitation[11] and indirect detection using Hyper-CEST.[12] These initial implementations suffer from limited spatial resolution and spectral selectivity. Selective excitation is strongly limited by the cage and ^{129}Xe concentration in several aspects. First, it requires relatively high cage concentrations (200–300 μM)[4,11] as it uses conventional signal averaging, with SNR increasing only with the square root of the number of acquisitions. Second, to increase cage occupancy, high ^{129}Xe concentrations (ca. 4.5 mM in solution at 1 atm Xe)[4] are often applied. This necessitates batch mode production to obtain high purity hyperpolarized Xe. Third, when using slice selection, the magnetic field gradient broadens the cage resonance and the method loses spectral selectivity.[11] The Hyper-CEST approach on the other hand preserves slice selection and has been demonstrated with lower Xe concentrations (ca. 200 μM). It utilizes the reversible binding in a more efficient way, by encoding the Xe@cage signal in the Xe@solution peak. As it is a differencing technique, it requires a minimum of two acquisitions (reference and on-resonant saturation) with comparable starting conditions, which necessitates reliable delivery of Xe into solution. Previous implementations of Hyper-CEST have been hampered by long acquisition times with multiple Xe re-deliveries over several minutes per image.[12] This made the method sensitive to instabilities in Xe delivery into solution and limits further encoding of the spectral dimension of different sensors.[13]

Herein, we demonstrate that ^{129}Xe concentrations as low as about 100 μM are sufficient to perform single-shot MRI. This allows Xe to be used directly from the polarizer in continuous flow without purification, thus improving reproducibility of delivery of hp Xe. Re-delivery can now be reduced to its absolute minimum; that is, one dissolution per CEST image. With batch-mode production and single filling of the NMR tube with Xe gas, CEST would not be possible owing to signal loss from repetitive excitation and relaxation.

To demonstrate the detection limits of this technique, we performed measurements at physiological temperature (310 K) to accelerate the chemical exchange and increase Hyper-CEST efficiency. Hp Xe was bubbled into a phantom (Supporting Information, Figure S1) containing 250 nM solution of cryptophane-A monoacid cages (CrA-ma, Figure 1 a; a precursor for biosensor synthesis) in 95 % H_2O/5 % DMSO. The CrA-ma was imaged using an EPI sequence (Supporting Information, Figure S2) with a CEST saturation pulse of $B_1 = 19\ \mu T$ for 26 s (total imaging time including gas deliveries ca. 102 s). The CEST data show excellent response (Figure 1 c) with clear localization of CrA-ma in the image (Figure 1 d). Under these conditions, [Xe@solution] is about 361 μM (ca. 95 μM ^{129}Xe) and circa 45 % occupancy of cages, the concentration of NMR-active cages is only 30 nM (see the Supporting

---

[*] M. Kunth,[+] J. Döpfert,[+] Dr. C. Witte, F. Rossella, Dr. L. Schröder
ERC Project BiosensorImaging
Leibniz-Institut für Molekulare Pharmakologie (FMP)
13125 Berlin (Germany)
E-mail: lschroeder@fmp-berlin.de
Homepage: http://www.fmp-berlin.de/schroeder/

[+] These authors contributed equally to this work.

[**] This work has been supported by the European Research Council under the European Community's Seventh Framework Programme (FP7/2007-2013)/ERC grant agreement no. 242710 and the Human Frontier Science Program. The authors would like to thank Stefan Klippel for fruitful discussions regarding the dialysis tubing.

Supporting information for this article is available on the WWW under http://dx.doi.org/10.1002/anie.201202481.

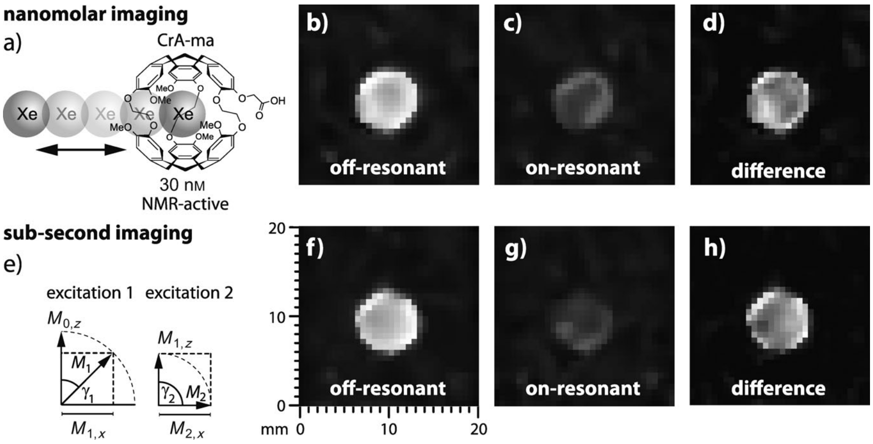

Figure 1. Detection limits of Hyper-CEST EPI acquired at $T=310$ K. a) CrA-ma for fast reversible binding of hyperpolarized Xe. b–d) ^{129}Xe CEST imaging of the distribution of the cage molecules at a total concentration of 250 nM and an NMR-active fraction of 30 nM. The images were acquired employing a cw-saturation pulse (length $t_{sat}=26$ s, amplitude $B_1=19$ μT), once off-resonant (b) ($SNR_b \approx 5$) and once on-resonant (c) ($SNR_c \approx 3$) with Xe@CrA-ma. Prior to each scan, fresh hp ^{129}Xe was bubbled into solution for 25 s. d) Difference image illustrating localization of the caged ^{129}Xe ($SNR_{CEST,d} \approx 2$). e)–h) Subsecond imaging of 50 μM CrA-ma with single delivery of hp ^{129}Xe ($SNR_f/SNR_g/SNR_{CEST,h} \approx 6/2/2$). e) CEST data of the solution was collected with shared magnetization after single hyperpolarization (smashCEST; see also the Supporting Information) using a variable flip angle excitation. With a saturation pulse length of $t_{sat}=450$ ms ($B_1=19$ μT) and an EPI scan time of 19.8 ms per image, the total acquisition time adds up to only 940 ms. Although the post-processed images are shown, all SNR specifications refer to the raw ^{129}Xe images.

Information). This significantly improves on the fastest approach so far, selective excitation with [Xe@solution] of about 4500 μM, circa 96 % occupancy, circa 83 μM NMR-active cages and comparable spatial resolution in 15 s.[4] Using selective excitation for nM cage detection would require multiple re-deliveries of Xe, with acquisition times of well over 100 s. The circa 2750-fold decrease in concentration compared to Reference [4] does not require 2750^2-fold increase in acquisition time when making optimized use of the chemical exchange through Hyper-CEST.

A second experiment was performed to explore minimum acquisition times; subsecond MRI after a single delivery of hp ^{129}Xe ([CrA-ma] = 50 μM, Xe gas fraction = 5 %). To acquire two measurements, we combined Hyper-CEST EPI with a variable flip angle[14] (Figure 1 e; Supporting Information, Figure S4). A first saturation pulse is applied off-resonant prior to excitation with a 45° flip angle (Figure 1 f), and the second saturates CrA-ma on-resonant before exciting the residual longitudinal magnetization with a 90° flip angle (Figure 1 g). Figure 1 h shows the difference image for CEST pulses of 450 ms and $B_1 = 19$ μT. The total acquisition time for the two scans was about 940 ms. This demonstrates snap-shot NMR localization of caged Xe at fairly low concentrations (8.9 μM NMR-active cage; [^{129}Xe@solution] ca. 238 μM). This sensitivity improvement allows new imaging applications, such as acquisition of full z-spectra images, that is, sweeping the saturation frequency to encode the chemical shift dimension. To demonstrate chemical selectivity, we developed a model system to tune the Xe@cage chemical shift. This is achieved by varying the DMSO/water ratio of the solvent (Supporting Information, Figure S6). To simulate multiplexing of differently functionalized cages, we used a two compartment phantom (Supporting Information, Figure S1) and tuned the Xe@cage peak in the different compartments to be about 131 Hz ($\delta = 1.2$ ppm) apart (Figure 2 a). This was achieved by using 10 % vol. DMSO in the outer and 20 % vol. DMSO in the inner compartment. Data were acquired with a saturation pulse of $B_1 = 1$ μT, $t_{sat} = 4$ s and steps of 20 Hz in saturation frequency taking images every 33 s after Xe re-delivery. Figure 2 b shows the z-spectrum calculated from area-normalized signal intensities of different regions of interest (ROIs), and Figure 2 c,d show ^{1}H and ^{129}Xe reference images. The method clearly separates the two different solutions with CEST response in one compartment while the other remains untouched (Figure 2 e,f).

False-color encoding of the separate responses (Figure 2 g) illustrates good sensitivity with unprecedented high chemical specificity while still performing slice selection (selective readout of resonances separated by about 235 Hz was demonstrated in Reference [4], but without the ability to perform slice selection). Only the red area shows some blue contributions, which is possibly due to bleeding of the broader left saturation dip into the right dip. The CEST profile for the higher DMSO content shows a broader response and a stronger absolute signal decrease (Supporting Information, Figure S7). This solution has a higher concentration of Xe (ca. 25–30 % according to the baselines in Figure 2 b), which might increase the cage occupancy if the binding constant is not reduced significantly by the higher DMSO concentration. In any case, the CEST effect seems to benefit from faster exchange, as represented by the increased dip width.

As another application of fast MRI of caged Xe we performed time-resolved studies of CrA-ma diffusion through dialysis tubing. Such tubing with MWCO = 10 kDa containing 500 μM cage in DMSO was placed inside the phantom at $t = 0$ min to provide a strong concentration gradient. Outside the tubing was DMSO, initially with no CrA-ma. Xe was bubbled into both volumes. Figure 3 a shows a series of images (acquired every 33 s) with an increasing CEST response in the outer compartment. The signal from this area shows an exponential decay (Figure 3 b). Further analysis reveals good agreement with a monoexponential increase in CEST response (time constant $\tau = 53$ min). This could be accelerated to $\tau = 17$ min or 4 min by piercing the membrane 2 or 3 times with a 350 μm needle (Figure 3 c). False-color encoding of the increasing CEST response from CrA-ma diffusion to the outer compartment is depicted in Figure 3 d (for animated versions, see the Supporting Information, Figure S8). The CEST approach detects quite low cage concentrations (15 μM) in the outer compartment, as confirmed by

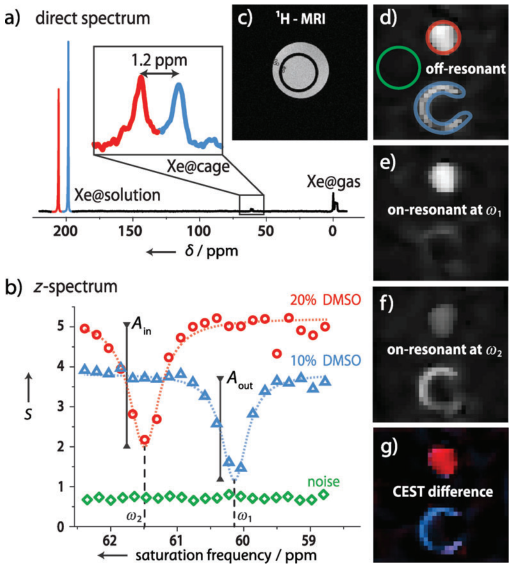

Figure 2. Chemically selective ^{129}Xe NMR imaging at $T = 293$ K. a) Direct ^{129}Xe NMR spectrum (16 averages) of a 10 μM cage dissolved in water with different DMSO fractions in the inner (20%) and the outer compartment (10%) of the bubbling phantom (see ^{1}H MRI (c)), leading to a chemical shift separation for both the Xe@cage and the Xe@solution peaks. The Xe@cage resonances are separated by $\omega_2 - \omega_1 = 1.2$ ppm (131 Hz at 9.4 T). The *z* spectrum with 20 Hz ($\delta = 0.18$ ppm) increments of the saturation frequency depicted in (b) illustrates the high selectivity and sensitivity of the CEST response. The data points result from averaging the signal over the ROIs shown in the off-resonant CEST image (d) for each saturation frequency. The amplitudes of the CEST response $A_{in} = 3.2$ and $A_{out} = 2.7$ are obtained from Lorentzian fits (dashed lines). Subtraction of the two on-resonant images (e) and (f) from the off-resonant image (d) yields the color-encoded CEST difference image (g), which allows for a clear spatial discrimination of the two Xe@cage resonances ($SNR_{CEST,red}/SNR_{CEST,blue} \approx 3/2$ refer to the raw ^{129}Xe images). The displacement between the inner and the outer compartment in (d)–(g) is a chemical shift artefact that originates from the frequency separation of the Xe@solution peaks (805 Hz; ca. 17 pixel shift).

UV spectrometry (see the Supporting Information). Cage occupancy at the given Xe concentration (ca. 2.40 mM) should not exceed 93% (based on $K_M = 6000\,\mathrm{L\,mol^{-1}}$), as K_M in DMSO is expected to be lower than in water. Therefore, the concentration of NMR-active cages is ≤ 3.6 μM at $t = 4$ min and changes in the CEST response can be seen quite soon. This experiment demonstrates the feasibility of time resolved biosensor uptake studies for future in vivo applications. Such a model experiment would be extremely difficult with selective excitation owing to replacing the pure Xe atmosphere after a few images of which each would require too much time compared to the diffusion time scale.

This technique is also applicable with other fast encoding schemes, for example, balanced steady-state free precession, which may be better suited to in vivo or in vitro applications, as EPI will be affected by a reduced T_2*.

In conclusion, we demonstrated that optimized use of reversible Xe binding to a host allows significant improvement for ^{129}Xe NMR imaging. It allows efficient NMR detection even if the fraction of caged Xe is < 2% and is in the range of 10^{-8} M. In fact, efficient contrast can be easily achieved once the Xe concentration threshold for single-shot imaging is surpassed. Although the fraction of occupied cages decreases with reduced concentration of Xe@solution, the amplification through CEST can compensate for this allowing for snap-shot MRI of caged Xe while preserving high chemical selectivity. This technique could find various applications in future biosensor applications in vivo and in vitro.

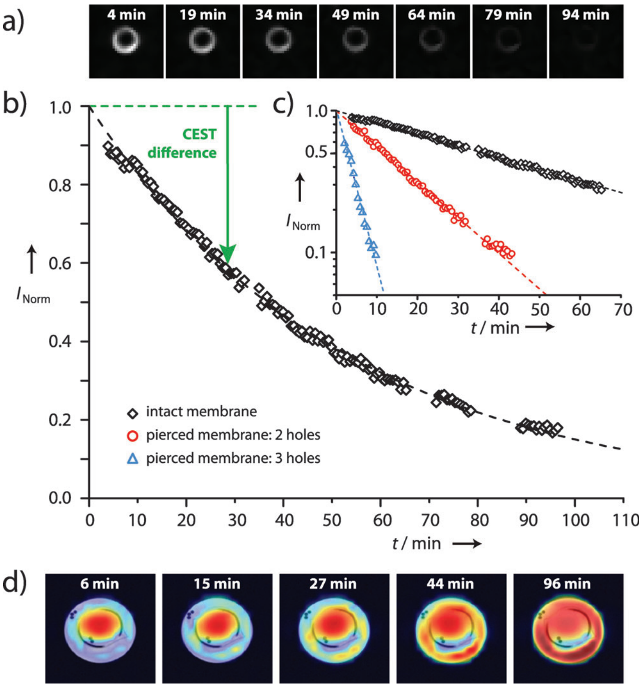

Figure 3. Visualization of CrA-ma diffusion at $T = 295$ K through dialysis tubing with Hyper-CEST EPI. At $t = 0$, CrA-ma is only present in the inner compartment (500 μM concentration). a) ^{129}Xe Hyper-CEST EPI images with presaturation at the Xe@cage frequency ($t_{sat} = 7$ s, $B_1 = 12$ μT) at different times *t* illustrates the gradual decay of the signal in the outer compartment owing to diffusion of cage molecules through the intact membrane ($SNR_{image1} \approx 16.7$). b) The time-dependent mean signal of a ROI in the outer compartment shows an exponential decay. The dashed green line represents the extrapolated off-resonant signal intensity; the length of the green arrow corresponds to the CEST difference which increases in time. Missing data points in the plot are due to acquisitions of high-resolution multislice proton images to monitor the position of the membrane. c) Signal decays show good agreement with monoexponential behavior (dashed lines) for the intact membrane (black diamonds) and intentionally pierced membranes with two (red circles) and three (blue triangles) 350 μm holes. The obtained decay constants of $\tau_{intact} = 53$ min, $\tau_{2\ holes} = 17$ min, and $\tau_{3\ holes} = 4$ min, respectively, indicate faster diffusion through damaged membranes. d) Visualization of the increase in cage concentration in the outer compartment for the intact membrane by overlaying a ^{1}H-MR image with CEST difference images. (A movie of the diffusion process for all three complete datasets can be found in the Supporting Information, Figure S8.)

Experimental Section

NMR experiments were performed on a 9.4 T NMR spectrometer (Bruker Biospin, Ettlingen, Germany) with gradient coils for imaging and a variable temperature unit. A 10 mm inner-diameter double-resonant probe (^{129}Xe and ^{1}H), was used for excitation and detection.

The gas flow was controlled by flow controllers at the sample gas outlet. Hyperpolarized ^{129}Xe was generated by spin exchange optical pumping (ca. 16% polarization) in a custom-designed continuous-flow setup using a gas mixture of 2% Xe (26.4% natural abundance of ^{129}Xe), 10% N_2, and 88% He (5%/10%/85% for the smashCEST experiment). The gas mix was directly bubbled into solution after polarization (Supporting Information, Figure S1). When not mentioned otherwise, for each image the samples were bubbled for 20 s at a total flow rate of 0.07 SLM followed by an 8 s delay (to allow bubbles to collapse) before signal acquisition. ^{129}Xe Hyper-CEST EPI images were acquired with a slice-selective 90°gaussian shaped excitation pulse, 20 × 20 mm^2 field of view, 32 × 32 matrix size, Fourier acceleration factor of 1.68 resulting in 19 phase encoding lines, double sampling, 20 mm slice thickness, echo time = 5.7 ms, and an acquisition time of 19.8 ms (Supporting Information, Figure S2). All images were acquired with 625 μm in plane resolution and processed using an adaptive weights smoothing filter with a local quadratic model. SNR determination of the ^{129}Xe raw images is given in the Supporting Information.

Received: March 30, 2012

Keywords: biosensors · imaging agents · magnetic resonance imaging · NMR spectroscopy · xenon

---

[1] B. M. Goodson, *J. Magn. Reson.* **2002**, *155*, 157 – 216.
[2] T. Brotin, J. P. Dutasta, *Chem. Rev.* **2009**, *109*, 88 – 130.
[3] M. M. Spence, S. M. Rubin, I. E. Dimitrov, E. J. Ruiz, D. E. Wemmer, A. Pines, S. Q. Yao, F. Tian, P. G. Schultz, *Proc. Natl. Acad. Sci. USA* **2001**, *98*, 10654 – 10657.
[4] N. Kotera, N. Tassali, E. Léonce, C. Boutin, P. Berthault, T. Brotin, J. P. Dutasta, L. Delacour, T. Traoré, D. A. Buisson, F. Taran, S. Coudert, B. Rousseau, *Angew. Chem.* **2012**, *124*, 4176 – 4179; *Angew. Chem. Int. Ed.* **2012**, *51*, 4100 – 4103.
[5] J. M. Chambers, P. A. Hill, J. A. Aaron, Z. Han, D. W. Christianson, N. N. Kuzma, I. J. Dmochowski, *J. Am. Chem. Soc.* **2009**, *131*, 563 – 569.
[6] Q. Wei, G. K. Seward, P. A. Hill, B. Patton, I. E. Dimitrov, N. N. Kuzma, I. J. Dmochowski, *J. Am. Chem. Soc.* **2006**, *128*, 13274 – 13283.
[7] V. Roy, T. Brotin, J. P. Dutasta, M. H. Charles, T. Delair, F. Mallet, G. Huber, H. Desvaux, Y. Boulard, P. Berthault, *ChemPhysChem* **2007**, *8*, 2082 – 2085.
[8] A. Schlundt, W. Kilian, M. Beyermann, J. Sticht, S. Günther, S. Höpner, K. Falk, O. Roetzschke, L. Mitschang, C. Freund, *Angew. Chem.* **2009**, *121*, 4206 – 4209; *Angew. Chem. Int. Ed.* **2009**, *48*, 4142 – 4145.
[9] C. Boutin, A. Stopin, F. Lenda, T. Brotin, J. P. Dutasta, N. Jamin, A. Sanson, Y. Boulard, F. Leteurtre, G. Huber, A. Bogaert-Buchmann, N. Tassali, H. Desvaux, M. Carriere, P. Berthault, *Bioorg. Med. Chem.* **2011**, *19*, 4135 – 4143.
[10] C. Hilty, T. J. Lowery, D. E. Wemmer, A. Pines, *Angew. Chem.* **2006**, *118*, 76 – 79; *Angew. Chem. Int. Ed.* **2006**, *45*, 70 – 73.
[11] P. Berthault, A. Bogaer *t*Buchmann, H. Desvaux, G. Huber, Y. Boulard, *J. Am. Chem. Soc.* **2008**, 130, 16456 – 16457.
[12] L. Schröder, T. J. Lowery, C. Hilty, D. E. Wemmer, A. Pines, *Science* **2006**, *314*, 446 – 449.
[13] T. Meldrum, L. Schröder, P. Denger, D. E. Wemmer, A. Pines, *J. Magn. Reson.* **2010**, *205*, 242 – 246.
[14] L. Zhao, R. Mulkern, C. H. Tseng, D. Williamson, S. Patz, R. Kraft, R. L. Walsworth, F. A. Jolesz, M. S. Albert, *J. Magn. Reson. Ser. B* **1996**, *113*, 179 – 183.

Angewandte Chemie
Eine Zeitschrift der Gesellschaft Deutscher Chemiker

Supporting Information

69451 Weinheim, Germany

Optimized Use of Reversible Binding for Fast and Selective NMR Localization of Caged Xenon**

*Martin Kunth, Jörg Döpfert, Christopher Witte, Federica Rossella, and Leif Schröder**

anie_201202481_sm_miscellaneous_information.pdf

Supporting Information

Contents

1. Hyper-CEST EPI Pulse Sequence

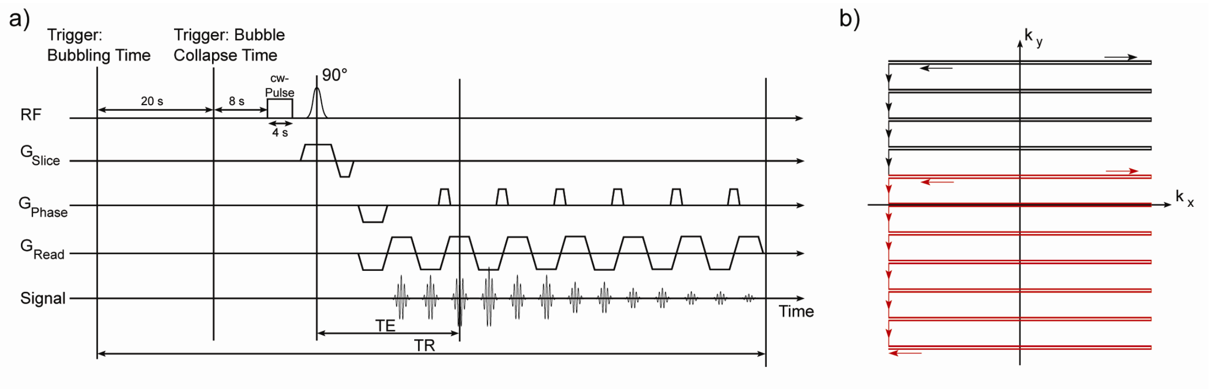

Figure S1: a) Hyper-CEST EPI pulse sequence. The phantom bubbling was controlled by trigger pulses in the pulse sequence. After 20 s of bubbling and 8 s bubble collapse time a cw saturation pulse with a particular carrier frequency was turned on for 4 s if not otherwise stated in the text. Slice selection and excitation was achieved by a selective 90° gaussian shaped radio frequency pulse of 1 ms duration. b) k-space trajectory for EPI readout with partial Fourier acceleration (red) to make more efficient use of the available hyperpolarized magnetization and double sampling [Yang1996] to suppress ghost artefacts (as can be seen by the phase encoding gradient blips for every second readout gradient plateau). The black trajectory shows the hypothetical fully sampled k-space.

2. Bubbling Phantoms

Bubbling phantoms are connected directly to the outlet of the polarizer and kept at the same pressure (4.4 bar abs.) as the optical pumping cell. When the gas is not flowing into the phantom during the bubble collapse time, it is vented through a bypass to keep ongoing flow through the pumping cell.

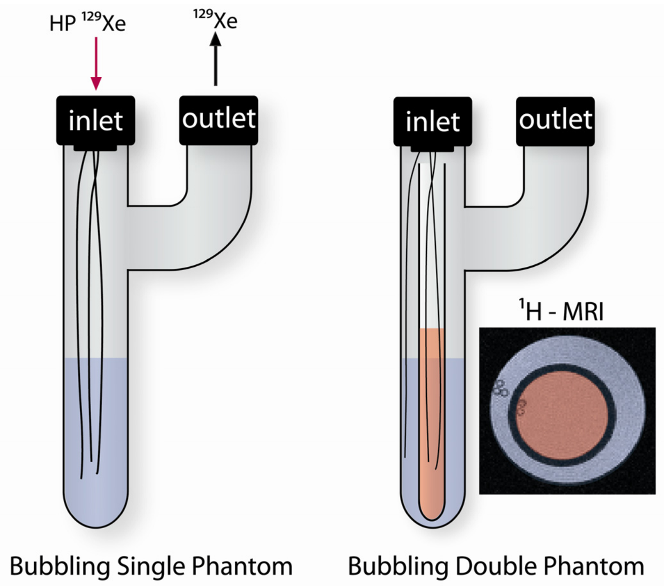

Bubbling Single Phantom

Bubbling Double Phantom

Figure S2: The bubbling single phantom consists of a 10 mm NMR glass tube with a second opening as outlet. Hyperpolarized ^{129}Xe is bubbled through five fused silica capillaries into solution (for illustration purposes only three are shown). The bubbling double phantom consists of the bubbling single phantom with an additional 5 mm NMR tube inserted inside the 10 mm tube in order to generate two separate compartments. As can be seen in the ^{1}H-MR image (colours manually added), two capillaries are in the inner and three are in the outer compartment.

3. Calculations for Xe Concentrations

The solubility of Xe in water at 310 K is 0.0834 L/atm [Clever1979] or 3.28 mM/atm. Knowing that the solubility for DMSO is ca. 6 times higher [Ladefoged1967], we calculated the approximate solubility of Xe in solution to 3.58 mM/atm as the arithmetic average of these values. For the diffusion experiment in DMSO at 295 K, the literature value of 0.66 L/atm published for this temperature was used.

4. Calculations of the Binding Constant, Cage Occupancy and Concentration of NMR active cages

a) Conditions at 310 K in 5% DMSO / 95% H_2O (Figure 1): Using the above calculated solubility constant (3.58 mM/atm Xe), the Xe concentrations are ca. 361 µM for the images in Figure 1 b-d (2% Xe mix), and ca. 902 µM for those in Figure 1 f-h (5% Xe mix). The peak ratio of 100 : 1.56 for a spectrum of 12.5 µM CrA-ma in 5% DMSO / 95% H_2O (Figure S3) at 310 K indicates a binding constant $K_M \approx 2270\ M^{-1}$ for [Xe@solution] = 361 µM (2% Xe mix). This number yields a cage occupancy of ca. 45%, i.e., ca. 30 nM for the NMR-active cage fraction (natural abundance of ^{129}Xe is 26%).

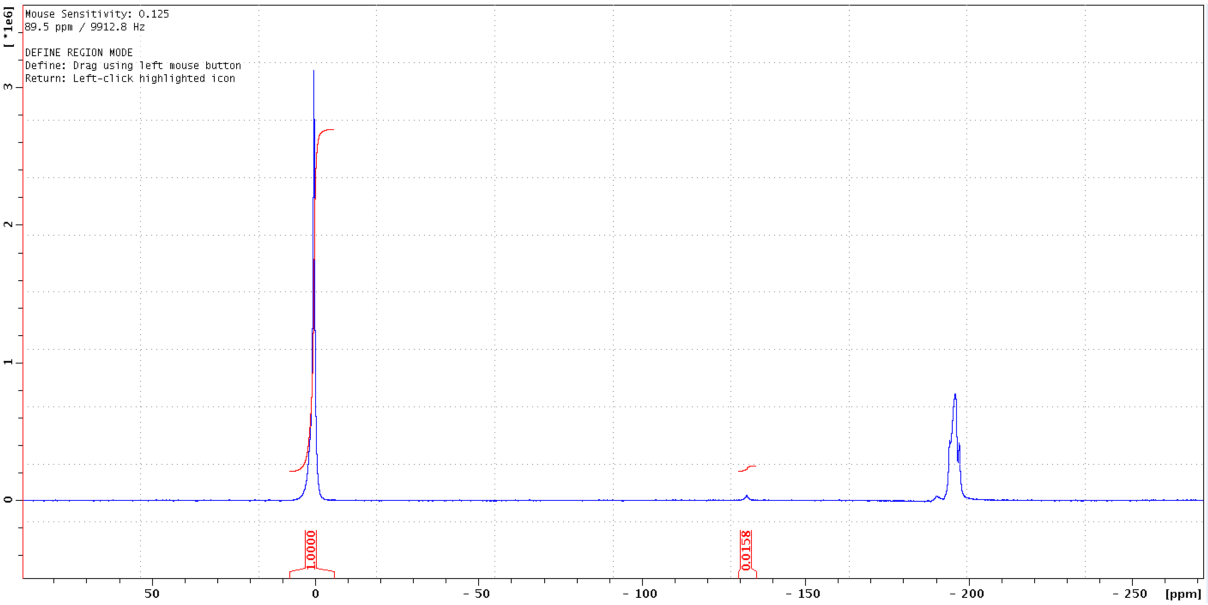

Figure S3: Direct NMR spectrum of ^{129}Xe with a CrA concentration of 12.5 µM at a temperature of 310 K with 32 averages. The red numbers show the peak areas relative to Xe@solution.

b) Conditions for 295 K in pure water (as in ref. [4]): The published Ostwald coefficient of 0.11 L/atm Xe for these conditions yields [Xe@solution] ~4.5 mM/atm. With 1 atm of Xe and $K_M \approx 6000\ M^{-1}$, the Xe@cage peak amounts to ca. 4.28 % of Xe@solution peak and the total Xe concentrations yields a cage occupancy of 96%. Using 200 µM total cage concentration and 86% enriched ^{129}Xe, the concentration of NMR-active cages is ca. 166 µM.

c) Condition for 295 K in pure DMSO: Using the above solubility constants (27.25 mM/atm Xe for pure DMSO at 295 K), the concentration of xenon in solution is ca. 2398 µM for the images in Figure 3. This yields a cage occupancy of 93.5% based on $K_\mathrm{M} \approx 6000\ \mathrm{M}^{-1}$ at 295 K (the published value for CrA in water); this should be an upper limit since the affinity of Xe to the cage cavity is expected to be lower in DMSO than in water.

Formula used to for the above estimations:

$$K_\mathrm{M} = \frac{[\text{occupied cages}]}{[\text{Xe in solution}]\,[\text{unoccupied cages}]}$$

5. smashCEST Preparation

After dissolution of hp xenon, the first excitation generates an amount of $M_{1\mathrm{x}}$ = sin(45°)*M_0 transverse magnetization, which is used up in the first EPI readout. The second excitation flips all the remaining z-magnetization, i.e. cos(45°)*M_0 = $M_{2\mathrm{x}}$ into the transverse plane where it is read out again. Since cos(45°) = sin(45°), the initial transverse magnetization for both encodings is the same, when relaxation effects are negligible (see figure S4).

By introducing off-resonant saturation prior to the first excitation and on-resonant saturation prior to the second excitation, a CEST difference image can be obtained requiring only a single xenon dissolution. When the on-resonant saturation pulse is applied at $\Delta\nu$ Hz downfield from the Xe@solution peak, then the off-resonant saturation pulse is applied symmetrically at $\Delta\nu$ Hz up field in order to account for possible spillover effects.

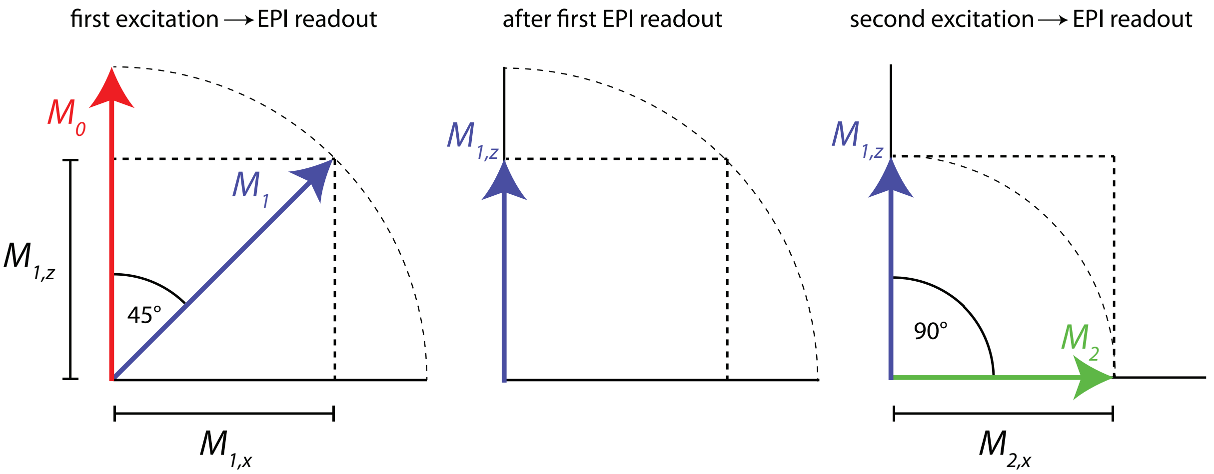

Figure S4: Visualization of the smashCEST approach

6. ^{129}Xe Image Post-Processing

After 2D Fourier transform of the acquired *k*-space data, the images were filtered by adaptive weights smoothing with a local quadratic model using the *R*-package *adimpro* [Polzehl2007]. Filter parameters were $h_\mathrm{max} = 5$ and $\lambda = 0.3$ for all images and $h_\mathrm{max} = 5$ and $\lambda = 0.15$ for the diffusion movies. No thresholding was applied. Diffusion overlay images were additionally scaled to the underlying flash image matrix size using bicubic interpolation and colour encoded using standard functions available in Matlab (R2012a). Possibly appearing negative pixel intensities in the CEST difference images were set to zero. Figure S5 shows some representative unfiltered images.

7. Raw ^{129}Xe Image Series for Spectral Selectivity

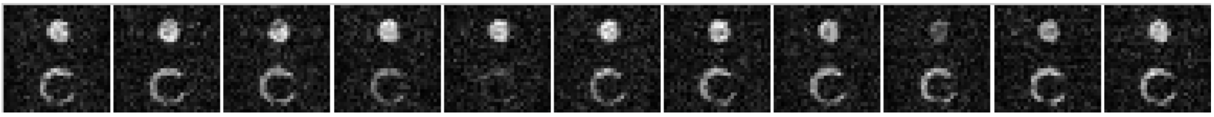

Figure S5: Series of ^{129}Xe selected raw images without post-processing for the application of different cw-saturation frequencies swept in a range between 59 and 62 ppm. The z-spectrum shown in Figure 2 is generated from these.

8. Chemical Shift Adjustment of Xe@CrA-ma using DMSO

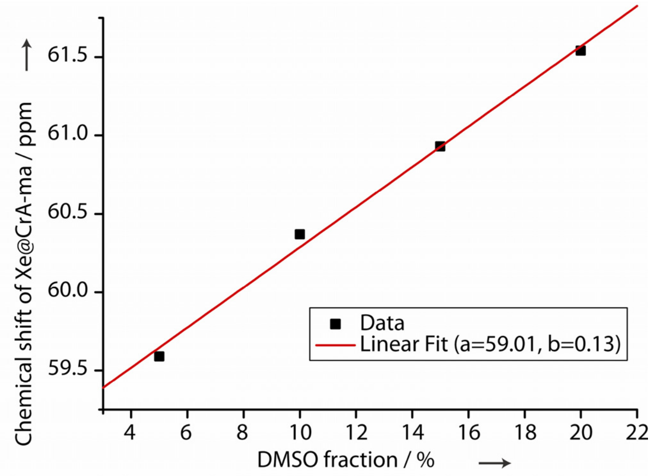

Figure S6: The chemical shift of Xe@CrA-ma is a function of the fraction of DMSO in H_2O. As a consequence, it is possible to tune the resonance frequency of Xe@CrA-ma by adjusting the concentration of DMSO. This enables the generation of multiple CrA-ma resonances with arbitrary chemical shifts to “simulate” multiplexing experiments with different biosensors.

9. Fit Analysis of Muliplexing (CrA-ma in 10% and 20% vol. DMSO)

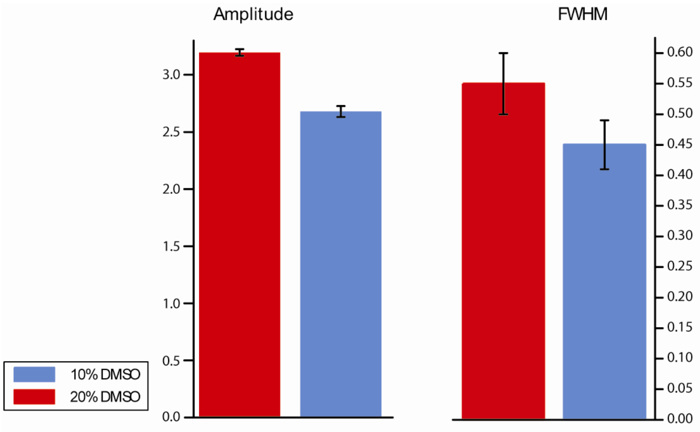

Figure S7: Fit results for lorentzian line shapes approximating the z-spectra shown in Figure 2b.

10. Cryptophane-A Diffusion through Dialysis Tubing (Movie)

Fig. 3 b/c show short interruptions of data acquisition due to necessary restarts of the hyperpolarizer control software. This happens within 2 s and does not affect signal stability.

a) intact membrane

b) damaged membrane
(2 holes)

c) damaged membrane
(3 holes)

Figure S8: Animated datasets for diffusion-driven uptake of CrA-ma under different membrane conditions (a: intact membrane; b: 2 holes; c: 3 holes).

11. CrA-ma Concentration Determination with UV Spectrometer

To investigate starting and ending concentrations of CrA-ma in the outer compartment of the diffusion setup, the experiment from Figure 3b) was repeated outside the NMR spectrometer with comparable conditions while analyzing samples from the outer compartment by UV spectrometry (see Figure S9 for the calibration curve). Measuring the absorption at 290 nm (the absorption wavelength of CrA-ma) yielded ca. 15 µM concentration at *t* = 3 min and ca. 45 µM at *t* = 96 min for the intact membrane (data not shown).

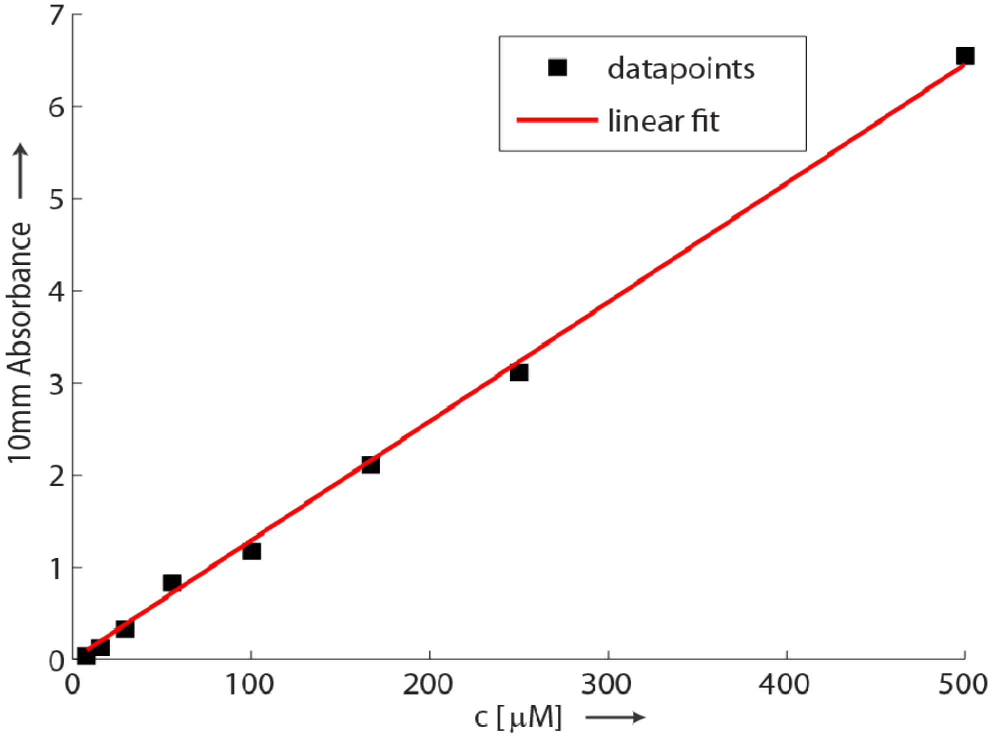

Figure S9: Calibration curve for CrA-ma in DMSO at λ = 290 nm using a UV NanoDrop spectrometer (Thermo Fisher Scientific) showing a linear increase of the absorbance with the CrA-ma concentration. The linear fit yields a molar extinction coefficient of $12.9 \cdot 10^{-3}$ $M^{-1}cm^{-1}$**.**

12. Signal-to-Noise Ratio (SNR) Determination

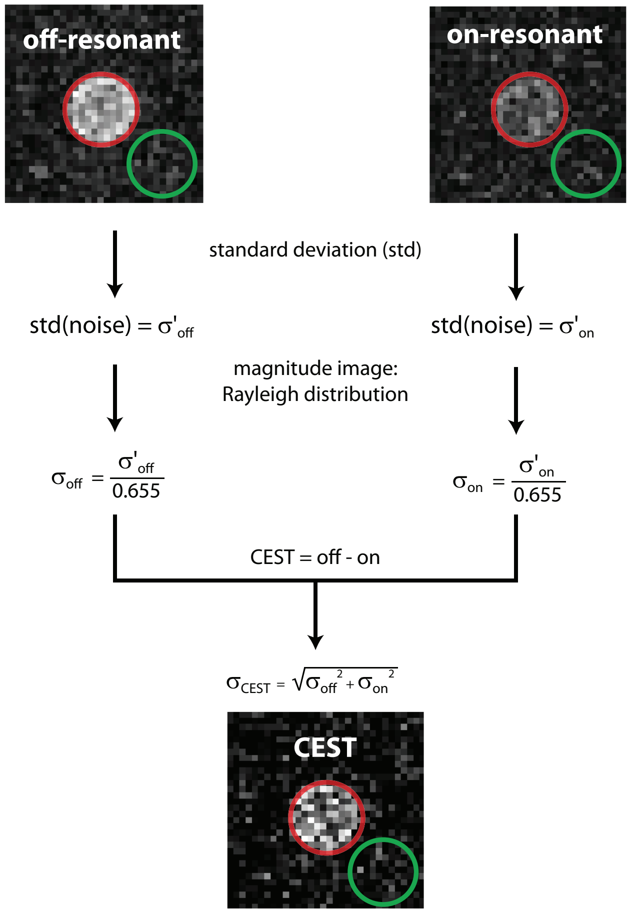

Figure S10: Signal-to-noise ratio determination workflow for CEST images. The standard deviation (std) for the noise (green ROI) for both off- and on-resonant images was calculated. Since the data are magnitude images the noise is not Gaussian distributed, but follows the Rayleigh distribution which can be corrected for by a factor of 1/0.655 to achieve the true noise. Error propagation of the subtraction of two magnitude images yields σ_{CEST}.

The SNR for the raw images can now be calculated for magnitude as well as difference (CEST) images according to

$$\mathrm{SNR}_{\mathrm{off/on}} = \frac{S}{noise} = 0.655 \cdot \frac{S}{\sigma_{off/on}}$$

and

$$\mathrm{SNR}_{\mathrm{CEST}} = \frac{S}{noise_{CEST}} = \frac{S}{\sigma_{CEST}}$$

where *S = mean(signal)* of the red ROI.

13. References

[Clever1979] Clever H (ed.). Krypton, Xenon, and Radon—Gas Solubilities, vol. 2.Oxford: Pergamon Press 1979.

[Ladefoged1967] Ladefoged J; Andersen A. Solubility of ^{133}Xe at 37°C in water, saline, olive oil, liquid paraffin, solutions of albumin, and blood. *Phys. Med. Biol.* **1967**, *12*, 353–358.

[Polzehl2007] Polzehl, J; Tabelow, K; Adaptive Smoothing of Digital Images: The R Package adimpro. *J Stat Softw*, **2007**, 19(1), 1-17. URL http://www.jstatsoft.org/v19/i01/.

[Yang1996] Yang, Q. X.; Posse, S.; Bihan, D. L. & Smith, M. B.
Double-Sampled Echo-Planar Imaging at 3 Tesla; *J Magn Reson Series B,* **1996**, *113*, 145 – 150.
URL http://www.sciencedirect.com/science/article/pii/S1064186696901673

[Zhao1996] Zhao, L.; Mulkern, R.; Tseng, C.; Williamson, D.; Patz, S.; Kraft, R.; Walsworth, R.; Jolesz, F. & Albert, M.; Gradient-Echo Imaging Considerations for Hyperpolarized 129Xe MR; *J Magn Reson B,* **1996***, 113*, 179-183. URL http://walsworth.physics.harvard.edu/publications/1996_Zhao_JMRB.pdf

D.2 QUANTITATIVE HYPER-CEST MRI

FULL REFERENCE:
Martin Kunth, Christopher Witte, and Leif Schröder. Quantitative chemical exchange saturation transfer with hyperpolarized nuclei (qHyper-CEST): Sensing xenon-host exchange dynamics and binding affinities by NMR. *The Journal of Chemical Physics*, 141:194202, 2014; Kunth *et al.*[129].

AUTHOR CONTRIBUTIONS: M.K. designed research and analyzed data; M.K. and C.W. performed research; M.K., C.W. and L.S. wrote the paper.

On the following 26 pages, the original publication and its Supplemental Material is attached.

- Full Article: Reproduced with permission from *J. Chem. Phys.*, 141: 194202 (2014). Copyright 2014, AIP Publishing LLC.

THE JOURNAL OF CHEMICAL PHYSICS **141**, 194202 (2014)

Quantitative chemical exchange saturation transfer with hyperpolarized nuclei (qHyper-CEST): Sensing xenon-host exchange dynamics and binding affinities by NMR

M. Kunth,[a] C. Witte, and L. Schröder[b]
ERC Project BiosensorImaging, Leibniz-Institut für Molekulare Pharmakologie (FMP),
13125 Berlin, Germany

(Received 23 July 2014; accepted 30 October 2014; published online 21 November 2014)

The reversible binding of xenon to host molecules has found numerous applications in nuclear magnetic resonance studies. Quantitative characterization of the Xe exchange dynamics is important to understand and optimize the physico-chemical behavior of such Xe hosts, but is often challenging to achieve at low host concentrations. We have investigated a sensitive quantification technique based on chemical exchange saturation transfer with hyperpolarized nuclei, qHyper-CEST. Using simulated signals we demonstrated that qHyper-CEST yielded accurate and precise results and was robust in the presence of large amounts of noise (10%). This is of particular importance for samples with completely unknown exchange rates. Using these findings we experimentally determined the following exchange parameters for the Xe host cryptophane-A monoacid in dimethyl sulfoxide in one type of experiment: the ratio of bound and free Xe, the Xe exchange rate, the resonance frequencies of free and bound Xe, the Xe host occupancy, and the Xe binding constant. Taken together, qHyper-CEST facilitates sensitive quantification of the Xe exchange dynamics and binding to hydrophobic cavities and has the potential to analyze many different host systems or binding sites. This makes qHyper-CEST an indispensable tool for the efficient design of highly specific biosensors. © *2014 AIP Publishing LLC*. [http://dx.doi.org/10.1063/1.4901429]

I. INTRODUCTION

The nuclear magnetic resonance (NMR) signal of the noble gas isotope ^{129}Xe is extremely sensitive to its molecular environment, due to the high polarizability of its large electron cloud, resulting in remarkably large chemical shifts.[1] Xe has thus been used as an atomic probe for different molecular environments.[2,3] In X-ray crystallography, Xe has found applications for defining and characterizing hydrophobic sites in different proteins. For instance, Xe has served as a gas probe in protein crystals for identification of putative diffusion channels of O_2.[4,5] In general, such mechanisms include aspects of exchange dynamics which, though inaccessible to x-ray crystallography, are accessible through solution NMR. Hence, NMR based techniques can go beyond the pure mapping of such binding sites. Similar related applications are valuable for the characterization of molecular hosts (such as cryptophane-A monoacid (CrA_{ma})) that have been used for the design of smart Xe NMR biosensors[6–10] for which dissolved Xe is used. Beyond its use as a biosensor for molecular imaging, Xe has also been used to sense model biomembrane fluidity.[11]

However, when working with Xe in solution, identification of resonances from bound Xe using conventional NMR spectroscopy can be impaired by the limited solubility of Xe and by the consequently low total NMR signal intensity. This is particularly true for exchanging spins systems which occur when Xe interacts with host molecules. In such systems deriving the Xe binding and exchange constants is of particular interest but has only been performed at relative high host concentrations[12–14] and as such has limited use for molecular imaging experiments and the investigation of hosts with low binding constants.

An excellent technique to overcome this limitation is the chemical exchange saturation transfer (CEST, originally proposed for protons[15]) approach. In CEST NMR, an abundant pool (free Xe in solution, pool A, see Fig. 1(a)) is used to detect a dilute pool (bound Xe, pool B). This is achieved by initially depleting the spin polarization of pool B (i.e., the magnetization is "saturated") for a certain duration by a (selective) radiofrequency saturation pulse. This induced depolarization is transferred to pool A via chemical exchange followed by detection of the large pool A for which the spin polarization is cumulatively decreased. A reference measurement without the radiofrequency pulse reveals the intensity of the saturation transfer. Critically, the selective manipulation of pool B prior to detection of pool A is easy to achieve with Xe due to its large chemical shift range. This results in an effective amplification of the signal of Xe bound to the host. Moreover, in combination with spin hyperpolarized Xe (produced by spin exchange optical pumping[16]), a significantly increased dynamic range between the initial condition and the depolarized final state is achieved. This technique is called Hyper-CEST[17] and allows for the detection of extremely low concentrations of bound Xe.[18–21]

---

[a] Electronic mail: kunth@fmp-berlin.de. Telephone: +49 30 947 93 279.
[b] Author to whom correspondence should be addressed. Electronic mail: lschroeder@fmp-berlin.de. Telephone: +49 30 947 93 121.

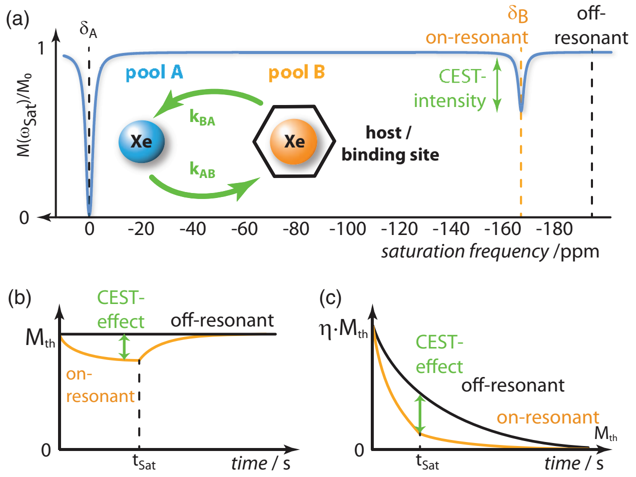

FIG. 1. (a) z-Spectrum of free Xe (at δ_A) and Xe bound to a host molecule or binding site (orange curve; signal at δ_B well shifted from that of free Xe (blue line)). The Xe exchange rate from pool B to A is k_{BA} and vice versa. Comparison of CEST signal build-up (b) with thermally polarized protons (^{1}H-CEST) and (c) hyperpolarized Xe (Hyper-CEST). After saturation, in ^{1}H-CEST, the system relaxes back to (higher) thermal magnetization M_{th} while in Hyper-CEST, the system starts from a hyperpolarized system (enhancement factor $\eta \sim 10^4$, $M_0 = \eta \cdot M_{th}$) and relaxes to (negligible) thermal magnetization M_{th}.

The CEST effect can be modeled by the Bloch-McConnell (BM) equations[22,23] which describe the time evolution of the detected macroscopic magnetizations given by the spin polarization of A and B under the effect of a saturation pulse. The parameters included therein allow for quantification of the exchange dynamics at low host concentrations. These equations have been previously used to study Xe host-guest interactions but without considering the intrinsic decay of the hyperpolarization.[21,24] Such evaluation is incomplete especially when utilizing long CEST durations to detect low host concentrations or to achieve high spectral resolution with weak/narrow pulses. A more comprehensive way to perform quantitative Hyper-CEST analysis (qHyper-CEST) is therefore still lacking. Whereas the BM equations are solved numerically (for which various approaches have been discussed[25–27]), a simplified analytical solution has been derived from the BM equations specifically for hyperpolarized nuclei, the so-called full Hyper-CEST (FHC) solution.[28] A further approximation of the FHC solution is an exponential decay with a Lorentzian lineshaped rate,[28] which has already been used to qualitatively describe experimental Hyper-CEST data.[29] Further experimental validation of the FHC model and its application to quantitative studies is therefore necessary.

Our work aims to present a qHyper-CEST approach which delivers comprehensive information about the Xe-host exchange dynamics and binding properties. We begin by introducing the necessary mathematical tools and the general procedure of qHyper-CEST, followed by briefly describing the BM equations and the FHC solution. We further present an approximation to the FHC solution. This analytical expression gives uncomplicated insight into the complex Hyper-CEST dynamics which becomes important in planning the appropriate set of experiments to perform. We then use simulated data to explore the sensitivity of our qHyper-CEST approach to noise and choice of saturation parameters. These results are used to guide our experiments and as an example to compare the fitting performance of the BM equations and the FHC solution. As a result we demonstrate the sensitivity of this method for quantifying the Xe exchange dynamics for cryptophane-A monoacid (CrA$_{ma}$) in dimethyl sulfoxide (DMSO), in particular the ratio of bound and free Xe, f_B, the Xe exchange rate, k_{BA}. In addition to this, the resonance frequencies of free and bound Xe, δ_A and δ_B, the longitudinal and transverse relaxation times of free Xe, $T^A_{1,2}$ can also be determined. Finally, we determine the previously unquantified binding constant, K_A, of Xe to CrA and the host occupancy, β, as an exemplary Xe host-guest system in this solvent.

II. MATHEMATICAL TOOLS

A. General qHyper-CEST approach

Accessing Xe-host exchange dynamic and binding parameters through qHyper-CEST requires acquisition of z-spectra (see Fig. 1(a)). Each data point within a z-spectrum is collected by saturating at a specific frequency, followed by detection of the resulting z-component of the magnetization of the large pool A. To cover a whole chemical shift range this is repeated multiple times by iterative variation of the specific frequency (saturation frequency in ppm). All detected magnetizations $M(\omega_{sat})$ are referenced to the initially available magnetization M_0. The characteristic shape of the z-spectrum is influenced by all of the above mentioned exchange parameters: f_B = [Xe@host]/[Xe in solution], k_{BA}, $\delta_{A,B}$, and $T^A_{1,2}$. For the experimental conditions used here, the ratio of bound and free Xe, f_B, was $<1/10\,000$. This renders the Hyper-CEST z-spectrum insensitive to the longitudinal and transverse relaxation times of the bound Xe, $T^B_{1,2}$ (see Table I in the supplementary material[30]). As it is discussed in the results and discussion section multiple z-spectra may need to be acquired with different saturation pulse strengths.

When analyzing a Hyper-CEST z-spectrum, it should be noted that in contrast to ^{1}H-CEST, Hyper-CEST experiments have (1) a hyperpolarized initial magnetization, i.e., a non-equilibrium condition giving a large enhancement of the detected signal (enhancement factor $\eta \sim 10^4$), and (2) the gyromagnetic ratio of ^{129}Xe ($\gamma/(2\pi) = -11.77$ MHz/T), which we account for. Consequently, the natural decay of the Hyper-CEST signal (time constant: T^A_1) is accelerated by the saturation pulse, whereas for ^{1}H-CEST these two effects oppose each other (illustrated in Figs. 1(b) and 1(c)), orange on-resonant curve). We introduced a method that takes the T^A_1 decay into account by acquiring reference data with no saturation pulses (similar to a Xe density map) at the beginning of each z-spectrum acquisition (T^A_1 correction). After the T^A_1 correction was applied the data were fitted using a mathematical model to retrieve the Xe exchange dynamic and binding parameters.

B. Xe exchange model

The Xe-host exchange (as it is shown in the inlay of Fig. 1(a)) is described by two processes: (1) when Xe meets a host not occupied by Xe: $Xe_{aq} + host_{noXe} \underset{\kappa_-}{\overset{\kappa_+}{\rightleftarrows}}$ Xe@host, and (2) when Xe meets an occupied host:

$\mathrm{Xe}^*_{\mathrm{aq}} + \mathrm{Xe@host} \underset{\kappa}{\overset{\kappa}{\rightleftarrows}} \mathrm{Xe}_{\mathrm{aq}} + \mathrm{Xe}^*\mathrm{@host}$ (the so-called kick-out exchange[31]). We mathematically modeled and fitted these exchange dynamics using the FHC solution[28] as a first experimental validation of this approximation. To validate the FHC solution we also fitted these exchange dynamics with the BM equations making minimal approximations. Since the FHC solution was derived from the BM equations, we first introduce the BM equations.

1. Model 1: The Bloch-McConnell equations

The BM equations for a 2-spin pool model[22,23] (pool A: free Xe; pool B: bound Xe) are given in S1 in the supplementary material.[30] The effect of a saturation pulse is to rotate the macroscopic magnetization with a specific strength $|\vec{B}_1| = B_1$ and for a specific time t_{sat} and in the case of Hyper-CEST induce an accelerated loss of spin polarization. It should be noted that the effects of B_1 field inhomogenieties can introduce CEST quantification errors. For the micro imaging system used here the results were not significantly affected by such inhomogenieties (see S6 in the supplementary material[30]), but these must be taken into account for larger animal and/or clinical scanners.[32,33] In addition to the Larmor precession term, the BM equations contain three other terms: one term describes the damping of the length of the magnetization vectors by both the intrinsic longitudinal and transverse relaxation times $T_{1,2}^{\mathrm{A,B}}$ in absence of exchange, to the magnetization at thermal equilibrium, $\vec{M}_{\mathrm{th}}^{\mathrm{A,B}}$. The remaining two terms describe the magnetization exchange between both pools and are linear in k_{AB} and k_{BA}. These exchange rates $k_{\mathrm{AB,\,BA}}$ are effective exchange rates consisting of $k_{\mathrm{BA}} = \kappa_{-} + \kappa \cdot [\mathrm{Xe}]$ (see S1 in the supplementary material[30]).

By solving the BM equation system numerically using a matrix operation[26] (which is faster than a previously proposed method[25]), Hyper-CEST *z*-spectra for known saturation pulse strength, B_1, and time, t_{sat}, were fitted to these Xe exchange parameters. To validate our ^{129}Xe Hyper-CEST *z*-spectra fitting routine we used simulated ^{1}H-CEST data generated by a BM equations implementation by Craig Jones from the Johns Hopkins University (JHU), Baltimore, USA.[34] We then used this ^{1}H-CEST data as input to our simulations. By replacing in our code (1) $\gamma\,^{129}\mathrm{Xe} \rightarrow \gamma\,^{1}\mathrm{H}$ and (2) $M_0^{\mathrm{A,B}} = M_{\mathrm{th}}^{\mathrm{A,B}} \cdot \eta \rightarrow M_0^{\mathrm{A,B}} = M_{\mathrm{th}}^{\mathrm{A,B}}$, we could recover the initial ^{1}H-CEST simulation parameters (full description and validation available in S1 in the supplementary material[30]).

2. Model 2: The full Hyper-CEST solution

In general, the BM equations can only be solved numerically which makes identifying trends difficult without running excessive numbers of simulations. If the magnetization is always much larger than the stationary solution (as in Hyper-CEST), than the complicated BM equations can be approximated analytically and yield a FHC solution.[28]

Analogous to the BM equations, we applied the FHC fitting to Hyper-CEST *z*-spectra for known saturation parameters of the exchanging Xe system (full description in S1 in the supplementary material[30]).

3. Approximation of the FHC solution

Whereas the FHC solution[28] gives an analytical but complex solution, an approximation has been found to the FHC model in which the different Xe exchange parameters manifest themselves in the Hyper-CEST effect intuitively.

When $k_{\mathrm{BA}} \gg R_2^{\mathrm{B}}$ (e.g., $k_{\mathrm{BA}} = 270\ \mathrm{s}^{-1}$ and $R_2^{\mathrm{B}} = 2\ \mathrm{s}^{-1}$ as listed in Table I and indeed, realistic parameters for $\mathrm{CrA}_{\mathrm{ma}}$ in DMSO at room temperature) then $M(\omega_{\mathrm{sat}})/M_0 = e^{-t_{\mathrm{sat}} \cdot \lambda_{\mathrm{depol}}}$ with the Lorentzian lineshaped ^{129}Xe depolarization rate (for large relative chemical shifts)

$$\lambda_{\mathrm{depol}}(B_1, \omega_{\mathrm{sat}}) = f_{\mathrm{B}}\, k_{\mathrm{BA}} \frac{(\gamma\, B_1)^2}{(\gamma\, B_1)^2 + k_{\mathrm{BA}}^2 + (\omega_{\mathrm{sat}} - \delta\omega_{\mathrm{B}})^2}. \tag{1}$$

Here, $\delta\omega_{\mathrm{B}} = \delta_{\mathrm{B}} \cdot \gamma B_0$ is the conversion from ppm scale to Hz. By Taylor expanding the exponential in $M(\omega_{\mathrm{sat}})/M_0$ and discarding higher order terms we find $M(\omega_{\mathrm{sat}})/M_0 = 1 - t_{\mathrm{sat}} \cdot \lambda_{\mathrm{depol}}$. Therefore, when the saturation is small this follows a Lorentzian lineshape; when saturation is large it deviates from this lineshape as we can no longer discard higher order terms. In the on-resonance case ($\omega_{\mathrm{sat}} = \delta\omega_{\mathrm{B}}$), the ^{129}Xe depolarization rate λ_{depol} of the CEST resonance with respect to the applied saturation pulse strength, B_1, is

$$\lambda_{\mathrm{depol}}(B_1) = f_{\mathrm{B}}\, k_{\mathrm{BA}} \frac{(\gamma\, B_1)^2}{(\gamma\, B_1)^2 + k_{\mathrm{BA}}^2}. \tag{2}$$

This simplified solution can give unique insights and generalizations that are difficult to observe using the more complex (and accurate) FHC solution. We find two limits of Eq. (2) regarding the saturation pulse strength:

- strong saturation ($\gamma\, B_1 \gg k_{\mathrm{BA}}$): $\lambda_{\mathrm{depol,\,max}} = f_{\mathrm{B}}\, k_{\mathrm{BA}}$.
- weak saturation ($\gamma\, B_1 \ll k_{\mathrm{BA}}$): $\lambda_{\mathrm{depol}}(B_1) = f_{\mathrm{B}} \cdot (\gamma\, B_1)^2 / k_{\mathrm{BA}}$.

TABLE I. Parameters for simulated Hyper-CEST *z*-spectra of $[\mathrm{CrA}_{\mathrm{ma}}] = 100\ \mu\mathrm{M}$ in DMSO ($f_{\mathrm{B}} = 0.00027$) at room temperature ($T = 295$ K) as used for Figs. 2 and 3. The size of pool A was set to $f_{\mathrm{A}} = 1$. Each set of simulated multiple *z*-spectra was globally fitted five times each time with a new randomly distributed set of initial values within the initial value range (bottom line).

	Pool A				Pool B				
	δ_{A} (ppm)	f_{A}	R_1^{A} (s^{-1})	R_2^{A} (s^{-1})	δ_{B} (ppm)	f_{B}/10 000	k_{BA} (s^{-1})	R_1^{B} (s^{-1})	R_2^{B} (s^{-1})
Sim. values	− 1	1 (fixed)	1/70	1/5	− 166	2.7	270	1/10	1/0.5
Value range (±)	0.25	0	20%	75%	0.25	60%	60%	20%	75%

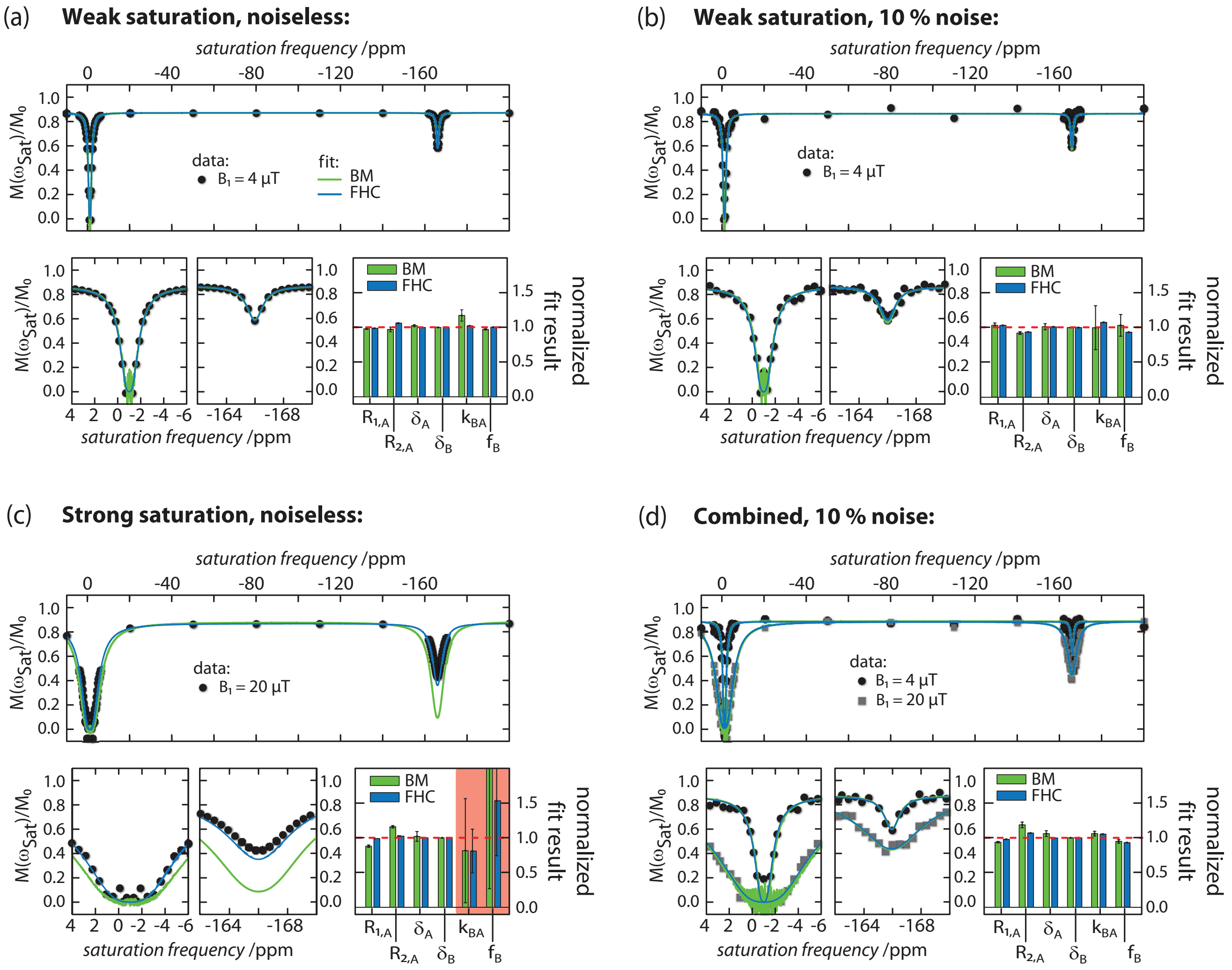

FIG. 2. Individual versus global fitting of BM simulated Hyper-CEST *z*-spectra. The simulation parameters used are listed in Table I. The saturation pulse duration was $t_{sat} = 10$ s and the strength is shown in each inset. (a) A Hyper-CEST *z*-spectrum was simulated (dots: data) without noise and fitted (green line: BM equations; blue line: FHC solution) with $B_1 = 4$ μT (top). A zoom in of the Xe in solution (bottom left) and Xe@host (bottom middle) resonance is shown below. The fit results normalized to the simulation values are shown in the bar plot (bottom right, green: BM equations, blue: FHC solution). A perfect retrieval returns all normalized fit values as 1 (red dashed line). The error bars represent the standard deviation of the individual results of fitting five times, each time with a new randomly distributed set of initial values (see Table I). (b) The same as in (a) but with 10% noise on the Hyper-CEST *z*-spectrum. (c) The same as in (a) but with $B_1 = 20$ μT (noiseless Hyper-CEST *z*-spectrum). Note, k_{BA} and f_B were not accurately determined (red box). (d) The simultaneous fitting (global fitting) of the combined Hyper-CEST *z*-spectra ($B_1 = \{4$ (circles), 20 (rectangles)$\}$ μT) with 10% noise.

III. RESULTS AND DISCUSSION

A. Hyper-CEST responsiveness and dynamic range of the ^{129}Xe depolarization rate

To investigate the robustness of qHyper-CEST, *z*-spectra including the T_1^A correction were simulated for a $B_1 = 4$ μT and $t_{sat} = 10$ s, once perfectly noiseless (Fig. 2(a)) and once with 10% noise, as it might occur in the experiment (Fig. 2(b)). The *z*-spectra were then fitted five times, each time with a new randomly distributed set of initial values (within a fixed range; see bottom line in Table I) to ensure the global minimum of the corresponding fit parameters was reached. The final fitting curves, which were plotted in Figs. 2 and 3, correspond to the mean fit value of each parameter. For the evaluation (bar diagram), all fitted values were normalized to the actual simulation parameter (see red dashed line) including error bars calculated from the standard deviation of the five repetitions. (Therefore, δ_A was artificially set to −1 ppm, rather than the more commonly chosen 0 ppm, to allow normalisation.) As can be seen in Fig. 2(b), using both the BM and FHC models we recovered all relevant exchange parameters, both with and without noise, demonstrating the utility of qHyper-CEST even in the presence of large amounts of noise. In the case with 10% noise, the precision of the results was somewhat reduced for the BM model, though still accurate, while the FHC model performed well. In contrast, when the saturation pulse strength was increased to $B_1 = 20$ μT, even in the completely noiseless case both models fail, Fig. 2(c). In particular, the exchange rate, k_{BA}, and ratio of bound and free Xe, f_B, were almost completely undetermined, as highlighted by the red box in Fig. 2(c). We recovered a successful fit by combining both the low and high strength simulations

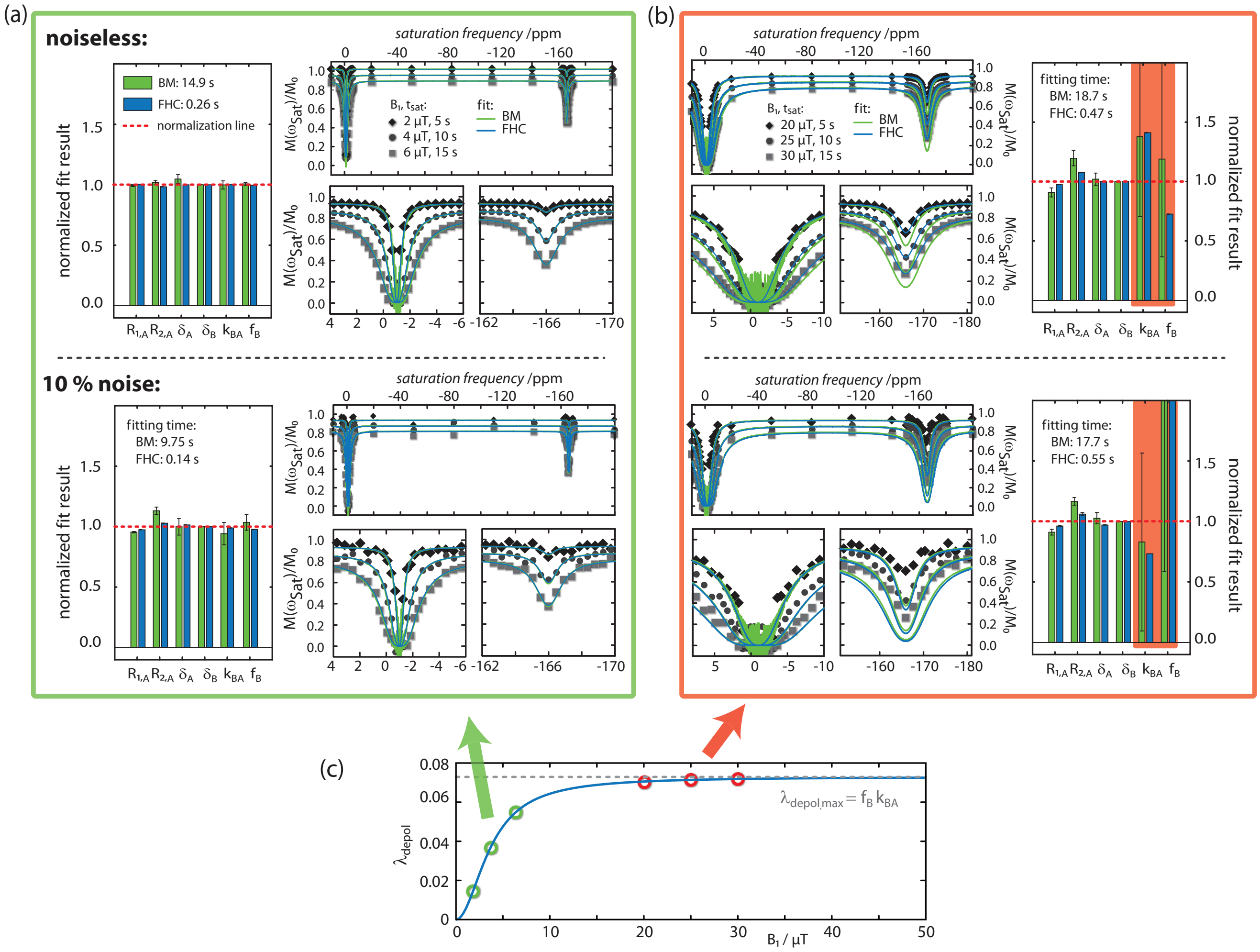

FIG. 3. Quantitative information range in Hyper-CEST *z*-spectra based on simulations and global fitting. The data simulation and analysis was performed as described in Fig. 2. (a, green frame) Low B_1 values allowed for global fitting with separate determination of f_B and k_{BA} for both the BM equations (green in bar plot; including fitting time) and the FHC solution (blue in bar plot; including fitting time) even for 10% noise on *z*-spectra. (b, red frame) For large B_1 values the global fit was not able to determine f_B and k_{BA} individually (transparent red boxes) and fails in the correct quantification of the system even for noiseless *z*-spectra. (c) Depolarization rate λ_{depol} calculated with Eq. (2) using the parameters listed in Table I. The maximum possible Hyper-CEST depolarization for a specific Xe-host system is $\lambda_{depol,\,max}(B_1 \to \infty) = f_B\, k_{BA}$, indicated by the dashed gray line. For B_1 values within the transition regime of λ_{depol} (green circles), global fitting recovered all simulation parameters (green frame). For B_1 values within the plateau of λ_{depol} (red circles), global fitting was not able to individually determine f_B and k_{BA} (red frame).

and performing a global fit to both data sets, Fig. 2(d). It could be suggested that this was merely due to the acquisition of more data but, as we shall see in the following, this was not the case.

We performed further simulations for three different combinations of B_1 as before, both without and with 10% noise. In addition, we simultaneously varied t_{sat}; this has the added benefit of enabling an estimation of T_1^A (see S4 in the supplementary material[30]). Again we saw that we successfully recovered the exchange parameters, Fig. 3(a), even in the presence of large amounts of noise. In this case, the additional data appeared to have improved the precision of the BM model compared to individual fitting, though the FHC model still appears to perform better. Curiously we still found cases in which the fit fails even for global fitting. In Fig. 3(b), where three high B_1 strengths were used, k_{BA} and f_B were again almost undetermined, even though we have the same amount of data to base the fit on as in Fig. 3(a). Further, although the fitting curves may look fine as in Fig. 3(b) for the FHC solution without noise, the numbers of k_{BA} and f_B were incorrect. Clearly the data has some redundancies preventing the retrieval of the desired exchange parameters.

To understand this it was instructive to examine the simpler approximation to the FHC model, Eq. (2) for the parameters listed in Table I. As can be seen from the plot in Fig. 3(c), λ_{depol} is sigmoidal with an extended plateau for large saturation strengths. In particular if $\gamma \cdot B_1 \gg k_{BA}$, Eq. (2) reduces to $\lambda_{depol} = f_B \cdot k_{BA}$ and we could no longer independently recover k_{BA} and f_B, but only their product. As can be seen in Fig. 3(c), if all measurements were taken where λ_{depol} was in the plateau region we failed to recover the exchange parameters. Thus, to individually extract k_{BA} and f_B, *z*-spectra with B_1 values that produce different depolarization rates are needed. The problem of separating k_{BA} and f_B is also well known in some ^{1}H-CEST systems and has been studied with different approaches.[35] Our data shows that the dynamic range of depolarizing hyperpolarized nuclei allowed easier access to these parameters compared to the characterization of exchangeable protons.

Whereas the BM equations and the FHC solution accurately agreed with each other, the FHC solution was about 30–70 times faster (dependent on the set of initial fit values) and more precise (see bar plots in Fig. 3(a)). While the fitting time is not paramount in this work, for pixelwise fitting of imaging data this becomes of greater concern. Further, when the saturation time is longer than the inverse of the B_1 field frequency and all transverse coherences to the effective fields are averaged out, the full 6 BM equations can be reduced to 2 equations,[36] which can potentially accelerate its fitting time.

Consequently, our measurements were taken within the dynamic range of the depolarization rate, and we exclusively used global fitting. To verify if a collected data set for qHyper-CEST fulfills this condition, three different saturation strengths (but the same saturation time) should be compared for sufficient differences in CEST intensity (see CEST intensity in Fig. 1(a)). Saturation conditions within the plateau regime mainly differ in width of the CEST resonance and are only useful if they are combined with weaker saturation strengths.

B. Full Hyper-CEST analysis with variable host concentrations

We evaluated the Xe-CrA$_{ma}$ interaction for [CrA$_{ma}$] = {1, 5, 10, 50, 100, 150} μM in DMSO at $T = 295$ K by both direct ^{129}Xe NMR spectra and qHyper-CEST. Fig. 4(a) illustrates the detection limit of direct ^{129}Xe NMR spectra (each with 64 scans), which is approximately 100 μM. The aim of qHyper-CEST is to determine the Xe exchange and binding parameters well below that detection limit.

As an example, experimental Hyper-CEST z-spectra ([CrA$_{ma}$] = 100 μM for three combinations of B_1 and t_{sat}), obtained from a ^{129}Xe Hyper-CEST echo planar imaging (EPI)[18] image series (Fig. 4(b)), are shown in Fig. 4(c). The B_1 strengths were chosen such that λ_{depol} was well below its maximum. They were fitted globally by the BM equations (green line) and the FHC solution (blue line). A comprehensive description of the host-guest system was then retrieved by evaluating sets of z-spectra at different concentrations. It should be emphasized that even at concentrations <10 μM we could still successfully retrieve the exchange parameters. This is well below the detection limit of direct NMR as illustrated in Fig. 4(a). The [CrA$_{ma}$] dependent fit results for the Xe exchange parameters were plotted in Figs. 4(d)–

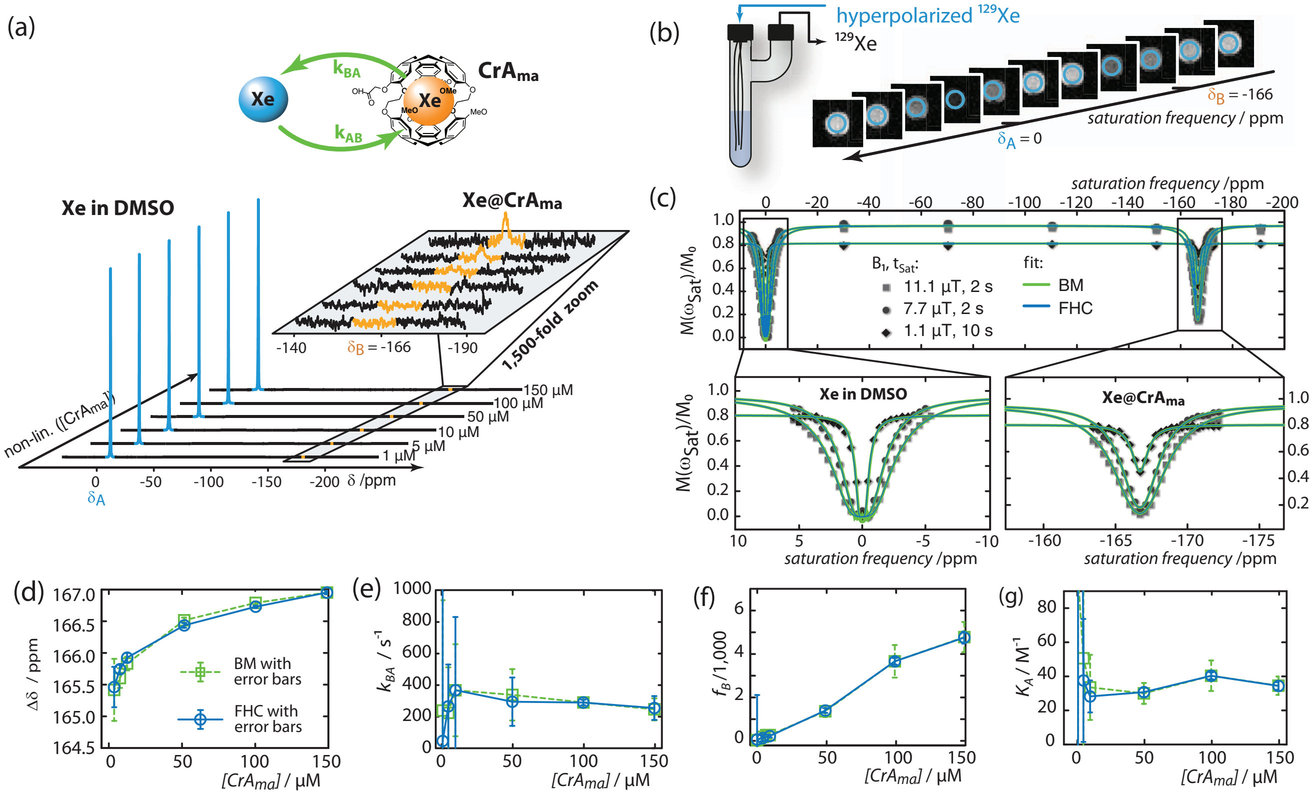

FIG. 4. qHyper-CEST results for different concentrations of CrA$_{ma}$ in DMSO at room temperature $T = 295$ K. (a) Illustrations of the detection limit of direct ^{129}Xe NMR spectra (64 averages) for [CrA$_{ma}$] < 100 μM. The Xe@CrA$_{ma}$ resonated upfield at $\delta_B \sim -166$ ppm. (b) Bubbling phantom (including capillaries and sample (blue)) and axial ^{129}Xe Hyper-CEST EPI image series with respect to the saturation frequency. Hyper-CEST z-spectra were obtained by integrating the signal within the region-of-interest (blue circle) and normalization according the T_1^A correction (see Fig. 1(c)). (c) Hyper-CEST z-spectra of exemplary [CrA$_{ma}$] = 100 μM for three different saturation pulses B_1,t_{sat} = {11.1, 2 (rectangles); 7.7, 2 (circles); 1.1, 10 (diamonds)} μT,s including global fitting with the BM equations (green line) and the FHC solution (blue line). Note that the fit for both models performed almost identically and there was significant overlay of the two lines. Fitting results as a function of [CrA$_{ma}$] using the BM equations (green) and the FHC solution (blue) including error bars (standard error of the fit) are shown in (d) for the relative chemical shift difference $\Delta\delta$, (e) for the exchange rate of Xe out of CrA$_{ma}$, k_{BA}, and (f) the ratio of bound and free Xe, f_B. (g) Association constant K_A calculated with Eq. (4) (error propagation described in S5 in the supplementary material[30]).

TABLE II. qHyper-CEST results exemplary for $[\mathrm{CrA_{ma}}] = 100\ \mu\mathrm{M}$ in DMSO at $T = 295$ K.

Model	$\Delta\delta$ (ppm)	$f_B/1000$	k_{BA} ($\mathrm{s^{-1}}$)	β (%)[a]	K_A ($\mathrm{M^{-1}}$)[b]	Fitting time (s)
BM	-166.73 ± 0.02	3.7 ± 0.7	290 ± 30	9	40 ± 9	29.6
FHC	-166.69 ± 0.02	3.7 ± 0.2	290 ± 20	9	40 ± 2	0.23

[a] According to Eq. (3).

[b] According to Eq. (4).

4(g), which represents the full quantification of this Xe-host system.

Two parameters were dependent on the host concentration, namely, the relative chemical shift between free and bound Xe, $\Delta\delta$, and the ratio of bound and free Xe, f_B. We attributed the increase in $\Delta\delta$ (Fig. 4(d)) to the large difference in size of the free Xe pool compared to bound Xe (asymmetric two-site exchange). The smaller the size of pool B is, the more the coalescence point of the two peaks, $\delta_{\mathrm{average}} \sim f_A \cdot \delta_A + f_B \cdot \delta_B$, moved towards the resonance of pool A. Hence as the $\mathrm{CrA_{ma}}$ concentration decreases, so does $\Delta\delta$. The ratio of bound and free Xe, f_B, increased linearly with $[\mathrm{CrA_{ma}}]$ (compare with Fig. 4(f)). This was expected, as long as the concentration of free Xe in solution was kept stable. Indeed, Fig. 4(f) agreed well with previously published ^{1}H-CEST results for labile protons showing that the labile proton fraction was proportional to the CEST agent concentration.[37] However, f_B does not directly represent the total amount of $[\mathrm{CrA_{ma}}]$, instead it is indicative of the concentration of occupied Xe hosts, $[\mathrm{Xe@CrA_{ma}}]$. We can recover the fractional occupancy by linear-fitting to the equation

$$f_B([\mathrm{CrA_{ma}}]) = \frac{\beta}{[\mathrm{Xe}]} \cdot [\mathrm{CrA_{ma}}], \tag{3}$$

where [Xe] is the Xe concentration in solution (given in Sec. V). We found the Xe host occupancy β, which has only been estimated so far, to be: $\beta_{\mathrm{CrA}}^{\mathrm{DMSO}} \approx 8\%$ at $T = 295$ K (derivation given in S3 in the supplementary material[30]). Implicit in this is an assumption that the occupancy is independent of the concentration of $\mathrm{CrA_{ma}}$ in solution. This was supported by the linear behavior observed in Fig. 4(f), justifying the use of this assumption within the $[\mathrm{CrA_{ma}}]$ range we studied.

In contrast, the longitudinal relaxation time of free Xe, T_1^A (data shown in S4 in the supplementary material[30]), and the Xe exchange rate, k_{BA} (shown in Fig. 4(e)) were insensitive to the host concentration. A similar result has again previously been observed in ^{1}H-CEST for labile protons, showing that the CEST agent concentration has a negligible effect on the exchange rate.[37] With this Xe exchange rate and relative chemical shift, the Xe-$\mathrm{CrA_{ma}}$ exchange dynamics in DMSO were slow on the NMR time scale ($k_{BA}/\Delta\omega = 0.014 \ll 1$, with $\Delta\omega = \Delta\delta \cdot 10^{-6} \cdot \gamma/(2\pi) \cdot B_0 = \Delta\delta \cdot 10^{-6} \cdot 11.77\ \mathrm{MHz/T} \cdot 9.4\ \mathrm{T}$). Therefore, in contrast to some ^{1}H-CEST systems (e.g., diamagnetic (DIACEST) or paramagnetic (PARACEST)), this Hyper-CEST system is an "ideal" CEST system which greatly fulfills the slow exchange regime condition.

In addition, we derived other quantities of interest from the exchange parameters determined by qHyper-CEST. In particular, we found the Xe binding constant K_A to be

$$K_A = \frac{f_B}{[\mathrm{CrA_{ma}}] - f_B \cdot [\mathrm{Xe}]} \tag{4}$$

(derivation including error estimation in S5 in the supplementary material[30]) which is shown in Fig. 4(g). Given the appearance of $[\mathrm{CrA_{ma}}]$ in the denominator of Eq. (4) it is surprising that K_A appeared to be insensitive to $[\mathrm{CrA_{ma}}]$. This can be explained by noting that f_B also depends on $[\mathrm{CrA_{ma}}]$. Using Eq. (3) to rewrite Eq. (4) as $K_A = [\mathrm{Xe}]^{-1} \cdot (\beta/(1-\beta))$ shows that K_A is, as expected, insensitive to $[\mathrm{CrA_{ma}}]$.

The comparison between the BM results and FHC fitting is listed in Table II which confirmed the acceleration of the fitting time and the higher precision (also apparent in Fig. 3(a)) of the FHC solution as already shown by the simulations.

IV. CONCLUSION

We presented quantitative experimental validation of the FHC model and a concept for sensitive quantification of Xe exchange dynamic and binding parameters for $\mathrm{CrA_{ma}}$ in DMSO as a host model.

We found that multiple Hyper-CEST z-spectra acquired with different saturation pulse strengths within the dynamic range of the ^{129}Xe depolarization rate allowed accurate and precise quantification of multiple parameters simultaneously such as the ratio of bound and free Xe, f_B; the Xe exchange rate, k_{BA}; the resonance frequencies of free and bound Xe, $\delta_{A,B}$; the longitudinal and transverse relaxation times of free Xe, $T_{1,2}^A$ (by variation saturation pulse length). These results were stable even in the presence of large amounts of noise on the data (here 10%). In addition, we derived other quantities of interest from the exchange parameters determined by qHyper-CEST, such as the previously unquantified binding constant, K_A, and the Xe host occupancy, β. This was possible because Hyper-CEST is an "ideal" CEST system, greatly fulfilling the slow exchange regime condition ($k_{BA}/\Delta\omega = 0.014 \ll 1$) in contrast to some ^{1}H-CEST systems (e.g., diamagnetic (DIACEST) or paramagnetic (PARACEST)). Whereas the fitting parameters found by the BM equations and the FHC solution accurately agreed with each other, the FHC solution was more precise (see Fig. 3(a)) and about 100 times faster (see Table II). Additionally, approximations to the FHC solution are a valuable tool and offer a straightforward, though approximate, analysis of Hyper-CEST z-spectra. Furthermore, they give uncomplicated insight into complex Hyper-CEST dynamics such as the dynamic range of the Xe depolarization rate we found here. Further, with localized NMR, as we used here, multiple samples could potentially be quantified simultaneously.

This approach can be easily extended to various other hydrophobic host systems or binding sites. We so far considered a model with 2-spin pools. The extension to multiple pools is straightforward,[38,39] thus complex Hyper-CEST systems, e.g., biomembranes[11] or cells,[40] could be understood in more detail by qHyper-CEST analysis, enabling the optimization of such complex systems or multiplexed ^{129}Xe MR imaging.[18,20]

Taken together, qHyper-CEST delivers sensitive quantification of the Xe exchange and binding to hydrophobic cavities and has the potential to analyze many different host systems or binding sites. This makes qHyper-CEST an indispensable tool for the efficient design of highly specific biosensors.

V. MATERIALS AND METHODS

A. Data processing and fitting

All simulations, calculations and fitting routines were implemented and performed in MATLAB 7 (The Mathworks, Natick, MA) with non-optimized code, on a standard desktop PC (64 bit, 8 cores each at 2.80 GHz, 4 GB RAM). To account for magnitude images a Rician correction was applied to the experimental Hyper-CEST *z*-spectra (more details are given in S2 in the supplementary material[30]). The fitting with the BM equations and the FHC solutions was done by the MATLAB function *lsqcurvefit*.

B. Sample preparation

Samples were prepared by dissolving cryptophane-A monoacid (CrA_{ma}) into DMSO at room temperature achieving concentrations of {1, 5, 10, 50, 100, 150} μM.

C. Hyperpolarization and ^{129}Xe delivery

Circa 25% Xe spin-hyperpolarization of a Xe gas mix ({2/10/88 vol. % Xe/N_2/He}, ^{129}Xe natural abundance: 26.4%) was obtained by a continuous-flow (0.35 SLM (standard liters per minute)) custom-designed polarizer[41] via spin exchange optical pumping with rubidium atoms. The electrons of Rb were excited by a 150 W continuous-wave laser (795 nm, 0.5 nm bandwidth, QPC Lasers) at a total pressure of $p = 4.5$ atm. Before signal acquisition, the samples were bubbled for 10 s at a flow rate of 0.1 SLM followed by a 2 s delay in order to allow the bubbles to collapse. The Xe concentration in DMSO, assuming Xe saturation, was [Xe] = 2.34 mM ($[\mathrm{Xe}] = L \cdot p \cdot \mathrm{Xe}_{pc}/(0.0254\,\mathrm{L/mM})$, with the Xe Ostwald solubility coefficient in DMSO $L = 0.66$ L/atm and $\mathrm{Xe}_{pc} = 0.02$). For our system, the shot-to-shot noise, corresponding to the reproducibility of the Xe concentration in solution, is <1%.[42] Hence, this setup provided excellent conditions for quantifying Xe-host systems with qHyper-CEST.

D. NMR experiments

NMR experiments were performed on a $|\vec{B}_0| = 9.4$ T NMR spectrometer (Bruker Biospin, Ettlingen, Germany) equipped with gradient coils for imaging and a variable temperature unit. All samples were measured at room temperature ($T = 295$ K $\sim 22\,^\circ$C). For excitation and detection a 10 mm inner-diameter double-resonant probe (^{129}Xe and ^{1}H) was used. For each sample a flip angle calibration and shimming was performed. The Xe in DMSO resonance was denoted by the chemical shift, $\delta_A = 0$ ppm and used as reference. The ^{129}Xe Hyper-CEST images were obtained with a ^{129}Xe Hyper-CEST echo-planar imaging[18] pulse sequence with the following parameters: Fourier acceleration: 1.68; double sampling; echo time: 5.7 ms; acquisition time: 19.8 ms; no smoothing filter was applied to the images. The geometry was: field of view: 20 × 20 mm^2; matrix size: 32 × 32; in plane resolution: 625 μm, slice thickness: 20 mm. The saturation pulse strengths and lengths used are mentioned in the figure captions. The total acquisition time of Fig. 4(c) ([CrA] = 100 μM in DMSO) was: number of frequency offsets: 55 (25 around solution peak, 25 around host dip, 5 for baseline offsets), three *z*-spectra: ($t_{sat,1} = t_{sat,2} = 2$ s and $t_{sat,3} = 10$ s), Xe delivery bubbling time = 10 s, bubbling collapse time = 2 s. Additionally, three images with no saturation time were acquired for normalization to correct for T_1^A relaxation. Therefore, the total acquisition time per sample adds up to <47 min.

ACKNOWLEDGMENTS

This work has been supported by the European Research Council under the European Community's Seventh Framework Programme (FP7/2007-2013)/ERC Grant Agreement No. 242710 and the Human Frontier Science Program. The authors gratefully thank Moritz Zaiss for helpful discussions and Jabadurai Jayapaul for sample preparation.

[1] B. M. Goodson, J. Magn. Reson. **155**, 157 (2002).

[2] L. Dubois, P. Da Silva, C. Landon, J. G. Huber, M. Ponchet, F. Vovelle, P. Berthault, and H. Desvaux, J. Am. Chem. Soc. **126**, 15738 (2004).

[3] E. Locci, J. Reisse, and K. Bartik, ChemPhysChem **4**, 305 (2003).

[4] T. Prang, M. Schiltz, L. Pernot, N. Colloc'h, S. Longhi, W. Bourguet, and R. Fourme, Proteins: Struct., Funct., Bioinf. **30**, 61 (1998).

[5] M. Svensson-Ek, J. Abramson, G. Larsson, S. Trnroth, P. Brzezinski, and S. Iwata, J. Mol. Biol. **321**, 329 (2002).

[6] M. M. Spence, S. M. Rubin, I. E. Dimitrov, E. J. Ruiz, D. E. Wemmer, A. Pines, S. Q. Yao, F. Tian, and P. G. Schultz, Proc. Natl. Acad. Sci. U. S. A. **98**, 10654 (2001).

[7] M. M. Spence, E. J. Ruiz, S. M. Rubin, T. J. Lowery, N. Winssinger, P. G. Schultz, D. E. Wemmer, and A. Pines, J. Am. Chem. Soc. **126**, 15287 (2004).

[8] J. L. Mynar, T. J. Lowery, D. E. Wemmer, A. Pines, and J. M. J. Fréchet, J. Am. Chem. Soc. **128**, 6334 (2006).

[9] T. Meldrum, K. L. Seim, V. S. Bajaj, K. K. Palaniappan, W. Wu, M. B. Francis, D. E. Wemmer, and A. Pines, J. Am. Chem. Soc. **132**, 5936 (2010).

[10] P. D. Garimella, T. Meldrum, L. S. Witus, M. Smith, V. S. Bajaj, D. E. Wemmer, M. B. Francis, and A. Pines, J. Am. Chem. Soc. **136**, 164 (2014).

[11] M. Schnurr, C. Witte, and L. Schröder, Phys. Chem. Chem. Phys. **15**, 14178 (2013).

[12] R. M. Fairchild, A. I. Joseph, K. T. Holman, H. A. Fogarty, T. Brotin, J.-P. Dutasta, C. Boutin, G. Huber, and P. Berthault, J. Am. Chem. Soc. **132**, 15505 (2010).

[13] H. A. Fogarty, P. Berthault, T. Brotin, G. Huber, H. Desvaux, and J.-P. Dutasta, J. Am. Chem. Soc. **129**, 10332 (2007).

[14] G. Huber, L. Beguin, H. Desvaux, T. Brotin, H. A. Fogarty, J.-P. Dutasta, and P. Berthault, J. Phys. Chem. A **112**, 11363 (2008).

[15] K. Ward and R. Balaban, Magn. Reson. Med. **44**, 799 (2000).

[16] T. G. Walker and W. Happer, Rev. Mod. Phys. **69**, 629 (1997).

[17] L. Schröder, T. J. Lowery, C. Hilty, D. E. Wemmer, and A. Pines, Science **314**, 446 (2006).

[18] M. Kunth, J. Döpfert, C. Witte, F. Rossella, and L. Schröder, Angew. Chem., Int. Ed. **51**, 8217 (2012).
[19] Y. Bai, P. A. Hill, and I. J. Dmochowski, Anal. Chem. **84**, 9935 (2012).
[20] M. G. Shapiro, R. M. Ramirez, L. J. Sperling, G. Sun, J. Sun, A. Pines, D. V. Schaffer, and V. S. Bajaj, Nat. Chem. **6**, 629 (2014).
[21] T. K. Stevens, R. M. Ramirez, and A. Pines, J. Am. Chem. Soc. **135**, 9576 (2013).
[22] H. M. McConnell, J. Chem. Phys. **28**, 430 (1958).
[23] D. E. Woessner, J. Chem. Phys. **35**, 41 (1961).
[24] R. M. Ramirez, T. K. Stevens, M. A. Smith, D. E. Wemmer, and A. Pines, in *Proceedings of ISMRM 19th Annual Meeting, Montreal, 2011*, Vol. 19, p. 3542.
[25] D. E. Woessner, S. Zhang, M. E. Merritt, and A. D. Sherry, Magn. Reson. Med. **53**, 790 (2005).
[26] K. Murase and N. Tanki, Magn. Reson. Imaging **29**, 126 (2011).
[27] M. Zaiss and P. Bachert, Phys. Med. Biol. **58**, R221 (2013).
[28] M. Zaiss, M. Schnurr, and P. Bachert, J. Chem. Phys. **136**, 144106 (2012).
[29] M. Schnurr, K. Sydow, H. M. Rose, M. Dathe, and L. Schröder, "Brain endothelial cell targeting via a peptide-functionalized liposomal carrier for xenon hyper-CEST MRI," Adv. Healthcare Mater. (published online).
[30] See supplementary material at http://dx.doi.org/10.1063/1.4901429 for additional details regarding Xe exchange theory, Rician correction, host occupancy, longitudinal relaxation time, and the binding constant.
[31] K. Bartik, M. Luhmer, J.-P. Dutasta, A. Collet, and J. Reisse, J. Am. Chem. Soc. **120**, 784 (1998).
[32] P. Z. Sun, C. T. Farrar, and A. G. Sorensen, Magn. Reson. Med. **58**, 1207 (2007).
[33] A. Singh, K. Cai, M. Haris, H. Hariharan, and R. Reddy, Magn. Reson. Med. **69**, 818 (2013).
[34] C. K. Jones, D. Polders, J. Hua, H. Zhu, H. J. Hoogduin, J. Zhou, P. Luijten, and P. C. van Zijl, Magn. Reson. Med. **67**, 1579 (2012).
[35] P. Z. Sun, Y. Wang, Z. Dai, G. Xiao, and R. Wu, Contrast Media Mol. Imaging **9**, 268 (2014).
[36] J. F. Jacquinot and M. Goldman, Phys. Rev. B **8**, 1944 (1973).
[37] P. Z. Sun, Y. Wang, G. Xiao, and R. Wu, Contrast Media Mol. Imaging **8**, 246 (2013).
[38] A. X. Li, R. H. Hudson, J. W. Barrett, C. K. Jones, S. H. Pasternak, and R. Bartha, Magn. Reson. Med. **60**, 1197 (2008).
[39] P. Z. Sun, J. Magn. Reson. **205**, 235 (2010).
[40] S. Klippel, J. Döpfert, J. Jayapaul, M. Kunth, F. Rossella, M. Schnurr, C. Witte, C. Freund, and L. Schröder, Angew. Chem., Int. Ed. **53**, 493 (2014).
[41] C. Witte, M. Kunth, J. Döpfert, F. Rossella, and L. Schröder, J. Visualized Exp. **67**, e4268 (2012).
[42] C. Witte, M. Kunth, F. Rossella, and L. Schröder, J. Chem. Phys. **140**, 084203 (2014).

Supplemental Material
for
Quantitative chemical exchange saturation transfer with hyperpolarized nuclei (qHyper-CEST): Sensing xenon-host exchange dynamics and binding affinities by NMR

Martin Kunth,* Christopher Witte, and Leif Schröder

ERC Project BiosensorImaging, Leibniz-Institut für
Molekulare Pharmakologie (FMP), 13125 Berlin, Germany

CONTENTS

S1: THEORY

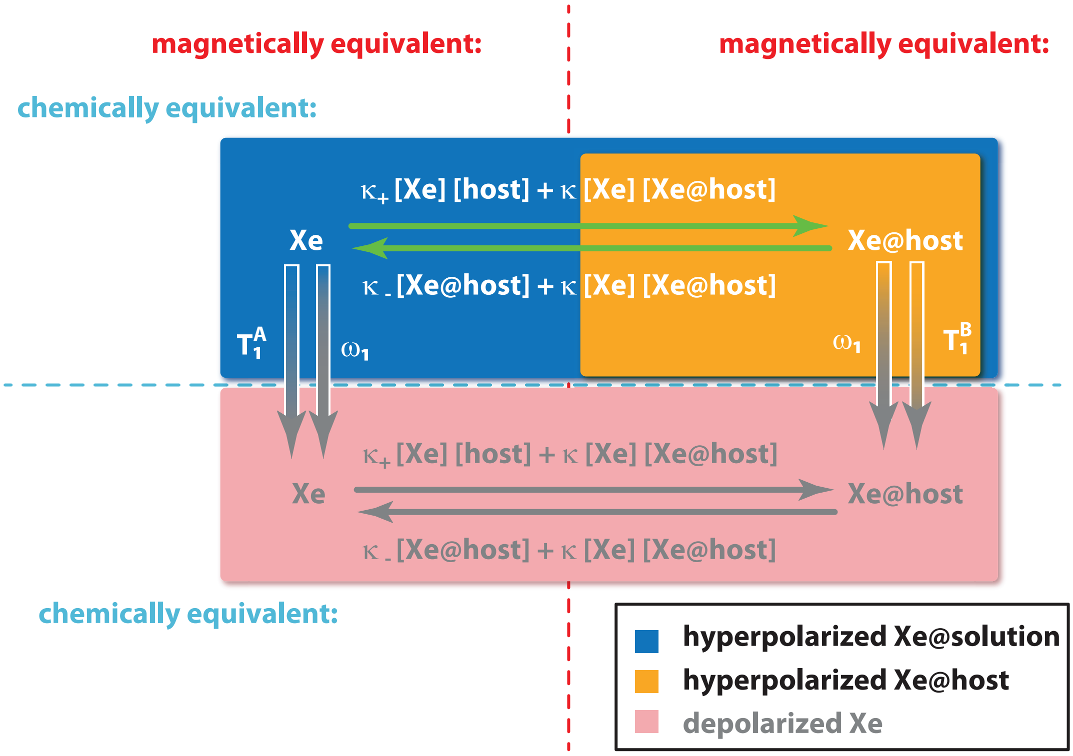

FIG. 1. Combined model of a Xe-host pseudo-first order exchange model $\kappa_{+,-}$ and a kick-out model κ while depolarization of hyperpolarized Xe occurs.

Xe Exchange Model

As written in the main manuscript (section II: Mathematical Tools), the Xe-host exchange is described by two processes: 1) when Xe meets a host that is not occupied by Xe and 2) when Xe meets an occupied host (so-called kick-out exchange[1]). As there is the possibility for both processes to occur simultaneously we included both in our evaluation of Hyper-CEST experiments. The Xe flux Φ_- from pool Xe@host to the pool of free Xe is

$$\Phi_- = \kappa_-[\text{Xe@host}] + \kappa[\text{Xe}]\,[\text{Xe@host}].$$

Hence, the loss rate per occupied host is

$$\frac{d\,\Phi_-}{d\,[\text{Xe@host}]} = K_- = \kappa_- + \kappa[\text{Xe}]. \tag{1}$$

The Xe flux Φ_+ from pool Xe → pool Xe@host is

$$\Phi_+ = \kappa_+[\mathrm{Xe}]\,[\mathrm{host}_{\mathrm{noXe}}] + \kappa[\mathrm{Xe}]\,[\mathrm{Xe@host}].$$

and here the loss rate per Xe atom is

$$\begin{aligned} \frac{d\,\Phi_+}{d\,[\mathrm{Xe}]} = K_+ &= \kappa_+[\mathrm{host}_{\mathrm{noXe}}] + \kappa[\mathrm{Xe@host}] \\ &= \kappa_+[\mathrm{host}_{\mathrm{noXe}}] + \kappa f_B[\mathrm{Xe}] \\ &= \kappa_- f_B + \kappa f_B[\mathrm{Xe}] \\ &= f_B\,K_- \end{aligned} \tag{2}$$

using the ratio of free and bound Xe, $f_B = \frac{[\mathrm{Xe@host}]}{[\mathrm{Xe}]}$, $\frac{\kappa_+}{\kappa_-} = \frac{[\mathrm{Xe@host}]}{[\mathrm{Xe}]\,[\mathrm{host}_{\mathrm{noXe}}]} \Rightarrow \kappa_+[\mathrm{host}_{\mathrm{noXe}}] = \kappa_-\,f_B$ and Equation 1.

Hence, for the combined exchange model, the ratio of free and bound Xe is $f_B = \frac{K_+}{K_-}$. This is similar to an exclusive Xe second-order exchange model with $f_B = \frac{\kappa_+}{\kappa_-}$ and no kick-out model (i.e., $\kappa = 0$).

The exchange rates $k_{AB,BA}$, which we achieve with the BM equations, are therefore effective exchange rates consisting of $k_{BA} = \kappa_- + \kappa[\mathrm{Xe}]$.

Bloch-McConnell (BM) Equation Fitting

The Bloch-McConnell (BM) equations[2, 3]

$$\begin{aligned}\frac{d\vec{M}^A(t)}{dt} &= \gamma\,\vec{M}^A(t)\times(\vec{B}_0+\vec{B}_1(t)) \quad -\hat{R}^A(\vec{M}^A(t)-\vec{M}^A_{\text{th}}) \quad -k_{AB}\vec{M}^A(t)+k_{BA}\vec{M}^B(t)\\ \frac{d\vec{M}^B(t)}{dt} &= \gamma\,\vec{M}^B(t)\times(\vec{B}_0+\vec{B}_1(t)) \quad -\hat{R}^B(\vec{M}^B(t)-\vec{M}^B_{\text{th}}) \quad -k_{BA}\vec{M}^B(t)+k_{AB}\vec{M}^A(t)\end{aligned} \tag{3}$$

empirically describe proton CEST experiments. Without loss of generality, we choose the saturation pulse to be applied along the x-direction and $\vec{B}_0$ along the z-direction. Thus, with $\vec{B}_0=(0,\,0,\,B_0)$ and corresponding relaxation rate matrices

$$\hat{R}^{A,B}=\begin{pmatrix}\frac{1}{T_2^{A,B}} & 0 & 0\\ 0 & \frac{1}{T_2^{A,B}} & 0\\ 0 & 0 & \frac{1}{T_1^{A,B}}\end{pmatrix}, \tag{4}$$

In the rotating lab frame, this explicitly yields to

$$\begin{aligned}\frac{dM_x^A(t)}{dt} &= -R_2^A M_x^A(t)+\Delta\omega_A M_y^A(t)-k_{AB}M_x^A(t)+k_{BA}M_x^B(t)\\ \frac{dM_x^B(t)}{dt} &= -R_2^B M_x^B(t)+\Delta\omega_B M_y^B(t)-k_{BA}M_x^B(t)+k_{AB}M_x^A(t)\\ \frac{dM_y^A(t)}{dt} &= -R_2^A M_y^A(t)-\Delta\omega_A M_x^A(t)+\omega_1 M_z^A(t)-k_{AB}M_y^A(t)+k_{BA}M_y^B(t)\\ \frac{dM_y^B(t)}{dt} &= -R_2^B M_y^B(t)-\Delta\omega_B M_x^B(t)+\omega_1 M_z^B(t)-k_{BA}M_y^B(t)+k_{AB}M_y^A(t)\\ \frac{dM_z^A(t)}{dt} &= -R_1^A(M_z^A(t)-M_{\text{th}}^A)-\omega_1 M_y^A(t)-k_{AB}M_z^A(t)+k_{BA}M_z^B(t)\\ \frac{dM_z^B(t)}{dt} &= -R_1^B(M_z^B(t)-M_{\text{th}}^B)-\omega_1 M_y^B(t)-k_{BA}M_z^B(t)+k_{AB}M_z^A(t),\end{aligned}$$

with the saturation RF irradiation field of $\vec{B}_1=(\omega_1/\gamma,0,0)$, the rotating frame rotation frequency ω_{rf} the irradiation frequency offset of $\Delta\omega_{A,B}=\omega_{rf}-\omega_{A,B}$ with $\omega_{A,B}$ being the Larmor frequency, $\omega_{A,B}=\gamma\cdot B_0$, of each pool in Hz. The intrinsic longitudinal and transverse relaxation rates in s^{-1} of both pools are $R_{1,2}^{A,B}$, the chemical exchange rates k_{AB} from A → B and vise versa in s^{-1}, obeying the rate equation in steady state $k_{AB}=\frac{M_B^0}{M_A^0}k_{BA}$. Two aspects are different for ^{129}Xe compared to ^{1}H-CEST: 1) The initial magnetization is the product of the thermally polarized magnetization M_{th} and the signal enhancement factor η due to hyperpolarization (for our system $\eta \sim$ 25,000 [4]) to $M_0^{A,B} = M_{th}^{A,B} \cdot \eta$, and 2) the gyromagnetic ratio (from $\gamma^{^1H} = 2.6752 \cdot 10^8$ rad/sT $\rightarrow$ $\gamma^{^{129}Xe} = \text{-}0.73997 \cdot 10^8$ rad/sT). Relative pool sizes are obtained with the ratio $\frac{M_0^B}{M_0^A} = f_B$.

For fitting, z-spectra were solved as shown by Murase et al. [5]. The BM equations can be rewritten in matrix form to

$$\frac{d\mathbf{M(t)}}{dt} = \mathbf{A} \cdot \mathbf{M(t)}$$

where

$$\mathbf{M(t)} = \begin{pmatrix} M_x^A(t) & M_x^B(t) & M_y^A(t) & M_y^B(t) & M_z^A(t) & M_z^B(t) & 1 \end{pmatrix}^T$$

and

$$\mathbf{A} = \begin{pmatrix} -(R_2^A + k_{AB}) & +k_{BA} & +\Delta\omega_A & 0 & 0 & 0 & 0 \\ +k_{AB} & -(R_2^B + k_{BA}) & 0 & +\Delta\omega_B & 0 & 0 & 0 \\ -\Delta\omega_A & 0 & -(R_2^A + k_{AB}) & +k_{BA} & +\omega_1 & 0 & 0 \\ 0 & -\Delta\omega_B & +k_{AB} & -(R_2^B + k_{BA}) & 0 & +\omega_1 & 0 \\ 0 & 0 & -\omega_1 & 0 & -(R_1^A + k_{AB}) & +k_{BA} & R_1^A M_{\text{th}}^A \\ 0 & 0 & 0 & -\omega_1 & +k_{AB} & -(R_1^B + k_{BA}) & R_1^B M_{\text{th}}^B \\ 0 & 0 & 0 & 0 & 0 & 0 & 0 \end{pmatrix},$$

which has the analytical solution

$$\mathbf{M}(t_{\text{sat}}) = e^{\mathbf{A}t_{\text{sat}}}\mathbf{M}(0), \tag{5}$$

with $\mathbf{M}(0)$ being the initial magnetization $\mathbf{M}(0) = \eta \cdot \mathbf{M}_{\text{th}}$. The extension to multiple pools is straight forward, as demonstrated by others [6, 7].

Validation of BM Equations Implementation

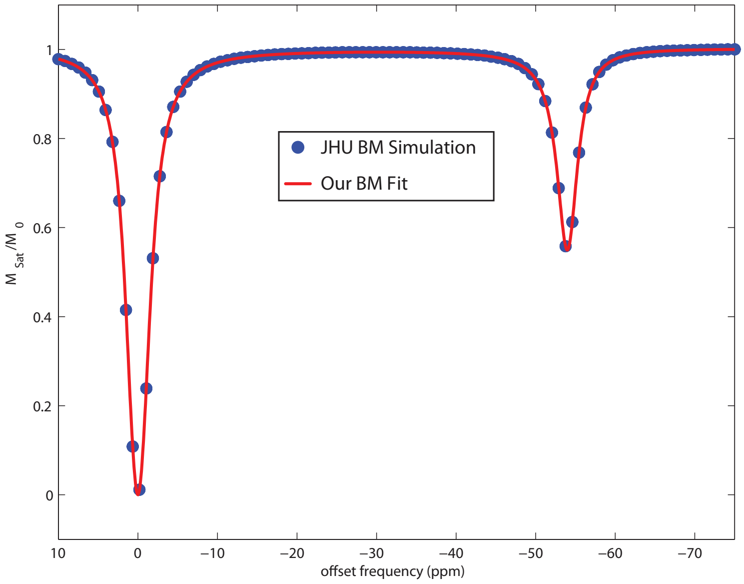

FIG. 2. Validation of our BM equations implementation. We fitted ^{1}H-CEST data, simulated independently by an implementation of Craig Jones from the John-Hopkins University (JHU), Baltimore, USA[8], for saturation pulse parameters of $B_1/t_{\text{sat}} = 2.5\ \mu\text{T}/4$ s and ^{1}H-CEST system properties (listed in Table I) with our Hyper-CEST z-spectra BM equations fitting routine used in the main manuscript after it was adapted to ^{1}H-CEST ($\gamma^{^{129}Xe} \to \gamma^{^1H}$ and $M_0^{A,B} = M_{th}^{A,B} \cdot \eta \to M_0^{A,B} = M_{th}^{A,B}$). The results are shown in this figure and listed in Table I. We acknowledge the website: http://www.nirbhay.info/ with grant support: NIH/NIBIB grants P41 EB015909 and RO1 EB015032.

TABLE I. Parameters for BM equations simulation (JHU) and fitting results of the BM equations implementation used in this manuscript (relaxivities for pool B were not accessible).

	pool A				pool B				
	δ_A / ppm	f_A	R_1^A / s^{-1}	R_2^A / s^{-1}	δ_B / ppm	f_B	k_{BA} / s^{-1}	R_1^B / s^{-1}	R_2^B / s^{-1}
JHU	0	1	0.333	10	-54	0.0022	3000	0.333	10
Our	6.789e-5	1	0.34488	10.2379	-54.0004	0.002329	3044	1.403	0.33336
BM	± 0.00165	-	± 0.00645	± 0.151	± 0.0035	± 2.5e-5	± 20	± 1.14	± 16

Full Hyper-CEST (FHC) Solution

As shown by Zaiss et al. [9], the complex BM equations can be approximated analytically, when the magnetization is always much larger than the stationary solution (as in Hyper-CEST). Therefore, the full Hyper-CEST (FHC) model function is

$$\frac{M_z^A(t_{sat})}{M_z^A(t_{sat}=0)}(\Delta\omega) = e^{-\lambda_{depol}(\Delta\omega)\cdot t_{sat}}, \tag{6}$$

with the full Hyper-CEST depolarization rate

$$\lambda_{depol}(\Delta\omega) = -\lambda_{direct}(\Delta\omega) - \lambda_{CEST}^{AB}(\Delta\omega)$$

and

$$\begin{aligned} -\lambda_{direct}(\Delta\omega) &= R_1^A\ \cos^2(\theta) + R_2^A\ \sin^2(\theta) \\ -\lambda_{CEST}^{AB}(\Delta\omega) &= \frac{S_1+S_2}{S_3+S_4+S_5+S_6+S_7+S_8} \end{aligned}$$

$$\begin{aligned} S_1 &= \omega_1^2\frac{k_{AB}\cdot k_{BA}}{k_{AB}+k_{BA}}\cdot(\delta\omega_B-\delta\omega_A)^2 & S_2 &= \frac{R_2^B}{k_{AB}+k_{BA}}\cdot\omega_1^2 k_{AB}(\Delta\omega_A^2+(k_{AB}+k_{BA})^2+k_{BA}R_2^B+\omega_1^2) \\ S_3 &= (\Delta\omega_A(k_{BA}+R_2^B)+\Delta\omega_B k_{AB})^2 & S_4 &= (k_{AB}+k_{BA}+R_2^B)^2\omega_1^2 \\ S_5 &= (\Delta\omega_A\Delta\omega_B-k_{AB}R_2^B)^2 & S_6 &= \Delta\omega_B^2\omega_1^2 \\ S_7 &= k_{AB}R_2^B\omega_1^2 & S_8 &= \frac{k_{AB}+k_{BA}+R_2^B}{k_{AB}+k_{BA}}(\Delta\omega_A^2\omega_1^2+\omega_1^4). \end{aligned}$$

In the rotating frame, the saturation RF irradiation field is $\vec{B}_1 = (\omega_1/\gamma, 0, 0)$. With the rotating frame rotation frequency, ω_{rf}, the irradiation frequency offset, $\Delta\omega_{A,B} = \omega_{rf} - \omega_{A,B}$ and $\omega_{A,B}$ being the Larmor frequency of each pool in Hz. The intrinsic longitudinal and transverse relaxation rates in s^{-1} of both pools are $R_{1,2}^{A,B}$ and the chemical exchange rates are given by k_{AB} from A → B and vise versa in s^{-1}. The system obeys the rate equation in steady state $k_{AB} = \frac{M_B^0}{M_A^0}k_{BA}$ and experiences an effective tip angle of $\theta = \tan^{-1}(\omega_1/\Delta\omega_A)$.

S2: RICIAN CORRECTION

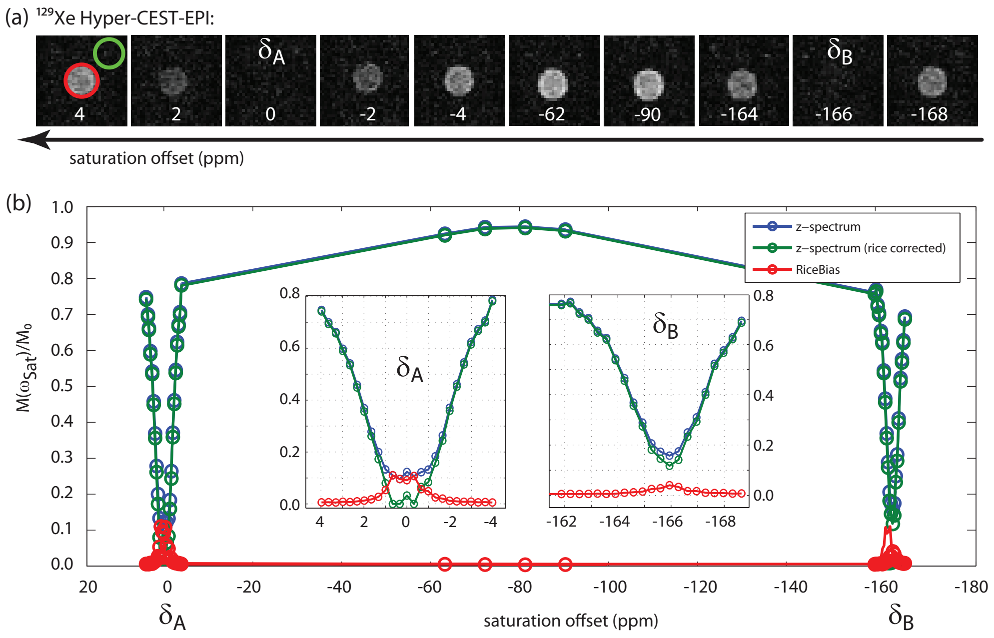

FIG. 3. Principle of the Rician correction.

(a) shows a series of ^{129}Xe Hyper-CEST echo planar image (EPI)[10] magnitude images for different saturation offsets, ω_{sat}, with a noise level above zero. (b) To correct for this, a Rician correction was implemented minimizing the function

$$\begin{aligned}
A_{\text{true}} &= e^{(-\omega_{\text{sat}}^2/2/\sigma^2)/2} \\
&\cdot [(1 - (-\omega_{\text{sat}}^2/2/\sigma^2)) \ \cdot \ \text{besseli}(0, -(-\omega_{\text{sat}}^2/2/\sigma^2)/2) \\
&- (-\omega_{\text{sat}}^2/2/\sigma^2) \ \cdot \ \text{besseli}(1, -(-\omega_{\text{sat}}^2/2/\sigma^2)/2)] \\
&\cdot \sigma \cdot \sqrt{\pi/2} \qquad (7)
\end{aligned}$$

$$A_{\text{rice bias}} = A_{\text{measured}} - A_{\text{true}}, \qquad (8)$$

with σ the true noise measured in the green region-of-interest (ROI), A_{measured} the mean signal amplitude as measured in the ROI containing signal (red ROI) and besseli the modified Bessel function of first-kind in Matlab. The measured z-spectrum (blue) was corrected (green) by the calculated Rician bias (red). The green data were fitted by the BM equations and the FHC solution in the main manuscript.

S3: XENON HOST OCCUPANCY

The Xe host occupancy, β, is introduced as the ratio of the concentration of hosts occupied by Xe, [Xe@host], and the total host concentration, [host],

$$\beta = \frac{[\mathrm{Xe@host}]}{[\mathrm{host}]} \;\Rightarrow\; [\mathrm{Xe@host}] = \beta\,[\mathrm{host}].$$

Rewriting the ratio of free and bound Xe, f_B, yields

$$f_B = \frac{[\mathrm{Xe@host}]}{[\mathrm{Xe}]} = \beta\,\frac{[\mathrm{host}]}{[\mathrm{Xe}]}. \tag{9}$$

Assuming that [Xe] = constant (the concentration in solution is given by the Ostwald coefficient, [Xe] = 2,340 μM), then $\beta/[\mathrm{Xe}]$ is the linear slope of f_B versus [host] (here $\mathrm{CrA_{ma}}$ in pure DMSO; compare with Fig. 4(f) in the main manuscript):

$$f_B([\mathrm{CrA_{ma}}]) = (3.3 \pm 0.1)/\mu\mathrm{M} \cdot [\mathrm{CrA_{ma}}] \cdot\; 10^{-5}.$$

Therefore, at room temperature the Xe-$\mathrm{CrA_{ma}}$ occupancy in DMSO is

$$\beta = \frac{3.3 \cdot\; 10^{-5}}{\mu\mathrm{M}} \cdot 2,340\,\mu\mathrm{M} = 0.077 \sim 8\%.$$

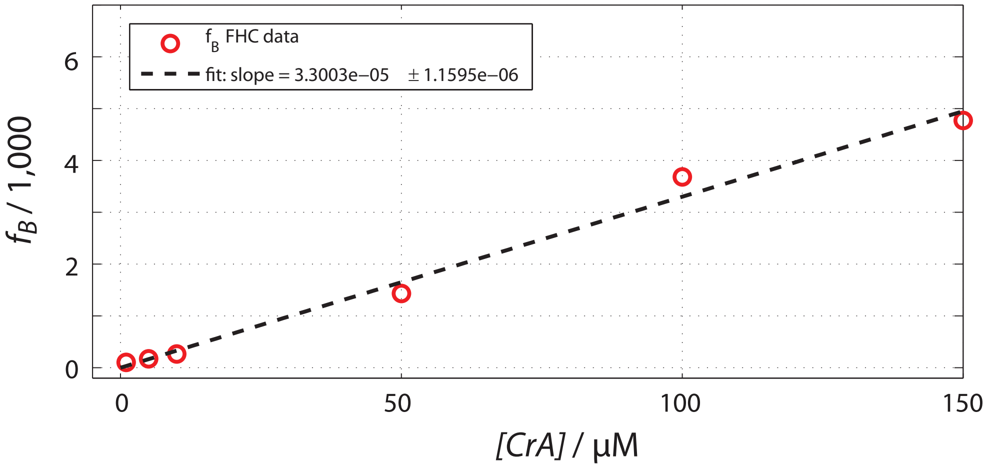

FIG. 4. f_B versus $[\mathrm{CrA_{ma}}]$ data (red circles) (shown in Fig. 4(f) in the main manuscript) and the linear fit (black dashed line).

S4: XENON LONGITUDINAL RELAXATION TIME T_1^A IN DMSO

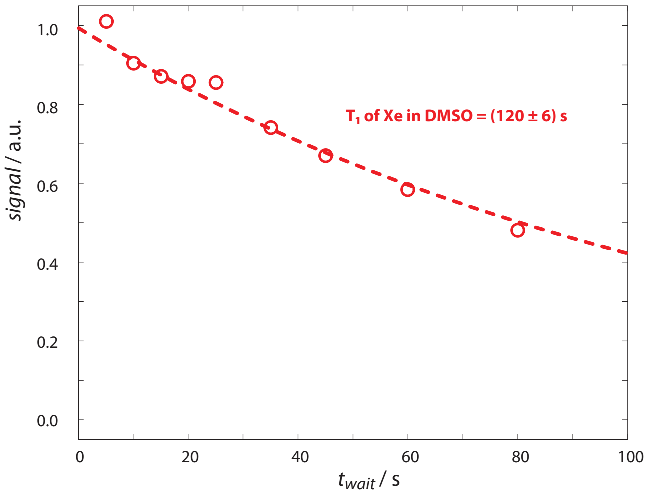

FIG. 5. Longitudinal relaxation time T_1^A of Xe in DMSO. For each data point, fresh HP Xe was bubbled into solution and after a variable waiting time t_{wait}, we measured the Xe@solution signal and fitted the normalized results for different waiting times to $S(t_{\mathrm{wait}}) = a \cdot \exp(-t_{\mathrm{wait}}/T_1^A)$. The T_1^A of Xe in DMSO was (120 ± 6) s.

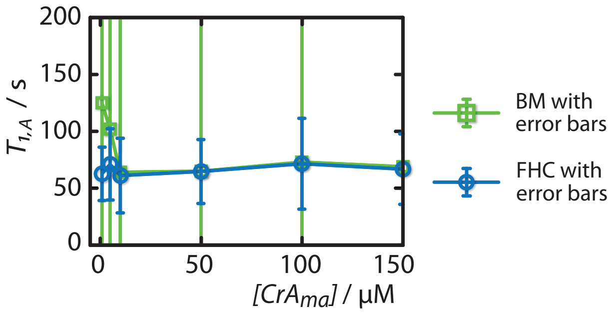

FIG. 6. qHyper-CEST based determination of the longitudinal relaxation time T_1^A of Xe in DMSO (achieved from the same data set as for Fig. 4 of the main manuscript). T_1^A was determined to $T_1^A \sim 60$ s. From the T_1^A measurement in DMSO (see Fig. 5), we achieved a $T_1^A = (120 \pm 6)$ s. Considering that the baseline of the z-spectrum was used to extract T_1^A, its observation is therefore limited to the duration of the saturation pulse t_{sat}. Since the longest t_{sat} was 10 s, it is difficult to sample a decay over 120 s and this deviation becomes obvious. However, in comparison with the simulation resluts in Fig. 3 of the main manuscript, T_1^A can be quantified reasonably accurate with qHyper-CEST.

S5: ASSOCIATION CONSTANT (BINDING CONSTANT)

Considering the combined Xe-exchange model as written in the main manuscript (section II: Mathematical Tools). The $[\mathrm{Xe}_{aq}]$ time evolution is

$$\frac{d\,[\mathrm{Xe}_{aq}]}{d\,t} = -\kappa_+[\mathrm{host}_{\mathrm{noXe}}]\,[\mathrm{Xe}_{aq}] + \kappa_-[\mathrm{Xe@host}] - \kappa[\mathrm{Xe}_{aq}]\,[\mathrm{Xe@host}] + \kappa[\mathrm{Xe}_{aq}]\,[\mathrm{Xe@host}].$$

In chemical equilibrium we have $\frac{d\,[\mathrm{Xe}]}{d\,t} = 0$ which yields $\kappa_+[\mathrm{host}_{\mathrm{noXe}}]\,[\mathrm{Xe}_{aq}] = \kappa_-[\mathrm{Xe@host}]$. Hence, the Xe association or binding constant is

$$K_A = \frac{\kappa_+}{\kappa_-} = \frac{[\mathrm{Xe@host}]}{[\mathrm{Xe}_{aq}]\,[\mathrm{host}_{\mathrm{noXe}}]}. \tag{10}$$

With the total host concentration, [host], being the sum of the concentration of hosts occupied by Xe, [Xe@host], and not occupied by Xe, $[\mathrm{host}_{\mathrm{noXe}}]$:

$$[\mathrm{host}] = [\mathrm{Xe@host}] + [\mathrm{host}_{\mathrm{noXe}}].$$

The binding constant is then:

$$\begin{aligned} K_A &= \frac{[\mathrm{Xe@host}]}{[\mathrm{Xe}_{aq}]\,[\mathrm{host}_{\mathrm{noXe}}]} = \frac{f_B}{[\mathrm{host}_{\mathrm{noXe}}]} = \frac{f_B}{[\mathrm{host}] - [\mathrm{Xe@host}]} \\ &= \frac{f_B}{[\mathrm{host}] - f_B\,[\mathrm{Xe}]}. \end{aligned} \tag{11}$$

Error Estimation of K_A

The errors are assumed to be $\Delta[\mathrm{Xe}] = 0.001\ \mathrm{M} = 1\ \mu\mathrm{M}$ (due to inaccuracies in the pressure reading), $\Delta[\mathrm{host}] = 2\ \mu\mathrm{M}$, and standard error from fitting in Δf_B. The error of the association constant can then be estimated to

$$\begin{aligned} \frac{\partial K_A}{\partial f_B} &= \frac{[\mathrm{host}]}{([\mathrm{host}] - f_B \cdot [\mathrm{Xe}])^2} \\ \frac{\partial K_A}{\partial [\mathrm{host}]} &= -\frac{f_B}{([\mathrm{host}] - f_B \cdot [\mathrm{Xe}])^2} \\ \frac{\partial K_A}{\partial [\mathrm{Xe}]} &= \frac{f_B^2}{([\mathrm{host}] - f_B \cdot [\mathrm{Xe}])^2} \\ \Delta K_A &= \sqrt{\left(\frac{\partial K_A}{\partial f_B}\Delta f_B\right)^2 + \left(\frac{\partial K_A}{\partial [\mathrm{host}]}\Delta[\mathrm{host}]\right)^2 + \left(\frac{\partial K_A}{\partial [\mathrm{Xe}]}\Delta[\mathrm{Xe}]\right)^2}. \end{aligned} \tag{12}$$

S6: RADIO-FREQUENCY FIELD HOMOGENEITY

B_1 Mapping

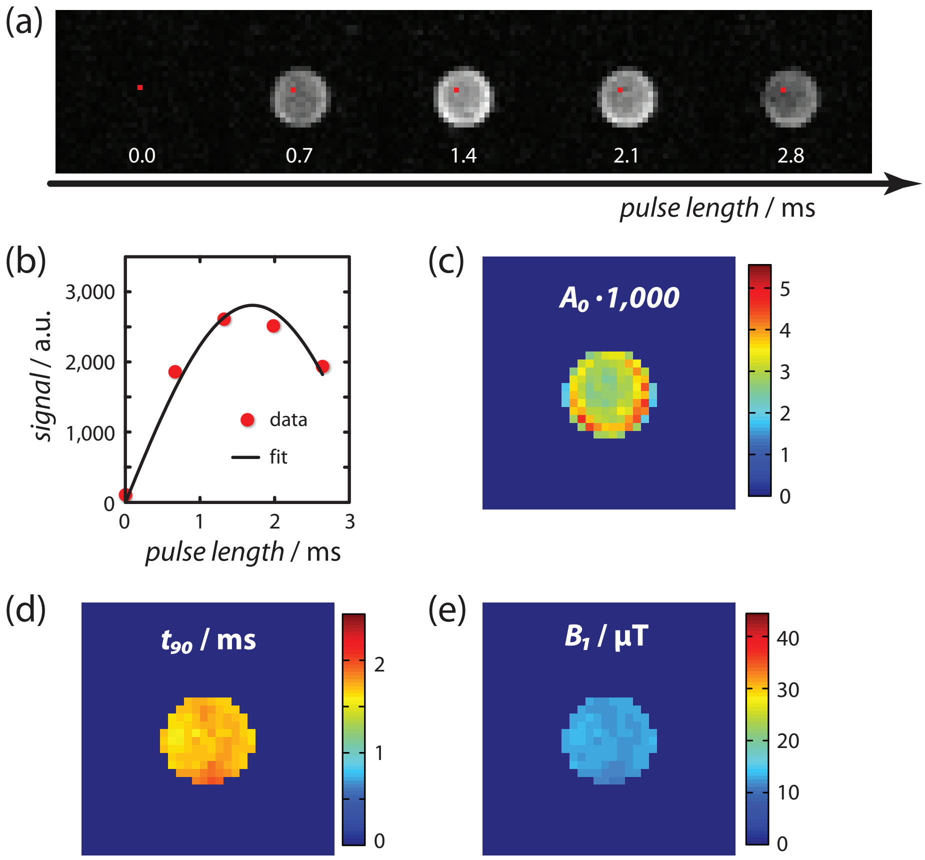

FIG. 7. Principle of B_1 mapping. (a) shows the image series obtained from a ^{129}Xe EPI pulse sequence with increased block pulse shaped excitation pulse length (PL). (b) shows the signal, S, (red dots) of the red pixel in (a) which was fitted to the function $S(PL) = A_0 \cdot |\sin\{(\pi/2 \cdot PL/t_{90} \cdot 1{,}000\}|$ (black line) with an amplitude of $A_0 = 2{,}640 \pm 130$ and the 90° time, $t_{90} = (1{,}800 \pm 70)$ μs. (c) shows the fitting results of A_0 and t_{90} for each pixel of the whole phantom (c, d). The B_1 values (e) were calculated by $B_1 = (\pi/2)/(2 \cdot \pi \cdot 11.777\ \mathrm{MHz/T} \cdot t_{90})$.

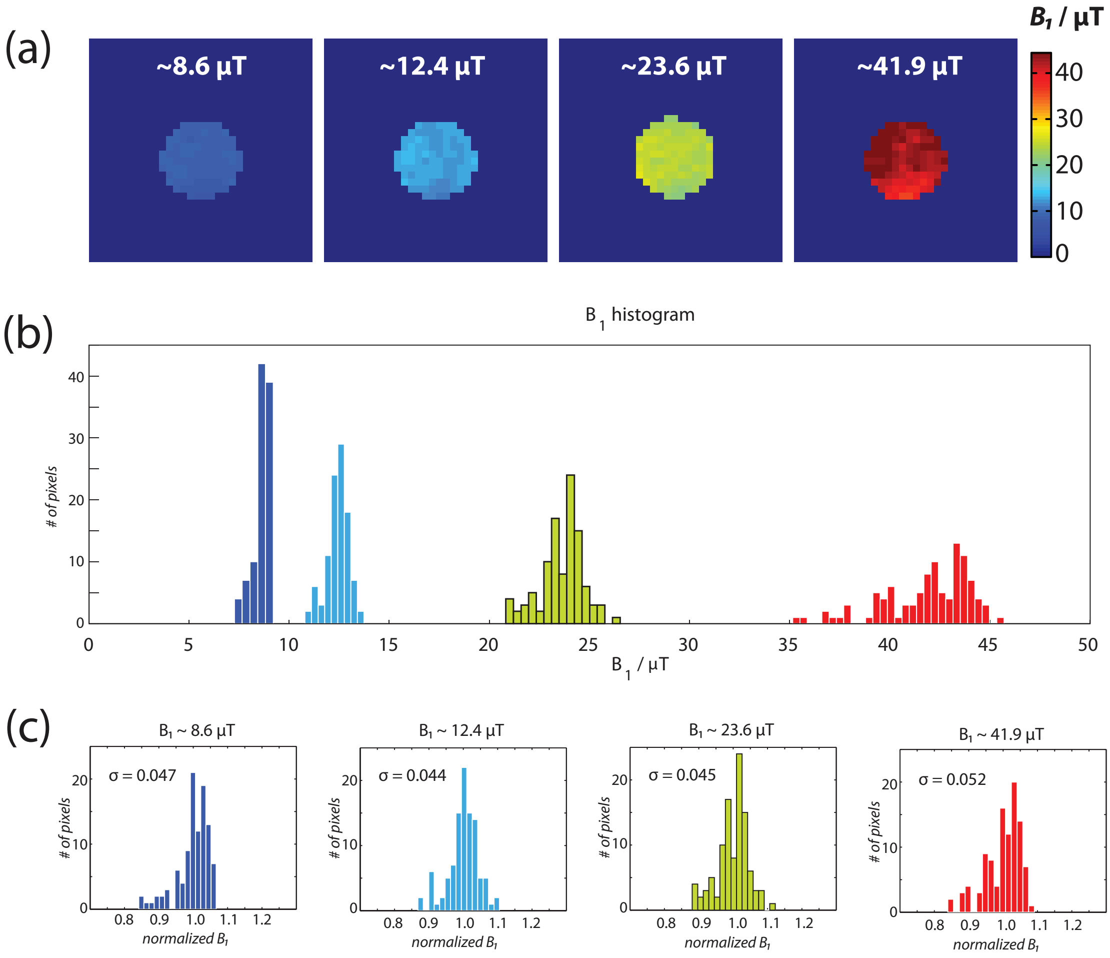

FIG. 8. Measured B_1 maps and homogeneity analysis. (a) shows B_1 maps as obtained in Fig.(7) for pulse strengths of $B_1 \sim \{8.6, 12.4, 23.6, 41.9\}$ μT. (b) shows the histogram analysis for each B_1 map with adaptive bin number to keep the bin size constant. The results do not follow a Gaussian distribution. (c) shows these histogram values normalized to its mean value and displayed with a constant bin number of 14. The results show a trend of slightly increased inhomogeneities at higher strength.

Simulation and Fitting of z-Spectra with B_1 Inhomogeneities

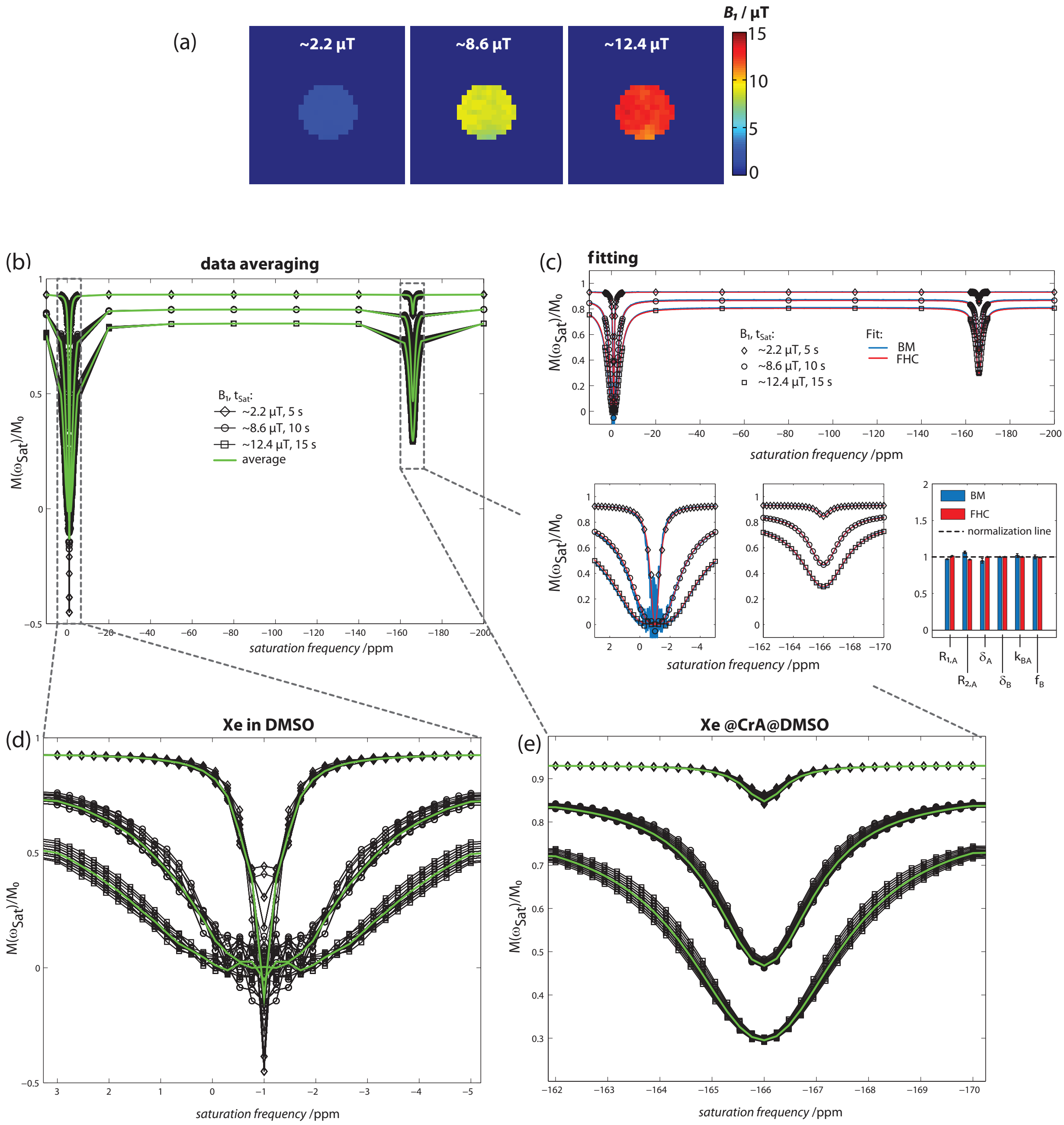

FIG. 9.

Simulation of experimental data analysis by averaging over multiple z-spectra with different effective B_1 strengths. (a) shows B_1 maps with Gaussian mean values of $B_1 \sim \{2.2, 8.6, 12.4\}$ μT. The maps with 8.6 μT and 12.4 μT were directly measured as shown in Fig. 7. The B_1 map for 2.2 μT could not be recorded due to bandwidth limitations and was extrapolated from the 8.6 μT map by dividing by 4. These B_1 maps were used for z-spectra simulation and fitting. They were evaluated by an histogram analysis and a total of 104 z-spectra were simulated with parameters listed in Table I in the main manuscript for the combinations of t_{sat} and B_1 given in the legend (diamonds: 2.2 μT and 5 s; circles: 8.6 μT and 10 s; rectangles: 12.4 μT and 15 s). The averaged z-spectra (green line; zoom in of Xe in DMSO (f) and Xe@CrA$_{\mathrm{ma}}$@DMSO (e)) is not centered with the individual z-spectra (black data) because of the non-Gaussian inhomogeneity distribution as shown in Fig.8(b). The global fitting of these averaged z-spectra showed excellent parameter recovery (c) indicating that the method is robust in the presence of RF inhomogeneities (of the magnitude observed in (a)).

---

* kunth@fmp-berlin.de

[1] Bartik, K., Luhmer, M., Dutasta, J.P., Collet, A., Reisse, J. *Journal of the American Chemical Society* **1998**, *120*, 784-791.

[2] H.M. McConnell *Journal of Chemical Physics* **1958**, *28*, 430-431.

[3] D.E. Woessner *Journal of Chemical Physics* **1961**, *35*, 41-48.

[4] Witte, C., Kunth, M., Döpfert, J., Rossella, F., Schröder, L. *Journal of Visualized Experiments* **2012**, *67*, e4268.

[5] K. Murase, N. Tanki *Magnetic Resonance Imaging* **2011**, *29*, 126-131.

[6] Li, A. X., Hudson, R. H., Barrett, J. W., Jones, C. K., Pasternak, S. H., Bartha, R. *Magnetic Resonance in Medicine* **2008**, *60*, 1197-1206.

[7] Sun, P. Z. *Journal of Magnetic Resonance* **2010**, *205*, 235-241.

[8] Jones, C.K., Polders, D., Hua, J., Zhu, H., Hoogduin, H.J., Zhou, J., Luijten, P., van Zijl, P.C. *Magnetic Resonance in Medicine* **2012**, *67*, 1579-1589.

[9] Zaiss, M., Schnurr, M., Bachert, P. *The Journal of Chemical Physics* **2012**, *136*, 144106.

[10] Kunth, M., Döpfert, J., Witte, C., Rossella, F., Schröder, L. *Angewandte Chemie International Edition* **2012**, *51*, 8217-8220

D.3 OPTIMAL SATURATION FOR HYPER-CEST MRI

FULL REFERENCE:
Martin Kunth, Christopher Witte, and Leif Schröder. Continuous-wave saturation considerations for efficient xenon depolarization. *NMR in Biomedicine*, 28: 601-606, 2015; Kunth *et al.*[127].

AUTHOR CONTRIBUTIONS: M.K. designed research, performed research and analyzed data; M.K., C.W. and L.S. wrote the paper.

On the following 13 pages, the original publication and its Supplemental Material is attached.

- Full Article: *NMR Biomed*, 28: 601-606, 2015 – Reprinted with permission. Copyright © 2015 John Wiley & Sons, Ltd.

Rapid communication

NMR
IN BIOMEDICINE

Received: 16 January 2015, Revised: 6 March 2015, Accepted: 18 March 2015,

(wileyonlinelibrary.com) DOI: 10.1002/nbm.3307

Continuous-wave saturation considerations for efficient xenon depolarization

Martin Kunth, Christopher Witte and Leif Schröder*

The combination of hyperpolarized Xe with chemical exchange saturation transfer (Hyper-CEST) is a powerful NMR technique to detect highly dilute concentrations of Xe binding sites using RF saturation pulses. Crucially, that combination of saturation pulse strength and duration that generates the maximal Hyper-CEST effect is *a priori* unknown. In contrast to CEST in proton MRI, where the system reaches a steady-state for long saturation times, Hyper-CEST has an optimal saturation time, i.e. saturating for shorter or longer reduces the Hyper-CEST effect. Here, we derive expressions for this optimal saturation pulse length. We also found that a pulse strength, B_1, corresponding to five times the Xe exchange rate, k_{BA} (i.e. $B_1 = 5\ k_{BA}/\gamma$ with the gyromagnetic ratio of ^{129}Xe, γ), generates directly and without further optimization 96 % of the maximal Hyper-CEST contrast while preserving spectral selectivity. As a measure that optimizes the amplitude and the width of the Hyper-CEST response simultaneously, we found an optimal saturation pulse strength corresponding to $\sqrt{2}$ times the Xe exchange rate, i.e. $B_1 = \sqrt{2}\,k_{BA}/\gamma$. When extremely low host concentration is detected, then the expression for the optimum saturation time simplifies as it approaches the longitudinal relaxation time of free Xe. Copyright © 2015 John Wiley & Sons, Ltd.
Additional supporting information may be found in the online version of this article at the publisher's web site.

Keywords: xenon; biosensor; hyperpolarization; CEST; Hyper-CEST; Bloch–McConnell; quantification

INTRODUCTION

Dissolved xenon (Xe) binds non-covalently to various binding sites or hosts and continuously undergoes exchange for many of these systems, including synthetic macromolecular hosts and protein cavities (1,2). The well-studied Xe encapsulating molecule cryptophane can be functionalized for biological relevant targets and acts as a Xe biosensor (3,4). However, a high biosensor concentration is required for direct Xe NMR detection. Using the sensitive chemical exchange saturation transfer (CEST) with hyperpolarized xenon (Hyper-CEST) MRI technique, which combines chemical exchange saturation transfer with hyperpolarized Xe (5), extremely dilute bound Xe signals can be measured compared with direct NMR. Many different Xe biosensors have been developed, with detection limits down to the nano and pico molar regimes. Such Xe biosensors include genetically encoded gas vesicles (6), perfluoroctyl bromid nano emulsion (7,8), bacterial spores (9) or cryptophanes (10–12). It is noteworthy that cryptophanes can further sense biomembrane fluidity (13). However, build-up of the measured Hyper-CEST effect is complex and relies on the specific Xe-host system properties and the applied saturation pulse strength and duration. For the case of proton (^{1}H)-CEST, there have been numerous analytical studies that investigated the conditions for CEST signal build-up (14–18). However, for the case of Hyper-CEST it has not been fully investigated. In particular, the combination of saturation pulse strength and duration that generates the maximal Hyper-CEST effect has not been reported.

Here, we propose optimal saturation pulse parameters for a maximum, but still spectrally narrow, Hyper-CEST effect using continuous-wave (cw) saturation for dilute Xe host systems. We demonstrate our method on the well studied Xe-host system cryptophane-A monoacid (CrA) in dimethyl sulfoxide (DMSO). We provide evidence that saturation times longer than our proposed optimal time reduce the Hyper-CEST effect. Additionally, we demonstrate that the CEST effect should be built up on a time-scale faster than the competing longitudinal relaxation of free Xe, T_1^A, i.e. saturation times exceeding T_1^A make the detected effect increasingly ineffective.

MATERIALS AND METHODS

Data fitting

All simulations, calculations and fitting routines were implemented and performed in Matlab 7 (The Mathworks, Natick, MA, USA) on a standard desktop PC (64 bit, 8 cores each at 2.80 GHz, 4 GB RAM), as described in (22).

Full qHyper-CEST results

The full quantitative Hyper-CEST (qHyper-CEST) results in the section on quantification of Xe exchange dynamics by qHyper-CEST

---

* Correspondence to: L. Schröder, ERC Project BiosensorImaging, Leibniz-Institut für Molekulare Pharmakologie (FMP), 13125 Berlin, Germany.
E-mail: lschroeder@fmp-berlin.de

M. Kunth, C. Witte, L. Schröder
ERC Project BiosensorImaging, Leibniz-Institut für Molekulare Pharmakologie (FMP), 13125 Berlin, Germany

Abbreviations used: *CEST, chemical exchange saturation transfer; CrA, cryptophane-A monoacid; cw, continuous-wave; DMSO, dimethyl sulfoxide; FHC, full Hyper-CEST; Hyper-CEST, chemical exchange saturation transfer with hyperpolarized xenon; qHyper-CEST, quantitative chemical exchange saturation transfer with hyperpolarized nuclei; RF, radio-frequency; SLM, standard liters per minute; Xe, xenon.*

and Fig. 1 were as follows: longitudinal relaxation time of free Xe, $T_1^A = (125 \pm 26)$ s; transverse relaxation time of free Xe, $T_2^A = (2.6 \pm 0.2)$ s; fractional size of pool B, $f_B = (13.4 \pm 0.4) \times 10^{-4}$; exchange rate, $k_{BA} = (317 \pm 17)$ s^{-1}; relative chemical shift, $\Delta\delta = -(165.18 \pm 0.01)$ ppm; binding constant, $K_A = (29 \pm 2)$ M^{-1}; and occupancy of $\beta = 6\,\%$.

Sample preparation

Samples were prepared by dissolving cryptophane-A monoacid (CrA, provided by Kang Zhao, Tianjin University, China) into dimethyl sulfoxide (DMSO) at room temperature to a concentration of [CrA] = 50 μM.

Hyperpolarization and ^{129}Xe delivery

Hyperpolarized Xe was generated in continuous-flow mode (0.35 SLM (standard liters per minute) using a custom-designed polarizer (31,32) with a Xe gas mix ((2/10/88 vol.– % Xe/N_2/He), ^{129}Xe natural abundance 26.4 %) at a total pressure of $p = 4.5$ atm. This set-up achieves ca. 25 % Xe spin hyperpolarization via spin-exchange optical pumping with rubidium atoms. A 150 W cw laser (795 nm, 0.5 nm bandwidth, QPC Lasers) is used for excitation of the rubidium valence electron. The hyperpolarized gas mix is bubbled for 13 s at a flow rate of 0.1 SLM into the sample, followed by a 2 s delay in order to allow the bubbles to collapse and subsequent signal acquisition. The Xe concentration in DMSO, assuming Xe saturation, was [Xe] = 2340 μM ([Xe] = $L\,p\,Xe_{pc}$/(0.0254 L/mM), with an Xe Ostwald solubility coefficient in DMSO of L = 0.66 L/atm and $Xe_{pc} = 0.02$).

NMR experiments

NMR experiments were performed on a $|\vec{B_0}| = 9.4$ T NMR wide-bore spectrometer (Bruker Biospin, Ettlingen, Germany) equipped with gradient coils for imaging. All samples were measured at room temperature ($T = 295$ K) by using the variable temperature unit to maintain stable conditions. RF excitation and detection were achieved with a 10 mm inner-diameter double-resonant probe (^{129}Xe and ^{1}H). The B_1 field inhomogeneities can significantly affect the CEST quantification and these must be known. However, as shown in (22), B_1 field inhomogeneities are negligible for our micro-imaging system. ^{129}Xe Hyper-CEST MRI scans were obtained with a ^{129}Xe Hyper-CEST echo-planar imaging pulse sequence (10) with the following parameters: Fourier acceleration 1.68; double sampling; echo time 5.7 ms; acquisition time 19.8 ms; no smoothing filter was applied to the images. Image geometry parameters were as follows: field of view 20×20 mm^2; matrix size 32×32; in-plane resolution 625×625 μm^2; slice thickness 20 mm. The saturation pulse strengths and durations used are given in the figure captions. We performed the qHyper-CEST analysis based on the imaging series that yielded *z*-spectra from region-of-interest averaged signals containing pixels in each MRI scan.

THEORY

The time evolution of the detectable macroscopic magnetization of an exchanging two-pool spin system with interaction under application of a (selective) saturation pulse (continuous-wave RF pulse) with a specific strength, B_1, and for a certain time, t_{sat} (saturation duration), is described by the Bloch–McConnell equations (19,20). We follow a powerful analytical approximation of the Bloch–McConnell equations for the case of Hyper-CEST: the full Hyper-CEST (FHC) solution (21), describing the detected Hyper-CEST signal for a saturation frequency offset, $\Delta\omega$, relative to the detection resonance of free Xe as

$$\text{Hyper}-\text{CEST signal}(\Delta\omega, B_1, t_{\text{sat}}) = 1 - e^{-\lambda_{\text{depol}}(\Delta\omega, B_1)t_{\text{sat}}} \qquad [1]$$

with the Lorentzian line shaped Xe depolarization rate

$$\lambda_{\text{depol}}(\Delta\omega, B_1) = C(\Delta\omega) + \frac{\lambda_{\text{on-res}}(B_1)\frac{\Gamma(B_1)^2}{4}}{\frac{\Gamma(B_1)^2}{4} + (\Delta\omega_B(\Delta\omega) + x_0(B_1))^2} \qquad [2]$$

The saturation frequency offsets relative to pools A and B are $\Delta\omega_{A,B}(\Delta\omega) = \Delta\omega - \delta\omega_{A,B}$, with $\delta\omega_{A,B}$ being the resonance frequencies of both pools in Hz, or, normalized with the Larmor frequency, ω_{gas}, to ppm: $\delta_{A,B} = \delta\omega_{A,B}/\omega_{gas}$. The longitudinal and transverse relaxation rates of unbound Xe, $R_{1,2}^A$, determine the baseline $C(\Delta\omega)$. Excessive saturation pulse strength, B_1, might impact the position of the maximum CEST response, $x_0(B_1)$. However, with some reasonable assumptions this shift away from the true resonance frequency of bound Xe, $\delta\omega_B$, approximates 0 (see Supplementary Material S1). The Xe exchange rates from free to bound state and from bound to free state are k_{AB} and k_{BA}, respectively. They obey the law of initial magnetization conservation, $k_{AB} = k_{BA}(M_{0,B}/M_{0,A})$. The fractional size of pool B, f_B, is the ratio of bound and free Xe. In the limit $k_{BA} \gg R_2^B$ (with R_2^B denoting the transverse relaxation rate of bound Xe), the Lorentzian line shaped Xe depolarization rate, λ_{depol}, on-resonant with the bound Xe signal, reduces to (21,22)

$$\lambda_{\text{on-res}}(B_1) \approx f_B\, k_{BA} \frac{(\gamma\, B_1)^2}{(\gamma\, B_1)^2 + k_{BA}^2} \qquad [3]$$

with the gyromagnetic ratio of Xe ($\gamma/(2\pi) = -11.77$ MHz/T). In the same limit, the full width at half-maximum of the depolarization rate is (21)

$$\Gamma(B_1) \approx 2\sqrt{(\gamma\, B_1)^2 + k_{BA}^2} \qquad [4]$$

Similarly to Equation [2], an even more general framework has been developed for ^{1}H-CEST, where $\lambda_{depol} = R_{1\rho} = R_{eff} + R_{ex}$, with longitudinal relaxation rate of the detection pool in the rotating frame $R_{1\rho}$, effective relaxation rate R_{eff} and exchange-dependent relaxation rate in the rotating frame R_{ex} (14,23). Also here the R_{ex} part should be dominant through the saturation pulse in order to produce a CEST effect before the R_{eff} part intrinsically cancels the total signal. For ^{1}H-CEST analysis, it has also been shown that it is beneficial to remove the steady-state signal (24) or to perform the measurement in the transient state (14). In contrast to ^{1}H-CEST, Hyper-CEST is special, since a negligible steady-state amplitude exists and the system is always in the transient state. Thus, this work aims to find the conditions to encode the CEST effect rapidly enough before the steady state, i.e. vanishing thermal magnetization, is reached. By looking at Equation [1], the experimental parameters for a specific saturation frequency, $\Delta\omega$, straightforwardly influencing the Hyper-CEST signal are the saturation pulse strength, B_1, and duration, t_{sat}. In the following, using Equations [3] and [4] we derive guidelines for the determination of useful saturation pulse parameters that allow efficient Xe depolarization.

RESULTS AND DISCUSSION

Quantification of Xe exchange dynamics by qHyper-CEST

To determine the unknown parameters in Equations [3] and [4], we characterize the fundamental Xe exchange dynamics using the qHyper-CEST method (22) (Fig. 1). For our sample of [CrA] = 50 µM in DMSO at $T = 295$ K, we calculated a Xe concentration in solution of [Xe] = 2340 µM (see Materials and Methods section). The relevant parameters quantified by qHyper-CEST were the longitudinal relaxation time of free Xe, $T_1^A = (125 \pm 26)$ s, the fractional size of pool B, $f_B = (13.4 \pm 0.4) \times 10^{-4}$, and the exchange rate, $k_{BA} = (317 \pm 17)$ s^{-1}. They agreed well with previously reported results (22). For the sake of completeness, all qHyper-CEST results are given in the Material and Methods section.

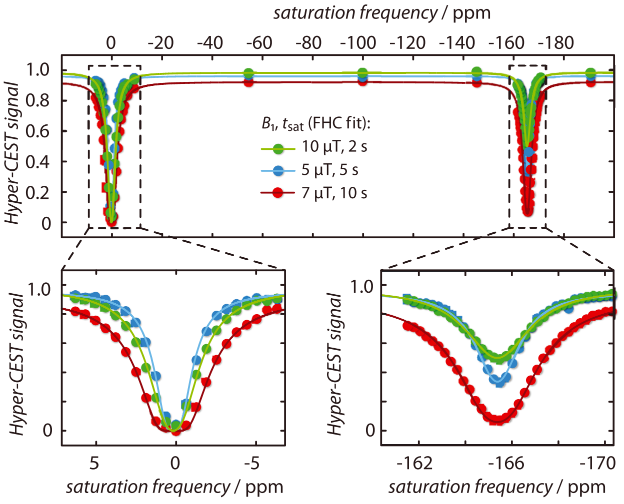

Figure 1. qHyper-CEST analysis of [CrA] = 50 µM in DMSO at $T = 295$ K by simultaneously fitting z-spectra obtained from the Xe MR image series with the full Hyper-CEST (FHC) solution (solid lines) for multiple z-spectra having saturation pulse strengths, B_1, and times, t_{sat}, such that B_1/t_{sat} = {10/2 (green), 5/5 (blue), 7/10 (red)} µT/s.

Saturation pulse-strength optimization

We investigate the maximal depolarization rate, $\lambda_{\text{on-res}}$, as given by Equation [3] with the values quantified by qHyper-CEST in the previous subsection and calculate the Xe-host system intrinsic maximum saturation transfer onto free Xe to be $f_B k_{BA}$ = 0.425 s^{-1} in the limit of infinitely high saturation pulse strength (i.e. $B_1 \rightarrow \infty$). In a generalized case, $\lambda_{\text{on-res}}$ can be plotted as a function of the unitless parameter $B_1\gamma/k_{BA}$ (see top x-axis label in Fig. 2(b)–(d)). Using this scale, we derive the following general regimes for the behavior of the Xe depolarization rate:

- $B_1 \gg k_{BA}/\gamma$: then $\lambda_{\text{on-res}} \approx f_B\, k_{BA}$ reaches the maximum possible depolarization rate.
- $B_1 = k_{BA}/\gamma$: then $\lambda_{\text{on-res}} = (f_B\, k_{BA})/2$ is 50% of the maximum possible depolarization rate.
- $B_1 \ll k_{BA}/\gamma$: then $\lambda_{\text{on-res}} \approx (f_B / k_{BA})(\gamma B_1)^2$, which is parabolic in saturation pulse strength, B_1.

In the high strength regime ($B_1 \gg k_{BA}/\gamma$; also referred to as the strong-saturation power or full-saturation limit (23)), all Xe that binds to CrA is already saturated and higher strength is

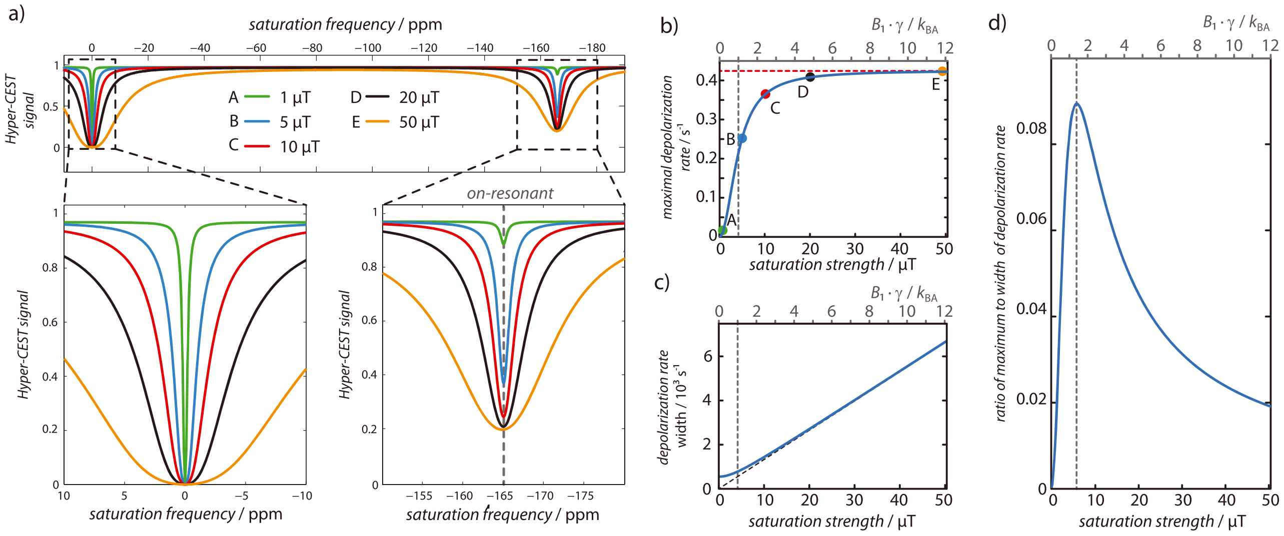

Figure 2. Optimal saturation pulse strength. (a) Simulated Hyper-CEST z-spectra using the FHC solution (21) with simulation parameters as given in the qHyper-CEST section. The saturation pulse strengths were B_1 = {1 (green; A), 5 (blue; B), 10 (red; C), 20 (black; D) and 50 (orange; E)} µT, while the saturation time was 5 s and the same for all. The resonance frequency of bound Xe is indicated by the gray dashed line, for which the data points corresponding to the Xe depolarization rate are shown in (b). Note that, between 20 and 50 µT, the difference in on-resonant Hyper-CEST response is small but the loss of spectral selectivity is significant. The system intrinsic maximum depolarization rate (red dashed line) is given by $f_B k_{BA}$ (i.e. $B_1 \rightarrow \infty$). Already half of the maximal depolarization rate (i.e. 50 %) is reached at the point of inflection at $B_1 = k_{BA}/\gamma \sim 4.3\,\mu$T (gray dashed line). However, 96 % of the maximum possible depolarization rate is reached for $B_1 = 5\,k_{BA}/\gamma \sim 21.4\,\mu$T. Panel (c) shows the full width at half-maximum of the depolarization rate, Γ, with respect to the saturation pulse strength, B_1. The y-intercept is $\Gamma(B_1 \rightarrow 0) = 2\,k_{BA} \sim 634$ s^{-1}. Whereas the vertical gray dashed line marks $B_1 = k_{BA}/\gamma$, the diagonal black dashed line illustrates linearly increasing line broadening without an exchange contribution. (d) The ratio of the maximal depolarization rate and its full width at half-maximum, $\lambda_{\text{on-res}}/\Gamma$, as a function of B_1 shows a distinct maximum for $B_1 = \sqrt{2}\,k_{BA}/\gamma \approx 1.4\,k_{BA}/\gamma$ (gray dashed line).

unnecessary. In this case, further increases in the saturation strength only serve to broaden the *z*-spectra resonances, causing a loss of spectral resolution. To illustrate this, we simulated Hyper-CEST *z*-spectra using the FHC solution (21), with simulation values as quantified in the previous qHyper-CEST section and the saturation parameters given in Fig. 2(a). Note that, between 20 µT (ca. 4–5 k_{BA}/γ) and 50 µT (ca. 12 k_{BA}/γ), the difference in the depolarization rate, $\lambda_{\text{on-res}}$, is small but the loss of spectral selectivity of the CEST resonance is significant. Thus, we analyze the full width at half-maximum of the depolarization rate, Γ, as given by Equation [4] with respect to the saturation pulse strength, B_1. We do not analyze the shape of the CEST resonance in the *z*-spectrum because that behaves in a difficult way as an argument of the exponential function of the Hyper-CEST signal given by Equation [1]. However, the general behavior is similar for both. As shown in Fig. 2(c), we found the following dependence of the full width at half-maximum of the depolarization rate, Γ, with the saturation pulse strength, B_1:

- $B_1 \gg k_{BA}/\gamma$: $\Gamma \approx 2\,\gamma\,B_1$ and depends linearly on the saturation pulse strength, B_1;
- $B_1 \ll k_{BA}/\gamma$: $\Gamma \approx 2\,k_{BA}$, which is the minimum possible width given by the Xe exchange rate (i.e. for CrA in DMSO at $T = 295$ K: $\Gamma(B_1 \rightarrow 0) = 634\ \text{s}^{-1}$).

Since both λ_{depol} and Γ increase monotonically with B_1, it can be constructive to look at the ratio of the maximal Xe depolarization rate and its full width at half-maximum, $\lambda_{\text{on-res}}/\Gamma$, as a function of B_1 strength (see Fig. 2(d)). This gives a measure of how much CEST effect is gained, in relation to how much spectral resolution is lost, for a given increase in the saturation strength. We found that pulses with $B_1 = \sqrt{2}\,k_{BA}/\gamma \approx 1.4\,k_{BA}/\gamma$ show the best ratio of $\lambda_{\text{on-res}}/\Gamma$ as shown in Fig. 2(d) (and derived in S2 in the Supplementary Material). Excluding spillover, this best ratio should not alter with the static magnetic field, B_0, since (i) Hyper-CEST is already reasonably in the large-shift limit and (ii) Equations [3] and [4] consider only the depolarization rate of the CEST pool itself under B_1 irradiation, without taking the distance to the observed pool A into account. Furthermore (and not only important for multiplexing experiments), a saturation pulse strength with $B_1 = 5\,k_{BA}/\gamma$ already reaches 96% of the Xe-host system intrinsic maximal Hyper-CEST effect while (at least to some extent) preserving spectral selectivity (in Fig. 2(a) and (b), compare the *z*-spectra for 20 µT (black, D) and 50 µT (orange, E)). If, however, $B_1 = 5\,k_{BA}/\gamma$ exceeds the subject specific absorption rate (SAR) or the transmitter coil limitations (e.g. for our system $B_1 < 40$ µT) or both, then a maximal B_1 value has to be chosen that fulfils both limitations.

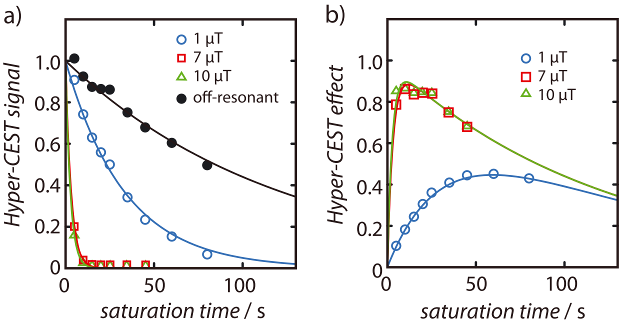

Figure 3. Optimal saturation time for the maximal Hyper-CEST effect. (a) The Hyper-CEST signal with respect to the saturation time, t_{sat}, for on-resonant saturation on bound Xe with three different saturation pulse strengths: $B_1 = \{1$ (blue open circles), 7 (red rectangles) and 10 (green triangles)$\}$ µT. The signal with off-resonant saturation (black closed circles) corresponds to a pure longitudinal relaxation time of free Xe, T_1^A. (b) The Hyper-CEST effect (which is the difference the off-resonant and on-resonant signal) versus the saturation time, t_{sat}, for these three different saturation pulse strengths. Regarding these B_1 values, the optimal saturation times were $t_{\text{sat}} = \{59.3,\ 11.8,\ 10.6\}$ s, respectively.

Optimal saturation time for maximal Hyper-CEST effect

Whereas in ^{1}H-CEST the longitudinal relaxation opposes the CEST effect, in Hyper-CEST it accelerates the driven depolarization further, due to non-equilibrium starting conditions (22). Therefore, Hyper-CEST has an optimal saturation time. We acquired data with saturation off-resonant (black closed circles in Fig. 3(a)) and on-resonant with bound Xe for three saturation pulse strengths: $B_1 = \{1$ (blue open circles), 7 (red rectangles), 10 (green triangles)$\}$ µT with respect to the saturation time. The off-resonant signal is pure longitudinal relaxation-driven depolarization of free Xe, T_1^A. We calculated (not fitted) these Hyper-CEST signal curves (solid lines) using Equation [1] with the depolarization rate, λ_{depol}, for on-resonant saturation with bound Xe, i.e. $\lambda_{\text{depol}} \rightarrow \lambda_{\text{on-res}}$, and the qHyper-CEST results from the previous section on quantification of Xe exchange dynamics by qHyper-CEST. They agree excellently with the data. As expected and shown more intuitively in Fig. 3(b), the Hyper-CEST effect, which is the difference between the off- and on-resonant Hyper-CEST signals, becomes maximal for specific saturation times. This is given by

$$
\begin{aligned}
t_{\text{sat}} &= \frac{1}{\lambda_{\text{on-res}}} \ln\left(\lambda_{\text{on-res}} \cdot T_1^A + 1\right) \\
&= \frac{\left((\gamma\,B_1)^2 + k_{BA}{}^2\right)}{f_B k_{BA} (\gamma\,B_1)^2} \\
&\quad \times \ln\left(\frac{f_B k_{BA} (\gamma\,B_1)^2}{(\gamma\,B_1)^2 + k_{BA}{}^2} \cdot T_1^A + 1\right)
\end{aligned}
\qquad [5]
$$

(the derivation is given in the Supplementary Material in S3), which is $t_{\text{sat}} = \{59.3,\ 11.8,\ 10.6\}$ s, respectively. In contrast to ^{1}H-CEST, excessively long saturation decreases the Hyper-CEST effect. When $\lambda_{\text{on-res}} \rightarrow 0$ (i.e. highly dilute concentrations of bound Xe or weak saturation pulse strengths), then $t_{\text{sat}} \rightarrow T_1^A$. When $\lambda_{\text{on-res}} \rightarrow \infty$, then $t_{\text{sat}} \rightarrow 0$. Thus, one should always saturate for less than T_1^A, independently of the exchange rate, k_{BA} (see S4 in the Supplementary Material). Although the qHyper-CEST procedure predicts the optimal saturation time, t_{sat}, fully according to Equation [5], in some studies it might be too detailed. For such cases, one can rely on the fact that the Xe depolarization was assumed to be monoexponential (21). We therefore validated this assumption experimentally by fitting the data of Fig. 3(a) monoexponentially, used the decay rates, τ, as the inverse of $\lambda_{\text{on-res}}$ and calculated the optimal saturation times, t_{sat}, for a specific preselected B_1 condition and sample concentration (see S3 in Supplementary Material). Recording this simple exponential decay can therefore be used to achieve a quick estimate for the optimum saturation time.

CONCLUSION

We demonstrated that Hyper-CEST has an optimal saturation time. When extremely low host concentration is detected ($f_B \rightarrow 0$) then the optimal saturation time approaches the longitudinal relaxation time of free Xe, T_1^A. However, saturating for longer than T_1^A becomes unproductive. After quantification of the Xe-host system-specific exchange dynamics, our presented cw saturation pulse using $B_1 = 5\,k_{BA}/\gamma$ achieves, directly and without further optimization, 96 % of the maximal Hyper-CEST contrast, while preserving spectral selectivity. In addition, we found that the ratio of CEST depolarization to CEST response width is best for a saturation pulse strength of 1.4 times the exchange rate (i.e. $B_1 = \sqrt{2}k_{BA}/\gamma$). Whereas the cw saturation considered in this work is the most common form of Hyper-CEST, because it is the most efficient saturation scheme and should be used when no SAR or hardware limitations exist, Xe depolarization with pulsed shaped saturation pulses has been shown to (i) reduce the energy deposition of the saturation pulse and (ii) improve spectral selectivity (25). The translation of our results achieved by cw saturation to pulsed saturation via the cw power equivalent, $B_{1,\mathrm{cwpe}}$, should be similar in its behavior of Xe labeling (26,27). In this context also pulses with rising amplitude waveforms could be promising (28). Our theory is applicable for any exchanging Xe-host system with a single binding site (i.e. spin pools). However, if several pools are present or a whole distribution of exchange rate exists for one pool, the straightforward extension of qHyper-CEST to multiple pools (29,30) may enable even broader applications.

Acknowledgements

This work has been supported by the European Research Council under the European Community's Seventh Framework Programme (FP7/2007-2013)/ERC grant agreement no. 242710 and the Human Frontier Science Program no. LT000858/2010-C.

REFERENCES

1. Dubois L, Da Silva P, Landon C, Huber JG, Ponchet M, Vovelle F, Berthault P, Desvaux H. Probing the hydrophobic cavity of lipid transfer protein from nicotiana tabacum through xenon-based NMR spectroscopy. J. Am. Chem. Soc. 2004; 126(48): 15 738–15 746.
2. Chambers JM, Hill PA, Aaron JA, Han Z, Christianson DW, Kuzma NN, Dmochowski IJ. Cryptophane xenon-129 nuclear magnetic resonance biosensors targeting human carbonic anhydrase. J. Am. Chem. Soc. 2009; 131(2): 563–569.
3. Spence MM, Rubin SM, Dimitrov IE, Ruiz EJ, Wemmer DE, Pines A, Yao SQ, Tian F, Schultz PG. Functionalized xenon as a biosensor. Proc. Natl. Acad. Sci. U. S. A. 2001; 98(19): 10 654–10 657.
4. Spence MM, Ruiz EJ, Rubin SM, Lowery TJ, Winssinger N, Schultz PG, Wemmer DE, Pines A. Development of a functionalized xenon biosensor. J. Am. Chem. Soc. 2004; 126(46): 15 287–15 294.
5. Schröder L, Lowery TJ, Hilty C, Wemmer DE, Pines A. Molecular imaging using a targeted magnetic resonance hyperpolarized biosensor. Science 2006; 314: 446–449.
6. Shapiro MG, Ramirez RM, Sperling LJ, Sun G, Sun J, Pines A, Schaffer DV, Bajaj VS. Genetically encoded reporters for hyperpolarized xenon magnetic resonance imaging. Nat. Chem. 2014; 6: 626–634.
7. Wolber J, Rowland IJ, Leach MO, Bifone A. Perfluorocarbon emulsions as intravenous delivery media for hyperpolarized xenon. Magn. Reson. Med. 1999; 41(3): 442–449.
8. Stevens TK, Ramirez RM, Pines A. Nanoemulsion contrast agents with sub-picomolar sensitivity for xenon NMR. J. Am. Chem. Soc. 2013; 135(26): 9576–9579.
9. Bai Y, Wang Y, Goulian M, Driks A, Dmochowski IJ. Bacterial spore detection and analysis using hyperpolarized 129-Xe chemical exchange saturation transfer (Hyper-CEST) NMR. Chem. Sci. 2014; 5: 3197–3203.
10. Kunth M, Döpfert J, Witte C, Rossella F, Schröder L. Optimized use of reversible binding for fast and selective NMR localization of caged xenon. Angew. Chem. Int. Ed. 2012; 51(33): 8217–8220.
11. Klippel S, Döpfert J, Jayapaul J, Kunth M, Rossella F, Schnurr M, Witte C, Freund C, Schröder L. Cell tracking with caged xenon: Using cryptophanes as MRI reporters upon cellular internalization. Angew. Chem. Int. Ed. 2014; 53(2): 493–496.
12. Rose HM, Witte C, Rossella F, Klippel S, Freund C, Schröder L. Development of an antibody-based, modular biosensor for 129-Xe NMR molecular imaging of cells at nanomolar concentrations. Proc. Natl. Acad. Sci. U. S. A. 2014; 111(32): 11 697–11 702.
13. Schnurr M, Witte C, Schröder L. Functionalized 129-Xe as a potential biosensor for membrane fluidity. Phys. Chem. Chem. Phys. 2013; 15: 14 178–14 181.
14. Zaiss M, Bachert P. Exchange-dependent relaxation in the rotating frame for slow and intermediate exchange – modeling off-resonant spin-lock and chemical exchange saturation transfer. NMR Biomed. 2013; 26: 507–518.
15. Jin T, Kim SG. Advantages of chemical exchange-sensitive spin-lock (CESL) over chemical exchange saturation transfer (CEST) for hydroxyl– and amine–water proton exchange studies. NMR Biomed. 2014; 27: 1313–1324.
16. Zaiss M, Xu J, Goerke S, Khan IS, Singer RJ, Gore JC, Gochberg DF, Bachert P. Inverse *Z*-spectrum analysis for spillover-, MT-, and T1-corrected steady-state pulsed CEST-MRI – application to pH-weighted MRI of acute stroke. NMR Biomed. 2014; 27: 240–252.
17. Zaiss M, Zu Z, Xu J, Schuenke P, Gochberg DF, Gore JC, Ladd ME, Bachert P. A combined analytical solution for chemical exchange saturation transfer and semi-solid magnetization transfer. NMR Biomed. 2015; 28: 217–230.
18. Roeloffs V, Meyer C, Bachert P, Zaiss M. Towards quantification of pulsed spinlock and CEST at clinical MR scanners: an analytical interleaved saturation–relaxation (ISAR) approach. NMR Biomed. 2015; 28: 40–53.
19. McConnell HM. Reaction rates by nuclear magnetic resonance. J. Chem. Phys. 1958; 28: 430–431.
20. Woessner DE. Nuclear transfer effects in nuclear magnetic resonance pulse experiments. J. Chem. Phys. 1961; 35(1): 41–48.
21. Zaiss M, Schnurr M, Bachert P. Analytical solution for the depolarization of hyperpolarized nuclei by chemical exchange saturation transfer between free and encapsulated xenon (HyperCEST). J. Chem. Phys. 2012; 136(14): 144 106.
22. Kunth M, Witte C, Schröder L. Quantitative chemical exchange saturation transfer with hyperpolarized nuclei (qHyper-CEST): Sensing xenon-host exchange dynamics and binding affinities by NMR. J. Chem. Phys. 2014; 141(19): 194 202.
23. Zaiss M, Bachert P. Chemical exchange saturation transfer (CEST) and MR *Z*-spectroscopy in vivo: a review of theoretical approaches and methods. Phys. Med. Biol. 2013; 58(22): R221.
24. Sun PZ. Simplified quantification of labile proton concentration-weighted chemical exchange rate (k_{ws}) with RF saturation time dependent ratiometric analysis (QUESTRA): Normalization of relaxation and RF irradiation spillover effects for improved quantitative chemical exchange saturation transfer (CEST) MRI. Magn. Reson. Med. 2012; 67: 936–942.
25. Meldrum T, Bajaj VS, Wemmer DE, Pines A. Band-selective chemical exchange saturation transfer imaging with hyperpolarized xenon-based molecular sensors. J. Magn. Reson. 2011; 213(1): 14–21.
26. Sun PZ, Wang E, Cheung JS, Zhang X, Benner T, Sorensen AG. Simulation and optimization of pulsed radio frequency irradiation scheme for chemical exchange saturation transfer (CEST) MRI–demonstration of pH-weighted pulsed-amide proton CEST MRI in an animal model of acute cerebral ischemia. Magn. Reson. Med. 2011; 66(4): 1042–1048.
27. Zu Z, Li K, Janve VA, Does MD, Gochberg DF. Optimizing pulsed-chemical exchange saturation transfer imaging sequences. Magn. Reson. Med. 2011; 66(4): 1100–1108.
28. Rancan G, Nguyen T, Glaser S. Gradient ascent pulse engineering for rapid exchange saturation transfer. J. Magn. Reson. 2015; 252C: 1–9.
29. Li AX, Hudson RH, Barrett JW, Jones CK, Pasternak SH, Bartha R. Four-pool modeling of proton exchange processes in biological systems in the presence of MRI-paramagnetic chemical exchange saturation

transfer (PARACEST) agents. Magn. Reson. Med. 2008; 60(5): 1197–1206.

30. Sun PZ. Simplified and scalable numerical solution for describing multi-pool chemical exchange saturation transfer (CEST) MRI contrast. J. Magn. Reson. 2010; 205(2): 235–241.
31. Witte C, Kunth M, Döpfert J, Rossella F, Schröder L. Hyperpolarized xenon for NMR and MRI applications. J. Vis. Exp. 2012; 67: e4268.
32. Witte C, Kunth M, Rossella F, Schröder L. Observing and preventing rubidium runaway in a direct-infusion xenon-spin hyperpolarizer optimized for high-resolution Hyper-CEST (chemical exchange saturation transfer using hyperpolarized nuclei) NMR. J. Chem. Phys. 2014; 140(8): 084 203.

SUPPORTING INFORMATION

Additional supporting information may be found in the online version of this article at the publisher’s web-site.

Supplemental Material
for
Continuous-wave saturation considerations for efficient xenon depolarization

Martin Kunth,* Christopher Witte, and Leif Schröder†

ERC Project BiosensorImaging, Leibniz-Institut für
Molekulare Pharmakologie (FMP), 13125 Berlin, Germany

CONTENTS

S1: ASSUMPTIONS FOR SIMPLIFICATION OF XE DEPOLARIZATION RATE

As shown by Zaiss et al. [1], the longitudinal and transverse relaxation rates of unbound Xe, $R^{\mathrm{A}}_{1,2}$, determine the baseline $C(\Delta\omega) = R^{\mathrm{A}}_1 \cos^2\theta(\Delta\omega) + R^{\mathrm{A}}_2 \sin^2\theta(\Delta\omega)$ which approximates $R^{\mathrm{A}}_1 = 1/T^{\mathrm{A}}_1$, when the angle of the tilted magnetization vector off the z axis in the rotating frame $\theta(\Delta\omega) = \tan^{-1}(\frac{\omega_1}{\Delta\omega_{\mathrm{A}}(\Delta\omega)}) \rightarrow 0$ and is negligible for saturation frequencies far off-resonant of the unbound Xe resonance, with $\omega_1 = \gamma \cdot B_1$ and γ the gyromagnetic ratio for Xe ($\gamma/(2\pi)$ = -11.77 MHz/T). The shift away from the true resonance frequency of bound Xe, $\delta\omega_{\mathrm{B}}$, is $x_0(B_1) = \frac{(\delta\omega_{\mathrm{B}}-\delta\omega_{\mathrm{A}})k_{\mathrm{AB}}k_{\mathrm{BA}}}{(\gamma\, B_1)^2+(\delta\omega_{\mathrm{B}}-\delta\omega_{\mathrm{A}})^2}$ and approximates 0 for the weak saturation pulse strengths we used here compared to the relative chemical shift of both pools, $\delta\omega_{\mathrm{B}} - \delta\omega_{\mathrm{A}}$.

S2: DERIVATION FOR LARGE BUT NARROW HYPER-CEST RESPONSE

We find the maximum of the ratio of the maximal Xe depolarization rate and its full width at half maximum, $\lambda_{\max}/\Gamma$, as a function of B_1 strength by setting its derivation in ω_1 to zero:

$$\begin{aligned} \frac{\partial}{\partial\,\omega_1}\left(\frac{\lambda_{\max}(\omega_1)}{\Gamma(\omega_1)}\right) &= \frac{\partial}{\partial\,\omega_1}\left(\frac{f_{\mathrm{B}}\,k_{\mathrm{BA}}\,\omega_1^2}{(\omega_1^2+k_{\mathrm{BA}}^2)\cdot\left(2\sqrt{\omega_1^2+k_{\mathrm{BA}}^2}\right)}\right) \\ &= \frac{f_{\mathrm{B}}\,k_{\mathrm{BA}}(2\,k_{\mathrm{BA}}^2\,\omega_1 - \omega_1^3)}{2\,(k_{\mathrm{BA}}^2+\omega_1^2)^{5/2}} \\ &= 0 \\ \Leftrightarrow \qquad \omega_1 &= \{\pm\sqrt{2}\cdot k_{\mathrm{BA}}, 0\}. \end{aligned} \tag{1}$$

Whereas $\omega_1 = 0$ is the saddle point at (0,0), $\omega_1 = -\sqrt{2}\cdot k_{\mathrm{BA}}$ is a minimum since the second derivative turns from negative sign to positive. Thus, a saturation pulse strength of $B_1 = +\sqrt{2}\cdot k_{\mathrm{BA}}/\gamma$ produces the strongest while most narrow Hyper-CEST response.

S3: DERIVATION OF THE OPTIMAL SATURATION TIME

In addition to the full Hyper-CEST (FHC) solution to the Bloch-McConnell (BM) equations, Zaiss et al. also developed an approximate analytical solution of the BM equations for Hyper-CEST[1]. In this approximation, the z-magnetization of the free Xe in solution (denoted by pool A) after the application of a saturation pulse with duration t_{sat} is given by

$$M_{\mathrm{z}}^{\mathrm{A}} = e^{-t_{\mathrm{sat}}(\lambda_{\mathrm{direct}}+\lambda_{\mathrm{CEST}})},$$

where $\lambda_{\mathrm{direct}} = 1/T_1^{\mathrm{A}}$ (compare with Eq. 14 of Zaiss). When the saturation pulse is nearly resonant with the CEST pool, λ_{CEST} is determined by the exchange rates, k_{BA}, between the two pools, the relaxation rates of the CEST pool, R_2^{B}, and the amplitude and frequency of the saturation pulse (Eq. 15 from Zaiss). When the saturation pulse is sufficiently off-resonant from the CEST pool then $\lambda_{\mathrm{CEST}} = 0$. Assuming the saturation pulse is weak enough that there is no spillover, the Hyper-CEST effect is then

$$M_{\mathrm{z,off}}^{\mathrm{A}} - M_{\mathrm{z,on}}^{\mathrm{A}} = e^{-t_{\mathrm{sat}}/T_1^{\mathrm{A}}} - e^{-t_{\mathrm{sat}}(1/T_1^{\mathrm{A}}+\lambda_{\mathrm{CEST}})}. \tag{2}$$

We can find the optimal saturation time by differentiating Eq. 2, equating this to zero and then solving for t_{sat}. We then find the greatest Hyper-CEST effect when

$$\begin{aligned} t_{\mathrm{sat}} &= \frac{\ln(1+T_1^{\mathrm{A}}\lambda_{\mathrm{CEST}})}{\lambda_{\mathrm{CEST}}} \\ &= \frac{\left(w_1{}^2+k_{\mathrm{BA}}{}^2\right)}{f_{\mathrm{B}}\,k_{\mathrm{BA}}\,w_1{}^2}\cdot\ln\left(\frac{f_{\mathrm{B}}\,k_{\mathrm{BA}}\,w_1{}^2}{w_1{}^2+k_{\mathrm{BA}}{}^2}\cdot T_1^{\mathrm{A}}+1\right) \end{aligned} \tag{3}$$

with the approximation that $k_{\mathrm{BA}} \gg R_2^{\mathrm{B}}$.

In addition, the Xe depolarization was assumed to be monoexponential[1]. We therefore fitted the data of Figure 3a in the main manuscript (here in FIG. 1) to a monoexponential decay and retrieved decay constants of $\tau_{1\mu\mathrm{T}} = (58 \pm 2)$ s, $\tau_{7\mu\mathrm{T}} = (4.7 \pm 0.1)$ s, $\tau_{10\mu\mathrm{T}} = (3.6 \pm 0.1)$ s and $\tau_{\mathrm{off-res}} = T_1^{\mathrm{A}} = (121 \pm 6)$ s, respectively. Using the inverse decay constants, i.e., the depletion rates, $\lambda_{\mathrm{on-res}} = 1/\tau$, we calculated the optimal saturation times with

$$t_{\mathrm{sat}} = \frac{1}{\lambda_{\mathrm{on-res}}} \cdot \ln\left(\lambda_{\mathrm{on-res}} \cdot T_1^{\mathrm{A}} + 1\right).$$

They agree well with the predicted values calculated with Eq. (2) in the main manuscript[1, 2]

$$\lambda_{\mathrm{on-res}} \approx f_{\mathrm{B}}\, k_{\mathrm{BA}} \frac{(\gamma\, B_1)^2}{(\gamma\, B_1)^2 + k_{\mathrm{BA}}^2}$$

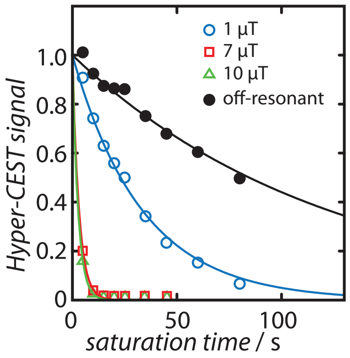

FIG. 1. Data of Figure 3a of the main manuscript.

and the qHyper-CEST results in the main manuscript, as listed in Table I. The error estimation of $\lambda_{\mathrm{on-res}}$ assuming only errors in f_{B} and k_{BA} is:

$$\frac{\partial \lambda_{\mathrm{on-res}}}{\partial f_{\mathrm{B}}} = k_{\mathrm{BA}} \frac{(\gamma\, B_1)^2}{(\gamma\, B_1)^2 + k_{\mathrm{BA}}^2}, \qquad \frac{\partial \lambda_{\mathrm{on-res}}}{\partial k_{\mathrm{BA}}} = f_{\mathrm{B}}\, (\gamma\, B_1)^2\, \frac{(\gamma\, B_1)^2 - k_{\mathrm{BA}}^2}{\left((\gamma\, B_1)^2 + k_{\mathrm{BA}}^2\right)^2},$$

$$\Delta\lambda_{\mathrm{on-res}} = \sqrt{\left(\frac{\partial \lambda_{\mathrm{on-res}}}{\partial f_{\mathrm{B}}} \Delta f_{\mathrm{B}}\right)^2 + \left(\frac{\partial \lambda_{\mathrm{on-res}}}{\partial k_{\mathrm{BA}}} \Delta k_{\mathrm{BA}}\right)^2}.$$

The deviation to $1/\tau$ results from the $\lambda_{\mathrm{on-res}}$ calculation, since it was determined with multiple qHyper-CEST parameters.

TABLE I. Whereas the depolarization rate, $\lambda_{\mathrm{on-res}}$, was calculated from the qHyper-CEST results and Eq. (4) in the main manuscript, $1/\tau$ is the inverse of the decay time, τ, of the monoexponential fit in FIG. 1. The optimal saturation times, were calculated with Eq. (5) in the main manuscript.

	depolarization rate / s^{-1}		saturation time / s	
$B_1/\mu\mathrm{T}$	$\lambda_{\mathrm{on-res}}$	$1/\tau$	$\lambda_{\mathrm{on-res}}$	$1/\tau$
1	(0.022 ± 0.001)	(0.017 ± 0.001)	59.1	65.4
7	(0.31 ± 0.01)	(0.213 ± 0.005)	11.8	15.4
10	(0.36 ± 0.02)	(0.278 ± 0.008)	10.6	12.8

S4: XE DEPOLARIZATION RATE: SATURATION TIME

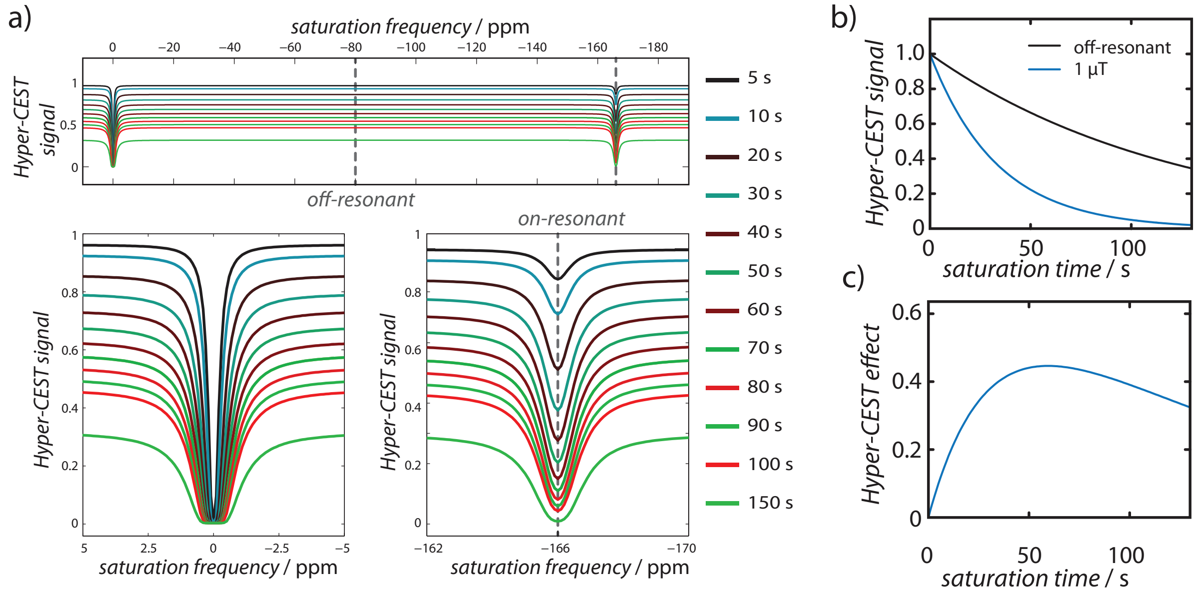

FIG. 2. Xe depolarization rate with respect to the saturation time, t_{sat}, for [CrA]=50 μM in DMSO at $T = 295$ K. a) Simulated Hyper-CEST z-spectra using the FHC solution[1] with simulation parameters as given in the qHyper-CEST section in the main manuscript (section 3.1). The saturation pulse strength was 1 μT and kept constant, while different saturation times (listed in the Figure legend) were employed. The frequencies for off- and on-resonant experiments are indicated by the gray dashed lines, and the respective signal evolutions correspond to the Xe depolarization curves shown in b). The resulting difference between the off- and on-resonant signal, the Hyper-CEST effect, is shown in c). Note that the Hyper-CEST z-spectra in a) were simulated with the full Hyper-CEST solution, but the curves in b) and c) were calculated using Eq. (1) from the main manuscript with the depolarization rate, λ_{depol}, for on-resonant saturation with bound Xe, i.e., $\lambda_{\mathrm{depol}} \rightarrow \lambda_{\mathrm{on-res}}$, and the qHyper-CEST results in section 3.1 in the main manuscript. Further, saturating for longer than the longitudinal relaxation rate of free Xe, T_1^{A}, decreases the Hyper-CEST effect (see z-spectrum for $t_{\mathrm{sat}} = 150$ s, while T_1^{A} of the simulation was 125 s). In this model, we observed a negligible increase of the full width at half maximum of the CEST response in the z-spectra with increased saturation time, as can be seen in a).

---

[*] kunth@fmp-berlin.de

[†] lschroeder@fmp-berlin.de

[1] Zaiss, M., Schnurr, M., Bachert, P. *The Journal of Chemical Physics* **2012**, *136*, 144106.

[2] Kunth, M., Witte, C., Schröder, L. *The Journal of Chemical Physics* **2014**, *141*, 194202.

D.4 HIGH GAS TURNOVER HYPER-CEST MRI

FULL REFERENCE:
Martin Kunth, Christopher Witte, Andreas Hennig, and Leif Schröder. Identification, classification, and signal amplification capabilities of high-turnover gas binding hosts in ultra-sensitive NMR *Chemical Science*, 6:6069-6075, 2015; Kunth *et al.*[126].
(highlighted as front cover article)

AUTHOR CONTRIBUTIONS: M.K. designed research and analyzed data; M.K. and C.W. performed research; A.H. provided CB6; M.K., C.W., A.H. and L.S. wrote the paper.

On the following 18 pages, the original publication and its Electronic Supporting Information is attached.

- Cover: *Chem. Sci.*, 6:6025-6025, 2015 – Reprinted with permission. Published by The Royal Society of Chemistry.
- Full Article: *Chem. Sci.*, 6:6069-6075, 2015 – Reprinted with permission. Published by The Royal Society of Chemistry.

Volume 6 | Number 11 | November 2015 | Pages 6025–6680

Chemical Science

www.rsc.org/chemicalscience

ISSN 2041-6539

ROYAL SOCIETY OF CHEMISTRY

EDGE ARTICLE

Leif Schröder *et al.*

Identification, classification, and signal amplification capabilities of high-turnover gas binding hosts in ultra-sensitive NMR

Image created by Barth van Rossum at Leibniz-Institut für Molekulare Pharmakologie.

Chemical
Science

EDGE ARTICLE

View Article Online
View Journal | View Issue

Cite this: *Chem. Sci.*, 2015, **6**, 6069

Identification, classification, and signal amplification capabilities of high-turnover gas binding hosts in ultra-sensitive NMR†

Martin Kunth,[a] Christopher Witte,[a] Andreas Hennig[b] and Leif Schröder*[a]

Received 17th April 2015
Accepted 5th July 2015

DOI: 10.1039/c5sc01400j

www.rsc.org/chemicalscience

Nuclear Magnetic Resonance (NMR) can be a powerful tool for investigating exchange kinetics of host–guest interactions in solution. Beyond conventional direct NMR detection, radiofrequency (RF) saturation transfer can be used to enhance the study of such chemical exchange or to enable signal amplification from a dilute host. However, systems that are both dilute and labile (fast dissociation/re-association) impose specific challenges to direct as well as saturation transfer detection. Here we investigate host–guest systems under previously inaccessible conditions using saturation transfer techniques in combination with hyperpolarized nuclei and quantitative evaluation under different RF exposure. We further use that information to illustrate the consequences for signal amplification capabilities and correct interpretation of observed signal contrast from comparative exchange data of different types of hosts. In particular, we compare binding of xenon (Xe) to cucurbit[6]uril (CB6) with binding to cryptophane-A monoacid (CrA) in water as two different model systems. The Xe complexation with CB6 is extremely difficult to access by conventional NMR due to its low water solubility. We successfully quantified the exchange kinetics of this system and found that the absence of Xe signals related to encapsulated Xe in conventional hyperpolarized ^{129}Xe NMR is due to line broadening and not due to low binding. By introducing a measure for the gas turnover during constant association–dissociation, we demonstrate that the signal amplification from a dilute pool of CB6 can turn this host into a very powerful contrast agent for Xe MRI applications (100-fold more efficient than cryptophane). However, labile systems only provide improved signal amplification for suitable saturation conditions and otherwise become disadvantageous. The method is applicable to many hosts where Xe is a suitable spy nucleus to probe for non-covalent interactions and should foster reinvestigation of several systems to delineate true absence of interaction from labile complex formation.

Introduction

The noble gas xenon (Xe) undergoes non-covalent interactions with hydrophobic cavities of natural biomacromolecular and artificial supramolecular structures.[1–4] It has consequently been used in a large variety of contexts, for example, to explore protein surfaces[5–9] and the structure of bacterial spores,[10] to study gas diffusion through nanotubes[11] and gas adsorption by metal–organic frameworks,[12–14] as well as a probe for understanding the driving forces of supramolecular host–guest systems.[15,16] In addition, biosensing using ^{129}Xe nuclear magnetic resonance (NMR) is an emerging field with great potential for medically important applications[17–19] and has led to the development of Xe contrast agents for magnetic resonance imaging (MRI). Hence, the characterization of such Xe–host interactions is extremely important to supramolecular chemists, materials scientists and biochemists, as it allows access to the driving forces of non-covalent interactions.

Popular methods to characterize Xe binding include X-ray crystallography and isothermal titration calorimetry (ITC). They provide structural information in the solid state and thermodynamic parameters in solutions, respectively, and thus complement each other. An alternative method to study both dynamic and structural aspects of Xe host–guest systems in solution is ^{129}Xe NMR spectroscopy. The high polarizability of the large Xe electron cloud renders the chemical shift of the NMR-active ^{129}Xe isotope extremely sensitive to its molecular environment,[20] and ^{129}Xe NMR can thus report on small structural changes. Moreover, ^{129}Xe NMR spin labeling allows the study of exchange kinetics and thereby provides dynamic parameters of Xe binding such as binding constants,

---

[a] *ERC Project BiosensorImaging, Leibniz-Institut für Molekulare Pharmakologie (FMP), 13125 Berlin, Germany. E-mail: lschroeder@fmp-berlin.de; Tel: +49 30 947 93 121*

[b] *Jacobs University Bremen, Department of Life Sciences and Chemistry, Campus Ring 1, 28759 Bremen, Germany*

† Electronic supplementary information (ESI) available: CB6 modeling, Xe–CrA exchange kinetics in water, CB6 line broadening, Xe–CrA exchange kinetics in DMSO, Xe–host properties for efficient Hyper-CEST detection, commercially CB6 sample and the Xe delivery into water and DMSO. See DOI: 10.1039/c5sc01400j

association and dissociation rate constants. In addition, Xe can be hyperpolarized, which leads to a 10^5-fold NMR signal enhancement and enables the direct detection of micromolar quantities of Xe-binding hosts.[21,22]

However, the study of dynamic Xe binding and exchange in aqueous solution by conventional NMR detection often remains problematic. Known binding sites were typically determined from NMR observations under conditions where either (a) complex formation and dissociation is slow enough to yield a sharp NMR resonance of the (at least temporarily) bound Xe or (b) in the case that there is no unique observable peak from the complex, the existence of a complex can be inferred from (small) shifts in the signal of free Xe when high concentrations of the host are present. Utilizing these methods is particularly challenging for hosts with poor solubility. In addition, new labile systems or known hosts under conditions with accelerated Xe exchange might easily be overlooked, even though a high exchange rate might be of considerable interest. For instance, Xe can be used as a probe for oxygen binding pockets related to reactive centers in biological systems but exchange in such systems is expected to be rapid. To overcome these limitations, the Hyper-CEST technique was developed[19] by combining hyperpolarized Xe with chemical exchange saturation transfer (CEST).[23] The Hyper-CEST method also utilizes the Xe–host as an MRI contrast agent and enhances its detection sensitivity down to the picomolar range using the dynamic nature of the Xe–host interaction;[9,24–26] however, it does not *per se* provide quantitative information about Xe complexation. For example, the recent study of bacterial spores reported in this journal[10] used Hyper-CEST to confirm the existence of a Xe complex but detailed quantification of the Xe exchange remained elusive. To address this shortcoming, we recently introduced a concept to comprehensively analyze the Hyper-CEST signal of a host where a clear NMR signal from bound Xe is easy to identify for a system well within the slow exchange regime. Data acquired at varying saturation pulse strengths and durations provide a quantitative method for Hyper-CEST (qHyper-CEST).[27]

Herein, we quantify the Xe exchange kinetics for two different Xe–host systems, cryptophane-A monoacid (CrA) and cucurbit[6]uril (CB6), with unprecedented sensitivity in water. Thus, we demonstrate that qHyper-CEST is not only applicable in the slow regime (Xe in CrA), but becomes even more valuable in the intermediate regime (Xe in CB6). In particular, the interaction of Xe with CB6 is otherwise impractical to access owing to its inherently low water solubility in combination with its labile complex formation, which is a typical property of many gas binding substances. By characterizing the previously unquantified, labile and barely soluble version of the Xe–CB6 system we demonstrate that such systems are indeed detectable by NMR and, as a consequence, we believe that other Xe–host systems may be worth reinvestigating. We then compare these two systems with each other. To enhance the discussion, we additionally include a third Xe–host system that has been previously quantified (CrA in dimethyl sulfoxide, DMSO, which is in the slow exchange regime).[27] To facilitate an objective comparison between these different systems we propose to rank them according to their gas turnover rate. We find that in water, CB6 exhibits a *ca.* 100-fold increased gas turnover rate in comparison to CrA and is therefore, under appropriate conditions, a significantly more sensitive Hyper-CEST biosensor and superior Xe-MRI contrast agent. Finally, we discuss which saturation conditions are needed to fully realize the potential of the superior gas turnover rate of CB6.

Results and discussion

Quantifying exchange kinetics with qHyper-CEST

In Hyper-CEST, an abundant pool (free Xe in solution, pool A, see Fig. 1) is used to detect a dilute pool (bound Xe, pool B) by application of a (selective) radiofrequency (RF) saturation pulse with a specific strength, B_1, and for a certain duration, t_{sat}, on-resonant with pool B. In this study, we used continuous-wave (cw) saturation. The induced spin depolarization is transferred to pool A *via* chemical exchange, which results in a cumulative decrease in the large detection pool A. A reference measurement with off-resonant RF saturation reveals the intensity of the saturation transfer. The qHyper-CEST technique takes advantage of the spectral dimension by iterative variation of the saturation frequency to cover a whole range of chemical shifts. The normalized Hyper-CEST signal with respect to the saturation pulse frequency is referred to as a *z*-spectrum. In qHyper-CEST, multiple *z*-spectra acquired with different saturation pulse conditions are fit with the full Hyper-CEST (FHC) solution[28] which is an analytical solution of the Bloch–McConnell equations.[29,30] This enables the sensitive and simultaneous quantification of Xe exchange kinetic and binding parameters such as: the ratio of bound to free Xe, f_B, the Xe exchange rate, k_{BA}, the chemical shifts of free and bound Xe, $\delta_{A,B}$, the Xe association (binding) constant, K_A, and the Xe host occupancy, β (see Table 1).

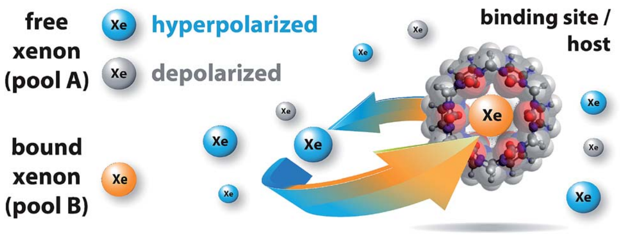

Fig. 1 Probing reversible, labile binding in a molecular cavity with xenon: free xenon atoms (pool A, where blue indicates hyperpolarized Xe and gray indicates depolarized Xe) undergo constant exchange with the binding site/host (*i.e.*, cucurbit[6]uril, CB6; transparent overlay of the ball-stick-model of the molecule with its van der Waals radius representation; molecular modeling in Fig. S1 in the ESI†). The NMR signal of bound Xe shows a remarkably large chemical shift (indicated by orange xenon atoms; pool B). The host geometry with the two opposing portals facilitates fast dissociation of the complex. This causes detrimental line broadening, precluding conventional NMR detection.

Table 1 qHyper-CEST results of Xe exchange kinetic and binding parameters for three Xe–host systems: CrA in DMSO, CrA in water and CB6 in water (at $T = 295$ K). Listed parameters are: the solvent, the Xe concentration in this solvent, [Xe] (determined by the Xe Ostwald solubility coefficient), the Xe host molecule, the host molecule concentration, [host], the relative chemical shift between free and bound Xe, $\Delta\delta$, the ratio of bound and free Xe, f_B, the Xe exchange rate, k_{BA}, the Xe host occupancy, β, the Xe binding (association) constant, K_A, the host concentration occupied by Xe, $[\text{host}_{occ}] = \beta[\text{host}]$, and the host system efficiency for Hyper-CEST detection in terms of the maximal ^{129}Xe depolarization rate per μM host concentration at a given Xe concentration (the gas turnover rate, $\beta\, k_{BA}$)

Solvent	$[\text{Xe}]^a$ (μM)	host	$[\text{host}_{tot}]$ (μM)	$\Delta\delta$ (ppm)	f_B (10^{-4})	k_{BA} (s^{-1})	β^b (%)	$K_A{}^c$ (M^{-1})	$[\text{host}_{occ}]$ (μM)	$\beta\, k_{BA}$ (% s^{-1})
Water	390	CB6	3.4	-96.1 ± 0.1	43 ± 1	2100 ± 300	49	2500 ± 400	1.7	1029
Water	390	CrA	11	-132.06 ± 0.02	70 ± 11	38 ± 6	29	850 ± 250	3.2	11
DMSO	2340	CrA	50	-166.37 ± 0.04	18 ± 1	250 ± 130	9	38 ± 4	4.5	23

[a] Calculation given in the Experimental Section. [b] As given by eqn (3) in ref. 27. [c] As given by eqn (4) in ref. 27.

Xenon exchange kinetics for cryptophane-A in water

One prominent synthetic host often used in ^{129}Xe NMR studies is CrA. Its Xe binding constant has been measured using ITC[31] and the kinetics has been studied by direct detection of the caged Xe in organic solvent[32,33] and in water.[18,34] We have recently used CrA in an organic solvent to validate qHyper-CEST,[27] and now apply quantitative saturation transfer to this system in water to have a reference for the subsequently studied more labile system and to illustrate the consequences in saturation transfer performance under different RF exposures. A direct ^{129}Xe NMR spectrum (see Fig. S2a in the ESI†) and qHyper-CEST analysis for $[\text{CrA}] = 11$ μM can be found in the S2 section in ESI†. The determined exchange rate k_{BA} of (38 ± 6) s^{-1} is in excellent agreement with previous studies.[18,34] As such, the Xe–CrA complexation in water is well within the slow exchange regime ($k_{BA}/\Delta\omega = 0.0024 \ll 1$). The results for the other parameters are listed in Table 1.

Xenon exchange kinetics for cucurbit[6]uril in water

Another class of macrocycles where ^{129}Xe NMR spectroscopy can be used to probe Xe–host binding are cucurbit[*n*]urils.[35–38] Cucurbiturils are highly important in the fields of molecular self-assembly and nano-technology.[39] Due to their non-toxicity[40] new biological applications are currently emerging for cucurbiturils, such as drug carriers, as molecular recognition units for insulin or β-amyloid fibers,[41] as well as pH-responsive supramolecular nanovalves[42] or in fluorescence assays.[43,44] A cucurbit[*n*]uril homologue with promising Xe binding capabilities is CB6, which, however, suffers from a low water solubility (<30 μM (ref. 45)). Without qHyper-CEST, high contents of inorganic salt are compulsory to solubilize sufficient amounts for CB6 detection. This complicates the quantification of actual binding constants[45] because of competitive binding of cations to the carbonyl portals of the macrocycle. However, we now demonstrate that reversible occupation of the cavity happens already at fairly low concentrations.

To exemplify, we recorded a direct ^{129}Xe NMR spectrum of CB6 (3.4 μM) with 64 signal averages in pure water, which, contrary to CrA at comparable concentration, shows no signal from the Xe–CB6 complex (Fig. 2a). In contrast, Hyper-CEST *z*-spectra at varying saturation pulse conditions obtained with CB6 at the same concentration clearly revealed a distinct signature of the Xe–CB6 complex at −95.6 ppm upfield from free Xe (Fig. 2b), which facilitated the corresponding qHyper-CEST analysis (Table 1). This clearly demonstrates that studying hosts at the low concentrations used here may be misleading with direct NMR and easily lead to the wrong assumption of no complexation.

Both the exchange rate, k_{BA}, and association constant, K_A, obtained by the qHyper-CEST analysis are in good agreement with expectations based on literature results with a water-soluble CB6 derivative, which has been measured by

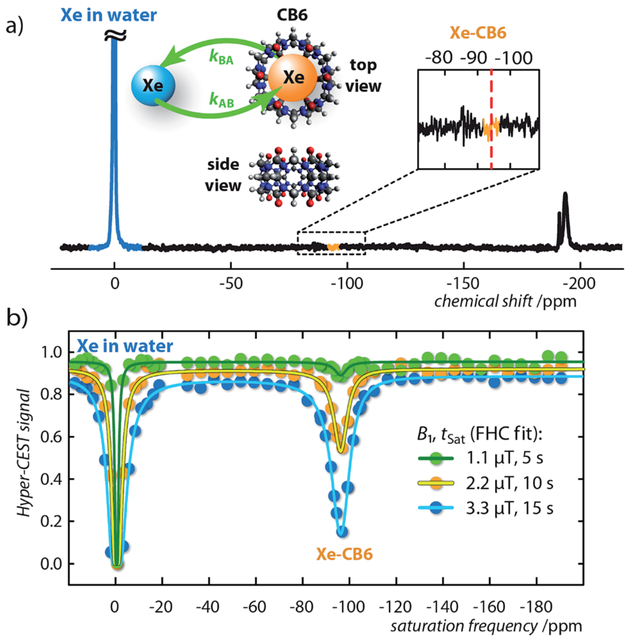

Fig. 2 Direct and indirect (Hyper-CEST) ^{129}Xe NMR measurements for cucurbit[6]uril (CB6) at a concentration of 3.4 μM dissolved in pure water. (a) ^{129}Xe NMR spectrum with 64 averages at $T = 295$ K. Retrospectively, the Xe–CB6 resonance is expected to appear at *ca.* $\delta_B = -95$ ppm (red dashed line). The insert shows the CB6 structure as top and side view including the Xe exchange, $k_{AB,BA}$. (b) Hyper-CEST *z*-spectra (dots) for continuous-wave (cw) saturation of $B_1/t_{sat} = \{1.1/5$ (green), 2.2/10 (orange), 3.3/15 (blue)$\}$ μT/s including fitting curves of the full Hyper-CEST (FHC) solution (solid lines); results are listed in Table 1.

conventional hyperpolarized ^{129}Xe NMR spectroscopy at 10^3-fold higher concentration.[37,46–48] Most strikingly, only the qHyper-CEST analysis was able to reveal that CB6 has a higher occupancy ($\beta = 49\%$) than CrA ($\beta = 29\%$) under the given experimental conditions suggesting that Xe binding to CB6 is more efficient than to CrA in pure water where the portals are freely accessible. Moreover, the Xe–CB6 system enters the intermediate exchange regime on the NMR time scale ($k_{BA}/\Delta\omega = 0.2 < 1$; the corresponding value for CrA in water is 100-fold lower and in the slow regime), which should additionally contribute to a higher Hyper-CEST signal compared to CrA. As a consequence, the signal of bound Xe in the direct ^{129}Xe NMR spectrum is most likely only below the noise level because of extreme line broadening and not because of insufficient binding (for more details see section S3 in the ESI†).

Overall, we believe that it might be worthwhile to revisit some previously studied host systems with qHyper-CEST, since their performance may have been similarly overlooked as is the case for CB6. This extends also to systems where Xe is used as a probe for other guests by competitive binding studies. Our findings apply in particular to numerous low binding, but rapidly exchanging host–guest systems, in which Xe NMR was so far restricted to organic solvents (or at least admixtures thereof) to achieve sufficient signal. Since results from organic solvents have limited transferability for conditions in aqueous solution,[27,49] this corroborates the strong motivation for the use of carefully designed Hyper-CEST, which now provides the sensitivity for the re-investigation of labile/dilute Xe–host systems under more realistic conditions.

Comparison of supramolecular Xe-binding hosts

In addition to the optimization of the saturation pulse conditions[50] the choice of the Xe–host can also greatly influence the sensitivity of Hyper-CEST detection. Intuitively, the saturation transfer increases by both a large number of Xe atoms continuously moving through the host during the saturation period, *i.e.*, a high Xe exchange rate, k_{BA}, and moreover, a large amount of Xe atoms that bind in chemical equilibrium to the hosts, *i.e.*, a high Xe association constant, K_A. Unfortunately, an increase in one parameter is often associated with a decrease in the other and, as a consequence, make the sensitivity improvement insignificant. Consider for example the Xe exchange kinetics for CrA in the two solvents water and previously quantified dimethyl sulfoxide (DMSO; Fig. S4 in the ESI†)[27] in Table 1. While the Xe exchange rate can be improved by more than 6-fold when switching from water to DMSO, the binding constant, in contrast, decreases by a factor of 22. Thus, the Xe exchange rate of CrA improves at the cost of the binding constant. The question of which system provides superior ^{129}Xe depolarization becomes even more complex considering that in DMSO, 6 times more free Xe atoms are in solution (Table 1) and the manipulation of this large signal *via* saturation transfer becomes less sensitive. Moreover, as a surprising result, we found that CB6 in pure water has both a superior Xe exchange rate of, $k_{BA} = 2100\ \mathrm{s}^{-1}$, and a superior Xe binding constant, $K_A = 2500\ \mathrm{M}^{-1}$.

To allow an objective comparison of these systems in terms of their Hyper-CEST performance and to specifically classify and engineer Xe–host systems with highly optimized properties for Hyper-CEST detection, we propose to use the maximum depolarization rate per host molecule for a given Xe concentration, *i.e.*, the gas turnover rate, $\beta\ k_{BA}$, as an appropriate measure for the performance of a given Xe–host system (see Table 1; S5 in the ESI†). Here, the host occupancy, β, can be related to the binding constant, $K_A = [\mathrm{Xe}]^{-1}\{\beta/(1-\beta)\}$.[27] The gas turnover rate gives the maximum possible Hyper-CEST effect for an infinitely strong saturation pulse. In terms of this measure, CB6 is 100 times more efficient than CrA. Hence, it has the potential to be a much better Hyper-CEST agent. Yet the question remains, if CB6 has superior Hyper-CEST performance under all saturation conditions?

Signal amplification strategies

Care has to be taken to consider what saturation parameters and Xe host were used when interpreting Hyper-CEST contrast. Only saturation pulses that are strong enough to depolarize the Xe magnetization during the rather short residence time within CB6 will fully take advantage of its signal amplification potential (see Fig. S5a in the ESI†). Having said that, this aspect at the same time has consequences for the image contrast similar to the film speed in optical detection but with a somewhat inverse behavior: efficient amplification build-up at high RF "exposure" comes along with poor sensitivity at low exposure (for 1 : 1 Xe–host complexation and occupancy of $\leq 100\ \%$). To illustrate this, we compare the gas turnover of two dilute host structures side by side in an inhomogeneous setup. Two solutions were prepared and studied under different exposure conditions: one of CB6 and the other CrA (both at [CB6] = [CrA] = 12.9 μM). These solutions were placed into separate, concentric compartments, CrA in the inner compartment and CB6 in the outer compartment (Fig. 3a) and studied by MRI. As can be seen (Fig. 3b), when increasing the saturation pulse strength from 5.5 μT to 33.3 μT (both with 2 s saturation duration) there is almost no change in the CrA Hyper-CEST effect. Due to its slower exchange rate (Table 1) CrA has reached its intrinsic depolarization maximum (*i.e.*, 60 % Hyper-CEST effect). In contrast, with its faster exchange, there is a significant amplification in the CB6 Hyper-CEST effect as the saturation strength is increased, namely from < 30 % to ~ 100 % (Fig. 3c). Best comparison of the gas turnover and the related signal amplification is possible for high RF exposure. It should, however, be noted that CrA can still remain the host of choice, if saturation pulse strength is limited, *e.g.*, due to specific absorption rate concerns, (Fig. S5a in the ESI†). Weak pulses are only capable of saturating Xe with longer residence times, as is the case for the slower exchange of the Xe–CrA system. In such cases, the Hyper-CEST performance as a function of the saturation pulse strength, B_1, should also be considered (Fig. S5a in the ESI†).

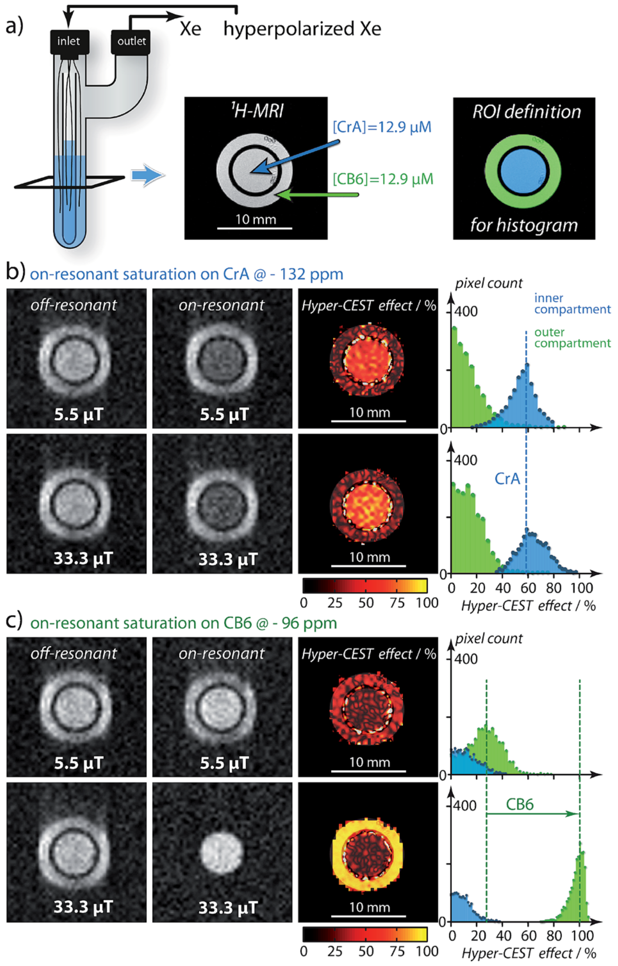

Fig. 3 Hyper-CEST effect mapping for equal concentrations of [CB6] = [CrA] = 12.9 μT in water at $T = 295$ K. (a) shows the proton (^{1}H)-MRI as a cross-section (tilted black square) of the double bubbling phantom and the region-of-interest (ROI) definition for histogram analysis. (b) Hyper-CEST effect maps of CrA for 5.5 μT ("low RF exposure") and 33.3 μT ("high RF exposure") both for 2 s of cw saturation calculated as the difference of the on-resonant image (saturation at − 132 ppm) and the off-resonant image (saturation at + 132 ppm) with respect to the free Xe in solution resonance. The Hyper-CEST effect of 60 % for both RF exposures is significant but unchanged. (c) CB6 Hyper-CEST effect maps for identical RF exposure but the on-resonant image (saturation at − 96 ppm) and the off-resonant image (saturation at + 96 ppm) with respect to the free Xe in solution resonance. Whereas the Hyper-CEST effect for 5.5 μT saturation strength was below 30 %, the stronger saturation resulted in ~ 100 % Hyper-CEST effect, thus revealing significantly higher gas turnover for the Xe–CB6 complex. The Xe-MR images were acquired with 64^2 resolution and cubic spline interpolated to 256^2. The slight blurring in phase encoding direction originated from faster T_2 relaxation with CB6 in the outer compartment.

Conclusion

We demonstrated that a dilute host providing a binding site for labile complex formation with Xe (in the intermediate exchange regime) can be identified and classified by saturation transfer NMR where conventional detection fails. The gas turnover rate is accessible through qHyper-CEST as a highly sensitive method for the comprehensive quantification of Xe exchange kinetics and binding affinities. In particular, we successfully quantified the Xe interaction with CB6 in pure water, a Xe–host system which is extremely difficult to access by conventional NMR owing to the exceedingly low solubility of CB6. This indicated that CB6 can be a much more efficient Hyper-CEST agent than previously presumed, because the absence of a detectable signal from the Xe–CB6 complex in direct NMR precluded its comprehensive characterization. Given proper saturation conditions, CB6 is 100 times more efficient than CrA, which is the most prominent contrast agent used so far in Xe biosensing. We could attribute the superior performance of CB6 to its fast exchange rate, k_{BA}, and high occupancy, β. We additionally suggest that other Xe–host systems are valuable to be reinvestigated, since their performance may have similarly been overlooked, if the combination of a high exchange rate and low solubility led to the absence of a signal in direct Xe NMR. In addition, we provide the gas turnover rate, $\beta\ k_{BA}$, as a simple parameter to classify the constant complex association/dissociation and to assess the prospective Hyper-CEST performance of particular Xe–host systems. This is not restricted to macrocyclic host systems, but will be similarly applicable to other emerging potential contrast agents such as bacterial spores,[10] nanodroplets[26] or genetically encoded gas vesicles (gas-binding protein nanostructures).[9] It is also noteworthy that the different exchange parameters (Table 1) in combination with their determination at low concentrations by Hyper-CEST, paves the way for analytical multiplexing applications by exploiting these parameters as unique fingerprints assignable to different Xe–host systems.

Experimental section

Data processing and fitting

All simulations, calculations and fitting routines were implemented and performed in Matlab 7 (The Mathworks, Natick, MA, USA) on a standard desktop PC (64 bit, 8 cores each at 2.80 GHz, 4 GB RAM) as described in ref. 27.

Sample preparation

Cucurbit[6]uril (CB6) was synthesized as described.[51] The synthesized product was characterized by ^{1}H-NMR and ESI mass spectrometry and agreed with the literature.[52] Noteworthy, qHyper-CEST analysis of a commercial CB6 sample gave a binding constant and host occupancy, which was inconsistent with results from literature and those reported herein (S6 in ESI†), which we ascribe to an unknown impurity in the commercial sample such as cations. Cryptophane-A monoacid (CrA, provided by Kang Zhao, Tianjin University, China) samples in water were prepared at room temperature followed by 25 minutes of sonication. Due to the higher solubility of CrA in dimethyl sulfoxide (DMSO), this sample could be readily prepared at room temperature.

Hyperpolarization and Xe delivery

Using a continuous-flow (0.35 standard liters per minute (SLM)) custom-designed polarizer[53] *via* spin exchange optical pumping with rubidium atoms, circa 25 % Xe spin-hyperpolarization of a Xe gas mix (2/10/88 vol % Xe/N_2/He, ^{129}Xe natural abundance: 26.4 %) were obtained. At a total pressure of $p = 4.5$ atm, the electrons of Rb were excited using a 150 W continuous wave-laser (795 nm, 0.5 nm bandwidth, QPC Lasers, Sylmar, CA, USA). Before signal acquisition, the samples were bubbled with the hyperpolarized Xe gas mixture with the following conditions: DMSO sample: bubbling time 10 s, bubble collapse time 2 s, at a flow rate of 0.1 SLM; CrA in water sample: bubbling time 12 s, bubble collapse time 2 s, at a flow rate of 0.1 SLM; For Fig. 2: bubbling time 7 s, bubble collapse time 3 s, at a flow rate of 0.18 SLM (S7 in ESI†). For Fig. 3: bubbling time 11 s, bubble collapse time 4 s, at a flow rate of 0.07 SLM. We triggered these bubbling delays from the NMR spectrometer. The Xe concentration, assuming Xe saturation, was in DMSO $[\mathrm{Xe}] = 2340\ \mu\mathrm{M}$, and in water $[\mathrm{Xe}] = 390\ \mu\mathrm{M}$ ($[\mathrm{Xe}] = \Gamma\, p\, \mathrm{Xe}_{\mathrm{pc}}/(0.0254\ \mathrm{L\ mM}^{-1})$, with the Xe Ostwald solubility coefficient in DMSO, $\Gamma = 0.66\ \mathrm{L\ atm}^{-1}$, and in water, $\Gamma = 0.11\ \mathrm{L\ atm}^{-1}$, and $\mathrm{Xe}_{\mathrm{pc}} = 0.02$). The shot-to-shot noise, corresponding to the reproducibility of the Xe concentration in solution, is < 1 % for our system.[54]

NMR experiments

NMR experiments were performed on a $B_0 = 9.4$ T NMR wide bore spectrometer (Bruker Biospin, Ettlingen, Germany) equipped with gradient coils for imaging and a variable temperature unit which was adjusted to room temperature ($T = 295\ \mathrm{K} \sim 22\ ^\circ\mathrm{C}$) for all samples. A 10 mm inner-diameter double-resonant probe (^{129}Xe and ^{1}H) was used for excitation and detection and a flip angle calibration was performed for all samples. Since the B_1 field inhomogeneities can significantly affect the CEST quantification, these must be known. As shown in ref. 27, B_1 field inhomogeneities were not significant for our micro imaging system. For the DMSO sample (S4 in ESI†), ^{129}Xe Hyper-CEST data was obtained in form of images using a Hyper-CEST echo-planar imaging[24] pulse sequence with the following parameters: Fourier acceleration: 1.68, EPI echo time: 5.7 ms, acquisition time: 19.8 ms, field of view: $20 \times 20\ \mathrm{mm}^2$, matrix size: 32×32; in plane resolution: 625 μm and slice thickness: 20 mm. No smoothing filter was applied to the images. The ^{129}Xe Hyper-CEST images for water were obtained from a single-shot Cartesian rapid acquisition with relaxation enhancement pulse sequence modified for Hyper-CEST, with the following parameters: centric encoding, effective echo time: 12.17 ms, no Fourier acceleration, 90° hermite excitation pulse (length = 3.375 ms, bandwidth = 1600 Hz) and 180° mao refocusing pulse (length = 3.105 ms, bandwidth = 2000 Hz), field of view: $20 \times 20\ \mathrm{mm}^2$, matrix size: 64×64; in plane resolution: 321 μm, slice thickness: 20 mm. The saturation strength and saturation length used varies and are mentioned in the figures. The exchange regime on the NMR time scale, $k_{\mathrm{BA}}/\Delta\omega$, was calculated with $\Delta\omega = \Delta\delta \times 10^{-6} \times \gamma/(2\pi)\, B_0 = \Delta\delta \times 10^{-6} \times 11.77\ \mathrm{MHz\ T}^{-1} \times 9.4\ \mathrm{T}$.

Acknowledgements

This work has been supported by the European Research Council under the European Community's Seventh Framework Programme (FP7/2007–2013)/ERC grant agreement no. 242710 and the Human Frontier Science Program no. LT000858/2010 C. The authors thank Dr. Jabadurai Jayapaul and Matthias Schnurr for the helpful discussions regarding sample preparation. We gratefully thank the World Molecular Imaging Congress (WMIC) committee for generous support enabling Martin Kunth the presentation of parts of this work at the WMIC meeting 2014 in Seoul, Korea.

References

1 L. Dubois, P. Da Silva, C. Landon, J. G. Huber, M. Ponchet, F. Vovelle, P. Berthault and H. Desvaux, *J. Am. Chem. Soc.*, 2004, **126**, 15738–15746.

2 H. Desvaux, L. Dubois, J. G. Huber, M. L. Quillin, P. Berthault and B. W. Matthews, *J. Am. Chem. Soc.*, 2005, **127**, 11676–11683.

3 C. Gröger, A. Möglich, M. Pons, B. Koch, W. Hengstenberg, H. R. Kalbitzer and E. Brunner, *J. Am. Chem. Soc.*, 2003, **125**, 8726–8727.

4 J. M. Chambers, P. A. Hill, J. A. Aaron, Z. Han, D. W. Christianson, N. N. Kuzma and I. J. Dmochowski, *J. Am. Chem. Soc.*, 2009, **131**, 563–569.

5 C. R. Bowers, V. Storhaug, C. E. Webster, J. Bharatam, A. Cottone, R. Gianna, K. Betsey and B. J. Gaffney, *J. Am. Chem. Soc.*, 1999, **121**, 9370–9377.

6 S. M. Rubin, M. M. Spence, B. M. Goodson, D. E. Wemmer and A. Pines, *Proc. Natl. Acad. Sci. U. S. A.*, 2000, **97**, 9472–9475.

7 S. M. Rubin, M. M. Spence, I. E. Dimitrov, E. J. Ruiz, A. Pines and D. E. Wemmer, *J. Am. Chem. Soc.*, 2001, **123**, 8616–8617.

8 S. M. Rubin, S.-Y. Lee, E. Ruiz, A. Pines and D. E. Wemmer, *J. Mol. Biol.*, 2002, **322**, 425–440.

9 M. G. Shapiro, R. M. Ramirez, L. J. Sperling, G. Sun, J. Sun, A. Pines, D. V. Schaffer and V. S. Bajaj, *Nat. Chem.*, 2014, **6**, 629–634.

10 Y. Bai, Y. Wang, M. Goulian, A. Driks and I. J. Dmochowski, *Chem. Sci.*, 2014, **5**, 3197–3203.

11 C.-Y. Cheng and C. R. Bowers, *J. Am. Chem. Soc.*, 2007, **129**, 13997–14002.

12 S. Pawsey, I. Moudrakovski, J. Ripmeester, L.-Q. Wang, G. J. Exarhos, J. L. C. Rowsell and O. M. Yaghi, *J. Phys. Chem. C*, 2007, **111**, 6060–6067.

13 J. J. Perry, S. L. Teich-McGoldrick, S. T. Meek, J. A. Greathouse, M. Haranczyk and M. D. Allendorf, *J. Phys. Chem. C*, 2014, **118**, 11685–11698.

14 L. Chen, P. S. Reiss, S. Y. Chong, D. Holden, K. E. Jelfs, T. Hasell, M. A. Little, A. Kewley, M. E. Briggs, A. Stephenson, K. M. Thomas, J. A. Armstrong, J. Bell, J. Busto, R. Noel, J. Liu, D. M. Strachan, P. K. Thallapally and A. I. Cooper, *Nat. Mater.*, 2014, **13**, 954–960.

15 T. Adiri, D. Marciano and Y. Cohen, *Chem. Commun.*, 2013, **49**, 7082–7084.

16 J. Roukala, J. Zhu, C. Giri, K. Rissanen, P. Lantto and V.-V. A. Telkki, *J. Am. Chem. Soc.*, 2015, **137**, 2464–2467.

17 M. M. Spence, S. M. Rubin, I. E. Dimitrov, E. J. Ruiz, D. E. Wemmer, A. Pines, S. Q. Yao, F. Tian and

Identification, classification, and signal amplification capabilities of high-turnover gas binding hosts in ultra-sensitive NMR

– Electronic Supporting Information –

Martin Kunth,* Christopher Witte, and Leif Schröder†
ERC Project BiosensorImaging, Leibniz-Institut für
Molekulare Pharmakologie (FMP), 13125 Berlin, Germany

Andreas Hennig
Jacobs University Bremen, Department of Life Sciences and Chemistry,
Campus Ring 1, 28759 Bremen, Germany

CONTENTS

S1: CB6 MODELING

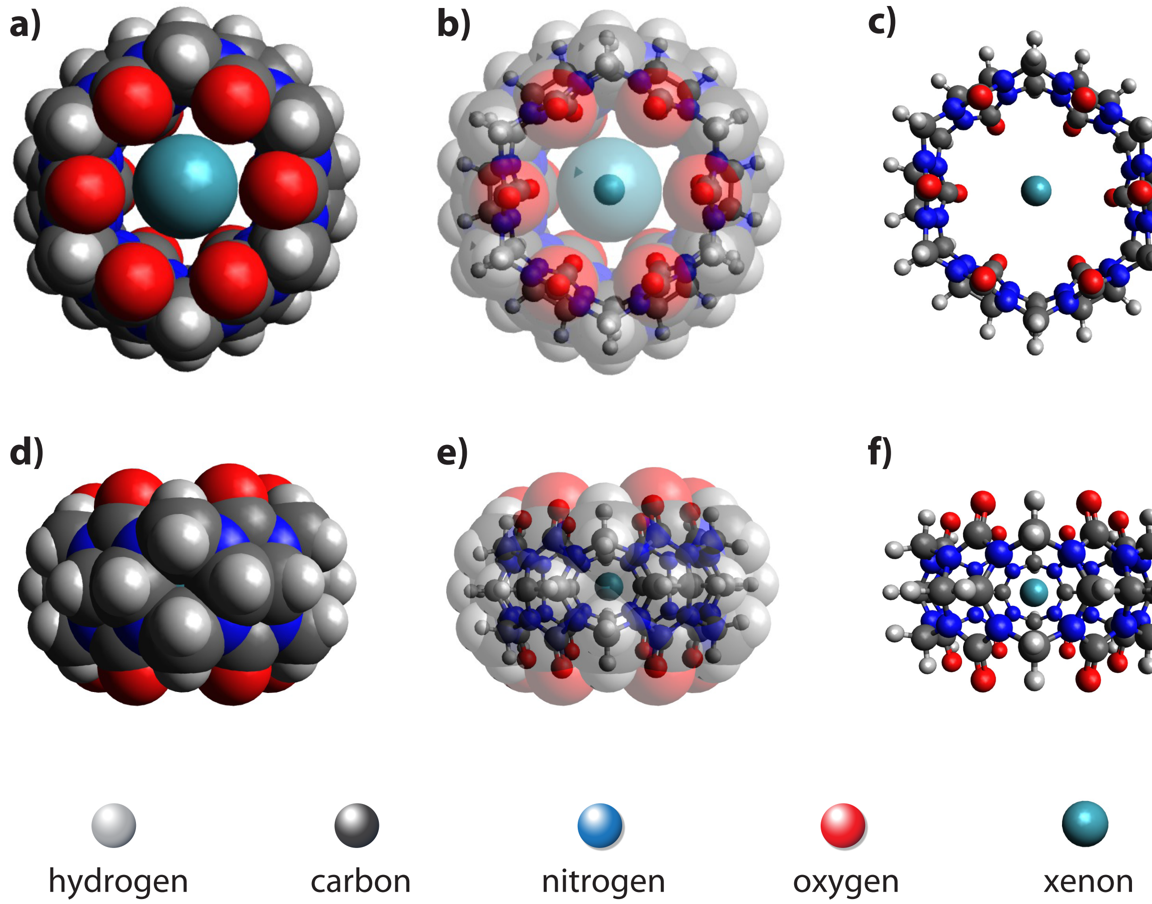

FIG. S1. Cucurbit[6]uril (CB6) ($C_{36}H_{36}N_{24}O_{12}$) and xenon (Xe) modeling using the open-source molecular builder and visualization tool, Avogadro – Version 1.1.1[1] (`http://avogadro.openmolecules.net`). a) Xe encapsulation by CB6 in the van der Waals radius representation from the top view of the molecule. b) transparent overlay of the van der Waals radius representation shown in a) with the ball-and-stick model that is solely shown in c). d-f) displays the side view representation of a-c), respectively.

S2: XE-CRA EXCHANGE KINETICS IN WATER

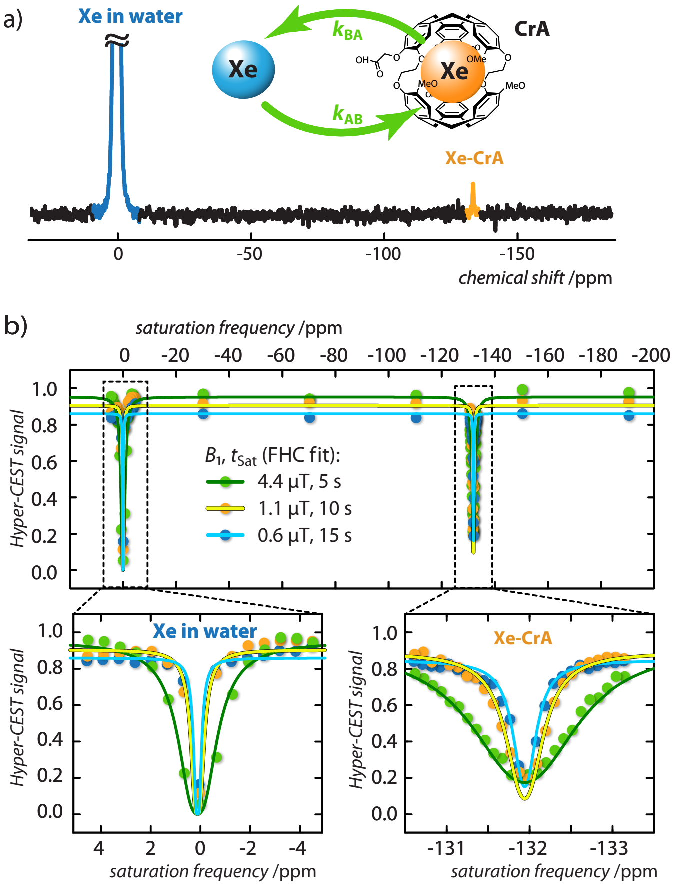

FIG. S2. Direct and indirect Hyper-CEST ^{129}Xe NMR measurements for [CrA] = 11 μM dissolved in pure water at room temperature, T = 295 K. a) ^{129}Xe NMR spectrum with 64 averages. The Xe-CrA resonance appears at δ_B = -132 ppm. b) Hyper-CEST z-spectra (dots) for continuous-wave (cw) saturation of B_1/t_{sat} = {4.4/5 (green), 1.1/10 (orange), 0.6/15 (blue)} μT/s including global fitting curves of the full Hyper-CEST (FHC) solution (solid lines). The fitting results are listed in Table 1 in the main manuscript.

S3: CB6-LINE BROADENING

In chemical equilibrium the following equation holds

$$[\mathrm{Xe}]\,\underbrace{[\mathrm{CB6}]\;k_{\mathrm{AB}}}_{k'} = [\mathrm{Xe@CB6}]\;k_{\mathrm{BA}}\ .$$

We therefore have

$$k' = \frac{[\mathrm{Xe@CB6}]}{[\mathrm{Xe}]}\;k_{\mathrm{BA}} = f_{\mathrm{B}}\;k_{\mathrm{BA}}\ .$$

The linewidth (full width at half maximum, FWHM) for each spin pool is influenced by the transverse relaxation and the exchange rate out of the particular spin pool according to the following equation (M.T. McMahon *et al.*[2] and citations therein),

$$\mathrm{FWHM} = (k + R_2)/\pi.$$

The FWHM of the solution pool yields

$$\begin{aligned}\mathrm{FWHM}_{\mathrm{sol}} &= (k' + R_{2,\mathrm{sol}})/\pi \\ &= (f_{\mathrm{B}} \cdot k_{\mathrm{BA}} + R_{2,\mathrm{sol}})/\pi\end{aligned}$$

Thus, the exchange broadening contribution is

$$\begin{aligned}\Delta\nu_{\mathrm{sol,ex}} &= (0.0043 \cdot 2,100\,\mathrm{s}^{-1})/\pi \\ &\sim 3\ \mathrm{Hz}\ ,\end{aligned}$$

using the numbers listed in Table 1 in the main manuscript. We measured the $\mathrm{FWHM}_{\mathrm{sol}}$ (of Figure 2a in the main manuscript) to be 22 Hz (at 9.4 T) for a 10 mm NMR tube; ca. 1.5 mL solution. Thus, we can see that the contribution of exchange broadening to the solution pool linewidth is not significant.

In contrast, the line broadening of the CB6-bound Xe resonance is significant:

$$\begin{aligned}\mathrm{FWHM}_{\mathrm{CB6}} &= (k_{\mathrm{BA}} + R_{2,\mathrm{CB6}})/\pi \\ \Rightarrow\quad \Delta\nu_{\mathrm{CB6,ex}} &= (2,100\,\mathrm{s}^{-1})/\pi \\ &\sim 670\ \mathrm{Hz}\ .\end{aligned}$$

Intuitively, the majority of the pool of Xe@CB6 is participating in exchange at any time, leading to a large linewidth, but the residence time in the much larger solution pool is significantly longer, thus leading to a narrow resonance.

S4: XE-CRA EXCHANGE KINETICS IN DMSO

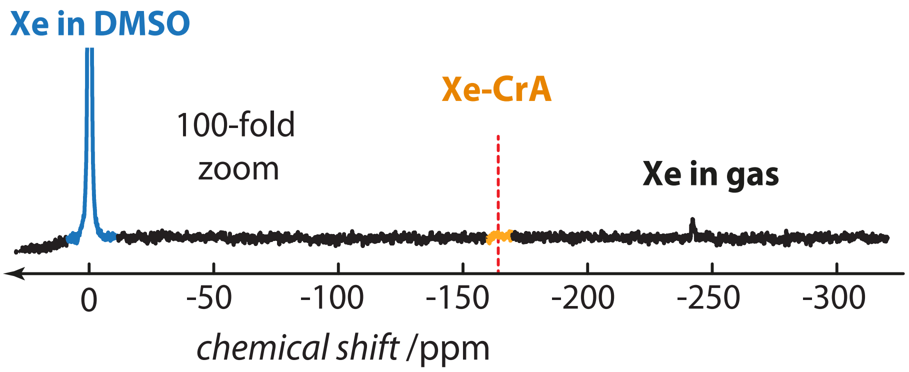

FIG. S4. Direct ^{129}Xe NMR spectrum with 100-fold zoom as average of 16 scans of 50 μM of CrA in dimethyl sulfoxide (DMSO) at T = 295 K. The red dashed line indicates the chemical shift of the Xe-CrA in DMSO resonance. The results of a qHyper-CEST analysis of this sample are listed in Table I which agree well with previously reported results[3].

TABLE I. qHyper-CEST results for CrA in DMSO (at T = 295 K). The listed parameters are identical with those of Table 1 in the main manuscript.

solvent	$[\mathrm{Xe}]^a$ (μM)	host	$[\mathrm{host}_{\mathrm{tot}}]$ (μM)	$\Delta\delta$ (ppm)	f_B (10^{-4})	k_BA (s^{-1})	β (%)^b	K_A (M^{-1})^c	$[\mathrm{host}_{\mathrm{occ}}]$ (μM)	$\beta \cdot k_\mathrm{BA}$ (% s^{-1})
DMSO	2,340	CrA	50	-166.37 ± 0.04	18 ± 1	250 ± 130	9	38 ± 4	4.5	23

[a] Calculation given in the Experimental Section. [b] As given by Eq. 3 in Ref. 3. [c] As given by Eq. 4 in Ref. 3.

S5: XE-HOST PROPERTIES FOR EFFICIENT HYPER-CEST DETECTION

We derive the depolarization rate per host molecule from the ^{129}Xe depolarization rate, λ_{depol}, for on-resonant saturation (in the limit of $k_{\mathrm{BA}} \gg R_2^{\mathrm{B}}$), as reported in Ref.[3], divided by total host concentration, [host], and multiplied by Xe concentration free in solution, [Xe], to

$$\begin{aligned} \lambda_{\mathrm{depol}}(B_1, k_{\mathrm{BA}}) &= f_{\mathrm{B}}\, k_{\mathrm{BA}} \frac{(\gamma\, B_1)^2}{(\gamma\, B_1)^2 + k_{\mathrm{BA}}^2} & (1) \\ \Leftrightarrow \qquad \lambda_{\mathrm{depol}}(B_1, k_{\mathrm{BA}}) \cdot \frac{[\mathrm{Xe}]}{[\mathrm{host}]} &= \beta \cdot k_{\mathrm{BA}}\, \underbrace{\frac{(\gamma\, B_1)^2}{(\gamma\, B_1)^2 + k_{\mathrm{BA}}^2}}_{=\,\alpha}, & (2) \end{aligned}$$

with saturation pulse strength, B_1, the exchange rate, k_{BA}, the ratio of bound and free Xe, f_{B}, the gyromagnetic ratio, γ, and the host occupancy, β. We used the identity $f_{\mathrm{B}} = \beta \cdot \frac{[\mathrm{host}]}{[\mathrm{Xe}]}$ for rewriting Eq.(1) to obtain the gas turnover rate, $\beta \cdot k_{\mathrm{BA}}$. Figure 4a shows the dependence of Eq.(2) with respect to the saturation pulse power, B_1, for the Xe-host systems: CB6 in water (blue), CrA in water (green) and CrA in DMSO (red) using the values reported in Table 1 of the main manuscript. Figures S5b-c show its dependence versus the exchange rate, k_{BA}. Note, the maxima of these curves occur for the saturation pulse strength calculated in Hz.

In terms of Xe-host design for Hyper-CEST detection, Eq.(2) can be very useful because it shows that CB6 in water is indeed the superior system due to both relatively high occupancy and high exchange rate compared to CrA in water and in DMSO.

It also shows that at low saturation strength the Hyper-CEST performance is better for lower exchange rates (compare in the insert of Figure S5a; CrA in water and CB6 in water (green and blue, respectively)), since the Hyper-CEST labeling efficiency, α, in the limit of $k_{\mathrm{BA}} \gg R_2^{\mathrm{B}}$ is increased for decreased exchange rates, k_{BA} [4, 5].

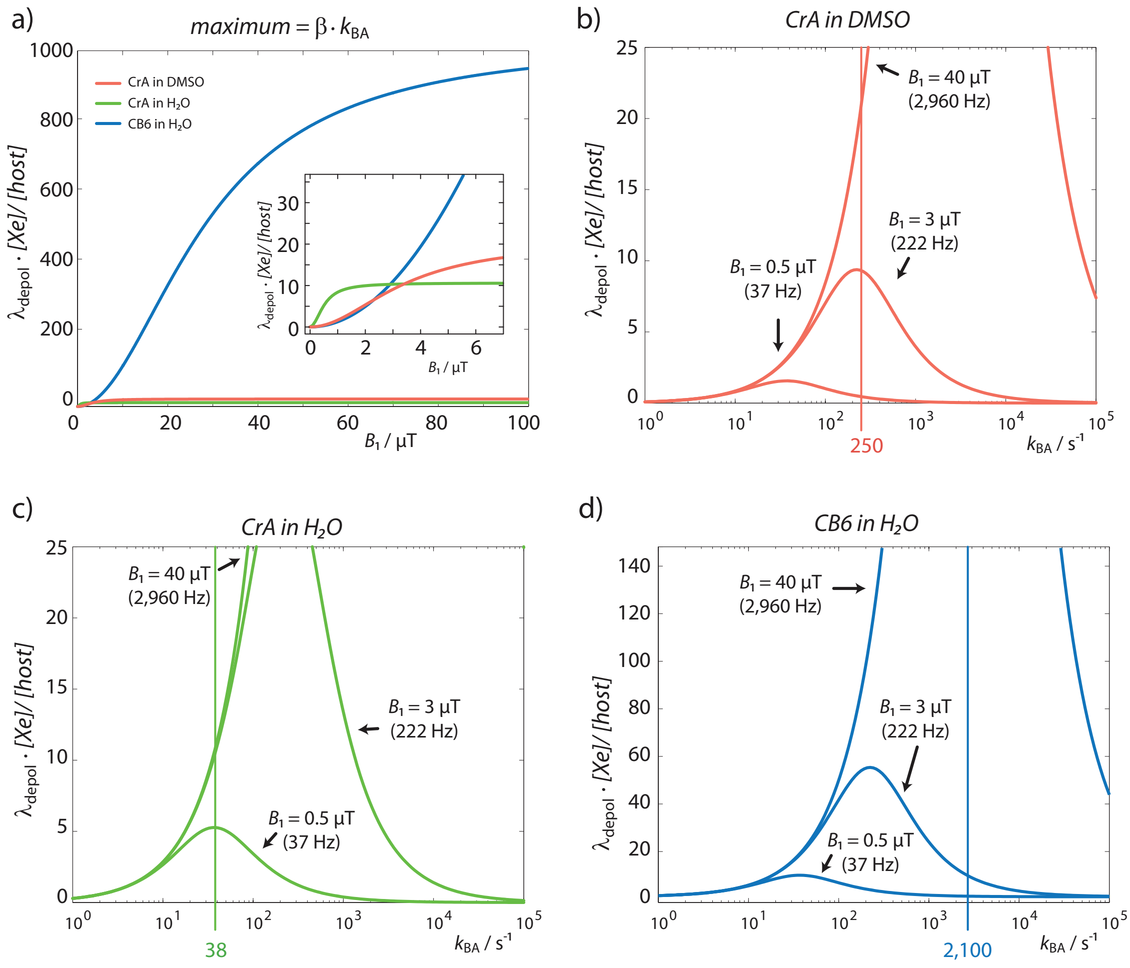

FIG. S5. Maximal on-resonant ^{129}Xe depolarization per host concentration in given Xe concentration for the Xe-host systems: CrA in DMSO (red), CrA in H_2O (green) and CB6 in H_2O (blue). The simulation parameters are listed in Table 1 in the main manuscript. (a) Xe depolarization curve per host molecule as a function of the saturation pulse strength, B_1. (b-d) Xe depolarization curve divided by [host] versus the exchange rate, k_{BA}, for the individual Xe-host systems with three different saturation pulse strengths, $B_1 = \{0.5,\ 3,\ 40\}\ \mu\mathrm{T} \rightarrow \omega_1 = \gamma \cdot B_1 = \{37,\ 22,\ 2960\}$ Hz, respectively. The system intrinsic Xe exchange rates are indicated by the straight line.

S6: COMMERCIALLY AVAILABLE CUCURBIT[6]URIL SAMPLE BY SIGMA-ALDRICH

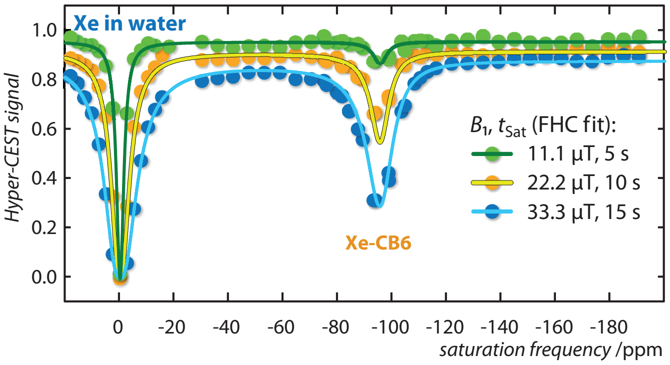

FIG. S6. qHyper-CEST analysis and results listed in Table II of the commercially available cucurbit[6]uril (CB6) sample (ordered by Sigma-Aldrich, product number: 94544, CAS Number: 80262-44-8, LOT Number: BCBH8803V) in water at room temperature (T = 295 K). In contrast to Figure 2b in the main manuscript, note that the saturation pulse strength values, B_1, are increased and the Hyper-CEST z-spectra spectrally broadened.

While the relative chemical shift between free and bound Xe, $\Delta\delta$, and the Xe exchange rate, k_{BA}, agree with the pure CB6 sample (see main manuscript), the ratio of bound and free Xe, f_{B}, the Xe host occupancy, β, the Xe binding (association) constant, K_{A}, the host concentration occupied by Xe, $[\mathrm{host}_{\mathrm{occ}}] = \beta \cdot [\mathrm{host}]$, and the gas turnover $\beta \cdot k_{\mathrm{BA}}$ disagree (see Table II). This particular change of the specific Xe exchange kinetics indicates a blocking of Xe exchange for the CB6 portals for the commercially available sample.

TABLE II. qHyper-CEST results for the Sigma-Aldrich available CB6 sample in water (at T = 295 K). The listed parameters are identical with those of Table 1 in the main manuscript except for the host occupancy, β, the binding constant, K_{A} and its continuative values.

solvent	[Xe]^a (μM)	host	[host$_{\mathrm{tot}}$] (μM)	$\Delta\delta$ (ppm)	f_{B} (10^{-4})	k_{BA} (s^{-1})	β (%)^b	K_{A} (M^{-1})^c	[host$_{\mathrm{occ}}$] (nM)	$\beta \cdot k_{\mathrm{BA}}$ (% s^{-1})
water	390	CB6	4.6	(-95.6 ± 0.2)	(0.7 ± 0.07)	(2,100 ± 500)	0.6	(15 ± 7)	28	13

[a] Calculation given in the Experimental Section in the main manuscript;

[b] As given by Eq. 3 in Ref.[3]; [c] As given by Eq. 4 in Ref.[3].

S7: XE DELIVERY INTO H_2O AND DMSO

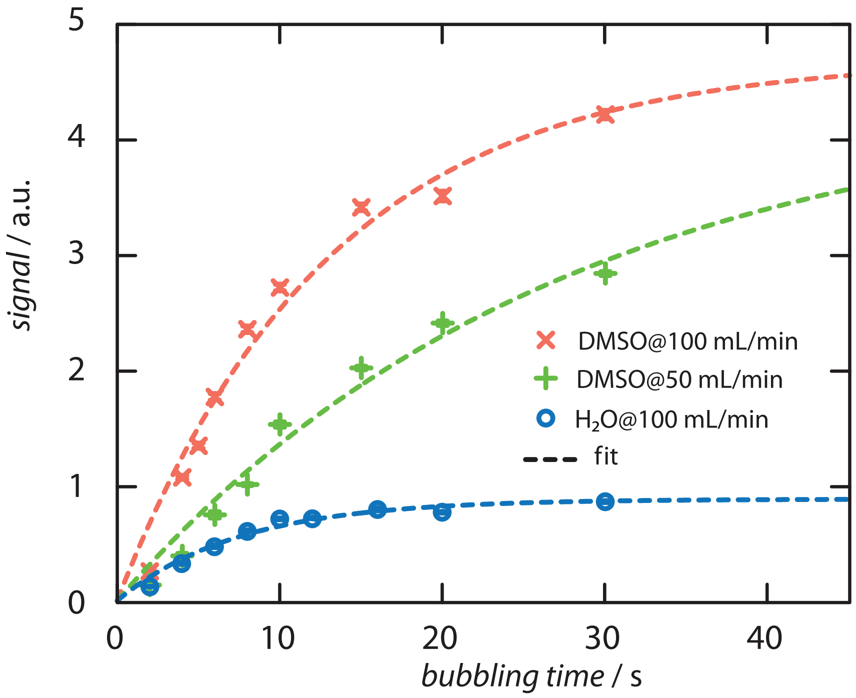

FIG. S7. Xe signal build up in H_2O and DMSO versus the bubbling time for flow rates of 50 mL per minute and 100 mL per minute including error bars.

Fit function with respect to the bubbling time, BT: $S(BT) = A_0 \cdot (1 - \exp\{-BT/\tau\})$. The total measured signal is influenced by the build up due to hp Xe bubbling while hp Xe starts to decay with its longitudinal relaxation time, ${T_1}^{\mathrm{A}}$ ($\sim$ 125 s for both solvents). Therefore, the ratio of $A_{0,\mathrm{DMSO}}/A_{0,\mathrm{H_2O}} \sim 5$ and differs from the value 6, as expected from the ratio of both Ostwald solubility coefficients.

- H_2O at 100 mL per minute: $\mathrm{A}_0 = (0.88 \pm 0.04)$, $\tau = (8 \pm 1)$ s.
- DMSO at 100 mL per minute: $\mathrm{A}_0 = (4.7 \pm 0.4)$, $\tau = (13 \pm 2)$ s.
- DMSO at 50 mL per minute: $\mathrm{A}_0 = (4.4 \pm 0.9)$, $\tau = (27 \pm 8)$ s.

---

* kunth@fmp-berlin.de

† lschroeder@fmp-berlin.de

[1] Hanwell, Marcus D.; Curtis, Donald E.; Lonie, David C.; Vandermeersch, Tim; Zurek, Eva; Hutchison, Geoffrey R. *Journal of Cheminformatics* **2012**, *4*, 17, `http://www.jcheminf.com/content/4/1/17`, `http://avogadro.openmolecules.net`.

[2] McMahon, M.T.; Gilad, A.A.; Zhou, J.; Sun, P.Z.; Bulte, J.W.M.; van Zijl, P.C.M. *Magnetic Resonance in Medicine* **2006**, *55*, 863, `http://dx.doi.org/10.1002/mrm.20818`.

[3] Kunth, M.; Witte, C.; Schröder, L. *The Journal of Chemical Physics* **2014**, *141*, 194202, `http://dx.doi.org/10.1063/1.4901429`.

[4] Sun, P.Z.; Farrar, C.T.; Sorensen, A.G. *Magnetic Resonance in Medicine* **2007**, *58*, 1207-1215, `http://dx.doi.org/10.1002/cmmi.1524`.

[5] Zaiss, M.; Bachert, P. *NMR in Biomedicine* **2012**, *26*, 507-518, `http://dx.doi.org/10.1002/nbm.2887`.

VERSICHERUNG

Hiermit versichere ich, daß ich alle verwendeten Hilfsmittel und Hilfen angegeben und die vorliegende Arbeit auf dieser Grundlage selbstständig verfasst habe. Ich versichere außerdem, daß diese Dissertation noch nicht anderweitig als Dissertation eingereicht worden ist.

Berlin, den 07. Januar 2016

Martin Kunth